

28411

**DEVELOPMENT
OF A
THERMAL PROTECTION SYSTEM
FOR THE WING
OF A
SPACE SHUTTLE VEHICLE**

NASA-MSC CONTRACT NAS9-11224

**PHASE II FINAL REPORT
VMSC REPORT NO. T143-5R-00124**

1k
(NASA-CR-148908) DEVELOPMENT OF A THERMAL
PROTECTION SYSTEM FOR THE WING OF A SPACE
SHUTTLE VEHICLE, PHASE 2 Final Report, 19
May 1971 - 30 Apr. 1972 (Vought Missiles and
Space Co., Dallas, Tex.) 441 p

N76-78647

Unclas
50823

00/98



**VOUGHT MISSILES
AND SPACE COMPANY**

REPRODUCED BY
NATIONAL TECHNICAL
INFORMATION SERVICE
U.S. DEPARTMENT OF COMMERCE
SPRINGFIELD, VA. 22161

446

ABSTRACT

AST-62821 R2

TITLE OF REPORT Development of a Thermal Protection System for the Wing of a Space Shuttle Vehicle - Phase II Final Report.				
ORIGINATING AGENCY AND LOCATION Vought Missiles and Space Company LTV Aerospace Corporation P.O. Box 6267 Dallas, Texas 75222		CLASSIFICATION		
		REPORT None	ABSTRACT None	TITLE None
AUTHORS D. M. While	ISSUE DATE 30 April '72	LIMITATIONS ON DISTRIBUTION (IF ANY) Distribution List Included		
ORIGINATING AGENCY'S REPORT NO. T143-5R-00124	DOD REFERENCES			OTHER IDENTIFYING REPORT NOS. NASA-MSC Number MSC-02557
	CONTRACT NO. NASA MSC NAS9-11224	PROJECT NO. T-143	TASK NO. BA	
INDEXING Preliminary designs and analyses are shown for an oxidation inhibited RPP shuttle wing leading edge. Test results from development of an oxidation resistant coating for Reinforced Pyrolyzed Plastics are given. Full scale leading edges were fabricated and successfully tested to EXPERIMENTAL maximum load and temperature conditions.				
B. Key Words: Oxidation Inhibitors, Reinforced Pyrolyzed Plastic (RPP), Leading Edge Design, Plasma Testing, Catalytic Phenomenon, Diffusion Coatings, Non-Destructive Test, Shuttle Thermal Protection System.				
WEAPON SYSTEMS NUMBERS, MODEL NUMBERS, ETC. N/A				
ABSTRACT <p>A preliminary design and supporting analysis is given for the wing leading edge of a NASA delta wing shuttle configuration employing oxidation inhibited RPP as structure. A baseline geometry, representing one of the proposed shuttle vehicles, is specified for use in point design. Design criteria are provided and show that boost airload pressures, half of which are from venting lag, are critical for design. Maximum design radiation equilibrium temperature is 2740°F, at 0.85 emittance. Temperature gradients experienced during entry are found to produce relatively small thermoelastic stresses, primarily because of the low thermal expansion and low elastic modulus of RPP.</p> <p>Coating development approaches and preliminary results are presented. A diffusion coating employing constituents of alumina, silicon carbide, and silicon is selected for continued development. A melt impregnation coating of hafnium and tantalum with 4000°F temperature capability is found to offer limited reuse capability when applied to RPP that has not been densified.</p> <p>Trials show that joining RPP by bonding in the virgin state is promising and relatively high bond tensile strengths can be achieved.</p> <p>Studies of oxidation of the siliconized coating system in the entry environment show that if the boundary layer air is not dissociated, the resultant reaction of molecular constituents with the coating system should be orders of</p>				

magnitude less than achieved by plasma testing. Alternately, if the boundary layer air is dissociated, the low catalytic reaction rate at the surface of the coating can reduce surface temperature by hundreds of degrees and mass loss rate is reduced an order of magnitude. It is concluded that current plasma arc testing, controlled to a given temperature, is conservative.

Fatigue data demonstrates oxidation inhibited RPP is highly resistant to fatigue loading. Mechanical strength of the material was obtained for a wide range of properties and shows good strength capability over the full operating range.

Two different leading edge configurations were fabricated for test. One represents a wing tip region and has been tested by NASA-MSFC in a plasma arc facility. The other configuration (three were fabricated) is a full scale leading edge and approximates the size of the root region on the current expendable tank shuttle. One of these leading edges was tested to the critical boost pressure loading and two were subjected to the entry temperature profile. Both leading edges passed the tests without failure or anomaly.

DEVELOPMENT OF A THERMAL PROTECTION
SYSTEM FOR THE WING OF A
SPACE SHUTTLE VEHICLE
NASA-MSC CONTRACT NAS9-11224
PHASE II FINAL REPORT

VMSC REPORT NO. T143-5R-00124

30 APRIL 1972



D. M. While
Prepared By



G. B. Whisenhunt
Approved By

Vought Missiles and Space Company
LTV Aerospace Corporation
P.O. Box 6267
Dallas, Texas 75222

ACKNOWLEDGEMENT

This report was prepared by the Vought Missiles and Space Company of LTV Aerospace Corporation for the National Aeronautics and Space Administration - Manned Spacecraft Center, under Contract No. NAS9-11224. The period of performance was 19 May 1971 through 30 April 1972.

Mr. J. E. Pavlosky of the Structures and Mechanics Division, NASA-MSC was Technical Manager for the program. Mr. B. A. Forcht was the VMSC Program Manager.

The technical work was directed by D. M. While, Project Leader, while I. E. Harder and D. C. Rogers were responsible for materials development. Thermal analysis and analytical evaluation of coating systems were conducted by J. E. Medford; design was performed by V. J. Kramar and F. D. Tarsia with W. E. Agan providing the structural and thermoelastic analysis.

Mr. B. A. Forcht also acted as consultant on materials development, while structures design consultation was provided by J. J. King and H. E. Brougham, all from VMSC.

The Space Division, North American Rockwell supported the program by providing design conditions and assisting in establishment of design criteria.

TABLE OF CONTENTS

	<u>Page No.</u>
1.0 INTRODUCTION	1
2.0 SUMMARY	5
2.1 <u>LEADING EDGE DESIGN</u>	8
2.2 <u>MATERIALS DEVELOPMENT</u>	19
2.3 <u>FABRICATION</u>	34
2.4 <u>CONCLUSIONS</u>	37
3.0 DESIGN SYNTHESIS	39
3.1 <u>DESIGN CRITERIA</u>	39
3.2 <u>DESIGN CONCEPT</u>	49
3.3 <u>PROTOTYPE DESIGN</u>	54
3.4 <u>THERMAL ANALYSIS</u>	57
3.4.1 Thermal Properties	58
3.4.2 Aerodynamic Heating	61
3.4.3 Surface Recession of Bare RPP	73
3.4.4 Gap Leakage	73
3.4.5 Conclusions and Recommendations	80
3.5 <u>STRUCTURAL ANALYSIS</u>	81
3.5.1 Mechanical Properties	82
3.5.2 Airloads Analysis	90
3.5.3 Thermoelastic Analysis	104
3.5.4 Dynamic Analysis - Prototype Leading Edge	108
3.5.5 Conclusions	113
4.0 MATERIALS DEVELOPMENT	115
4.1 <u>RPP SUBSTRATE</u>	116
4.1.1 Baseline System	116
4.1.2 Processing Complex Shapes	123
4.1.3 Laminate Improvement	127

TABLE OF CONTENTS (Cont'd.)

	<u>Page No.</u>
4.2 <u>BONDING AND RIVETING</u>	131
4.3 <u>COATINGS</u>	136
4.3.1 Developmental Coatings	137
4.3.2 Refinement of the Silicon System	143
4.3.3 Hafnium Tantalum Coating	173
4.4 <u>CONCLUSIONS AND RECOMMENDATIONS</u>	180
5.0 MATERIALS EVALUATION	183
5.1 <u>COATING MISSION LIFE PERFORMANCE</u>	184
5.1.1 Catalycity and Molecular Oxidation	184
5.1.2 Wedge Heating	196
5.1.3 Plasma Arc Evaluation of Heat Treated 10/60/30 Material	201
5.1.4 Mission Life Prediction for Heat Treated 10/60/30 Material	209
5.2 <u>PHYSICAL/MECHANICAL PROPERTIES</u>	214
5.2.1 Physical Properties	214
5.2.2 Mechanical Properties	218
5.2.3 Joints	231
5.2.4 Thermal/Oxidation Cycling	238
6.0 NON DESTRUCTIVE EVALUATION (NDE) AND INSPECTION	245
6.1 <u>LAMINATE INVESTIGATIONS</u>	245
6.1.1 NDE Studies	
6.1.2 Preliminary Standards	257
6.2 <u>HARDWARE EVALUATION</u>	262
7.0 LEADING EDGE HARDWARE	280
7.1 <u>WING TIP LEADING EDGE PANELS</u>	280
7.1.1 Design and Instrumentation	282
7.1.2 Fabrication	287

TABLE OF CONTENTS (Cont'd.)

	<u>Page No.</u>
7.1.3 Test Plans	293
7.2 <u>PROTOTYPE LEADING EDGE</u>	293
7.2.1 Fabrication	294
7.2.2 Test	300
REFERENCES	319
DISTRIBUTION	321
APPENDIX A - MATERIALS TESTS SUMMARY	A-1
APPENDIX B - TEST SPECIMEN CONFIGURATION	B-1
APPENDIX C - PROTOTYPE LEADING EDGE TEST DATA	C-1

LIST OF FIGURES

<u>Figure No.</u>	<u>Title</u>	<u>Page No.</u>
1-1	Phase II Task Flow	3
2-1	Shuttle Leading Edge Preliminary Design	9
2-2	Prototype Leading Edge Segments Prior to Coating	10
2-3	Prototype Leading Edge Segments After Coating & Prior to Temperature Test	11
2-4	Prototype Leading Edge Segments After Boost Pressure and Entry Temperature Tests	12
2-5	Weight Preliminary Leading Edge Design	14
2-6	Airloads Analysis Prototype Leading Edge	14
2-7	Boost Pressure Test Rib Stress Prototype Leading Edge	16
2-8	Boost Pressure Test Deflections Prototype Leading Edge	16
2-9	Dynamic Analysis Prototype Leading Edge Stresses	17
2-10	Temperature Distribution Around Leading Edge	17
2-11	Thermal Stresses Entry Condition	20
2-12	Entry Temperature Test Thermal Profile	20
2-13	Lug Joint Maximum Temperatures	21
2-14	Temperature Effect on Strength Coated RPP	21
2-15	Temperature Effect on Elastic Modulus Coated RPP	25
2-16	Tension Fatigue and Inplane Shear Fatigue $R = 0$	25
2-17	Flexure Fatigue	27
2-18	Interlaminar Fatigue Strength $R = 0$	27
2-19	Emittance	29
2-20	m/h Correlation Plasma Arc Tests	31
2-21	Cumulative Mass Loss Typical	31
2-22	Coating Mission Life	32
2-23	Coated Wing Tip Panel	35

LIST OF FIGURES (Cont'd.)

<u>Figure No.</u>	<u>Title</u>	<u>Page No.</u>
2-24	Coated RPP Fuselage Panel	36
3-1	Wing Leading Edge Section Comparison	40
3-2	Leading Edge Geometry Phase I vs Phase II Comparison	42
3-3	Ascent Trajectory Data	44
3-4	Entry Design Trajectory	44
3-5	Limit Boost Pressures	
3-6	Limit Entry Pressure Maximum Angle of Attack	46
3-7	Limit Cruise Condition Loads	46
3-8	Local Heat Flux Ratio	47
3-9	Shuttle Leading Edge Temperatures - Time of Peak Reentry Temperature	47
3-10	Boost Phase Random Vibration	48
3-11	Shuttle Leading Edge Preliminary Design	51
3-12	Preliminary Leading Edge Design	53
3-13	Prototype Leading Edge Assembly	55
3-14	Prototype Leading Edge Design Details	56
3-15	Thermal Conductivity, Coated RPP	59
3-16	Boost Aerodynamic Heating	63
3-17	Entry Aerodynamic Heating	63
3-18	Skin Temperature at Peak Heating Location, $\epsilon = 0.85$	65
3-19	Skin Temperatures Around Leading Edge - Initial Skin Temperature = -170°F	65
3-20	Thermal Model, Leading Edge With Cross Radiation	66
3-21	Shuttle Leading Edge Temperatures - Time of Peak Reentry Temperature	66
3-22	Rib Temperature Drop - Cavity Areas	68
3-23	Rib Temperature Drop - Cavity Areas	68
3-24	Rib Temperature Drop, Attachment Areas	71
3-25	Attachment Temperature	71

LIST OF FIGURES (Cont'd.)

<u>Figure No.</u>	<u>Title</u>	<u>Page No.</u>
3-26	Entry Surface Recession of Bare RPP	74
3-27	Surface Recession Distribution of Bare RPP	74
3-28	Distribution Function for Mass Flow into Cavity	77
3-29	Air Flow Into Leading Edge Cavity	77
3-30	Distribution Function for Energy Entering Cavity	78
3-31	Total Energy Influx into Leading Edge Cavity	78
3-32	Calculated Coated Design Properties	84
3-33	Coated RPP Stress Allowables - Warp Prototype Design	86
3-34	Coated RPP Modulus - Warp Prototype Design	86
3-35	Coefficient of Thermal Expansion	89
3-36	Leading Edge Weight Variation with Span	91
3-37	Summary of Minimum Margins of Safety Preliminary Design 30 Inch Segment Span	91
3-38	Summary of Minimum Margins of Safety Prototype Design - 15 Inch Segment Span	93
3-39	NASTRAN Model - Leading Edge	95
3-40	Pressures Used in Static Load Analysis	96
3-41	Ultimate Loads - Rib	97
3-42	Ultimate Loads - Beams	97
3-43	Lug Reactions and Margins of Safety	98
3-44	Maximum Hoop Direction Skin Stresses - Ultimate	100
3-45	Maximum Spanwise Direction Skin Stresses - Ultimate	100
3-46	Relative Skin Deflections at Limit Load	101
3-47	Compressive Membrane Stresses	102
3-48	Shear Stress Distribution on Leading Edge Skin Panel - Ultimate Load Case II	103

LIST OF FIGURES (Cont'd.)

<u>Figure No.</u>	<u>Title</u>	<u>Page No.</u>
3-49	Shear Stress Distribution on Leading Edge Due to Thermal Load - $t = 400$ Sec. Ultimate	103
3-50	Rib Thermoelastic Model	105
3-51	Thermoelastic Stresses in Skin Hoop Direction $t = 400$ Sec	106
3-52	Thermoelastic Stresses in Skin Spanwise Direction $t = 400$ Sec	106
3-53	Thermal - Axial Rib Stresses	107
3-54	Panel Expansion at Maximum Temperatures - 400 Seconds	109
3-55	Hinge Point Reactions - Thermal Loads	109
3-56	Space Shuttle Leading Edge Nodal Locations - Vibration Analysis	111
3-57	Vibrationally Induced Stress Envelope of RMS Values 32 Grms	111
4-1	Process Flow Chart for Baseline RPP Substrate Material	117
4-2	RPP Laminates Showing Delamination and Areas of High Porosity 10X Magnification	120
4-3	Acceptable RPP Laminate 10X Magnification	120
4-4	Illustration of a Delamination Defect 5X Magnification	121
4-5	A 90° Corner With Wrinkling at the Inside Radius	125
4-6	Multi-Piece Tool for Forming a Section With Vertical Reinforcing Webs	125
4-7	Compaction Aids to Fabricate Wing Tip Panels	126
4-8	RPP Section Illustrating Delamination & Distortion	126
4-9	Graphite Restraining Fixtures Used During Pyrolyzation of a Belly Panel Component	126
4-10	Boron-Silicon System	138
4-11	Zirconium-Boron-Silicon (ZBS) System	140

LIST OF FIGURES (Cont'd.)

<u>Figure No.</u>	<u>Title</u>	<u>Page No.</u>
4-12	Silicon System	142
4-13	Scanning Electron Microscope Evaluation of Silicon Carbide	151
4-14	Typical Thermal Cycle Curves for 12" Diameter Furnace	154
4-15	Typical Thermal Cycle Curves for 24" Diameter Furnace	154
4-16	Percent Weight Gain During Coating Cycle	156
4-17	Thermal Model of Retort	157
4-18	Thermal and Mechanical Performance Data for Selected RPP Inhibitor System	161
4-19	Oxidation Relationship to Weight Gain During Coating, 10/60/30 Siliconized System	162
4-20	Flexure Strength Relationship to Weight Gain During Coating, 10/60/30 Siliconized System	162
4-21	Mission Life Relationship to Weight Gain During Coating, 10/60/30 Siliconized System	162
4-22	Photomicrograph of Specimen Showing Coating (Darkened Area) Diffusion Depth	166
4-23	Green Silicon Carbide Characterization	168
4-24	Green Silicon Carbide - Heat Treated Characteristics	168
4-25	Black Silicon Carbide Characterization	169
4-26	Black Silicon Carbide - Heat Treated Characterization	169
4-27	Green Silicon Carbide Mission Life	170
4-28	Black Silicon Carbide Mission Life	170
5-1	Correlation of Surface Temperatures Inhibited vs Bare Material	186
5-2	Heating Reduction Due to Low Catalytic Efficiency Surface	186
5-3	Skin Temperature at Peak Heating Location - $\epsilon = 0.85$	188

LIST OF FIGURES (Cont'd.)

<u>Figure No.</u>	<u>Title</u>	<u>Page No.</u>
5-4	State of Boundary Layer Flow Re-Entry	188
5-5	Temperature Dependence of SiC Mass Loss Rate	192
5-6	Mass Loss Rate of SiC in Molecular Oxygen	192
5-7	Mass Loss Rate of SiC at 3100°F	193
5-8	Wedge Heating Specimen Holder	197
5-9	Comparison of Aerodynamic Shear Entry and Plasma Arc Test	197
5-10	Aerodynamic Shear During Entry	198
5-11	Entry Aerodynamic Shear Distribution	198
5-12	Low Temperature Wedge Heating Data	200
5-13	High Temperature Wedge Heating Data	200
5-14	Comparison of Plasma Arc Test With Entry Heating Conditions	203
5-15	Plasma Arc Test Mass Loss Rate Data For Oxidation Inhibited Carbon-Carbon	204
5-16	Mass Change vs Time Final Evaluation Data	205
5-17	Mass Loss vs Time Final Evaluation Data	205
5-18	Mass Loss vs Time Final Evaluation Data	206
5-19	Mass Loss vs Time Final Evaluation Data	207
5-20	Plasma Arc Test Mass Loss Rates Final Evaluation Data	207
5-21	Thickness Loss vs Mass Loss Siliconized RPP	210
5-22	Mass Loss Rate During Entry	210
5-23	Predicted Mission Capability High Cross Range Mission Final Evaluation Data	212
5-24	Peak Temperature of Inhibited RPP During Entry vs Peak Radiation Equilibrium Temperature	213
5-25	Comparison of Predicted Mission Capability With Actual Exposure Times High Cross Range Mission	213

LIST OF FIGURES (Cont'd.)

<u>Figure No.</u>	<u>Title</u>	<u>Page No.</u>
5-26	Emittance of Coated RPP	215
5-27	Specific Heat of Coated RPP	215
5-28	Thermal Conductivity of Coated RPP Parallel to Lamina Direction	217
5-29	Thermal Conductivity of Coated RPP Normal to Lamina Direction	217
5-30	Strength Data Siliconized RPP Heat Treated 13 Ply	220
5-31	Elastic Modulus Siliconized RPP Heat Treated 13 Ply	222
5-32	Strain to Failure Siliconized RPP Tension and Compression	222
5-33	Typical Stress-Strain Curves Tension-Warp	224
5-34	Typical Stress-Strain Curves Compression - Warp 13 Ply Siliconized RPP	225
5-35	Typical Load-Deflection Curves Flexure - Warp 13 Ply Siliconized RPP	225
5-36	Coefficient of Thermal Expansion Siliconized RPP	226
5-37	Tension Fatigue and Inplane Shear Fatigue $R = 0$	228
5-38	Flexure Fatigue $R = 0$ and $R = -1$	228
5-39	Interlaminar Fatigue Strength $R = 0$	229
5-40	Failed Lug Specimens	234
5-41	Failed Tension Angles - Tested With Washer Fitted to Radius	234
5-42	Failed Tension Angles - Tested With Squared Washer	234
5-43	Mission Thermal and Oxidation Simulator	239
5-44	Thermal/Oxidation Test Facility Utilizing Graphite Resistance Heater Elements	242
5-45	Thermal/Oxidation Test Environment	243

LIST OF FIGURES (Cont'd.)

<u>Figure No.</u>	<u>Title</u>	<u>Page No.</u>
6-1	Photograph of Panel No. LE68 Radiographic Film, Taken After Immersion of Panel in Carbon Tetrachloride for 30 Minutes. Test Specimens are Shown Overlayed	248
6-2	Photograph of Radiographic Film From Panel # 1-8, RPP-0 Condition. Determination of Delaminated Areas is Not Possible Due to Saturation of Carbon Tetrachloride Throughout Available Porosity	250
6-3	Photograph of Radiographic Film From Panel # 1-8 RPP-1 Condition. Outlined Areas Were Noted to be Delaminated by Visual Examination and Tapping. Carbon Tetrachloride Saturation is Evident in Available Porosity and Delamination	251
6-4	Ultrasonic C-Scan Recording of Panel # 1-8, RPP-1 Condition. Approximately Half of the Available Porosity Volume Has Been Filled by Initial Impregnation. White Areas are Porous Which Give High Attenuation Levels.	252
6-5	Photograph of Radiographic Film From Panel # 1-8, RPP-2 Condition. Delamination Areas And The Available Porosity Have Been Filled With Carbon Tetrachloride.	253
6-6	Ultrasonic C-Scan Recording of Panel # 1-8, RPP-2 Condition. Re-Impregnation Has Decreased Size of Delaminated Area When Compared to Figure 6-4 RPP-1 Condition. Major Amount of Available Porosity Volume Has Been Filled During Re-Impregnation	254
6-7	Photograph of Radiographic Film From Panel # 1-8, RPP-3 Condition. Delamination And Available Porosity Volume Has Decreased In Size When Compared to Figure 6-3 and 6-5, RPP-1 and RPP-2 Conditions.	255
6-8	Ultrasonic C-Scan Recording of Panel # 1-8, RPP-3 Condition. Re-Impregnation Has Further Decreased Size of Delaminated Area When Compared to Figure 6-6 RPP-2 Condition.	256

LIST OF FIGURES (Cont'd.)

<u>Figure No.</u>	<u>Title</u>	<u>Page No.</u>
6-9	Non-Destructive Evaluation Standard Samples. Typical Defects - Large Delamination, Multiple Ply Delaminations and Excessive Porosity. Correlation Was Established by Visual, Photomicrographic, Radiographic and Ultrasonic Examination of Defective Areas.	258
6-10	Non-Destructive Evaluation Standard Sample. Delaminations and Porosity of Low Density Area Defects.	259
6-11	Photograph of RPP-3 Panel From Radiographic Film Using Carbon Tetrachloride Immersion With Standard Sample. No Defective Areas Present in Panel, However Defects in Sample Are Readily Observed.	260
6-12	Ultrasonic C-Scan Recording of RPP-3 Panel With Standard Sample. No Defective Areas Present in Panel, However Defects in Sample Are Readily Observed.	261
6-13	Dimensional Data Collected for Prototype Leading Edge	263
6-14	Radiographic X-Ray Views Taken For Prototype Leading Edges	266
6-15	Ultrasonic C-Scan Recording of Doubler Area and T-Seal Bond of Leading Edge S/N -1 at RPP - 3 Stage	267
6-16	Ultrasonic C-Scan Recording of Doubler Area And T Seal Bond of Leading Edge S/N-2 at RPP-3 Stage	268
6-17	Ultrasonic C-Scan Recording of Doubler and T-Seal of Leading Edge S/N-3 at RPP-3 Stage	269
6-18	Ultrasonic C-Scan Recording of Doubler Area and T-Seal Bond of Leading Edge S/N-1 After Coating	270
6-19	Ultrasonic C-Scan Recording of Leading Edge Seal Strip S/N - 1 at RPP-3 Stage	271

LIST OF FIGURES (Cont'd.)

<u>Figure No.</u>	<u>Title</u>	<u>Page No.</u>
6-20	X-Ray View 1 Leading Edge Skin S/N-1	273
6-21	X-Ray View of Leading Edge S/N-1 After Coating	274
6-22	X-Ray of Leading Edge S/N-1 After Coating	275
6-23	Ultrasonic C-Scan Recording of Wing Tips S/N's 1 and 2	277
6-24	X-Ray of Wing Tip Panel S/N-1 Showing Lower Surface, Ribs & Intercostal - RPP-3	278
6-25	X-Ray of Wing Tip Panel S/N-2 Showing Lower Surface, Ribs and Intercostal RPP-3	279
7-1	Wing Tip Leading Edge Panel	283
7-2	Wing Tip Leading Edge	284
7-3	Spring Loaded Thermocouples For Wing Tip Assemblies	286
7-4	Wing Tip Molding Tools	288
7-5	Wing Tip Section Showing Bonded Reinforcing Angles	289
7-6	Graphite Holding Fixtures for Pyrolyzation of the Wing Tip	289
7-7	Wing Tip Panel S/N-1 Following Coating	291
7-8	Bare Wing Tip Panel Assembly Showing Thermocouple Installation	292
7-9	Prototype Leading Edge Layup Mold	295
7-10	Seal Strip Mold	295
7-11	Leading Edge Section Showing RPP Rivet	297
7-12	Rivet Debulking Mold	297
7-13	As-Cured Plug Used to Form the Head of an RPP Rivet	298
7-14	Graphite Restraining Fixtures for Prototype Leading Edge in Pyrolyzation Retort	298
7-15	Prototype Leading Edge Assembly and Seal Strip Ready for Coating	299

LIST OF FIGURES (Cont'd.)

<u>Figure No.</u>	<u>Title</u>	<u>Page No.</u>
7-16	Shaped Graphite Retort Used For Coating Prototype Leading Edge Assemblies	299
7-17	Strain Gage Installation Boost Pressure Load Test	301
7-18	Strain Gage Installation Lower Panel Boost Pressure Load Test	302
7-19	Strain Gage Installation Rib and Lug Boost Pressure Load Test	303
7-20	Deflectometer Installation Boost Pressure Load Test	304
7-21	Ribs Stresses - Upstanding Leg Computation Versus Experimental Boost Pressure Load Test	306
7-22	Comparison of Predicted and Experimental Skin Stresses Boost Pressure Load Test	307
7-23	Comparison of Predicted and Measured Deflections Boost Pressure Load Test	307
7-24	Entry Temperature Test Setup Leading Edges Rotate Into Heater Cavity for Heating	309
7-25	Entry Temperature Test Setup Showing Thermo- couple Installation on Leading Edge	310
7-26	Thermocouple Locations Entry Temperature Test	312
7-27	Temperature Profile Desired vs Actual Entry Temperature Test	313
7-28	Prototype Leading Edges - Front View Following Entry Temperature Test	316
7-29	Prototype Leading Edges - Rear View Following Entry Temperature Test	317
B-1	Tensile Specimen Configuration	B-2
B-2	Flexure Specimen Configuration	B-2
B-3	Axial Compressive Specimen Configuration	B-3
B-4	Interlaminar Shear Specimen Configuration (Short Beam Shear) VMSC Tests	B-3
B-5	Interlaminar Shear Specimen Configuration (Compression/Shear) SRI Tests	B-3

LIST OF FIGURES (Cont'd.)

<u>Figure No.</u>	<u>Title</u>	<u>Page No.</u>
B-6	Interlaminar Tension Specimen Configuration Elevated Temperature SRI Tests	B-4
B-7	Interlaminar Tension Specimen Configuration Room Temperature and Fatigue VMSC Tests	B-4
B-8	Bearing Specimen	B-4
B-9	Inplane Shear Specimen	B-5
C-1	Static Load Test Instrumentation	C-2
C-2	Thermal Test of Prototype Leading Edge Panel	C-4
C-3	Thermal Test of Prototype Leading Edge Panel	C-5
C-4	Thermal Test of Prototype Leading Edge Panel	C-6
C-5	Thermal Test of Prototype Leading Edge Panel	C-7
C-6	Thermal Test of Prototype Leading Edge Panel	C-8
C-7	Thermal Test of Prototype Leading Edge Panel	C-9

LIST OF TABLES

<u>Table No.</u>	<u>Title</u>	<u>Page No.</u>
2-1	Room Temperature Strength Coated RPP 13 Ply Laminates	23
2-2	Flexure Strength 13 Ply Laminates - Warp Direction Room Temperature	24
2-3	Static Strength After Fatigue Cycling	26
3-1	Changes Between Phase I and Phase II Design Criteria	50
3-2	Emittance of Coated RPP	60
3-3	Coating and Substrate Specific Heat	61
3-4	Specific Heat, Dynaflex Insulation	61
3-5	Thermal Conductivity of Dynaflex Insulation 6.2 Lb/Ft ³ Density Conductivity Units, BTU/Ft Hr °F	62
3-6	Support Joint Configurations	70
3-7	Support Joint Peak Temperatures	72
3-8	Properties Used for Preliminary Design and Assessment of Design Validity	83
3-9	Properties Used for Prototype Design and Assessment of Design Validity	87
3-10	Margins of Safety	94
3-11	Space Shuttle Leading Edge Panel Node Spatial Location	112
3-12	Space Shuttle Orbiter Leading Edge Reaction at Attach Points	114
4-1	Strength of RPP-3 Laminates of Various Thicknesses	118
4-2	Strength of RPP Substrate Material at Various Processing Steps	122
4-3	Laminate Improvement Results	129
4-4	Flexure Strength of Heat Treated and Siliconized RPP	131
4-5	Bond Strength Results	133
4-6	Single Lap Shear Strength	135

LIST OF TABLES (Cont'd.)

<u>Table No.</u>	<u>Title</u>	<u>Page No.</u>
4-7	Selection of 10 AL ₂ O ₃ /60SiC/30Si Qualitative Comparison	145
4-8	Silicon Metal Powder Particle Size Distribution Weight Percent	149
4-9	Trace Metal Impurities of Pack Material Powders	152
4-10	Correlation Data Plasma Arc and Pereny Weight Loss	158
4-11	Results of Hafnium-Tantalum Coating Application to RPP	175
4-12	Results of Multiple Hafnium/Tantalum Coating Application of RPP-0 (Vacuum Bay Fabricated)	179
5-1	Plasma Arc Test Conditions	201
5-2	Typical Room Temperature Strength Values 13-Ply Siliconized RPP	221
5-3	Static Strength Following Fatigue Cycling	231
5-4	Summary of Lug Tests 13-Cross Ply Laminates	232
5-5	Tension Angle Test Data	233
5-6	Bonded Joint Strength	236
5-7	Typical RPP Riveted Joint Strengths	237
5-8	Siliconized RPP Strength Following Thermal/Oxidation Cycling Warp Direction - 13-Ply	243
6-1	Flexure Strength of Bare and Coated RPP 4-Point Loading	247
6-2	Strength Data of Component Test Panels	263
6-3	Prototype Leading Edge Dimensional Data	265
7-1	Comparison of Predicted and Measured Temperature Gradients at 230 Sec Test Time	314
A. 1-1	Diffusion Coating Runs Early Series	A-3
A. 1-2	Diffusion Coating Runs Alumina/Silicon Carbide/Silicon Systems	A-7
A. 1-3	Heat Treat Runs Alumina/Silicon Carbide/Silicon System	A-25
A. 2-1	Flexure Test Data	A-34

LIST OF TABLES (Cont'd.)

<u>Table No.</u>	<u>Title</u>	<u>Page No.</u>
A.3-1	Summary, Plasma Arc Test Data	A-52
A.3-2	Summary, Plasma Arc Test Final Evaluation Data Heat Treated 10/60/30 Material	A-63
A.4-1	Weight Change During Thermal Cycle at 2300°F (When 6th Cycles are listed it is at 2500°F or 2600°F)	A-66
A.4-2	Weight Change During Thermal Cycle at 2300°F	A-72
A.4-3	Weight Change of Heat Treated Specimens During Thermal Cycle at 2300°F	A-76
A.4-4	Weight Change During Thermal Cycle at 2300°F For Used Pack Materials	A-79
A.4-5	Thermal Treatments After Coating Applied	A-80
C-1	Stress Outputs Boost Pressure Test Limit Load (100%)	C-3

1.0 INTRODUCTION

This report summarizes the technical work accomplished by the Vought Missiles and Space Company (VMSC) of LTV Aerospace Corporation under Phase II of a two-phase program, "Development of a Thermal Protection System for the Wing of a Space Shuttle Vehicle", NASA-MSC Contract No. NAS9-11224, reference (1). The thermal protection system, directed toward application to the leading edge structure of the NASA Orbiter wing and tail surfaces, must sustain multiple exposure to all environments through earth launch, orbital operation, entry and landing. The goal was to achieve a reliable leading edge design and material system with 100-mission life capability, while withstanding a maximum temperature level up to 4000°F.

Thermal protection system development in this program was restricted to the oxidation resistant carbon-carbon reinforced pyrolyzed plastic (RPP) composites. This class of materials has shown the potential for long-term exposure in an oxidizing atmosphere at temperatures exceeding the limits of coated metals. In addition, the substrate materials, comprised of graphite cloth and carbon binder, offer low density (90 lb/ft³) with good strength (15000 psi flexure) at operational temperatures. In addition to the materials development task, the program effort included consideration of all aspects of design, fabrication, and inspection relative to realistic flight hardware.

Phase I consisted of Materials Development and Design Synthesis tasks. Materials Development was concerned with the selection of candidate inhibitor and substrate materials, the integration and fabrication of these into RPP composites, and the testing and subsequent modification of these composites to develop a system(s) potentially suitable for the Orbiter wing leading edge application. Design Synthesis was devoted to the generation of design concepts, the analysis of these concepts to determine best approaches, and the establishment of materials property performance goals and material structural composite configurations. The Phase I portion of the program was completed in February 1971.

Phase II consisted of three major tasks: (1) Materials Evaluation, (2) Design Synthesis and (3) Prototype Leading Edge design and fabrication. Materials Evaluation was devoted to the continued development of the oxidation inhibited carbon-carbon systems, selected from the Phase I program, and the gathering of preliminary design data for the selected siliconized WCA cloth material system.

Design Synthesis was directed toward the preliminary design and thermal/structural analysis of a practical leading edge concept for the

delta wing Orbiter. The Phase I program concentrated on the straight wing vehicle leading edge; however, with the NASA selection of the high cross range delta wing Orbiter configuration, emphasis on this program was shifted accordingly.

Prototype leading edge design and fabrication demonstrated the ability to fabricate full scale leading edge segments that withstood the critical design boost pressure and entry thermoelastic stress conditions. In addition, two small leading edge assemblies were fabricated for testing in a NASA-MSC plasma arc facility.

The interrelationship of the various program tasks is illustrated by the task flow in Figure 1-1. Significant accomplishments achieved during the Phase II program are summarized as follows:

(1) The leading edge design was further simplified by removal of return flanges on the ribs and elimination of intercostals.

(2) Improvement of the siliconized coating system was obtained which produced higher strengths and reduced substrate oxidation. Mechanical properties throughout the operating temperature range were found to be high and fatigue strength is outstanding.

(3) A deeper understanding of the factors affecting coating performance has been obtained. These include such items as the quality of starting ingredients, cleanliness of furnace environments, time/temperature relationships, and retort design.

(4) Bonding potential was established for use in attaching secondary structure, and RPP rivet application was demonstrated to add design flexibility.

(5) Fabrication capability was confirmed with three full scale coated leading edge assemblies complete with bonded and riveted trailing edge seal strips and curved seal strips.

(6) Adequacy of the design and hardware to withstand the critical load and thermal stress environments was demonstrated by test of full scale leading edge assemblies. No failure or anomalies were observed.

(7) Fabricability of small units was also proven when two assemblies representing wing tip regions were fabricated for NASA test.

(8) It was demonstrated by plasma arc and thermal/oxidation cycling tests that the coated RPP material can meet the 100-mission capability for Phase II requirements from both coating erosion and strength standpoints.

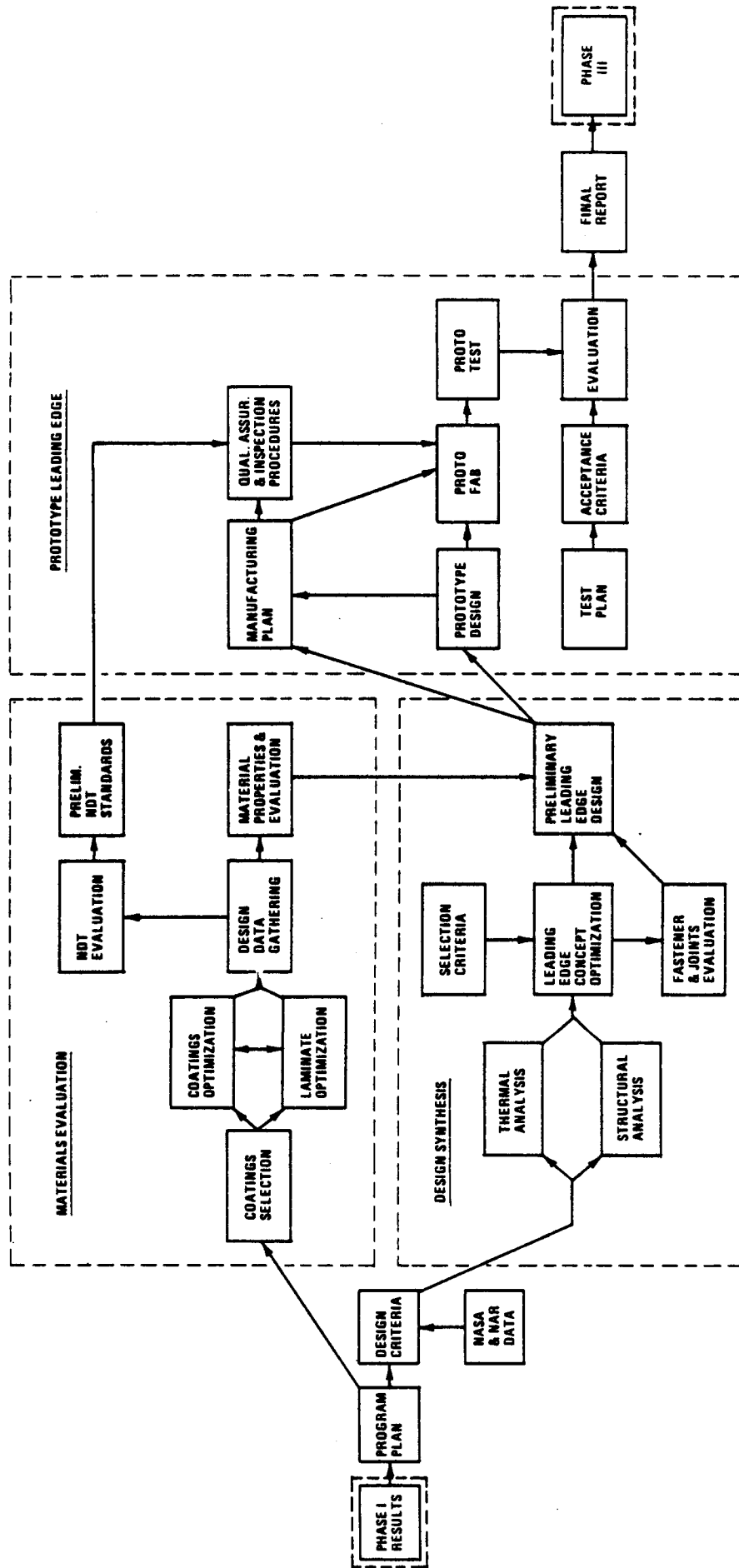


FIGURE 1-1 PHASE II TASK FLOW

While considerable progress was made in Phase II, there are areas of importance requiring increased emphasis. Among these are:

- (1) Procurement of specification controlled coating materials.
- (2) Establishment of the true state of the boundary layer air during entry, be it predominately molecular or mainly atomic, and attainment of material performance data in the correct environment.
- (3) Improvement of the bonding technique to completely eliminate debonding tendencies.
- (4) Refinement of fabrication techniques to improve corner molding and reduce restraint tooling.
- (5) Examination of thicker laminates to determine capabilities and provide flexibility to the designer.
- (6) Further refinement of the coating/substrate system to reduce coating crazing.

2.0 SUMMARY

This program is concerned with the development of an oxidation inhibited carbon-carbon leading edge suitable for the wing of a Space Shuttle vehicle. It is being conducted in three phases. Phase I, which was completed in February, 1971, sought to develop a material system(s) and design concept that could be employed on a straight wing, short range shuttle and meet a 100-mission life requirement. Phase II, which is documented herein, refined the leading edge design concept for the high cross range delta winged vehicle, fabricated and tested representative full scale leading edge segments, and further developed the coated RPP material system. Phase III will examine thicker laminate leading edges in an effort to achieve a one mission return capability in the event of coating failure, prove the feasibility of fabricating such a concept by producing full scale coated leading edge segments, and further refine the coating system to achieve improved uniformity and reproducibility. In addition, Phase III will expand the systems aspect of the leading edge and address the heat shield insulation design to protect wing structure, having a 350°F limitation. (This requirement is more stringent than in Phase II, where a 650°F limit was imposed on wing structure).

The approach taken in this technology program was to channel materials development along those avenues having direct application to the leading edge baseline design and design criteria. This had the advantage of narrowing the materials activity within performance bounds pertinent to the Shuttle to achieve more rapid development.

The primary objectives of the Phase II program were to:

- (1) Develop a preliminary design for the wing leading edge of a high cross range delta winged Orbiter.
- (2) Develop physical and mechanical property data for the baseline material system for use in preliminary designs and evaluations.
- (3) Demonstrate by full scale article fabrication and test the feasibility of the design and material system to meet the structural requirements of the Orbiter.

End products of this study include the following:

- (1) Material property data covering a spectrum of mechanical, physical, and thermal performance over the applicable temperature range (-250°F to 3000°F) of the coated material system.
- (2) Typical strength data for lug, tension-angle, bonded, and RPP riveted joints.

- (3) Preliminary and Prototype leading edge designs.
- (4) Three full scale Prototype leading edge assemblies, complete with trailing edge and between-segment seal strips. One assembly was delivered to NASA-MSC.
- (5) Full scale demonstration tests and data covering maximum boost load and entry thermal stress conditions.
- (6) Two wing tip panels, one bare and one coated, for NASA-MSC plasma arc tests.

Since Phase I represented the point of departure for Phase II, a brief summary of the Phase I program is given below. This is followed by a summary of Phase II activities.

Phase I - A variety of design concepts was examined in Phase I including sandwich or solid laminate configurations, multi-layered designs with replaceable components, those involving multiple ribs or intercostals, and those using trussed ribs. It was concluded that a segmented solid laminate leading edge configuration, employing stiffening ribs at the edges of each segment, offered the greatest advantages of all concepts considered. This type of design permits the use of thicker, stronger laminates, promotes internal cross radiation to reduce stagnation temperature and increased mission life, and presents a rather simple design concept (reference 2).

Materials investigations in Phase I were divided into two categories: substrates and coatings, with the final test of feasibility being their combined performance as a materials system. Substrate investigations included evaluation of carbon and graphite filaments and cloths with high and low elastic moduli. Delamination was experienced with the high modulus fiber laminates, and carbon cloth showed poor strength in the coated condition compared to graphite cloth. Only two substrate materials showed acceptable and equal performance, WCA graphite cloth and Kreha KGF-200 fibers. Because the WCA material was controlled by specification and was in a form (cloth) more suitable to leading edge fabrication, further work baselined the WCA substrate.

Phase I coatings activity involved evaluation of carbides and oxides of a number of metals applied by diffusion coating, chemical vapor deposition (CVD), plasma spray overlay, mixing with the resin during laminate fabrication (add-mix), and certain combinations of these. Overlay coatings were found to be limited to one or two missions and the CVD coating test results indicated insufficient temperature or

mission life capability. The add-mix systems were plagued with low interlaminar strength and poor oxidation resistance unless combined with an outer layer of diffusion coating. VMSC elected to concentrate on the diffusion coating system primarily because it offered the best plasma arc test performance, the highest strength, and the least complexity. However, another coating system was examined briefly that showed promise of multimission capability in the 4000°F surface temperature region. This was a hafnium-tantalum melt impregnation coating that was further examined in Phase II. However, it was found to have reuse capability limited to about five missions because of coating crumble and was therefore not pursued beyond plasma arc test evaluation.

Two diffusion coatings emerged from Phase I with the potential of satisfying shuttle requirements. These were the zirconium-boron-silicon (ZBS) system and the silicon system. The silicon system showed outstanding high temperature (3000°F) oxidation resistance of the coating but suffered from poor substrate oxidation protection. The ZBS coating by contrast was insensitive to oxidation attack of the substrate but coating erosion resistance was only half that of the siliconized coating. Further, it was handicapped by being a more complex system, requiring two separate coating processes. Reproducibility was therefore a potential problem.

Phase II - Each of these diffusion systems were examined in Phase II until it became clear that one of them could be brought to fruition for the Shuttle application. Data showed that with the proper starting ingredients and good process control, high temperature performance could be retained, while subsurface oxidation could be retarded on the siliconized coating to the point where 100 mission life appeared feasible for the Phase II design requirements. Further study was therefore concentrated on the silicon coating.

Component fabrication was a significant feature of the Phase II program. Three full size leading edge segments were successfully fabricated. One was tested to the critical air load condition and two were subjected to the entry temperature environment without failure. Fabrication established that sound and warp-free leading edge segments can be produced for the shuttle. In addition, two smaller wing tip models were produced for NASA test. The ability to fabricate and coat such large, sophisticated, and structurally sound RPP components is considered a milestone in coated carbon-carbon technology. Further demonstration of fabrication capability was exemplified by two coated RPP fuselage panel assemblies, produced under contract to North American Rockwell (reference 9). After successfully completing 100 cycles of a typical time/temperature profile simulating entry, one of these panels was tested to ultimate load without failure.

This section of the report summarizes the results of the Phase II program and presents significant findings covering design, fabrication, test, and materials performance. Substantiating detail and background data will be found in the design discussion of Section 3.0, materials development activities in Section 4.0, evaluation of the selected baseline material system in Section 5.0, NDE and Inspection Studies in Section 6.0, and finally, in Section 7.0 the fabrication and test efforts on the Prototype leading edges and wing tip panels are documented.

2.1 LEADING EDGE DESIGN

Phase II design activities centered on the detail design of the RPP portion of the leading edge and the means by which it would be supported by the wing box structure. Analyses were conducted to define temperature levels of wing support fittings and the insulating heat shield to determine the reasonableness of their requirements. Phase III will analyze these elements in more detail and test representative designs.

Design - The Preliminary design of a typical leading edge is shown in Figure 2-1. A Prototype design, which was fabricated and tested, is similar in concept to the Preliminary design but with 15 in. rather than 30 in. span to conform to current VMSC coating facility size limitations. Prototype leading edges are pictured in Figures 2-2, 2-3 and 2-4 before coating, after coating and following boost pressure and entry temperature tests. (In Figure 2-4 the dark spots on one of the leading edge segments are the result of subsequent charring of strain gages.) The design follows closely that established during Phase I (reference 2) except that it has been simplified by removing return flanges on the ribs and by eliminating intercostals. This was permitted because of the more favorably curved geometry and 50% lower pressures compared to the Phase I design. The concept features a solid laminate construction with integrally fabricated ribs and trailing edge cross beams. Trailing edge "T" Section seal strips to overlap the adjacent RSI panels are bonded and riveted with RPP rivets to the basic structure. A curved "T" section seal strip closes the expansion gap between leading edge segments and blocks direct flow of boundary layer air into the leading edge cavity. The adequacy of the seal strip design will be evaluated by plasma test in Phase III.

Each leading edge segment is supported at the corners by single bolt lug attachments. Metal wing support fittings are shared by adjacent segments as well as the curved seal strip. One side of each segment is anchored against side movement while the opposite side is free to slide on the lug bolt to accommodate thermal expansion. This concept was successfully demonstrated by the entry temperature test

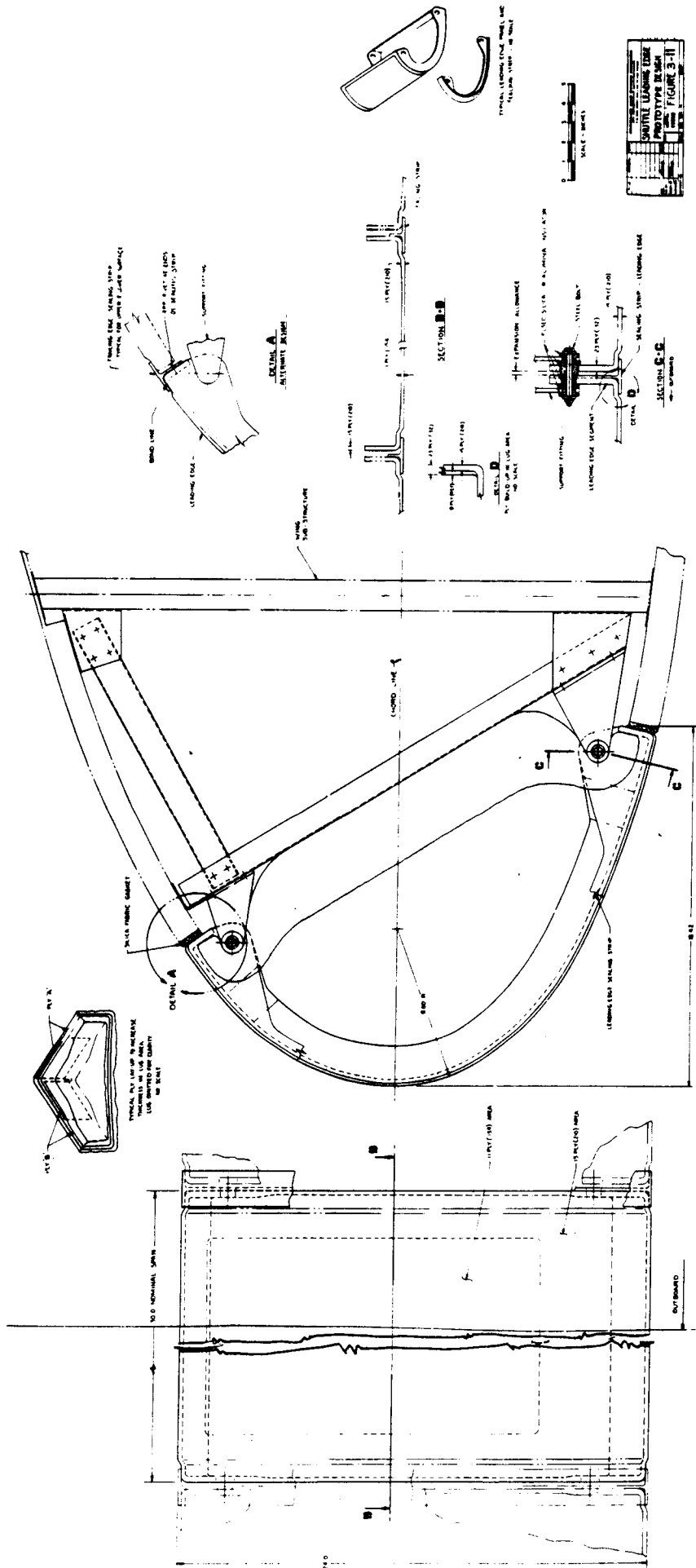


FIGURE 2-1 SHUTTLE LEADING EDGE PRELIMINARY DESIGN

q-b

q-a

q-b

9



FIGURE 2-2 PROTOTYPE LEADING EDGE SEGMENTS PRIOR TO COATING

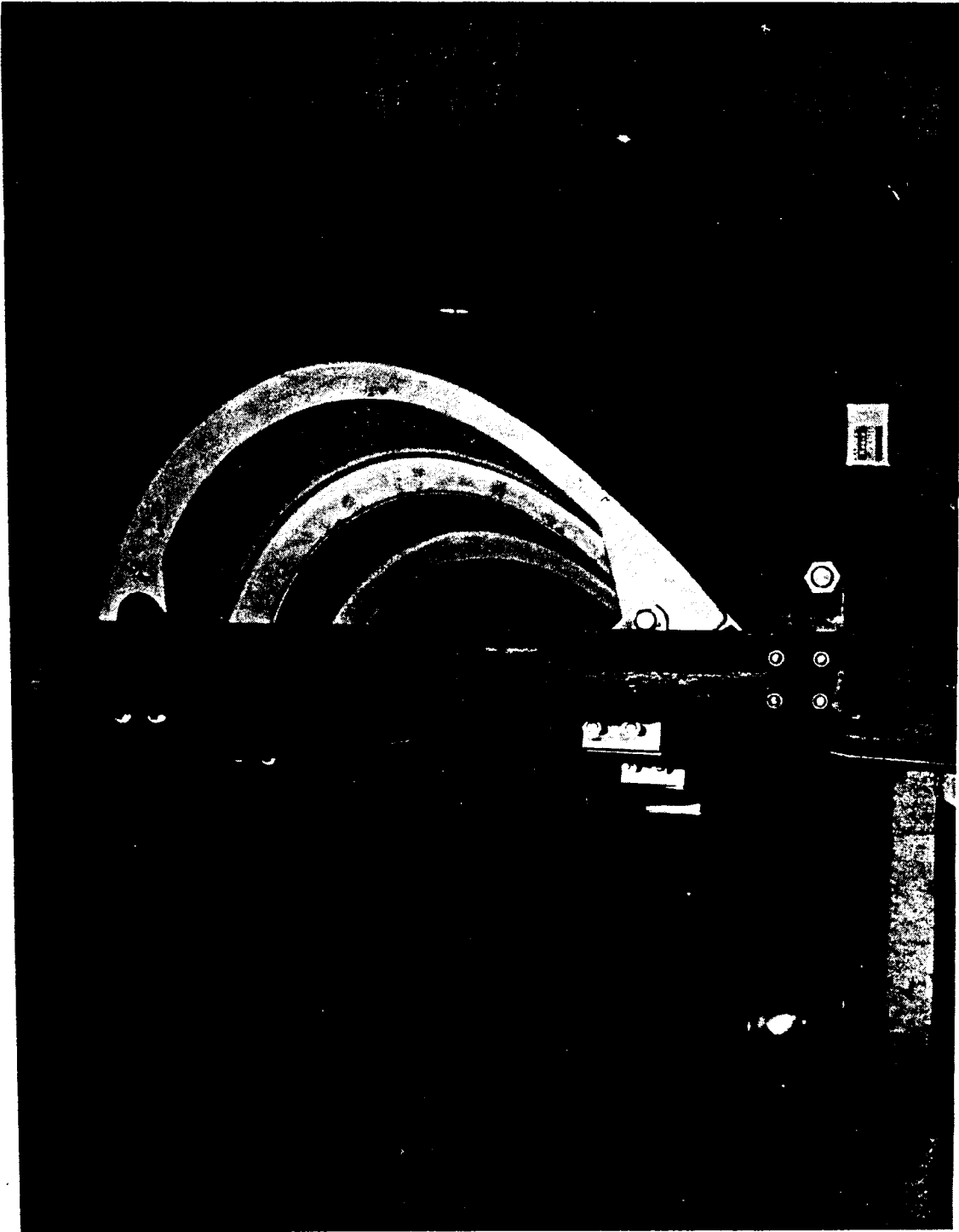


FIGURE 2-3 PROTOTYPE LEADING EDGE SEGMENTS AFTER COATING & PRIOR
TO TEMPERATURE TEST



FIGURE 2-4 PROTOTYPE LEADING EDGE SEGMENTS AFTER BOOST PRESSURE
AND ENTRY TEMPERATURE TESTS

of two adjacent Prototype leading edge segments (Figures 2-3 and 2-4). The lug bolt and fittings are protected thermally by wrapping the insulation blanket around each joint to block direct radiation from the skin. Conduction through the RPP rib lug is sufficiently low that lug bolt temperature can be maintained below 1200°F, an acceptable level for superalloys. Verification of this design will be established in Phase III with a thermal test of the joint.

With a 2800°F ($\epsilon = .80$) stagnation temperature it has been computed that the combined effects of internal cross radiation and an 0.85 emittance (used for preliminary analysis) reduces the stagnation temperature to 2600°F. A further reduction of over one hundred degrees is realizable with the higher 0.90 emittance more recently measured on the siliconized RPP and low catalytic effects. (Low catalycity is a property of the coated RPP material system that prevents recombination of dissociated flow at the surface of the material and results in a lower heating rate being imposed to the leading edge.) Insulations such as Dynaflex or RSI meet the heatshield temperature requirements, although perhaps not for a 100 mission service life.

Analysis - The Prototype leading edge was fully analyzed using the NASTRAN finite element computer routine for critical airloads and thermoelastic stresses; a thermal electrical analogy technique computed temperature distribution; and a finite element approach was employed for vibration response.

A weight optimization study, conducted to determine the optimum segment span for a Preliminary design, showed the minimum weight to occur at 30 in. span, including nonoptimum effects of the curved seal strips and 1 lb allowance for fastener hardware. Weight variation with span, shown in Figure 2-5, indicates that an increase of less than 0.1 lb/ft² is realized for span variations of ± 10 in. With this moderate penalty it appears that optimum span will ultimately be selected on the basis of cost or fabricability, rather than weight alone.

The Prototype design, which was based on somewhat different loads, design allowables, and thickness limits than those used for the weight optimization study and Preliminary design, was calculated to weigh less than 2 lb/ft² of wetted external surface area, including contributions from the seal strip, but excluding attachment hardware. This remains in the same range as computed for the Phase I design. Measured weight of a leading edge segment after coating was 7.2 lb, while seal strips weigh 0.9 lb each.

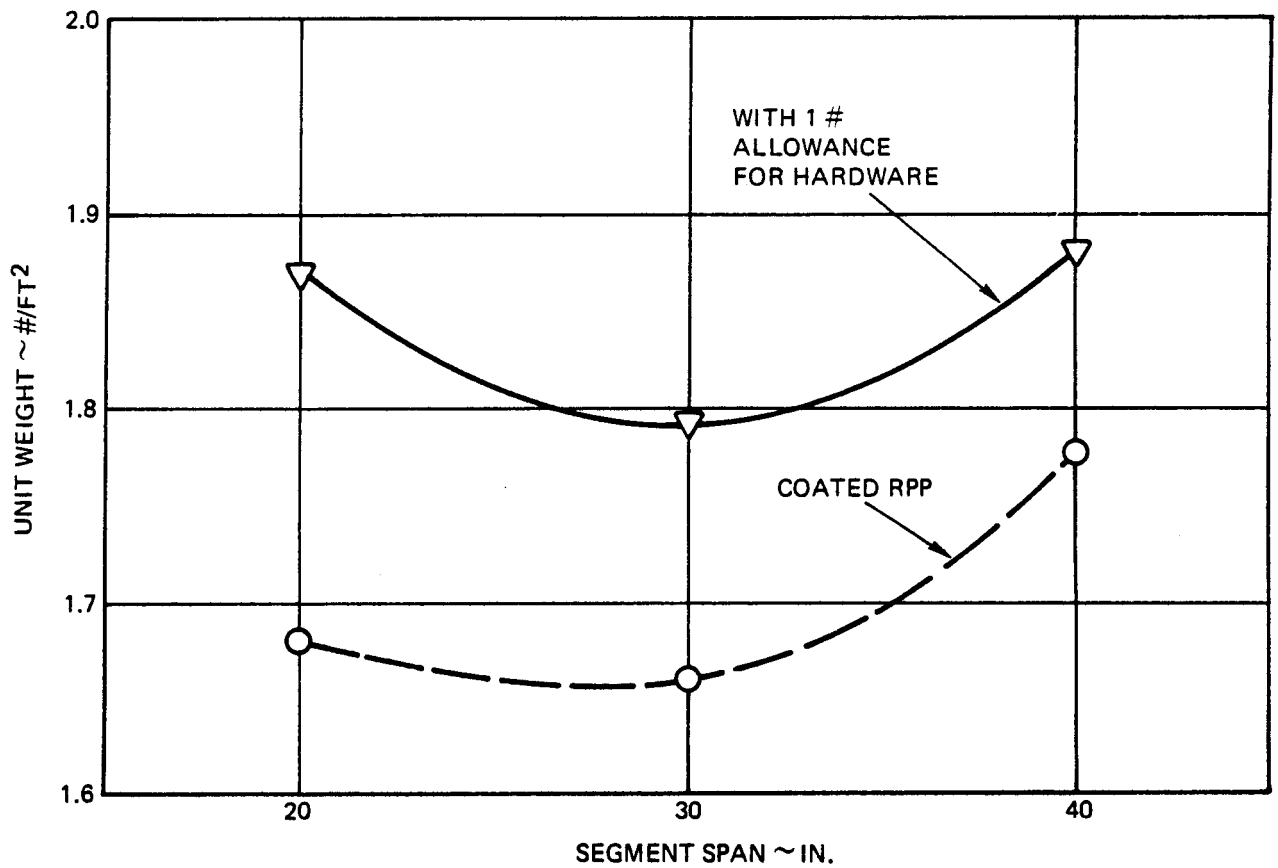


FIGURE 2-5 WEIGHT PRELIMINARY LEADING EDGE DESIGN

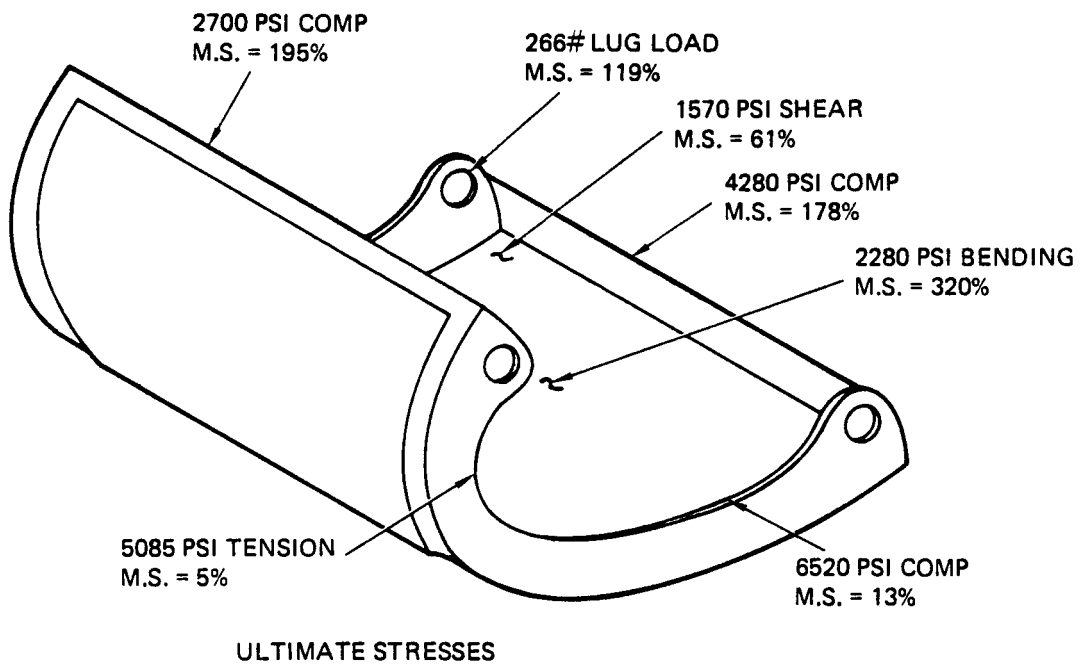


FIGURE 2-6 AIRLOADS ANALYSIS PROTOTYPE LEADING EDGE

Three 15 in. span Prototype design segments were fabricated and tested in this phase. Analyses were, therefore concentrated on the 15 in. span configuration. Design criteria were documented by report (reference 3) and approved by NASA-MSC. Critical design loads occur during boost, when a venting lag of 1.0 psi limit is assumed. This produces differential design burst pressures on the lower surface of the leading edge of 3.7 psi ultimate and 4.0 psi ultimate on the upper surface. Maximum collapse pressure in the stagnation region is 2.8 psi ultimate, but this is calculated to be not critical. The vibration design level which occurs during boost is 32 GRMS applied at the lugs in each axis. The entry trajectory employed in analyses was the North American Rockwell trajectory No. 935, which produces a peak radiation equilibrium temperature for the baseline airfoil section of 2800°F ($\epsilon = 0.80$), and remains at this maximum level for about 15 minutes. Entry time from an altitude of 400,000 ft until the leading edge temperature is reduced to 1000°F is 40 minutes.

Selected maximum stresses from boost pressure airload analysis computed for the Prototype leading edge design, and associated ultimate margins of safety based on the latest materials data, are summarized in Figure 2-6. Minimum calculated margins are found on the ribs, where tension and compression values are 5% and 13% respectively. All other margins are high because of other factors contributing to design, such as minimum thickness allowance or deflection limits.

Comparative stress data, obtained from the boost pressure test of a Prototype leading edge segment, are illustrated in Figure 2-7. The NASTRAN analysis is seen to predict the tensile stresses accurately but compression stresses are overstated, possibly because of assumptions regarding effective skin material acting with the rib. This can be improved with a different modeling approach.

Deflection measurements made during test are shown in Figure 2-8. Rib deflection is greater and panel deflection lower than computed. Apparently the "picture frame" effect of the ribs and cross beams cause the skin panel to operate more efficiently by carrying a greater proportion of the load as membrane stress, rather than bending.

Vibration analysis indicates that stresses from this load condition will be reasonably low by comparison to static stresses from the boost phase. Maximum values of rib and beam stresses, shown in Figure 2-9, are only 1500 psi. While a local bending stress of 4400 psi was computed for the lower lug from spanwise vibration (Y load), it is believed that this is more a result of modeling, rather than an actual stress. In any event the local nature of this stress means that it can be

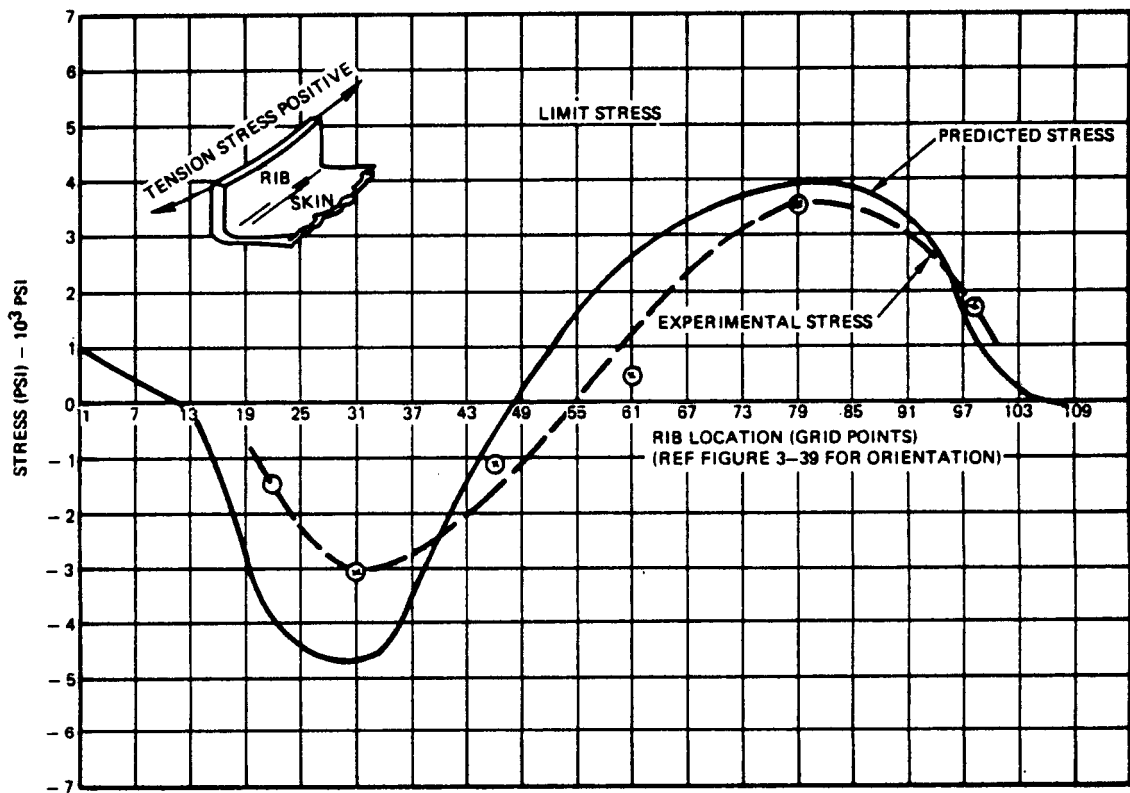


FIGURE 2-7 BOOST PRESSURE TEST RIB STRESS PROTOTYPE LEADING EDGE

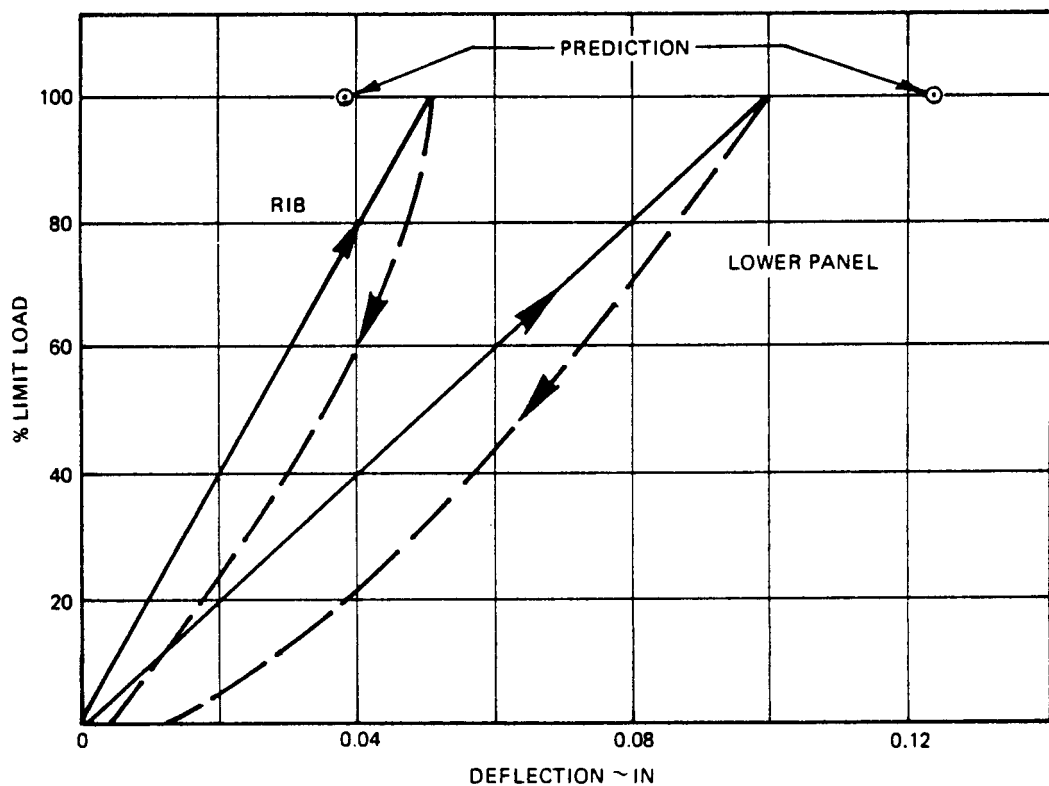


FIGURE 2-8 BOOST PRESSURE TEST DEFLECTIONS PROTOTYPE LEADING EDGE

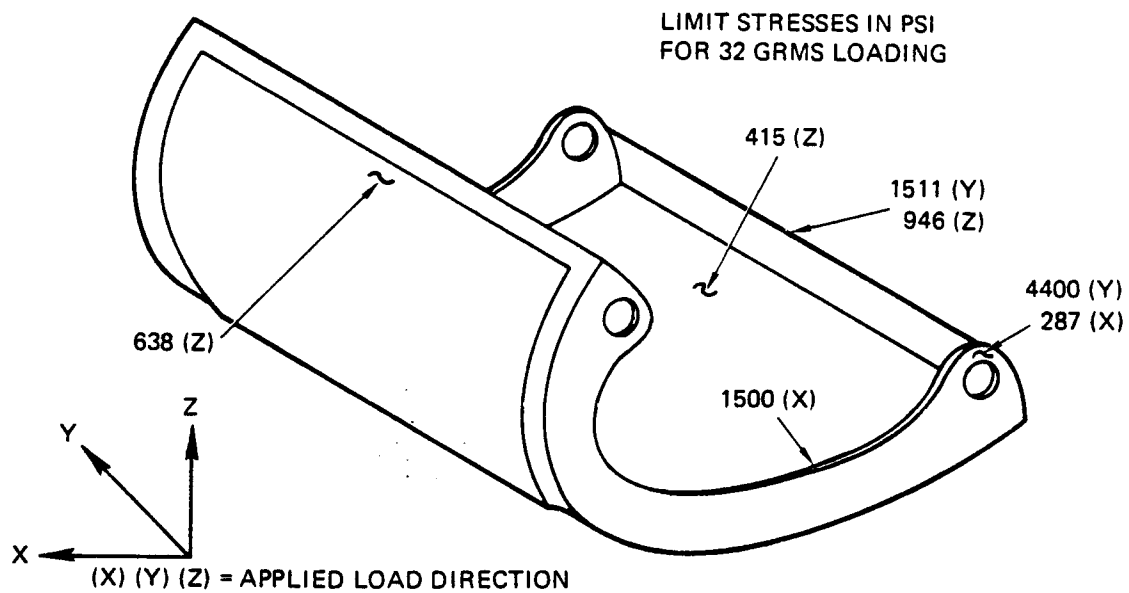


FIGURE 2-9 DYNAMIC ANALYSIS PROTOTYPE LEADING EDGE STRESSES

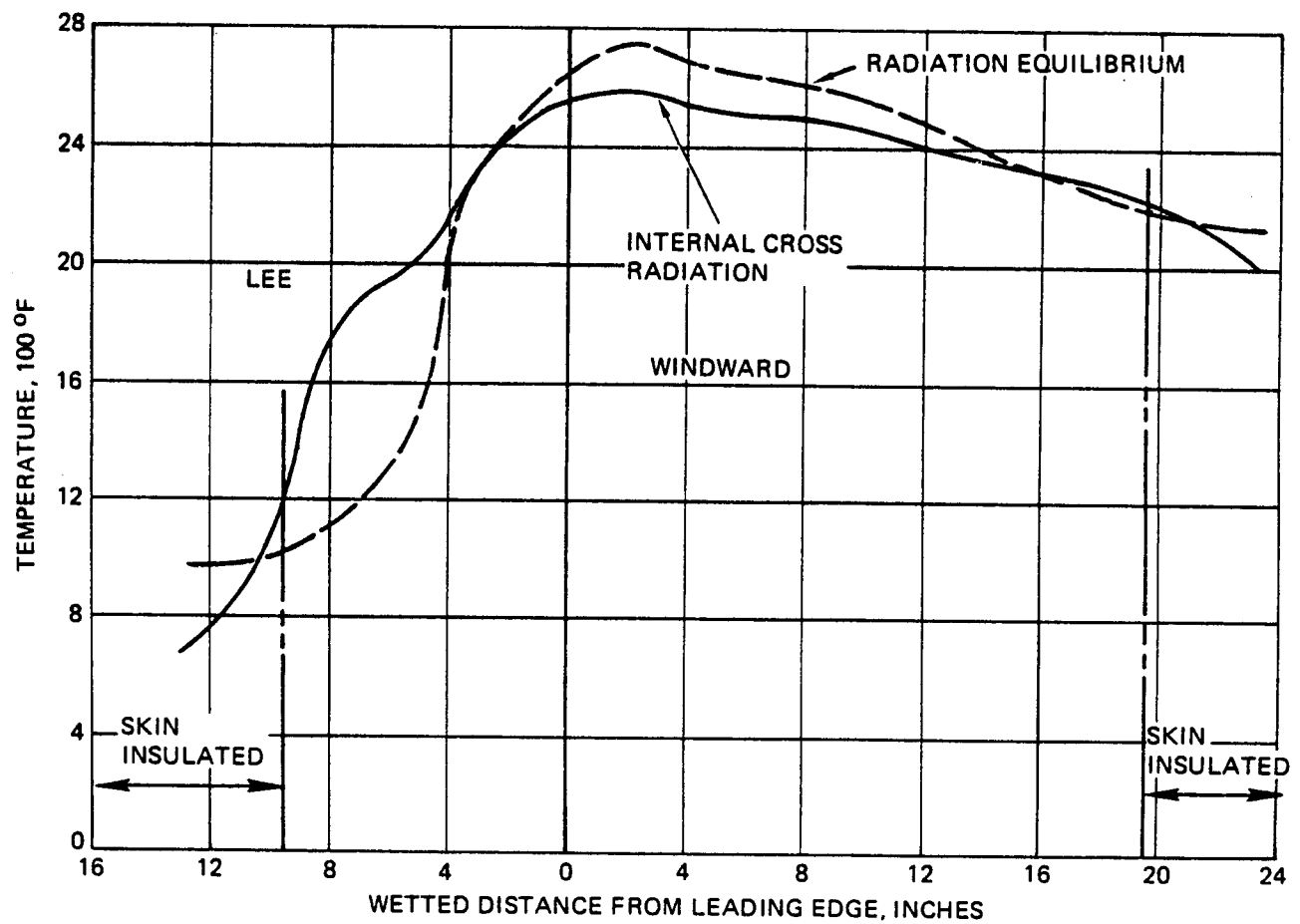


FIGURE 2-10 TEMPERATURE DISTRIBUTION AROUND LEADING EDGE

readily lowered with insignificant weight penalty. The vibration stresses shown are one-sigma values. For fatigue analysis two-sigma stresses, which are double those on Figure 2-9, are normally employed. As will be seen fatigue stresses in the 3000 psi should pose no problem because of the outstanding fatigue properties of coated RPP.

Thermal stresses induced in the leading edge during entry were of concern because of the rather severe gradients around the leading edge during entry as illustrated in Figure 2-10. The radiation equilibrium temperature distribution produces a temperature gradient around the skin at the stagnation point of $513^{\circ}\text{F}/\text{in.}$ However, internal cross radiation analysis predicts a 53% reduction in this region to $241^{\circ}\text{F}/\text{in.}$ Actually, with cross radiation a maximum gradient of $325^{\circ}\text{F}/\text{in.}$ is computed on the leeward side in the region of the rear beam and is due to the heat sink effect of the beam and trailing edge seal strip as well as the insulation, which blocks cross radiation heat from the hotter regions.

With these thermal gradients and those computed for the ribs a NASTRAN thermoelastic analysis was conducted for the two worst conditions. The first condition occurs during heatup, 230 sec after entry, where maximum temperature gradients are experienced by the ribs. These gradients tend to close the rib section but the restraint provided at the lugs prevents this and results in tensile stresses being induced in the outstanding leg of the ribs. The second and most critical condition occurs when the leading edge reaches maximum temperature. Under these conditions temperature gradients in the ribs are minimal; however, with the entire leading edge expanding but constrained at the cool lug supports, significant compression stresses are developed in the outstanding leg of the ribs. Maximum skin gradients are encountered for the second condition but these were found to produce rather small thermoelastic stresses in the skins.

A summary of maximum thermal stresses computed for the two conditions is given in Figure 2-11. Maximum compression stress is a relatively low value of 2570 psi (compared with an allowable of around 11,000 psi at these temperatures) and the maximum tensile stress is still lower at 1100 psi. Skin stresses are shown to be insignificantly low.

Two of the leading edge segments were tested together to a time-temperature profile simulating one entry. The purpose of the entry temperature test was to demonstrate that the Prototype leading edges would survive the thermal stress conditions without failure. Strain measuring techniques could not be employed because of the high temperature and inaccessibility of the leading edges in the test facility. Therefore,

the test was essentially "go,no-go". A measure of the accuracy of the test is in the time-temperature profile achieved versus that predicted. This comparison is illustrated on Figure 2-12. The two critical periods occur when the stagnation temperature reaches 1500°F and the time when maximum steady state temperatures are reached. Each of these conditions were adequately satisfied by the test. No failures or damage were observed.

In addition to the temperature gradients computed for the thermal stress analysis the joint region was examined thermally to ascertain lug joint insulation requirements. Results are tabulated in Figure 2-13 for three different conditions. Phase II design criteria permitted the wing structure to which the bracket attaches to reach 650°F. (This requirement will be reduced to 350°F in Phase III). It is apparent from the calculated temperatures that the lug bolt can be maintained below 1200°F (acceptable for super alloys) and the wing structure limited to 650°F for the Prototype design, where the bolt is 2.7 in. from the skin compared to the 2.0 in. and 3.3 in. dimensions analyzed. Note in Figure 2-13 that there is a modest change to the bolt temperatures as the RPP conduction path is shortened. It appears that the key to joint thermal protection is the soft insulation wrapping around the joint to protect against direct radiation from the skin.

Even when the hard insulators are removed from around the bolt, bolt temperature remains reasonable, but a greater burden is placed on insulation that must be placed between the bracket and the wing structure. Thus it appears that for the future 350°F wing structure limit, hard insulators at the lug joint will be required. These can also function as bushings, where drilling on assembly is necessary for leading edge installation on the vehicle.

Based on structural/thermal analyses and the supporting test data, the Prototype leading edge design appears to be a viable approach for the shuttle.

2.2 MATERIALS DEVELOPMENT

Materials activities in Phase II were concentrated on both facets of the material system, each interrelated: (1) Phase I coating systems performance improvement, and (2) WCA laminate refinement to provide a more compatible base for the coating. The coating task investigated both of the diffusion coatings from Phase I (reference 2) until evidence was found that the siliconized coating modifications could cure the deficiencies of the Phase I M30 siliconized coating system. Improvements to the zirconium-boron-silicon system did not materialize and it was discontinued when

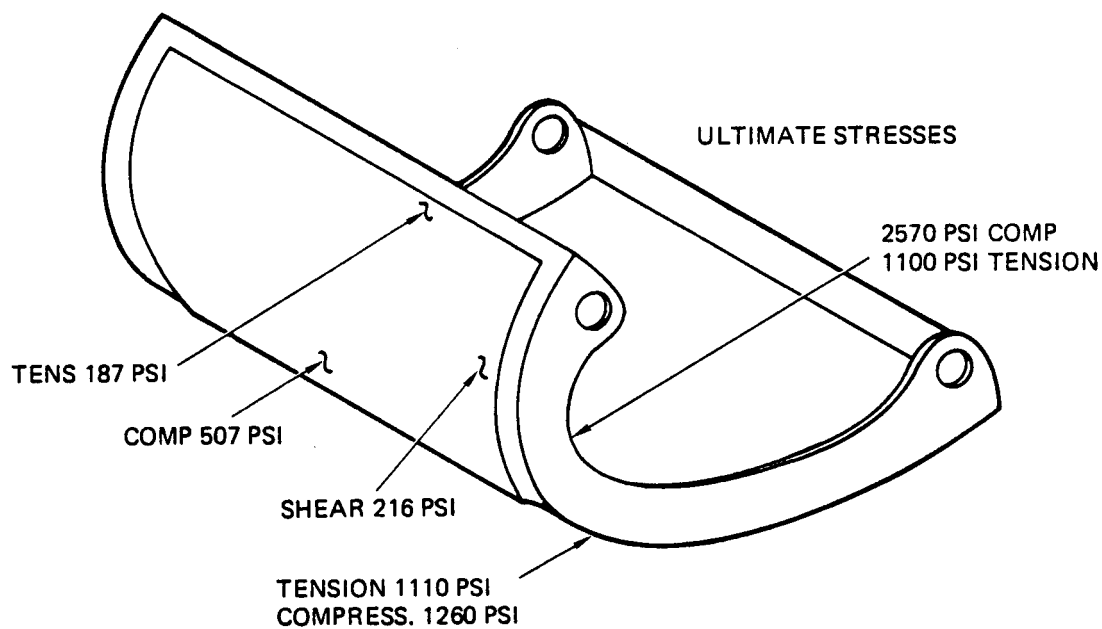


FIGURE 2-11 THERMAL STRESSES ENTRY CONDITION

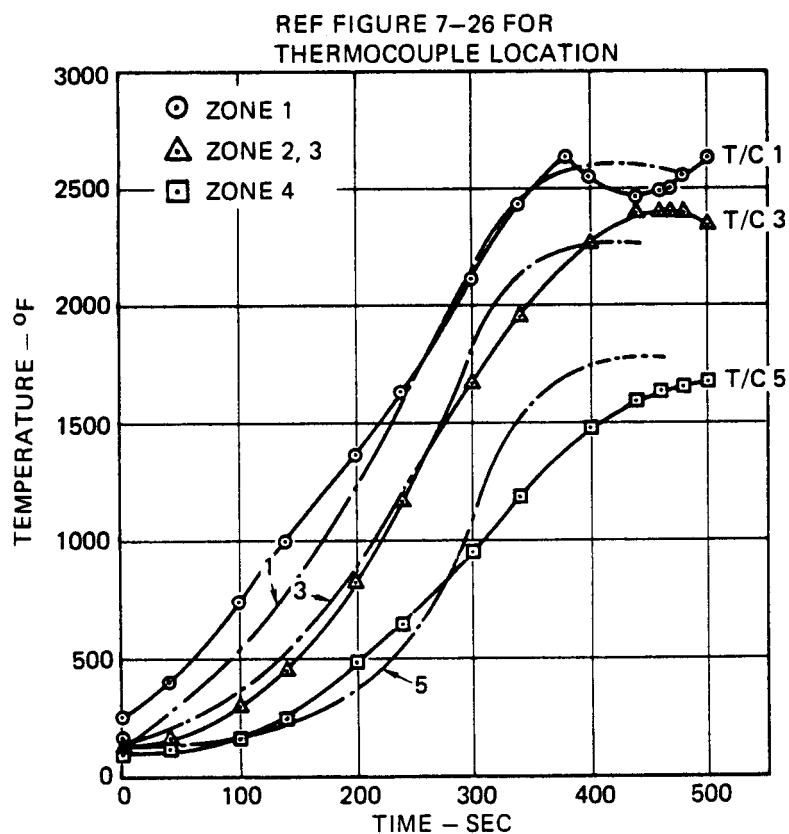


FIGURE 2-12 ENTRY TEMPERATURE TEST THERMAL PROFILE

COMPONENT	BASELINE °F	BOLT 1.3" OUTBD °F	NO BOLT INSUL °F
BRACKET			
T4	782	830	1111
T1	635	659	>717
BOLT			
T6	1107	1177	1175
T13	1042	1104	1161
RPP			
T16	1691	1793	1225
T33	2100	2100	2100
DIMENSION "D"	3.3"	2.0"	3.3"

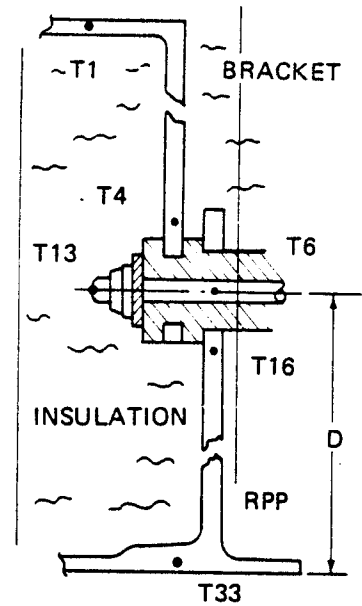


FIGURE 2-13 LUG JOINT MAXIMUM TEMPERATURES

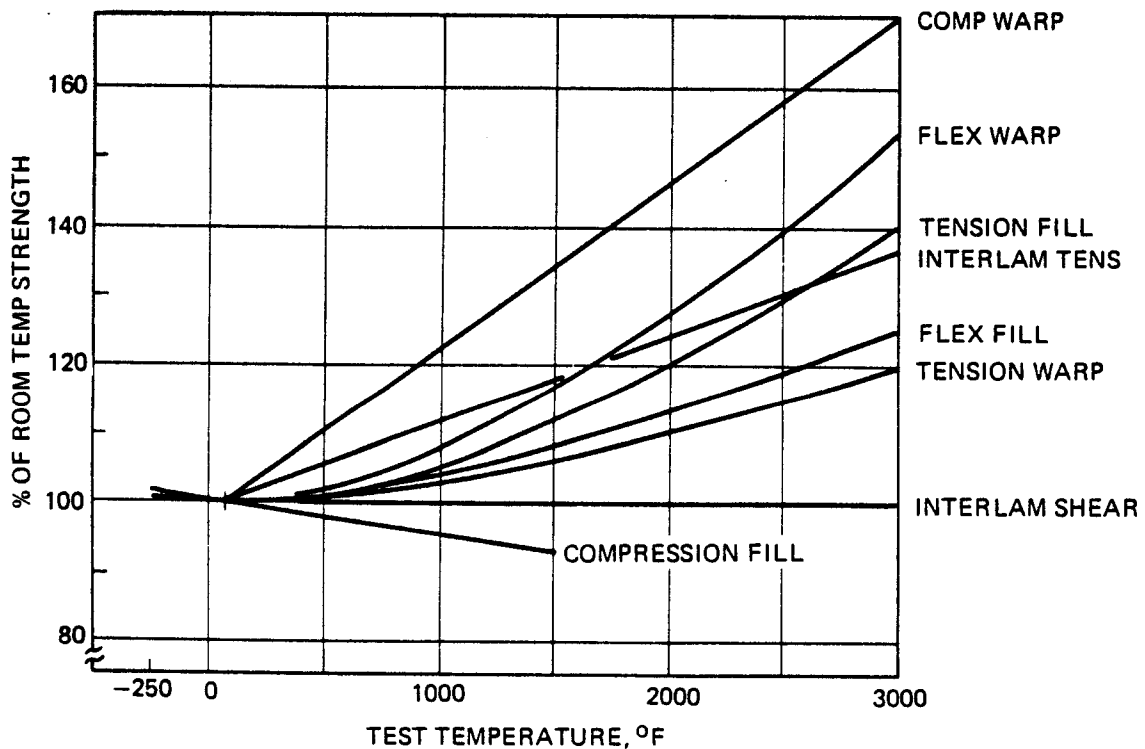


FIGURE 2-14 TEMPERATURE EFFECT ON STRENGTH COATED RPP

the siliconized system showed promise of meeting the 100-mission requirement. The Phase I hafnium-tantalum melt impregnation coating that permitted 4000°F operating temperature was also studied further to determine techniques for impregnating various conditions of RPP (i. e., RPP-0 through RPP-3) but plasma tests showed a life limit of only 5 or 6 high cross range missions before excessive crumbling of the coating was experienced. Because of this, investigation of this system was limited to plasma test evaluation only.

Laminate studies were concerned with densification of the surface and modification of the expansion characteristics to more closely match those of the coating, and reduce coating crazing which has been observed on most parts. However, results of these investigations were inconclusive because of inordinately deep coating penetration, and therefore additional activity along this line of investigation is planned for Phase III. It should be noted, however, that crazed material tests demonstrate that strength and oxidation resistance for 100-missions can be satisfied with the current material system.

The siliconized coating system applied to WCA graphite cloth laminate was selected for development on the basis of the coating's high temperature oxidation resistance, good system strength, and the promise of satisfactory substrate oxidation protection to meet the 100 mission service life goal without significant ($<15\%$) strength degradation. The baseline silicon coating is diffused into the laminate by the pack cementation process. The pack consists of a mixture of powders containing 10% alumina, 60% silicon carbide, and 30% silicon. Coating is conducted at about 3100°F for a nominal period of 2 1/2 hours, the exact conditions being governed by the particular part to be coated. A coating depth of 0.020 in. was the goal, 0.010 in. of which is assumed the allowance for oxidation in service before part replacement. This is somewhat arbitrary because it has been demonstrated that greater coating thicknesses can be obtained. This means that greater recession allowance and mission life can be increased as required. However, the 0.020 in. thick coating was found to satisfy Phase II design criteria.

In order to gain good mass loss rate performance in plasma arc testing the coating was post heat treated to 3200-3400°F. Little strength loss in the as-fabricated condition occurred due to heat treating but plasma performance was enhanced by a factor of five, while subsurface oxidation resistance (based on strength reduction data) was degraded by about 30% as determined by furnace tests. However, 100-mission thermal/oxidation tests proved the heat treated material to have little or no strength loss after exposure.

Recent but limited data indicates that heat treating may not be required for high temperature performance if processing is modified slightly and all of the factors involved with the coating process are adequately controlled. However, the design strength data reported in this phase were obtained on heat treated material.

Considerable knowledge has been gained regarding the factors that control coating performance and reproducibility. These include types of starting materials, furnace control, retort design, retort packing techniques, and time/temperature profiles. Desirable features for each of these factors have been established and are discussed in detail in Section 4.3. However, further work is required to establish material and process tolerance limits and their control to consistently produce quality coatings.

Mechanical, physical and thermal performance of the baseline 10/60/30 siliconized coated system were obtained in Phase II and are summarized below in Table 2-1.

TABLE 2-1

ROOM TEMPERATURE STRENGTH
COATED RPP
13 PLY LAMINATES

<u>Property</u>		<u>Average Test Value, PSI</u>	<u>*Revised Design Value, PSI</u>
Flexure	Warp	14200	9600
	Fill	12200	8130
Tension	Warp	8500	5680
	Fill	4500	3000
Compress	Warp	11500	7670
	Fill	11000	7340
Shear	Warp	3800	2530
	Fill	3900	2600
Bearing	Warp	13500	9000
	Fill	13800	9200
Interlam	Shear	2200	1470
	Tens	400	270

* Revised Design Value = Average \div 1.5

Mechanical property data was obtained on coated RPP over the temperature range of -250°F to 3000°F. Typical room temperature values for 13 ply laminates are listed in Table 2-1. All but the bearing and shear (in plane) were tested by Southern Research Institute (SRI). Bearing and inplane shear tests were conducted by VMSC. Strengths obtained are reasonably high and result in light weight designs (2 lb/ft²). These data show a substantial improvement over the Phase I data (reference 2), where strength measurements were made only on coated 13 ply flexure bars in the warp direction. The comparison is indicated below in Table 2-2.

TABLE 2-2
FLEXURE STRENGTH 13 PLY LAMINATES - WARP
DIRECTION ROOM TEMPERATURE

Phase I		Phase II	
Typical	Scatter	Typical	Scatter
10710 psi	610 - - 14000 psi	14200 psi	14050 - 15010 psi

Note that the scatter has been reduced considerably, mostly through a better understanding of furnace control and retort design to achieve better coating uniformity.

Assuming a 33% strength reduction to account for data scatter and service life strength loss, preliminary design values shown in Table 2-1 were obtained for computation of the margins of safety for the Prototype design noted on Figure 2-6. This reduction has recently been confirmed by a statistical analysis of flexure strength data compiled on 53 specimens from 17 different coating runs. This showed the 99% probability, 95% confidence strength value to be 33% below the mean.

Strength variation with temperature (Figure 2-14) shows all properties except compression in the fill direction are equal to or higher than the room temperature strength. The preponderance of data suggests that the compression-fill anomaly is either the result of test technique or the individual group of specimens tested. Note that the low strength problem encountered at 1500°F in the Phase I program (reference 2) no longer exists and all, but interlaminar shear and the compression-fill anomaly already cited, exhibit higher strength at 1500°F than at room temperature.

Elastic modulus data (Figure 2-15) shows reasonable design values which in general increase with temperature to 2500°F and then

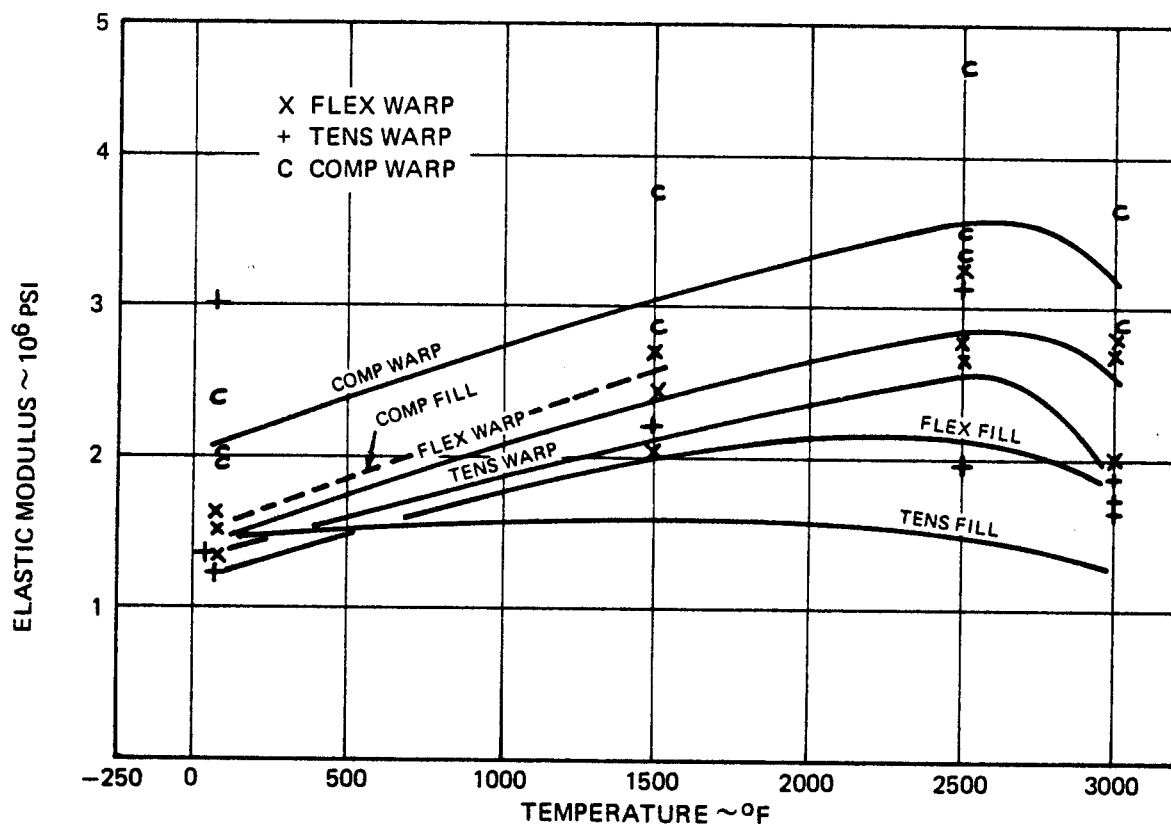


FIGURE 2-15 TEMPERATURE EFFECT ON ELASTIC MODULUS COATED RPP

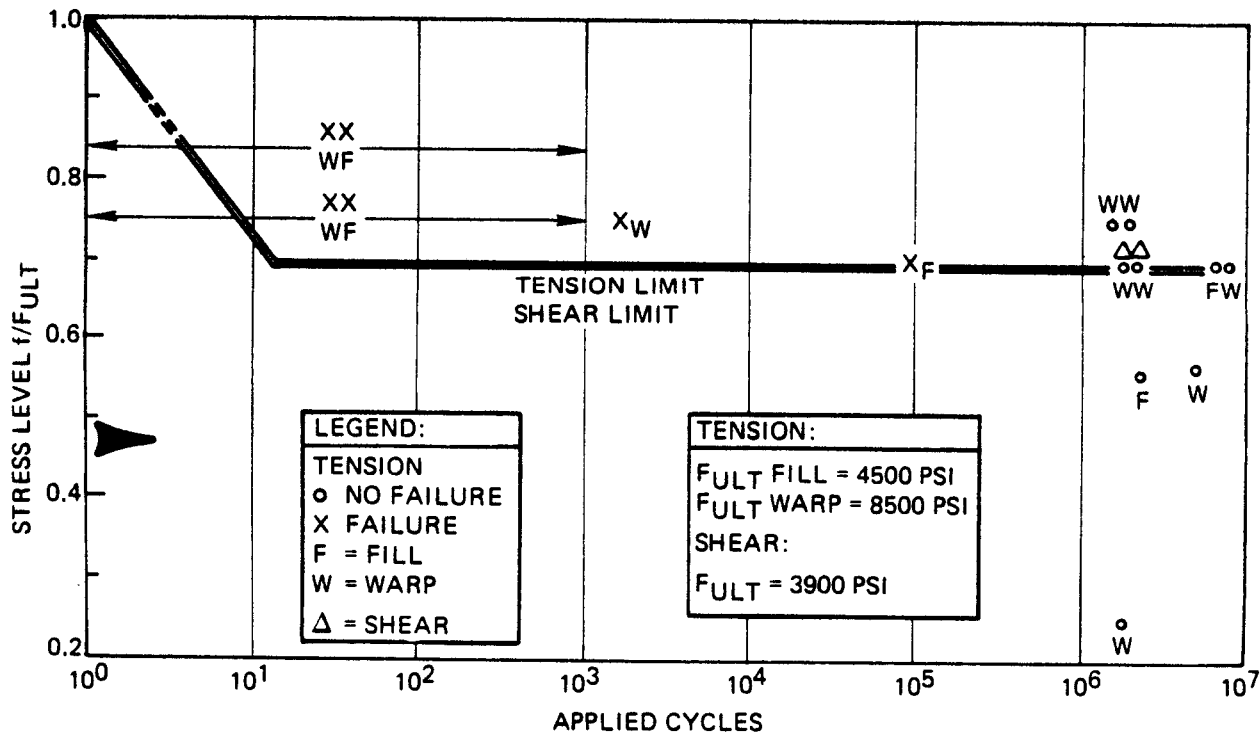


FIGURE 2-16 TENSION FATIGUE AND INPLANE SHEAR FATIGUE $R = 0$

break over to a reduced value at 3000°F. The reason for the 2500°F break is not clear; however, bare material exhibits the same characteristic. Thermal stress calculations have included these temperature effects, and show that increased stiffness obtained above room temperature is not detrimental.

Fatigue strength for coated RPP is outstanding and even after two-million cycles of load at substantial stress levels the static test data showed that the strength of the material was not degraded. Fatigue strength was obtained for tension, flexure, inplane shear, interlaminar shear and interlaminar tension. Both warp and fill direction properties were examined. Data is shown in Figures 2-16, 2-17 and 2-18. Applied stress levels were well above anticipated limit design stress levels which are indicated by the symbol on the figures. Preliminary endurance limits are indicated by the limit level lines on the figures. The transition between one-cycle (static strength) and the endurance limit is undefined but is represented by a dashed line. Transition between no failure for millions of cycles and early failure was found to be rather abrupt as load was increased. Since applied stress levels in practice will be much lower than test endurance limits, this sensitivity to load level becomes unimportant. Several specimens which had not failed during fatigue cycling were static tested to failure to ascertain fatigue damage. Results, listed in Table 2-3, show no degradation within reasonable data scatter and only one specimen shows a lower value than typical static strength values (reference Table 2-1). (Note that a load ratio $R = -1$ indicates reversed loading while $R = 0$ indicates stress is varied between zero and maximum).

TABLE 2-3
STATIC STRENGTH AFTER FATIGUE CYCLING

Specimen	Loading	Fatigue Load				Static Failing Strength, PSI
		Stress PSI	%F _{ULT}	Applied Cycles	Load Ratio R	
F-8	Flexure	5710	40	2.43×10^6	-1	19000
F-9	Flexure	5710	40	2.50×10^6	-1	20700
F-4	Flexure	5710	40	2.49×10^6	-1	19600
F-19	Flexure	8570	60	3.32×10^6	-1	19800
S-8	Inplane Shear	2720	70	2.33×10^6	0	3630
TL - /1	Interlam Tens	280	70	1.74×10^6	0	702
TL - /2	Interlam Tens	280	70	2.45×10^6	0	725

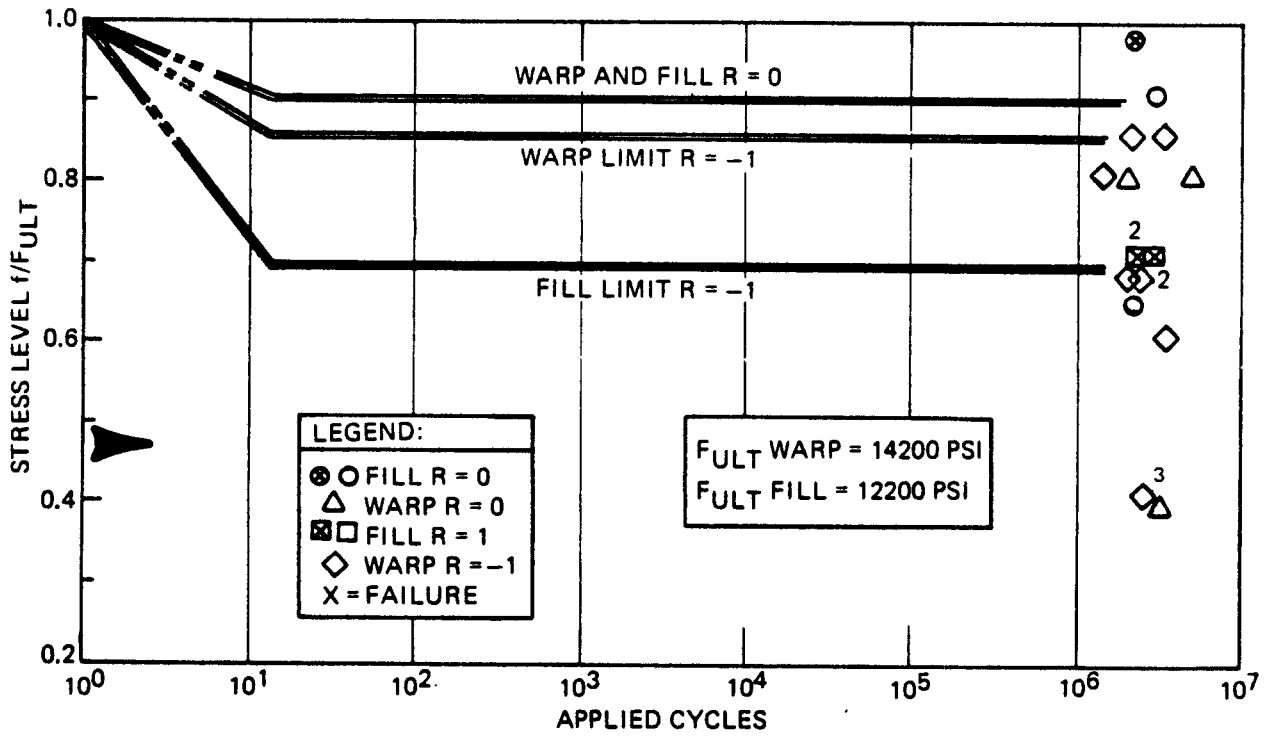


FIGURE 2-17 FLEXURE FATIGUE

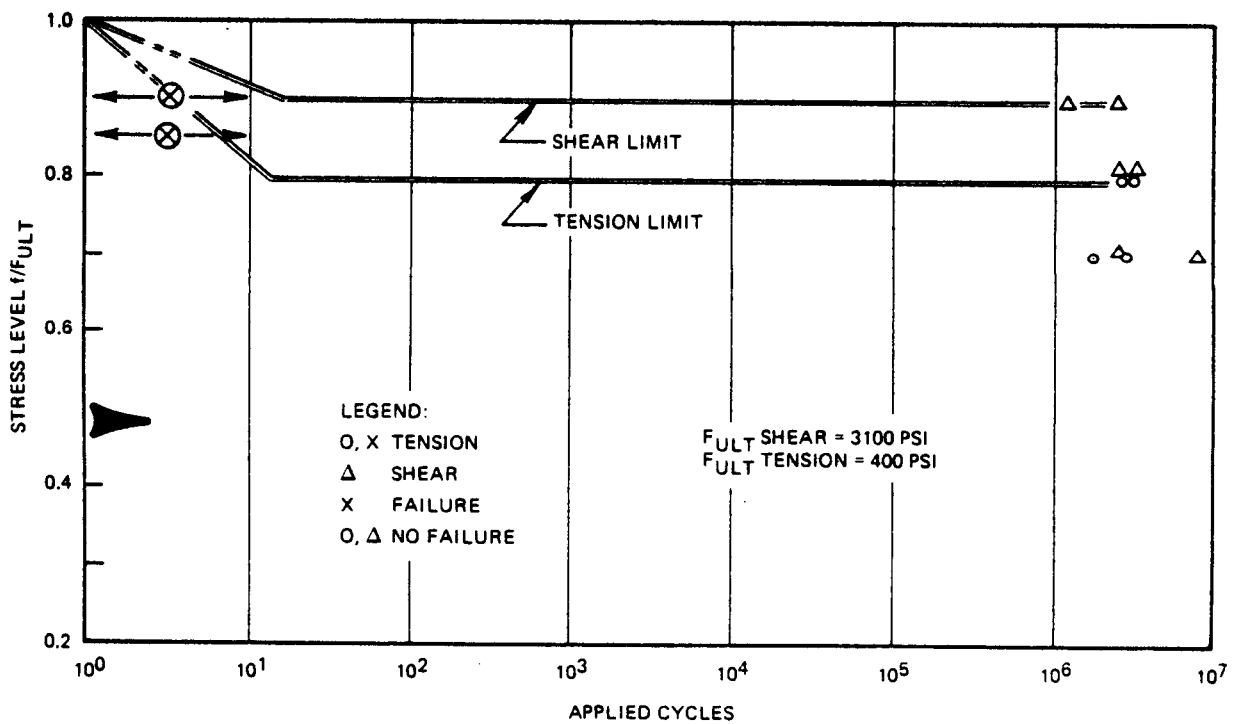


FIGURE 2-18 INTERLAMINAR FATIGUE STRENGTH $R=0$

It is concluded from the fatigue test program that fatigue will not be a problem for the leading edge and furthermore it appears that realistic fatigue stress levels will not result in degraded static strength at the conclusion of the service life of the leading edge.

Joint tests were also performed in this phase to gather sufficient data to obtain a "feel" for the design limits with coated RPP. Lug joints representative of the Preliminary and Prototype design, tension-angle joints, bonded joints, and riveted joints were examined experimentally. All but the tension-angle joint is employed on the Prototype design. Tension-angle data was obtained to offer the designer some flexibility in conceptual design with possible application to fuselage panels or vertical tail leading edges.

Lug tests using a 0.75 dia. pin and 13-ply cross ply laminates produced failures ranging from 484 lb to 603 lb depending upon the direction of loading. Load direction was axial, transverse, and 45°. Data indicates that lug design with coated RPP is similar to sand casting design in terms of strength reduction factors. Failing loads are far in excess of the 266 lb. ultimate applied lug load for the Prototype design.

Bonded joints, wherein the parts are bonded in the as-molded state and subsequently pyrolyzed and strengthened by the reimpregnation approach, produced strengths approaching interlaminar tension strength. This technique was employed in the attachment of trailing edge seal strips to the Prototype leading edge segments and intercostals to the wing tip panels. Bond tensile strength averaging 472 psi and bond single lap shear strength of 792 psi were obtained. Lap shear tests were accompanied by significant joint rotation, which is typical of single lap specimens, and induced tensile stresses, believed to be responsible for the low shear values. Shear strength in the 2000 psi region should be possible with double lap specimens, and would be adequate for design.

Riveted joints were tested to establish the strength potential of rivets fabricated from RPP. These joints were riveted in the as-molded condition and then pyrolyzed and strengthened. The rivet is squeezed into place while in the uncured condition. Single lap shear strength over 1100 psi and double lap shear strength of 2000 psi were obtained. Tensile strength over 1100 psi was also measured. These values are believed suitable for the leading edge application, where rivets are used only in conjunction with a bonded joint. They serve to clamp the bonded joint during processing and act as a peel stopper in the event of bond separation in service.

Tension-angle data gathered on joints employing 1/4 in. dia. tension bolts and 0.24 in. thick coated RPP produced failing strengths between 450 and 640 lb. depending upon the washer used with the bolt.

Considerable deflection of the RPP angle was noted during test which tended to concentrate the stresses close to the bolt so that the effective width of the angle was perhaps as small as one inch.

Physical property data was obtained on coated RPP over a temperature range from -250°F to 3000°F . The most important property measured was emittance, which showed rather high values as noted on Figure 2-19. In the region of maximum re-use surface temperature (2500 - 2800°F) emittance is above 0.9 as measured by SRI. This is beneficial in lowering operating temperature and extending mission life. Conductivity was measured both in the plane of the laminate (warp direction) and normal to the laminate. Values were lower than anticipated but sufficiently high to cause no thermal stress problems. At 2500°F for example, inplane conductivity was $102 \text{ BTU-in/ft-hr-}^{\circ}\text{F}$ and conductivity normal to the laminate was $47 \text{ BTU-in/ft-hr-}^{\circ}\text{F}$. Specific heat values were normal for this material and followed the predicted trend very closely, varying from $0.18 \text{ BTU/lb-}^{\circ}\text{F}$ at room temperature to $0.41 \text{ BTU/lb-}^{\circ}\text{F}$ at 2500°F .

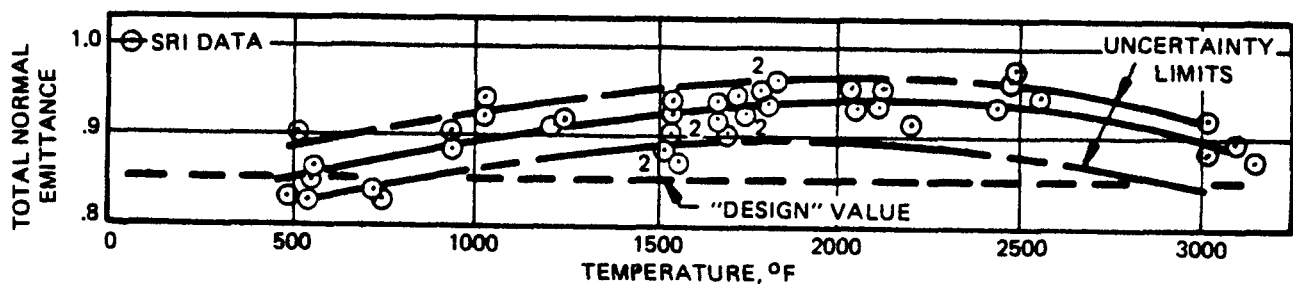


FIGURE 2-19 EMITTANCE

The low thermoelastic stresses computed for coated RPP are largely a function of the low thermal expansion. In the warp direction for example, expansion values of $1.7 \times 10^{-6} \text{ in/in-}^{\circ}\text{F}$ through 3000°F were measured. This, coupled with a fairly low elastic modulus, produces small thermal strains.

One of the main aspects of the coated RPP system is its reuse capability in the entry environment. Mission life of the coated RPP is established by one of two failure mechanisms: (1) Coating oxidation/erosion which will ultimately lead to exposure of the bare substrate and then rapid oxidation and (2) subsurface oxidation caused by oxygen diffusing through the coating to attack the bare substrate beneath. This can result in either lowered

strength or loss of the coating bond or both. Plasma arc test data has been used to establish coating erosion life, while thermal/oxidation cycling in a molecular environment was employed to determine capability of the system to survive 100 missions without serious strength loss from subsurface attack. Long term exposure in plasma arc (atomic environment) conditions has also been performed to determine differences between atomic and molecular constituents on coating and subsurface attack.

Plasma arc coating mass loss data converted to the standard presentation of mass loss rate divided by heat transfer coefficient is shown in Figure 2-20. The curve indicates rather small data scatter and a logarithmic function of mass loss with temperature. This curve was generated from cumulative average mass loss data for eleven specimens over four temperature regions with exposure up to five hours on a given sample in the VMSC 180-KW plasma arc. Typical cumulative mass loss data is shown in Figure 2-21. Note that at low heat flux rates mass gains are obtained and it is only after several hours exposure that a steady state mass loss rate condition is established. This trend tended to make the Phase I data too optimistic at low temperature because insufficient test time was involved. At the higher heat flux conditions stabilization occurs sooner. The earlier non linearity is believed due to the establishment of a thin silica layer which eventually reaches an equilibrium condition between buildup and removal. This silica layer is believed responsible for the low catalytic behavior of the coating.

Utilizing the mass loss rate data generated by test, mission life of the material system was computed (Figure 2-22) for various assumptions of effectiveness of factors controlling surface temperature. The mission life calculations in Figure 2-22 are based on high cross range missions and are plotted against radiation equilibrium temperature at the stagnation point for an emittance of 0.8. The mission life curves, however, incorporate in them the effect of having an actual measured coating emittance of 0.9. The most optimistic curve includes both internal cross radiation relief (150°F) and low catalytic effects (250°F) and assumes for the 0.020 in. thick coating that only half of it is consumed before leading edge segment replacement. Under these conditions a 100 mission life can be obtained with a computed peak radiation equilibrium temperature of 3070°F . On the other hand, if no temperature relief is assumed, which is the most pessimistic and unrealistic assumption that can be made, a maximum radiation equilibrium value of only 2690°F can be tolerated to achieve 100 missions. This is raised 150°F to a value of 2840°F with the cross radiation effect included.

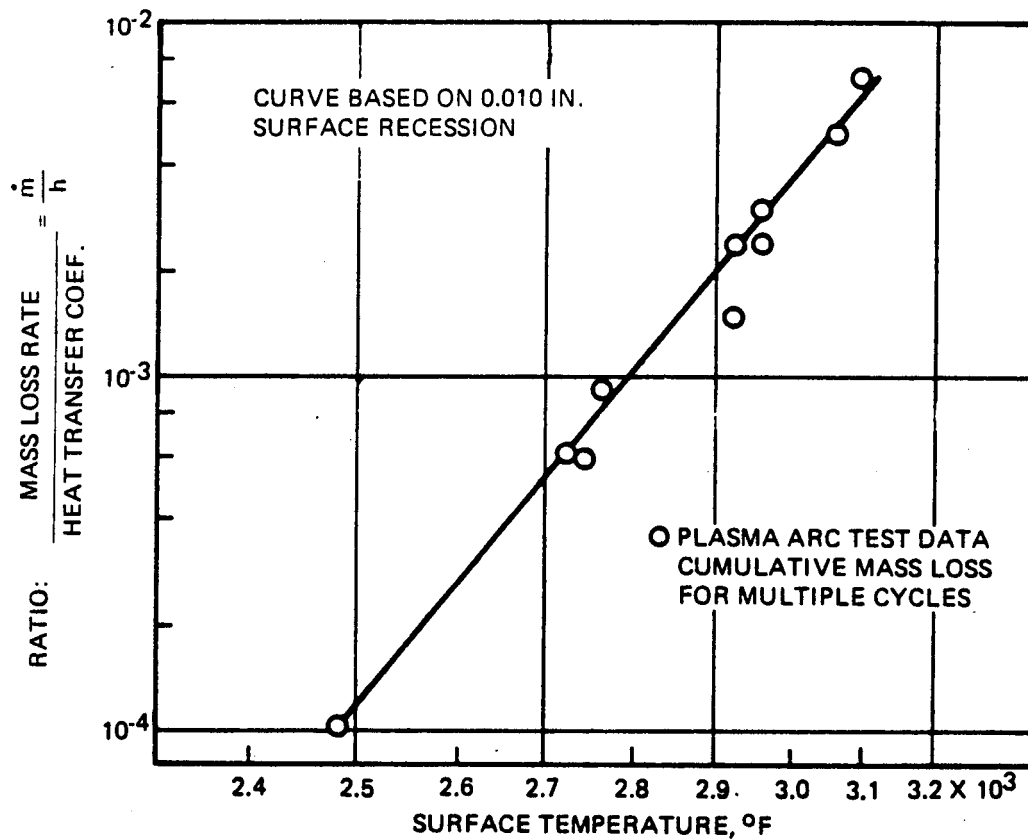


FIGURE 2-20 m/h CORRELATION PLASMA ARC TESTS

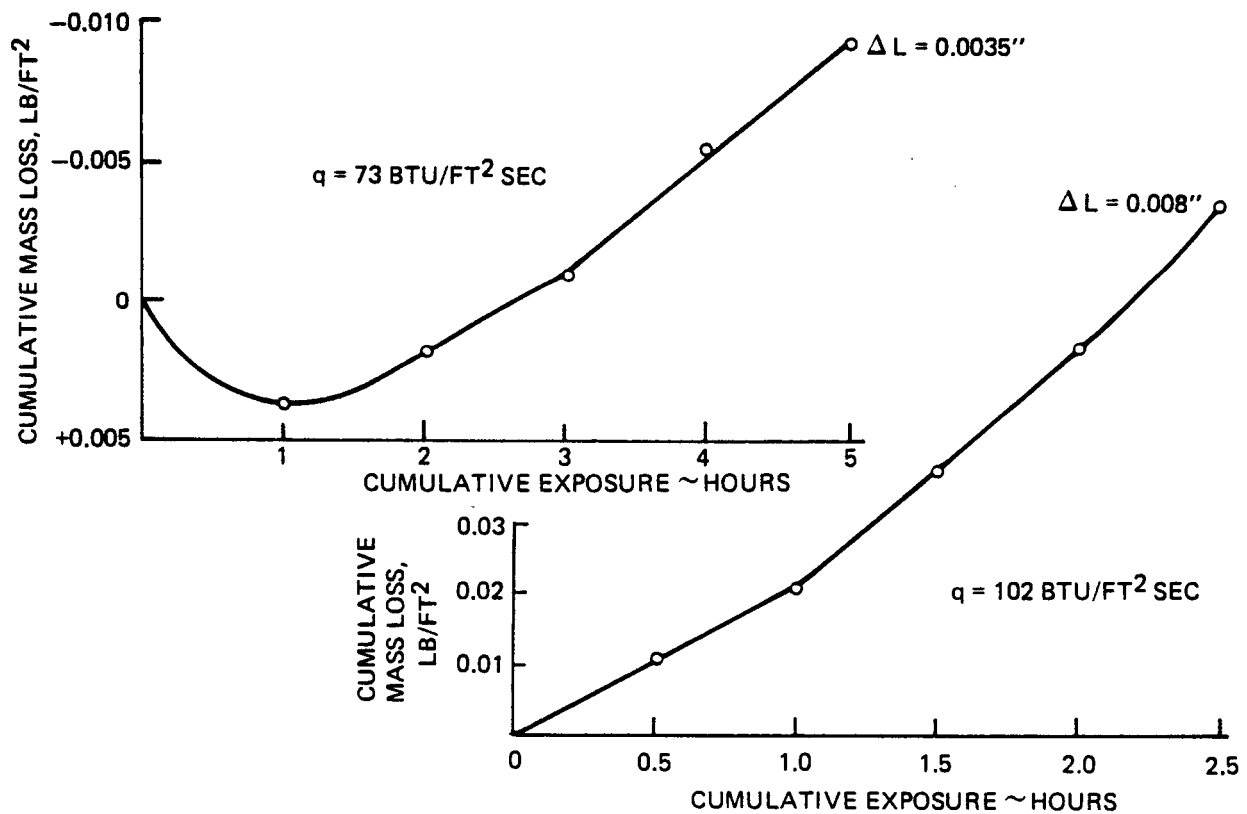


FIGURE 2-21 CUMULATIVE MASS LOSS TYPICAL

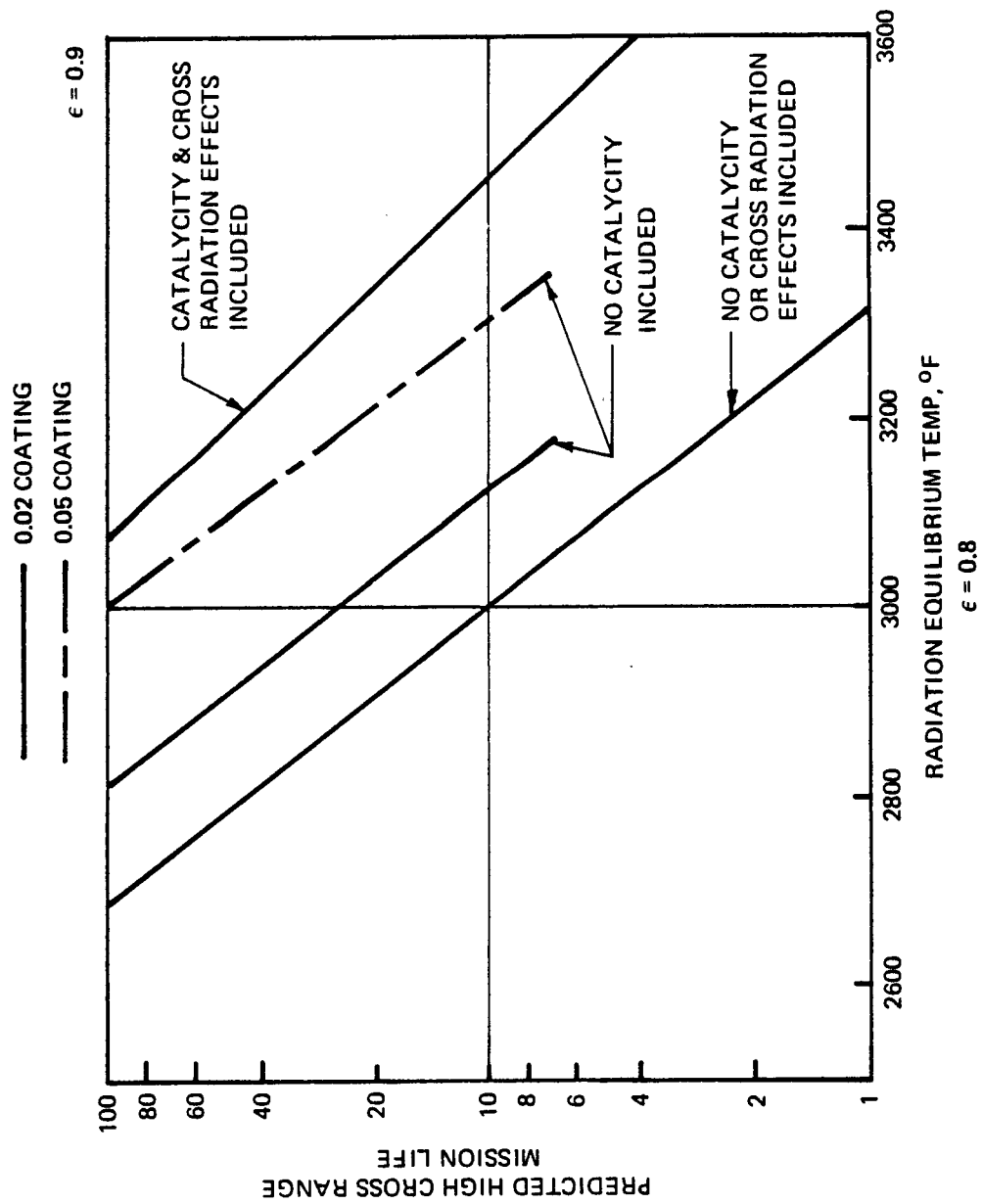


FIGURE 2-22 COATING MISSION LIFE

The latest information on shuttle design indicates that leading edge temperatures will be higher than the 2800°F ($\epsilon = 0.8$) design criteria for Phase II and that a value as high as 3000°F ($\epsilon = 0.8$) is warranted. This, as noted on Figure 2-22, will require a 0.05 in. thick coating (if no catalycity relief is assumed) with replacement required after 0.04 in. is consumed. Development test data has shown that substrate thickness must increase to retain good structural properties if the coating depth is increased. Coating thickness in this range is practical and has been produced. Coating run M103, given in Appendix A, is an example.

The catalycity work was extended in Phase II to obtain a better understanding of the nature of the phenomenon. Calculations made on the delta wing vehicle, assuming inviscid equilibrium flow, show a temperature reduction of 250°F over radiation equilibrium values as alluded to above. More recent calculations, however, made since the conclusion of the contractual effort, suggest that for the inviscid non-equilibrium flow conditions less dissociation is expected for the shuttle and a reduction of at least 70°F is more realistic. However, this will be greater when viscous flow effects are considered. Thus, initial calculations appear optimistic, but on the other hand all plasma arc data is conservative because it is obtained in a highly dissociated flow.

From tests conducted by outside sources and VMSC it has been demonstrated that at reuse surface temperatures a molecular environment is orders of magnitude less reactive with the coating than the atomic environment of a plasma arc. For example, 60 cycle exposure (45 hours) to a simulated entry environment peaking at 2600°F produced no measurable coating recession in a molecular environment, while 7.2 hours in a plasma arc at the same temperature produced 0.019 in. erosion. It is mandatory that more realistic and consistent evaluation criteria be established to determine the true life of the coating. It may well be that post coating heat treatment of the coating will not be required to meet mission life requirements if the environment is either predominately molecular or, if low catalytic effects can be included in coating evaluation. This could improve subsurface oxidation mission life beyond the 100-mission requirement. Both heat treated and non heat treated material were evaluated for 100 mission life in a thermal/oxidation environment to establish mission life capability and quantitative differences between the two processes. Results are discussed below.

Thermal/oxidation testing was conducted in a flowing nitrogen/oxygen environment with the partial pressure of the molecular oxygen maintained to average flight levels. The time/temperature profile simulated entry conditions with a peak temperature of 2600°F maintained for 15 minutes and a total cycle time of 45 minutes. A total of 100 missions

(cycles) were imposed on the test specimens. Resultant flexure strengths obtained by VMSC on heat treated material ranged between 12400 psi and 15800 psi with the mean at 14100 psi. Comparison data on non heat treated material averaged 15900 psi with the scatter falling between 14100 psi and 16900 psi. By contrast, average flexure strength obtained by SRI on as-fabricated heat treated material (Table 2-1) was 14200 psi. This indicates that little or no reduction in strength should be realized for the 100-mission service life of the leading edge.

Thickness changes, following 100-mission exposure in the molecular oxygen environment, varied between +0.004 in. and -0.003 in. This is within the estimated accuracy of measurement so it is concluded that essentially no surface recession was experienced.

2.3 FABRICATION

Fabricability of coated RPP components has been clearly demonstrated in Phase II, and in a companion program under contract to North American Rockwell to produce Shuttle fuselage panels. During this period of time three full scale Prototype leading edge assemblies were fabricated and coated (Figures 2-3 and 2-4 show two of the coated units); two wing tip panels were fabricated, one of which was coated (Figure 2-23); and two fuselage panels were fabricated and coated (Figure 2-24). Each of these units were held within allowable tolerances and none exhibited warpage or other gross defects during fabrication that would have precluded their useability.

RPP components are molded and cured much like fiberglass parts. Pyrolysis requires graphite restraining fixtures to prevent warpage of the parts as they undergo a slight thickness shrinkage. No restraint tooling was used during coating, yet all parts retained their shape well without warpage.

None of the large parts were particularly difficult to fabricate and no delaminations were experienced. Only the small wing tip panels presented problems due to the restricted access to the interior for debulking. One of these experienced partial delamination but this was repaired with resin injection. While improvements in tooling and fabrication techniques can be made, the experience gained in the fabrication of these components establishes the fact that quality RPP hardware can be made for the Shuttle.

The structural integrity of these components was established by both loads and thermoelastic tests. A Prototype leading edge was tested to the maximum limit airload condition and two leading edges and seal strip were assembled together in an entry temperature test. No

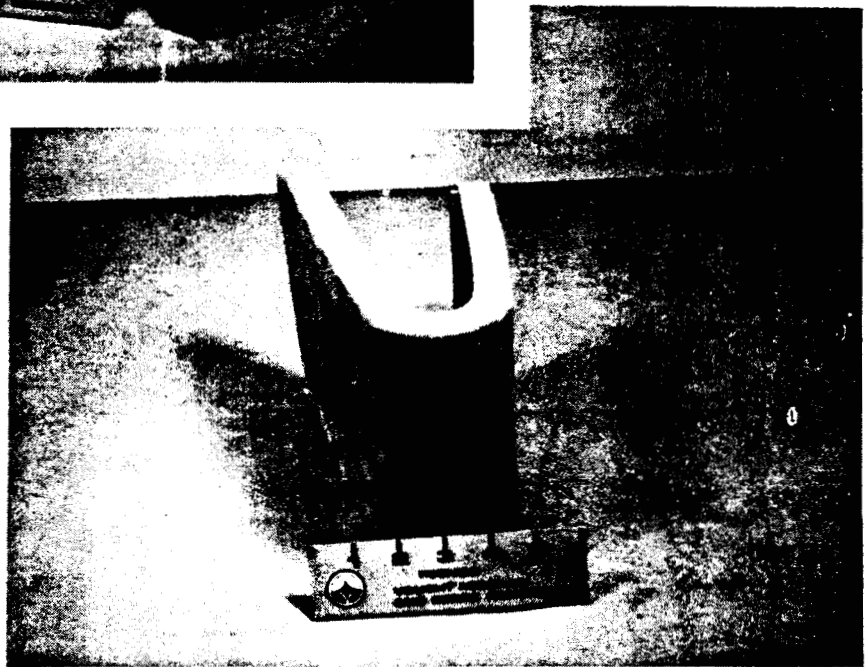


FIGURE 2-23 COATED WING TIP PANEL

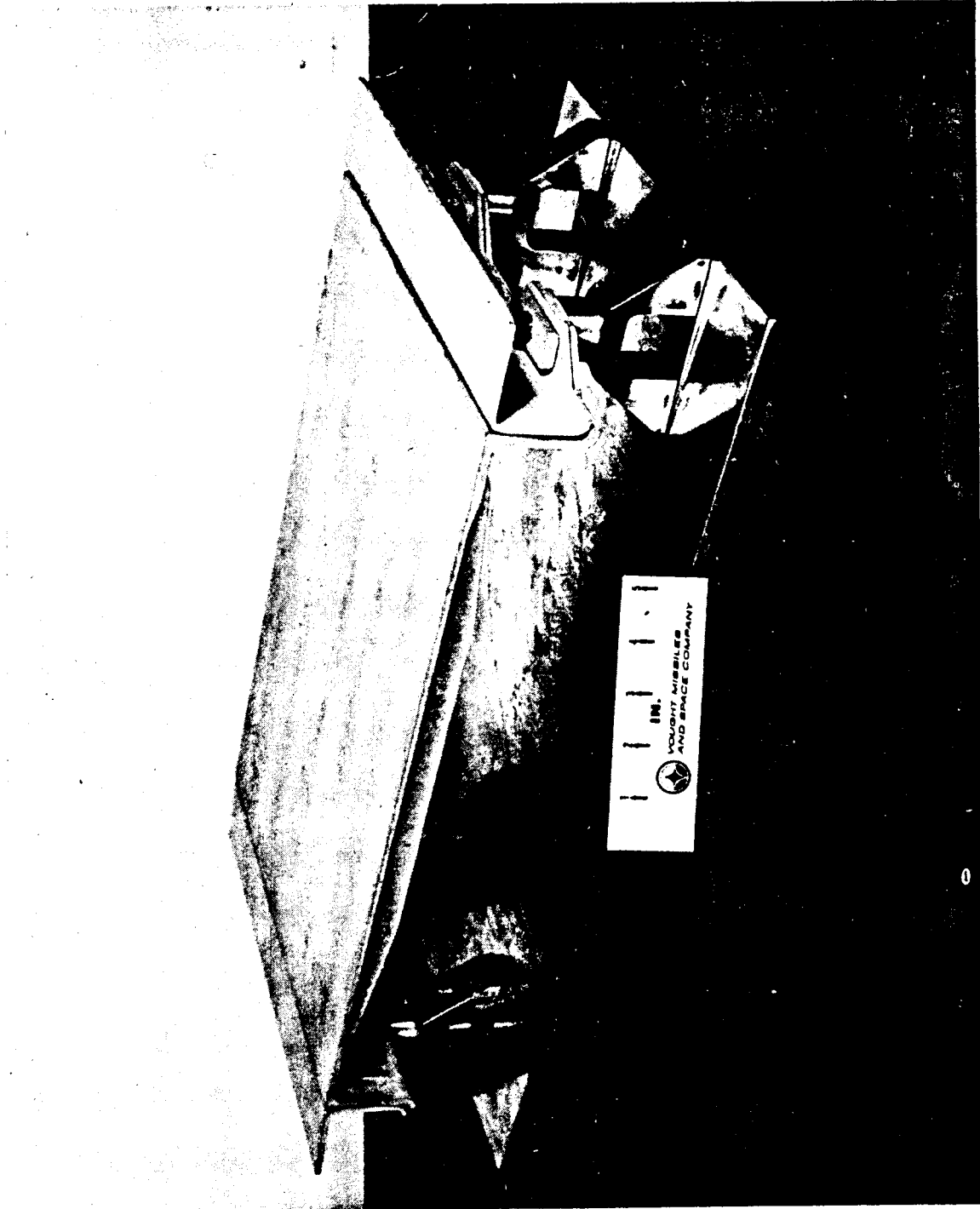


FIGURE 2-24 COATED RPP FUSELAGE PANEL

damage or failure was incurred in either test. North American Rockwell tested a belly panel assembly to 100 cycles of a simulated high cross range entry mission and then loaded the panel to ultimate stress (1.4 x limit load) without failure or damage. The wing tip panels were tested by NASA-MSC in a 10-MW plasma arc facility. The coated wing tip panel has been subjected to 18 separate exposures (2.6 hours) representing 27 equivalent missions, at surface stagnation temperatures of between 2700°F and 2800°F. Coating recession was negligible and, therefore, additional testing is anticipated.

The successful fabrication and test programs for this hardware should promote high confidence in the ability of coated RPP to meet Shuttle requirements.

2.4 CONCLUSIONS

The following summary conclusions are drawn from the work conducted during this study.

- (1) The siliconized RPP system was demonstrated by test to satisfy the representative Shuttle design requirements of Phase II.
- (2) The siliconized RPP system has been found to be the best system examined.
- (3) Coated RPP strength is adequate for lightweight and reliable leading edge designs. No low strength regions have been observed.
- (4) Fatigue properties of coated RPP exceed design requirements and based on test data, degradation following flight level cyclic stresses for the service life of the material should be negligible.
- (5) A 100 mission life of the coating and substrate can be achieved for the Phase II design and environment.
- (6) Coating oxidation/erosion is highly dependent upon the condition of the boundary layer air. If dissociated, low catalycity and lower temperatures will prevail. If molecular, low oxidation rates will exist.

- (7) Fabrication of coated RPP components of good quality can be accomplished and with good tolerance control.
- (8) Leading edges, fabricated from coated RPP and meeting Phase II requirements can be designed to weigh approximately 2 lb/ft² of surface area.
- (9) The hafnium-tantalum coating system has limited mission life (approximately 5 missions) even though it can operate at surface temperatures in the 3500°F to 4000°F range.

3.0 DESIGN SYNTHESIS

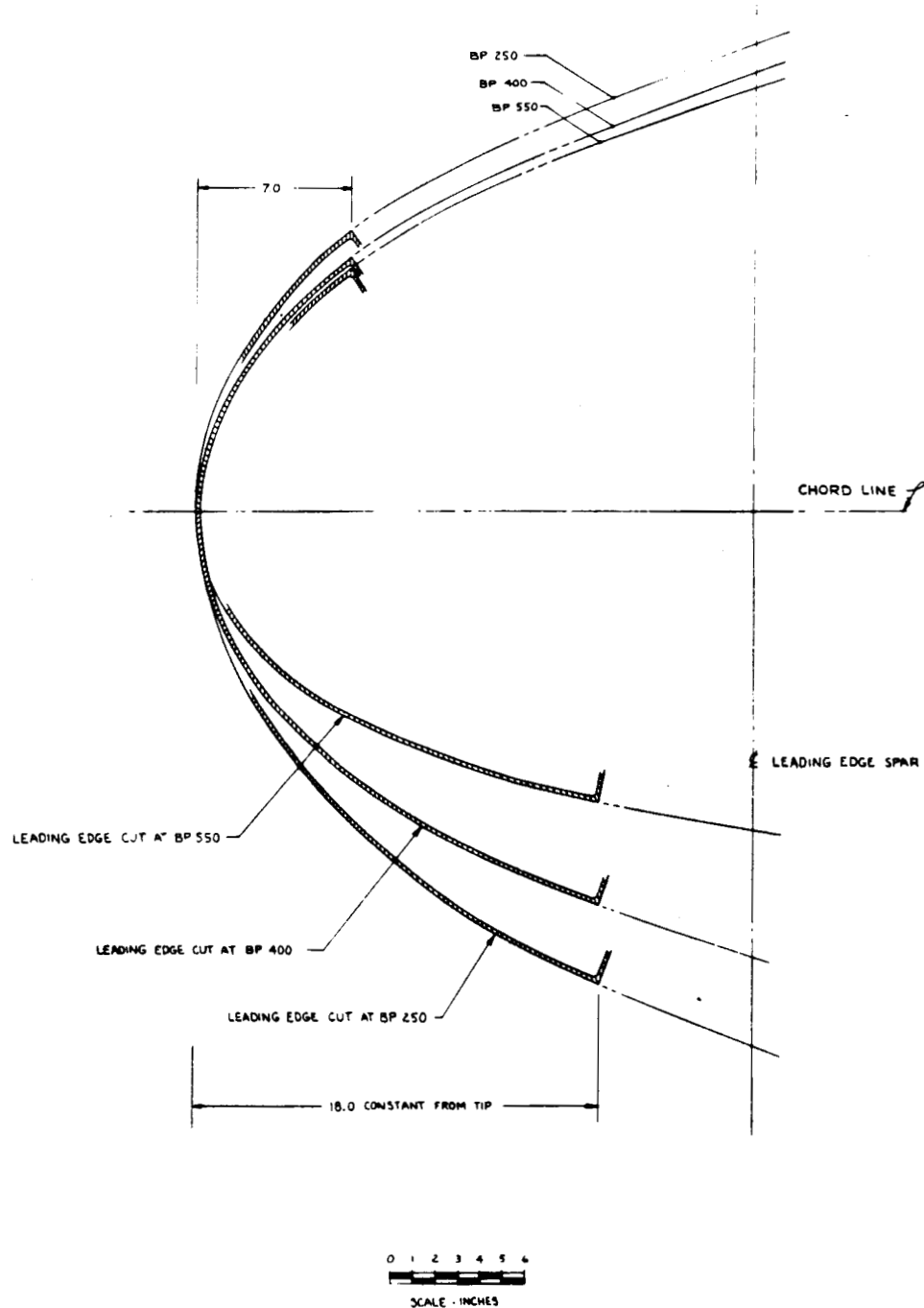
Design synthesis in Phase II has been directed toward re-examination and revision of the Phase I leading edge concept, because of the NASA change of emphasis from the straight wing to the delta winged vehicle. The delta wing leading edge geometry is deeper but has a shorter chord than the straight wing vehicle, and by virtue of the 60° sweep back angle both airload pressures and temperatures are reduced. These benefits result in a more simplified leading edge design, because intercostals are no longer required to stiffen the air load panels, and return flanges on the ribs can be eliminated. This should result in lower fabrication costs, and increased reliability. Optimum leading edge unit weight for a 30 in. segment span remains at 1.8 lb/ft^2 , the same as computed in Phase I and includes an allowance for fasteners, insulators, and a seal strip between leading edge segments. Because of coating facility limitations, the prototype leading edges were designed for 15 in. wide segments. Unit weight did not exceed 2.0 lb/ft^2 even with this non-optimum span.

Design, structural, and thermal analyses, conducted to establish and support the preliminary and prototype leading edge designs, are summarized in this section. All analyses were based on the North American Rockwell (NAR) SSV-161C vehicle configuration, environmental conditions, and flight profiles. Adequacy of the design was demonstrated by pressure testing one of the full scale prototype leading edges and subjecting two leading edge segments to the entry temperature profile.

3.1 DESIGN CRITERIA

Design criteria were specified by Reference (3) to provide consistent and realistic requirements for the design and evaluation of leading edge material and concepts. Significant aspects of the criteria are provided herein. Much of the design criteria is identical to that used in Phase I; however, revised aerodynamic and thermal environments, References (4) and (5), were obtained from NAR for the high L/D Delta Wing Orbiter, SSV-161C, to replace the Phase I design criteria, which were for the low L/D straight wing vehicle.

A baseline airfoil section at 75% exposed semi-span, measured from the fuselage intersection, was selected for design and analysis because (1) it was in the region of maximum interference heating for the noted delta wing vehicle, (2) the selected section was of sufficient size to ensure that design, thermal, and structural analyses are meaningful, (3) root and midspan leading edge geometry were not significantly larger, as shown in Figure 3-1, (4) the cross sectional shape and size were such that full scale prototype units could be built in Phase II with current



NOTES

1. LEADING EDGE SECTIONS ARE CUTS TAKEN NORMAL TO THE 60° SWEEPBACK ANGLE WING LEADING EDGE
2. SECTIONS SHOWN ARE APPROX FOR WING-FUSELAGE INTERSECTION (BP 250)
50% OF EXPOSED SEMI-SPAN (BP 400)
75% OF EXPOSED SEMI-SPAN (BP 550)

TITLE		WING LEADING EDGE SECTION COMPARISON	
DATE		10018	
BY		FIGURE 3-1	
CHECKED BY			
APPROVED BY			
CONTRACT NO.			

FIGURE 3-1 WING LEADING EDGE SECTION COMPARISON

coating facilities, and (5) designs, materials, and analytical techniques developed at the 75% span section should be readily scaleable to other span locations. Current Shuttle configurations are smaller than the SSV-161C vehicle so that the selected baseline geometry is now more representative of the wing root region.

The baseline airfoil geometry is as follows:

NASA 0012-64 airfoil section
 Chord Length = 310 inches
 Front Beam = 24 inches aft, measured normal to leading edge sweep
 Leading Edge Sweep Angle = 60°
 Local Incidence Angle = -5°

Baseline geometry, cut normal to the leading edge sweep line, is shown in Figure 3-2 and is compared with the Phase I baseline geometry for the straight wing vehicle. The delta wing leading edge is deeper but has a shorter chord and large nose radius than the corresponding straight wing leading edge. Upper and lower surface RPP trim lines were established by NAR from wing isotherms and represent the selected transition from RPP leading edge segments to wing panel TPS.

Ultimate factors of safety of 1.4 for boost and orbit conditions, and 1.5 for entry, aircraft flight, and landing were used for design and are in accordance with Phase B shuttle contractor criteria. These factors were assumed applicable for either mechanical stresses imposed from air and inertia loads, or thermoelastic stresses when acting independently. NASA-MSD criteria for combining these sources of stress is as follows, although combined conditions have not been found to be critical.

$$K \sigma_{LM} + K \sigma_{LT} \geq 1.35 \sum \sigma$$

where

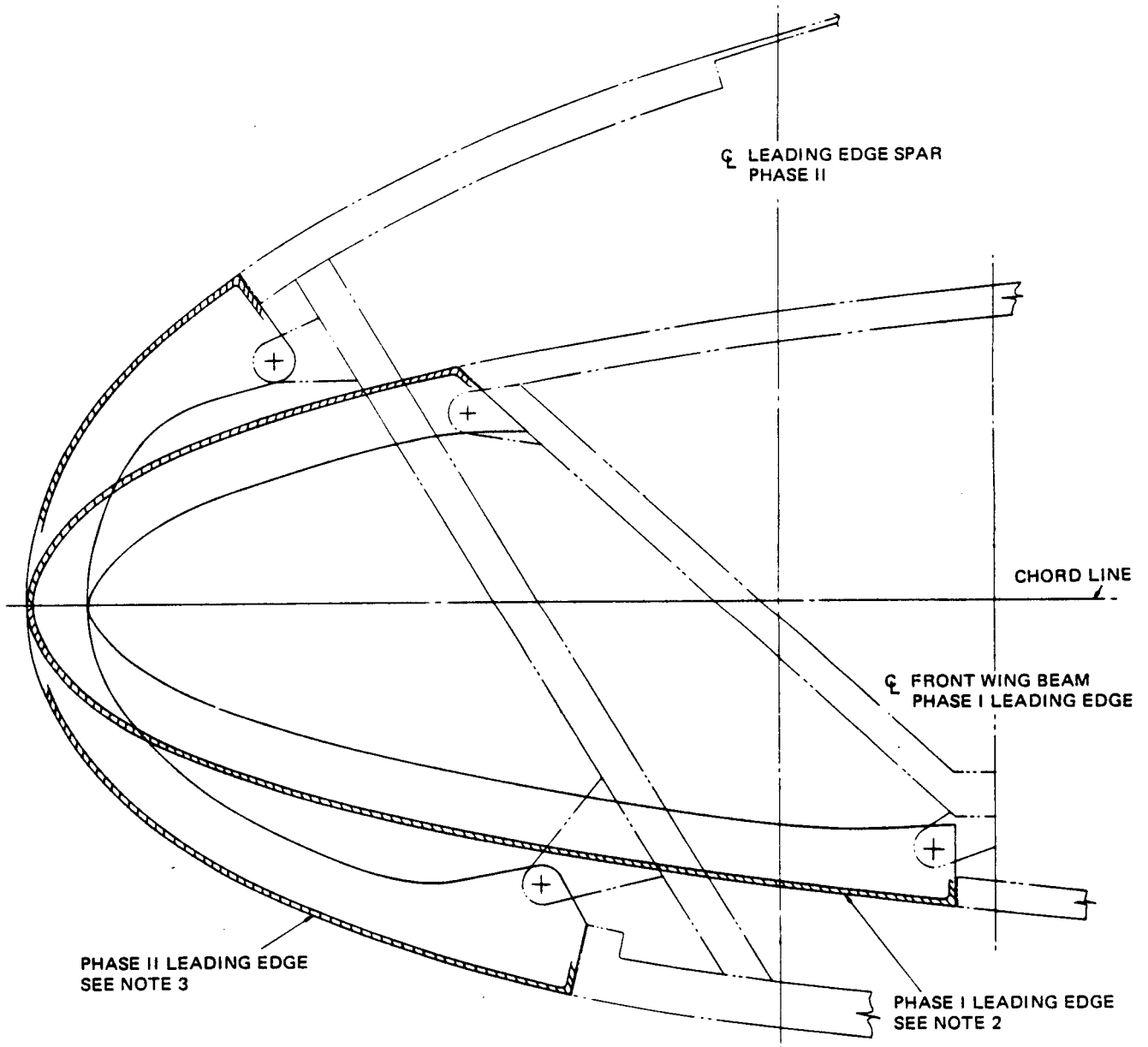
$$\sum \sigma = \text{algebraic sum of } \sigma_{LM} + \sigma_{LT}$$

$K = 1.0$ if stresses are subtractive

$K = 1.5$ if stresses are additive

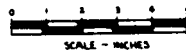
$\sigma_{LM} =$ Limit Mechanical Stress

$\sigma_{LT} =$ Limit Thermal Stress



NOTES:

1. SECTIONS SHOWN ARE THIN NORMAL TO THE WING LEADING EDGE, AND IN THE AREA OF MAXIMUM MEETING.
2. THE LEADING EDGE SECTION OF THE PHASE I STRAIGHT WING SHUTTLE IS CUT AT 25% EXPOSED SEMI-SPIN, 210 DEG CHORD, NACA 0008-04 AIRFOIL.
3. THE LEADING EDGE SECTION SHOWN FOR PHASE II 60° SWEEPBACK ANGULAR DELTA WING SHUTTLE IS CUT AT 75% EXPOSED SEMI-SPIN WITH A 310 DEG CHORD FOR A NACA 0012-64 AIRFOIL.



LEADING EDGE GEOMETRY PHASE I VS PHASE II COMPARISON	
FIGURE 3-2	

FIGURE 3-2 LEADING EDGE GEOMETRY PHASE I VS PHASE II COMPARISON

Margins of safety required at joints were established to be 15% and 50% for shear and tension joints, respectively.

Design trajectories obtained from reference 4 are given in Figures 3-3 and 3-4 for boost and entry, respectively. The high cross range entry trajectory is NAR's No. 935 for the SSV-161C vehicle, which produces maximum total heat load and for the leading edge, maximum heating rate as well. Design pressures and temperatures are based on these trajectories.

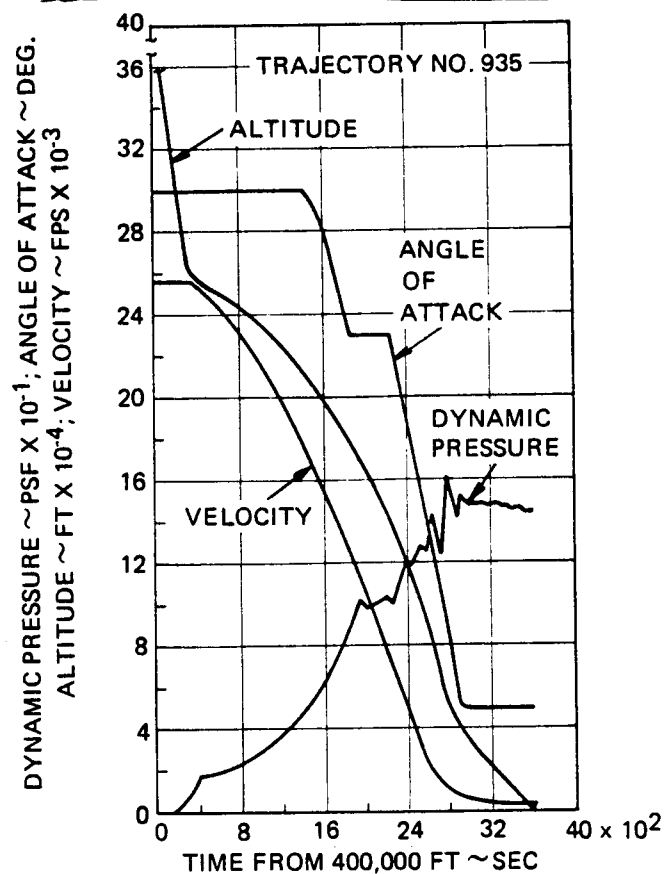
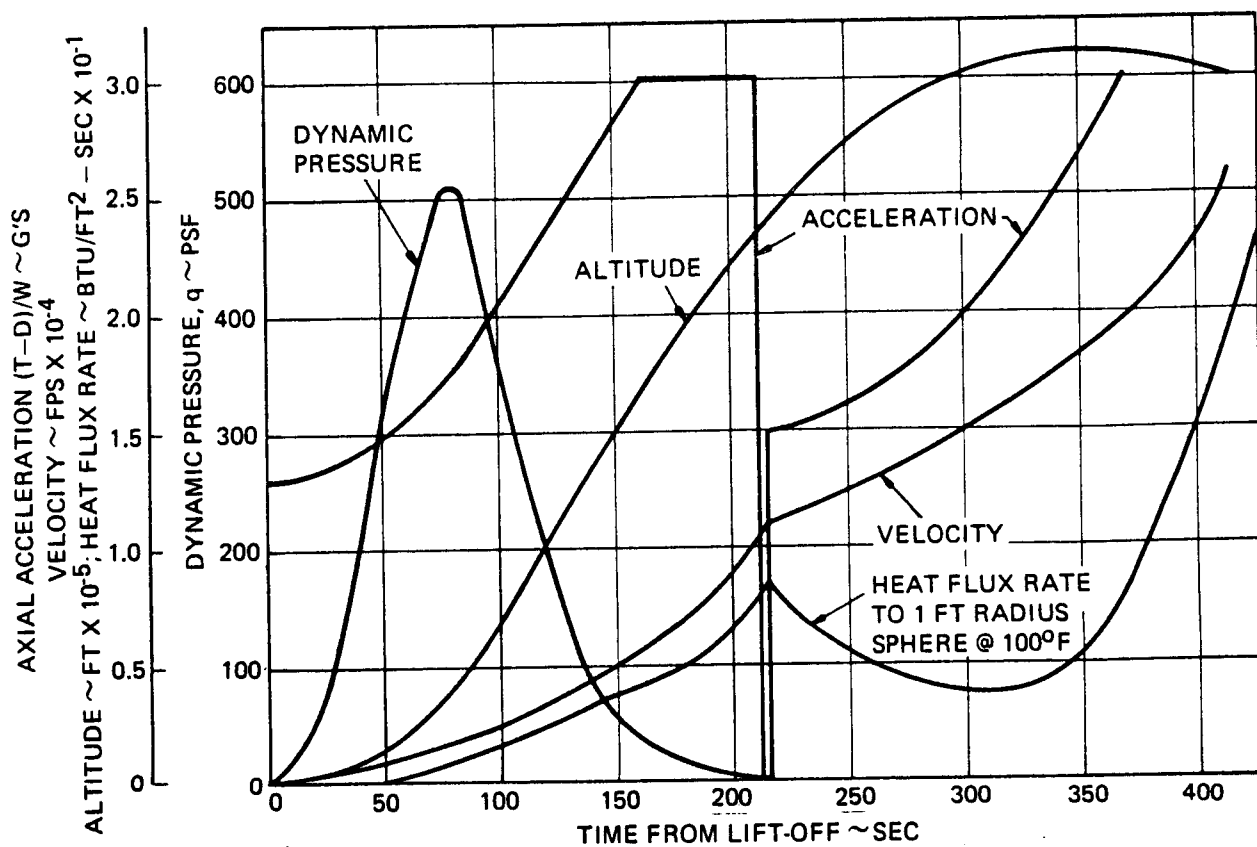
The critical design conditions result from airloads encountered at maximum dynamic pressure during boost. Limit airloads for design are shown in Figure 3-5 for two angles of attack at maximum dynamic pressure. Initially, burst pressure of 1.5 psi was assumed to account for venting lag and resulted in maximum local pressure of 3.4 psi limit. NASA-MSC subsequently revised the design venting pressure lag to 1.0 psi for the prototype leading edge design, which reduced maximum limit pressures by 0.5 psi. The final pressures are shown in Figure 3-5.

Airloads experienced during entry and subsonic cruise maneuvers are shown on Figures 3-6 and 3-7, respectively. The entry pressure loads are for high angle of attack while temperature is relatively high. This produces only 0.2 psi pressure differential on the flat area of the lower panel if internal pressure is assumed at ambient. However NASA-MSC requires that these pressure loads be increased ± 0.5 psi to account for the uncertainty in accurately predicting pressure differentials. Even with the increased pressure loading, the condition is not critical for design.

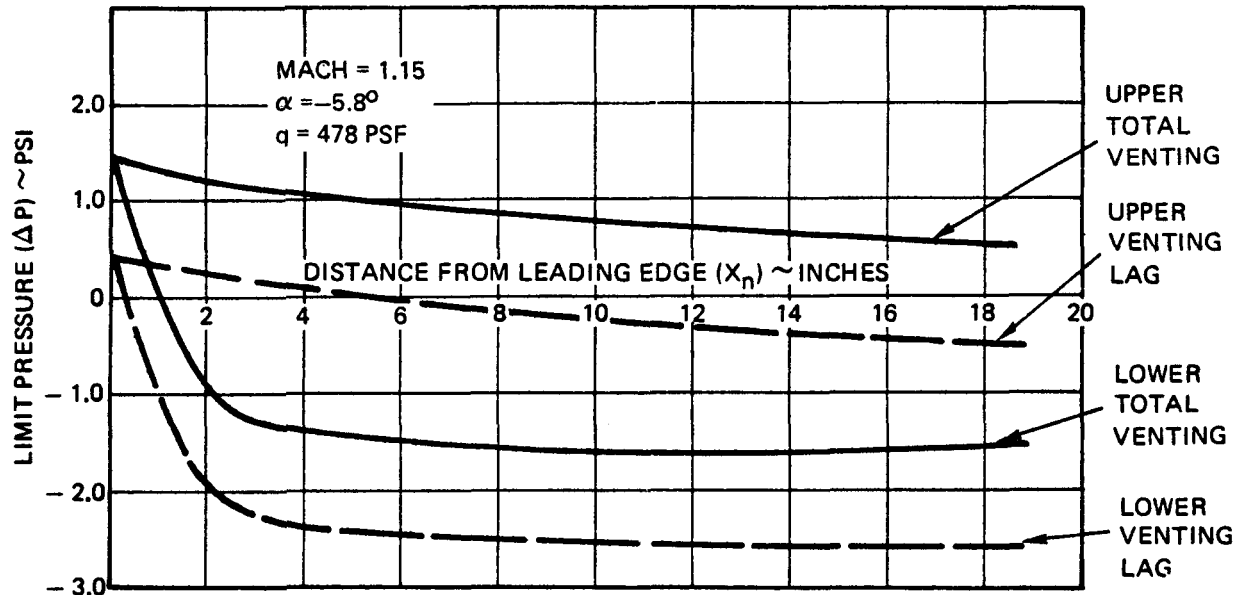
Maximum cruise condition airloads, given on Figure 3-7, are based on maneuver analysis of reference (5) and are for a limit load factor of 2.5 g. Assuming ambient internal conditions, peak pressure differential on the flat area of the lower panel is only 0.15 psi limit, but, as for the entry condition, these were increased by ± 0.5 psi. However, this condition is not critical.

Entry conditions produce the highest temperature and steepest thermal gradients around the leading edge. The local design heat flux ratio around the leading edge is presented in Figure 3-8. The corresponding cross radiation temperature distribution, computed using an emittance of 0.85 and NAR maximum heat load trajectory No. 935, is given in Figure 3-9, and is discussed in Section 3.4.2.

The highest dynamic loads occur during boost at maximum dynamic pressure. The design spectral vibration environment is shown in Figure 3-10. An rms value of 32G acting in each of the mutually perpendicular axes is indicated. Analysis showed this condition to be critical only for a local area of a lug. The maximum acoustic environment of 163 db



NOTE: PRESSURE DUE TO VENTING LAG IS ASSUMED
TO BE - 1.0 PSI (BURST)



ULT = LIMIT X 1.4

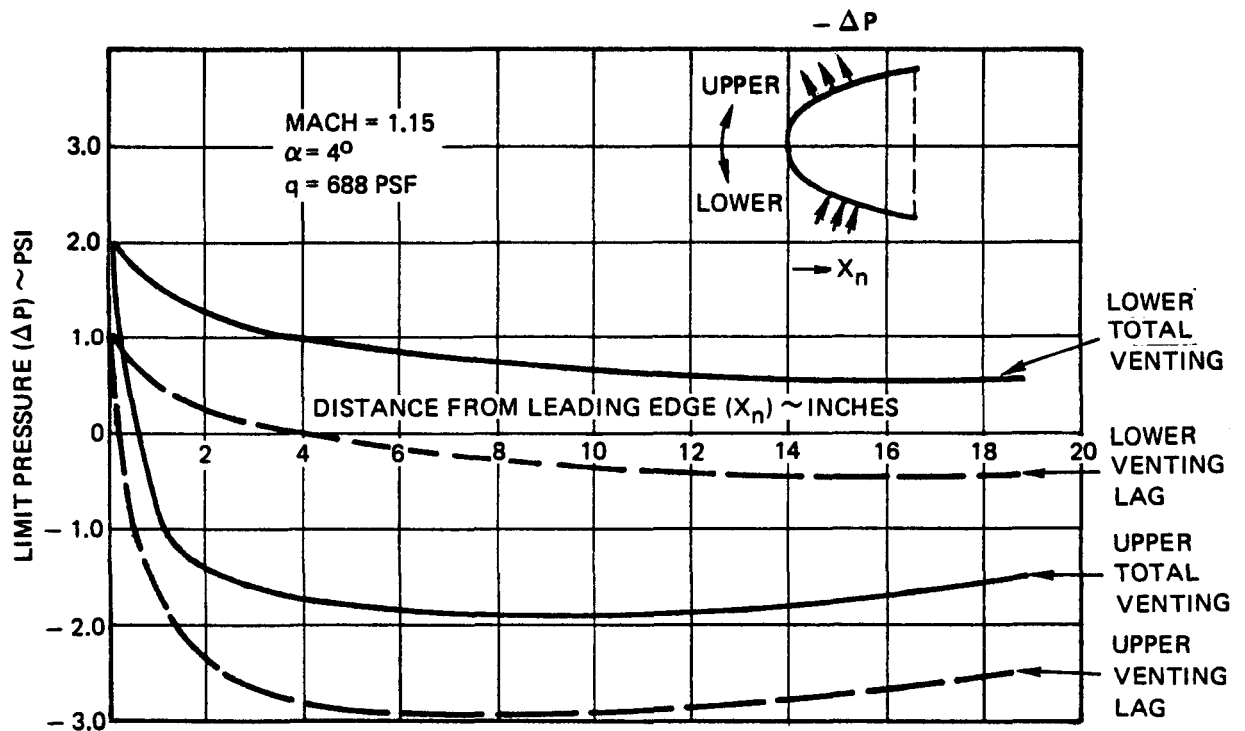


FIGURE 3-5 LIMIT BOOST PRESSURES

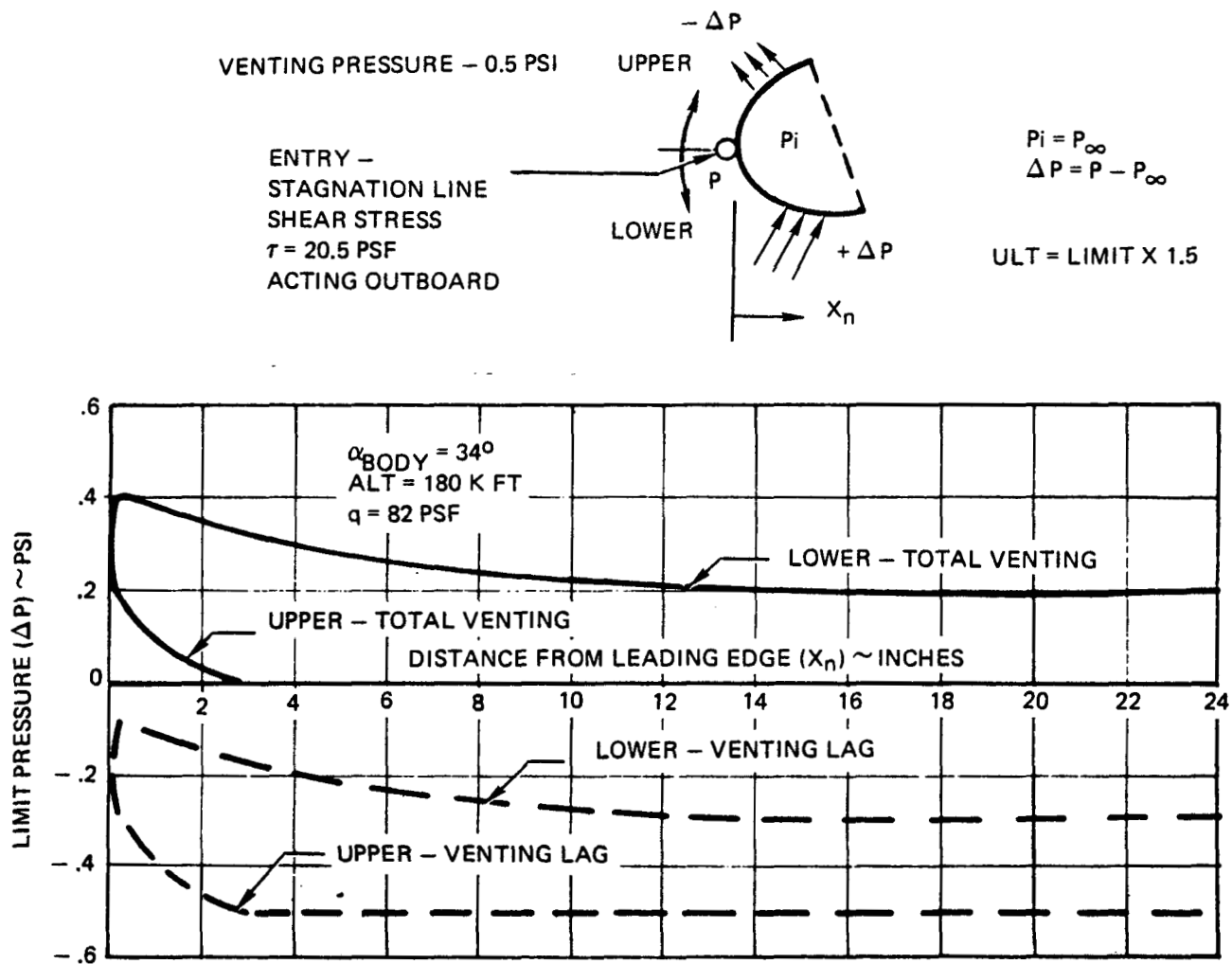


FIGURE 3-6 LIMIT ENTRY PRESSURE MAXIMUM ANGLE OF ATTACK

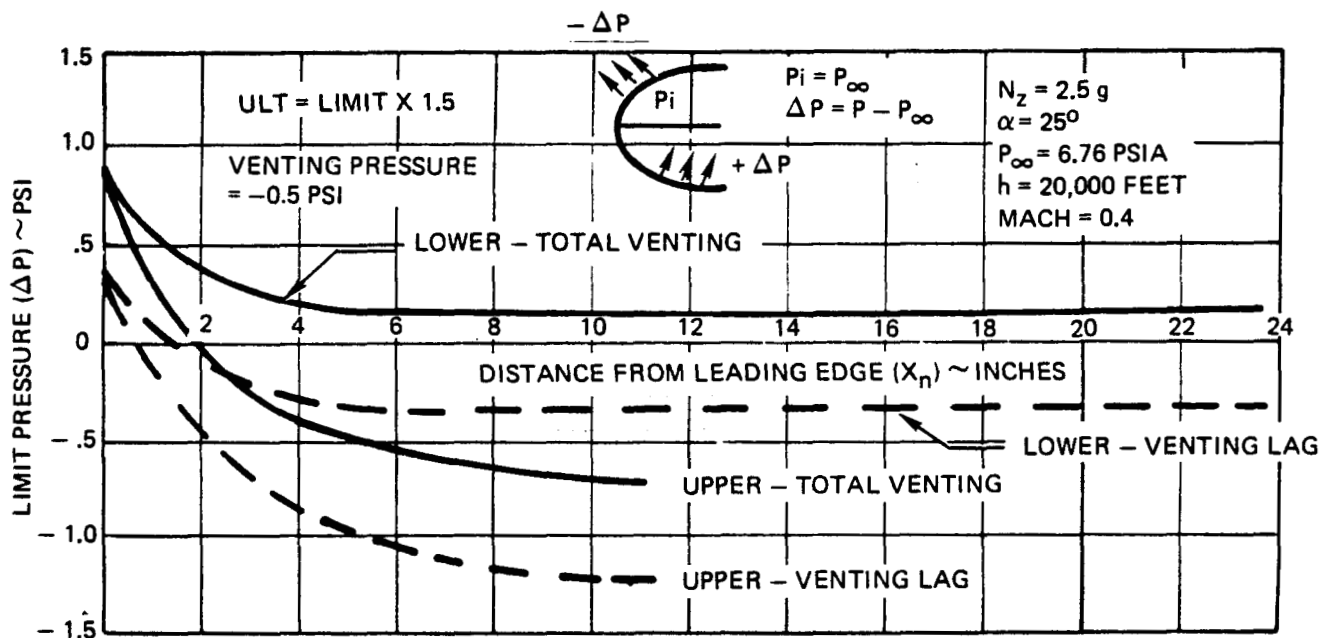


FIGURE 3-7 LIMIT CRUISE CONDITION LOADS

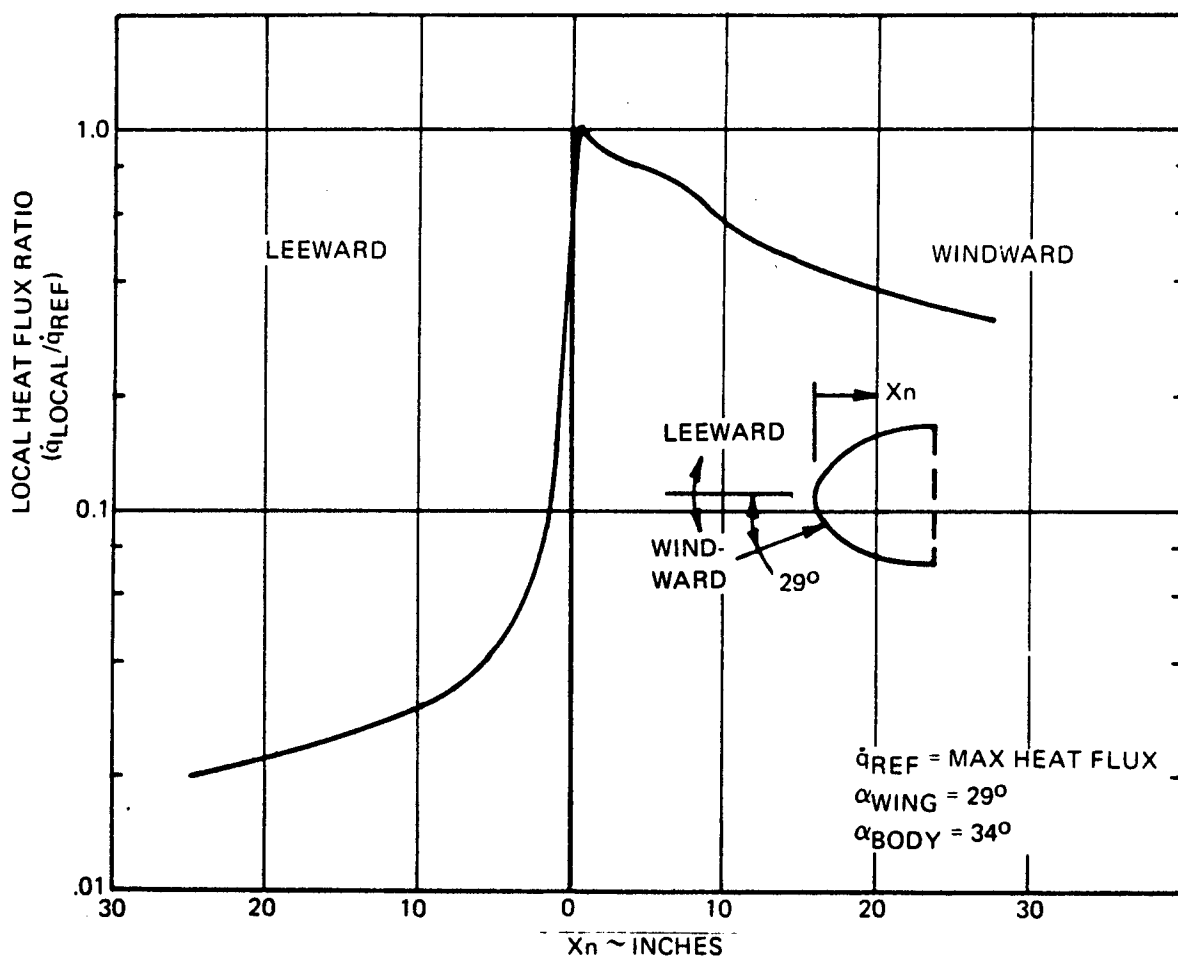


FIGURE 3-8 LOCAL HEAT FLUX RATIO

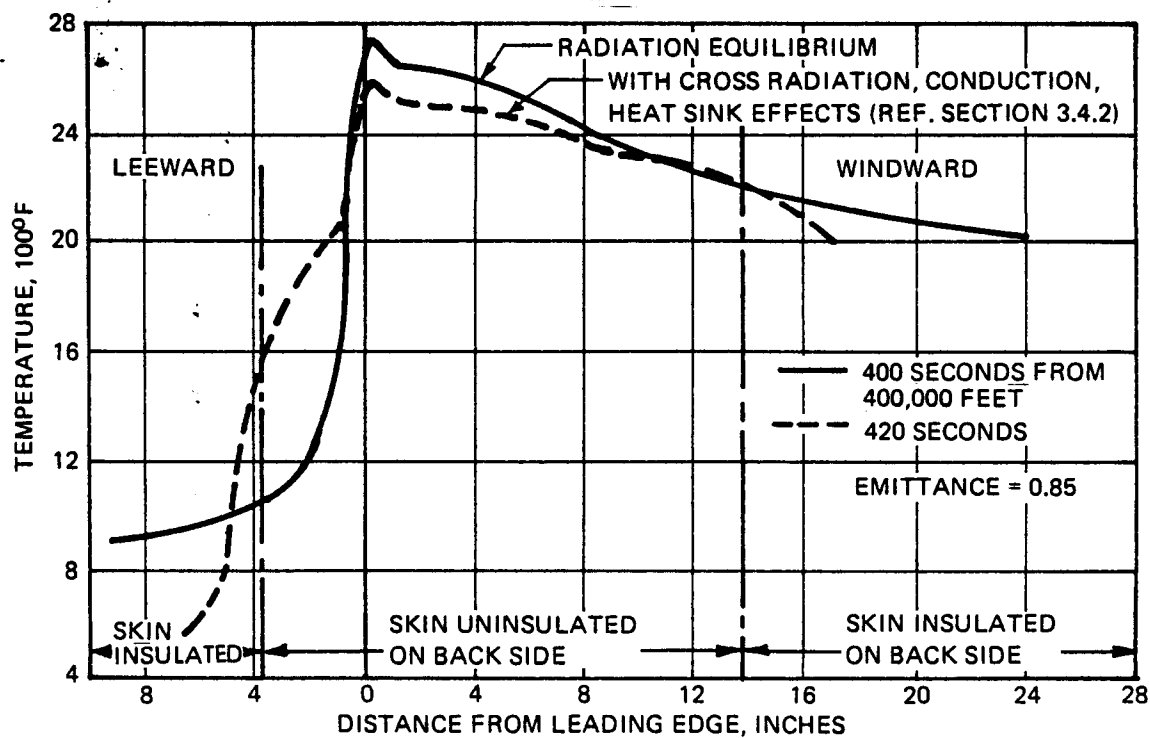


FIGURE 3-9 SHUTTLE LEADING EDGE TEMPERATURES – TIME OF PEAK REENTRY TEMPERATURE

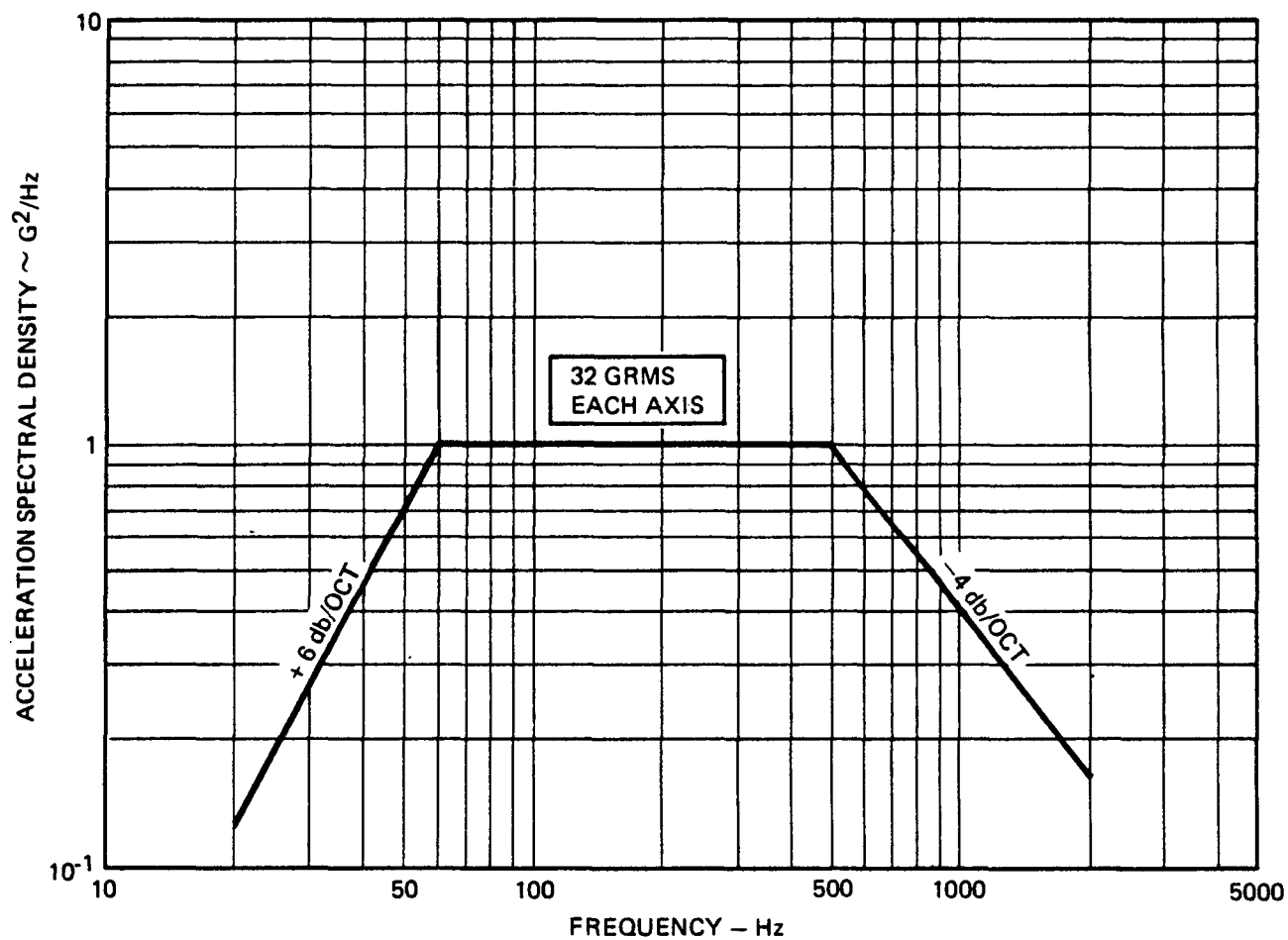


FIGURE 3-10 BOOST PHASE RANDOM VIBRATION

overall sound pressure level can also be experienced during boost. However, this should be less critical than the 32 GRMS vibration input and was not analyzed.

Significant changes between Phase I and Phase II Leading Edge programs are summarized in Table 3-1 to enable a comparison of Phase I and Phase II results.

These design criteria provided requirements for the design of leading edge concepts, which are discussed in the following paragraphs.

3.2 DESIGN CONCEPT

The basic design concept for the leading edge, shown in Figure 3-11, is the same as that developed in Phase I. Essentially, it consists of multiple segments fabricated as solid laminates with integrally formed ribs at the edges of each panel segment. Four lug type joints tie to the wing support structure. The thin solid laminate design and heatshield location promotes internal thermal cross radiation to reduce both peak stagnation temperature (by 148°F) and thermal gradients/stresses (by 37%). The upper surface chord is abbreviated to reduce RPP weight, and more importantly, to provide access to the internal heatshield and tie down bolts without having to provide entry through the main wing box. Gaps between adjacent leading edge segments are covered by a "T" section seal strip. This seal approach is designed to reduce flow of boundary layer gases into the leading edge cavity. Tests must be conducted to establish firm sealing requirements, or gap allowances, and establish acceptability of the proposed design. These are planned for Phase III.

Structural analysis showed that for the lower pressure loads experienced by the delta winged vehicle compared to the straight winged vehicle, it was feasible, by thickening the lower surface skin slightly, to remove the intercostals used in the Phase I concept design (Reference 2). While this may result in a small weight penalty, it is believed to be more than offset by increased reliability and reduced costs anticipated through the elimination of intercostals either integrally formed or bonded to the skin panel. The lower design loads have also permitted removal of the return flange on the airload ribs that was believed necessary in the Phase I design. This modification improves fabricability, simplifies tooling and should result in reduced costs.

The preliminary design for the delta wing vehicle leading edge (Figure 3-11) is segmented to provide expansion gaps for relief of thermal stresses that would result from differential expansion of the hot leading edge and cool wing structure. Each segment is comprised of five

TABLE 3-1

CHANGES BETWEEN PHASE I AND PHASE II DESIGN CRITERIA

Item	Phase I	Phase II	Effect on Leading Edge Design
Vehicle	Straight Wing, Low L/D	Delta Wing, High L/D	a) Longer duration of maximum temperatures b) Increased insulation requirements c) Reduced aerodynamic loads d) Decreased geometry variations along span
Design, Wing Location	25% Exposed Semi-Span, 30 in. chord	75% Exposed Semi-Span, 15 in. chord	a) Structurally more efficient b) Simplified design
Boost Vent Pressure	0 psi	0-1.0 psi burst (venting lag)	None
Boost Pressure	5.9 psi limit	2.9 psi limit (includes venting lag)	Reduced airloads, and thus weight, even though a venting lag has been added.
Random Vibration	6.3 g RMS	32 g RMS	May be significant only to lug region.

integrally fabricated structural elements; airload panel, two ribs with integral attachment lugs, and an upper and lower cross beam at the aft edges of the airload panel. These cross beams serve to support the airload panel against possible flutter, reduce airload panel thickness and weight, and stiffen the lug regions for side load. Wing interface geometry shown in Figure 3-11 is typical of support structure that could be employed to attach the leading edge to the wing. Details of the cloth layup for the basic integrally fabricated structural elements is illustrated by the design shown in Figure 3-12.

Seperate "floating" seal strips cover the gap between leading edge segments and prevent the direct flow of boundary layer air into the leading edge cavity. The seal strips are anchored to the same fittings that support each leading edge segment. There are a number of advantages to this approach, among them being: (1) fabrication costs are minimized by not having to fabricate the seal strip integrally with the panel, (2) cost of bonding and riveting a separately fabricated seal strip to a leading edge segment is eliminated, (3) reliability should be increased by elimination of a bond joint, (4) the strength of the skin panel rib flange radius is not degraded by using some of the plies to form an integrally fabricated seal, (5) it is believed that the floating seal would be more compliant to differential deflections of adjacent sections, thus improving sealing, and (6) the seal strip could be designed as a retainer strap to provide some degree of redundant support to a leading edge segment in the event of lug failure or rib cracking. This would be accomplished by using the seal to transfer load from the damaged segment to an adjacent segment.

Trailing edge seals to overlap the thermal protection system behind the leading edge segments are shown as an alternate approach if sealing becomes necessary at this point. These seals are fabricated as "T" sections and are subsequently bonded and riveted to the leading edge panel, while in the as-molded state. The rivets serve to hold the seal in place during further processing and act to prevent or terminate peeling in the event of bond failure. Fabrication feasibility has been demonstrated on the prototype leading edges, although additional development is believed required to produce a bond free from possible delamination.

As indicated above, the design concept of the leading edge permits integral fabrication of ribs and cross beams with the airload panel. This ensures that transfer of load from the skin panel to ribs or beams is through the continuity of each ply rather than through a seperate joint. This should enhance reliability and reduce cost. Differences in thickness requirements between upper and lower skin panels are accommodated by cutting a "window" in several plies where reduced thickness is permissible at the upper surface.

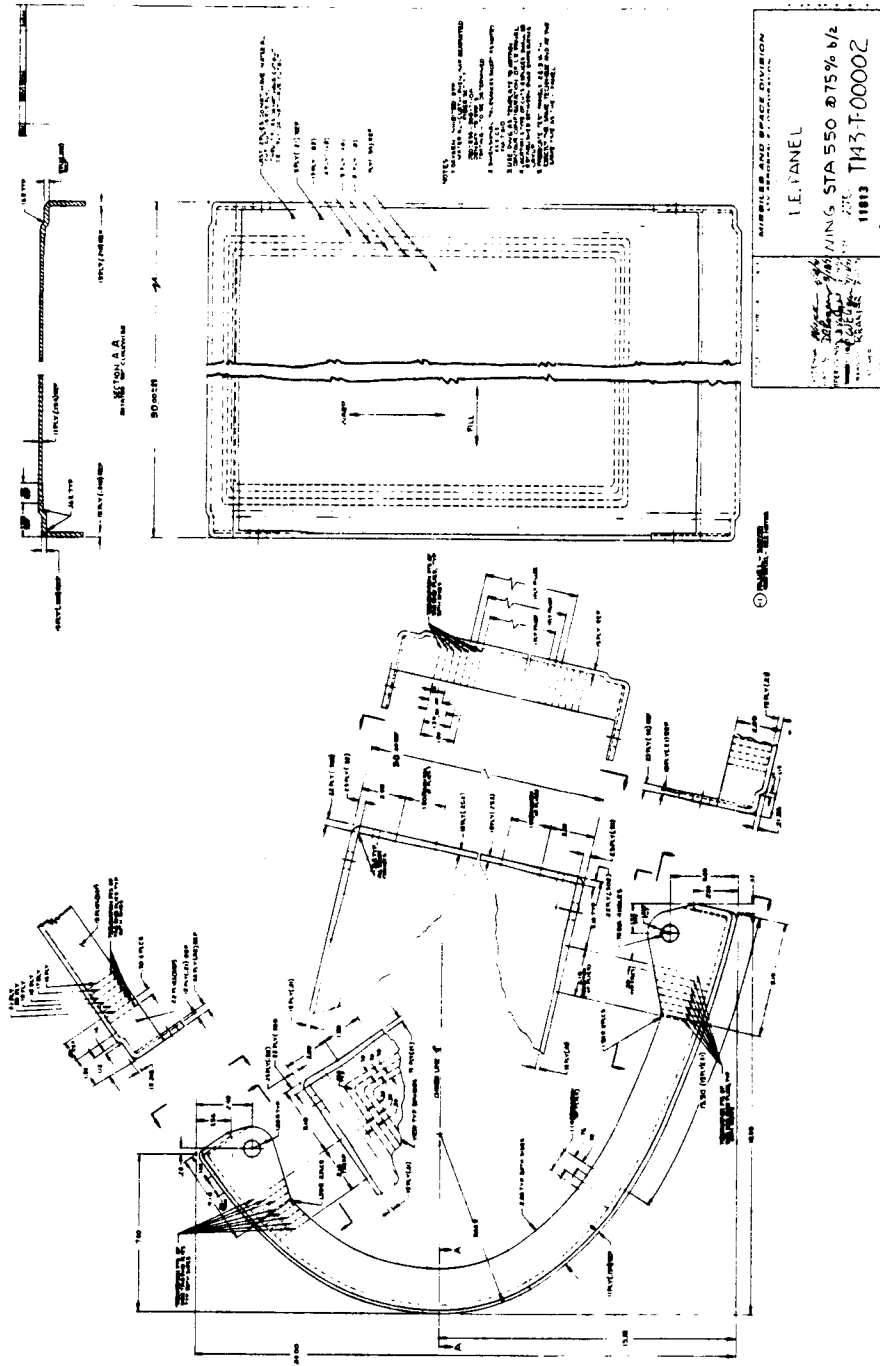


FIGURE 3-12 PRELIMINARY LEADING EDGE DESIGN

The inboard lugs of each leading edge segment are fixed against side movement, while the outboard lugs are free to slide on the insulators to accommodate thermal expansion. The thickened lug areas together with stiffened beam and rib intersections prevent rolling or jamming of the lug during thermal expansion. Further, very high margins are designed into the lugs to enhance reliability. The seal strip is trapped against the fixed lug of each leading edge segment and is not free to move spanwise. As noted previously, this can be designed as a redundant leading edge segment support.

Fused silica or alumina insulation washers have been assumed to protect the steel bolt and wing support fitting from high temperatures conducted from the skin. However, current thermal analyses show that the soft Dynaflex type heat shield insulation, which is wrapped around each joint, is sufficient to maintain metal temperatures to within acceptable limits without the use of hard insulators. It is believed, however, that some form of bushing will be required in the RPP to permit match drilling of the joints on either assembly or subassembly to offset tolerance accumulation during fabrication. The bushings may be either metallic or ceramic.

Structural analysis has shown that optimum segment weight occurs at a 30 inch segment span and this has therefore been selected for baseline preliminary design. This may vary in the future as other considerations such as cost, acoustic or vibration loads, and reliability are considered further.

3.3 PROTOTYPE DESIGN

Three full scale prototype leading edges were designed and fabricated on the program, two of which were tested to simulated design temperature and load environments. The initial purpose of these prototype units was to demonstrate full scale fabrication potential. However, by virtue of recent coating facility additions, VMSC was able to essentially double the size of the subscale (8 in. x 9 in. x 14 in.) units initially proposed, so that full scale segments could be fabricated. At the recommendation of NASA, these units, which have a segment span of 15 in. to fit the coating facility were designed as full scale components assuming 15 in. wide segments are employed on the vehicle. While this size does not represent the optimum span for minimum weight, unit weight is still a respectable 2 lb/ft².

The prototype design shown in Figures 3-13 and 3-14 follows closely the preliminary design discussed in Section 3.2. The main differences are the segment span as already noted, and the difference in boost condition venting pressure, which was 0.5 psi lower for the prototype design (Section 3.1). These two changes resulted in a design that is

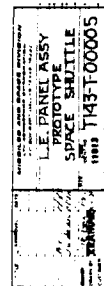


FIGURE 3-13 PROTOTYPE LEADING EDGE ASSEMBLY

9-55

REV	DATE	BY	CHKD	APP'D
1	10/10/54	W. J. B.		
2	11/10/54	W. J. B.		
3	12/10/54	W. J. B.		
4	1/10/55	W. J. B.		
5	2/10/55	W. J. B.		
6	3/10/55	W. J. B.		
7	4/10/55	W. J. B.		
8	5/10/55	W. J. B.		
9	6/10/55	W. J. B.		
10	7/10/55	W. J. B.		
11	8/10/55	W. J. B.		
12	9/10/55	W. J. B.		
13	10/10/55	W. J. B.		
14	11/10/55	W. J. B.		
15	12/10/55	W. J. B.		
16	1/10/56	W. J. B.		
17	2/10/56	W. J. B.		
18	3/10/56	W. J. B.		
19	4/10/56	W. J. B.		
20	5/10/56	W. J. B.		
21	6/10/56	W. J. B.		
22	7/10/56	W. J. B.		
23	8/10/56	W. J. B.		
24	9/10/56	W. J. B.		
25	10/10/56	W. J. B.		
26	11/10/56	W. J. B.		
27	12/10/56	W. J. B.		
28	1/10/57	W. J. B.		
29	2/10/57	W. J. B.		
30	3/10/57	W. J. B.		
31	4/10/57	W. J. B.		
32	5/10/57	W. J. B.		
33	6/10/57	W. J. B.		
34	7/10/57	W. J. B.		
35	8/10/57	W. J. B.		
36	9/10/57	W. J. B.		
37	10/10/57	W. J. B.		
38	11/10/57	W. J. B.		
39	12/10/57	W. J. B.		
40	1/10/58	W. J. B.		
41	2/10/58	W. J. B.		
42	3/10/58	W. J. B.		
43	4/10/58	W. J. B.		
44	5/10/58	W. J. B.		
45	6/10/58	W. J. B.		
46	7/10/58	W. J. B.		
47	8/10/58	W. J. B.		
48	9/10/58	W. J. B.		
49	10/10/58	W. J. B.		
50	11/10/58	W. J. B.		
51	12/10/58	W. J. B.		
52	1/10/59	W. J. B.		
53	2/10/59	W. J. B.		
54	3/10/59	W. J. B.		
55	4/10/59	W. J. B.		
56	5/10/59	W. J. B.		
57	6/10/59	W. J. B.		
58	7/10/59	W. J. B.		
59	8/10/59	W. J. B.		
60	9/10/59	W. J. B.		
61	10/10/59	W. J. B.		
62	11/10/59	W. J. B.		
63	12/10/59	W. J. B.		
64	1/10/60	W. J. B.		
65	2/10/60	W. J. B.		
66	3/10/60	W. J. B.		
67	4/10/60	W. J. B.		
68	5/10/60	W. J. B.		
69	6/10/60	W. J. B.		
70	7/10/60	W. J. B.		
71	8/10/60	W. J. B.		
72	9/10/60	W. J. B.		
73	10/10/60	W. J. B.		
74	11/10/60	W. J. B.		
75	12/10/60	W. J. B.		
76	1/10/61	W. J. B.		
77	2/10/61	W. J. B.		
78	3/10/61	W. J. B.		
79	4/10/61	W. J. B.		
80	5/10/61	W. J. B.		
81	6/10/61	W. J. B.		
82	7/10/61	W. J. B.		
83	8/10/61	W. J. B.		
84	9/10/61	W. J. B.		
85	10/10/61	W. J. B.		
86	11/10/61	W. J. B.		
87	12/10/61	W. J. B.		
88	1/10/62	W. J. B.		
89	2/10/62	W. J. B.		
90	3/10/62	W. J. B.		
91	4/10/62	W. J. B.		
92	5/10/62	W. J. B.		
93	6/10/62	W. J. B.		
94	7/10/62	W. J. B.		
95	8/10/62	W. J. B.		
96	9/10/62	W. J. B.		
97	10/10/62	W. J. B.		
98	11/10/62	W. J. B.		
99	12/10/62	W. J. B.		
100	1/10/63	W. J. B.		
101	2/10/63	W. J. B.		
102	3/10/63	W. J. B.		
103	4/10/63	W. J. B.		
104	5/10/63	W. J. B.		
105	6/10/63	W. J. B.		
106	7/10/63	W. J. B.		
107	8/10/63	W. J. B.		
108	9/10/63	W. J. B.		
109	10/10/63	W. J. B.		
110	11/10/63	W. J. B.		
111	12/10/63	W. J. B.		
112	1/10/64	W. J. B.		
113	2/10/64	W. J. B.		
114	3/10/64	W. J. B.		
115	4/10/64	W. J. B.		
116	5/10/64	W. J. B.		
117	6/10/64	W. J. B.		
118	7/10/64	W. J. B.		
119	8/10/64	W. J. B.		
120	9/10/64	W. J. B.		
121	10/10/64	W. J. B.		
122	11/10/64	W. J. B.		
123	12/10/64	W. J. B.		
124	1/10/65	W. J. B.		
125	2/10/65	W. J. B.		
126	3/10/65	W. J. B.		
127	4/10/65	W. J. B.		
128	5/10/65	W. J. B.		
129	6/10/65	W. J. B.		
130	7/10/65	W. J. B.		
131	8/10/65	W. J. B.		
132	9/10/65	W. J. B.		
133	10/10/65	W. J. B.		
134	11/10/65	W. J. B.		
135	12/10/65	W. J. B.		
136	1/10/66	W. J. B.		
137	2/10/66	W. J. B.		
138	3/10/66	W. J. B.		
139	4/10/66	W. J. B.		
140	5/10/66	W. J. B.		
141	6/10/66	W. J. B.		
142	7/10/66	W. J. B.		
143	8/10/66	W. J. B.		
144	9/10/66	W. J. B.		
145	10/10/66	W. J. B.		
146	11/10/66	W. J. B.		
147	12/10/66	W. J. B.		
148	1/10/67	W. J. B.		
149	2/10/67	W. J. B.		
150	3/10/67	W. J. B.		
151	4/10/67	W. J. B.		
152	5/10/67	W. J. B.		
153	6/10/67	W. J. B.		
154	7/10/67	W. J. B.		
155	8/10/67	W. J. B.		
156	9/10/67	W. J. B.		
157	10/10/67	W. J. B.		
158	11/10/67	W. J. B.		
159	12/10/67	W. J. B.		
160	1/10/68	W. J. B.		
161	2/10/68	W. J. B.		
162	3/10/68	W. J. B.		
163	4/10/68	W. J. B.		
164	5/10/68	W. J. B.		
165	6/10/68	W. J. B.		
166	7/10/68	W. J. B.		
167	8/10/68	W. J. B.		
168	9/10/68	W. J. B.		
169	10/10/68	W. J. B.		
170	11/10/68	W. J. B.		
171	12/10/68	W. J. B.		
172	1/10/69	W. J. B.		
173	2/10/69	W. J. B.		
174	3/10/69	W. J. B.		
175	4/10/69	W. J. B.		
176	5/10/69	W. J. B.		
177	6/10/69	W. J. B.		
178	7/10/69	W. J. B.		
179	8/10/69	W. J. B.		
180	9/10/69	W. J. B.		
181	10/10/69	W. J. B.		
182	11/10/69	W. J. B.		
183	12/10/69	W. J. B.		
184	1/10/70	W. J. B.		
185	2/10/70	W. J. B.		
186	3/10/70	W. J. B.		
187	4/10/70	W. J. B.		
188	5/10/70	W. J. B.		
189	6/10/70	W. J. B.		
190	7/10/70	W. J. B.		
191	8/10/70	W. J. B.		
192	9/10/70	W. J. B.		
193	10/10/70	W. J. B.		
194	11/10/70	W. J. B.		
195	12/10/70	W. J. B.		
196	1/10/71	W. J. B.		
197	2/10/71	W. J. B.		
198	3/10/71	W. J. B.		
199	4/10/71	W. J. B.		
200	5/10/71	W. J. B.		
201	6/10/71	W. J. B.		
202	7/10/71	W. J. B.		
203	8/10/71	W. J. B.		
204	9/10/71	W. J. B.		
205	10/10/71	W. J. B.		
206	11/10/71	W. J. B.		
207	12/10/71	W. J. B.		
208	1/10/72	W. J. B.		
209	2/10/72	W. J. B.		
210	3/10/72	W. J. B.		
211	4/10/72	W. J. B.		
212	5/10/72	W. J. B.		
213	6/10/72	W. J. B.		
214	7/10/72	W. J. B.		
215	8/10/72	W. J. B.		
216	9/10/72	W. J. B.		
217	10/10/72	W. J. B.		
218	11/10/72	W. J. B.		
219	12/10/72	W. J. B.		
220	1/10/73	W. J. B.		
221	2/10/73	W. J. B.		
222	3/10/73	W. J. B.		
223	4/10/73	W. J. B.		
224	5/10/73	W. J. B.		
225	6/10/73	W. J. B.		
226	7/10/73	W. J. B.		
227	8/10/73	W. J. B.		
228	9/10/73	W. J. B.		
229	10/10/73	W. J. B.		
230	11/10/73	W. J. B.		
231	12/10/73	W. J. B.		
232	1/10/74	W. J. B.		
233	2/10/74	W. J. B.		
234	3/10/74	W. J. B.		
235	4/10/74	W. J. B.		
236	5/10/74	W. J. B.		
237	6/10/74	W. J. B.		
238	7/10/74	W. J. B.		
239	8/10/74	W. J. B.		
240	9/10/74	W. J. B.		
241	10/10/74	W. J. B.		
242	11/10/74	W. J. B.		
243	12/10/74	W. J. B.		
244	1/10/75	W. J. B.		
245	2/10/75	W. J. B.		
246	3/10/75	W. J. B.		
247	4/10/75	W. J. B.		
248	5/10/75	W. J. B.		
249	6/10/75	W. J. B.		
250	7/10/75	W. J. B.		
251	8/10/75	W. J. B.		
252	9/10/75	W. J. B.		
253	10/10/75	W. J. B.		
254	11/10/75	W. J. B.		
255	12/10/75	W. J. B.		
256	1/10/76	W. J. B.		
257	2/10/76	W. J. B.		
258	3/10/76	W. J. B.		
259	4/10/76	W. J. B.		
260	5/10/76	W. J. B.		
261	6/10/76	W. J. B.		
262	7/10/76	W. J. B.		
263	8/10/76	W. J. B.		
264	9/10/76	W. J. B.		
265	10/10/76	W. J. B.		
266	11/10/76	W. J. B.		
267	12/10/76	W. J. B.		
268	1/10/77	W. J. B.		
269	2/10/77	W. J. B.		
270	3/10/77	W. J. B.		
271	4/10/77	W. J. B.		
272	5/10/77	W. J. B.		
273	6/10/77	W. J. B.		
274	7/10/77	W. J. B.		
275	8/10/77	W. J. B.		
276	9/10/77	W. J. B.		
277	10/10/77	W. J. B.		
278	11/10/77	W. J. B.		
279	12/10/77	W. J. B.		
280	1/10/78	W. J. B.		
281	2/10/78	W. J. B.		

basically a 12 ply layup with patch doublers on the lower flattened surface to stiffen that region and reduce deflection. The ribs are profiled in an effort to more closely match computed bending moment distributions although a slightly higher margin exists in the maximum compression section (lower portion) of the rib than the maximum tension or upper portion (Section 3.5.2).

Trailing edge overlap seals are bonded and riveted to the trailing edge beams to demonstrate the ability to fabricate such a configuration. Since the trailing edge seals are bonded to the beams, the seals become an integral part of the structure. This produces beams that are considerably stronger than required and high margins result. The "T" configuration of the seal provides two bonding surfaces to provide a strong joint with a minimum tendency toward peeling; thus, adding reliability to the joint. Likewise, rivets are used to prevent peeling as well as to provide clamping during RPP processing.

The leading edge panel assembly is shown in Figure 3-13. Overall dimensions are 27 in. x 12.5 in. x 15 in. exclusive of the curved seal strip. The contour was established by cutting the NASA 0012-64 airfoil section normal to the 60° sweep angle. Detail layup is similar to Figure 3-12. Note that the lug regions are strengthened by overlapping corner plies in the fashion illustrated on Figure 3-11. This boxed corner adds side stiffness to the lugs for airload drag and vibration loads. Details of the seal strips are shown in Figure 3-14.

Detail stress analysis results are summarized in Section 3.5, fabrication technique and experience are documented in Section 7.2.1 and full scale test results are discussed in Section 7.2.2.

3.4 THERMAL ANALYSIS

Thermal analyses were performed on the Space Shuttle wing leading edge with the following objectives:

- Support development of preliminary design
- Provide temperature histories for use in mission life predictions
- Provide temperature distributions for use in thermal stress analyses

Preliminary thermal properties were determined for use in these analyses based upon measurements from reference (6) and properties for expected constituents of the final material system. Subsequent to the thermal analyses, measurements were made of thermal properties for the selected material system, as reported in Section 5.2.1. The effect of differences between assumed and measured properties is discussed.

Aerodynamic heating rates were determined for boost and entry environments. Since entry heating is more severe, the remainder of the analysis was devoted to that portion of flight. Radiation equilibrium temperature distribution around the leading edge was computed as a function of entry time. Effects of internal cross radiation and circumferential heat conduction upon temperature distributions were also computed.

Predictions were made of temperature gradients in stiffening ribs and support joints. Surface recession of bare RPP was computed to indicate the thickness of substrate material required to provide a "fail safe" design in the event of coating failure. Air leakage rates through gaps at joints between adjacent panels were computed, and potential effects were assessed.

Results indicate that internal cross radiation and heat conduction effects will reduce peak temperatures by 148°F from radiation equilibrium values and will reduce peak circumferential temperature gradients by 37%. Support joint analyses indicate that insulating washers and bushings are not required, provided that bulk insulation is used between the skin and the joint area. Finally, analysis of bare RPP surface recession shows that 0.246 inch will be removed at the peak heating location during entry. Hence, a fail safe design would require a considerable increase in substrate material thickness. This surface recession is 2-1/2 times greater than for the Phase I straight wing baseline vehicle, because of the high cross range mission.

3.4.1 Thermal Properties

Emittance and thermal conductivity values for coated RPP were based upon measurements from reference (6) for the Phase I, Zr-B-Si system, since it was anticipated at the start of Phase II that the final coating would be similar to Zr-B-Si. Emittance values used for this design are listed in Table 3-2. Now, however, the final coating is siliconized RPP and measurements in Section 5.2.1 for the selected coating confirm that the design value of emittance was conservatively low.

The design value for thermal conductivity parallel to the lamina shown in Figure 3-15 agrees well with measurements made during Phase I for both Zr-B-Si and siliconized RPP above 2000°F and is somewhat higher than measurements for siliconized RPP below 2000°F. This property primarily effects the joint support analysis, where a high value of conductivity enhances heat conduction to the support point. Measurements in Section 5.2.1 for the selected coating indicate that the design value of conductivity is conservatively high at all temperatures.

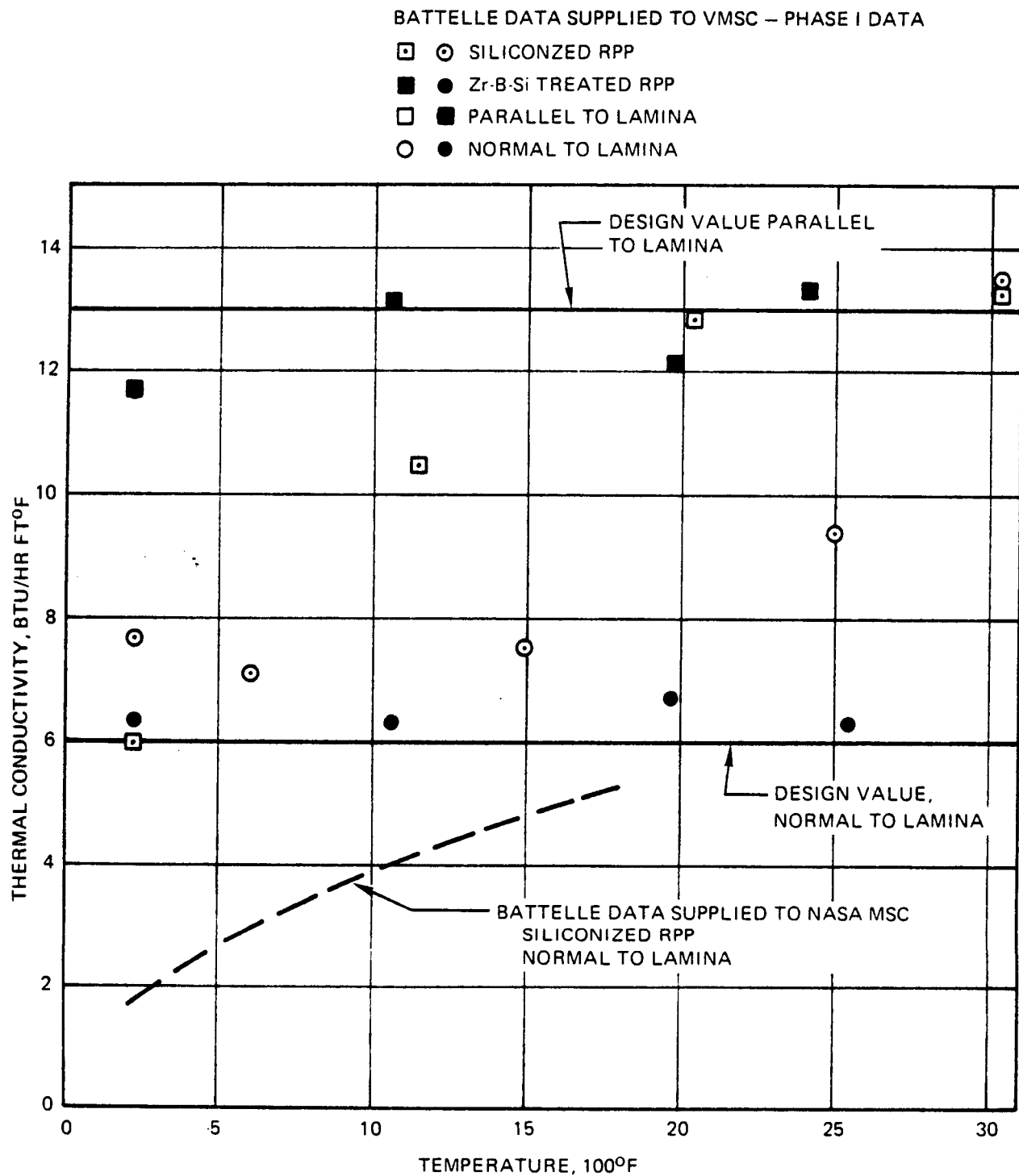


FIGURE 3-15 THERMAL CONDUCTIVITY, COATED RPP

TABLE 3-2

EMITTANCE OF COATED RPP

<u>Temperature °F</u>	<u>Zr-B-Si and Design</u>
1500	0.85
2000	0.86
2500	0.85
3000	0.86

The design value for conductivity normal to the lamina, as shown in Figure 3-15, is somewhat lower than measurements for siliconized RPP, particularly above 1500°F. This property primarily affects the cross radiation analysis, where a low value of conductivity inhibits heat conduction across the skin thickness and therefore diminishes the beneficial cross radiation effect. It should be noted that Battelle measured lower values of conductivity on siliconized RPP in tests for NASA-MSD than those reported in reference (6). This is shown in Figure 3-15 where it is seen that the difference is most pronounced below 1500°F. Some substantiation was provided for the higher conductivity measurements by early Southern Research Institute (SRI) data. SRI measured conductivity normal to lamina on RPP of similar density to the current material in 1965 for Air Force Materials Laboratory. Values for bare RPP varied from 8.35 to 10 BTU/Hr Ft °F at -50°F to 800°F, and were a factor of 2.5 to 4.5 higher for RPP coated with an early Si-SiC system. In view of this substantiating data and the lack of other evidence to indicate a higher accuracy for the data supplied to NASA-MSD, the design value of 6 BTU/Hr/Ft °F was selected. Measurements in Section 5.2.1 for the selected material are about 36% below the design value. This should reduce cross radiation results only slightly.

Specific heat values based upon data for expected constituents of the final system are shown in Table 3-3. These values are in good agreement with measurements in Section 5.2.1 for the selected coating.

Substrate density was calculated to be 80 Lb/Ft³ based upon weights and volumes of bare RPP specimens. Coating density was estimated to be 100 Lb/Ft³, and data presented in Section 5.1.3 confirms this value.

TABLE 3-3

COATING AND SUBSTRATE SPECIFIC HEAT

<u>Temperature, °F</u>	<u>SPECIFIC HEAT, BTU/LB°F</u>	
	<u>Substrate</u>	<u>Coating</u>
0	0.215	
100	0.230	0.132
500	0.300	0.195
1000	0.385	0.218
1500	0.446	0.235
2000	0.480	0.247
2500	0.500	0.260
3000	0.510	0.270

Thermal conductivity, density and specific heat of the fused silica support joint insulators were taken from reference (2). Properties of a candidate bulk insulation material for the wing structural box front beam and support joints are shown in Tables 3-4 and 3-5 and were obtained from reference (7).

TABLE 3-4

SPECIFIC HEAT, DYNAFLEX INSULATION

<u>Temperature °F</u>	<u>Specific Heat BTU/LB/°F</u>
0	0.200
400	0.229
1000	0.272
1800	0.292
2800	0.292

3.4.2 Aerodynamic Heating

Aerodynamic heating rates during boost and entry are based upon the trajectories presented in section 3.1. Boost heating rates were computed using the real gas, stagnation point theory of Fay and Riddell, developed in reference (10). Entry heating rates were obtained from reference (4)

TABLE 3-5

THERMAL CONDUCTIVITY OF DYNAFLEX INSULATION
6.2 LB/FT³ DENSITY
CONDUCTIVITY UNITS, BTU/FT HR °F

TEMPERATURE °F	PRESSURE, LB/FT ²			
	0.0003	0.2780	27.80	2120
- 200	0.009	0.011	0.018	0.021
0	0.0095	0.0115	0.0200	0.0235
200	0.0105	0.0125	0.022	0.027
400	0.012	0.014	0.025	0.0315
600	0.014	0.0165	0.0285	0.037
800	0.017	0.0195	0.0325	0.0435
1000	0.021	0.0235	0.0375	0.052
1200	0.026	0.029	0.0435	0.0625
1400	0.032	0.0355	0.051	0.075
1600	0.0419	0.044	0.0615	0.092
1800	0.0515	0.055	0.074	0.115
2000	0.065	0.068	0.091	0.149
2400	0.1025	0.1085	0.1585	0.218
2600	0.1305	0.138	0.2085	0.2395

Boost heat flux rates referenced to the stagnation point of a one foot radius sphere at 100°F are presented in Figure 3-16. Similar data for entry are given in Figure 3-17, except that a reference temperature of 2200°F was chosen and the heating rate applies to the maximum heating location on the leading edge. Air total enthalpy and local enthalpy and pressure at the stagnation line are also presented. Since maximum heating rates during entry are higher and of longer duration than those during boost, the bulk of the thermal analysis was devoted to entry. However, a calculation was made of the heat flux rate to the stagnation line of the leading edge at the time of peak heating during boost, 425 seconds from launch. This resulted in a value of 8.4 BTU/ft² sec, which corresponds to a radiation equilibrium temperature of 1700°F. The primary purpose of this calculation was to confirm that the RPP interface with the primary wing structure is located sufficiently far aft. Since the interface temperature will be well below the stagnation line value, boost conditions will not introduce a requirement for shifting the interface further aft.

Heating rates at local positions on the leading edge were normalized to that at the maximum heating location. They are presented in Figure 3-8 as a function of distance from the geometric leading edge. The local heat flux rate to a wall at temperature T_W is therefore given by:

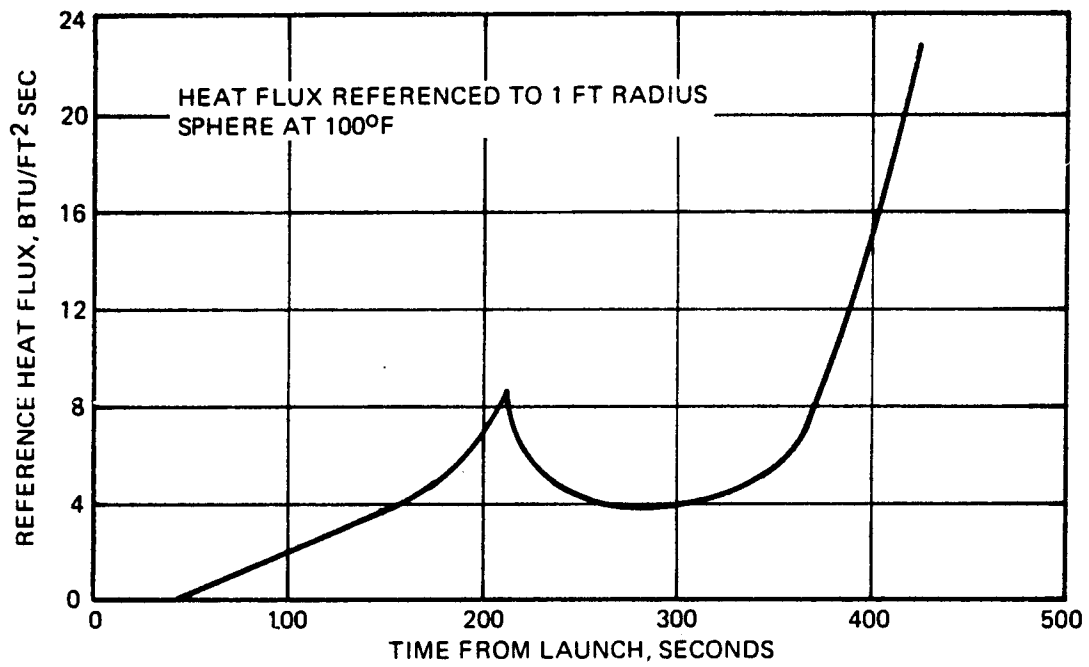


FIGURE 3-16 BOOST AERODYNAMIC HEATING

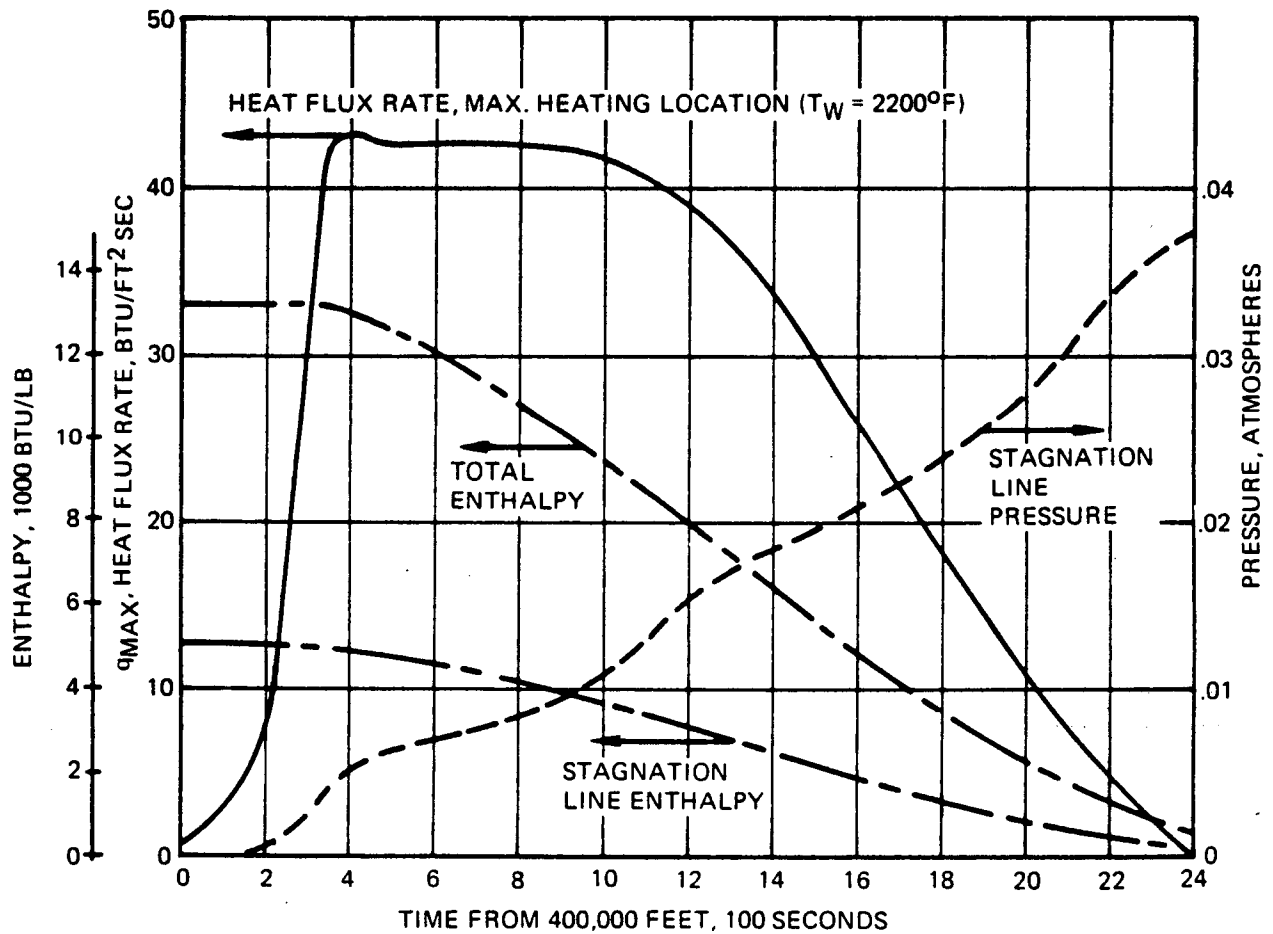


FIGURE 3-17 ENTRY AERODYNAMIC HEATING

$$\dot{q} = \dot{q}_{\max} \left(\frac{\dot{q}_{\text{local}}}{\dot{q}_{\max}} \right) \frac{(i_R - i_W)}{(i_R - i_C)}$$

where:

i_R = air recovery enthalpy, BTU/Lb

i_W = air enthalpy at T_W and local pressure

i_C = air enthalpy at 2200°F

Local pressures on the leading edge are given by the stagnation line pressure in Figure 3-17, together with pressure distribution from reference (4).

Radiation equilibrium temperatures were computed to provide an upper limit of expected temperatures on the leading edge. Radiation equilibrium temperatures assume that the incident heat is entirely removed by surface re-radiation to space. Hence, heat sink, conduction and internal cross-radiation effects are neglected. These effects are considered in more detailed analyses which follow.

Temperatures were computed as a function of both entry time and leading edge location as shown in Figures 3-18 through 3-21. Figure 3-18 presents a temperature-time plot for the maximum heat location, which reaches a peak temperature of 2740°F. Temperatures shown in Figure 3-21 are a function of location on the leading edge, at the time of peak heating. The peak circumferential temperature gradient, which is important from a thermal stress standpoint, is 513°F/inch.

Measured emittance for the selected coating as reported in Section 5.2.1, is actually 0.92 at 2740°F, as opposed to the design value of 0.85. This higher value reduces the peak radiation equilibrium temperature by 60°F to 2680°F.

Cross Radiation - A two-dimensional analysis was performed to determine the effects of internal cross radiation. Heat conduction through the skin in both circumference and thickness directions was included in the analysis. Figure 3-20 shows the 51 node thermal model which was employed. A constant 0.18 inch thick (14 ply) RPP laminate skin was assumed. The aft surface of the enclosure was assumed to be adiabatic to represent insulation over the wing support structure and support joints. All 24 interior nodes were permitted to participate in cross radiation. A portion of the skin interior surface near both windward and leeward support joints was assumed to be covered by insulation material to protect the joints. These surfaces were assumed to be adiabatic.

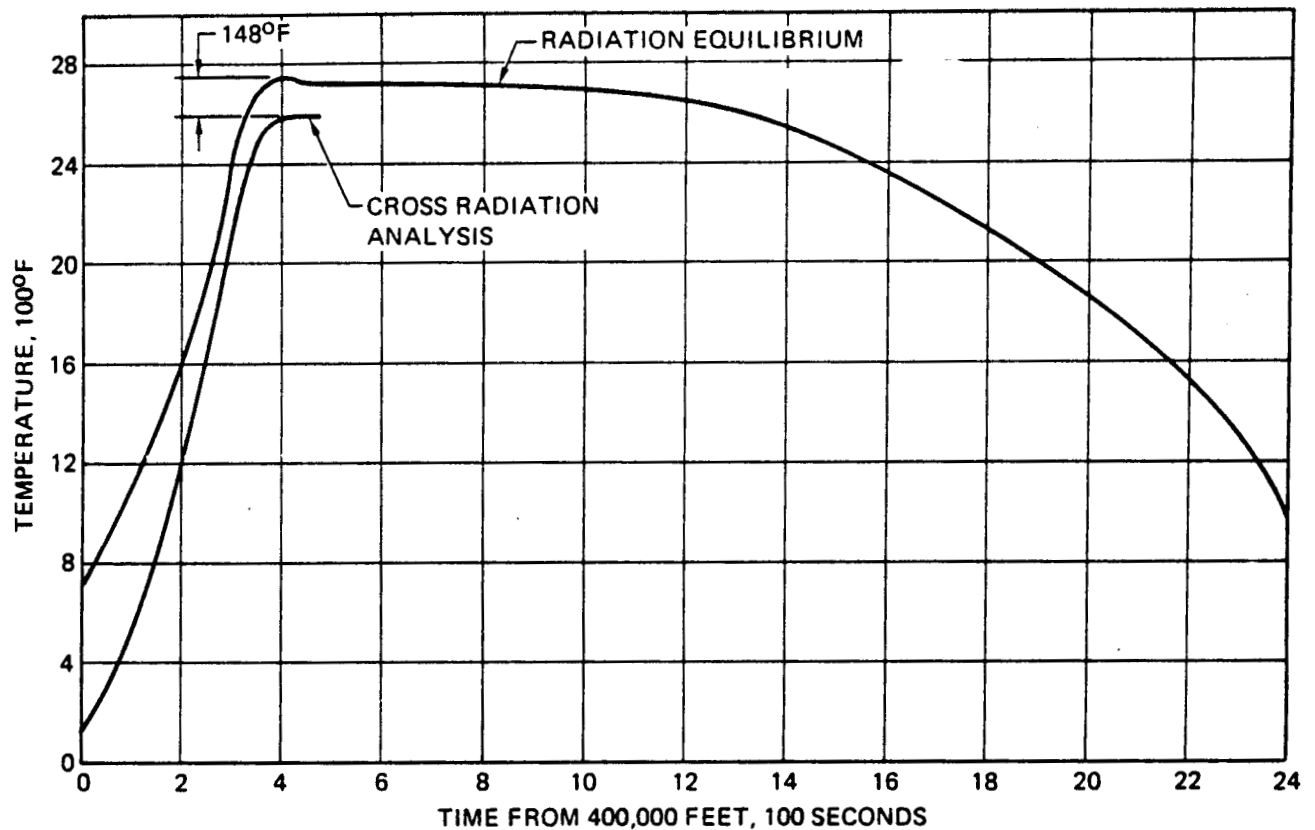


FIGURE 3-18 SKIN TEMPERATURE AT PEAK HEATING LOCATION, $\epsilon = 0.85$

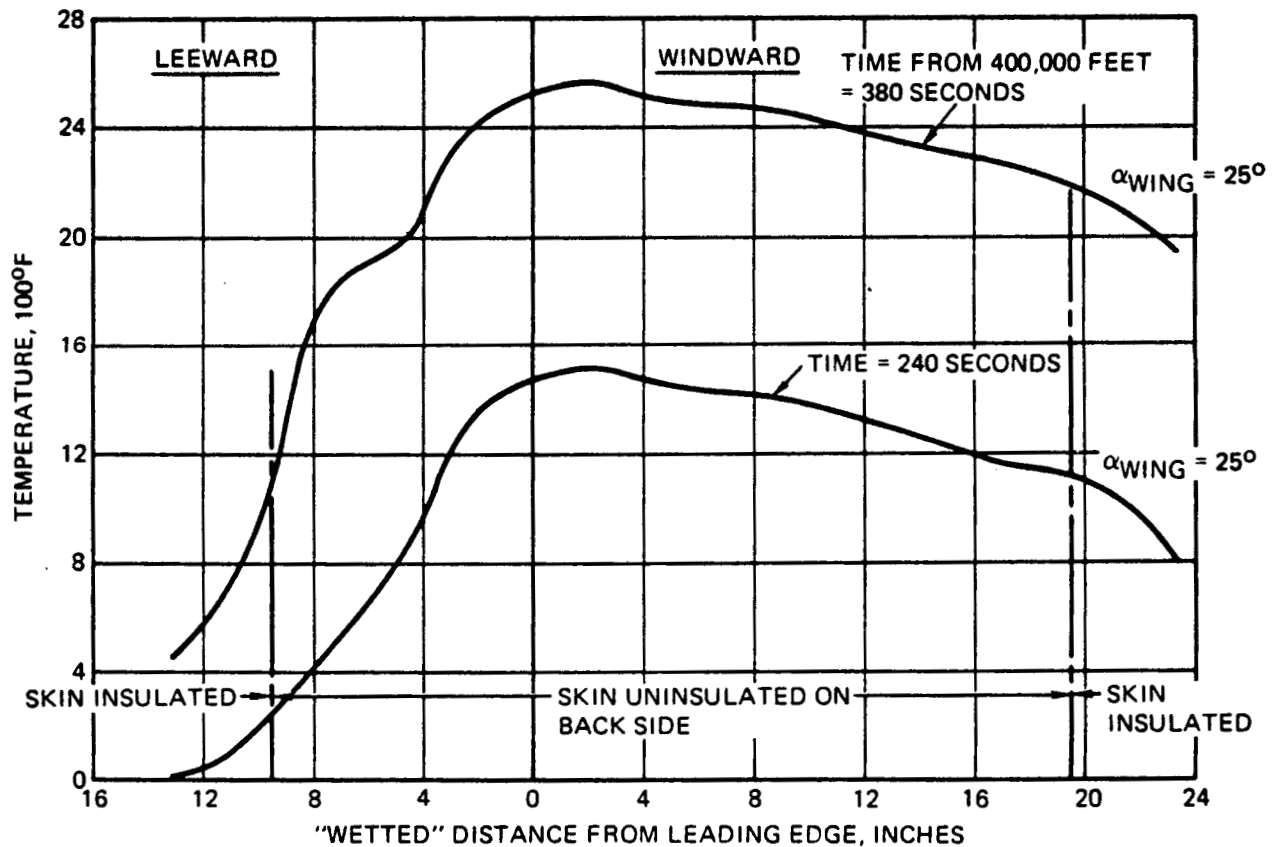


FIGURE 3-19 SKIN TEMPERATURES AROUND LEADING EDGE – INITIAL SKIN TEMPERATURE = -170°F

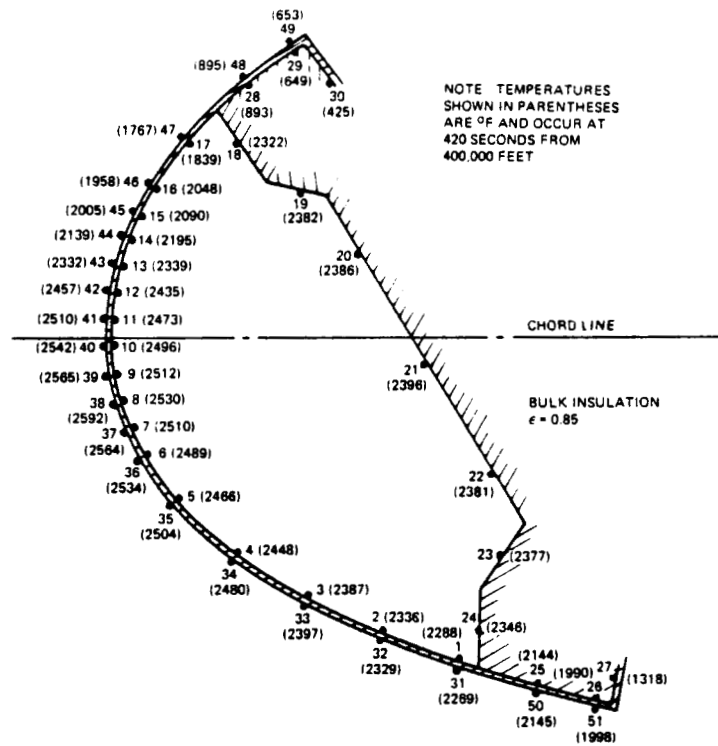


FIGURE 3-20 THERMAL MODEL, LEADING EDGE WITH CROSS RADIATION

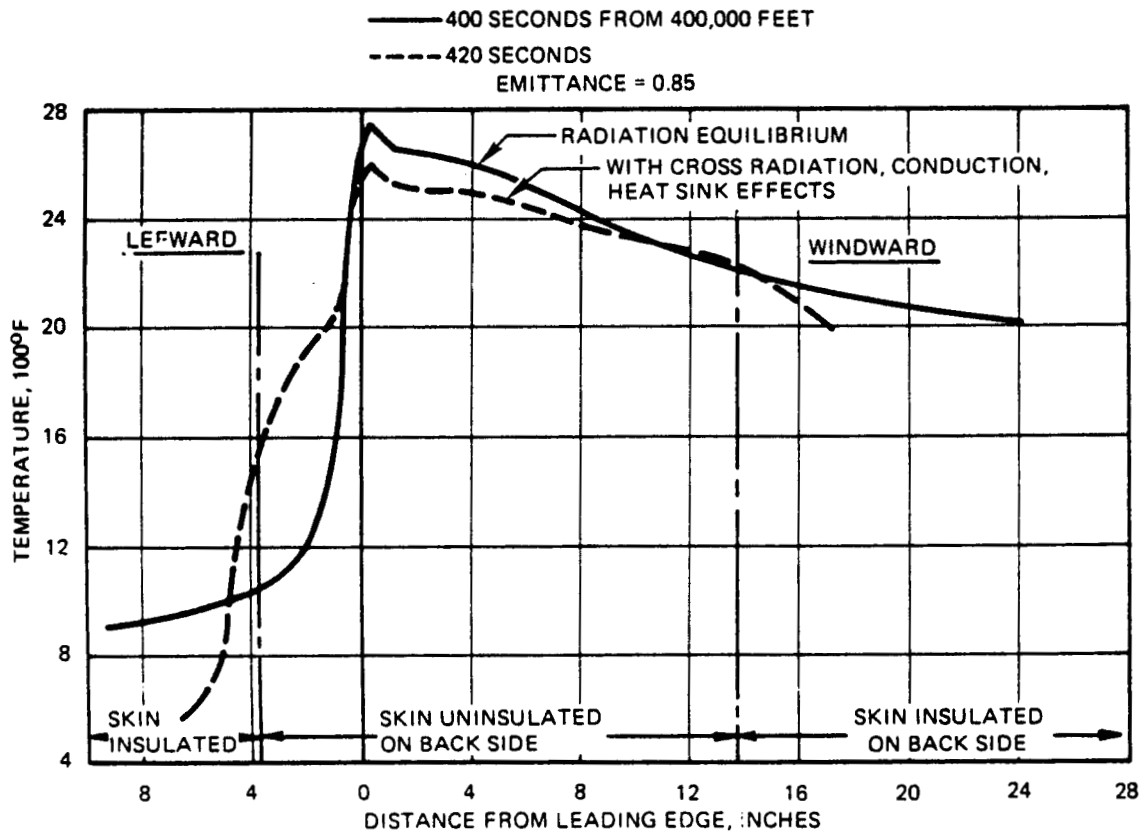


FIGURE 3-21 SHUTTLE LEADING EDGE TEMPERATURES — TIME OF PEAK REENTRY TEMPERATURE

Radiation view factors between nodes were computed using Hottel's "crossed string method" from reference (11). Numerical calculations were performed using a VMSC computer routine, which calculates coefficients for cross-radiation from the view factors and emittance using an exact net radiation method, rather than an approximation technique involving only a small number of reflections. All surfaces are assumed to be gray and diffuse reflectors, which is reasonable for the materials of interest.

Computed temperatures at each node location at 420 seconds, the time at which temperatures at the maximum heating location have peaked, are presented in Figure 3-20. It will be noted that the wing support structure insulation surface temperature reaches a maximum value of 2396°F, establishing the temperature capability required of this material. The temperature-time history at the peak heating location is compared with radiation equilibrium values in Figure 3-18. It is seen that cross radiation reduces the maximum skin temperature by 148°F to a value of 2592°F.

The temperature distribution around the leading edge at 420 seconds is compared with maximum radiation equilibrium values in Figure 3-21. The point of peak circumferential temperature gradient in the radiation equilibrium analysis was near the geometric leading edge. In the cross radiation analysis, this point shifts to the location on the leeward side where the wing support insulation begins. Insulation blocks cross radiation heat transfer from the windward side, causing skin temperatures to drop rapidly across the insulation interface. The peak temperature gradient actually occurs slightly earlier than peak absolute temperatures, at 380 seconds, when the gradient is 325°F/inch. This constitutes a 37% reduction from the radiation equilibrium value of 513°F/inch, which is significant from a thermal stress standpoint. Temperature distributions around the leading edge at two times during entry, 380 and 240 seconds are shown in Figure 3-19. Temperatures at 240 seconds are significant due to the fact that stiffener rib gradients peak at this time, as discussed below.

As discussed previously, measured emittance for the selected coating is higher than the design value and measured conductivity in the normal to lamina direction is lower than the design value. The net effect of these differences on the cross radiation analysis was calculated to be a 44°F reduction in maximum skin temperature from 2592°F to 2548°F.

Rib Gradients - Temperature distributions in rib stiffeners were computed for use in thermal stress analyses using a two-dimensional thermal model, shown in Figure 3-22. Heat conduction along the skin and across the rib, cross radiation between adjacent skin and the rib, and cross radiation to and from surrounding structure were considered. The mating surface of the rib with an adjoining rib was considered adiabatic

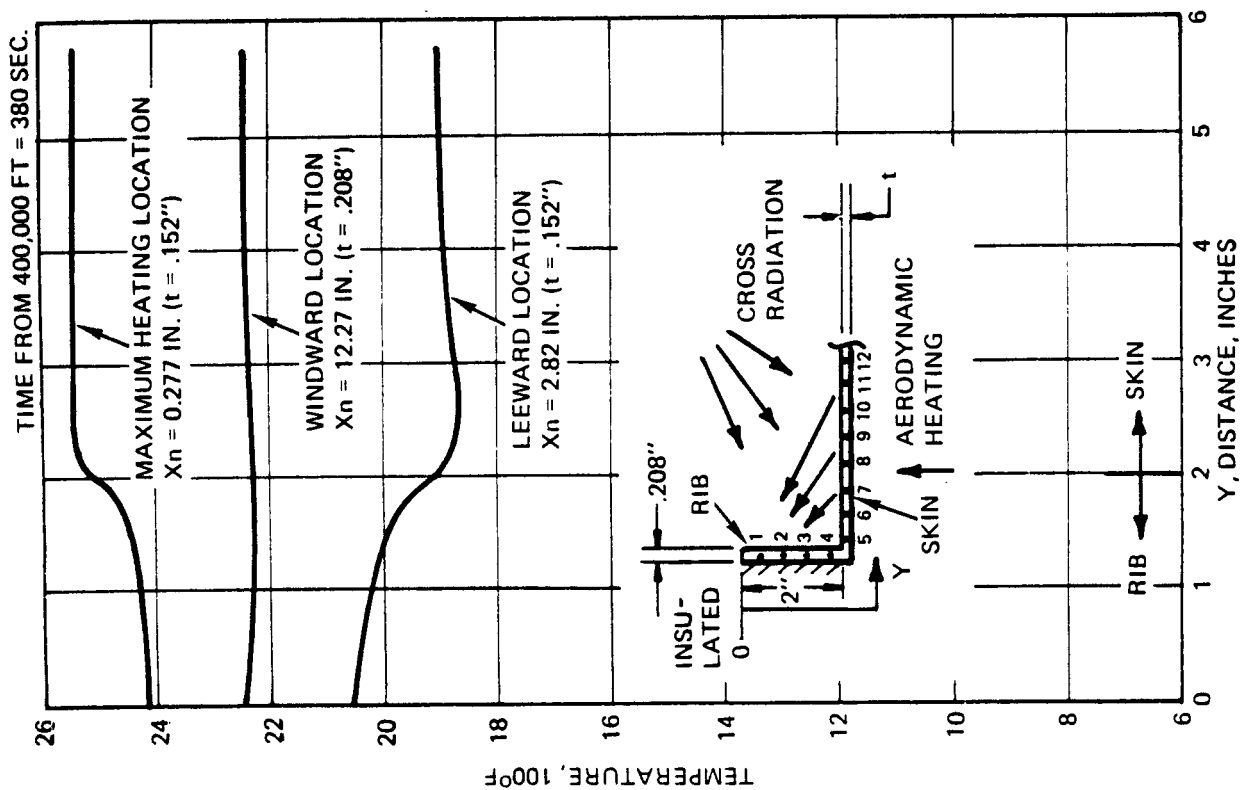


FIGURE 3-22 RIB TEMPERATURE DROP - CAVITY AREAS

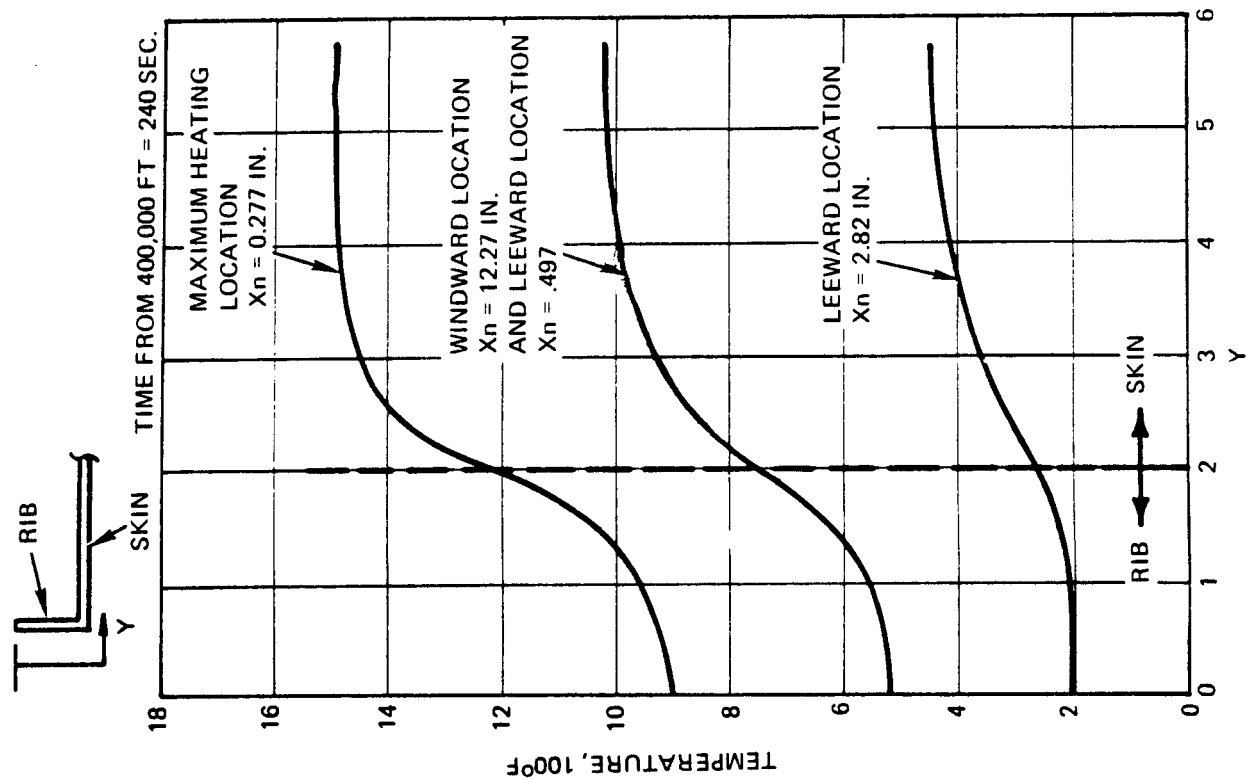


FIGURE 3-23 RIB TEMPERATURE DROP - CAVITY AREAS

by reason of symmetry. The temperature of surrounding structure radiating to the rib and skin was assumed to be equal to the temperature of the wing support insulation surface. This is a reasonable assumption, since the insulation surface maintains a temperature equal to the average temperature of the skin which radiates to it.

The temperature distribution across the rib and adjacent skin is shown in Figure 3-22 for three locations on the leading edge at an entry time of 380 seconds. This corresponds to the time of peak circumferential gradients around the leading edge. The three locations are defined as follows:

	Distance Aft of Leading <u>Edge In.</u>	\dot{q}/\dot{q}_{MAX}
Maximum heating	0.277	1.0
Windward location	12.27	0.482
Leeward location	2.82	0.059

Temperature variations across the rib are relatively low at 380 seconds and are governed primarily by cross radiation to and from surrounding structure. This surrounding structure is cooler than the skin adjacent to the rib at the maximum heating location, about equal at the windward location and hotter than the skin at the leeward location. Hence, the temperature drops from skin to rib at the maximum heating point, is essentially constant at the windward location, and rises from skin to rib at the leeward location.

Maximum temperature gradients across the rib occur at 240 seconds as shown in Figure 3-23. The temperature drops across the rib at this time are higher, amounting to 300°F at the maximum heating location. These temperature drops are governed primarily by heat conduction from adjacent skin into the rib, since skin temperatures at 240 seconds are too low for cross radiation effects to dominate. Therefore, for all three locations the temperature reduces, progressing from skin to rib.

To apply this data to thermal stress analysis some slight adjustment of the temperature in Figures 3-22 and 3-23 was required to match the skin temperatures computed with the rib model to those computed with the cross radiation model. This upward or downward shift of rib temperatures was small, in most cases less than 50°F and in no case was greater than 10%.

The rib temperatures in Figures 3-22 and 3-23 apply to the major portion of the rib which is free to participate in cross radiation with skin and other structure. However, in the support joint areas the rib and adjacent skin are covered with bulk insulation, and the thermal model used to generate the above rib temperatures is not applicable. Rib temperatures in the support areas were therefore computed using the thermal model described in the following paragraph on support joint analysis. Results are shown in Figure 3-24 for the windward and leeward attachment locations at 240 and 380 seconds. The maximum temperature drop across the rib occurs at 380 seconds on the windward attachment and is 1100°F. This drop is considerably higher than that in the uninsulated portion of the rib for three reasons.

- Heat transfer from skin to rib is by conduction only, since bulk insulation suppresses cross radiation.
- The rib height is 3.45 inches in the attachment area, compared to 2.00 inches for the remainder of the rib.
- Attachment hardware at the inboard side of the rib serves as a heat sink to maintain relatively low temperatures.

However, because of the localized region of these gradients, they have little effect on overall rib thermoelastic stresses.

Support Joint Analysis - The leading edge is attached to Haynes 188 brackets bolted to the wing box as illustrated in Figure 3-25 and Figure 3-11. Analyses were performed to determine the insulation required to protect the Haynes bracket and steel bolt from overheating and the required separation distance between the skin and the support joint. The area between the skin and support joint was assumed to be filled with 6.2 LB/FT³ density Dynaflex insulation. A baseline configuration, shown in Figure 3-25, and two alternate configurations were analyzed. Major features of the three configurations are listed in Table 3-6.

TABLE 3-6
SUPPORT JOINT CONFIGURATIONS

Configuration	Distance Skin to Bolt Centerline, Inches	Hard Insulator Material	Hard Insulator Dimensions Inches					
			Bushings in RPP		Bushings in Haynes 188		Washer	
			Thickness/Diameter	Thickness/Diameter	Thickness/Diameter	Thickness/Diameter	Thickness/Diameter	Thickness/Diameter
Baseline	3.3	Fused Silica	.55	1.00	.40	1.00	.10	0.70
Bolt Moved Outboard	2.0	Fused Silica	.55	1.00	.40	1.00	.10	0.70
Hard Insulators Removed	3.3	None	-	-	-	-	-	-

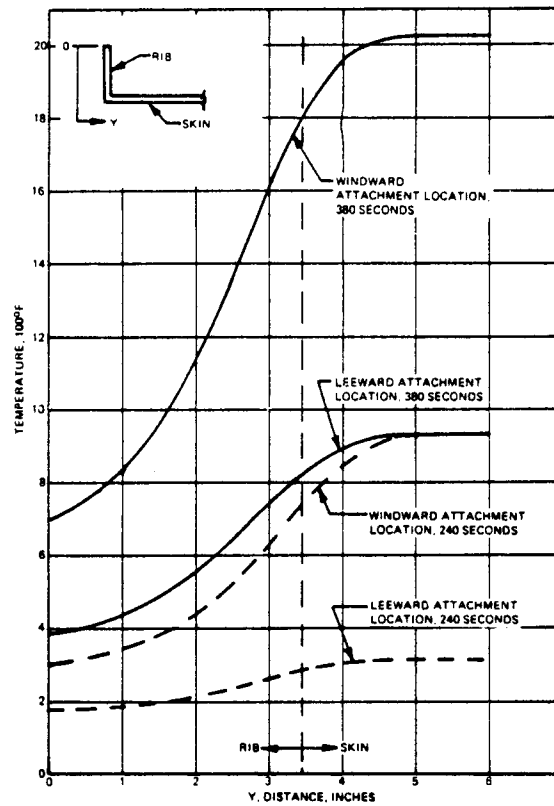


FIGURE 3-24 RIB TEMPERATURE DROP, ATTACHMENT AREAS

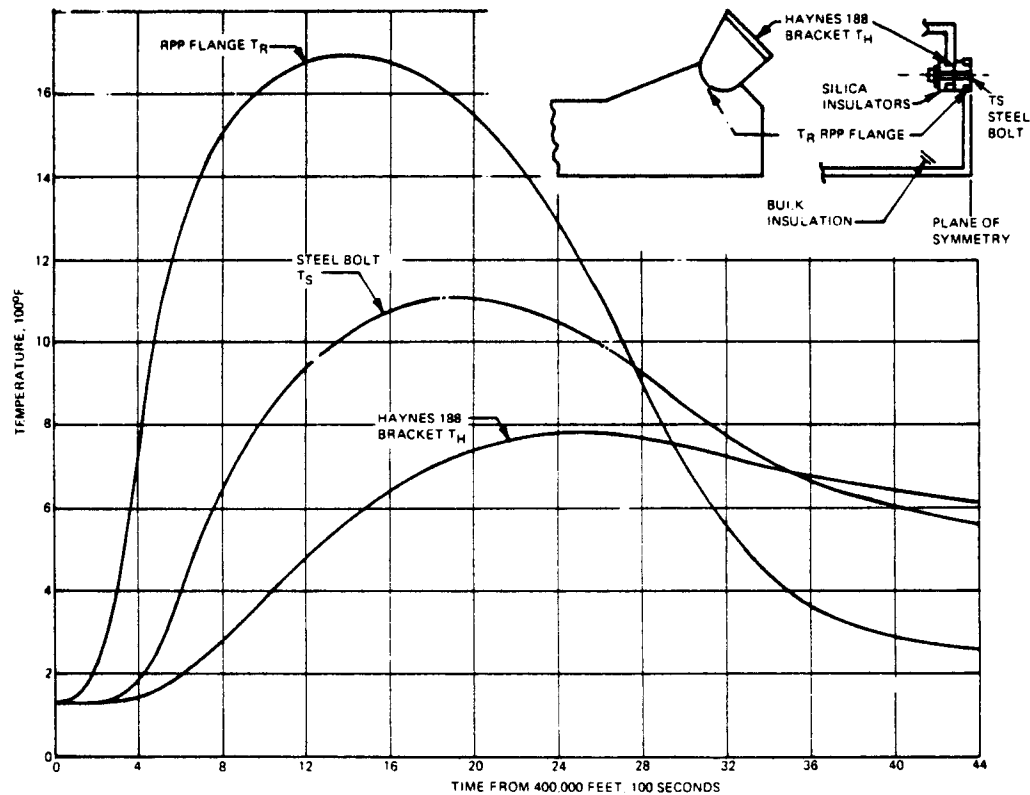


FIGURE 3-25 ATTACHMENT TEMPERATURES

These configurations were analyzed using a 55 node, three-dimensional thermal model which included heat conduction along the skin and RPP rib, across the hard insulators, and into the steel bolt and Haynes 188 bracket. Cross radiation from the skin to the portion of the RPP rib outside of the bulk insulation was also considered, as was heat conduction through the bulk insulation and into the support joint.

Computed temperatures as a function of entry time for the baseline configuration are shown in Figure 3-25. Temperature of the RPP rib at its interface with the hardware insulator peaks at 1691°F, which is tolerable for fused silica. The steel bolt temperature peaks at 1107°F, while the Haynes 188 bracket temperature peaks at 782°F, both of which are tolerable. The peak temperatures reached at various locations for all three configurations are summarized in Table 3-7.

TABLE 3-7 SUPPORT JOINT PEAK TEMPERATURES

		<u>Temperature, °F</u>		
		<u>Baseline</u>	<u>Bolt Moved Outboard</u>	<u>Hard Insulator Removed</u>
Haynes Bracket	Hot Side	782	830	1111
	Cold Side	635	659	717 at 2400 sec*
Steel Bolt	RPP End	1107	1177	1175
	Haynes Bracket End	1042	1104	1161
RPP	Interface with Insulator or Bolt	1691	1793	1225
	Skin Side	2128	2133	2127

* Temperature at this location rising at 2400 seconds, maximum temperature not computed.

None of the temperatures in Table 3-7 are considered excessive, including the temperatures with the hard insulators removed. Hence, it appears possible to remove these insulators. As shown in Table 3-7, the temperature at the cold side of the Haynes bracket is 717°F at 2400 seconds and is still rising. Insulation will therefore be required between this bracket and the titanium beam to which it attaches, since the titanium is limited to 650°F.

Measured values of thermal conductivity for the selected material system in the parallel to lamina direction, as given in Section 5.2.1 are significantly lower than the design value used in this analysis. This will have the effect of lowering temperatures in the lug area below calculated values.

3.4.3 Surface Recession of Bare RPP

In order to determine the thickness of substrate material required to provide a "fail safe" design in the event of general or local coating failure, calculations were made to predict surface recession of bare, uninhibited RPP during entry. A VMSC computer routine was utilized with RPP oxidation characteristics based upon plasma arc test data. Reaction rate control, transition and diffusion control oxidation regimes are accounted for in the routine.

Figure 3-26 presents the computed surface recession as a function of entry time for RPP with a density of 80 Lb/Ft³. Computer runs were made for the maximum heating location and for a location on the leeward side. Recession for intermediate heating conditions was scaled from the stagnation line results, based upon diffusion control for which recession is proportional to heat flux rate. Since reaction rate control is important at the lower heating rates, this procedure is slightly conservative.

Peak recession rate occurs at 1800 seconds and is 1.61×10^{-4} in/sec at the maximum heating location. Total recession is 0.246 inch at the maximum heating location and 0.0114 inch at the leeward location. This recession could be reduced about 20% by increased densification, graphitization, and consideration of cross radiation to reduce surface temperature. The distribution of surface recession around the leading edge is shown in Figure 3-27. These results indicate that a fail safe design would require a considerable increase in substrate material thickness on the windward side, but only a slight increase on most of the leeward side. It is also evident that bare RPP has a single mission capability in the high heating region and multi-mission capability on most of the leeward side.

3.4.4 Gap Leakage

A preliminary analysis was made of air leakage rates through joints between adjacent segments of the leading edge and potential effects of this leakage on leading edge temperatures. The joint design, shown in Figure 3-11, includes a sealing strip attached between adjacent panels. The outer surface of the strip is made flush with the outer surface of the panels by joggles in the panels. Each leading edge segment is fixed at the inboard end and is free to expand outboard. The total expansion

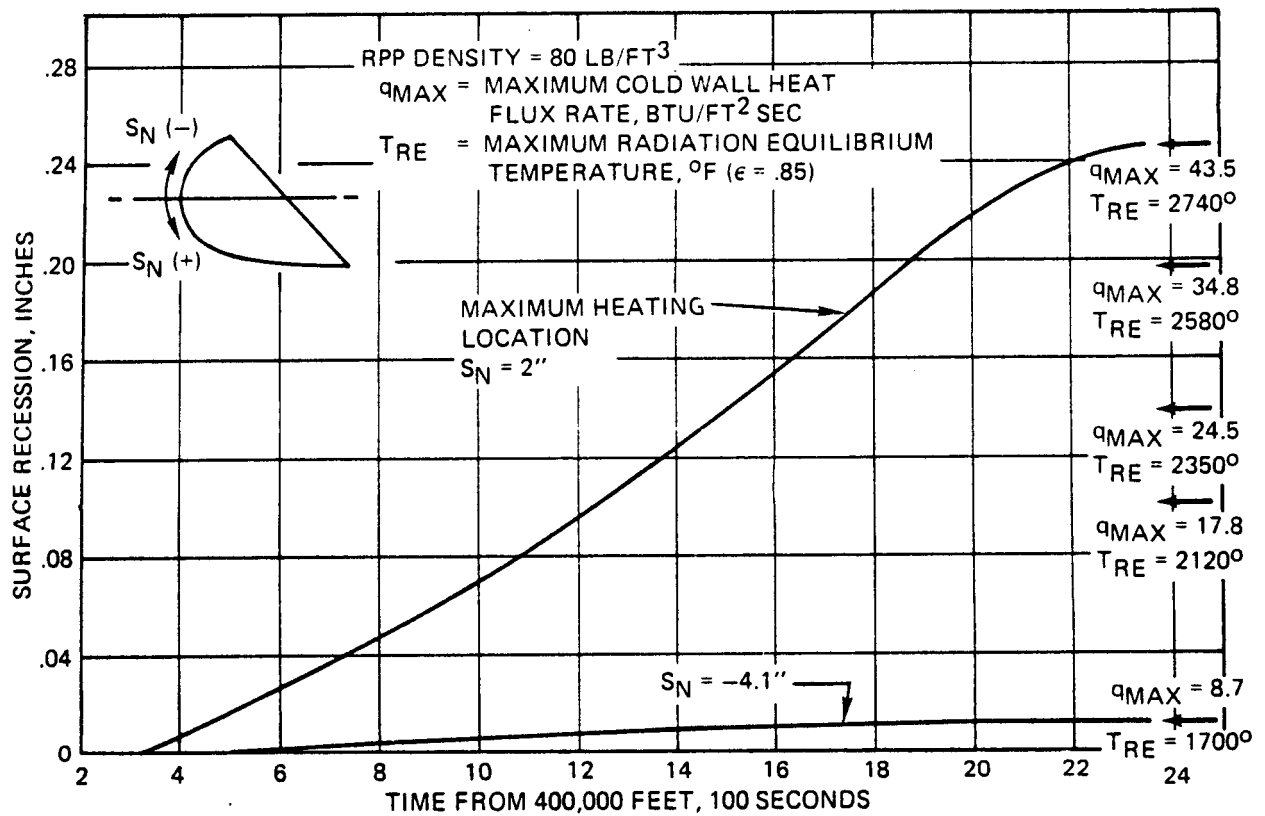


FIGURE 3-26 ENTRY SURFACE RESSION OF BARE RPP

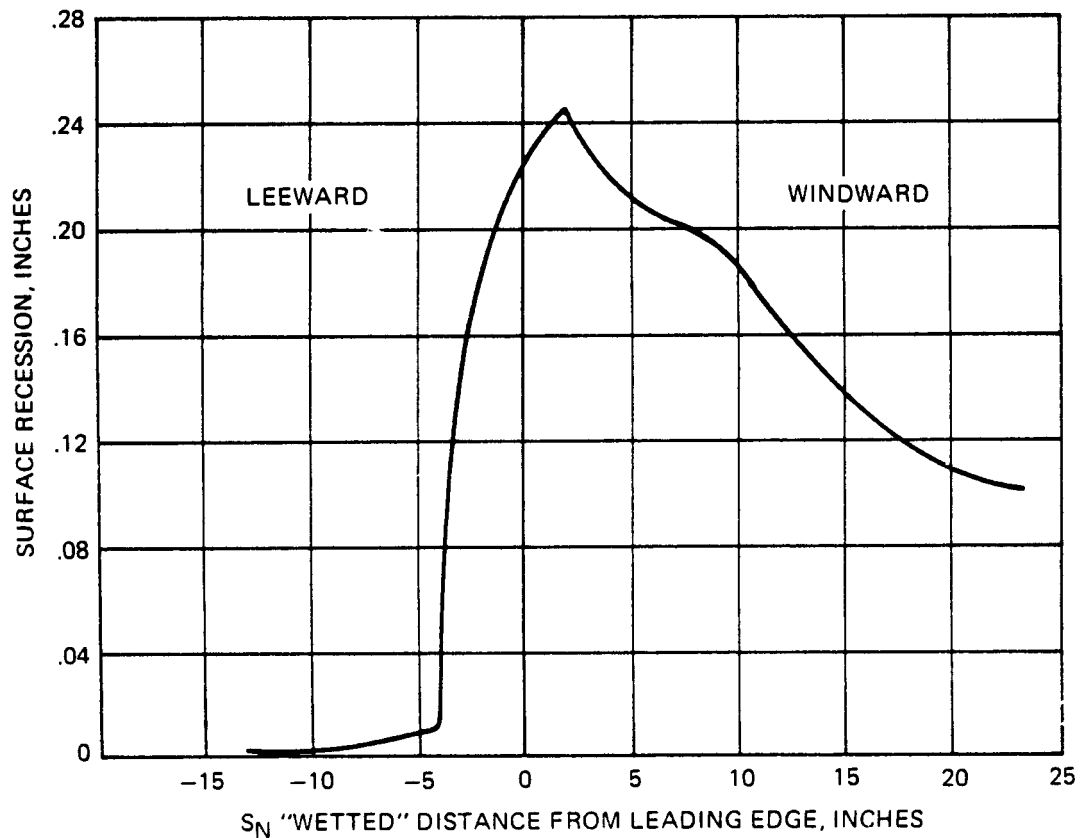


FIGURE 3-27 SURFACE RESSION DISTRIBUTION OF BARE RPP

allowance between panels is 0.128 inch to accommodate the stagnation region expansion for a 30 in. segment. The sealing strip is fixed against the fixed inboard end of each panel, although the reverse situation could be employed (i. e., allow panel to expand inboard and attach seal against the outboard side of the panel).

Ordinarily, air leakage will be controlled by the gap at the area where the seal strip overlaps the free end of the adjacent panel, that is, the joggled portion of the skin. As can be seen in Figure 3-11, this gap will usually be much smaller than the 0.128 inch expansion allowance gap between the seal strip and the lug at the free end of the adjacent panel. Since possible gap heights are currently uncertain, calculations of air leakage and temperature effects were made for a range of values.

Calculations were first made to determine air leakage rates and associated total energy influx into the leading edge cavity. An assessment was then made of potential effects of this leakage on leading edge temperatures.

Assumptions employed in the analysis are as follows:

- (1) For any given gap height, the gap exists around the entire leading edge wetted distance.
- (2) Pressure inside the leading edge cavity is sufficiently low to result in choked flow through the gap.
- (3) Air enters the gap at the local surface temperatures and pressure on the leading edge panel. (The effects of deviations from these conditions are also assessed.)

With these assumptions, the mass flow into the leading edge cavity can be written as follows:

$$\dot{W} = \frac{0.53}{144} h \sqrt{\frac{P_{SL}}{T_{SL}}} \int_S \left(\frac{P}{P_{SL}} \right) \left(\sqrt{\frac{T_{SL}}{T}} \right) ds \quad (2)$$

where:

\dot{W} = air flow rate, Lbs /Sec

h = gap height, inches

P = Local pressure on leading edge panel minus free stream static pressure, Lbs/Ft²

P_{SL} = stagnation line pressure minus free stream static pressure, Lbs/Ft²

T = local panel temperature, °R

T_{SL} = panel temperature at stagnation line, °R

S = wetted distance along panel, inches

The variation of the product under the integral is shown in Figure 3-28. Integration of the function yields a value of 18 inches. This is an effective gap length, relative to stagnation conditions. Utilizing the design entry trajectory to obtain the variation of stagnation line pressure and temperature with time, air flow rate into the cavity versus time was calculated for various gap heights. These results are shown in Figure 3-29.

Similarly, the total energy influx into the leading edge cavity can be written as follows:

$$\dot{Q} = \frac{0.53}{144} h C_P \sqrt{T_{SL}} P_{SL} \int_S \left(\frac{P}{P_{SL}} \right) \left(\sqrt{\frac{T}{T_{SL}}} \right) ds \quad (3)$$

where:

\dot{Q} = energy influx rate, BTU/Sec, total energy of air entering cavity, measured from absolute zero temperature base.

C_P = specific heat of air, BTU/Lb-°R

The remaining terms are as specified in equation (2). The variation of the product under the integral is shown in Figure 3-30. Integration of the function yields a value of 17.4 inches. Computed energy influx into the leading edge cavity is shown in Figure 3-31.

The preceding calculations are based on ideal gas conditions. Utilization of real gas pressures on the leading edge would increase the flow rate and energy influx by approximately 10%. The largest uncertainty in the analysis is the total temperature of the air entering the cavity. If the air is drawn off from a very thin portion of the boundary layer adjacent to the surface as assumed in the analysis, then the results presented are representative. In such a situation, the bulk total temperature of the air entering the cavity is approximately equal to the mean temperature of the panel and wing structure insulation at any given time; consequently, overheating of the panel and insulation would not occur. However, if air is

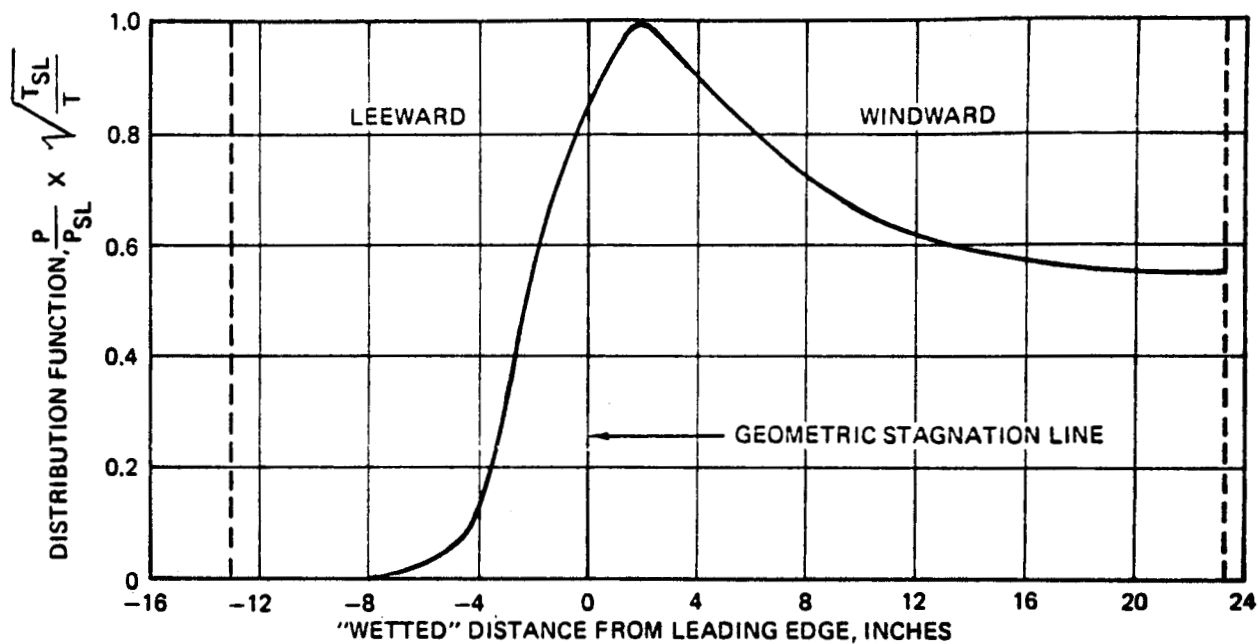


FIGURE 3-28 DISTRIBUTION FUNCTION FOR MASS FLOW INTO CAVITY

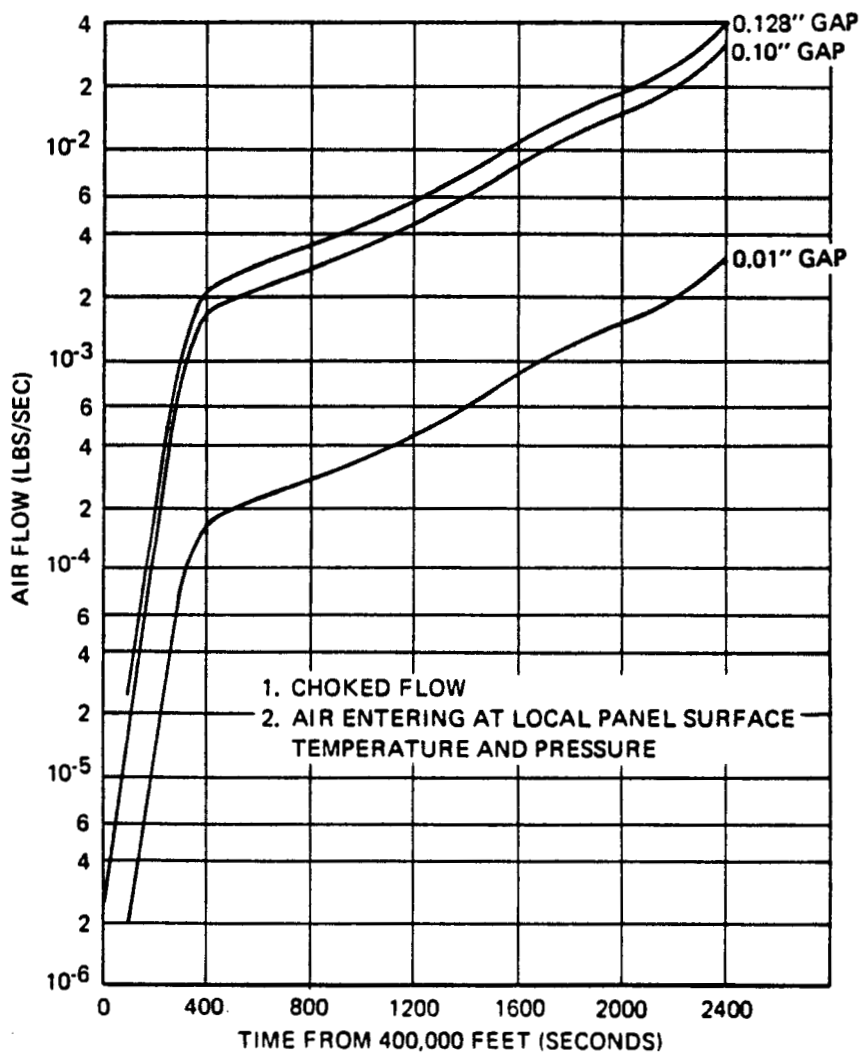


FIGURE 3-29 AIR FLOW INTO LEADING EDGE CAVITY

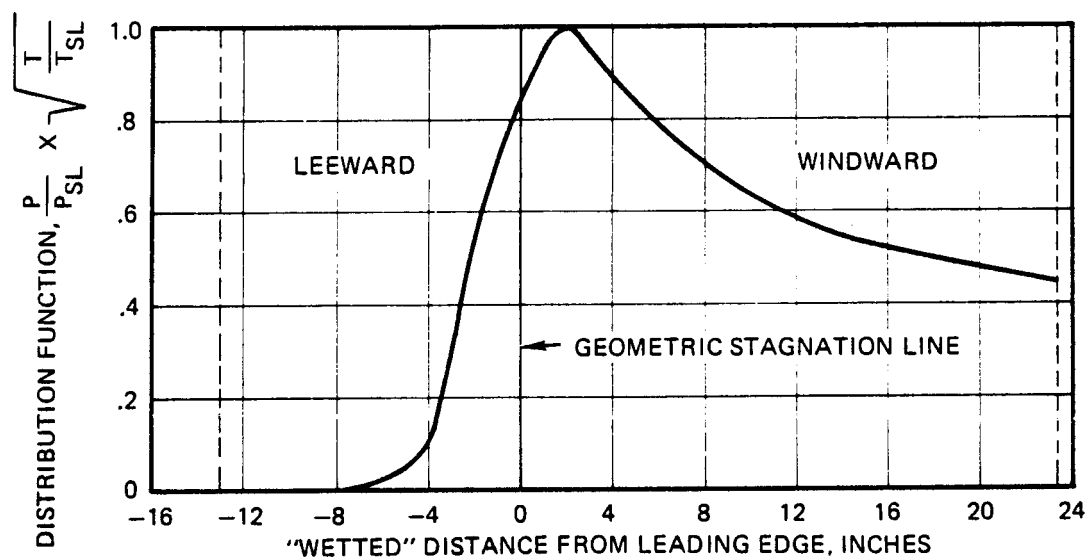


FIGURE 3-30 DISTRIBUTION FUNCTION FOR ENERGY ENTERING CAVITY

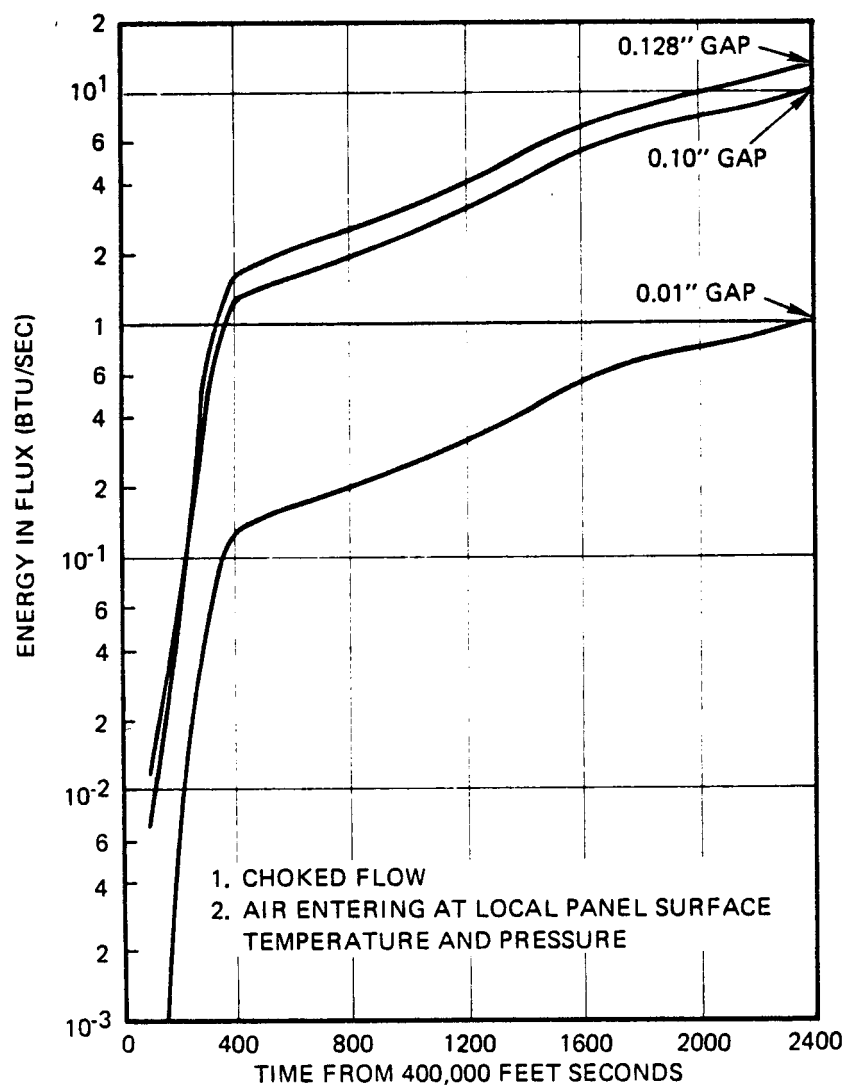


FIGURE 3-31 TOTAL ENERGY INFLUX INTO LEADING EDGE CAVITY

drawn off from a greater portion of the total boundary layer thickness, the bulk total temperature of the air entering the cavity is increased considerably due to the steep temperature gradient in the boundary layer, and local increased heating of panel and insulation would occur.

Areas of the leading edge which are subject to increased heating due to air leakage include the following:

- (1) Heat shield bulk insulation
- (2) Seal strip and RPP skin in overlap area at joggle
- (3) Front wing box structural beam (if air leaks around edges of bulk insulation)
- (4) Attachment bolts and fittings

Items (1) and (2) would be subjected to increased heating only if the total temperature of the leaked air is above the surface temperature, whereas items (3) and (4) would receive increased heating even if the air is at or near the surface temperature. Heating of items (3) and (4) can be controlled by maintaining a tight fit of insulation over these parts. However, heating of items (1) and (2) can be controlled only by design of the seal strip and joint. A preliminary assessment was therefore made of potential heating of the latter items.

A very conservative approach was used to estimate increased heating of the heatshield insulation. Air was assumed to enter the cavity at the local external recovery temperature. Since the velocity and pattern of air flow over the insulation surface is not known, an average heat transfer coefficient was calculated assuming that the maximum possible heat is extracted from the air and distributed uniformly over the insulation surface. That is, the air was assumed to leave the cavity at the temperature of the insulation surface. Even with these conservative assumptions the increase in temperature of the insulation surface due to air leakage was only 20°F for an 0.01 inch joint gap. This increases to 240°F for the extremely conservative assumption of a 0.128 inch gap. An additional conservatism was introduced into the calculations in that, with air entering at recovery temperature, the flow rate will be lower than that given by Figure 3-29, due to the lower air density. Hence, it appears that increased heating of the insulation will be minimal.

Heating of the seal strip and the mating skin surface at the gap is limited by two mechanisms; the convective heat transfer rate across the boundary layer and the total energy in the air flow. Two values of heat transfer coefficient in the gap were computed, based on the respective

mechanisms. A boundary layer convective heat transfer coefficient was computed, based upon duct heating relations. A second coefficient was computed, assuming the maximum possible energy is extracted from the air and distributed over the surfaces on each side of the gap. Since both mechanisms limit the heat transfer simultaneously, the actual heat transfer coefficient will be less than the lower of the computed values.

For reasonable gap heights (< 0.10 inch), it was found that the heat transfer will be limited by the total available energy. The value of the heat transfer coefficient was computed to be equal to the external coefficient for a gap of 0.016 inch. Therefore, it appears that if the air enters the gap at a temperature well above the local surface temperature, a substantial increase in overall heating to the seal and mating skin could occur.

Should tests prove this to be the case, the seal design of Figure 3-11 could be modified in a number of ways to prevent or minimize flow past the seal. For example, the seal could be held firmly against the downstream (outboard) side of each segment, placing the expansion joint and therefore the largest gap to the leeward side of the flow. Another approach would be to bond the seal strips to, or otherwise integrally fabricate them with, the outboard side of the segments to eliminate the potential for scooping air into the leading edge cavity. The latter approaches preclude individual removal of leading edge segments because of the resulting shingle type overlaps. Further study would be required if experimental data should dictate more stringent sealing requirements. Further analyses and plasma arc tests are planned for Phase III to better define the extent of air leakage at the joints and its effect upon leading edge temperatures.

3.4.5 Conclusions and Recommendations

The following conclusions are drawn from the foregoing analyses:

1. Internal cross radiation and heat conduction effects will reduce peak skin temperature at the stagnation line by 148°F from radiation equilibrium and will reduce peak circumferential temperature gradients by 37%.
2. Insulating washers and bushings are not required at the support joints, provided that bulk insulation is used between the skin and the joint area.
3. Front beam insulation will require 2396°F temperature capability.

4. A considerable increase in RPP substrate material thickness would be required to provide a fail safe design in the event of generalized coating failure in the maximum heating region. Effects on internal structure from localized coating loss and burnthrough have not been assessed.
5. Heating within the leading edge cavity due to air leakage through gaps does not appear to be a problem. Experimental air leakage data will be required to correlate with analyses to determine if heating at faying surfaces is serious.

3.5 STRUCTURAL ANALYSIS

Structural analyses were performed on two full scale leading edge designs, one with a computed weight optimum span of 30 inches, and the other with the span reduced to 15 inches to accommodate the size of the current coating facility. The 30 inch span unit is termed the "Preliminary" design configuration while the narrower version is the "Prototype" leading edge. The Prototype unit was fabricated and successfully tested to critical load and temperature conditions as reported in Section 7.2. This section of the report summarizes structural analysis results performed on the preliminary and prototype leading edges designs.

Airloads, thermoelastic and vibration analyses were conducted for the delta wing leading edge configurations to establish structural sizing and confirm design adequacy. It was found that the intercostals employed in the Phase I straight wing vehicle leading edge design (reference 2) could be eliminated on the delta wing configuration without incurring excessive thickness or weight penalties. Further, the reduced airloads permitted removal of return flanges on the airload ribs, thus simplifying fabrication.

Parametric analysis of leading edge segments with spans of 20, 30, and 40 inches resulted in identification of an optimum weight span of 30 inches, having a unit weight 1.8 lb/ft^2 . Detail analysis of the Preliminary design were therefore centered on this span. However, span variations up to ± 10 inches produce only nominal weight penalties not exceeding 0.10 lb/ft^2 .

Prototype leading edge design employed reduced venting pressure load levels compared with the Preliminary design, as discussed in Section 3.1. More conservative design allowables were also used. Even so, unit weight of the Prototype leading edge, including seal strips, was computed to be only 1.94 lb/ft^2 .

Thermoelastic analysis showed that thermally induced stresses are relatively low, producing margins of safety in excess of 100%. Vibrational stresses were likewise found to pose no problems, since margins were very high, except for one local area of a lower lug, where the computed margin is about 100% for root-mean-square (rms) loads.

Because design data for various coated RPP thicknesses and properties were not available at the beginning of Phase II, a scheme was devised for extrapolating Phase I flexure data for early preliminary design analysis until Phase II data became available for evaluation. The scheme is discussed in the Quarterly Report, reference 6, and summarized in section 3.5.1 herein. More conservative allowables were derived for the Prototype design. These proved to be reasonably good predictions if it is assumed that average test data obtained in Phase II is reduced 33% to establish design values. This reduction should cover data scatter and strength loss after a 100-mission service life.

Elaboration on these analyses, included in a discussion of the material property data employed, is provided in the following sections.

3.5.1 Mechanical Properties

Initial Allowables for the Preliminary Design - At the outset of design analysis the only mechanical property data available for diffusion coated RPP, upon which to base design, were those developed during the Phase I program. These data, however, were limited to flexure strength of coated 13 ply laminates. It was therefore necessary to extrapolate this data to other thicknesses and other properties to permit realistic leading edge sizing. Three pertinent observations had been made on this and other programs to guide the approach taken for data extrapolation:

- Coated RPP strength is generally lower than bare RPP strength.
- Coated RPP failing stress varies with laminate thickness and is significantly lower for thinner stock.
- Bare RPP failing stress varies with thickness and is lower for thinner stock, though the variation is much less severe than for coated material.

An approach was established wherein it was assumed that the coated portion of a laminate was ineffective as load carrying material and only the bare central core resisted bending, tension, and shear loads. This permitted preliminary analyses to be conducted assuming

bare RPP properties but final design thickness was determined by adding together the number of bare plies required to support loads and the number of plies assumed ineffective because of coating depth. Initial design effort assumed three ineffective plies per laminate thickness. This was ultimately proven to be too optimistic for all but flexure strength; however, high computed design margins offset the optimism so that thicknesses determined and weights calculated remain valid.

Since new design values can be established from the recent test data, Section 5.2., the actual values used for Preliminary design are important only for the purpose of validating the design and the weights computed. The particular flexure strength and flexure secant modulus used in computations are given in Figure 3-32. This illustrates the strong influence of thickness on strength, which should be typical (to varying degrees) of expected variations with other properties.

Values used for other mechanical properties are summarized in Table 3-8, baselined to 13-ply laminates for comparison with final test data. In this table is also shown an assessment of the maximum equivalent applied ultimate stress for the Preliminary design taking into account the computed margins of safety and adjusting for 13 ply data and for compression buckling. This permits a direct comparison with recent test data. Although this is not an exact technique, it is sufficient for the purpose intended.

TABLE 3-8
PROPERTIES USED FOR PRELIMINARY DESIGN AND
ASSESSMENT OF DESIGN VALIDITY

Property	Assumed Data		Test Data		
	Equivalent Allowable Stress Re: 13-Ply Coated Laminate	Margin of Safety Preliminary Design	Ultimate Applied Stress Re: 13-Ply Coated Laminate	Average Curve Fit Test Data Divided by 1.5	Revised Margin of Safety
Flexure Warp	9800	2.76	2600	9600	+2.69
Fill	5900	1.90	2000	8130	+3.07
Tension Warp	10200	0.87	5500	5680	+0.03
Fill	6100	4.60	1100	3000	+1.72
Compress Warp	9200	0.34	6900	7670	+0.11
Fill	8000	0.28	6250	7340	+0.17
Shear	2180	0.18	1850	2530	+0.37

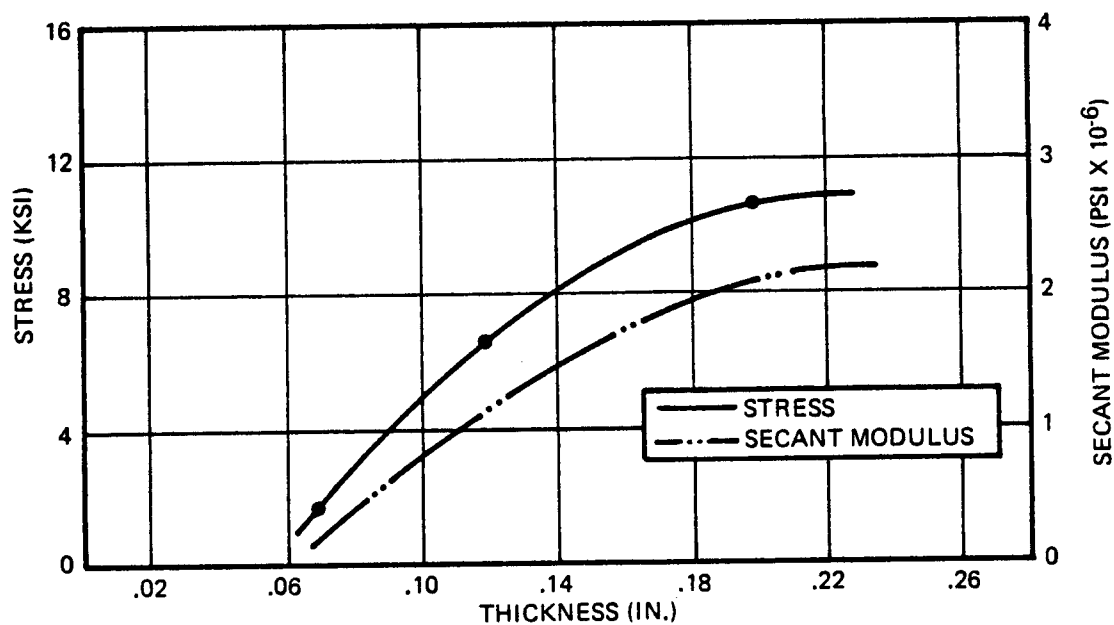


FIGURE 3-32 CALCULATED COATED DESIGN PROPERTIES

It is seen that all margins remain positive even when the assumed new allowables are established by arbitrarily reducing average test data by 33%. Therefore, the basic configuration and weights computed for the preliminary design leading edge appear to remain valid.

Revised Allowables for Prototype Design - The only data available to support the establishment of design allowables for the Prototype design were flexure data obtained from development trials of the baseline 10/60/30 silicon coating system, and limited bare RPP flexural data. More complete test data on the baseline system was not obtained until the design was committed to fabrication. An attempt was made to establish conservative allowables because simple, lightweight designs are possible with RPP even with pessimistic strength assumptions.

The approach employed was to assume that the strength of the coated system was governed by the bare, uncoated portion of the substrate, as was done for the Preliminary design. Thus, the coated layers became totally ineffective for load carrying. A total of four plies, two per laminate face, were assumed coated and non load bearing to establish design allowables. Further, a margin of safety of 25% was established for Prototype design. This has the effect of reducing the allowables by another 20%.

Design thickness data was revised for the Prototype design. Based on over three hundred measurements made on 58 panels fabricated in Phase II, a nominal thickness of 0.013 in/ply was determined to be a representative value for design. In addition a minimum of 10 plies for structural applications was established to avoid the large data scatter found in coated thinner laminates.

With these assumptions, and others summarized below, the design curves shown in Figures 3-33 and 3-34 were derived. The comparative flexure test data shown on the curves were obtained from variations of the 10/60/30 silicon coating and included such planned differences as batches of coating materials, packing densities, and retort configurations. These variations, which were being evaluated so that final processing could be established, accounts for the wide data scatter. The design points fall near the lowest test points experienced. It should be noted that test data was obtained from specimens with the edges coated to a depth of at least 0.05 inch per side. If the data is adjusted to correct for this edge effect in accordance with the assumptions of the ineffectivity of the coating material, the data band is raised 15% and the flexure strength and flexure secant modulus curves more nearly meet minimum test values obtained. This was believed to be suitably

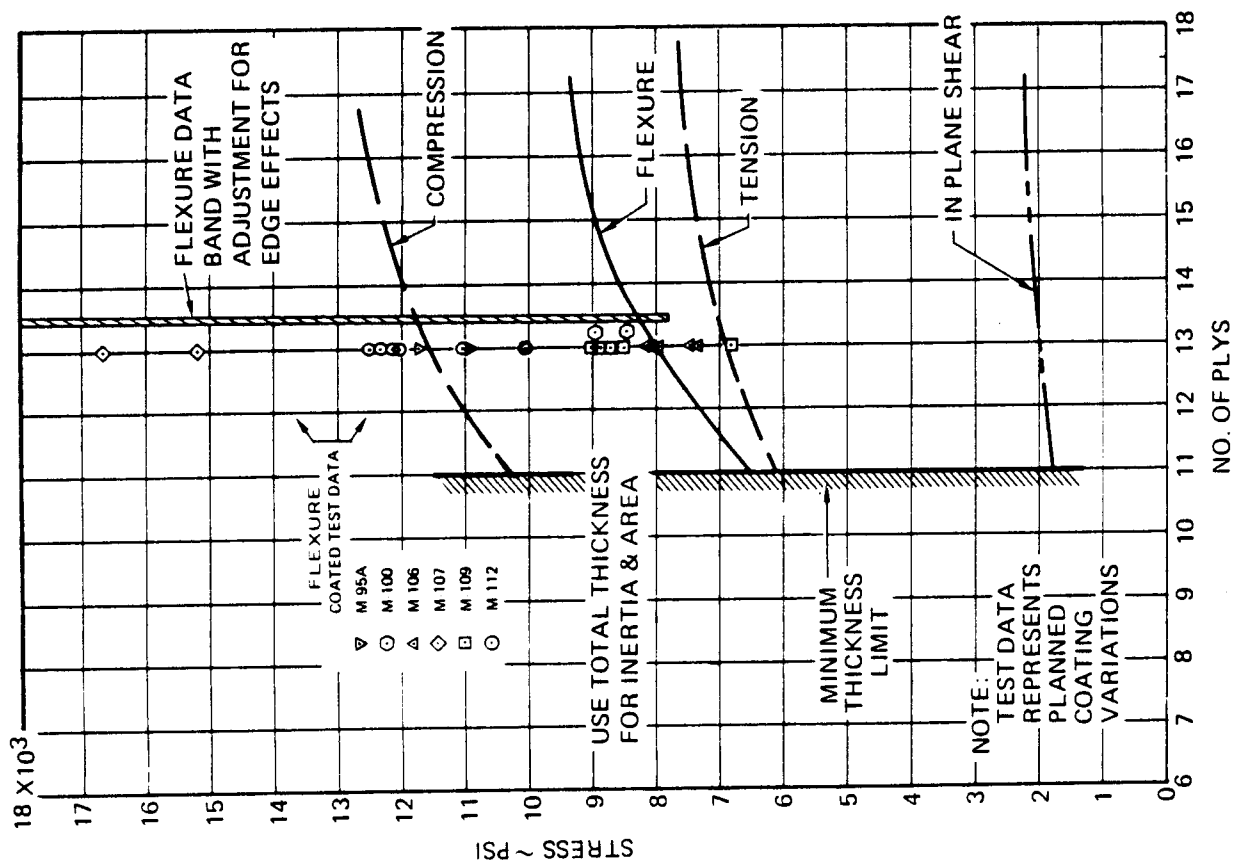


FIGURE 3-33 COATED RPP STRESS ALLOWABLES -- WARP PROTOTYPE DESIGN

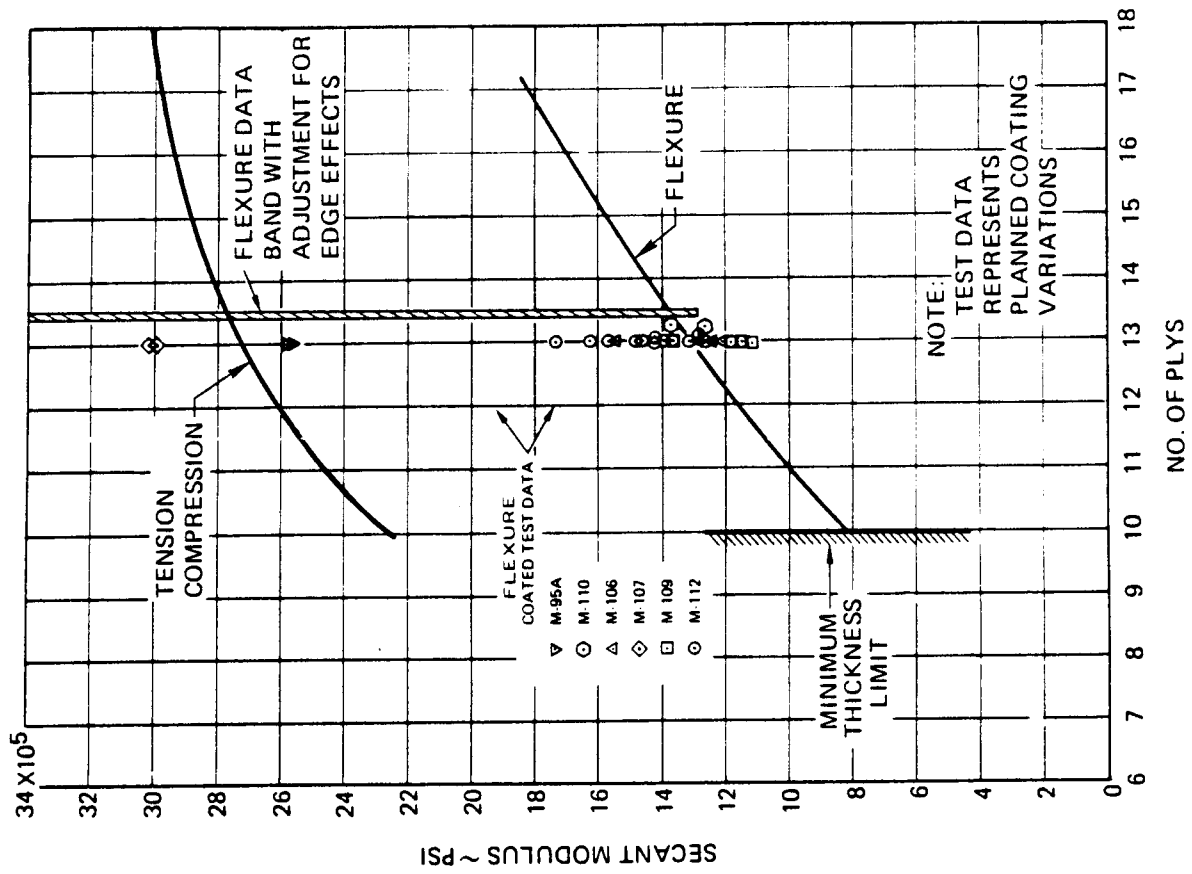


FIGURE 3-34 COATED RPP MODULUS -- WARP PROTOTYPE DESIGN

conservative because final process selection was expected to produce significantly better results than the lowest data points obtained in trial runs. This optimism was borne out by the test data reported in Section 5.2.

TABLE 3-9

PROPERTIES USED FOR PROTOTYPE DESIGN AND ASSESSMENT
OF DESIGN VALIDITY

Property	Design Allowable Employed Re: 13 Ply Laminate	Computed Margin of Safety	Ultimate Applied Stress Re: 13 Ply Laminate	Average Curve Fit Test Data Divided by 1.5	Revised Margin of Safety
<u>Strength</u>					
Flexure Warp	8000	2.51	2280	9600	High
Fill	4800	3.36	1430	8130	High
Tension Warp	6900	0.28	5400	5680	0.05
Fill	4200	4.44	770	3000	High
Compress Warp	11500	0.69	6800	7670	0.13
Fill	6900	1.12	3250	7340	1.26
Shear	1900	0.28	1500	2530	0.69
<u>Elastic Modulus</u>					
				<u>Average Test Value</u>	
Flexure Warp	1.31×10^6	N.A.	N.A.	1.45×10^6	
Fill	0.79×10^6	N.A.	N.A.	1.25×10^6	
Tension Warp	2.7×10^6	N.A.	N.A.	1.40×10^6	
Fill	1.63×10^6	N.A.	N.A.	1.48×10^6	
Compress. Warp	2.7×10^6	N.A.	N.A.	2.08×10^6	
Fill	1.63×10^6	N.A.	N.A.	1.53×10^6	
Shear	1.10×10^6	N.A.	N.A.	Not available	

The tension curve in Figure 3-33 was established assuming tensile strength of bare stock to be 60% of the flexure values and four plies rendered ineffective by the coating. Compression allowables were based

on the bare flexure value corrected for four ineffective plies, while inplane shear stress was based on 2830 psi strength for bare material (average $\div 1.15$), which when corrected for coating reduces to 1960 psi for a 13 ply laminate. Thickness variations of these properties are included on Figure 3-33.

Axial (tension and compression) elastic modulus for bare material was assumed equal to the values obtained on bare flexure bars. When adjusted to account for the four ineffective coated plies, the difference between axial and flexural elastic moduli for coated material becomes pronounced. Test data, summarized in Section 5.2, indicate that the axial moduli prediction was optimistic. This, however, should have little effect on the design.

In order to illustrate the comparison of these assumed allowables with the recent test data obtained for the selected coating system, the data in Table 3-9 is provided. This is similar to Table 3-8 in which data is shown referenced to 13 ply material and the actual computed margins of safety for the Prototype leading edge design. As can be readily seen by the data, positive margins exist on the Prototype units even when the average test data of Section 5.2 is reduced 33% to account for data scatter and mission life degradation. It is anticipated that this will prove to be a conservative assumption. Some degree of optimism on elastic modulus in the axial direction can be seen. This may have some effect on the stress distribution computed, but in view of the low operating stresses this is not believed to be significant.

A Prototype leading edge has been successfully tested to limit design pressure load. The applied stress levels, evaluated against computed stresses, indicates that the design operated at a maximum of 46% of average test data. This analysis is based on tension stresses in the warp direction being the most critical as the full scale test data indicated.

Coefficient of thermal expansion data for siliconized RPP was taken from the Phase I baseline siliconized system and is shown in Figure 3-35 for both warp and fill directions. Bare RPP data is plotted for comparison. A retest of the Phase I baseline M-30 system was conducted in Phase II and is designated on the figure as "retest". While the retest does not result in an exact duplication of the original data, the scatter band is not considered significant (especially in the fill direction) for the developmental status of the material. Below 2000°F, before the specimen begins glowing, data scatter could have been aggravated by shadows partially obscuring the control marks. This shadowing has since been corrected with specimen redesign. Design curves used in thermoelastic analysis are indicated on the figure and are approximate

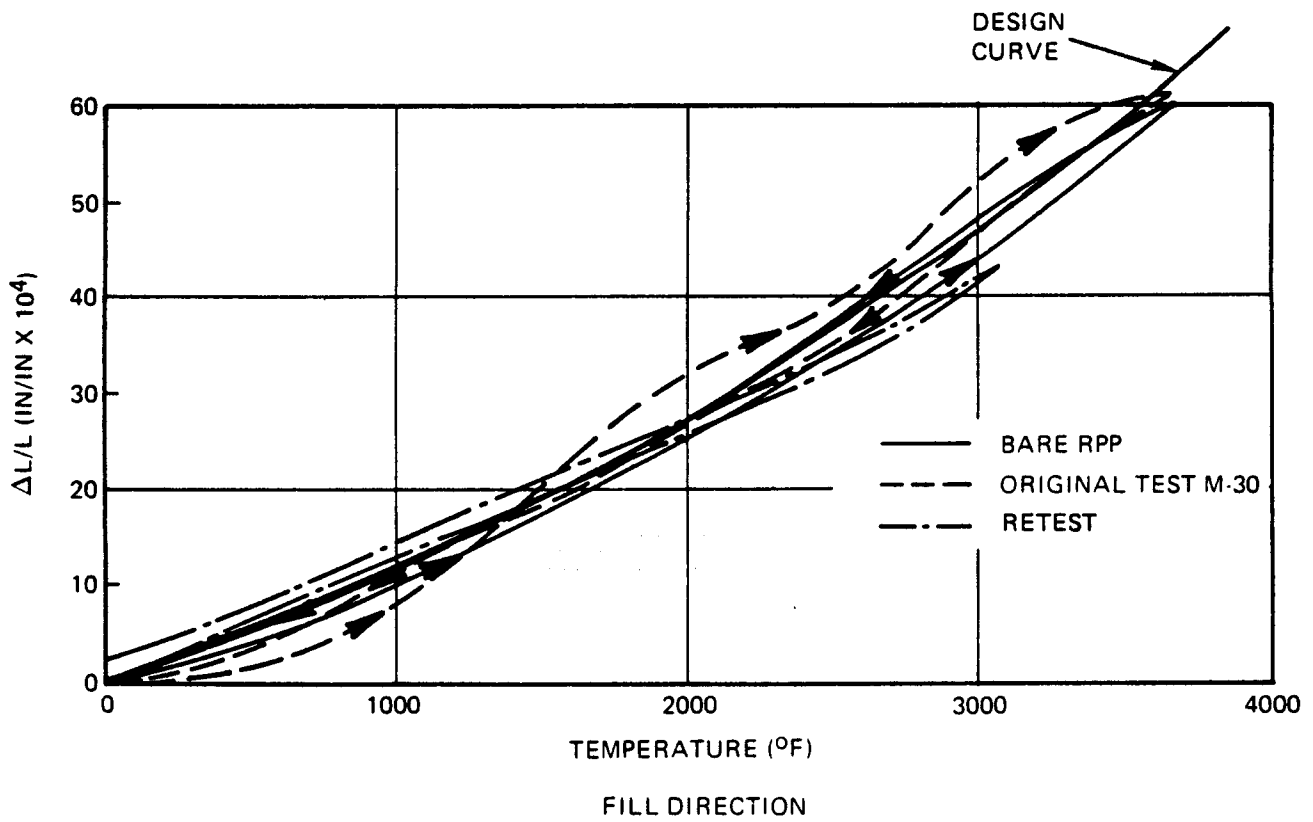
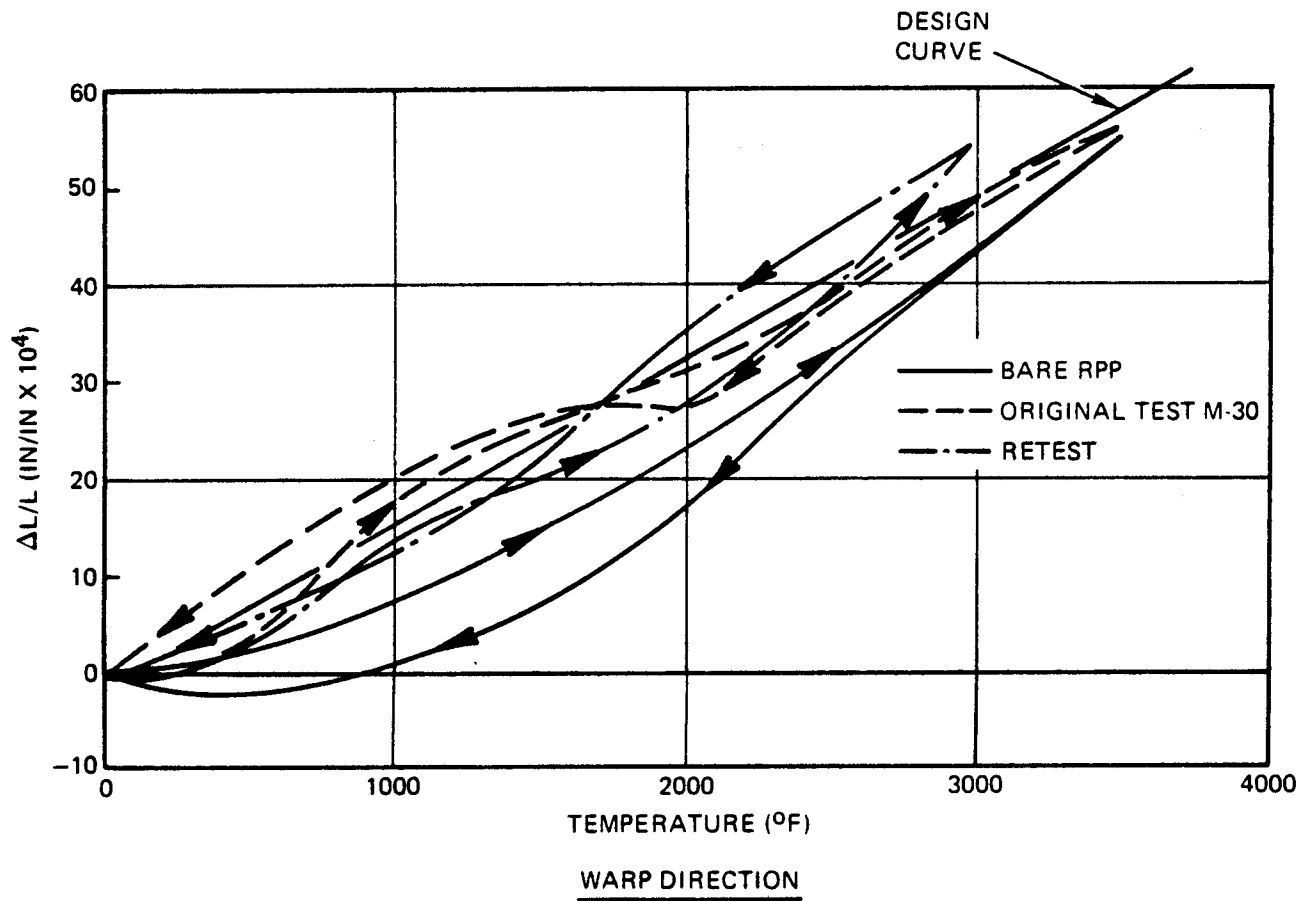


FIGURE 3-35 COEFFICIENT OF THERMAL EXPANSION

averages of the coated data. Thermal expansion is very low for the coated RPP material and, when combined with the low elastic moduli determined from test, produces relatively low thermoelastic stresses.

3.5.2 Airloads Analysis

The delta wing vehicle baseline leading edge configuration experiences lower airload pressure than the design analyzed in Phase I (reference 2) due to sweepback. By virtue of its more cylindrical shape, it is structurally more efficient, because more loads are carried in-plane as hoop loads rather than by flat panel bending. Initial Phase II analyses indicated that both the intercostals and return flanges on the ribs could be eliminated on the new geometry. Detail analyses proved this to be feasible, and it results in a simpler, more fabricable structure than that of Phase I. Further, it eliminates the need for stiffeners (intercostals), bonded to the airload panels, to gain efficiency.

The leading edge was sized by boost airload conditions and was subsequently checked for entry thermal gradients to ensure that thermoelastic stresses did not exceed allowables. Boost vibration analysis was also conducted to verify design adequacy. This section describes the airloads analysis conducted and summarizes results. Materials allowables used for design are presented in section 3.5.1.

The NASTRAN computer routine was employed in leading edge analysis. It uses finite element structural members in a displacement analysis, and includes both membrane and bending elements. Anisotropic materials can be included. Loads, stresses and displacements are outputs, but in addition, the routine offers geometry plots showing both the unloaded and loaded shapes. This provides a verification that the correct geometry is being analyzed.

Preliminary Design of 30 Inch Segment - Parametric analyses were conducted on 20, 30, and 40 inch leading edge segment spans to determine optimum span size. On the basis of weight alone, a 30 inch segment span produced the lowest unit weight and was selected for more detailed analysis. The unit weight variation with span is shown in Figure 3-36. A one-pound allowance was included for the attachment bolts and hard insulators. Unit weight is expressed in terms of outside curved surface area (not plan form area) and includes the weight of seal strips between each segment but excludes overlap type trailing edge seal strips, since these were not analyzed for the Preliminary design.

The 30 inch span Preliminary design was discussed in detail in the Quarterly Report, reference (6). Since the Prototype design supersedes the Preliminary design, only the Prototype design analysis will

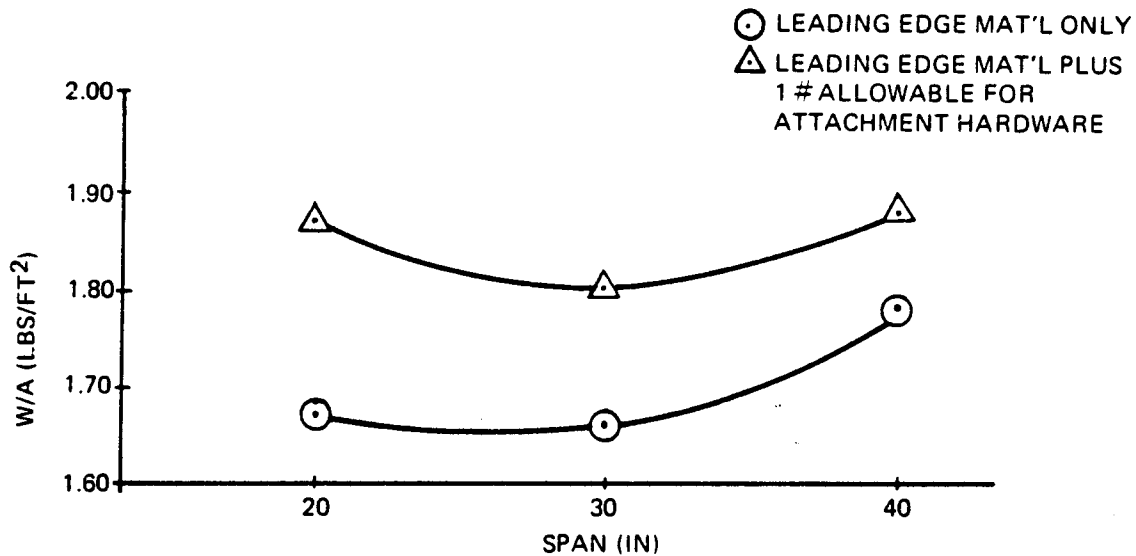


FIGURE 3-36 LEADING EDGE WEIGHT VARIATION WITH SPAN

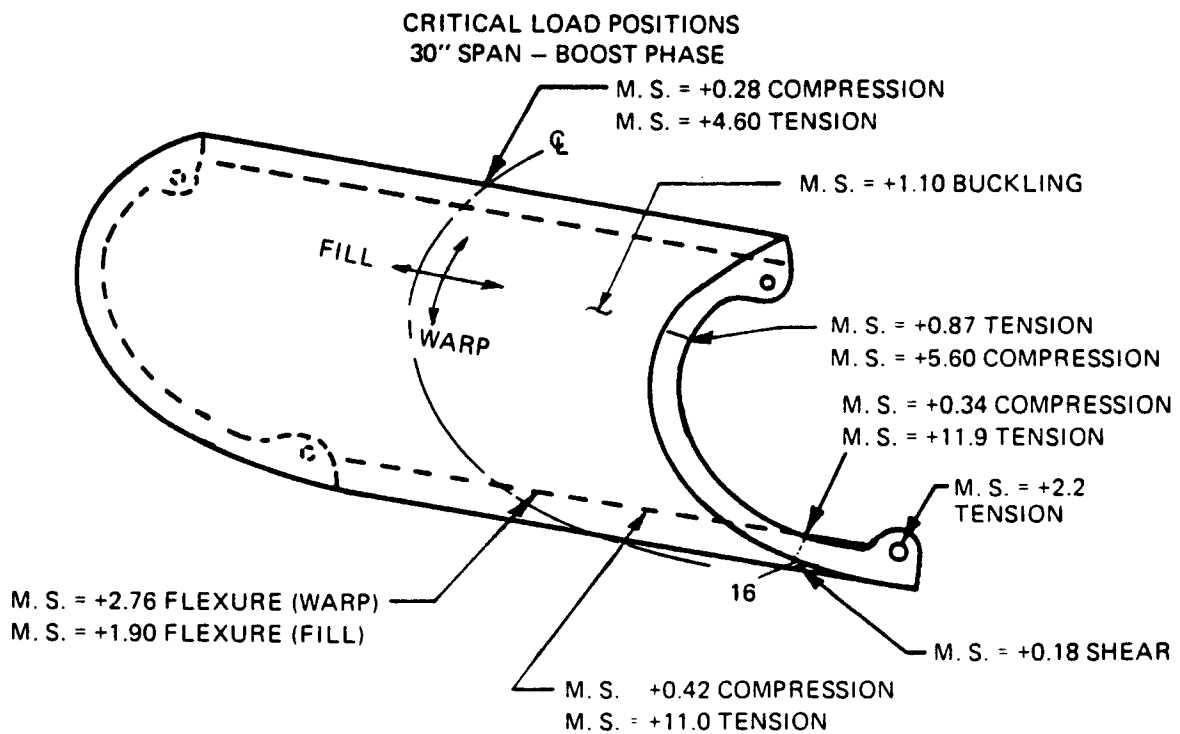


FIGURE 3-37 SUMMARY OF MINIMUM MARGINS OF SAFETY PRELIMINARY DESIGN 30 INCH SEGMENT SPAN

be covered in detail herein. However, margins of safety computed for the Preliminary design are summarized in Figure 3-37. These are given in terms of the initial allowables used for design. An assessment of the validity of these values in terms of recent test data is discussed in Section 3.5.1, and shown in Table 3-8 with a comparison of applied stresses. As discussed previously, all margins are positive.

Prototype Design - 15 Inch Segment - The Prototype leading edge was limited to 15 inch span because of coating facility size limitations. However, 15 inch segments could be utilized on the Shuttle, even though preliminary analysis indicates the optimum span to be twice this length. The Prototype units were designed and sized as though 15 inch segments would be employed on the vehicle. Materials design data is shown in Section 3.5.1, along with an assessment of the data used, compared with more current allowables (Table 3-9).

Computed margins of safety using the assumed design allowables are shown in Figure 3-38. Revised values based on recent test data reduced by 33%, are shown in Table 3-9 and Table 3-10.

The geometry used in the computer analysis is shown in Figure 3-39. Because of symmetry only one-half of the 15 inch span required modeling, since boundary conditions could be specified at the centerline. The skin is simulated by anisotropic quadrilateral elements, containing both membrane and bending plate properties. Rib and spanwise beams were modeled as bar (beam) elements. A total of 90 plate and 32 bar elements were used to describe one-half of the leading edge panel.

Ultimate boost pressure loads used in the NASTRAN analysis are shown in Figure 3-40 and were developed from the boost loads given in Figure 3-5. Load case II, which applies a maximum burst pressure on the lower panel of 3.70 psi ultimate, generally produces maximum stresses and deflections. Ultimate bending moment and axial load distributions for the rib and upper and lower spanwise beams are presented in Figures 3-41 and 3-42, respectively, for the critical boost loading conditions. The maximum moment is 980 in-lb for the rib and only 160 in-lb for the lower spanwise beam.

Upper and lower lug reactions for the four boost load conditions and a summary of lug margins of safety are given in Figure 3-43. The high margins shown are the result of two factors: (1) the method of fabrication of the corners of the leading edge produces an overlap of rib and beam plies (Figure 3-11) and inherently results in a thickened lug region, and (2) the uncertainty of lug allowables results in a conservative edge distance being employed. As part of the joint test

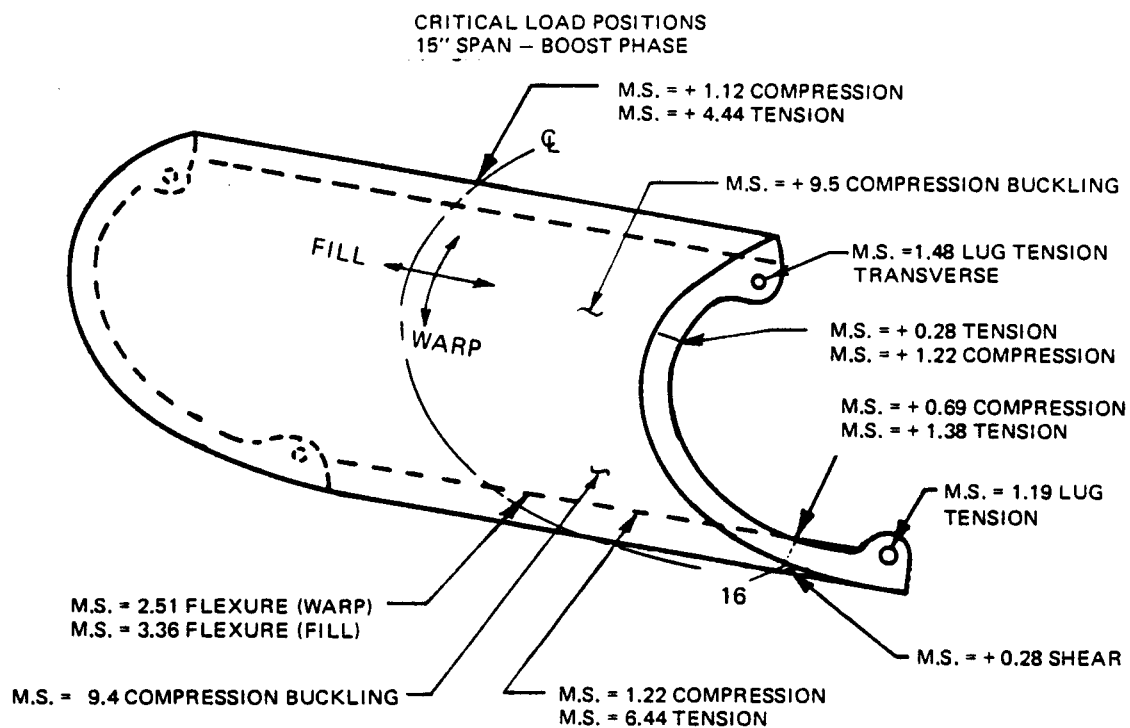


FIGURE 3-38 SUMMARY OF MINIMUM MARGINS OF SAFETY PROTOTYPE DESIGN - 15 INCH SEGMENT SPAN

TABLE 3-10

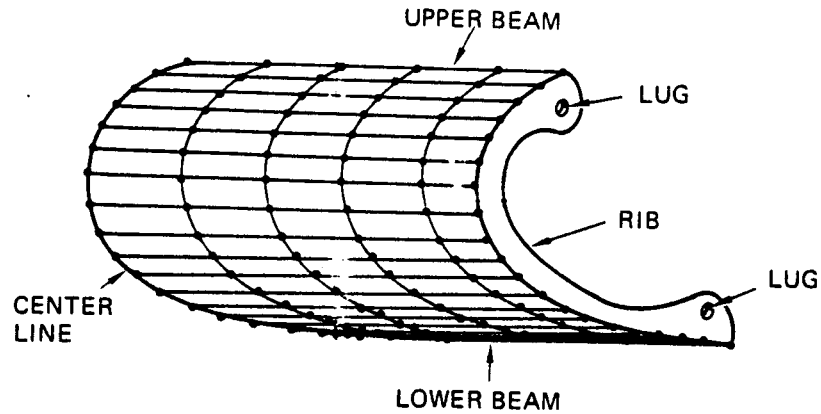
MARGINS OF SAFETY

ITEM	ULT APPLIED STRESS - PSI	CRITICAL LOAD CASE	ALLOWABLE STRESS - PSI	INITIAL ⁽¹⁾ MS	REVISED ⁽²⁾ MS
Rib	-6520 flexure, axial	Venting lag $\alpha = -5.8^\circ$	-11,000 Crippling (warp)	+0.69	+0.13
	5085 flexure, axial	Venting lag $\alpha = -5.8^\circ$	6,500 tension (warp)	+0.28	+0.05
Upper Beam	-2690 flexure, axial	Venting lag $\alpha = 4.0^\circ$	-7650 Compression (Fill)	+1.12	+1.26
			5900 Flexure (Fill)		
	865 flexure, axial	Vented $\alpha = -5.8^\circ$	4,700 tension (Fill)	+4.44	High
Lower Beam	-2475 flexure, axial	Venting lag $\alpha = -5.8^\circ$	-5,500 Crippling (Fill)	+1.22	+1.09
	630 flexure, axial	Vented $\alpha = 4^\circ$	4,700 tension (Fill)	+6.44	High
Skin	1570 shear	Venting lag $\alpha = 5.8^\circ$	2,000 inplane shear	+0.28	+0.69
	1390 flexure	Venting lag $\alpha = -5.8^\circ$	8,550 Flex. (Warp)	+2.51	High
	885 Tension		7,250 Tension (Warp)		
	1,110 flexure	Venting lag $\alpha = -5.8^\circ$	5,150 flexure (Fill)	+3.36	High
	60 Tension		4,400 Tension (Fill)		
	-400 compression	Venting lag $\alpha = 4.0^\circ$	4,400 Fill buckling	+10.0	High
	-220 compression	Vented $\alpha = 4.0^\circ$	2,300 Fill buckling	+9.4	High
Lug	232 Lbs Tension Lower Lug	Venting lag $\alpha = -5.8^\circ$	686 Lbs Axial	+1.19	1.26
	266 Lbs Trans Upper Lug		512 Lbs Trans	+1.48	1.56
Skin at Centerline	-510 compression	t = 400 sec	4,400 fill longitudinal buckling	+7.6	High
Rib	-2,580 compression	t = 380 sec	6,300 comp	1.44	2.06
	+1,100 tension	t = 240 sec	(warp) at 2170°F		
Skin at the Rib	+1,100 tension	t = 380 sec	5,930 tension	+4.4	High
	-1,260 compression	t = 240 sec	(warp) at 1400°F		

(1) Margins based on initial assumed prototype design allowables (Ref. Section 3.5.1)

(2) Margins of safety estimates based on recent test data Section 5.2

NASTRAN MODEL
FOR STATIC
ELASTIC LOAD
ANALYSIS



- Ⓝ BAR IDENTIFICATION
- ▢ QUADRILATERAL IDENTIFICATION
- N GRID POINT IDENTIFICATION

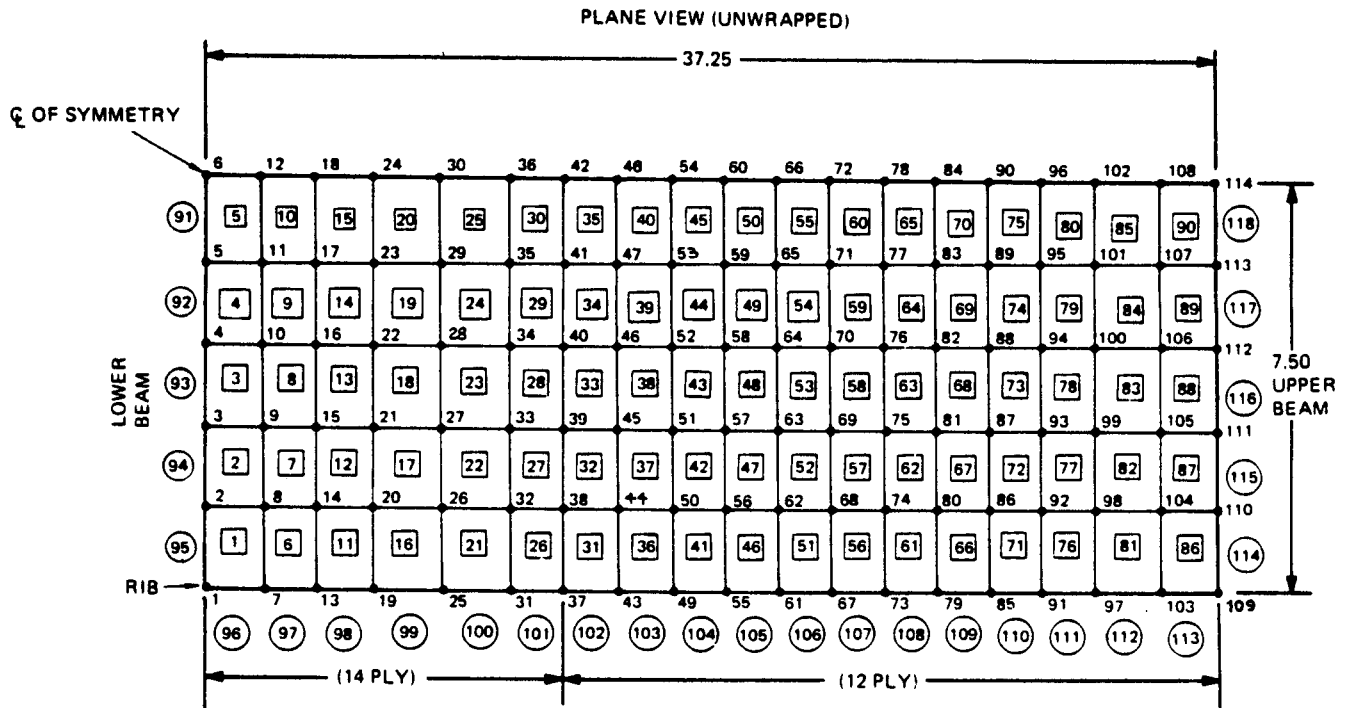


FIGURE 3-39 NASTRAN MODEL – LEADING EDGE

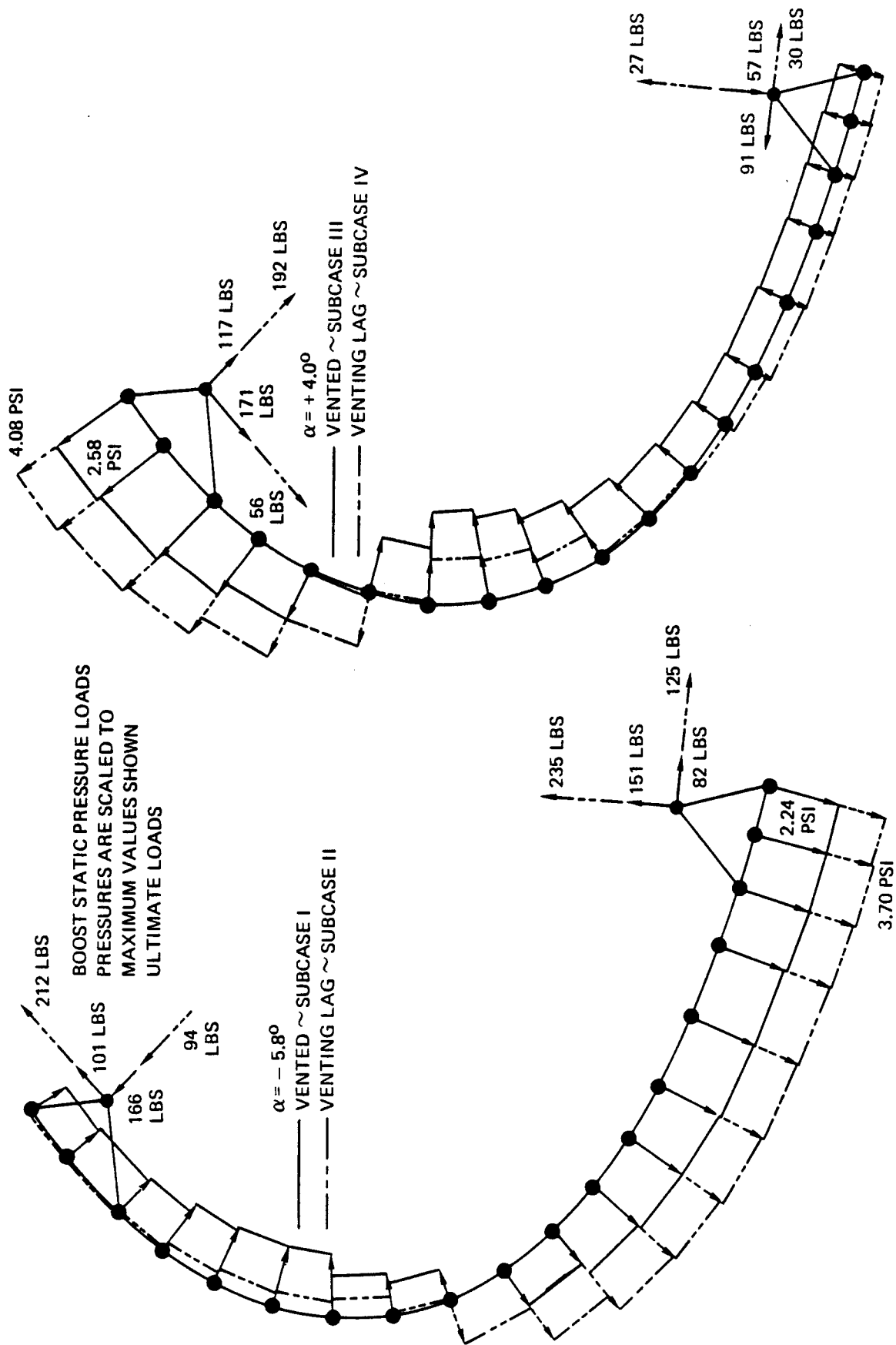


FIGURE 3-40 PRESSURES USED IN STATIC LOAD ANALYSIS

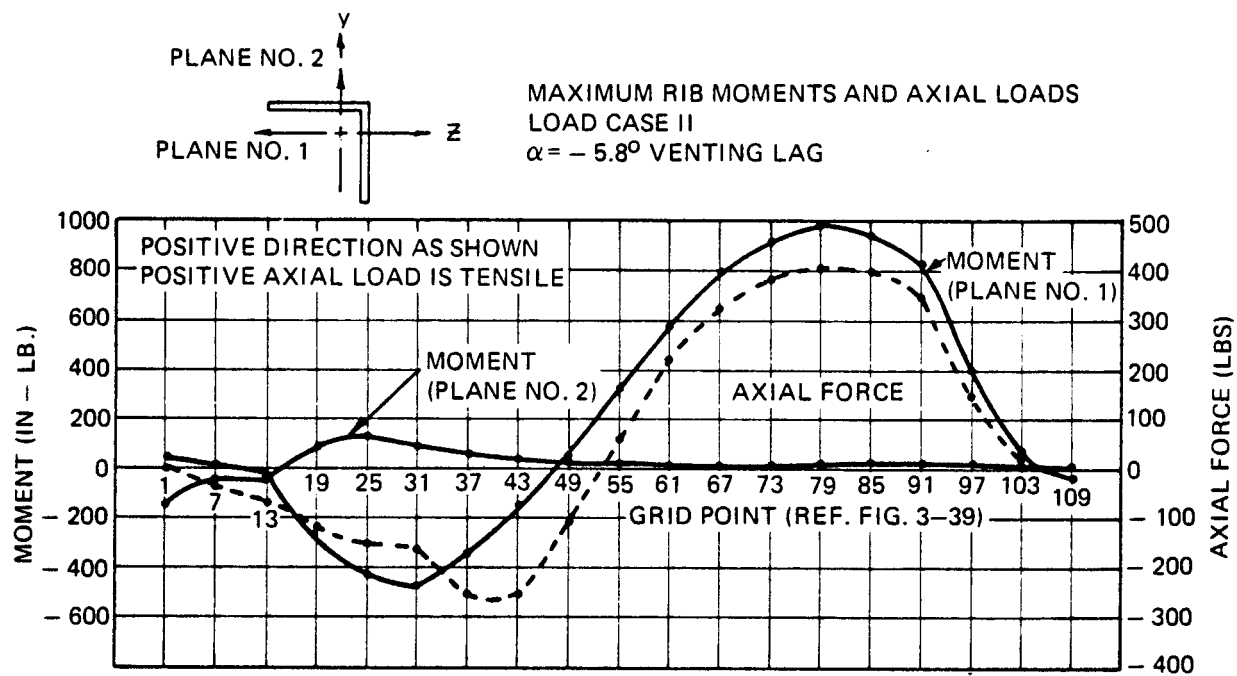


FIGURE 3-41 ULTIMATE LOADS - RIB

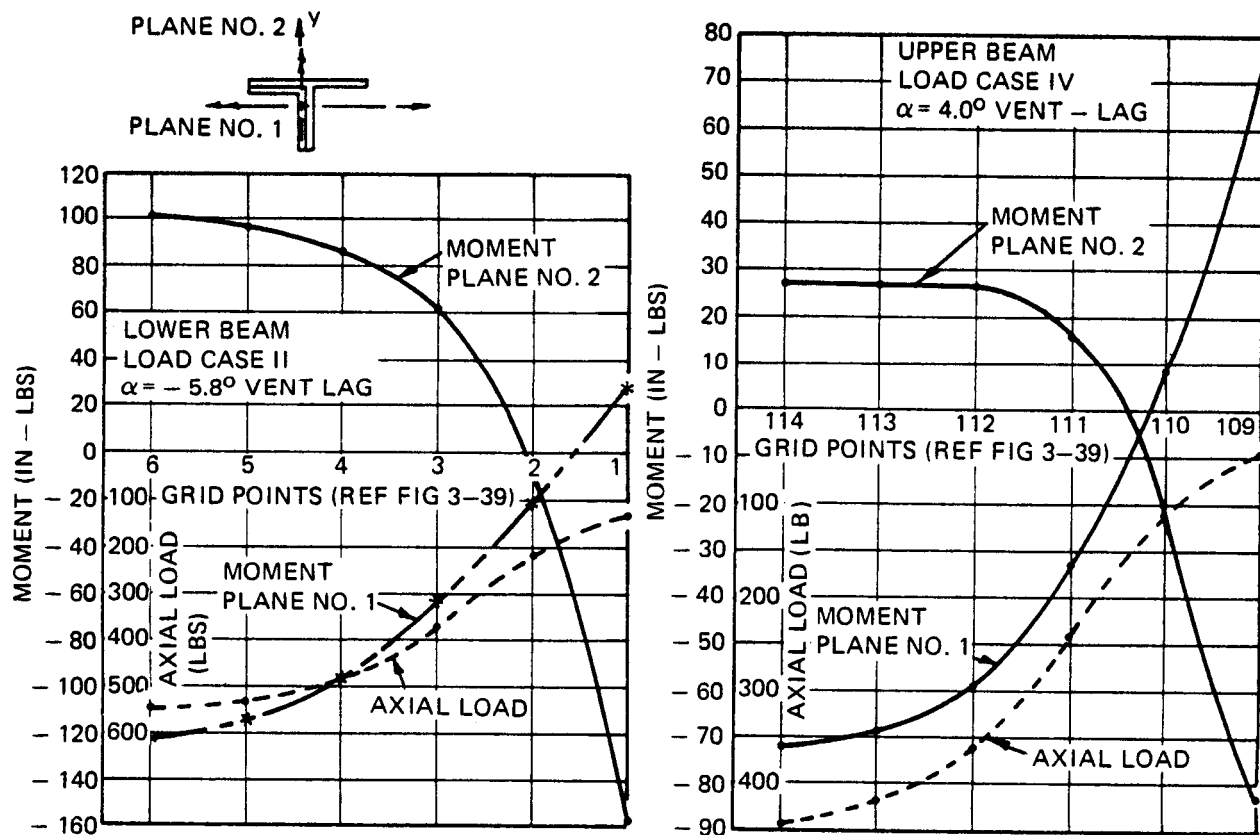
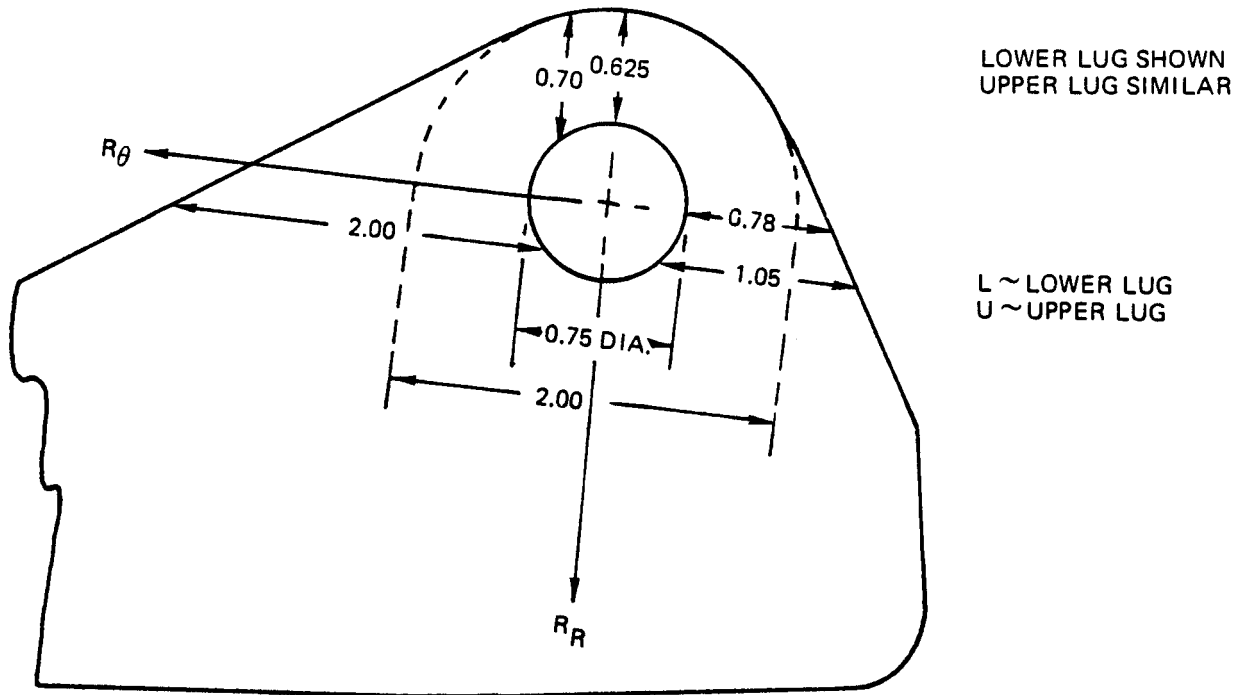


FIGURE 3-42 ULTIMATE LOADS - BEAMS



LOAD CASE	ULTIMATE LOAD – LBS				M.S.	
	R_{R_L}	R_{R_U}	R_{θ_L}	R_{θ_U}		
					L	U
I	- 151	165	- 8	101	3.50	4.08
II	- 235	93	- 124	211	1.19	1.48
III	57	- 116	90	- 170	4.62	1.49
IV	- 27	- 192	- 29	- 56	12.1	2.98

FIGURE 3-43 LUG REACTIONS AND MARGINS OF SAFETY

program (Section 5.2.3) lug design data was obtained and substantiates that the lug design is more than adequate.

Maximum airload panel (skin) stresses, which are comprised of bending and membrane stresses are presented in Figures 3-44 and 3-45. It can be seen that the skin stresses are relatively low and peak at the centerline in the flattened region of the lower panel, as would be expected. This particular area of the panel has the greatest deflection as shown in Figure 3-46 where the plotted deflections are amplified eight times. These deflections are lower than would be computed from a flat plate bending analysis, apparently due to the tension membrane loads transmitted from the more curved forward area of the leading edge. A maximum deflection of 0.123 inch occurs at the center of the segment. The deflection was limited by design to a value not to exceed one times the skin thickness. Deflection along the rib is a very small 0.038 inch.

The membrane portion of the skin stresses for the maximum collapse pressure boost conditions are shown in Figure 3-47 for chord (hoop) and spanwise components. The maximum spanwise value is 400 psi, while 220 psi is the maximum hoop value. These stresses were used in evaluating buckling stability of the airload panel, where allowable buckling stresses were established using the data contained in NASA CR-912, "Shell Analysis Manual", for axially and hydrostatically loaded cylinders.

Interaction of hoop and spanwise stress components employed the formulas from "Analysis and Design of Flight Vehicle Structures" by Bruhn. The stability analysis shows the panel to be highly stable, the minimum margin of safety being 940% as noted on Figure 3-47. However, due to the inability to evaluate the effect of bending stresses on compression buckling, testing is required to confirm panel integrity under compressive loading.

Maximum shear stresses in the airload panel for the critical boost condition are given on Figure 3-48. This shows that a maximum value of 1567 psi is developed at the intersection of the rib and beam on the lower surface. The shear stress shown is comprised of (1) the membrane portion, resulting from reacting the hoop loads generated by the curved forward part of the leading edge, and (2) a torsional component produced from lower panel deflection being restrained along the edge by the beam and rib. The margin of safety at this location is 0.28 and is one of the lowest computed margins on the leading edge. By comparison, thermoelastic induced shear stresses, discussed in section 3.5.3 are relatively insignificant as indicated in Figure 3-49.

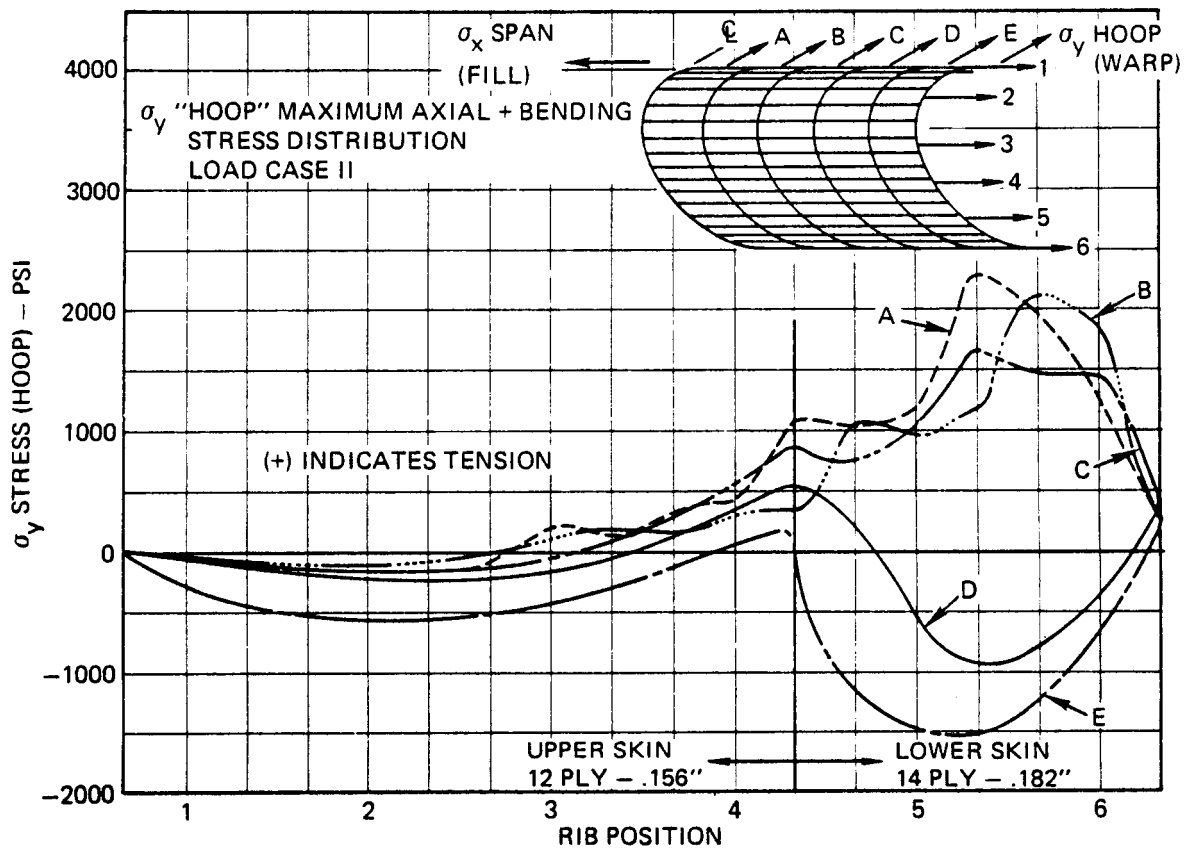


FIGURE 3-44 MAXIMUM HOOP DIRECTION SKIN STRESSES - ULTIMATE

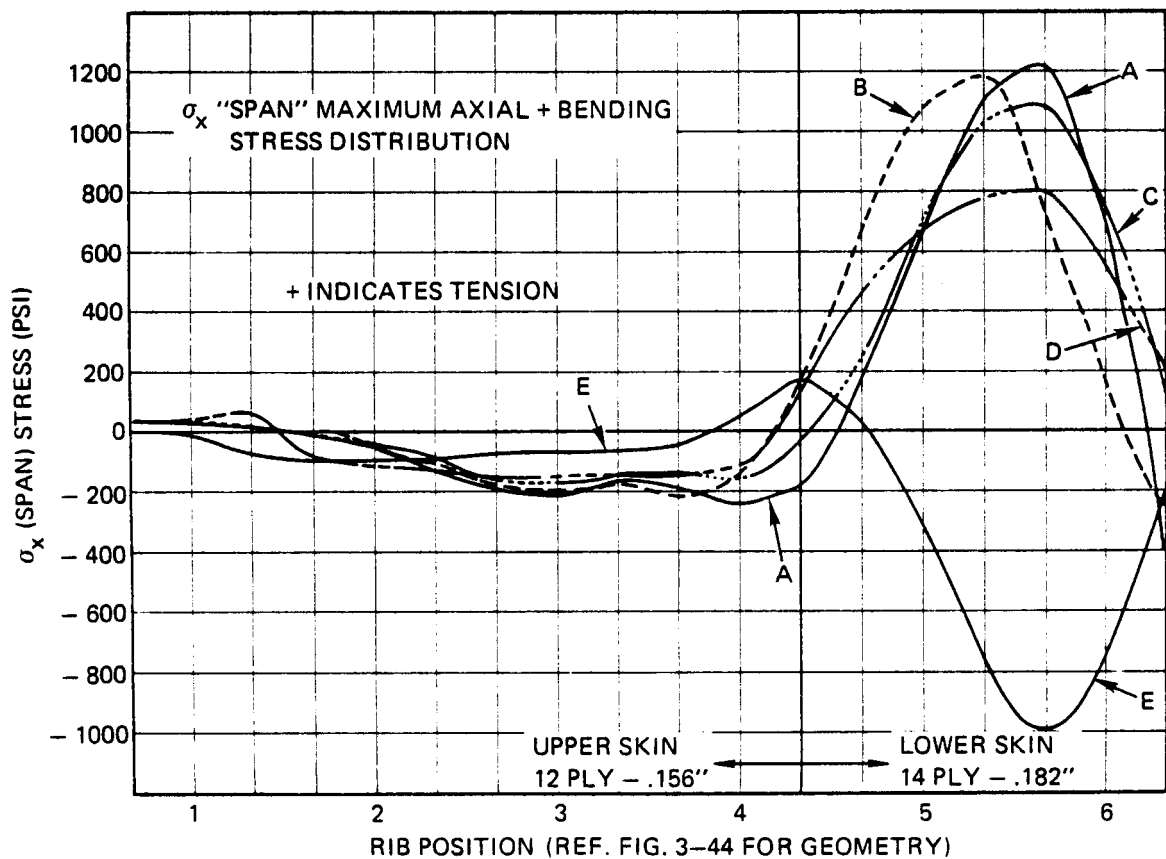


FIGURE 3-45 MAXIMUM SPANWISE DIRECTION SKIN STRESSES - ULTIMATE

SUBCASE II
 $\alpha = -5.8^\circ$
VENTING LAG

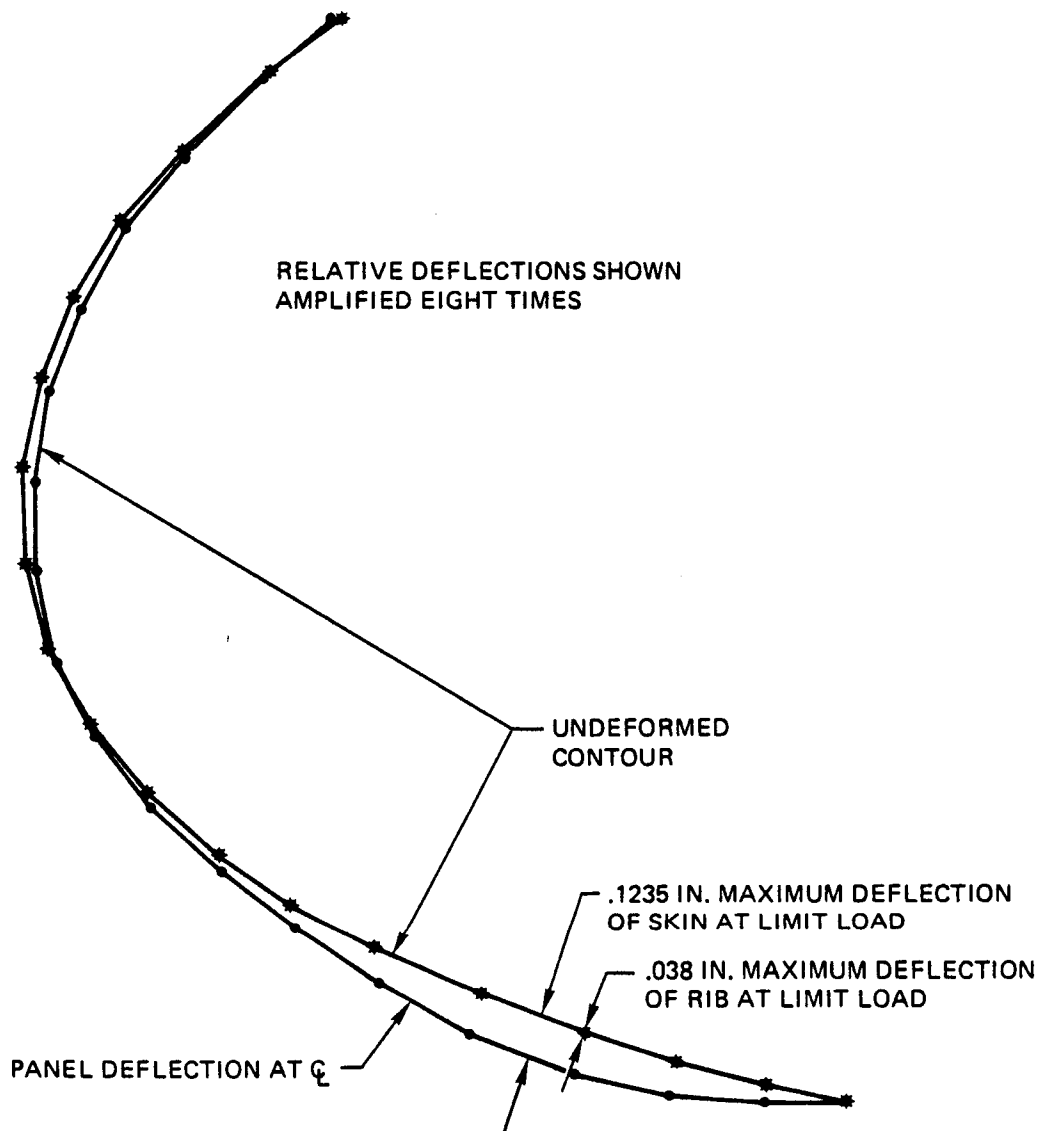


FIGURE 3-46 RELATIVE SKIN DEFLECTIONS AT LIMIT LOAD

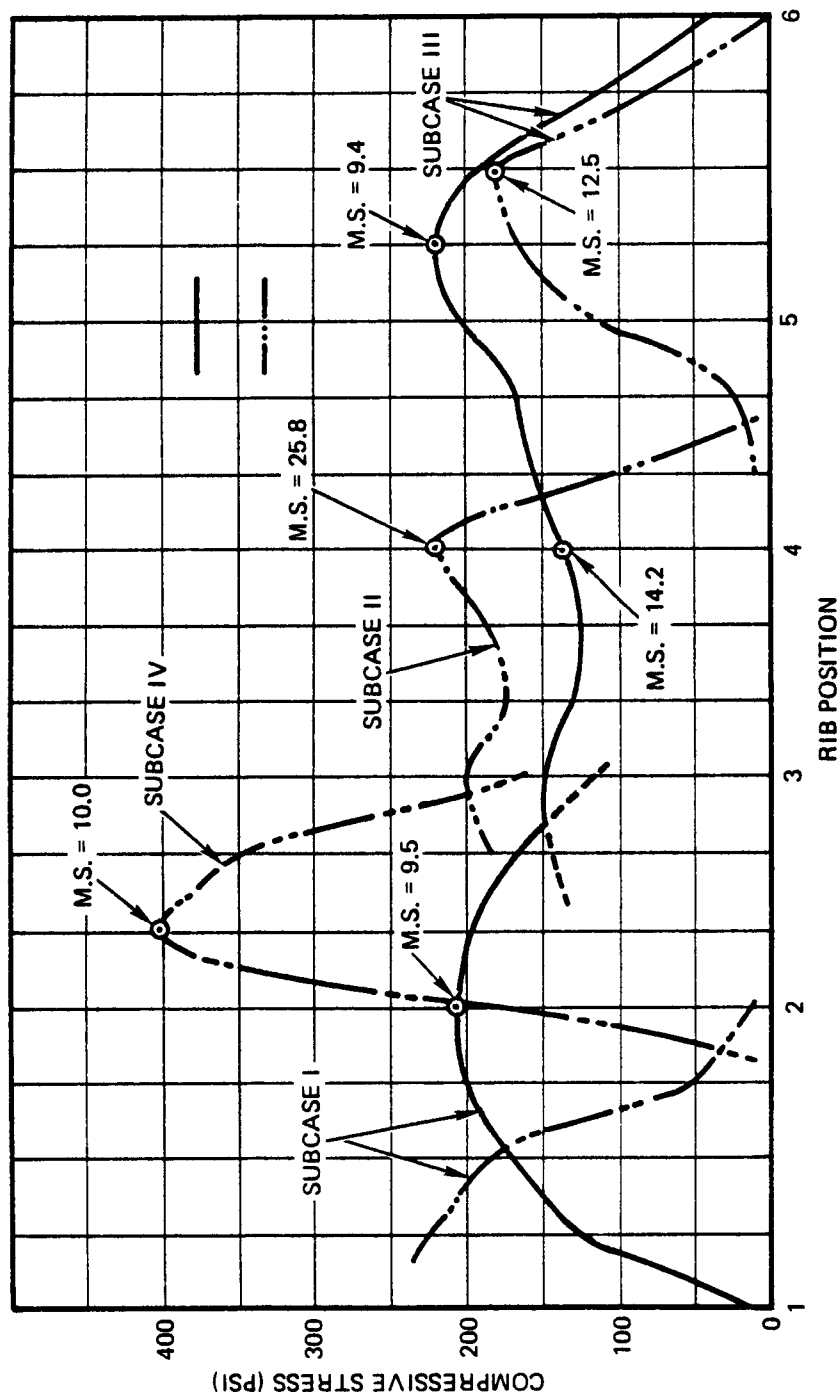
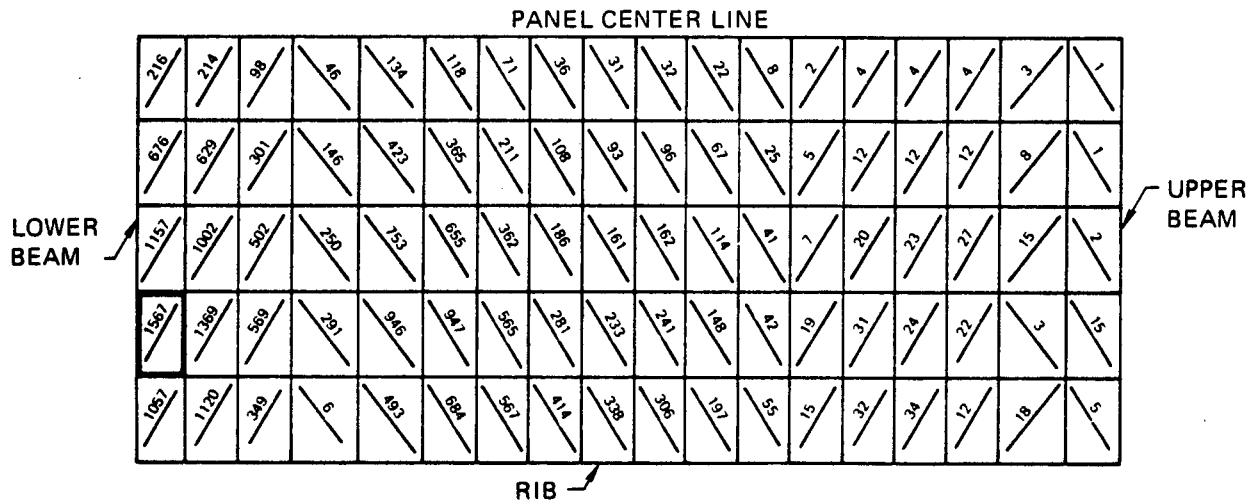
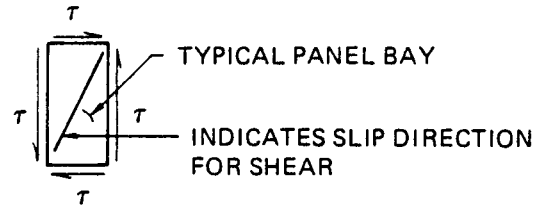
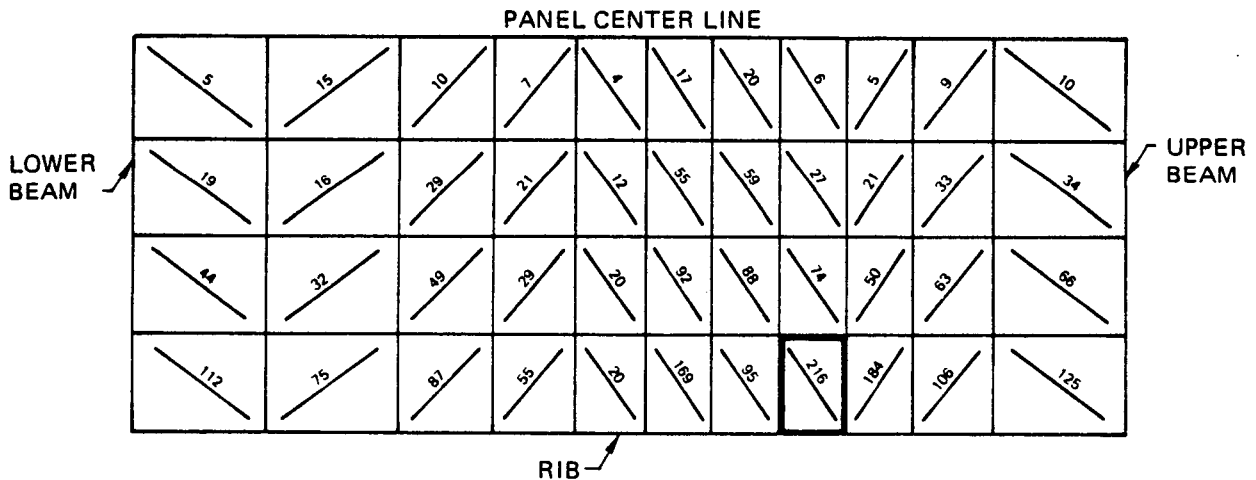


FIGURE 3-47 COMPRESSIVE MEMBRANE STRESSES
(REF. FIG. 3-44 FOR GEOMETRY)
(ALL CUTS TAKEN AT SECTION "A")



ELEMENT GEOMETRY IS THE SAME AS THAT SHOWN ON FIGURE 3-39
LOAD CASE II IS THE MOST CRITICAL CASE FOR SHEAR.

FIGURE 3-48 SHEAR STRESS DISTRIBUTION ON LEADING EDGE SKIN PANEL – ULTIMATE LOAD CASE II



NOTE: STRESSES AND GEOMETRY BASE ON 30" SPAN MODEL.
HOWEVER, RESULTS ARE APPLICABLE TO CURRENT
DESIGN.

FIGURE 3-49 SHEAR STRESS DISTRIBUTION ON LEADING EDGE DUE TO THERMAL LOAD – t = 400 SEC. ULTIMATE

A summary of margins of safety for the 15 inch span Prototype leading edge segment is given on Figure 3-38 for the assumed design allowables. These have been converted in terms of the more recent test data (reduced 33%) to provide the updated margins of safety listed in Table 3-10. The revised data shows the minimum margin of safety to be 5% for tension in the ribs and 13% for rib compression stress. Skin panel shear stresses produce a margin of 69%, while all other areas of the panel also have comfortably high computed margins.

3.5.3 Thermoelastic Analysis

Thermoelastic analyses were performed on the airload panels and ribs for conditions producing maximum thermal gradients encountered during entry. The NASTRAN computer routine, discussed previously, was used for these analyses and included the effect of temperature dependent properties. The airload panel was modeled in a fashion similar to that for the airloads analysis, but a finer grid, shown in Figure 3-50 was employed to describe the ribs. The grid size for the skin panel is indicated by the plot of resultant shear stresses shown in Figure 3-49.

The most severe temperature gradients in the airload panel skin occur at the maximum temperature condition 420 seconds after initiation of entry (measured from 400,000 feet altitude). The ribs were analyzed for two conditions: (1) maximum gradients at 240 seconds after initiation of entry, and (2) maximum temperatures occurring approximately 380 seconds after entry (reference, section 3.4.2). In no case are thermoelastic stresses high. This is attributed to the low coefficient of thermal expansion and low elastic modulus of RPP, as well as small gradients.

The maximum skin shear stresses computed are shown in Figure 3-49 for the thermal profile of Figure 3-21. As previously pointed out, shear stresses are very small with the maximum value being only 216 psi. Axial stresses in the skin were found to be correspondingly insignificant not exceeding 510 psi as can be noted in Figures 3-51 and 3-52.

Rib stresses, computed from the gradients given in Figures 3-22, 3-23, and 3-24 are illustrated in Figure 3-53. The rib model, Figure 3-50 is comprised of bar elements at the skin-rib intersection and membrane elements for the remainder of the rib. The stresses were found to be reasonably small with the maximum value being compression of the rib flange (2580 psi) in the stagnation region at 380 seconds after initiation of entry. Maximum computed tensile stress is 1110 psi on the flange and occurs during initial heatup (240 sec. after initiation of entry). These low stresses are apparently due to the relatively small rib

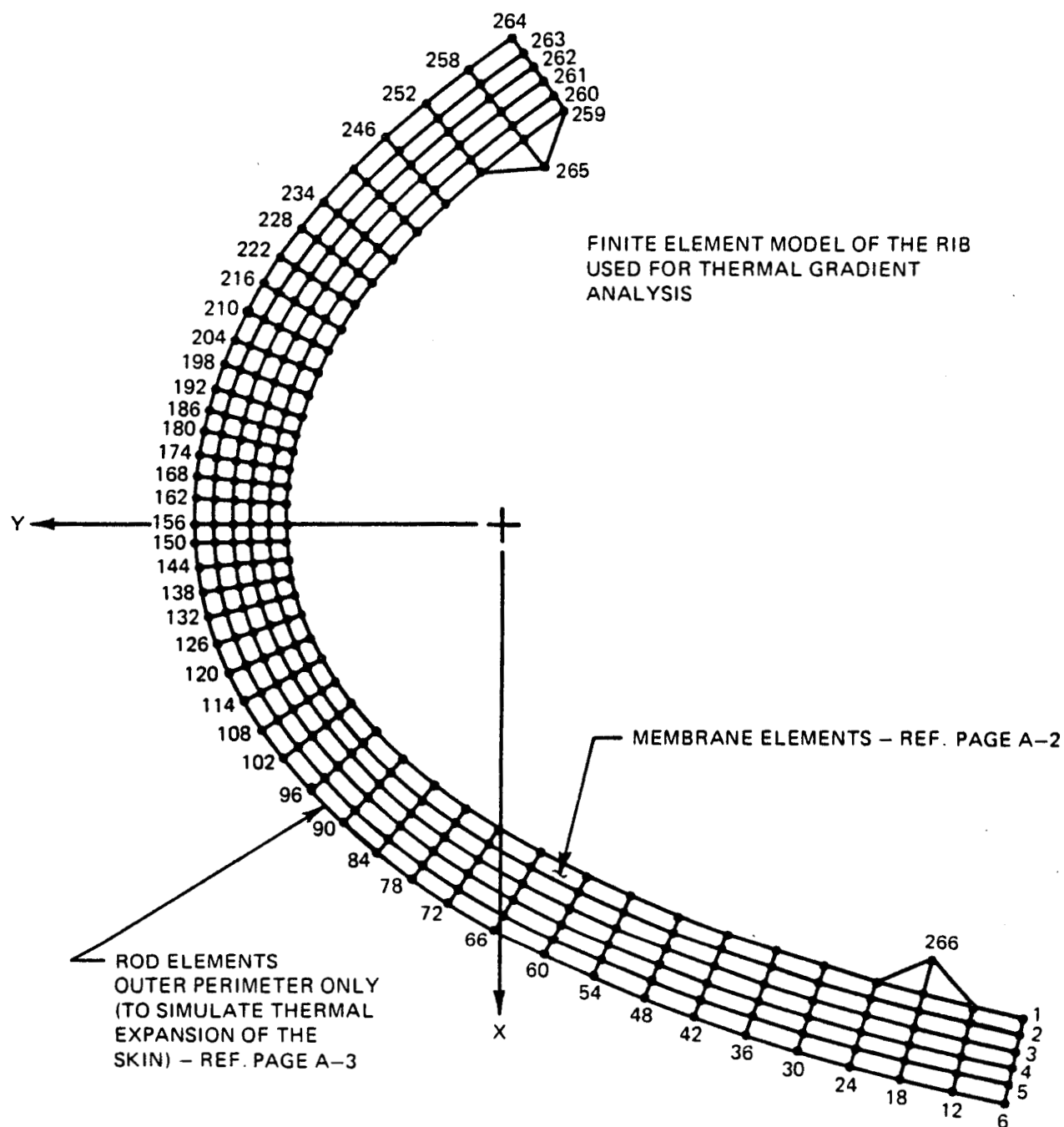


FIGURE 3-50 RIB THERMOELASTIC MODEL

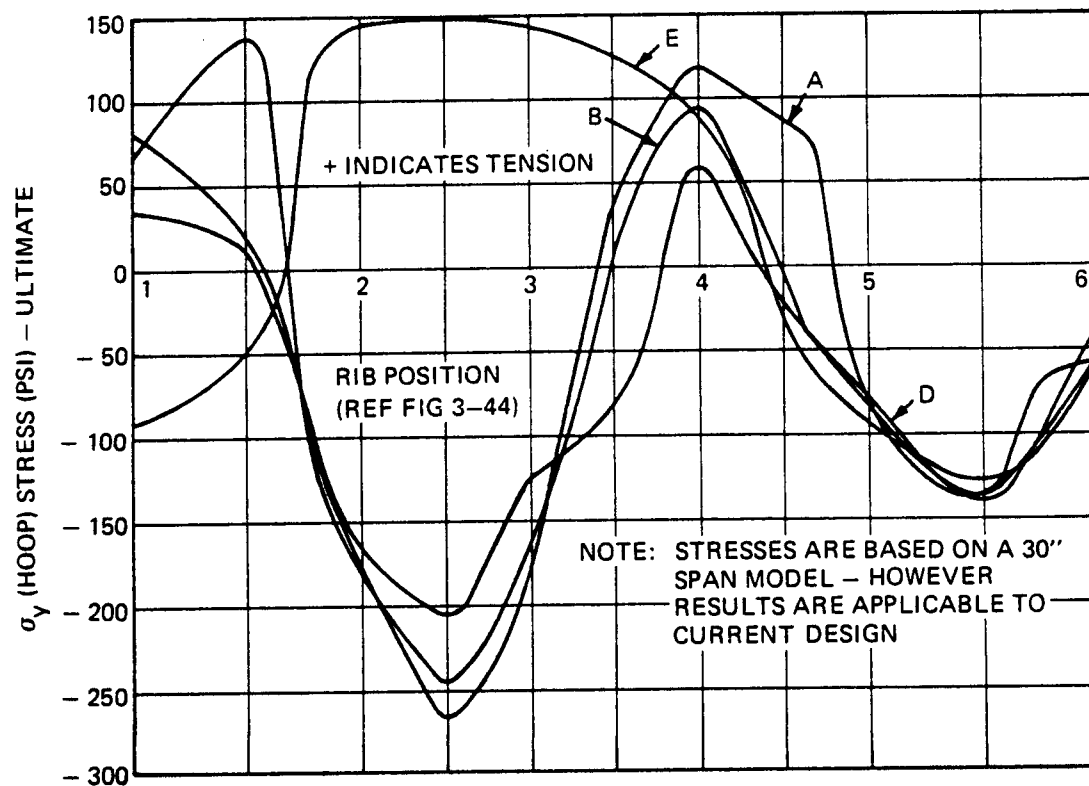


FIGURE 3-51 THERMOELASTIC STRESSES IN SKIN HOOP DIRECTION $t = 400$ SEC

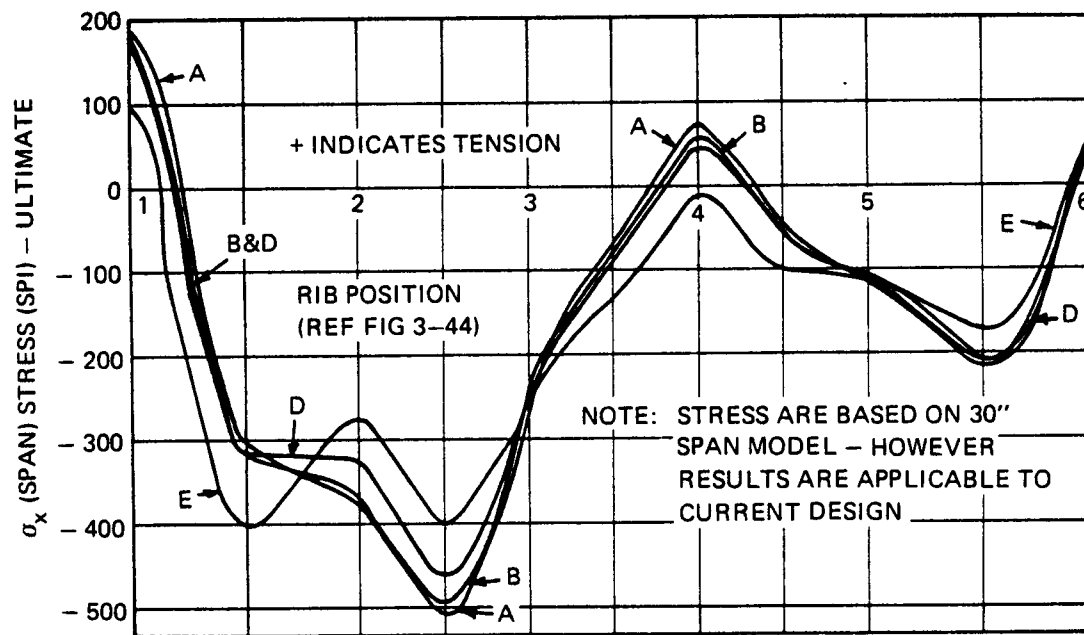


FIGURE 3-52 THERMOELASTIC STRESSES IN SKIN SPANWISE DIRECTION $t = 400$ SEC

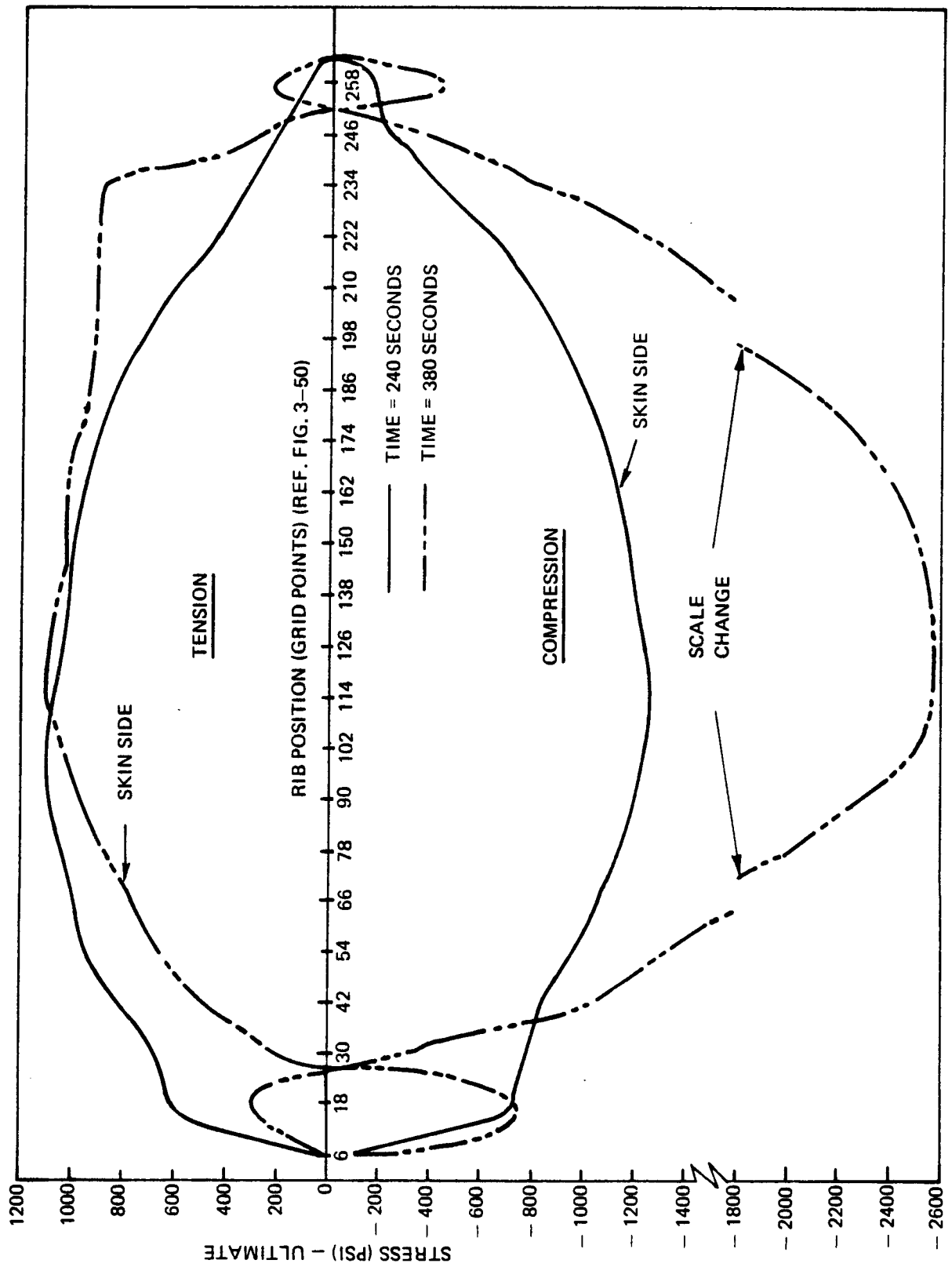


FIGURE 3-53 THERMAL-AXIAL RIB STRESSES

temperature gradients (300°F maximum) experienced by the delta wing vehicle and the characteristics of the material. Only in the attachment area, which is a fairly localized region, are gradients large, but these do not significantly effect overall rib stresses. The attachment region will require a more detailed examination to ensure that a local thermoelastic stress problem does not exist.

The thermoelastic analyses conducted assumed the initial temperature of the leading edge and support structure to be at room temperature. Additional stresses could be induced in the RPP by assuming the wing support structure to be at either cold or hot soak conditions. However, these stresses are so configuration oriented that they were neglected for this assessment of thermoelastic stresses. Should thermal stresses in the ribs ever become significant, slotted upper lug holes could be employed to provide relief.

Each leading edge segment is fixed at the inboard end and is free to expand outboard. The total expansion allowance is based on the thermal expansion of the hot airload panel relative to the cool support structure to which the panel is attached. From NASTRAN computations, spanwise expansion is given in Figure 3-54 for all spanwise elements around the leading edge. This shows a maximum overall growth of 0.064 inch at the stagnation region, when the wing lower support structure is at approximately 180°F. The initial orbital temperature of the skin panel was assumed to be -170°F. At the lug regions the expansion is less as shown because of the lower operating temperature. The lower outboard "floating" lug would be expected to slide a maximum of 0.05 inch, while the upper lug will slide less than 0.03 inch for a 15 inch span segment. This movement is relatively small and easily accommodated by the expansion gap.

Lug reactions computed for the thermal stress conditions are tabulated in Figure 3-55. These are also very small in comparison with those computed for the airloads conditions and given in Figure 3-34.

A summary of the significant margins of safety for thermal stresses is included in Table 3-10. This indicates the minimum margin to be 206% for compression in the ribs.

3.5.4 Dynamic Analysis - Prototype Leading Edge

The leading edge must ultimately sustain vibration and acoustic noise dynamic environments, as well as resist flutter. By virtue of the curved geometry and difficulties in describing the local environmental conditions, the leading edge is not amenable to flutter analysis and therefore requires flutter testing, which is beyond the scope of the current

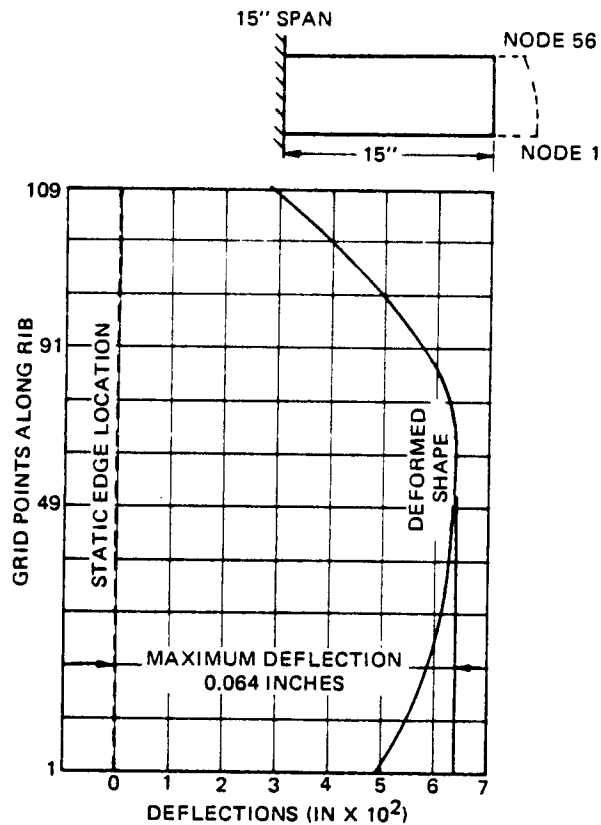
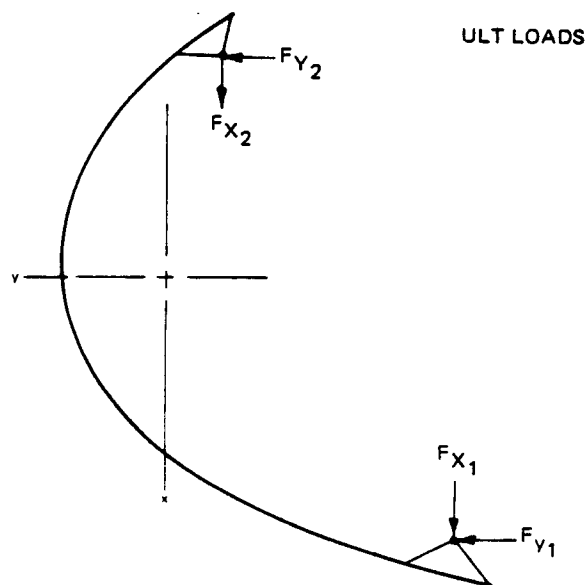


FIGURE 3-54 PANEL EXPANSION AT MAXIMUM TEMPERATURES - 400 SECONDS



LOAD CASE	F_{x1} (LBS)	F_{y1} (LBS)	F_{x2} (LBS)	F_{y2} (LBS)	MODEL
240 SECONDS	38.3	19.2	-38.3	19.3	RIB
380 SECONDS	-62.8	21.2	62.8	-21.2	RIB
400 SECONDS	-44.8	21.1	44.8	-21.7	RIB-SKIN

FIGURE 3-55 HINGE POINT REACTIONS - THERMAL LOADS

program. However, to obtain a "feel" for the significance of the dynamic environments on design, a vibration analysis was conducted on the 15" span Prototype configuration, using 32 GRMS as an x, y, and z axis input level to the support lugs. The spectral distribution of the acoustic noise environment is given in Figure 3-10.

Results show that the maximum computed one-sigma stress level is 4412 psi, which is a local flexure stress experienced on the lower fixed lug. This high local stress level may be more the result of modeling rather than an actual stress. In either event the stress is highly localized and can readily be reduced to a safer level. The next highest stress computed is only 1510 psi, occurring in the ribs and beams. With the excellent fatigue properties being exhibited by coated RPP (Section 5.2) these stress levels are not serious even when a two-sigma level of 3020 psi is considered. The lowest natural frequency for the leading edge is 22 Hz. The mode associated with this frequency is primarily bending in the "Z" direction.

The vibration analysis employed a finite element computer routine using 196 degrees of freedom to define the motion of the panel. Elements were composed of triangular and quadrilateral plates, and general beams. The plates carry membrane and bending loads and simulate orthotropic properties, while the general beams have bending capability in two planes, as well as axial and torsional stiffness. In developing the stiffness matrices the velocity field was assumed proportional to the displacement field, which is referred to as "consistent". The nodal locations used in the analysis of the leading edge are pictured in Figure 3-56, while the spatial coordinates are listed in Table 3-11. Orthotropic properties assumed for analysis were those used for static analysis of the Prototype leading edge and are summarized in Section 3.5.1. The structural damping coefficient was assumed to be 5% of critical.

Maximum RMS stress values computed for the skin, ribs, and beams are plotted in Figure 3-57. These show the envelope of maximum values. Skin stress peaks at 650 psi and is due to response to the vertical loading direction. Rib and beam maximum stresses are 1497 psi and 1510 psi, respectively. The rib is critical for fore and aft vibration, while the lower beam receives maximum stresses from response to side as well as fore and aft loading.

The lower fixed lug region is also critical for side (y) loading and produced a local bending stress of 4412 psi. This appears high considering that other elements in the lower lug region do not exceed 1775 psi and the maximum value on the upper lug is only 1281 psi. In addition the side load on the lower lug and upper lug is 67 lb. and 50 lb., respectively. These values would not suggest the wide variation between computed stresses

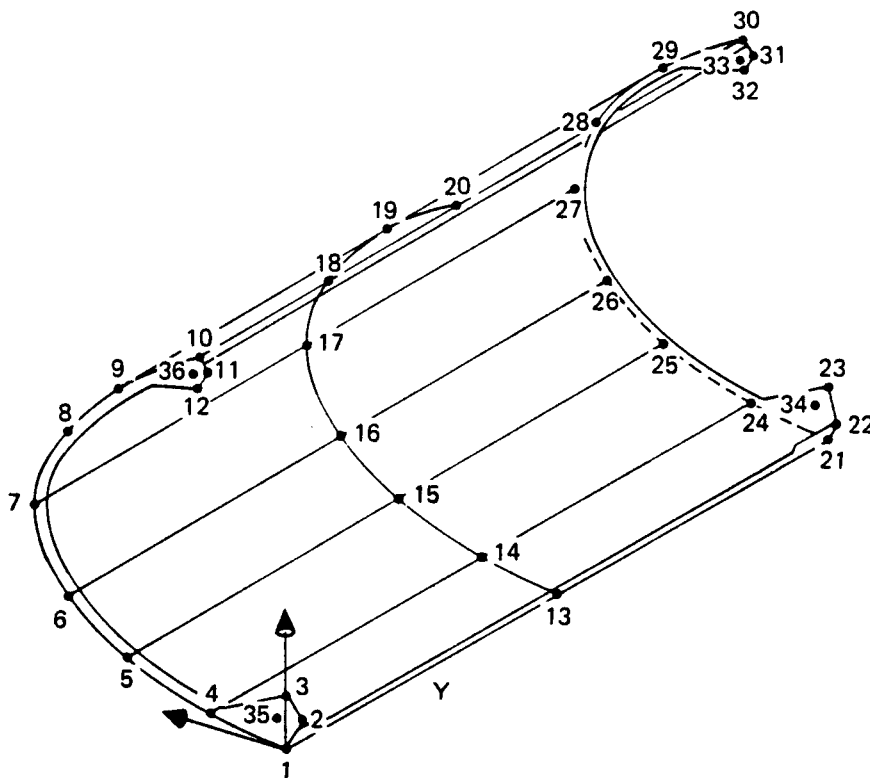


FIGURE 3-56 SPACE SHUTTLE LEADING EDGE NODAL LOCATIONS – VIBRATION ANALYSIS

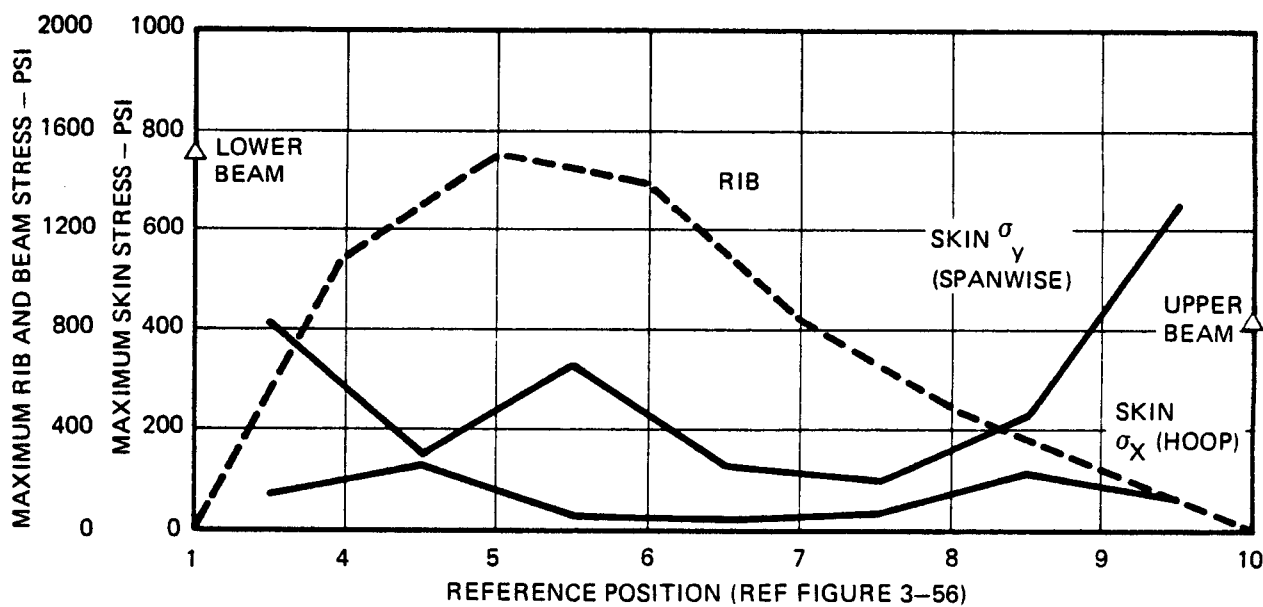


FIGURE 3-57 VIBRATIONALLY INDUCED STRESS ENVELOPE OF RMS VALUES 32 GRMS

TABLE 3-11

SPACE SHUTTLE LEADING EDGE PANEL
NODE SPATIAL LOCATION

<u>NODE NO</u>	<u>X</u>	<u>Y</u>	<u>Z</u>
1	0.0	0.0	0.0
2	- .33	0.0	1.50
3	0.0	0.0	4.25
4	6.14	0.0	1.81
5	11.95	0.0	4.38
6	16.55	0.0	8.69
7	18.00	0.0	13.18
8	17.05	0.0	17.57
9	14.29	0.0	21.41
10	11.00	0.0	24.00
11	10.10	0.0	22.77
12	9.45	0.0	20.89
13	0.0	7.50	0.0
14	6.14	7.50	1.81
15	11.95	7.50	4.38
16	16.55	7.50	8.69
17	18.00	7.50	13.18
18	17.05	7.50	17.57
19	14.29	7.50	21.41
20	11.00	7.50	24.00
21	0.0	15.00	0.0
22	- .33	15.00	1.50
23	0.0	15.00	4.25
24	6.14	15.00	1.81
25	11.95	15.00	4.38
26	16.55	15.00	8.69
27	18.00	15.00	13.18
28	17.05	15.00	17.57
29	14.29	15.00	21.41
30	11.00	15.00	24.00
31	10.10	15.00	22.77
32	9.45	15.00	20.89
33	10.72	15.00	21.52
34	.90	15.00	3.00
35	.90	0.0	3.00
36	10.72	0.0	21.52

for the two lug regions. It is therefore believed that the 4412 psi value is due primarily to modeling problems rather than being a real value. However, in the event that the value is realistic, it can be reduced to a more acceptable level (approximately 2000 psi) with slight geometry or stiffening changes.

Lug reactions are summarized in Table 3-12. These are very low compared with lug loads computed for the static load conditions (reference Section 3.5.3). Only the side load case discussed previously could offer a potential problem area by bending of the lug, but this can be improved by locally strengthening or clamping the lugs that carry side load.

In summary the vibration loads appear to be no serious factor in leading edge design except for the side load carrying lugs. This should be particularly true in view of the excellent resistance to fatigue loading demonstrated by coated RPP (section 5.2). While no vibration testing will be conducted in Phase II, it is believed that this should ultimately be performed on the Prototype leading edge to verify acceptability of the leading edge design and the analytical predictions.

3.5.5 Conclusions

As a result of performing these structural analyses a number of conclusions can be drawn. These are:

- (1) Airloads during boost establish the design of the leading edge and determine thickness requirements.
- (2) Thermally induced stresses are less than half of the load induced stresses and should pose no serious problem.
- (3) Leading edge segments in the optimum size range do not require intercostals, intermediate ribs, or excessive thickness to efficiently resist design pressures.

TABLE 3-12

SPACE SHUTTLE ORBITER LEADING EDGE
REACTION AT ATTACH POINTS

RMS LIMIT LOAD VALUES

RESPONSE IN X - DIRECTION

	<u>NODE</u>	F X <u>LBS</u>	F Y <u>LBS</u>	F Z <u>LBS</u>
Upper Lug	33	24.7	-	5.6
Lower Lug	34	33.6	-	14.8
Lower Lug	35	33.3	4.1	15.5
Upper Lug	36	24.4	6.4	5.8

RESPONSE IN Y - DIRECTION

Upper Lug	33	21.8	-	4.8
Lower Lug	34	24.2	-	11.1
Lower Lug	35	23.4	67.2	9.2
Upper Lug	36	20.0	50.0	4.9

RESPONSE IN Z - DIRECTION

Upper Lug	33	6.7	-	11.5
Lower Lug	34	14.7	-	11.5
Lower Lug	35	14.0	3.1	11.8
Upper Lug	36	5.8	4.4	11.6

4.0 MATERIALS DEVELOPMENT

At the conclusion of Phase I it had been established that diffusion coatings applied to laminates fabricated from WCA graphite cloth offered the best solution to the Shuttle leading edge thermal and structural requirements. An alternate coating system, employing melt impregnation of a mixture of hafnium and tantalum also showed promise for limited applications, where surface temperature reached 4000°F. Two diffusion coating systems from the Phase I development program appeared to have the potential of meeting the 100 mission life goal for the leading edge application. These coatings were the siliconized system and the zirconium-boron-silicon (ZBS) system. Each had its good and bad features.

The siliconized coating showed superior oxidation resistance, when tested in a plasma arc, but indicated a potential low temperature sub-surface oxidation problem when exposed to furnace heating in air up to 2300°F. Further, low strength apparently existed in the 1400°F temperature region. The ZBS coating by contrast was insensitive to furnace exposure or temperature conditions where strength was concerned but lacked the high temperature erosion resistance of the siliconized system. Further, the ZBS system suffered from non-uniformity and poor reproducibility, probably aggravated by the two stage coating process employed.

Initial Phase II activity concentrated on these two diffusion systems and sought to improve their deficiencies. Principle approaches to the siliconized system problems included addition of boron as a low temperature oxidation retardant, and variations to the materials and process while still relying on the basic coating constituents of alumina, silicon carbide, and silicon. It was believed that the solution to the ZBS coating deficiencies lay in the ability to fabricate the system in a one stage operation, where each ingredient would be introduced into the substrate in a single coating run.

Success in reducing low temperature oxidation was achieved on the siliconized system before the ZBS coating could be improved satisfactorily. Investigation of the ZBS coating was therefore terminated to permit full concentration of effort on further development of the siliconized coating. Strength data on the selected siliconized RPP system shows improved strength over the Phase I system and proves that there are no low strength temperature regions.

Another possible means of improving low temperature oxidation resistance of the siliconized system is to modify the substrate for better compatibility with the coating characteristics. Variations of the baseline WCA graphite laminate were examined in an effort to increase the thermal expansion and surface density. These two effects were expected to reduce

crazing and retard the migration of oxygen into the substrate. However, these have not proved successful, although continued exploration along these lines should be pursued.

The Phase I leading edge design concept required the use of bonded intercostals to achieve structural efficiency. This requirement has since been eliminated on the Phase II design; however, bonding studies were conducted in Phase II to develop the technology for use in bonding trailing edge seal strips. These show highly encouraging results. Rivets fabricated from RPP material were also being examined. The feasibility of fabricating rivets and using them in a component has now been demonstrated.

Attempts to achieve high mission life for the hafnium-tantalum coating proved disappointing, when exposure in the plasma arc facility showed mission life to be limited to about six missions. Still, this coating system could be employed in limited areas.

The following sections elaborate on each of these topics. Problems, solutions and conclusions are discussed. Final test results on the selected material system are covered in Section 5.0.

4.1 RPP SUBSTRATE

Phase I and Phase II development effort established materials and processes for general substrate requirements. It has been demonstrated that configurations of parts, that would present some challenges even in conventional fiberglass reinforced plastic layup, can be successfully fabricated from prepreg graphite fabric. Complex parts have been carried through all required cure, pyrolysis, and reimpregnation - repyrolysis strengthening processes, and have been successfully taken through the still higher temperature processing required for diffusion coating reactions and heat treatment. Processing has not imposed any serious constraints on desired designs, and in fact has offered such latitude that design features could be selected for simplicity, economy, and ease of fabrication.

4.1.1 Baseline System

The WCA graphite cloth/R-120 phenolic resin prepreg system remains as the baseline substrate material. Basic material lay up characteristics such as tack and drape, which in most cases can be controlled by degree of resin advancement (B-stage), are well defined in VMSC material specification 307-7-7. A process flow chart of the substrate RPP material is presented in Figure 4-1.

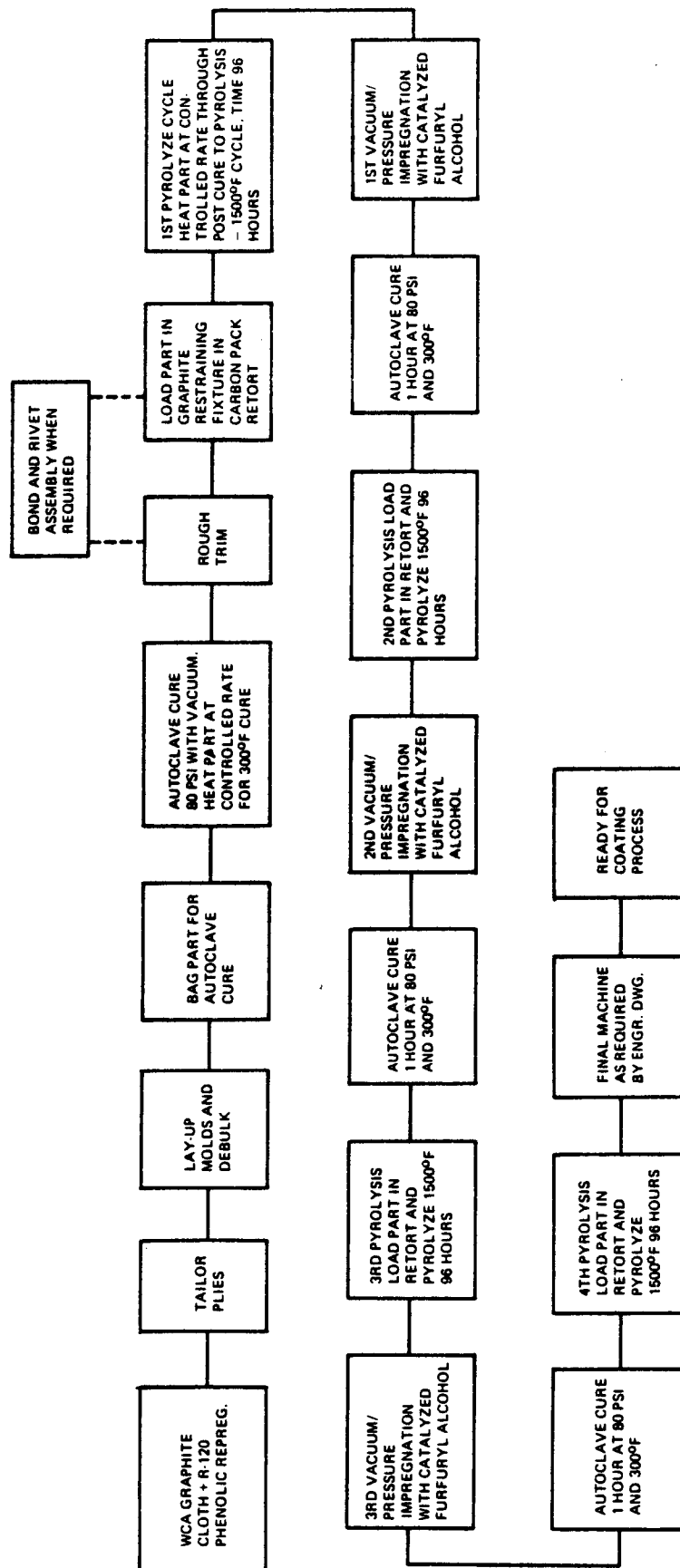


FIGURE 4-1 PROCESS FLOW CHART FOR BASELINE RPP SUBSTRATE MATERIAL

Lay-Up - Plies of graphite phenolic prepreg cloth are tailored to conform to the outside surface area of the part. These plies are placed in a mold one ply at a time and hand rolled for initial compaction. In order to improve surface quality for subsequent coating application, higher debulking pressures using molding type dies and pressure bags are desirable. It has been noted that the present resin content may be slightly excessive for this type of debulking and lower levels should be investigated. A method for improving surface conditions at the bend corner radii of parts has been investigated and shows promise. This method incorporates an RTV silicone strip, pre-molded to the desired inside radius shape, which is inserted after lay-up and prior to bagging. These strips give a localized matched die effect in these wrinkle prone areas. Further improvements are needed at the termination points of the pre-molded strips.

Cure - VMSC process specification 308-7-10 requires vacuum pressure, augmented by an additional 70 psi autoclave pressure during cure. The temperature profile was developed as a function of part thickness and mold mass to assure complete cure through the part and proper outgassing during resin flow and cure. Outgassing during the curing process is not considered a problem with thin laminates (13 plies); however, thick laminates do not outgas easily during cure and may require a more specialized "step" cure cycle or an interrupted pressure cycle to aid the removal of volatiles. It has also been noted that the strength of RPP laminates is sensitive to thickness. Thinner laminates have been found to have a lower measured flexure strength, as indicated in Table 4-1.

TABLE 4-1
STRENGTH OF RPP-3 LAMINATES
OF VARIOUS THICKNESSES

<u>Number of Plies</u>	<u>Thickness Inches</u>	<u>Flexure Strength psi</u>
5	.068	13,790
9	.120	16,050
13	.192	19,270

This condition may be due to excessive resin bleed out during the curing operation. Although the current leading edge design does not employ either the very thick or very thin laminates, some production hardware

designs may require a wider range of laminate thickness and should be examined to establish the technology.

Postcure and Pyrolyzation - Following cure, state of the art practice is to post cure and pyrolyze the part through a stepwise time-temperature profile up to a maximum temperature of 1500°F. The rate of temperature increase is slow to permit the decomposition gases formed during the pyrolyzation of the resin polymer to escape at a rate slow enough to avoid delamination due to build up of internal pressure. Conversion of the cured phenolic binder resin to a carbon structure results in a marked reduction in strength as indicated in Table 4-2.

Impregnation and Repyrolysis - Because of the low strength value of the as pyrolyzed (RPP-0) material, reimpregnation and repyrolysis processing steps were developed to increase strength of the laminate and to decrease laminate porosity for better coating conversion. These additional processing steps develop the desired results through densification of the carbon binder system. Impregnation is accomplished by placing the part in a closed chamber, drawing a vacuum to remove all air from the pores, and then flooding the part with the catalyzed furfuryl alcohol. An 80 psi positive pressure is then employed to drive the resin into the small pores of the pyrolyzed laminates. The parts are removed from the chamber, the excess resin removed from the parts by blotting with paper towels, and the part is cured in an autoclave at 80 to 100 psi for 1 hour at 300°F.

After cure the parts are again post cured and pyrolyzed using the same procedure as used for the as-cured parts. Strength increases at each successive step up to a limit. A typical example of this improvement is illustrated by the data of Table 4-2, which was taken from material processed with the prototype leading edges. Further reimpregnation/repyrolysis steps to produce RPP-4 or RPP-5 can be performed but the rate of strength increase is reduced and the risk of delamination is greater above the RPP-3 stage. This is due to increased chances of trapping decomposition gases, that have caused delamination. Further, strength afforded by RPP-3 is satisfactory for Shuttle leading edge or body panel components.

Defects Possible - Delamination and areas of high porosity are the major defects that are periodically found in simple RPP shapes. Both conditions can be seen in Figure 4-2 when compared to the acceptable laminate shown in Figure 4-3. A radiograph technique requiring submersion in carbon tetrachloride has been determined as an acceptable NDE method for detecting these types of defects. Light areas in Figure 4-4 illustrate delaminations discovered by the x-ray technique. Ultrasonic techniques have also been found to be useful in detecting these defects. This is discussed in detail in Section 6.0.

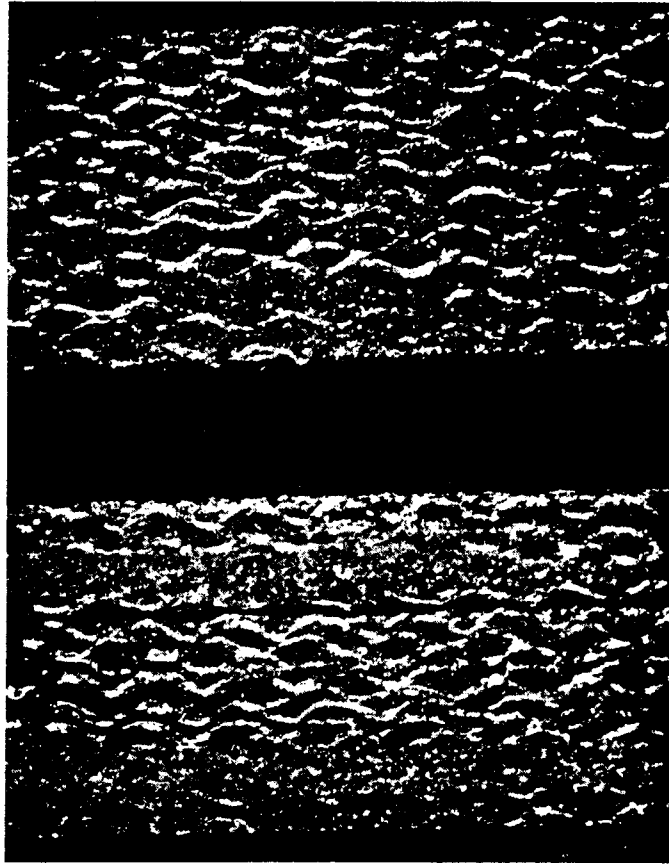


FIGURE 4-2 RPP LAMINATES SHOWING DELAMINATION AND AREAS OF HIGH POROSITY 10X MAGNIFICATION

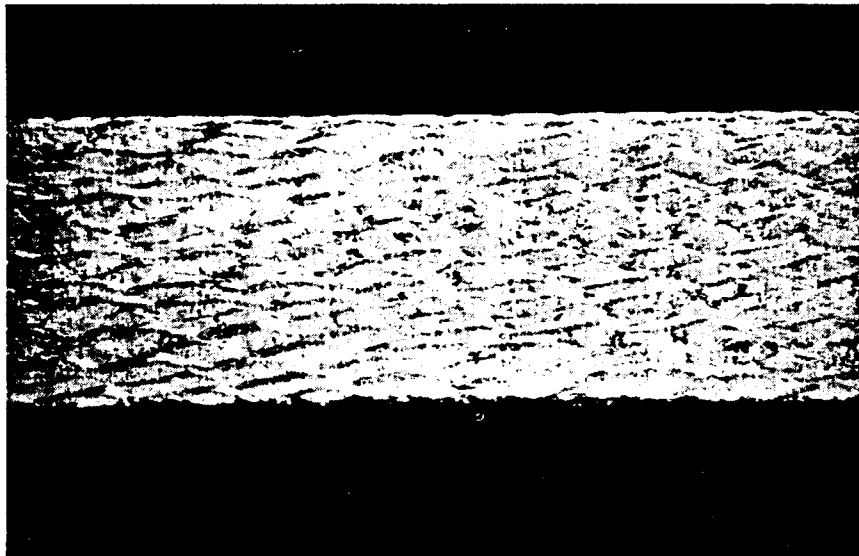
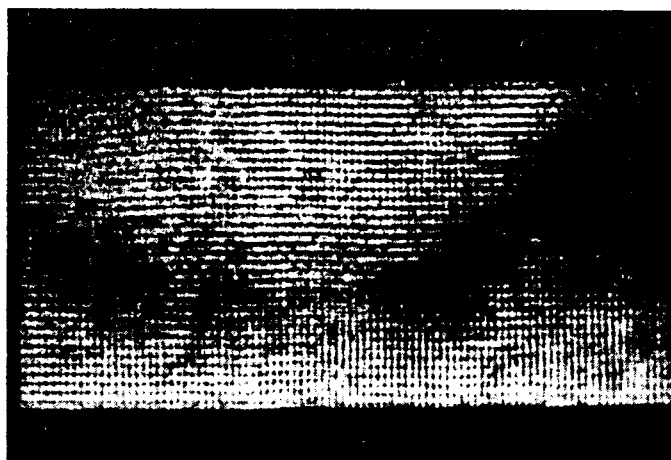
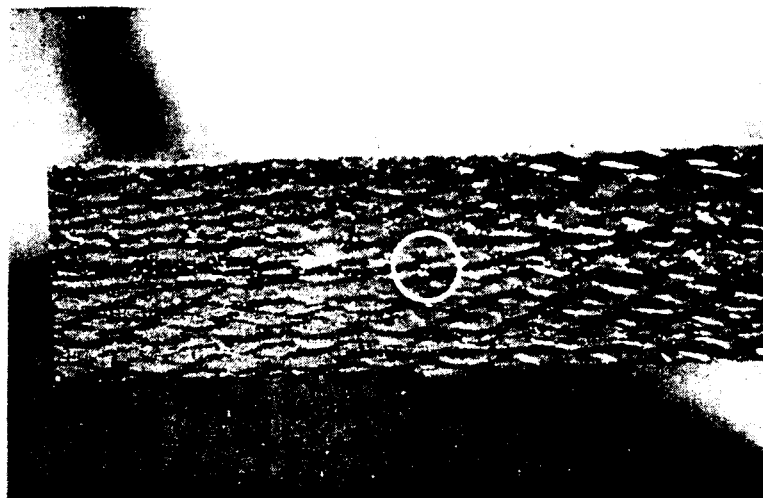


FIGURE 4-3 ACCEPTABLE RPP LAMINATE 10X MAGNIFICATION



X-RAY PHOTOGRAPH OF SECTION FROM PANEL 2-1



PHOTOGRAPH OF SECTION FROM ABOVE PANEL SHOWING DELAMINATION

**FIGURE 4-4 ILLUSTRATION OF A DELAMINATION DEFECT
5X MAGNIFICATION**

TABLE 4-2

STRENGTH OF RPP SUBSTRATE
MATERIAL AT VARIOUS PROCESSING STEPS

<u>Process Step</u>	<u>Flexure Strength * PSI</u>
As cured	20,780
RPP-0 (After 1st pyrolyzation)	4,300
RPP-1 (After one impregnation and repyrolysis steps)	9,630
RPP-2 (After two impregnation and repyrolysis steps)	14,820
RPP-3 (After three impregnations and repyrolysis steps)	17,900

* Average flexure strength of control specimens processed with 3 different leading edge segments.

Delamination is caused during pyrolysis when the decomposition gas pressure exceeds the interlaminar strength of the part. Excessive gas pressures can be developed when (1) volatiles, trapped during cure, expand, (2) rapid pyrolysis occurs, (3) little or no porosity is available for the gas to escape, or (4) the gas escape path is too long, such as found in large thick laminates. Low interlaminar strength is usually associated with very high or very low between-ply thicknesses. "High thickness" produces excessive low strength resin char while "low thickness" produces insufficient bonding between plies. Areas of high porosity are caused by (1) resin rich areas, (2) entrapped gases during cure, and (3) areas of insufficient resin (voids). Processing procedures have been developed to minimize these defects; however, additional work is required to eliminate defects and establish processing variations for thicker laminates.

Trapped volatiles are minimized during cure by allowing resin and volatile bleed-out through perforated cellophane into fiberglass and canvas bleeder material, and by limiting curing pressure to 80 psi. These molding conditions also produce some porosity which is available as a gas escape path during pyrolysis. Rapid pyrolysis is reduced through a stepwise postcure and pyrolysis cycle over a 96 hour period.

Very large interlaminar thickness is caused by high resin content, insufficient debulking, low molding pressure or insufficient bleed out during cure. Conversely, low interlaminar thickness is governed by low resin content, over debulking or excessive resin bleedout due to high molding pressure. Most of these variables are controlled by quantitized values in the process specifications; however, debulking is still somewhat of an art and requires a skilled operator to perform this task, unless "stops" are provided on debulking tools to control final thickness.

Resin rich areas in the cured laminate can be caused from improper bleed out during cure, low molding pressure and non-uniform resin content in the prepreg starting material. During lay-up bleed-out variations for the removal of excess resin and volatiles is examined and the molding pressure is closely controlled. However, some resin content variations in the prepreg materials have been noted.

Areas of insufficient resin that result in voids in the cured laminates are usually found in radius or wrinkled areas where improper debulking occurred or where low molding pressure resulted from "bridging" of the vacuum bag. Both problem areas require trained operators to recognize, identify, and overcome these deficiencies.

4.1.2 Processing Complex Shapes

Processing RPP into complex shapes has been demonstrated by VMSC but it requires close attention of certain factors. A number of

these factors are not unlike those encountered in fiberglass reinforced plastic technology; however, their severity or sensitivity to variables is increased in the RPP technology due to the lower strength of the graphite prepreg cloth and the demands of the subsequent conversion of the plastic binder to carbon.

Improper debulking during lay-up will result in areas of excessive porosity, delamination and wrinkles. Areas of small radius are very sensitive to wrinkling from improper debulking. This is shown in Figure 4-5 for a 90° corner with a protruding wrinkle at the inside radius. These areas create a region of excessive porosity in the carbon binder which is caused by resin richness between plies of graphite cloth.

Specialized molding tools and layup techniques are required to prevent wrinkling. The multi-piece tools shown in Figure 4-6 illustrate those developed for debulking and autoclave cure of a section of a Shuttle belly panel attachment concept (Reference (9)) with vertical reinforcing webs and joggle. It can be seen that this type of tooling results in a wrinkle free part with good radii.

The design of the prototype leading edge and wing tip sections do not lend themselves well to the matched die type tooling used in belly panel fabrication because of trapped tooling and excessive cost. The design of the prototype leading edge, Figure 3-8, shows the lay up pattern by ply used for the fabrication of this part. The large gently curved center area was not considered to be particularly difficult to debulk, since autoclave pressure and resin bleeding during cure on this type of section is very efficient. However, the rib and beam closures including the small corner radii were considered problem areas. Since the part was large enough to allow hand working, the radius areas were given an additional decompaction step using rollers after the part was bagged and preheated to 150°F in an autoclave. This technique aided the formation of the radii but still some wrinkling occurred. Further improvement of these parts should be accomplished with precast RTV shapes to form these radii as was done with the wing tip panels.

Debulking of the wing tip sections, Figure 7-1, was more difficult than for the leading edge because its smaller size excluded good hand roller compaction. Figure 4-7 shows the compaction aids used for this part. The rubber plug was employed for initial compaction after each 3 plies were layed up in the main section of the part. After the last ply was placed in the mold and debulked with the rubber plug, the end attachment sections were formed by the metal debulking angles, Figure 4-7, and clamping pressure. Final debulking of the entire layup was accomplished using the inflatable silicon rubber bag. The bag was pressurized to 50 psig and held for 30 minutes to allow final debulking

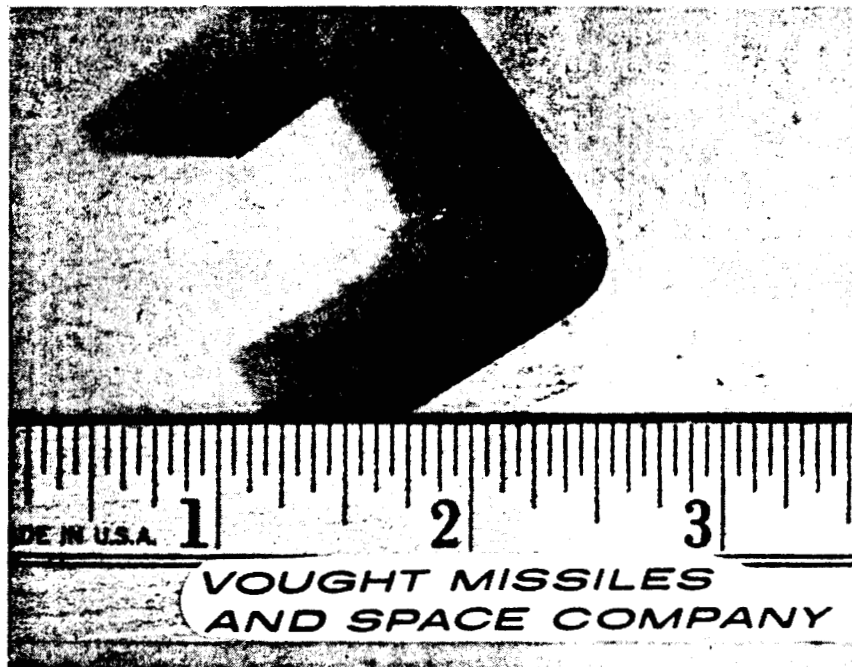


FIGURE 4-5 A 90° CORNER WITH WRINKLING AT THE INSIDE RADIUS

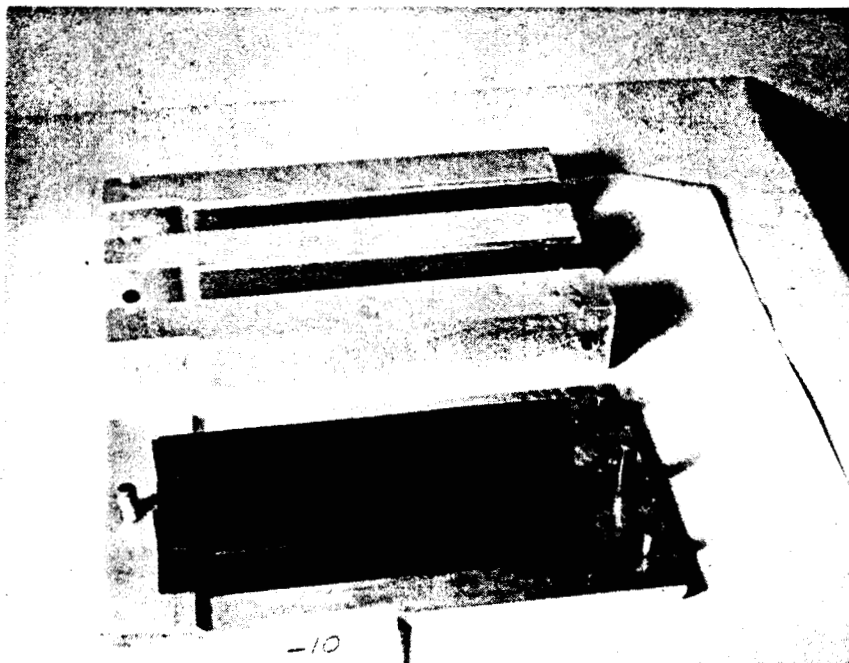
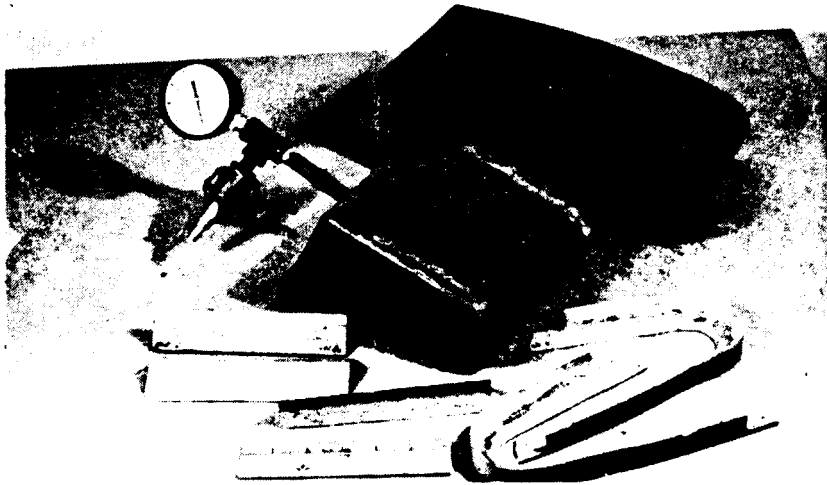
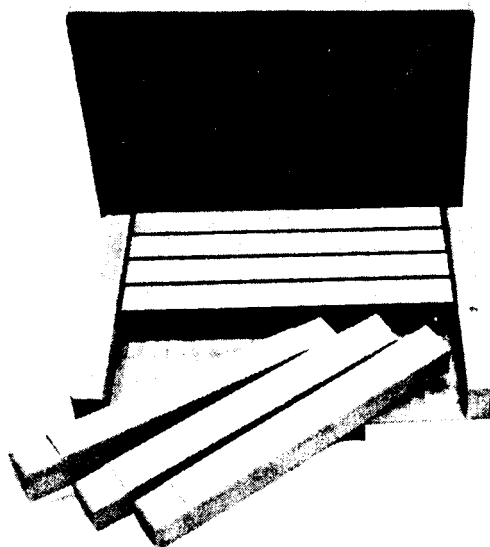
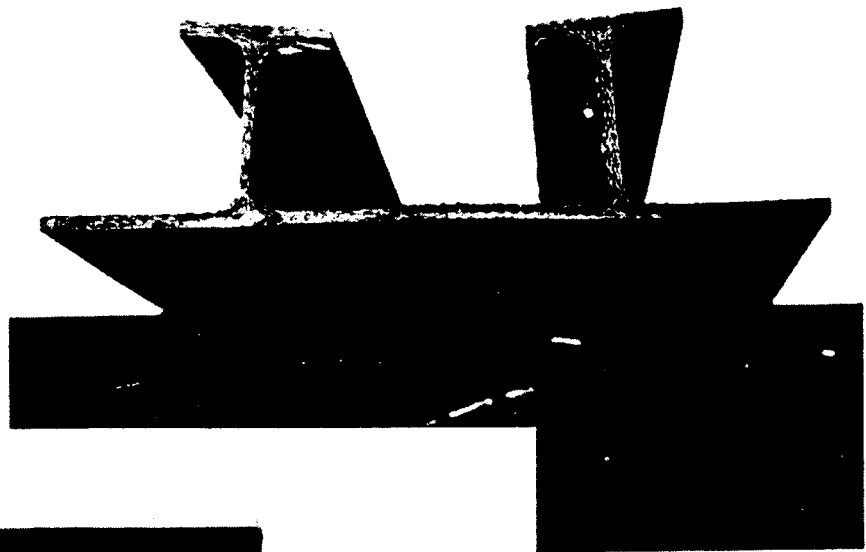


FIGURE 4-6 MULTI-PIECE TOOL FOR FORMING A SECTION WITH VERTICAL REINFORCING WEBS



**FIGURE 4-7
COMPACTION AIDS TO
FABRICATE WING
TIP PANELS**

**FIGURE 4-8
RPP SECTION
ILLUSTRATING
DELAMINATION
& DISTORTION**



**FIGURE 4-9
GRAPHITE RESTRAINING
FIXTURES USED DURING
PYROLYZATION OF A
BELLY PANEL
COMPONENT**

to occur. Precast silicone seal strips shown in Figure 4-7 were then placed over the lay-up prior to bagging to form the radius areas during cure. Good radii were formed in this manner; however, a slight "step" was apparent at the termination points of the silicone strips. It is believed that these steps can be eliminated by tapering the strips to less than .001 inch during the casting of the RTV.

Two major problems, delamination and distortion, can occur during the pyrolysis cycle when the binding resin is converted to carbon. Both of these conditions are shown in Figure 4-8. The most severe of these, delamination, is due to internal pressure of the decomposition gasses exceeding the interlaminar strength of the laminate. The causes of this condition are usually created during lay-up by improper bleeding during cure, under debulking, over debulking or thick lay-up over large surface areas. Distortion, which occurs as a result of pyrolyzation, can be controlled with proper restraining tools. Typical graphite restraining tools to control distortion are shown in Figure 4-9. These were used to form a belly panel having several ribs (Reference (9)). Shaped graphite restraining tools were also used during the pyrolyzation of the prototype leading edge sections and the wing tip sections. These are shown in Section 7.0.

From the result of having fabricated two complex belly panels (Reference (9)), three prototype leading edge panels, three curved seal strips, and two small wing tip panels, it is concluded that the designer has considerable latitude in designing parts fabricated from coated RPP. In general it may be stated that parts that can be fabricated with fiberglass can likewise be fabricated with RPP.

4.1.3 Laminate Improvement

The siliconized coating on RPP shows superior high temperature oxidation resistance to any other coating system tested under repeated exposure in plasma arc test conditions. However, there is experimental evidence that a mismatch in thermal expansion and contraction exists between the unreacted carbon matrix substrate and the outer portion which has accepted the diffusion coating. Modification of the RPP substrate to achieve improved expansion and density compatibility with the coating system is desired.

Two approaches investigated were (1) reduction of porosity on the laminate surface to decrease the ability for oxygen to diffuse through the coating to the bare substrate and (2) improve most of the thermal expansion match between coating and substrate.

Methods to Reduce Porosity - RPP laminates in the RPP-2 state were impregnated with a carbon filled furfuryl alcohol system to reduce surface porosity during the final RPP-3 processing step. Initial trials

showed that deep impregnation of the filler carbon was not achieved, because the fine particles of carbon filtered out of the furfuryl alcohol and remained on the surface while the resin achieved deep penetration into the RPP substrate. Pyrolysis resulted in severe "mud-cracking" of the concentrated surface carbon. An additional approach which appeared to be more satisfactory was to first impregnate the substrate with furfuryl resin and then coat the surfaces with a resin/carbon mix. This produced a smoother surface and appeared to be less porous. However, crazing was apparent after coating.

Another possible approach to improving surface porosity was to mold laminates with the outer plies of cloth being of finer weave than the WCA. This should minimize surface irregularities and change the porosity characteristics at the surface. WCL graphite cloth with an 8-hardness satin weave was chosen for this investigation because of its fine, close weave. However, this work was not completed due to more pressing priorities.

In addition to surface porosity, it has been observed that both large and small pores are formed during the first pyrolyzation cycle. The impregnation and repyrolysis of furfuryl alcohol was initially developed to increase laminate strength by reforming an interface bond between reinforcing fibers and matrix carbon. Furfuryl alcohol fills the small pores formed within the fiber bundles after pyrolysis, but although furfuryl alcohol does an excellent job of filling small pores, large porosity is only slightly filled. It was felt that to aid the compatibility of RPP with the siliconized coating an investigation to fill large pores should be initiated.

The approach employed involved the use of high char yielding materials and materials of high viscosity to selectively attack only the large pores during impregnation. Petroleum pitch and powdered phenolic resin impregnated into RPP-0 was one technique employed. Pitch impregnation was accomplished by using a viscous solution of pulverized pitch in toluene. After impregnation the toluene was evaporated from the RPP panels and then impregnated with furfuryl alcohol before pyrolyzation. A fine particle suspension of phenolic in furfuryl alcohol, pressure impregnated into RPP-0, cured and then pyrolyzed was another approach used. Both the pitch and the phenolic impregnated specimens were given two additional furfuryl alcohol impregnations and pyrolysis cycles to advance them to the RPP-3 state.

The flexure strength of the laminates resulting from these investigations are listed in Table 4-3. It can be seen that the flexure strengths are scattered. One explanation is that the treatments sealed the porosity, thereby preventing normal impregnation efficiency and hence, more scattered values. This theory is supported by a comparison of 013-6 and 013-7 where the higher percentage of carbon black produced lower

TABLE 4-3. LAMINATE IMPROVEMENT RESULTS

Series	System	Flexure Strength, Uncoated PSI	Sample No.	Wt. % Gain From Coating	Weight Change After Heat Treat, %	Weight Loss (1) After Oxidation Cycling, %	Flexure Strength Coated PSI	Flexure Strength After Oxidation Cycling, PSI	Remarks
013-1	RPP-2, impregnated and coated with resin and carbon black. Resulted in RPP-3.	14,873	1	47.4	0.69	3.7	4,718 5,878	2459	Crazed
			2	47.8	0.62	3.1			
			3	48.2					
			4	48.2					
013-2	RPP-3, impregnated and coated with resin and carbon black. Processed to RPP-4.	19,840	1	37.0	0.71	4.0	11,786 10,320	6223	Crazed
			2	39.7	0.61	3.7			
			3	37.1					
			4	40.0					
013-3	RPP-0, impregnated with furfuryl alcohol and phenolic then processed to RPP-3.	19,030	1	35.1	0.64	4.5	13,201 11,191	6589	Crazed
			2	35.4	0.65	4.5			
			3	33.6					
			4	34.4					
013-4	RPP-0, impregnated with pitch and then processed to RPP-3.	18,333	1	33.8	0.62	4.2	12,566 10,857	6781	Crazed
			2	33.9	0.75	4.8			
			3	33.5					
			4	35.9					
013-5	RPP-3 control.	15,286	1	58.2	0.36	1.7	4,800 4,626	9412	50% of specimens non-crazed
			2	54.4	0.44	2.3			
			3	52.7					
			4	52.7					
013-6	RPP-0 impregnated and then coated with resin and carbon black. Processed to RPP-3. (5 gm. carbon pickup)	11,500	1	59.4	0.18	1.2	3,445 4,691	8347	67% of specimens non-crazed
			2	57.9	0.29	1.8			
			3	50.1					
			4	53.3					
013-7	RPP-0 impregnated and then coated with resin and carbon black. Processed to RPP-3. (3 gm. carbon pickup)	13,324	1	56.2	0.38	2.1	4,928 4,728	6305	100% of specimens non-crazed
			2	53.9	0.46	2.6			
			3	51.3					
			4	52.8					
013-8	Cross ply construction RPP-3 condition.	15,062	1	40.2	0.69	4.1	7,927 6,282	3621	Crazed
			2	39.2	0.94	5.2			
			3	36.7					
			4	34.1					

(1) 5 cycles in furnace heated to 2300 °F

strength. This is believed due to carbon black acting as a barrier against reimpregnation.

The effectiveness of porosity control studies were directly shown by their coating response. All the specimens listed in Table 4-3 were crazed to a greater or lesser degree except numbers 013-5, 6, and 7. Number 013-7 showed no detectible crazing while 013-5 and 013-6 exhibited varying amounts as noted. It should also be noted that an excessive amount of coating was found on these series of specimens as indicated by weight percent coating. Subsequent treatment by thermally cycling in an oxidation environment caused no observable increase in crazing. At this point no conclusions based on crazing observed can be drawn regarding potential laminate improvements by the avenues explored. Those few cases which showed little or no crazing could not be interpreted as improvement because excessive coating weight gains occurred and the strength was low.

Strength behavior was mixed for the coated flexure bars in the as-processed state. In all cases, the coated composites showed a strength reduction, when compared with their uncoated values. This, of course, is normal. Thermal cycling of these composites in air further changed their flexure strength. It is interesting to note that the low strengths noted for systems 013-5, 6, and 7 showed an improvement in strength after thermal cycling. As noted in Table 4-3, these specimens also had low weight losses associated with thermal cycling.

Methods to Adjust the Thermal Expansion Characteristics of the RPP - Past experience has shown that the coefficient of thermal expansion (CTE) of RPP materials can be lowered and made more stable by heat treating to 4500°F. Four heat treat temperatures were selected to determine if a partial stabilization could be obtained that would enhance RPP coating compatibility. RPP test specimens were heat treated at 3400°F, 3600°F, 3900°F, and 4500°F for one hour. These substrates were then coated by an early Phase II siliconizing process and strengths were determined. Flexure strength results, shown in Table 4-4, indicate that no advantage is gained due to heat treatment and therefore current characterization test data for siliconized RPP was obtained on material which is not heat treated prior to coating.

TABLE 4-4
FLEXURE STRENGTH OF HEAT TREATED AND SILICONIZED RPP

<u>Heat Treat Condition</u>	<u>Flexure Strength PSI</u>
No heat treat above pyrolyzation temperature	8,960 8,450
3400°F heat treat	8,130 5,360
3600°F heat treat	6,990 6,820
3900°F heat treat	7,000 8,000
4500°F heat treat	7,670 6,260

Cross ply laminate material has been fabricated and examined as an additional approach to CTE modification. Results of CTE measurements of parallel laminates show a slight difference between the warp and fill direction (Reference (6)). Fabricating a laminate with the warp of each ply 90° to the previous ply results in a laminate with equal properties in both directions. The cross ply laminates were processed to the RPP-3 state prior to coating (items 013-8, Table 4-3). The coating on these laminates was severely crazed and was not considered an improvement method. However, it has been observed that when crazing occurs in a coating, the lines are invariably aligned with the warp and fill axes, but never at some other angle. This prompts the speculation that perhaps an isotropic lay up may change the expansion mismatch of the coating and substrate, and more closely match the 45° expansion properties of a parallel lay up laminate, thus avoiding crazing. Evaluation of isotropic material will be made in the future.

In summary, the depth of coating achieved on the laminate improvement specimens tended to mask the true potential benefits to be derived from alternate substrate processing. However, it appears that initial reimpregnation with phenolic resin and furfuryl alcohol will enhance RPP strength. Heat treating before coating showed no strength improvement for coated RPP, but all strengths including that of the control specimens were lower than values currently being obtained. It is therefore believed that these experiments should be repeated under more controlled processing before firm conclusions are drawn.

4.2 BONDING AND RIVETING

Bonding and riveting are commonplace in present aircraft design. These fabrication and assembly methods, when used in conjunction with

laminated parts, add a high degree of freedom to design shapes, which may otherwise be impossible to fabricate, due to limitation of processing and mold designs. It is evident, that if a bonding or riveting method could be developed for RPP, having the same high temperature resistance of the RPP material, new design concepts could be considered. VMSC has examined both of these fastening techniques with encouraging results.

Bonding - Bonding approaches were limited to carbonaceous material in order to maintain the temperature capability of RPP. Early investigations were performed on RPP-0 prior to the development of the higher strength RPP-3, and while a bond was obtained, strength results were not impressive. However, using the concept of increasing the interlaminar strength of RPP by reimpregnation and repyrolysis, a bonding program was developed. R-120 phenolic, X-2 furfuraldehyde, furfuryl alcohol and C-34, a Union Carbide carbon cement, were the chosen resin systems. WCA fabric was used as the adhesive carrier scrim cloth and in some cases carbon filler was added to increase viscosity and add body to the resin. The seven bonding systems evaluated in this investigation are listed in Table 4-5. After bonding, all parts were processed through a pyrolyzation cycle to convert the resin bond to its carbon structure. The RPP and bond lines were then strengthened to the RPP-3 state with furfuryl alcohol in the conventional manner.

Flatwise tensile test results are shown in Table 4-5. Three of the seven systems look very encouraging. One permits bonding in the as-molded condition, while the other two can be bonded after the parts have completed initial pyrolyzation. It should be noted that on two of the systems failure occurred in the laminate rather than in the bondline and a third system produced strengths nearly equal to the interlaminar strength of the base RPP-3. It is significant that bonding in either the molded or RPP-0 states are good candidates and may provide flexibility for design or fabrication processing. Leading edge and wing tip components were bonded in the as-molded condition because it was the simpler of the two approaches and if the bond did not hold well after pyrolysis, one of the other techniques could be employed as backup. (This appears to have been the proper choice because samples employing the RPP-0 approach tended to delaminate more severely following coating, while the other technique produced some good bonds on the full scale components.)

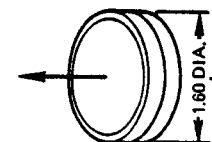
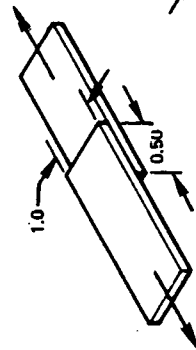
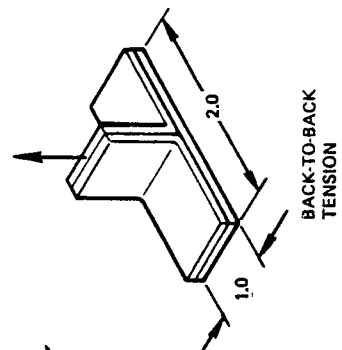
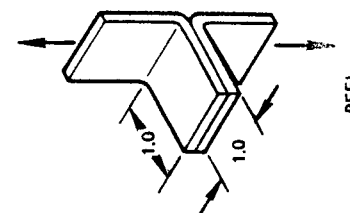
In addition to flatwise tensile tests three other specimen configurations were tested to further evaluate carbonaceous bonding as an attachment method. These were lap shear strength, back to back tension angle and peel strength tests as illustrated in Table 4-5. The lap shear results are consistent with the flatwise tensile data. All possibilities examined in the flatwise tensile tests were not checked in other tests, because only the most likely adhesive concepts were fabricated in all test configurations. The Furane X-2 approach exhibited considerably greater resistance to lap shear than the other two adhesives.

TABLE 4-5. BOND STRENGTH RESULTS

No.	Bond System	Flatwise Tension		Lap Shear			Tension Angle			
		Failing Strength, psi	Avg. psi	Failing Load, Lbs.	Failing Strength, psi	Avg. psi	Back to Back Tension Strength, psi	Avg. psi	Peel Strength (2) lb/in Width	Avg. lb/in
013-1	RPP-0 laminate bonded with WCA/phenolic	229 230 227	229.2							
013-2	Molded laminate bonded with WCA/phenolic, then pyrolyzed	422 498 494	471.8	385 391 430	762 773 840	792	103 122 104		36 24 20	27
013-3	RPP-0, bonded with Furane X-2 using WCA fabric in bond line	435 344 350	376.6	615 446 593	1112 835 1179	1042	128 118 127		30 32 32	31
013-4	RPP-0, bonded with Furane X-2 filled with 20% carbon black	384 330 596	439.9							
013-5	RPP-0, bonded with Furane X-2 filled with 20% carbon black using WCA in bond line	576 601 648	608.9							
013-6	RPP-0, bonded with furfuryl alcohol filled with 20% carbon black using WCA in bond line	241 161 274	225.6							
013-7	RPP-0, bonded with C-34 adhesive using WCA in bond line	205 266 88	186.7	260 262 303	495 521 601	539	95 118 153		65 61 74	67
	RPP-3 laminate	490 544	517							

(1) Interlaminar tensile failure in the RPP

(2) Breakaway force

FLATWISE
TENSIONLAP
SHEARBACK-TO-BACK
TENSION

PEEL

The results of two types of tension angle tests are more varied. As noted in the back to back tension tests, the Furane system shows a slightly greater strength with less variation than the other two systems. In these results the specimens failed predominately in tension. Some peel may have occurred as a result of RPP bending. The random partial bond line separation discovered after failure suggests some peel occurred or that the bond at the separation surfaces was not uniform. The carbonaceous adhesive C-34 (Union Carbide) was superior when tested in a simple peel test judging by its average break away force. For all adhesive systems tested, after break away was achieved, the peel loads dropped to 2 to 10 pounds per inch width until complete separation was achieved.

Carbonaceous bonds show great promise as a result of these tests and further investigation is warranted. The pure bond strength exhibited in flatwise tension was very encouraging as were the strengths noted in shear, recognizing that tensile stresses also were present. A scrim cloth of WCA enhances bond strength as does the introduction of carbon filler in the RPP-0 resin bond. Perhaps carbon filler will likewise improve bonding in the as-molded condition. Utilizing these properties in design will provide a means of secondary attachment. The peel results suggest that this type of loading should be avoided as expected, but the back to back tension angle data indicates that this design approach is feasible.

Flatwise tensile samples of the first two systems tested in Table 4-5 were also processed through coating. The purpose was to observe the coating reaction in the region of the bond line. After processing, the bond line in both types was cracked to varying degrees indicating adverse effects from the coating process. The molded laminate bonded with WCA/phenolic and then pyrolyzed exhibited significantly less bond line attack. Further work is required to correct this problem but the data indicates that good strengths can be achieved, when the process is perfected.

Riveting - Preliminary work has been initiated to develop an RPP rivet that can be used with RPP construction. Rivets fashioned from RPP are expected to be used in conjunction with bonded surfaces, and will serve as a means of preventing bond peel for higher reliability.

First attempts to prove the concept have been successfully fabricated. Narrow strips of phenolic impregnated WCA graphite cloth was placed in a cylindrical mold and debulked at 1000 psi. This debulked rod, which is not perfectly round at this point, was then frozen with liquid nitrogen and machined on a lathe to a 1/2 inch cylindrical rod.

The rod, extending 1/4" beyond two countersunk RPP parts to be riveted, was placed in a platen press after warming to room temperature and formed at a pressure of 200 psi. Heat was added and the rivet was cured at 300°F for one hour to form a double flush rivet assembly. Molds were also made for protruding head rivets. These were 3/4 inch diameter and 1/4 inch deep to form a rivet head. In the forming of protruding head rivets the rod is allowed to protrude 1/2 inch past the RPP surface. Three types of assemblies were fabricated: double flush rivets, flush on one side with a formed head on the other, and formed heads on both sides.

Single lap rivet shear specimens were fabricated for initial evaluation of the flush rivet concept. Results are provided in Table 4-6. Since these were installed in 1/4 in. thick RPP laminates single lap

TABLE 4-6

SINGLE LAP SHEAR STRENGTH

<u>Rivet* Approach</u>	<u>Failing load, lbs.</u>	<u>Shear Strength, psi</u>
Flush rivet only	226	1153
Flush rivet only	280	1429
Flush rivet with bond	818	204

* 0.5" diameter (area = 0.196 in²)

specimens, joint rotation was prevalent, adding a tensile component of stress. The shear strengths provided by the rivet tests were encouraging. However, when combined with a bonded joint, the results were less dramatic. This significant reduction in strength was attributed to snap loading of the rivet when the bond failed in shear, preventing the rivet from gradually picking up the load. This fortifies the position that the rivet's primary functions, when used in a bonded joint, are to prevent peel and act as a tooling clamp for the bonded joint.

Further work is required to perfect both the bonding and riveting concept, but the flexibility provided to the designer by having this technology developed will be of great value. Bonding and riveting are currently employed to attach the non-structural trailing edge seal strips to the prototype leading edge. Further back-to-back angle intercostals have been bonded to the wing tip panels as an early demonstration of the approach.

Phase I of the Shuttle Leading Edge Program was concluded with two coating candidates for the selected baseline RPP-3 substrate. Both coating systems possessed good and bad characteristics which needed further evaluation and modification to assure scale-up potential for fabrication of large, complex RPP-3 parts. Both coating systems were applied using standard pack cementation methods, adjusted to permit process temperatures above 3000°F to be reached and to reliably recover useable parts from the reacted pack. The two candidates were designated as a silicon-carbide system and a zirconium-boron-silicon system.

The silicon-carbide system was fabricated with a small amount of aluminum oxide incorporated into the coating from an alcohol slurry applied immediately prior to packing in a 70/30 silicon carbide/silicon pack. This coating system produced excellent plasma arc performance and flexure strength but had a basic oxidation problem in the 2300 to 2500°F temperature range when tested in air at one atmosphere. Unacceptable weight losses were encountered, accompanied by a corresponding strength decrease. Examination of tested specimens did not show clearly a preferential oxidation attack. However, since the principle protective mechanism for the siliconized system is probably due to the formation of an adherent layer of silicon dioxide at temperatures above 2500°F, it is possible that at lower temperatures this mechanism might not be performing at a rate sufficient to adequately protect the system. It is also probable that the coating was not dense enough to provide a totally impervious barrier to the oxidative gases surrounding the parts. Surface defects such as crazing within the coating were noted and could have been one source of oxygen entry into the RPP-3 substrate if the defects are more than surface phenomena. Coating depth and uniformity could have contributed to the oxidation resistance at the lower temperatures.

Temperature cycling tests to determine low temperature (2300°F) oxidation resistance were performed in a Pereny laboratory furnace, operating at one atmosphere pressure. These were considered to be conservative in light of the predicted in-flight shuttle pressure conditions where oxygen availability is an order of magnitude less than at ground level. However, a more quantitative comparison with flight conditions was not available and Pereny furnace data was used as a conservative evaluation technique.

The alternate Phase I coating system was composed of zirconium-boron-silicon (ZBS) applied in two furnace cycles. The boron was diffused into the RPP-3 substrate first, followed by cleanup of parts and application of the zirconium and silicon in the second cycle. Thus, it was necessary to pack, unpack, and diffusion coat twice to fabricate parts.

The finished coating system produced specimens that were non-uniform in appearance. Subsequent coating runs indicated that reproducibility problems existed. Plasma arc performance was inferior to the siliconized coating but the system was insensitive to low temperature oxidation tests. The boron content was thought to provide the desired degree of oxidation resistance at low temperatures, but degraded the plasma arc performance at higher temperatures. The protective mechanism, whereby boron oxide is formed at temperatures above 1000°F in air and protects up to 2500°F, failed at higher temperatures near 3000°F under low pressures. The formation of a silicon carbide/zirconium diboride system was probably achieved but possibly not in the proper proportion. A coating system containing near 85% zirconium diboride and 15% silicon carbide was sought to provide oxidation resistance for the full range of temperatures up through 3400°F.

An attempt was made to develop a "one cycle" ZBS system using boron and silicon carbide as the pack material with zirconium additions in a slurry coating. The base pack material, when used as a slurry, performed better than those with the zirconium additions. This led to an expanded evaluation of this system in Phase II.

The basic problems therefore to be solved at the beginning of Phase II were the low temperature oxidation resistance of the silicon carbide system and the non-uniformity and poor reproducibility of the zirconium-boron-silicon system. Initially in Phase II both systems were investigated concurrently to a point where one could safely be discontinued in favor of the other.

4.3.1 Developmental Coatings

Development of the Boron Silicon System - Boron carbide is noted for its good performance in air to 2500°F, stability in a carbon environment, and compatibility with silicon carbide. Combined with silicon carbide as a thin underlying layer adjacent to the RPP it could have functioned as a high temperature barrier to close out oxidative gases and seal in migrating carbons. One approach (shown in Figure 4-10) to the low temperature oxidation resistance of the siliconized system was to make boron additions in the form of slurries and packs on bare and siliconized RPP. Doping was employed to add small quantities of boron to the coatings. A single cycle boron carbide/silicon carbide system with and without slurry modifications showed good promise for low temperature protection. A greater success was achieved when the boron was added to the pack instead of to the slurry. However, boron additions to the coatings were not successful in producing plasma arc performance to compete with the siliconized system, although it is believed that the boron-containing system warrants further experimental work.

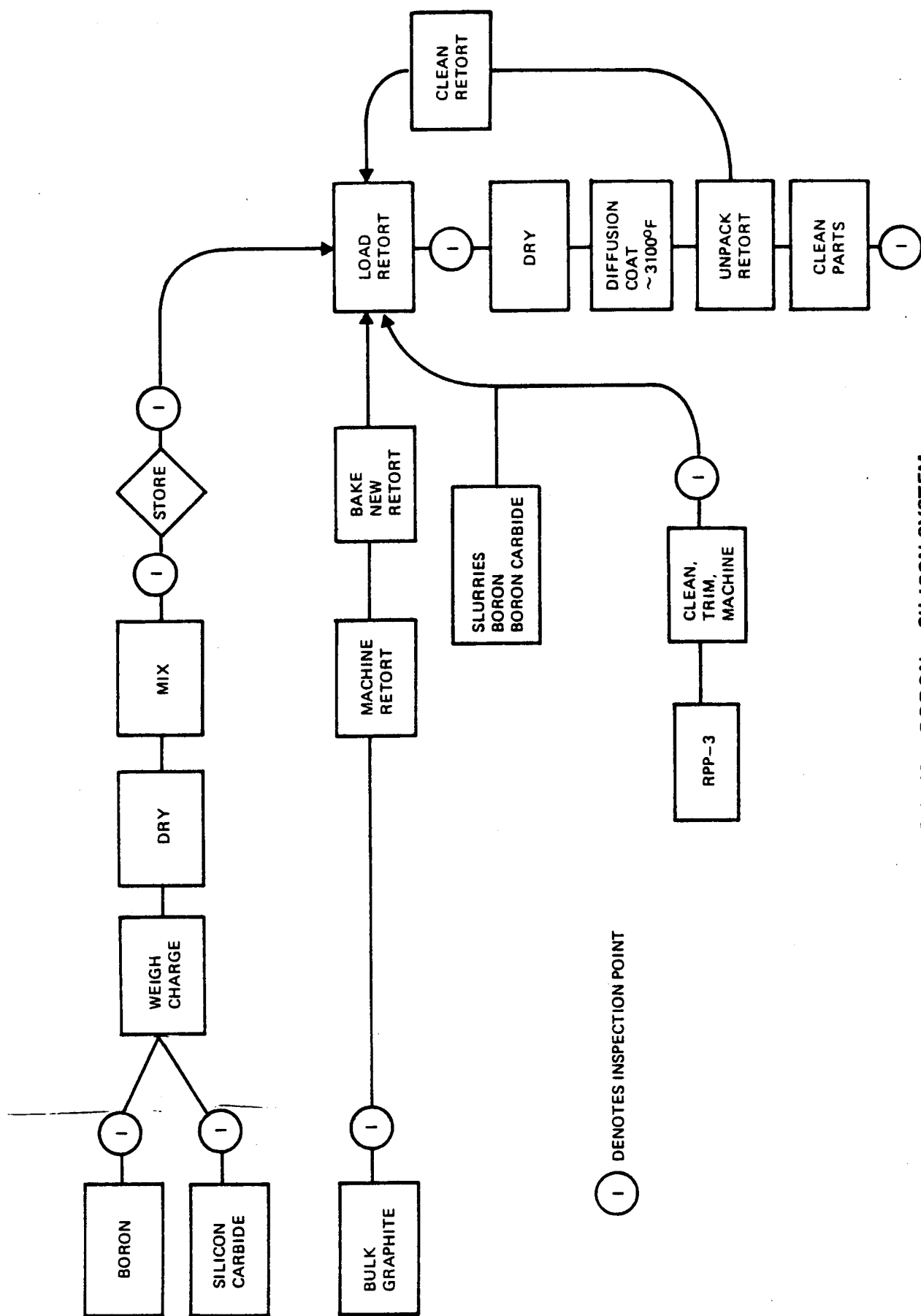


FIGURE 4-10 BORON - SILICON SYSTEM

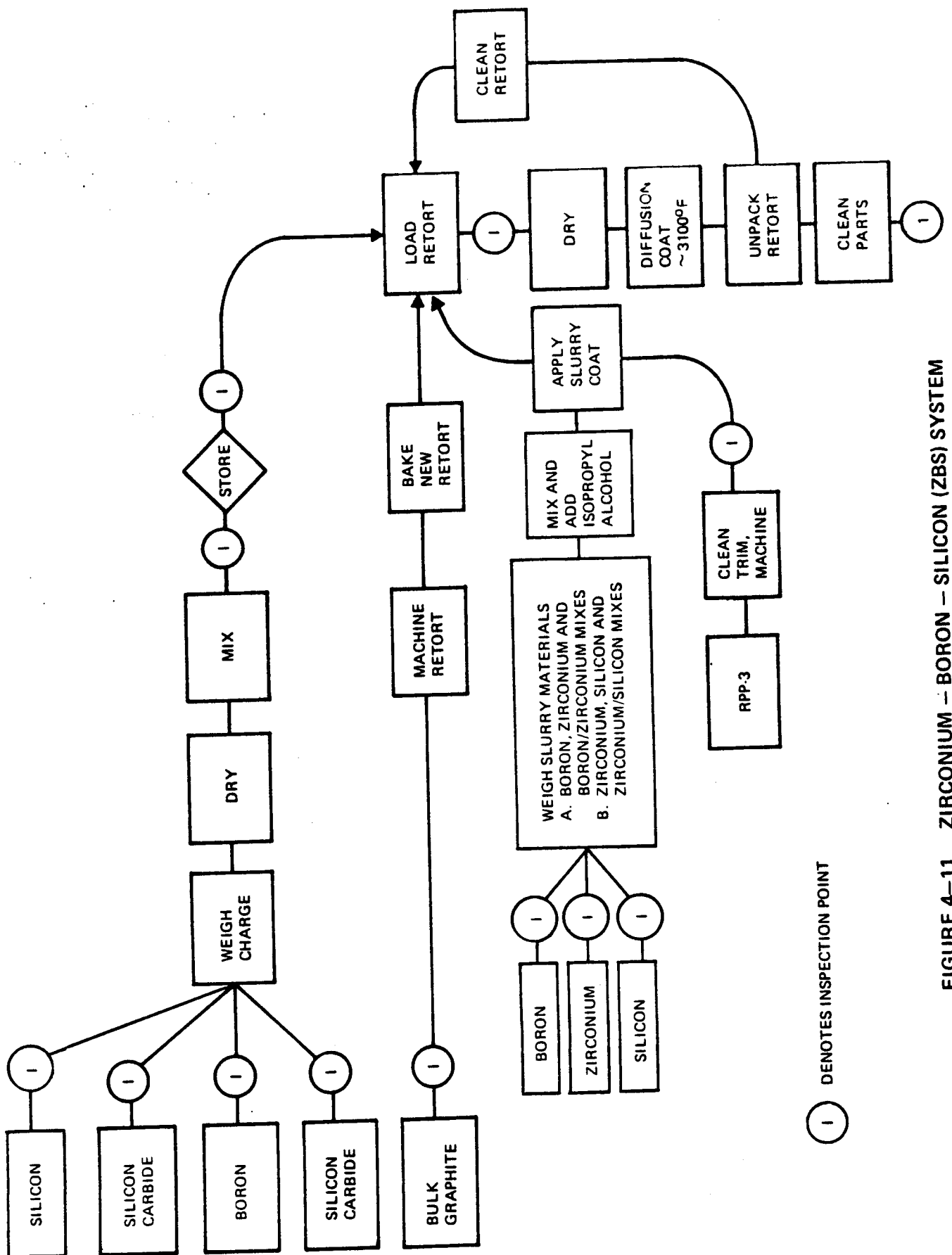
Experiment were conducted on the single cycle boron system with slurry modifications containing chromium, silicon molybdenum, tungsten, and zirconium additives. These did not produce specimens with acceptable plasma arc performance but did show that small amounts of these elements could be incorporated as modifiers to the boron coating.

The use of nitrogen or oxygen atmospheres at elevated temperature (1600°F) to stabilize coatings was evaluated on some of the boron-silicon systems with and without additives. The results indicated that treatment with nitrogen was ineffective, but treatment with oxygen can cause large (28%) increases in the weight of the coated part. These oxygen treated parts were relatively stable during subsequent thermal cycles at 2300°F in air. One specimen (M62-30, reference Appendix A for data), which was processed using a silicon-zirconium hydride slurry coating, lost weight during oxygen treatment. The parts processed with a chromium metal slurry mix were very stable after the oxygen treatment. For example, M62-14 was completely stable after the first thermal cycle at 2300°F . This indicates that the formation of the oxides of chromium may be used to develop a system which would be very stable for moderate (2500°F) temperature requirements. It should also be noted that the chromium treated RPP-3 systems had only a relatively small weight gain (about 10%) during the treatment with oxygen at 1600°F . Unfortunately, these systems did not possess satisfactory high temperature performance when exposed to temperatures of 2800°F - 3000°F in the plasma arc.

One of the best plasma arc performing boron-silicon systems tested was from run M56, (Appendix A). However, on this and other boron-silicon systems it was noted after furnace exposure that the coating was non-uniform and contained areas with poor oxidation protection. Solutions to these problems were not found before the final coating selection was made, and therefore, further investigation was discontinued.

Development of Zirconium-Boron-Silicon (ZBS) System - The approach used to further develop the ZBS system involved diffusion furnace runs consisting of boron/silicon carbide packs or silicon/silicon carbide packs. Slurries were used with both pack systems to place reactive powders in direct contact with the RPP substrate. The process flow diagram is illustrated in Figure 4-11.

Coating runs (Appendix A) M54, M56, M57, M58, M60, M61, M62 and M63 were utilized to develop further the boron-zirconium-silicon system from Phase I. Runs M54, M56, M57, and M58 used silicon/silicon carbide pack mix. Slurry mixes, containing powders of boron, zirconium and boron/zirconium were brushed on the surfaces. Furnace temperatures to 3900°F were employed. Generally, the resultant finished



1 DENOTES INSPECTION POINT

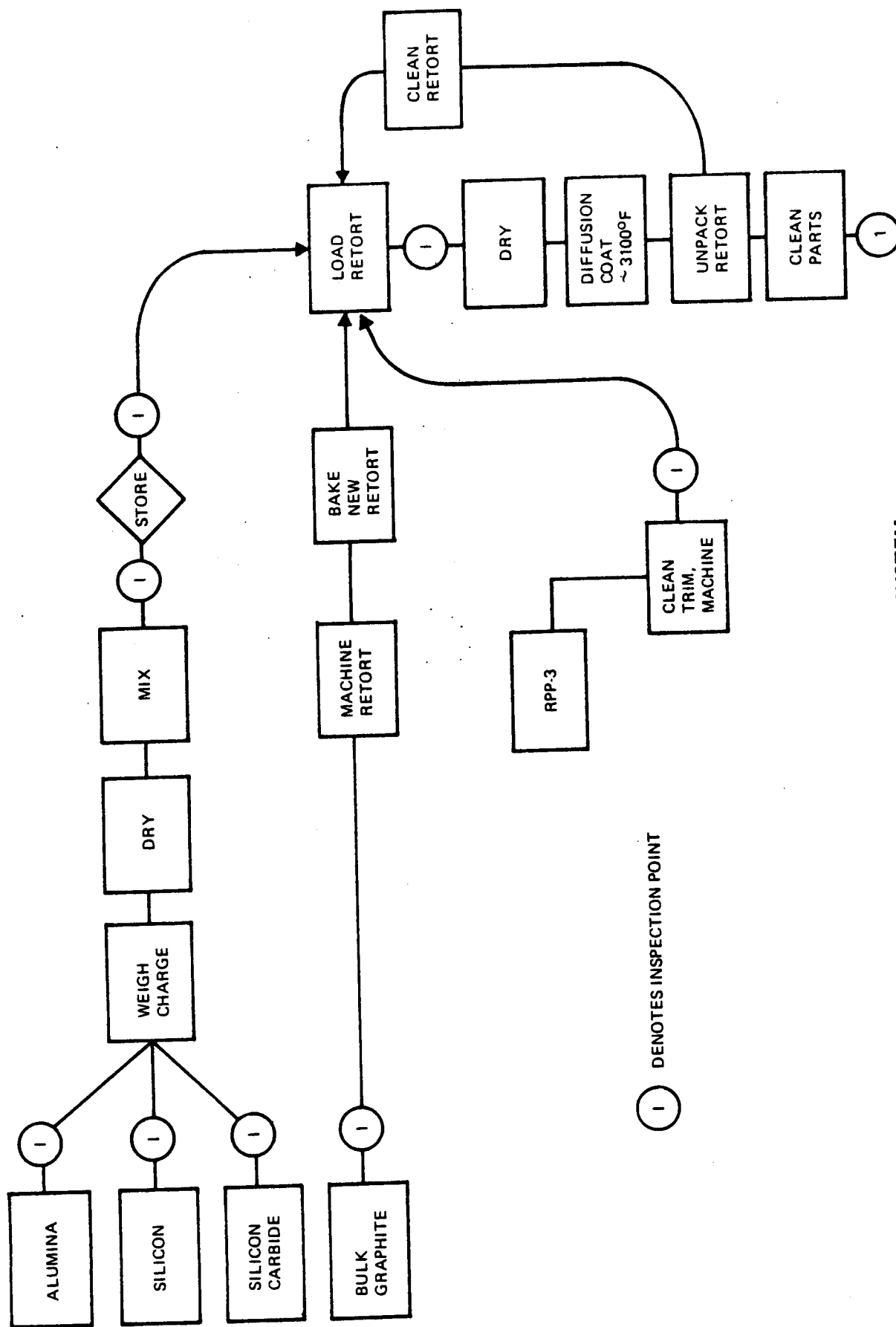
FIGURE 4-11 ZIRCONIUM - BORON - SILICON (ZBS) SYSTEM

coating was crystalline in nature and cleaned up well from the pack materials. Coating weight gains were of the order of 20 to 30%. Oxidation tests at 2300°F showed that after 5 cycles weight losses between 7% and 27% could be expected. Flexure strengths between 5000 and 8000 psi were the rule for these systems. Plasma arc tests confirmed the low temperature oxidation results, but higher than tolerable weight losses were experienced. There was an over-riding softening effect that was apparent only after low temperature oxidation tests and was the major deterrent to further development of these coating systems. The coated RPP surface after test would crumble in localized areas if thumb-nail pressure were applied. Silicides of boron and zirconium which can oxidize readily at 2300°F were probably formed instead of the desired high temperature SiC/ZrB₂ system.

Coating runs M60, M61, M62 and M63 were packed using boron/silicon carbide powder mixes with slurries of zirconium, silicon, and zirconium/silicon mixes. This pack system produced better performance results than the silicon/silicon carbide system. Specimens were as easy to remove from the pack after heat treating to 3400°F and oxidation resistance at 2300°F was improved many fold. In fact, weight gains up to 5% were experienced after 5 cycles at 2500°F and even up to 2600°F no ill effects were experienced. Flexure strengths near 10,000 psi and above were obtained. However, plasma arc performance was not as good as the M30 siliconized system from Phase I. It was felt that high temperature compounds had not formed in sufficient quantity to provide plasma arc resistance. This line of development was terminated when the siliconized system showed good promise of providing low temperature oxidation resistance.

Development of the Silicon System - A major thrust of the Phase II effort was to develop further the siliconized system from Phase I which performed well in plasma arc tests. This good performance was in part due to the aluminum oxide content added in slurry form to the surface of the RPP prior to packing in a mix of silicon and silicon carbide. Specimens fabricated without aluminum oxide did not perform as well. Since the slurry process is difficult to employ, coating trials where the alumina was added as a dry powder to the pack material were attempted and proved successful. By varying the alumina composition, over-sintering of the pack was restricted, while still maintaining high temperature performance. This process modification shown in Figure 4-12 has added greatly to the ease and controllability of processing. The alumina-containing dry pack will be continued in future development.

The siliconized coating process therefore utilizes a pack composed of alumina, silicon carbide and silicon. Silicon carbide has long



(1) DENOTES INSPECTION POINT

FIGURE 4-12 SILICON SYSTEM

been recognized for its superior refractoriness, thermal shock-resistance, and excellent resistance to abrasion at high temperatures. Aluminum oxide also has a refractory nature, having a melting point above 3600°F , and is used in high temperature furnaces as liners and domes. It is essentially chemically inert to most gases and molten metals until extremely high temperatures are reached. Silicon metal has a melting point slightly in excess of 2600°F at which point the vapor pressure rises appreciably. This vapor pressure is not only a function of the temperature but of the powder size and size distribution of the individual metal grains. Reaction of the silicon vapor with graphitic and carbonaceous materials is rapid because of their ability to combine directly. A somewhat slower reaction is expected to occur with metal oxides such as alumina, since direct combination is coupled with either oxygen transfer or release and recombination. In both cases a complex aluminum oxide-silicon dioxide compound can be formed under favorable conditions. Mullite of the form $3\text{Al}_2\text{O}_3 \cdot 2\text{SiO}_2$ with service temperatures near 3300°F in air could be expected.

The most significant accomplishment in the pursuit of the siliconized system was the reduction of weight loss when exposed to multi-thermal cycles in the Pereny furnace (see the discussion on Pereny furnace testing). The Phase I M30 baseline siliconized system produced 15% weight loss after 5 furnace cycles but current processing can reduce this to an acceptable range of between 5% loss to a few percent gain. Strength reduction varies roughly with weight loss. The reason for this improvement in low temperature oxidation resistance is attributed to the powder size and associated reactivity used in the starting ingredients. A greater percentage of fine particles has produced what appears to be a less porous surface and one with greater freedom from crazing.

With the subsurface oxidation problem apparently under control, the siliconized system was selected for Phase II hardware. This selection was based on the ability to control low temperature oxidation resistance while still providing excellent high temperature plasma arc oxidation resistance with good flexure strength. Attention was next directed to refinements in the coating process which would promote uniformity and reproducibility.

4.3.2 Refinement of the Silicon System

The selection of the $10\text{Al}_2\text{O}_3/60\text{SiC}/30\text{Si}$ pack material as the baseline system to be studied was based on test results from diffusion furnace runs M85B, M88, M95, M96, and M97. The data on each of these runs is given in Appendix A.

Once the basic system was chosen, the evaluation of factors which could affect the performance of the coated RPP-3 was undertaken. This evaluation included variations in the proportions of the three pack material constituents (alumina, silicon carbide and silicon) as well as the operating temperature of the diffusion furnace, the type of silicon carbide used, and the particle size of the silicon.

Thirty-seven diffusion coating furnace runs were made in order to develop and select the single best RPP coating system for Shuttle leading edge application. As noted previously, this system was selected on the basis that tested specimens indicated acceptable low temperature oxidation resistance, good strength and plasma arc performance, and a projected ease of fabrication. Slight variations to this formulation can be made as necessary to obtain an optimum composition without materially changing the coating. This coating system represents a simplified coating process, compared to the M30 siliconized system of Phase I, because coating ingredients are blended and packed dry. This eliminates the wet slurry application of powders to the surface of specimens prior to packing.

Synthesis of baseline coating was conducted at temperatures as high as 3400°F and as low as 2900°F, and from times of 2 hours to 6 hours. Techniques to investigate tight packing where the powder mix is firmly compressed about the RPP parts, as opposed to more loosely packed specimens, were examined, and will be further evaluated in Phase III when additional large parts will be coated. Pack thickness to provide adequate coating has been investigated as well. Evaluation of the response of RPP to the coating procedures was conducted on individual specimens which were examined before and after each step in the process. Weight changes were measured routinely. Dimensional changes have been found to be small.

Pack material composition variations were examined using diffusion furnace runs at 3000°F, 3200°F and 3400°F for 4 hours. The following composition (by weight %) pack material mixes were evaluated: 1Al₂O₃/69 SiC/30 Si, 10Al₂O₃/60 SiC/30 Si, and 33 Al₂O₃/33 SiC/33 Si. This alumina content was varied from 1% to 33% in this series of runs. The alumina fraction was considered the most critical because of its tendency to sinter readily under the proposed coating conditions. Therefore, the aluminum oxide portion was varied, in most cases, at the expense of the silicon carbide content, while the silicon fraction was held essentially constant.

The relative merits of the results are compared in Table 4-7. The use of any of the three levels of alumina eliminates the need for

TABLE 4-7 SELECTION OF 10 AL₂O₃/60SiC/30Si
QUALITATIVE COMPARISON

Item	10 AL ₂ O ₃ /SiC/Si	60 30 AL ₂ O ₃ /SiC/Si	1 69 30 AL ₂ O ₃ /SiC/Si	33 33 33 AL ₂ O ₃ /SiC/Si
Mixing of Powder	Mixes uniformly	Mixes uniformly	Mixes uniformly	Mixes uniformly
Retort Packing of Mixed Powder	Packs very well	Packs very well	Packs very well	Packs very well
Drying of Packed Retort	Drys without settling	Drys without settling	Drys without settling	Drys without settling
Pack Sintering in Argon				
After 3000°F Diffusion Run	Sinters slightly	Sinters very slightly	Sinters with slight shrinkage	
After 3200°F Diffusion Run	Sinters with slight shrinkage	Sinters slightly	Sinters with shrinkage	
After 3400°F Diffusion Run	Sinters with shrinkage	Sinters with slight shrinkage	Sinters hard	
Specimen Removal from Pack				
After 3000°F Diffusion Run	Specimens easily removed	Specimens easily removed	Specimens easily removed	
After 3200°F Diffusion Run	Specimens easily removed	Specimens easily removed	Specimens difficult to remove	
After 3400°F Diffusion Run	Specimens removed with some adherent pack material remaining on surface	Specimens easily removed	Specimens very difficult to remove from sinters pack	

TABLE 4-7 SELECTION OF 10 AL₂O₃/60SiC/30Si
QUALITATIVE COMPARISON (Cont'd.)

Item	10 AL ₂ O ₃ /SiC/Si	60 30 AL ₂ O ₃ /SiC/Si	1 69 30 AL ₂ O ₃ /SiC/Si	33 33 33 AL ₂ O ₃ /SiC/Si
Specimen Appearance after 3000°F diffusion coating	Uniform		Uniform	Uniform
After 3200°F diffusion coating	Uniform		Uniform	Uniform
After 3400°F diffusion coating	Fair		Uniform	Adherent pack Materials
Pereny Test of Specimens 5 Cycles @ 2300°F After 3200°F diffusion run	Slight weight gain		Slight weight loss	Slight weight loss cracking occurred
After 3400°F diffusion run	Slight weight loss		Slight weight gain	Slight weight loss
Flex Test Results after 3000°F	Greater than 10,000 PSI		Greater than 10,000 PSI	Greater than 10,000 PSI
After 3200°F diffusion run	Greater than 10,000 PSI		Greater than 10,000 PSI	Greater than 10,000 PSI
After 3400°F diffusion run	Less than 10,000 PSI		Less than 10,000 PSI	-
Plasmarc results mission life potential after 3000°F diffusion run	Less than 100		Less than 100	Less than 100
After 3200°F diffusion run	Greater than 100		Greater than 100	Greater than 100
After 3400°F diffusion run	Greater than 100		Greater than 100	Greater than 100

TABLE 4-7 SELECTION OF 10 AL₂O₃/60SiC/30Si
QUALITATIVE COMPARISON (Cont'd.)

Item	10 AL ₂ O ₃ /SiC/Si	60 30 AL ₂ O ₃ /SiC/Si	1 69 30 AL ₂ O ₃ /SiC/Si	33 33 33 AL ₂ O ₃ /SiC/Si
Coating wt. pick up after 3200°F diffusion run	Near 40%		Near 38%	Near 35%
After 3400°F diffusion run	Near 50%		Near 40%	Near 40%
Ease of specimen clean-up after 3000°F diffusion run	Very easy, brush only		Very easy, brush only	Very easy, brush only
After 3200°F diffusion run	Very easy, brush only		Very easy brush only	Adherent pack, material remains on specimen after brushing
After 3400°F diffusion run	Difficult to clean		Easy to clean - brush only	Can not clean adherent pack material from specimens

a slurry application. The 1% alumina powder mix has the greatest coating temperature range but sintering was not sufficient to keep the RPP parts and pack in intimate contact throughout the diffusion run. The 33% alumina mix sinters entirely too much at the coating temperatures employed. The 10% alumina mix sinters and shrinks at a more predictable rate under the test conditions although at 3400°F an over-sintered condition prevailed. Clean up of specimens was easy except for those coated at 3400°F in the 10% and 33% alumina mix.

Flexure strength, which is affected by coating depth and compatibility between RPP substrate and coating, was determined to be near 10,000 psi.

The low temperature oxidation problem, where excessive weight losses were encountered after cycling at 2300°F, can be minimized greatly if sufficient coating weight gain for any of the three systems is achieved. However, specimens coated with the 33% alumina system crazed when heat cycled at 2300°F, and were crack sensitive in the plasma arc test. The least sensitive was the 10% alumina system. Crazing is a condition normally created when expansion differences exist between the layers of multi-layered systems. Induced strains are relieved through crazing of one of the layered members when temperature changes are imposed on the system. Cool-down cracks and crazing during fabrication were less noticeable for the 10% alumina system.

As a further check on the 10% alumina pack composition, a test run comparing 5%, 10%, and 15% alumina was made. This coating run confirmed that small variations in the alumina content can be made without detrimental effects on performance.

The fabrication factors, which can affect the plasma performance, substrate oxidation, and strength of a coating system, are bulk material properties of powders, packing procedures, furnace temperature/time cycles, retort design and thermal distribution. Each of these factors must be standardized to achieve consistently good results. They are discussed individually on the following pages.

Evaluation of Coating Powders - The suppliers of powder materials were selected because of their interest in maintaining quality products which are commercially available. Discussions with key representatives from each company have shown a willingness on their part to cooperate with VMSC in qualifying their respective products to mutually acceptable specifications.

Silicon metal powder was purchased from three different sources. All three vendors have acceptable products. Two are producers of silicon, while the third is a processor. The processor at present does not have the capacity to handle the predicted quantity needs and cannot be seriously considered as a supplier. The producers are Union Carbide and Foote Minerals, both of which have demonstrated quantity deliveries in a timely fashion. Trial coating runs have shown equally successful performance behavior for RPP specimens coated with silicon metal powders from the two selected vendors.

Silicon powders were screened and classified at VMSC using a Ro-Tap machine and standard sieves. A comparison of the powder particle size distribution is shown in Table 4-8. The classification score is shown for nine of the silicon metal powder lots used in coating studies. The lots with large concentration of fines (powder size designated -325) were the most difficult to classify due to agglomeration, which was corrected in part by air drying at 250°F.

TABLE 4-8. SILICON METAL POWDER PARTICLE SIZE DISTRIBUTION WEIGHT PERCENT

SILICON LOT	<u>MESH SIZE</u>			
	<u>+140</u>	<u>-140 to +200</u>	<u>-200 to +325</u>	<u>-325</u>
404	1.5	16.1	75.2	7.8
468	0.1	3.1	86.9	10.4
721	0.0	1.5	34.5	65.2
532	0.1	5.9	88.1	5.9
708	0.0	0.4	33.2	65.0
741	1.0	17.0	71.1	10.0
833	0.2	15.7	71.6	12.5
1471	1.0	1.3	30.0	67.5
10939	7.2	19.9	52.1	20.4

A measure of silicon powder response in the coating process can be gained from a knowledge of the particle size distribution. The lots with a large fines concentration show a wider depletion zone within the pack adjacent to the part when examined after coating. Also, metal segregation within the pack is less likely to occur and coated parts have a more uniform appearance, indicating a more controlled rate at which the coating is applied.

Aluminum oxide powder was supplied by Aluminum Company of America and is a grade which can be purchased to an existing VMSC Materials Specification 307-15-2A, titled, "Alumina T-61". This alumina is an alpha crystal powder, commercially available in minus 325 mesh size with only 0.8 percent between the sizes, minus 200 to plus 325. This particle size distribution is compatible with vendor literature. Reactivity of the alumina T-61 powder is great enough to cause sintering at the temperature used for coating RPP. This sintering, attended by shrinkage, probably aids in maintaining the pack material in contact with the RPP parts during the diffusion coating process.

The silicon carbide powder, mesh size 1200 is a classification given to the proper particle size distribution by Carborundum Corporation of Niagara Falls, N. Y. A flotation process is used because the powder size is in the micron range and exceeds the capability of VMSC mechanical screens. Carborundum explained that silicon carbide of the 1200 mesh variety is supplied in color grades which indicate the amount of aluminum actually salted. Color grades are designated green (lowest aluminum content), green/black (low aluminum), and black (high aluminum content). The explanation for color variation from black to green previously reported by Carborundum (Reference 6) as being due to carbon migration into the powder mass from the chamber walls at the extremely high reaction temperatures employed during fabrication has been corrected, and aluminum content is now the reason offered.

Seven lots of silicon carbide were evaluated which includes the color variation from green through black. Emphasis was directed to the green, or more pure variety, than the black grade with its aluminum content. Selected powder batches representing the three color grades were examined using a Scanning Electron microscope (Figure 4-13). This technique doesn't readily show a striking difference. The photographs do, however, indicate that the green grade is slightly more uniform in particle size distribution and less angular in shape.

Metal impurities found in lot samples of silicon, silicon carbide and aluminum oxide powders are shown in Table 4-9. Generally, the metal impurities found are comparable to that expected from commercially available materials of this nature. There is no outstanding metal contaminate that causes alarm. This study of the powders was made by qualitative spectrochemical analysis using a DC arc excitation.

The final acceptance criteria for powders, however, was to employ them in standard coating cycle. This method was used to compare several lots of silicon and silicon carbide in one furnace run to minimize extraneous variables. Variations from lot to lot of the starting powders and the effect of particle size of the silicon were evaluated using plasma, flexure, and



A. SILICON CARBIDE
BLACK
LOT 00776
5000X



B. SILICON CARBIDE
GREEN
LOT 00774
5000X



C. SILICON CARBIDE
GREEN/BLACK
LOT A7058
5000X

FIGURE 4-13 SCANNING ELECTRON MICROSCOPE EVALUATION OF SILICON CARBIDE

TABLE 4-9. TRACE METAL IMPURITIES
OF PACK MATERIAL POWDERS

+ Element Detected

- Element not Detected

<u>POWDER LOT NO.</u>	<u>Si</u>	<u>Fe</u>	<u>Cu</u>	<u>Na</u>	<u>Ti</u>	<u>Zn</u>	<u>Ag</u>	<u>Ca</u>	<u>Sn</u>	<u>V</u>	<u>Al</u>	<u>Mg</u>	<u>Ni</u>
Silicon 007	+(1)	+	+	-	+	-	-	-	-	+	+	+	+
Silicon 404	+(1)	+	+	+	+	+	+	+	+	+	+	+	+
Silicon 464	+(1)	+	+	-	+	-	-	-	+	+	+	+	+
Silicon 468	+(1)	+	+	-	+	-	-	-	+	+	+	+	+
Silicon 503	+(1)	+	+	+	+	+	+	-	+	-	+	+	+
Silicon 532	+(1)	+	+	+	+	+	+	-	+	+	+	+	+
Silicon 538	+(1)	+	+	+	+	+	+	+	-	+	+	+	+
Silicon 602	+(1)	+	+	-	+	+	+	+	+	-	+	+	+
Silicon 708	+(1)	+	+	-	+	+	-	+	+	+	+	+	+
Silicon 721	+(1)	+	+	+	+	+	-	-	-	+	+	+	+
Silicon A-2 ⁽⁴⁾ Carbide	+(1)	+	+	-	+	+	-	-	-	+	+	+	+
Silicon 821700 Carbide	+(1)	+	+	-	+	-	-	-	-	-	+	+	+
Silicon 822992 ⁽²⁾ Carbide	+(1)	+	+	+	+	-	+	+	-	-	+	+	+
Silicon A7058 ⁽³⁾ Carbide	+(1)	+	+	+	+	+	+	+	-	-	+	+	+
Silicon 113 ⁽⁴⁾ Carbide	+(1)	+	+	+	+	+	+	-	-	-	+	+	+
Aluminum Oxide	+	+	+	-	+	-	-	-	-	-	+(1)	+	-

(1) Major Constituent

(2) Green Silicon Carbide RA1200

(3) Green Black Silicon Carbide RA1200

(4) Black Silicon Carbon RA1200

Pereny oxidation test results on coated RPP-3 to establish performance capabilities for each lot of material. This information will be used to determine the particular type of material to order in large quantity for future phases. To insure that the specified powder can be received from the suppliers, preliminary working agreements have been reached, where lot traceability, as needed, will be maintained. Further controls in the way of preliminary specifications to procure and process coating materials have been written and will be released to material suppliers for review and comment. In-house specifications to control coating processes have been developed.

Thermal Processing - The diffusion coating thermal process cycle controls the weight gain and other characteristics of the coating applied to the RPP-3 substrate material. Thus, to achieve reproducibility, it is essential to control the thermal cycle to achieve consistent furnace coating runs. This initially required the use of thermocouples embedded in the pack material because of erroneous pyrometer readings. However, reproducibility was ultimately achieved through several furnace modifications to improve optical reading reliability.

The positioning of the retort in the furnace is also very important to insure that parts are heated uniformly. The two furnaces used for the RPP coating process were a 12" diameter vertical loading furnace and a 24" diameter horizontal loading type. A typical diffusion coating cycle was developed for each furnace and adjusted for changes in both retort configuration and the amount of pack material being used in order to process parts successfully. Typical instrumented thermal cycle curves are shown in Figure 4-14 (12" dia. furnace) and Figure 4-15 (24" dia. furnace). The optical pyrometer readings shown have not been corrected to compensate for transmission loss through the sight glasses. Figure 4-14 shows one optical and two thermocouple curves for a stack of three "pancake" style retorts. These curves show that the center retort heats more slowly, but reaches a higher peak temperature. The optical temperature remains relatively constant throughout the coating cycle.

The large diameter (24") furnace, which was used to coat larger parts, like the leading edge segments, required a longer heat up cycle to heat the pack material to the proper coating temperature. This is shown by the temperature lag (relative to optical or furnace temperature) of the thermocouple in the pack material (Figure 4-15). There is evidence that after the pack reaches a certain temperature, it heats more rapidly than the optical temperature would indicate. This could indicate a change in the thermal properties of the pack material as the temperature increases.

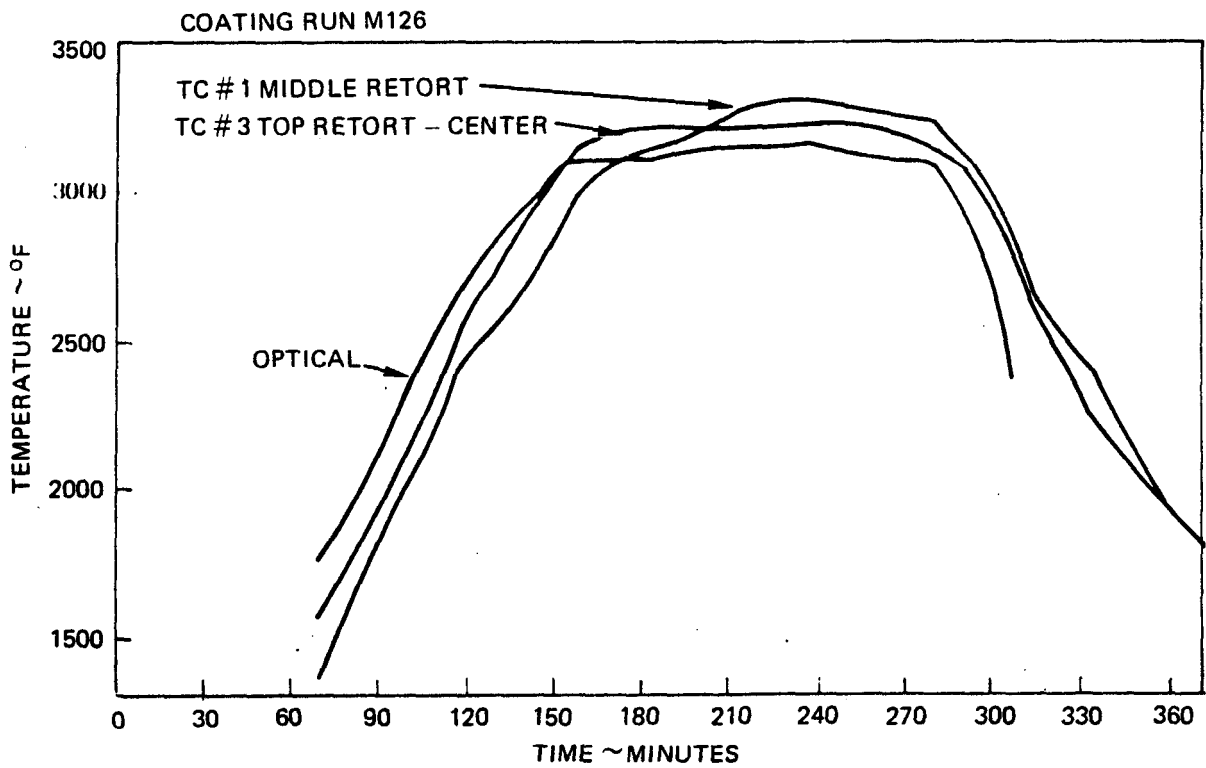


FIGURE 4-14 TYPICAL THERMAL CYCLE CURVES FOR 12" DIAMETER FURNACE

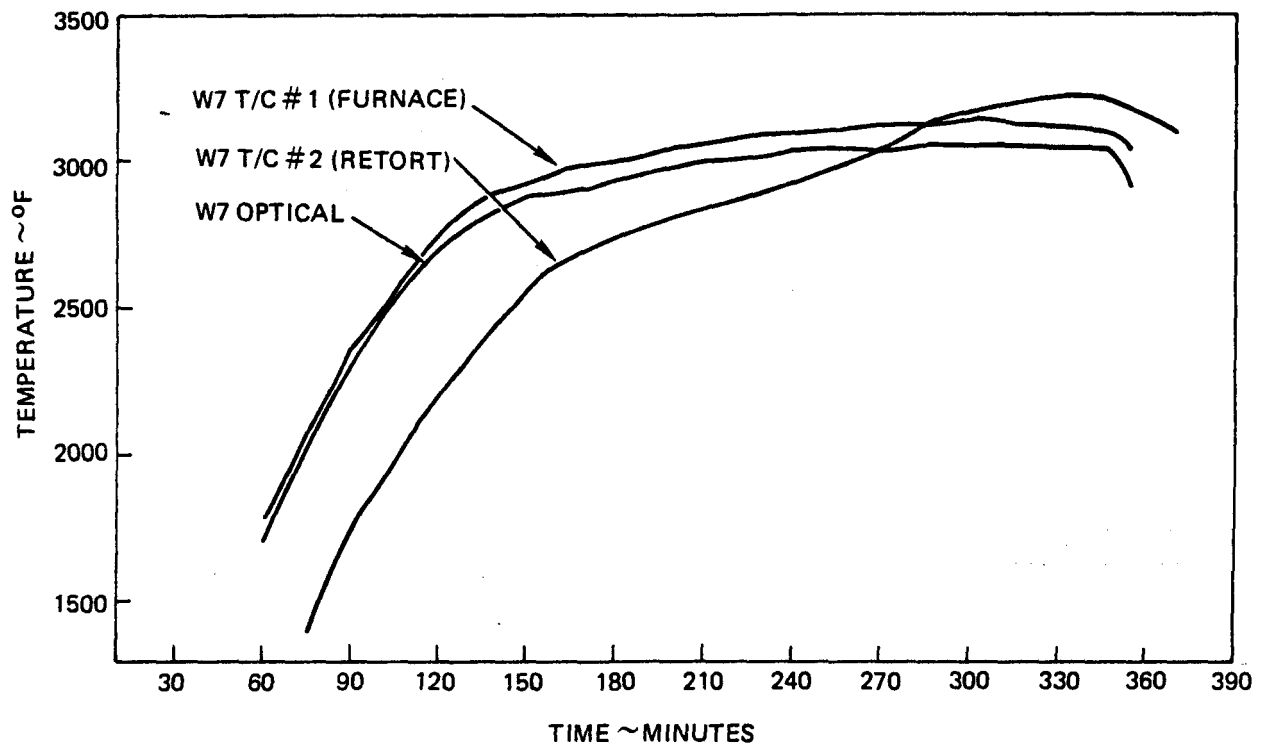


FIGURE 4-15 TYPICAL THERMAL CYCLE CURVES FOR 24" DIAMETER FURNACE

Weight gain of the RPP-3 substrate during a coating cycle is directly proportional to the dwell time at each temperature. The average weight percent gain measured for each processing temperature is given in Figure 4-16. This plot provides a means of predicting the weight gain for a planned thermal cycle. The data indicates that between 2900°F and 3100°F the percent weight gain is linear with temperature. However, above 3100°F the weight gain rate increases - then decreases as 3400°F is approached. The run (M168, Appendix A) at 3400°F has indicated that the surface "crazing" may be eliminated or greatly reduced by coating at higher temperature. Parts coated in this particular run had no "crazing" on the surface either in the as-coated condition or after they had been heat treated.

Heat treatment was developed as part of a test program to determine the effects of reheating the coated RPP to an elevated temperature in an inert atmosphere. This was done to determine the optimum temperature for formation of high temperature coating system reaction products, which would perform well in the plasma tests. Preliminary tests were carried out at 3000°F for 90 minutes and 3200°F for 45 minutes. The latter heat treatment gave the best plasma performance results.

The 3200°F for 45 minutes heat treating cycle was therefore adopted as the standard cycle for the remainder of the program. It is anticipated that the need for this post heat treatment can be eliminated by initially coating parts at a somewhat higher temperature. Coating runs at higher temperatures, such as M168, but for a shorter time period to control or limit the percent weight gain, may be used to alleviate "crazing", and eliminate the need for the post-coating heat treatment.

Another important concern with the coating process is heat distribution in the furnace and particularly in the retort. Early in the program it was suspected that, when using the large retorts for coating specimens, significant temperature variations occurred throughout the pack in terms of peak temperatures achieved. A calibration test and thermal analysis were therefore undertaken to establish the magnitude of gradients between the outer layer and interior of the pack. In addition, analyses were performed to predict the improvement to be realized from retort modifications. It was found, that by utilizing intermediate graphite plate conductors in contact with the retort walls to permit unrestricted radiation heat transfer, that variations in maximum temperature could be reduced from several hundreds of degrees Fahrenheit to less than 100°F.

The 30 node thermal model illustrated in Figure 4-17 was used to perform the two dimensional transient thermal analyses. This model included the graphite retort wall, pack material and graphite plate. The model included a symmetrical section of the retort from the centerline to

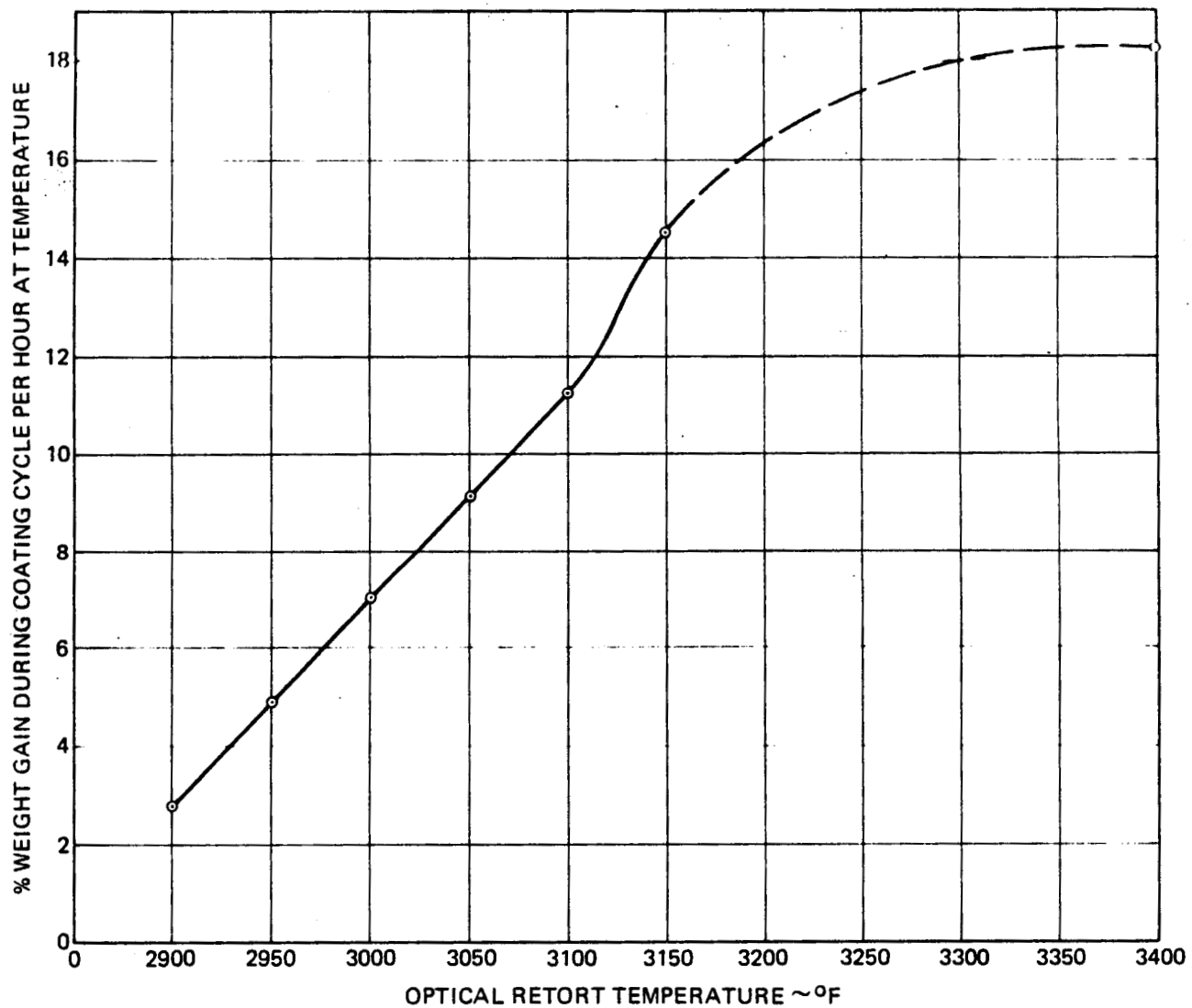


FIGURE 4-16 PERCENT WEIGHT GAIN DURING COATING CYCLE

the outside of the retort wall and from the mid-plane of one plate to a plane midway between parallel plates. Measured temperatures on the outside surface of the retort wall as a function of time were used as the driving temperature. This temperature history consisted of heatup to 3400°F over a three hour period, followed by 2.5 hours at 3400°F and subsequent cool down.

The greatest uncertainty in the analysis consisted of the thermal conductivity of the powdered pack material. Best available data in the literature on similar material was used to estimate a value of 0.10 BTU/hr ft°F for the pack conductivity. A furnace calibration run was made with the thermocouples in the pack material and on the graphite plate, which indicated a value of 0.077 to be more appropriate.

Computed maximum temperature in the retort, pack and plate, are shown in Figure 4-17 and it is seen that temperatures in the center of the pack reach only a little over 2800°F. Further, temperature gradients near the retort wall are severe. An analysis was made in which the heating cycle was extended an additional two hours, but this increased pack temperature to only 3000°F.

It is seen in Figure 4-17 that there is a severe temperature drop from the retort wall to the outside of the graphite plate. Temperature drop from outside to inside of the plate is very low, as is the drop from the plate into the pack material. Hence, the graphite plate acts as a fin to conduct heat into the retort, but its efficiency is severely impaired by the 0.50 inch of pack material between the retort wall and the plate. An

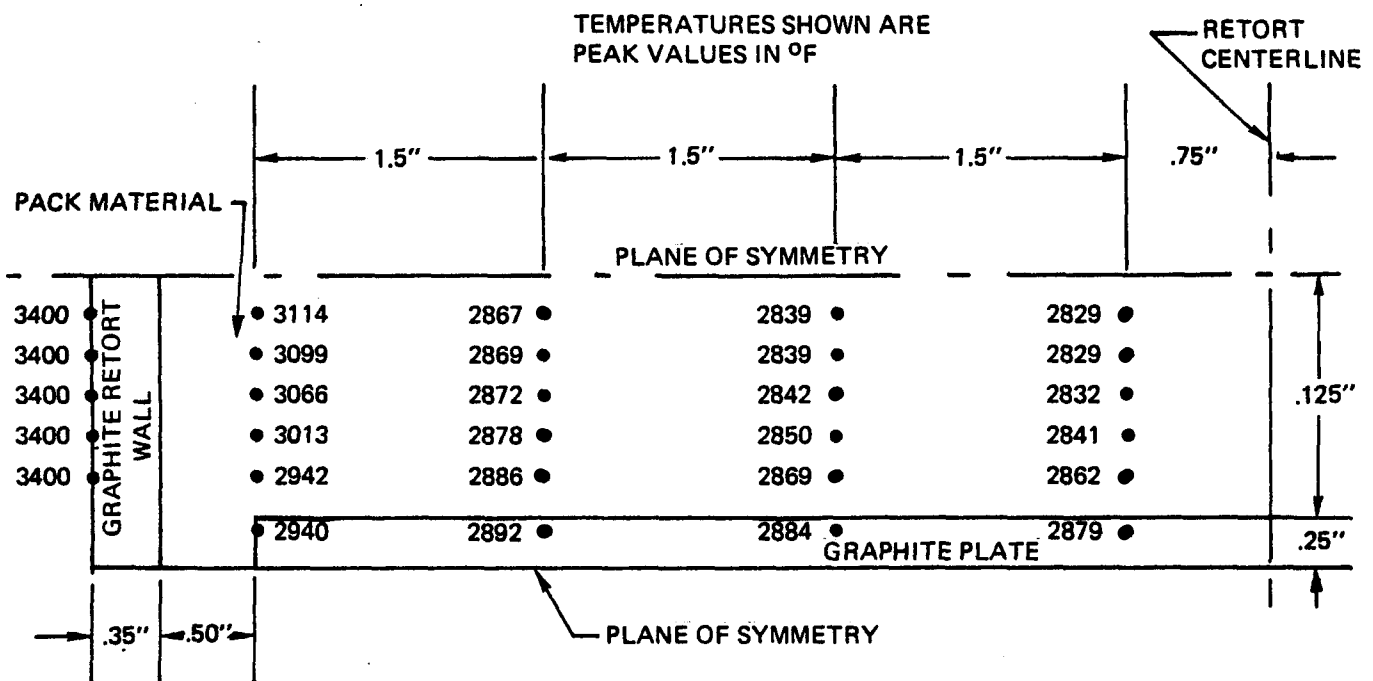


FIGURE 4-17 THERMAL MODEL OF RETORT

analysis was therefore performed to predict the effect of extending the plate to contact the retort wall. Contact resistance was simulated conservatively by assuming only radiation heat transfer from the retort to the plate. The results were highly encouraging, indicating that the inside of the pack would reach 3330°F with the original heating cycle.

The retort design was modified to allow the graphite plate to be machined integrally with the retort, such that no contact resistance existed between the retort and the plate. Furnace runs with this design confirmed that essentially uniform temperatures were obtained throughout the pack material.

Pereny Furnace Test - In an effort to ascertain the significance of specimen exposure in the Pereny furnace in terms of equivalent missions per exposure cycle, two separate correlation test experiments were conducted. The approach was to relate computed mass loss per mission to the mass loss data obtained in plasma arc testing, and then relate plasma arc mass loss to Pereny furnace mass loss. The mission/plasma arc relation is routinely calculated to estimate mission life for the various coating systems (reference section 5.1.3).

Experiments were conducted on specimens fabricated similar to the Phase I baseline siliconized coating. Specimens were exposed to the plasma environment continuously for 30 minutes, while a companion specimen was exposed to the same temperature and time in the Pereny furnace. The percentage weight loss comparison for these tests is given in Table 4-10. Furnace testing is noted to be 9 to 14 times more severe than exposure to the plasma arc.

TABLE 4-10. CORRELATION DATA
PLASMA ARC AND PERENY WEIGHT LOSS

Specimen Run	Avg. Exposure Temp °F	Avg. % Wt. Loss in Plasma	Avg. % Wt Loss in Furnace	Ratio Furnace Plasma
M71	2200	0.60	6.0	10.0
M86	2220	0.74	10.4	14.1
M86	1710	0.77	7.1	9.2

Analysis of the plasma arc testing by integrating incremental mass loss over the heating rate time history of the entry trajectory showed that 8.9 minutes of plasma arc exposure at maximum heat flux level is

equivalent to one shuttle mission. This equivalency is for the delta wing vehicle and is five times greater than for the short cross range vehicle, analyzed in Phase I.

Using the factor of 10 from the above data, a 100-mission life is equal to 890 minutes exposure in the plasma arc or roughly 89 minutes continuous exposure in the Pereny furnace. Since one standard cycle of testing in the Pereny consists of 10 minutes in a preheated furnace and 10 minutes outside, while cooling, an average period of severe oxidation is approximately 15 to 20 minutes. This means that roughly 4.5 to 6 cycles in the Pereny represents 100-mission life. It should be noted that this is a rather gross analysis of the correlation, but 5 cycle Pereny exposure has been used for coating evaluation as a guide to development until a more exact technique is established, even though it appears to be highly conservative.

The use of radiant heat lamps or graphite heaters as a heat source, and diluted atmosphere to represent the partial pressure of oxygen during entry, provides a more realistic thermal test to be imposed on the coated material. These tests are reported in section 5.2.4. Once these are thoroughly evaluated, modification to the simpler Pereny test can be made to be more realistic.

Characterization - Evaluation of the capability of the coated RPP system to meet Shuttle leading edge requirements was based on the following three main test criteria:

- (1) Plasma arc performance
- (2) Flexure strength
- (3) Oxidation cycle test in air at 2300°F

Example test results for the 10 Al₂O₃/60 SiC/30 Si system are summarized in Figures 4-18 through 4-21. These data are for early investigations of the 10/60/30 system and were used to determine the impact of certain variables on system performance. More recent data is discussed later.

Plasma arc performance, used to calculate the mission life shown in these figures, was based on 2750°F maximum radiation equilibrium temperature and includes no relieving effects from internal cross radiation or low catalycity. These factors are discussed in detail in Section 5.1.3.

Flexure strength was determined using a Tinius Olsen tensile test machine rigged with a four point loading fixture and deflectometer to continuously record applied load and deflection. Because of their simplicity, flexure tests were made to evaluate the effects of the coating process and variables on the strength of the material system.

The oxidation cycle test was performed in a Pereny Furnace controlled to maintain 2300°F during the test cycle. Each of the five cycles consisted of 10 minutes in the furnace at 2300°F and 10 minutes in ambient air, while cooling to less than 500°F, before the next cycle is started. Weight change was monitored at the end of the first and fifth cycles. This test is used to determine the degree of low temperature (less than 2300°F) protection afforded the substrate by the coating system and to ascertain the magnitude of subsurface oxidation.

The relative weight gain of the substrate during coating can be related to the weight gain or loss of the coated parts during the 2300°F temperature cycle tests in most cases. This can be shown by comparing the gain in weight for 13 ply flexure bars during the coating cycle to the weight change after five thermal cycles at 2300°F. Comparative values for various example configuration runs on the 10/60/30 siliconized system are given in Figures 4-18 and 4-19. In general, for each series of runs, in which the major variables were held constant, it is evident that an increase in coating weight up to approximately 35-40% (see Figure 4-19) results in

10 A701 60 S4 30 S
DEVELOPMENT RUNS

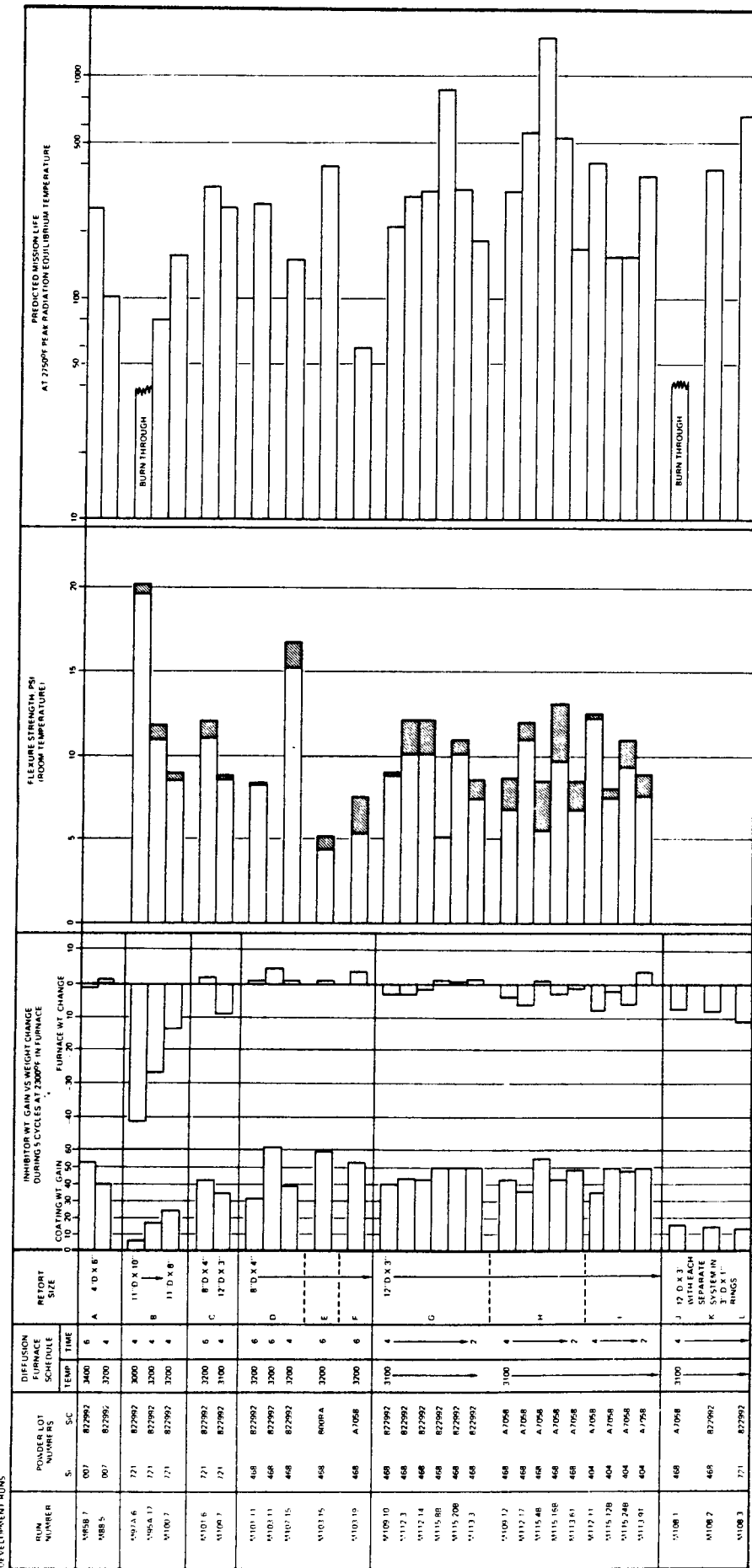


FIGURE 4-18 THERMAL AND MECHANICAL PERFORMANCE DATA FOR SELECTED RPP INHIBITOR SYSTEM

10 100

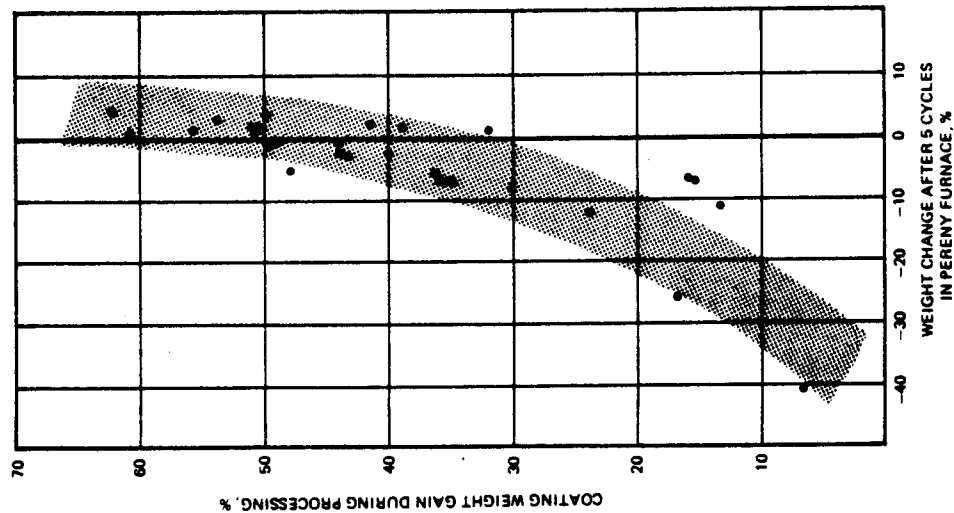


FIGURE 4-19 OXIDATION RELATIONSHIP TO WEIGHT GAIN DURING COATING, 10/60/30 SILICONIZED SYSTEM

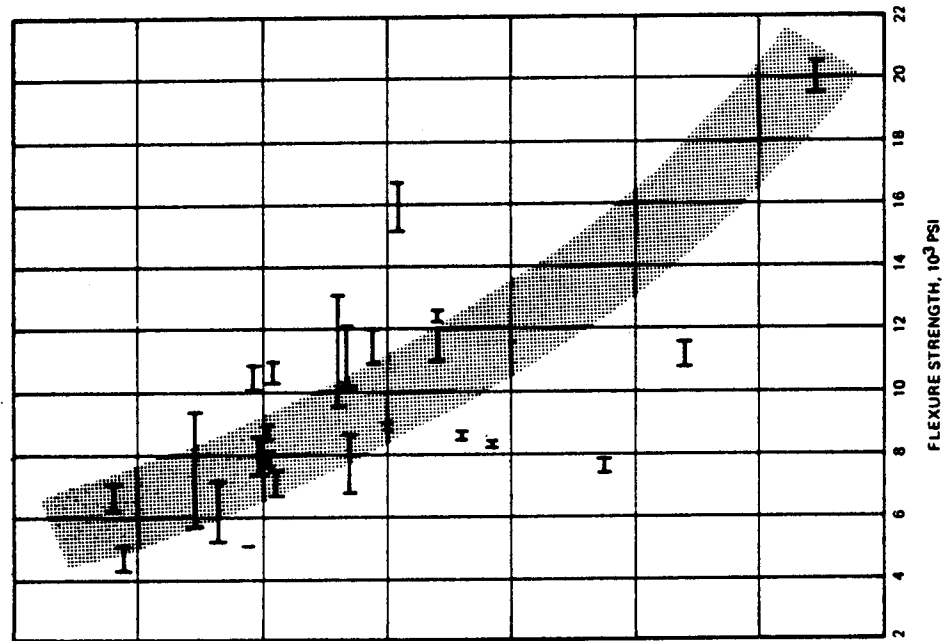


FIGURE 4-20 FLEXURE STRENGTH RELATIONSHIP TO WEIGHT GAIN DURING COATING, 10/60/30 SILICONIZED SYSTEM

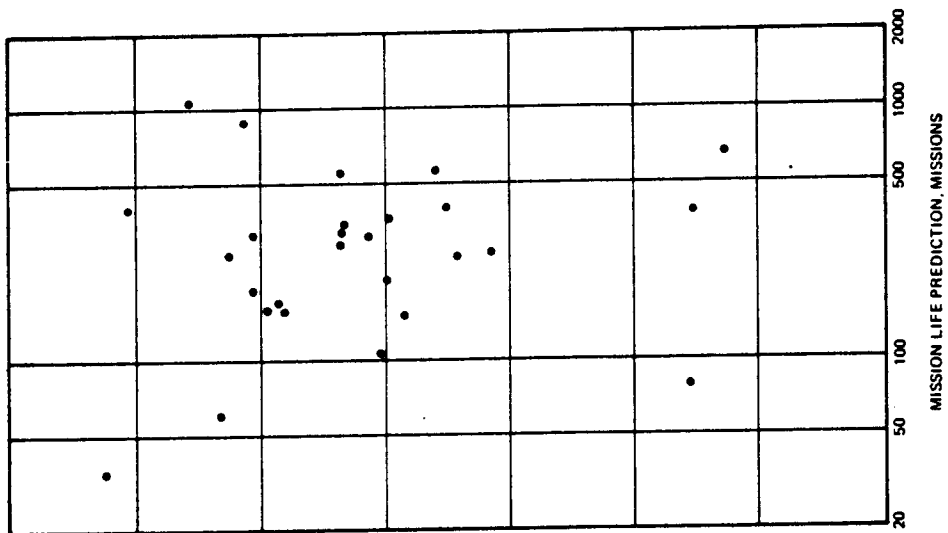


FIGURE 4-21 MISSION LIFE RELATIONSHIP TO WEIGHT GAIN DURING COATING, 10/60/30 SILICONIZED SYSTEM

an increased resistance to weight loss during the five thermal cycles at 2300°F. Higher weight gains during coating offer no added improvement. However, the necessary weight gain to achieve stability can be altered to some extent by time-temperature variations in the thermal cycles, by selection of proper retort configurations, and by retort packing procedures. Also, it should be noted that this weight gain percent can be decreased if thicker substrate materials are to be coated.

The oxidation test cycle (5 cycles at 2300°F) data summary given in Figure 4-18 shows the effects of many parameters on the test results. They have been given series letter designations A to L to facilitate the discussion of the results.

Series A is representative of the type of small retort runs which were used to evaluate and develop new pack cementation mixture ratios and to carry out material and process evaluations. Neither of the runs (M85B and M88) had a very significant change of weight during thermal cycling testing.

Series B shows the classic effect of weight gain during coating on the loss or gain of weight during thermal cycling test. In this series all the specimens had a relatively small weight gain during the coating cycle. All of these samples were coated in large 11-inch diameter x 1-inch thick wall retorts, which have been found to maintain the pack mixture at a somewhat lower effective operating temperature than other retort designs. The specimen listed in series L (using two other retort sizes) indicate that the pack materials used in series B will give good thermal cycle results when other coating cycle parameters are adjusted to increase the weight pick-up during the coating cycle.

Series D, E, and F were run in 8-inch diameter by 4-inch deep, thin walled (3/8 inch) retorts. These results indicate that increases in coating weight gain above 35% have less effect on the low temperature thermal protection mechanism than the initial portion of the coating weight gain. This means that large coating weight gains are not needed to achieve temperature stability when exposed to 2300°F thermal cycles. Run M103 gave similar results using three types of silicon carbide powders with the silicon metal being the same in all cases.

Flexure strength appears to be more strongly influenced by coating weight gain than by varying pack powders. This is shown on Figures 4-18 and 4-20. Series B illustrates this phenomenon and shows that flexure

strength decreases when coating weight increases are experienced. Coating penetration into the substrate evidently converts the available RPP carbon, forming a new combination of materials, which are dissimilar enough to reduce the system strength. Coating depth control is one facet to gaining higher strength without losing oxidation protection. Series C also shows this strength reduction as the coating weight increases. The superior behavior of the Series D M107-15 system indicates that coating weight gains near 38.7% were adequate enough to provide 2300°F oxidation protection, a mission life of 148 and flexure strength in excess of 15,000 psi. A weight gain of 62.3% reduced the strength 50% and cut the predicted mission life to 35, assuming mission life is based on an allowable coating recession of 0.010 in. The systems with the higher weight gain seem to embrittle the remaining virgin RPP, causing what would be severe mismatches between the coating and substrate. This has shown up as a reduced strength and lowered plasma arc performance. It would appear that coating thickness tolerance bands could be established and maintained by proper processing. Series G, H, and I generally confirm the results of Series B, C, and D that strengths above 10,000 psi can be consistently achieved if weight gains not exceeding 40% are maintained. The predicted mission life is also greater than the 100 missions required.

The weight gain in series J (M108-1) and B (M97A-6) of 6.4% and 15.8% was so slight that a completely sealed system was not obtained and coating discontinuities permitted oxygen penetration to the RPP substrate during plasma arc exposures. This resulted in coating collapse and early burn-through.

The room temperature flexure strength appears to be relatively insensitive to lot-to-lot variations and combinations of silicon and silicon carbide. Silicon lot 468 combined with silicon carbide lots 822992 and A7058 produced specimens with both low and high strength. The low strength performers had the highest weight gain. The weight increase experienced by RPP in the coating process is an indication of the relative coating depth to be expected.

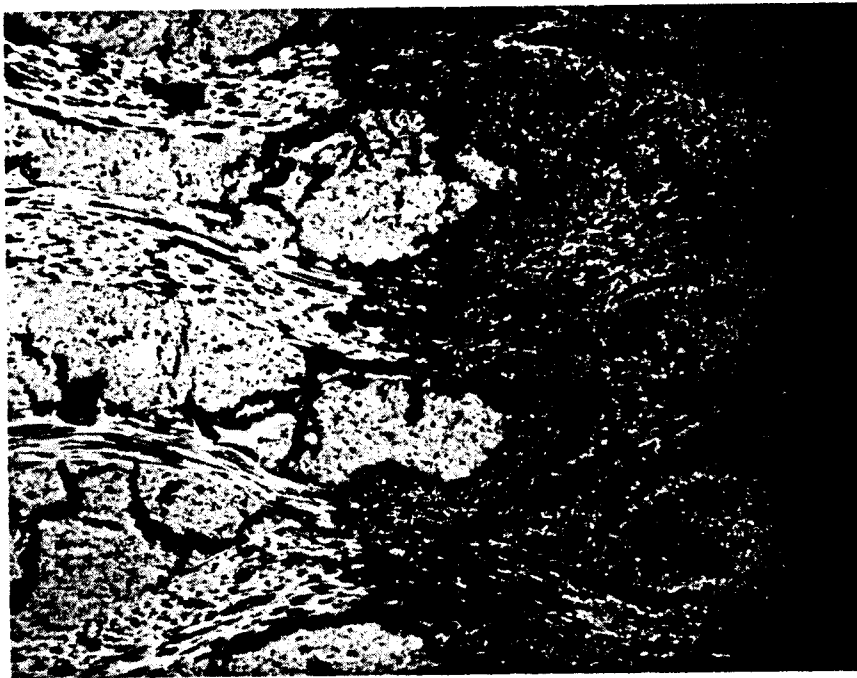
It is clear from examination of Figures 4-18 and 4-21 that there is no particular correlation between weight gain during coating and the predicted mission life (assume coating depth is in excess of 0.010 inch, since mission life is based on an allowable weight loss equivalent to 0.010 inch surface recession). It is noted, however, that the data predominately falls above the 100 mission life line, adding confidence that the shuttle requirements will be met. The mission life shown is based on

2750°F maximum radiation equilibrium temperature and includes no relieving effects from internal cross radiation or low catalycity.

It has been noted that coating depth has a significant effect on flexure strength. This may be partially due to coating/substrate mismatch. A typical coating/substrate interface is shown in Figure 4-22. The variation in coating depth between the edge and flat surface of RPP coated at 3100°F for four hours is shown. The flexure strength of the specimen was 7300 psi and coating weight gain was 25%. Photograph A shows preferential coating penetration along the fiber bundles to nearly 0.040 inch thick. It appears that coating entrance is mainly through the cut end of fiber bundles. Shallower areas, where coating depth is near 0.025 inch, are caused by the diffusion process meeting with localized across-fiber resistance. Photograph B shows a more uniform coating diffusion depth near 0.025 inch on the flat surface of the specimen where all fiber bundles are essentially across the coating flow direction. The coating appears tightly adherent to the RPP substrate and the coating/substrate interface is sharply defined. A density gradient of some depth, present at the interface, would be more likely to smooth out any existing mismatches between the coating and RPP substrate. The coating appears uniform throughout its depth and has filled well the natural pores of the RPP. The coating is continuous over the surface of the RPP with a very slight densification appearing at the coating surface. Visually, there is no splitting or separation of the fiber bundles.

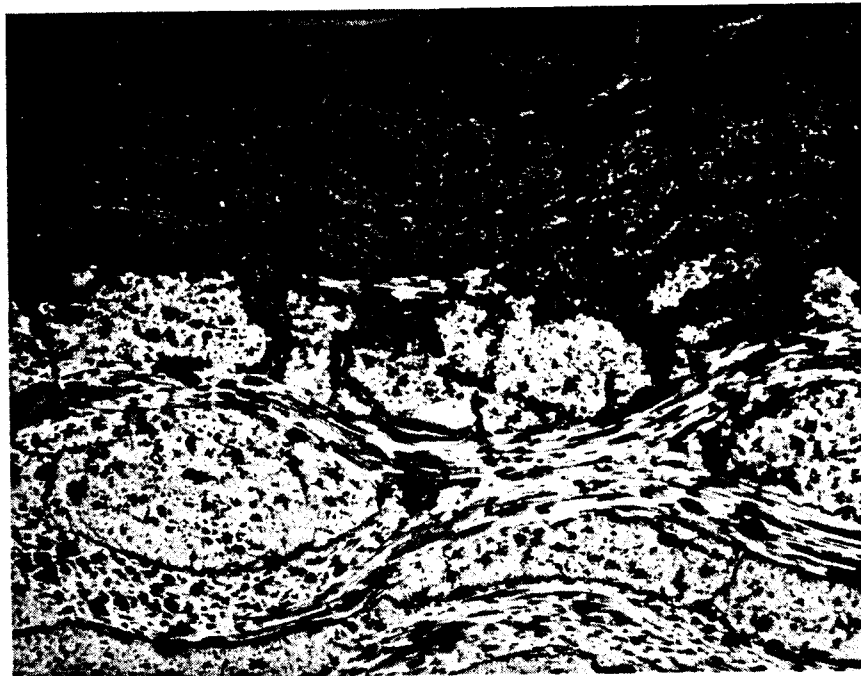
The temperature at which coating is performed has a pronounced effect on the depth and quality of the coating. A calibration and analysis of the coating process discussed previously was conducted to develop a better understanding of retort design to achieve uniform temperatures on all specimens during coating. Series G, H, I, J, K, and L in Figure 4-18 were run to confirm the analysis and prove that it was possible to achieve more uniform heat-up in retorts using graphite plates to conduct heat into the desired locations. This was accomplished with large diameter (12 inches) "pancake" (3-inch high) style stockable retorts. This allowed the retort surface temperature to be decreased by 100°F, while still achieving the same coating weight gain.

More recent investigations of factors affecting coating performance have centered on the differences between various starting ingredients. Both silicon and silicon carbide have been examined. It appears that the silicon quality has a significant effect on plasma arc performance but data is limited and at this point is somewhat inconclusive.



A – COATING DEPTH AT SPECIMEN EDGE

(50X)



B – COATING DEPTH AT ON FLAT SURFACE OF SPECIMEN

(50X)

**FIGURE 4-22 PHOTOMICROGRAPH OF SPECIMEN SHOWING COATING
(DARKENED AREA) DIFFUSION DEPTH**

Alumina variations have not been studied because only one lot of material has thus far been used. Examination of silicon carbide has, however, produced interesting and important results. Principally, the study compared green and black silicon carbide and the effects on post coating heat treatment.

Performance data for the silicon carbide variations are summarized in Figures 4-23 through 4-28. Flexural strength and weight loss after five cycles in the Pereny furnace at 2300°F for 10 minutes per cycle are plotted in Figures 4-23 through 4-26 for as-fabricated and heat treated material.

An analysis of Figures 4-23 and 4-24 for green silicon carbide indicates that there is very little change in the flexure strength when the heat treated strength is compared to the as-fabricated material. However, when the flexure strengths after five cycles at 2300°F are examined (Figure 4-24), it is evident that the present heat treating procedure reduces the capability to withstand oxidation at or below 2300°F to some extent. The decrease in flexure strength is more pronounced when the coating percent weight gain is less than 25%. This is also substantiated by the increased level of weight loss of the heat treated specimens during the five cycles at 2300°F when compared to the as-coated material.

The results using black silicon carbide given in Figures 4-25 and 4-26 are very similar to those for green silicon carbide. The major difference is that the black silicon carbide coated specimens appear to be slightly more susceptible to oxygen penetration, which results in a greater weight loss during the 5 cycle test at 2300°F than the green silicon carbide. Further, coating adherence after thermal exposure in the Pereny is poorer than with the green silicon carbide.

The plots of mission life versus coating percent weight gain are given in Figures 4-27 and 4-28. These plots do not show a mission life trend with coating percent weight gain. However, increased mission life is evident in these plots for both the green and black silicon carbide when a post coating heat treatment is employed. Recent runs have shown that it is possible to increase the mission life by raising the coating temperature in the retort without having to resort to heat treating.

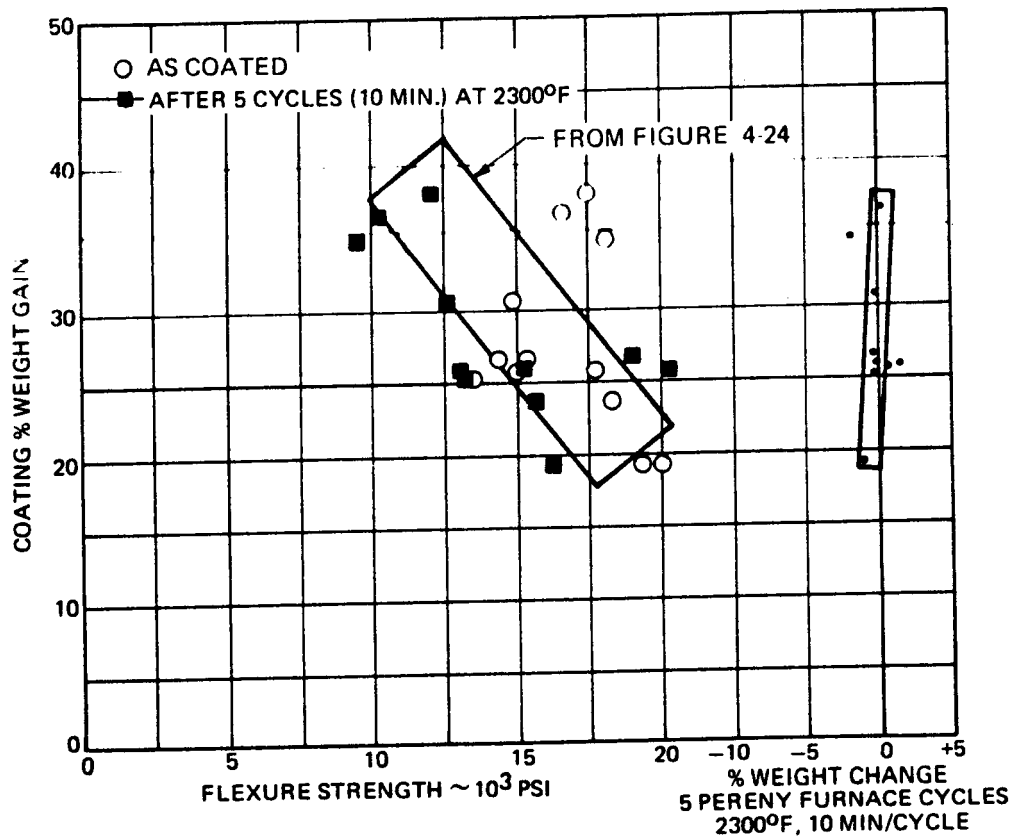


FIGURE 4-23 GREEN SILICON CARBIDE CHARACTERIZATION

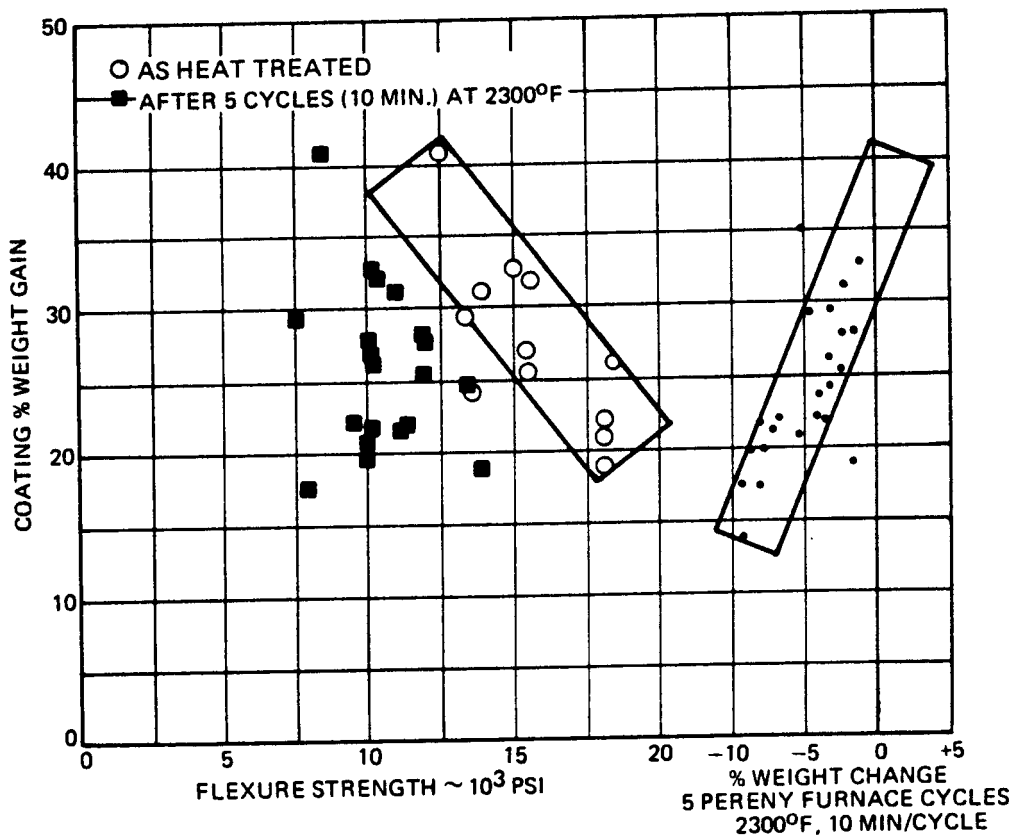


FIGURE 4-24 GREEN SILICON CARBIDE - HEAT TREATED CHARACTERISTICS

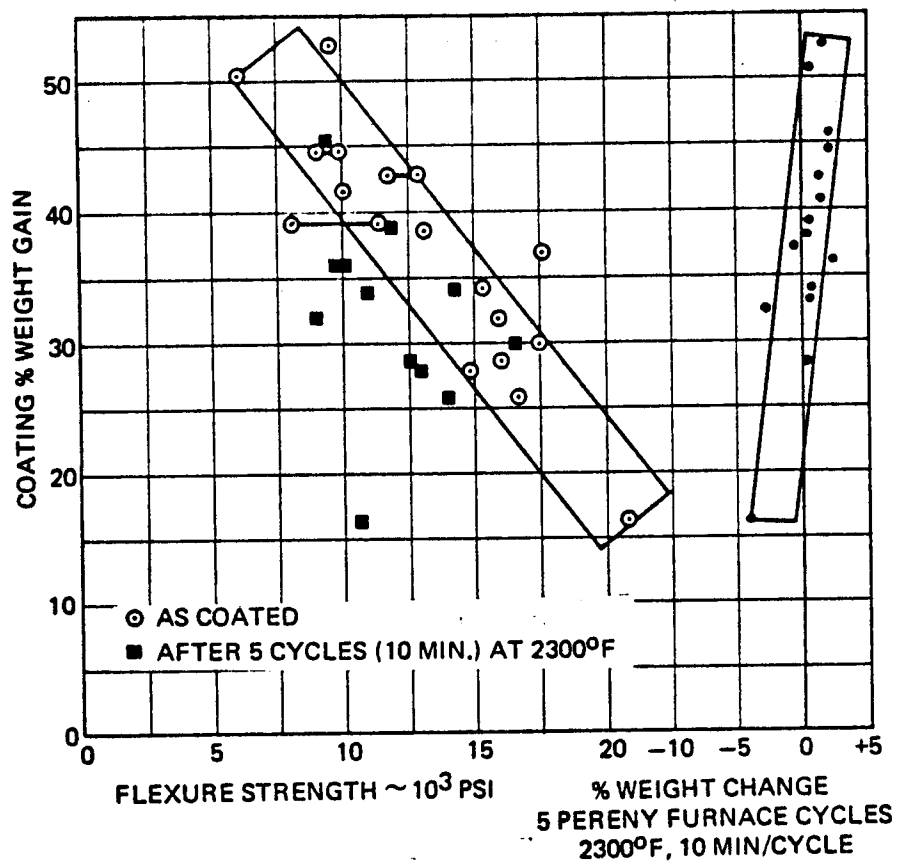


FIGURE 4-25 BLACK SILICON CARBIDE CHARACTERIZATION

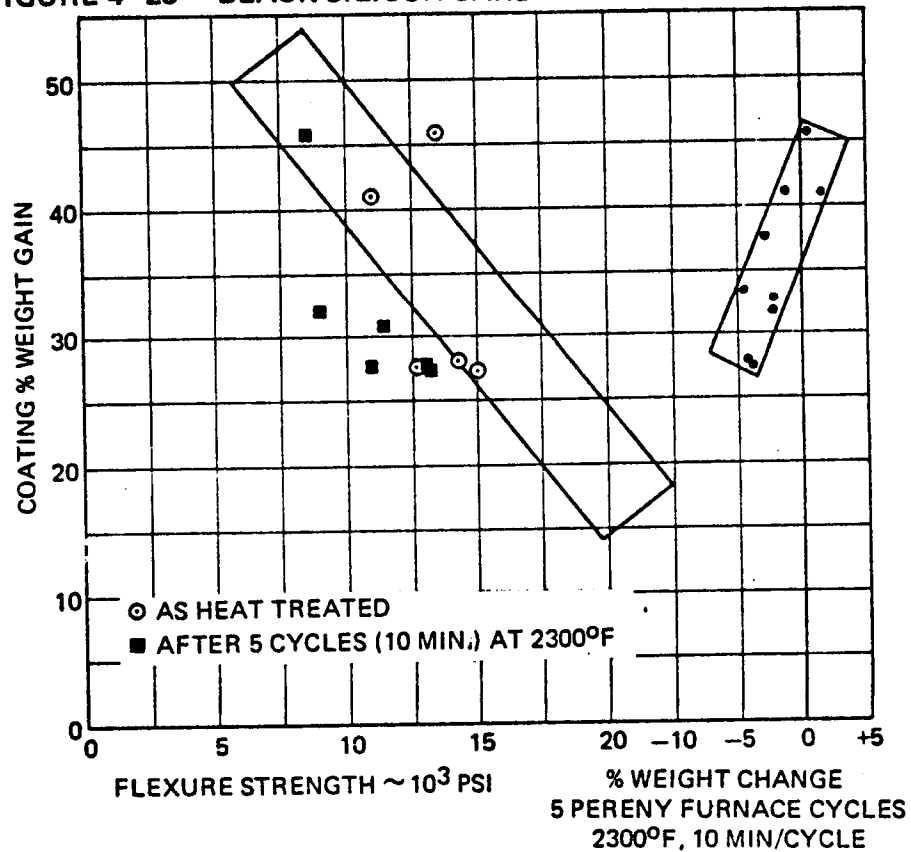


FIGURE 4-26 BLACK SILICON CARBIDE - HEAT TREATED CHARACTERIZATION

NOTE: FOR 2750°F SURFACE TEMPERATURE
AND 0.010 IN. ALLOWABLE RECESSION

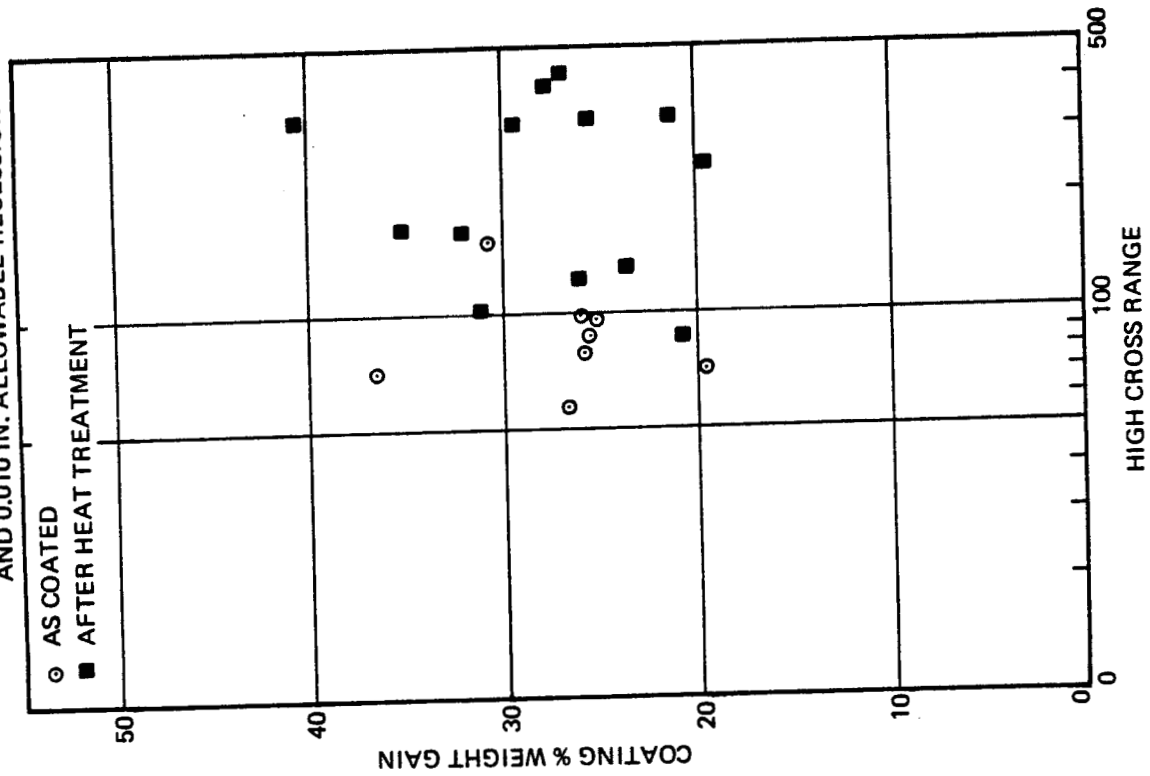


FIGURE 4-27 GREEN SILICON CARBIDE MISSION LIFE

NOTE: FOR 2750°F SURFACE TEMPERATURE
AND 0.010 IN. ALLOWABLE RECESSION

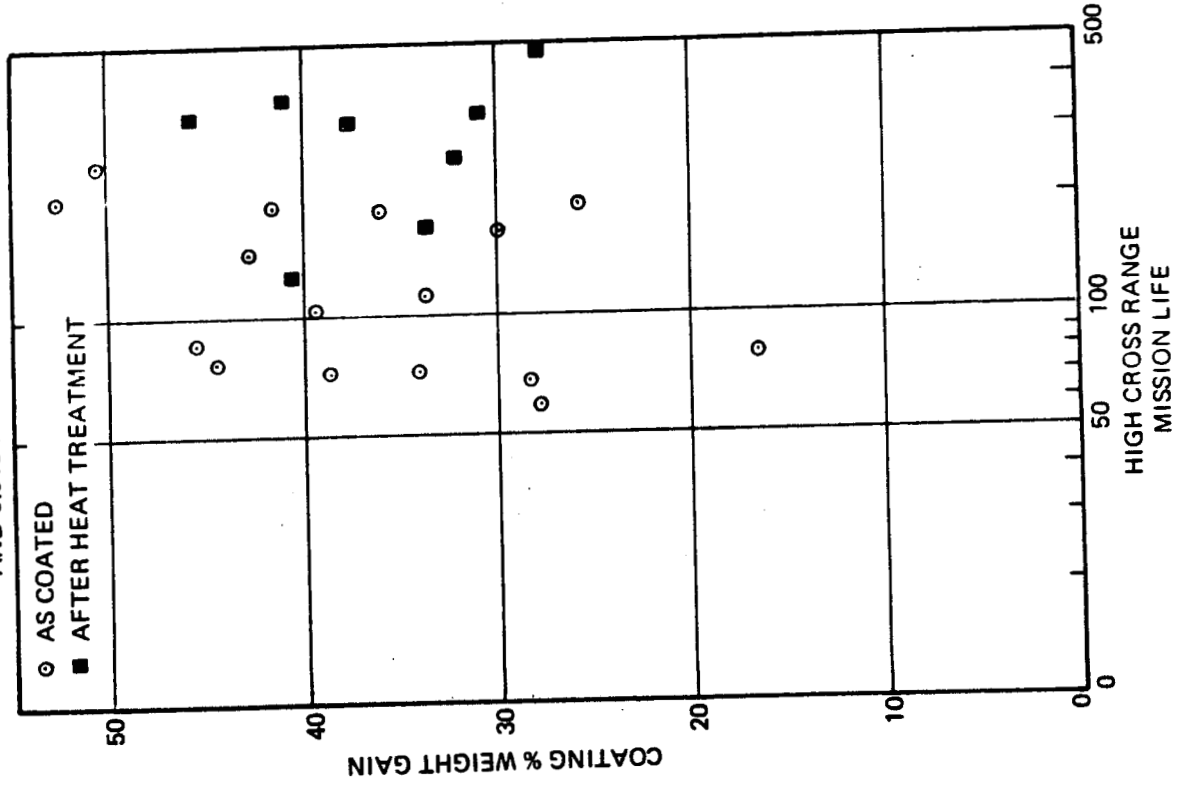


FIGURE 4-28 BLACK SILICON CARBIDE MISSION LIFE

Process Scale-Up - The abrupt shift in direction from coating many small RPP coupons to the larger size complex leading edge segments has been a revelation in processing carbon-carbon type hardware. Undoubtedly, the earlier premise that large complex parts could be fabricated successfully, utilizing pack techniques, has been proved. In fact, the ease with which the leading edge segments were coated lends confidence that the problem areas encountered can be worked to satisfactory conclusions. The process appears to have much more flexibility than that needed to coat components successfully. However, several areas of concern and attending problems are discussed below.

- (1) Blending of Powder Charge - A 100 lb. quantity of powder mix needed to load one large retort was blended on a ball mill in several smaller batches. It was found that a difference existed between the small batches blended for development work and the larger batches for scale-up. Much longer times were needed to thoroughly mix the thirty pound batches. Oven drying the powder solved the blending problem and was instituted as a standard. Ideally, a mixer large enough to handle a full charge is required, preferably one that functions by dividing the charge into equal parts and then re-combining it once per revolution as opposed to the cascading effect of the ball jars. A small mixer of this type is available for experimental material batches.
- (2) Coating Surface Craze - A craze condition has been noticed on large parts and small specimens. Generally, the pattern follows the fiber direction of the cloth and imparts a checkered appearance to the surface. It is heaviest in the warp direction. Crazeing has been observed to occur on small coated test parts after coating, after heat treating, and after thermal cycling. It was also observed on one of the three leading edge segments after coating and the coated wing tip panel. The effect of crazeing on system performance has not yet been proven detrimental since crazed parts have performed well in plasma arc test and air furnace test, and have good flexure strength. However, increased confidence in the RPP system will be gained if crazeing is diminished.

The crazed coating surface is probably the result of insufficient diffusion zone at the RPP/coating interface, which is controllable by adequate up-heat ramp time during coating run. This diffusion zone works as an expansion gradient to smooth out mismatches between the coating and RPP substrate. Effort will be required to continue investigation of the results of run M168, that produced craze free specimens after coating, after heat treat, and after five Pereny cycles at 2300° F.

- (3) Delamination - The introduction of good machine shop practices has greatly reduced the incidence of edge delamination or cracking noticed on coated parts. It was determined that grinding, instead of cutting the edges of uncoated RPP to fashion specimens, lessened the chance for delamination to occur. Coating tests on ground and cut surfaces clearly show this distinction.
- (4) Temperature Control of Coating Retort - More attention needs to be given to uniform heating of the packed RPP parts. Non-uniform heating can cause serious coating variations. In the design of retorts, it is important to place parts close to retort walls where packing procedures permit. Thermal analyses have been performed and additional analysis may be necessary to define critical pack thickness dimensions and ways to construct heat paths into the RPP parts. Packing techniques need to be explored further to determine pack thicknesses and pack densities that might aid in smoothing out temperature gradients. Packed retorts need to be instrumented with thermocouples to determine precisely the temperature profile obtained and needed for a chosen part.
- (5) Warpage of Parts - Warpage of RPP parts was a problem before the advent of the tight pack which, in effect, acts as a fixture to maintain the shape of the part. This was shown to be true when the leading edge segments and belly panels were coated. Little or no dimensional distortion due to coating was noticed.

- (6) Coating Uniformity - The visual appearance of the leading edge segments and wing tip panel after coating was generally good. However, coating thickness and uniformity are unknown. It will be necessary to destructively examine one of these parts in detail by sectioning to determine adequacy of the coating. Also, some discoloration was noted on the back side of two of the leading edges. It is advisable to chemically analyze these discolored areas to determine if some concentration of an unwanted chemical compound is present. Coating uniformity on large parts must be known to aid in the design of retorts and to refine time/temperature profiles.

4.3.3 Hafnium Tantalum Coating

In Phase I investigation of a 90% hafnium-10% tantalum eutectic mixture applied as a melt coating to RPP-0 was made. This coating withstood multi-cycle exposure in plasma arc testing at surface temperatures exceeding 4000°F. It was the only coating system examined or known that could withstand more than two or three exposures at these severe surface temperatures. The material system was prepared by pressing a wafer from a mixture of hafnium and tantalum powders with subsequent melt impregnation into RPP-0 in an inert atmosphere. Good wetting and depth of penetration of the substrate was achieved and the coating withstood five 5-minute cycles of exposure in the plasma arc at a heat flux rate of 140 BTU/ft² sec with no surface recession and a slight mass loss (Reference 2). The amount of coating applied was approximately 5 grams on a 3/4 inch disc of RPP-0. Attempts to apply the coating to RPP-3 at that time using the same techniques were unsuccessful because the melt did not wet and flow into the substrate.

In Phase II this investigation was continued using alternate approaches to determine if the coating could be successfully applied to the higher strength reimpregnated substrates RPP-1, RPP-2, and RPP-3. Test specimens were 3/4 inch discs, 13 plies thick, and an induction heater operating in a helium atmosphere was used to provide the melt temperature of approximately 3600°F. The effect of the following pre-conditioning treatments was evaluated: (a) pre-oxidation of the RPP to deglaze the surface, (b) heat treatment of the RPP to drive off possible contaminants and/or gasses that could block penetration and (c) graphitization of the RPP to achieve the same goals as (b) and to evaluate the wettability of the graphite structure of the resin char. The efficiency of two

fluxing agents combined with the hafnium-tantalum eutectic to provide a cleaning and wetting action on the RPP substrate, and a technique wherein the hafnium-tantalum was applied to the substrate as a slurry and subsequently melted were also investigated. RPP fabricated by the standard autoclave technique was examined as well as RPP fabricated by a vacuum bag technique, which produces a more porous material. A summary of the results of these investigations are listed in Table 4-11.

It was confirmed that the coating could be applied to RPP-0 with good penetration. However, numerous trials failed to achieve a 5 gram loading goal, which was accomplished in Phase I, and the specimens failed to withstand three 10-minute cycles in the plasma arc at a heat flux of 130 BTU/ft² sec. Limited success was realized with RPP-1 and RPP-2 using the pressed wafer technique. Some specimens showed fair penetration but there was a marked tendency for the melt to run off the specimen, and the desired five gram loading could not be obtained.

Pre-oxidation of RPP-3 was found to provide some degree of wetting and penetration. A specimen pre-oxidized at 1020°F for 45 minutes produced a coating with penetration but it was noted that approximately half of the melt ran off of the specimen indicating that penetration was shallow. A specimen pre-oxidized one hour at 1040°F showed some wetting of the substrate but a ridge of metal was left standing on the surface, indicating once again that penetration was minor. An attempt was made to apply a five gram coating to an RPP-3 specimen which had been pre-oxidized 57 minutes at 1040°F. The coating was applied in two separate melts in wafers of 2.5 grams each. The first application produced a thin coating with a large portion of the melt flowing off the specimen. Similar results were obtained in the second melt. The final coating weight was three grams. Examination of the specimen in cross section showed that penetration was limited to the first ply of the substrate. Most of the coating was concentrated in the cylindrical wall of the specimen, where the exposed ends of the graphite fiber bundles provide relatively large porosity. Penetration of the melt into the substrate is evidently dependent upon available porosity and pre-oxidation of the RPP-3 provides some surface porosity, but when this is filled, the excess melt flows over the side of the specimen and is lost. Severe pre-oxidation would allow greater penetration but this is equivalent to using RPP-0 as the substrate material.

The effect of heat treating RPP-3 at 4500 and 3900°F was found to be negligible. Melts applied to these specimens did not penetrate and lifted easily. Specimens graphitized at 4500°F showed the same lack of penetration.

TABLE 4-11 RESULTS OF HAFNIUM-TANTALUM
COATING APPLICATION TO RPP

Substrate	Application Form		Fabrication Results		Plasma Results
	Pellet or Slurry Wt. in Grams		Degree of Penetration	Coating Wt. Grams	HEAT FLUX 130 BTU/ft ² -sec 10 minutes/cycle
(Autoclave Fabricated)					
RPP-0	P	3.0	Good	1.8	-
RPP-0	P	2.0	Good	1.7	-
RPP-0	P	1.5	Good	1.4	-
RPP-0	P	1.3	Good	1.2	-
RPP-1	P	1.5	Fair	1.4	-
RPP-0	P	1.4	Fair	1.3	-
RPP-1	P	2.0	Fair	1.9	-
RPP-1	P	2.5	Fair	2.4	-
RPP-0	P	1.4	Good	1.4	-
RPP-0	P	1.7	Good	1.6	-
RPP-0	P	1.7	Good	1.6	2 cycle limit
RPP-0	P	1.7	Good	1.6	-
RPP-0	P	2.5	Good	2.4	3 cycle limit
RPP-1	P	2.5	Fair	2.4	-
RPP-1	P	3.0	Fair	2.9	coating destroyed first cycle
RPP-1	P	2.5	Fair specimen delaminated	2.4	-
RPP-2	P	3.0	None	2.9	-
RPP-2	P	2.5	Fair, coating cracked	2.4	-
RPP-2	P	2.0	Fair, coating cracked	1.9	-
RPP-2	P	2.2	Fair, coating cracked	2.1	-
RPP-3	P	2.2	None	2.0	-
RPP-2	P	2.4	Fair	2.3	1 cycle limit
RPP-2	P	2.5	Fair, Coating cracked	2.4	-
RPP-3	P(1% Ti)	2.4	None	2.2	-
RPP-3	P (1% Ti)	2.0	None	1.9	-

TABLE 4-11 RESULTS OF HAFNIUM-TANTALUM
COATING APPLICATION TO RPP (Cont'd.)

Substrate	Application Form		Fabrication Results		Plasma Results	
	Pellet or Slurry Wt. in Grams		Degree of Penetration	Coating Wt. Grams	HEAT FLUX 130 BTU/ft ² -sec 10 minutes/cycle	
RPP-3	P	2.2	None	1.9	-	
RPP-3 Pre-oxid. 1 Hr., 900°F	P	2.2	None	2.1	-	
RPP-3 Pre-oxid. 1 Hr., 1020°F	P	2.4	Good, coating cracked	2.4	-	
RPP-3 Pre-oxid. 30 min. 1020°F	P	2.4	Fair, coating cracked	2.1	-	
RPP-3 Pre-oxid. 45 min. 1020°F	P	2.5	Fair	2.0	-	
RPP-3 Pre-oxid. 35 min 1020°F	P	2.5	None	2.5	-	
RPP-3 Pre-oxid. 45 min. 1020°F	P	3.0	Good	2.1	-	
RPP-3 Pre-oxid. 45 min. 1020°F	P	3.0	Good	1.8	1 cycle limit	
RPP-3 Pre-oxid. 40 min. 1020°F	P	2.5	Good, specimen delaminated	2.5	-	
RPP-3 Pre-oxid. 55 min. 1000°F	P	3.0	Fair	2.5	-	
RPP-3 Pre-oxid. 57 min. 1040°F (2 applications)	P	5.0	Fair	3.0	-	
RPP-3 Pre-oxid. 45 min. 1030°F	P	3.0	Fair	1.7	-	
RPP-3 Heat Treat. 3400°F	P	1.0	None	1.0	-	
RPP-3 Heat Treat. 3900°F	P	2.5	None	2.2	-	
RPP-3 Graphitized	P	3.0	None	3.0	-	
RPP-3 Graphitized	P(1% Ti)	3.0	None	3.0	-	
RPP-3 Heat Treat. 00°F	S	2.7	None	2.6	-	

TABLE 4-11 RESULTS OF HAFNIUM TANTALUM
COATING APPLICATION TO RPP (Cont'd.)

Substrate	Application Form		Fabrication Results		Plasma Results
	Pellet or Slurry Wt. in Grams		Degree of Penetration	Coating Wt. Grams	HEAT FLUX 130 BTU/ft ² -sec 10 minutes/cycle
RPP-3	S	2.0	None	2.0	-
RPP-0 Pre-oxid. 20 min. 1000°F	S	2.9	Good, specimen delaminated	2.8	-
RPP-0 Pre-oxid. 15 min. 1000°F	S	2.0	Good, coating cracked	1.8	-
RPP-0	S	2.8	Fair, specimen delaminated	2.6	-
(Vacuum Bag Fabricated)					
RPP-0	P	3.2	Good	3.2	-
RPP-0	P	5.0	Good	4.8	-
RPP-0	S	3.1	Good	3.0	-
RPP-0	S	3.9	Good	3.8	2 cycle limit
RPP-0	P	5.0	Good	4.6	3 cycle limit
RPP-0	P	5.0	Good	4.4	-
RPP-0	P	5.0	Good	3.6	1 cycle limit
RPP-1	P	5.0	None	2.8	-
RPP-1	S	5.0	None	3.7	-

The effect of titanium powder mixed with the hafnium-tantalum eutectic in the amount of 1 weight percent to provide a fluxing action was also negligible in improving penetration into RPP-3. Negative results were also obtained with copper powder applied in the same proportion.

The application of the hafnium-tantalum eutectic in the form of a slurry did not appreciably improve penetration into RPP-3. The slurry was formed by mixing the hafnium-tantalum powders with an aqueous methocel solution to the consistency of a thick cream. Repeated brush applications, alternated with oven drying at 200°F, were required to build up a mass containing approximately 2.5 grams of the eutectic. Penetration was negligible but it was noted that the melt showed little tendency to flow off of the specimen.

All of the preceding work was done with RPP specimens fabricated by standard autoclave technique. Since it was not possible to achieve the desired five gram loading even with standard RPP-0, limited investigation was conducted with RPP-0 fabricated by vacuum bag technique where it was found that a five gram loading could be approached. Examination of the cross section of a specimen with approximately five gram loading revealed that the melt had penetrated completely through the specimen. Tests in the plasma arc showed that this type coating failed after three cycles. With the great amount of penetration there was a relatively small amount of coating left at the surface of the specimen to provide oxidation resistance. Coatings applied to vacuum bag fabricated RPP-1 failed to penetrate and lifted easily, indicating that the reimpregnation process had filled the available porosity. This investigation was continued to determine the feasibility of applying the coating by multiple applications in order to obtain a thicker coating on the surface. It was found that melts applied subsequent to the first coating showed considerable tendency to run off of the specimen surface. However, by varying the relative amount of coating applied during applications two specimens were prepared with coating weights of approximately 5 grams which exhibited a three to five cycle limit in the plasma arc. Table 4-12 summarizes the results of this investigation.

A limited amount of work was done to investigate the feasibility of applying the coating by melting the eutectic simultaneously onto the upper and lower surfaces of the specimen. The lower hafnium-tantalum wafer was supported on RPP-3 since it was known that the melt would not adhere to this material. The initial trial using this technique showed that the melt would wick up into the RPP-0 from the lower surface. A specimen was prepared with a 4.0 gram wafer on the top surface and 3.0 grams on the lower.

TABLE 4-12 RESULTS OF MULTIPLE HAFNIUM/TANTALUM
COATING APPLICATION OF RPP-0 (VACUUM
BAY FABRICATED)

Specimen No.	Coating Application No.	Pellet Weight, Grams	Degree of Penetration	Coating Weight, Grams	Plasma Results Heat Flux 130 BTU/ft ²	Remarks
HT-87	1	5.0	Good	4.8	-	Large amount of melt flowed off specimen in second application
	2	3.0	Poor	5.4	-	
HT-88	1	3.0	Good	2.9	-	Considerable overflow third application
	2	2.0	Good	4.8	-	
	3	2.0	Poor	5.2	-	
HT-89	1	4.0	Good	3.9	-	Small overflow second application
	2	1.5	Good	5.2	3 cycle limit 5 min. /cycle	
HT-90	1	4.0	Good	3.9	-	Small overflow second application
	2	1.5	Good	5.1	5 cycle limit 5 min. /cycle	
HT-93	1	4.0 Top 3.0 Bot.	Good	6.3	6 cycle limit 5 min. /cycle	Small overflow

Penetration of the melt into the specimen was good yielding a coating weight of 6.3 grams. The surface of the specimen which had contained the 4.0 gram wafer was exposed to the plasma arc. After four cycles the specimen showed a weight loss of 0.4%, after the fifth cycle it was 1.7% with slight flaking of the oxidized surface, and after the sixth cycle the total accumulated weight loss was 3.5% with considerable flaking of the surface. Six cycles represented one-half hour exposure in the plasma arc at surface temperatures in the 3200-3700°F range

It appears that the life of the hafnium-tantalum system is more closely associated with the number of exposures as opposed to the accumulated time of exposure. Using the technique of applying coating to both the top and bottom of the specimen, a life limit of five or six missions can be obtained at temperatures in the 4000°F region. The mission life of the Hf-Ta coating, therefore, falls far short of the 100-mission goal. However, for localized high temperature problem areas, the system may have merit. Because of the limited application, further work on this system was discontinued to concentrate on other program tasks.

4.4 CONCLUSIONS AND RECOMMENDATIONS

Full size hardware reflecting all requirements recognized at this stage of the space shuttle design has been built and tested in Phase II. It has been only a short time -- less than two years -- since small element buttons perhaps three inches or so in size represented the best state-of-the-art for oxidation protection of carbon/carbon composites. In process scale-up such as accomplished in Phase II, it is more the rule than the exception that unpredicted problems arise and these often seriously endanger successful completion of the hardware program. However, materials and processing problems encountered in Phase II have been relatively free from serious development problems.

The following list of significant conclusions reached from Phase II investigations is indicative of the very good posture for moving into Phase III of the program:

- (1) Large and complex shapes of good quality can be laminated with techniques adopted from standard reinforced plastic fabrication procedures.
- (2) Local debulking in wrinkle-prone areas to give good, smooth fillet areas, joggles, and upstanding flanges at 90° to the skin plane can be accomplished.

- (3) Scale-up of the pyrolyzation process and good dimensional control using graphite restraining tools was proven practical.
- (4) The feasibility of a rivet/bond attachment method was demonstrated and a pyrolyzed carbon/carbon bond line was shown to have good integrity.
- (5) The pack process is suitable for producing full size complex RPP shapes, and the coated surface appearance is acceptable and uniform.
- (6) The coating process does not cause dimensional changes and parts remain true in size and shape.
- (7) Diffusion depth of coating appears to be controllable.
- (8) Coating materials suppliers have been identified with production facilities to supply future powder quantity and quality requirements.
- (9) Random delamination which occurred on coated specimens can be minimized by revised machining techniques in the uncoated state.
- (10) Preliminary evaluation of reused pack material has indicated that large substantial savings are possible without performance loss of the finished product.
- (11) Experiments have indicated that a higher coating temperature will permit elimination of the heat-treat cycle while achieving the same performance level.
- (12) The hafnium-tantalum coating with high surface temperature capability (4000°F) has reuse capability limited to 5 or 6 missions.

The following recommendations are made in support of the continued refinement of the siliconized RPP system:

- (1) Increased emphasis should be placed on improving the thermal expansion match between coating and substrate to reduce coating crazing, which can add to mission life. This involves both coating and substrate improvement.

- (2) Detailed analysis of the coating should be conducted to better understand the factors affecting coating performance. This should lead to improved coating quality and reproducibility.
- (3) Continue refinement of processing to eliminate heat treating. This would reduce cost, simplify the process, and possibly add to mission life.

5.0 MATERIALS EVALUATION

In order to evaluate total mission performance capability of the selected diffusion coated carbon-carbon material system, consideration must be given to system strength before and after thermal and load exposure, and coating oxidation (recession) resistance in the entry environment. The Phase II materials test program explored a wide range of materials properties over the useful temperature range and examined fatigue, strength changes with thermal/oxidation mission life cycling, and coating removal rate with mission/temperature cycling. This section of the report summarizes the basic material property data gathered on the program and discusses the significance of the data on design and material system mission life. Only that data considered to represent the selected materials process is included in this section as design data. Development data on strength and plasma tests leading to process selection are included in other sections of the report or in the Appendices.

It is of prime importance to the evaluation of the coating system to analyze the ability to provide oxidation resistance to meet mission life requirements in the entry environment. In Phase I it was demonstrated by test and analysis that if the boundary layer air is dissociated low surface temperatures will result because of the low catalytic reaction rate at the surface of the VMSC coatings. The Phase I work has been extended to cover the alternate condition, wherein the boundary layer air is not dissociated. There is evidence that in this case, although temperatures are not reduced, the reactivity of the molecular constituents with the silicon carbide coating is orders of magnitude less than that of atomic oxygen and nitrogen encountered in plasma arc testing. In either event, whether the air is dissociated or not, current plasma arc test data appears highly conservative, when evaluated on a temperature rather than heat flux basis. Exploration of mass loss rates on specimens inclined to the flow to produce aerodynamic shearing stresses has shown the possibility that this can produce higher mass loss. Data is widely scattered so that firm conclusions on the performance of the selected coating formulation under high shear stress conditions cannot be made until extensive testing is performed.

Mission life predictions on the basis of coating recession alone is only one half of the answer to define life limits of the material system. Subsurface oxidation of the uncoated (prime load carrying) portion of the substrate can also occur by oxygen diffusing through the coating. This could produce two of possible effects: (1) the substrate could oxidize and reduce laminate strength or (2) the interface between coating and substrate could oxidize and result in coating peel. Either of these could limit system

life. Thermal/oxidation tests were conducted in an effort to determine if mission life would be restricted below the 100 goal. Results are included herein.

Materials static properties data were obtained over a wide temperature range to determine if problem areas existed in any test region. In Phase I there were indications that the siliconized system experienced a strength reduction in the 1400°F temperature region. The Phase II coating shows no such tendency and in general elevated and cryogenic temperature properties exceed room temperature values.

Fatigue tests conducted to establish life limits resulted in surprisingly high resistance to early failure. Experimental stress endurance limits ($> 10^6$ cycles) were substantially in excess of expected flight environments.

Details of the tests and their implications on design are discussed in the following sections.

5.1 COATING MISSION LIFE PERFORMANCE

Analyses of oxidation resistance of coated RPP were performed in order to guide materials development effort in selection of optimum coating constituents and processing variables and to provide a preliminary prediction of material mission life. These analyses included consideration of effects of coating surface catalytic activity, possible mechanisms controlling surface removal, effects of different reactants in the environment and effects of different flow configurations. Mission life predictions are presented as are comparisons of acceptable plasma arc test performance with final evaluation data for the heat treated 10-60-30 material system.

5.1.1 Catalycity and Molecular Oxidation

Surface Catalytic Effects - It was shown in the Phase I effort of reference (2) that siliconized and Zr-B-Si treated RPP have demonstrated in plasma arc tests at VMSC and NASA-MSC surface temperatures substantially below both radiation equilibrium values and values for bare RPP. Consideration of possible explanations for this phenomena led to the conclusion that a low level of surface catalytic activity on the coatings was the probable explanation for the low temperatures. Surfaces with low catalytic activity exposed to highly dissociated air with non-equilibrium boundary layers receive substantially lower convective heating rates than highly catalytic surfaces. This is due to the fact that these surfaces do not promote recombination reactions, and the atoms that reach the surface do not yield their heat of recombination.

Two conditions must be satisfied for the reduced convective heating rates to be realized on a low catalytic activity surface. A substantial portion of the total energy of the air must be dissociation energy, and the boundary layer must be frozen, or nearly so. A frozen boundary layer is one in which the time required for an atom to recombine is long compared to the time for it to diffuse through the boundary layer. The Phase I studies of reference (2) indicated, that for the conditions of the VMSC 180KW plasma arc tests, the boundary layer should indeed be frozen. Furthermore, the mode of operation of plasma arc tunnels assures that at the air enthalpies employed in the tests the air will be highly dissociated. Hence, the conditions in the plasma arc tests are suitable for substantial heating reductions on a low catalytic activity surface. Furthermore, the Phase I studies showed that the magnitude of heating reductions, as inferred from re-radiation heat fluxes on coated and uncoated RPP, were consistent with theoretical reductions as developed by Goulard in reference (12).

Plasma arc test data obtained in final evaluation of the heat treated 10-60-30 coating system, as shown in Figures 5-1 and 5-2 are in substantial agreement with the Phase I data for the M-30 siliconized system. Figure 5-1 presents measured surface temperature for the coated material versus bare RPP temperature. The Phase I correlation line for M-30 data is shown for comparison. It is seen that the current data shows somewhat greater temperature reduction for the coated material than the Phase I data for the M-30 material.

The ratio of heat flux on a finite catalycity surface to that on a fully catalytic surface $\dot{q}_s/\dot{q}_s, fc$ versus stagnation enthalpy is presented in Figure 5-2. The values for coated RPP were assumed equal to the ratio of reradiation heat flux for coated RPP to that for bare RPP. This is based upon the assumption that bare RPP is fully catalytic, and that specimen heat losses to the holder are comparable for coated and uncoated material. The values for the 10-60-30 heat treated system are compared with theoretical reductions corresponding to a catalytic reaction rate constant $K_W = 410$ cm/sec and with curves for zero and infinity catalycity. The plasma arc test data are well correlated by Goulard's theoretical relation with $K_W = 410$ cm/sec. This value of K_W was also found to correlate the Phase I data for the M-30 siliconized system.

Based upon the Phase I studies and the data presented above, it appears that low catalycity is the explanation for the low surface temperatures measured on coated RPP in plasma arc tests. Phase I analyses for the straight wing orbiter indicated that if the low catalytic effects are realized on the shuttle leading edge, order of magnitude increases in coating mission life could be realized as compared to those for the coating without low

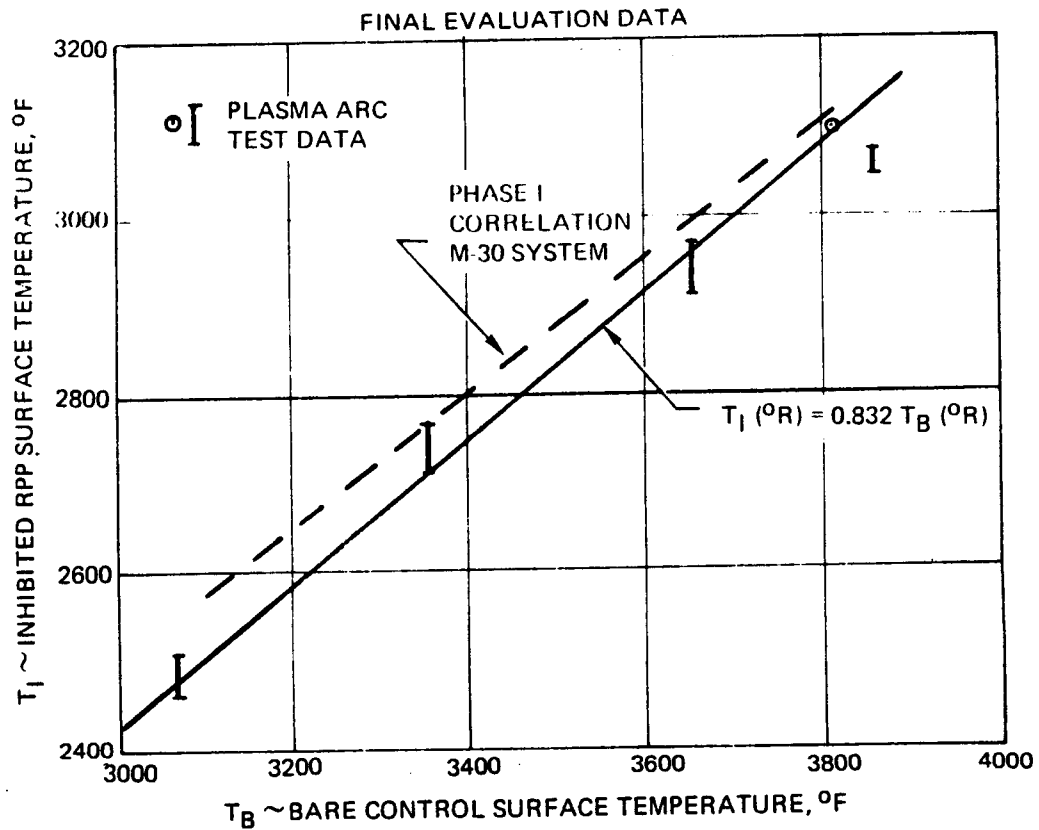


FIGURE 5-1 CORRELATION OF SURFACE TEMPERATURES INHIBITED VS BARE MATERIAL

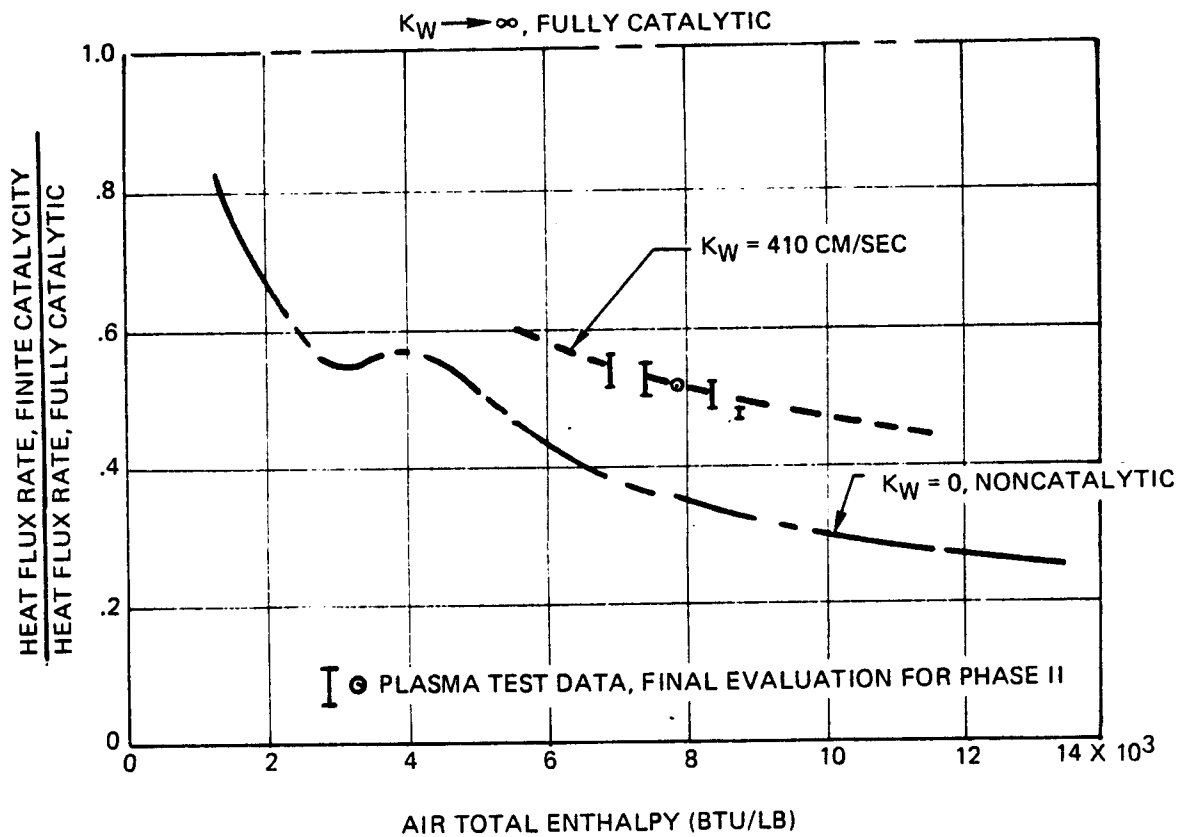


FIGURE 5-2 HEATING REDUCTION DUE TO LOW CATALYTIC EFFICIENCY SURFACE

catalycity effects. This is due to the extreme reduction in coating mass loss rate with reduced temperature. Analyses were therefore performed to predict surface temperature of coated RPP for the current delta wing vehicle at the maximum heating location on the wing, assuming that the low catalycity effects are realized.

Results are shown in Figure 5-3 which presents computed surface temperature as a function of entry time, compared with radiation equilibrium values. Calculations were based upon Goulard's theory of reference (12), with a catalytic reaction rate constant $K_w = 410$ cm/sec. Results indicate a 250°F reduction in peak temperature due to low catalycity. The time of peak temperature is shifted to a later point in the trajectory where low catalytic effects are less important than at 400 seconds, due to lower enthalpy and higher pressure. The temperature reduction, while quite significant, is considerably less than that predicted in Phase I for the straight wing orbiter. This is due to the lower local enthalpy at the stagnation line, and associated lower degree of dissociation for the highly swept leading edge on the delta vehicle as compared with the straight wing vehicle. The significance of the predicted 250°F temperature reduction to mission life will be discussed in section 5.1.4.

The predictions of entry low catalytic effects in Figure 5-3 are based upon the assumptions of a completely frozen boundary with thermal equilibrium conditions at the outer edge of the boundary layer. The Phase I studies for the straight wing orbiter indicated that, considering the trajectory flown, wing geometry, surface temperature and wall catalycity, shuttle entry conditions should result in a frozen boundary layer. The altitude-velocity plots in Figure 5-4 for the delta and straight wing vehicles show that the trajectory for the delta wing vehicle is only slightly less favorable for a frozen boundary layer than that for the straight wing orbiter. Furthermore, leading edge pressures for the delta wing vehicle are considerably lower than those for the straight wing vehicle, due to the high sweep back angle, which creates a more favorable condition for frozen boundary layer than that for the straight wing orbiter.

The primary uncertainty, at this point, regarding the extent of low catalytic effects to shuttle entry lies in the state of the flow at the boundary layer outer edge. If thermal equilibrium is not attained, the extent of dissociation will be reduced and the temperature reduction in Figure 5-3 will be corresponding diminished.

It is important to note that if thermal equilibrium is not attained at the outer edge of the boundary layer and the boundary layer flow is frozen,

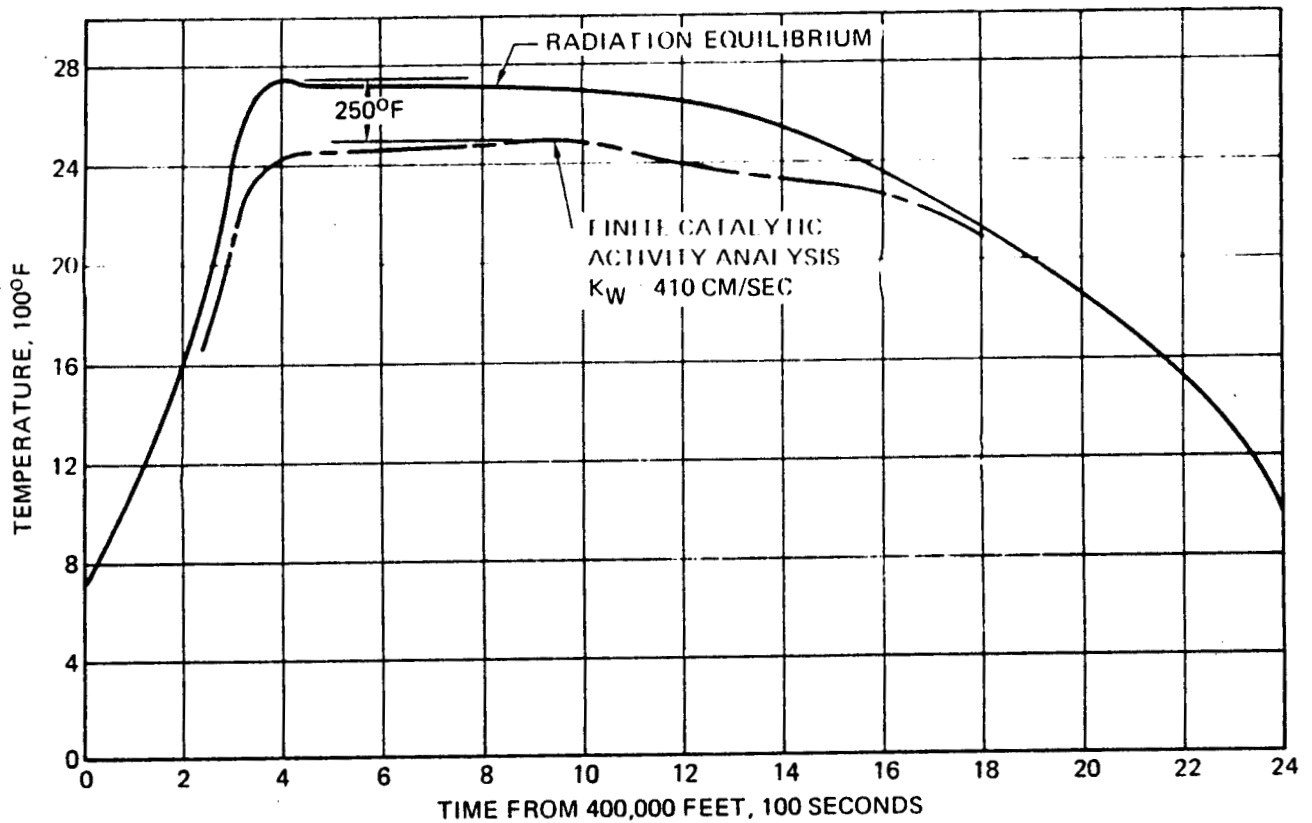


FIGURE 5-3 SKIN TEMPERATURE AT PEAK HEATING LOCATION — $\epsilon = 0.85$

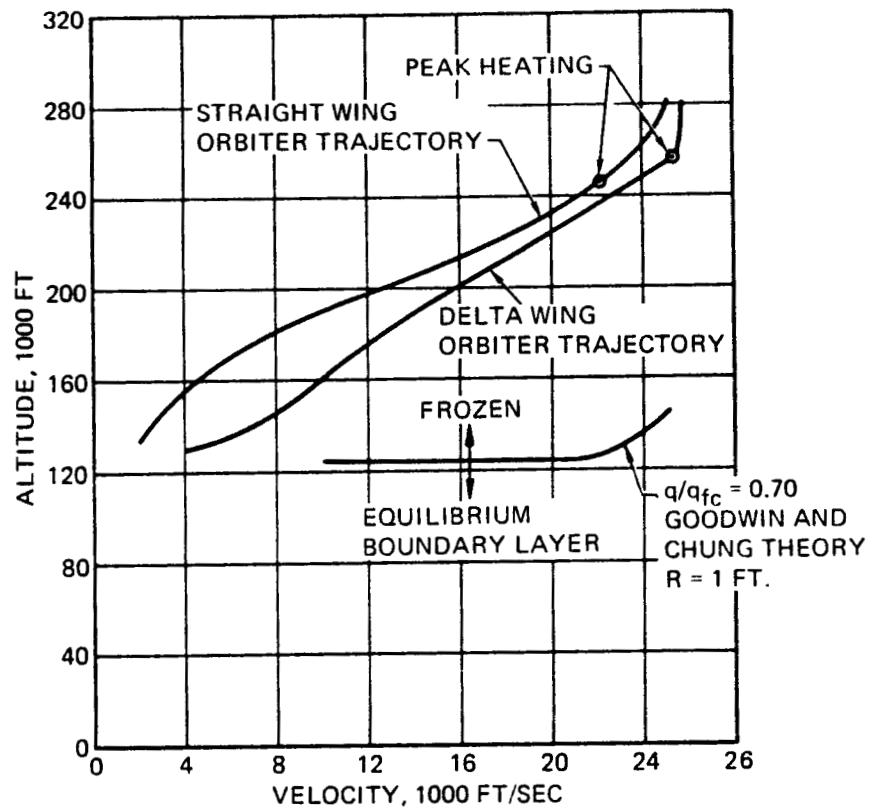


FIGURE 5-4 STATE OF BOUNDARY LAYER FLOW RE-ENTRY

not only will low catalytic effects be suppressed, but the composition of the gas reacting with the RPP coating will be altered. In the extreme case of frozen flow in the free stream, shock wave, shock layer and boundary layer, the coating surface would be exposed to only molecular oxygen and nitrogen. Since the plasma arc tests used for evaluation of coating mass loss rates subject the coating to predominately dissociated air, it is worthwhile to consider the relative reactivities of oxygen and nitrogen, atoms and molecules. This is discussed in the following section, which indicates that molecular reactants will probably be less reactive with coated RPP than atomic reactants.

It would be most desirable to perform a detailed, non-equilibrium flow field analysis to determine the extent of dissociation around the leading edge as a function of entry time for use in the catalycity analysis. Plasma arc tests could then be performed to evaluate coating mass loss performance with the predicted dissociation levels. Coating mission life performance could then be predicted based on realistic entry temperatures and plasma test data for the proper dissociation levels.

Unfortunately, a detailed non-equilibrium flow field analysis will be expensive and time consuming; hence, such results are not expected to be available until well into Phase C/D. It should be possible to bound the problem during Phase III, however, by considering two limiting cases, (1) The catalycity analysis will be based upon equilibrium dissociation behind the shock. Mission life will then be predicted based upon predicted surface temperatures with low catalytic effects and plasma arc tests data with dissociation levels corresponding to entry equilibrium values; (2) Mission life will also be predicted based upon no low catalytic effects and plasma arc test data obtained under conditions where the flow is not dissociated. Both predictions will therefore be consistent with respect to flow chemistry and its effects upon catalycity and coating oxidation rates.

During the early stages of Phase C/D, before detailed flow field analysis results are available, it will be possible to estimate the degree of dissociation and heat transfer at the stagnation line using a method developed in reference (17). This approximate, closed form, analytical solution includes effects of non-equilibrium chemical reactions throughout the shock layer. A computer routine will probably be necessary to facilitate calculations using this method; however, it will provide earlier results than the detailed flow field analysis.

The discussion above relates to the stagnation line of the leading edge. Once the atom concentration at the outer edge of the boundary layer

has been established, Chung's theory of References 18 and 19 can be employed to determine heating downstream of the stagnation line, including effects of low catalycity. The primary problem to be solved is determining the atom concentration, α , at the surface and location of interest. Once this is accomplished, the heat transfer rate due to atom diffusion and surface recombination, \dot{q}_D , is simply computed from the air density at the surface, ρ_w , reaction rate constant, K_w , and recombination energy, h_r , using the relation,

$$\dot{q}_D = \rho_w K_w \alpha h_r$$

The total heat transfer to the surface is simply the sum of \dot{q}_D and the heat transfer due to convection of frozen thermal and kinetic energy.

Chung has obtained a solution for the atom concentration, α , in terms of a Volterra integral equation. This equation is solved by subdividing the leading edge surface into small sections and integrating the Volterra equation analytically for each section, based upon the local flow conditions and reaction rate constant. The segmentized solutions are summed numerically, step by step, beginning at the stagnation line, to obtain a continuous solution for the atom distribution over the leading edge. A computer code would facilitate the numerical calculations. The calculations can be extended across the interface between the leading edge and main wing to determine the effect of low catalycity of the RPP on main wing in the event that the main wing surface is highly catalytic.

Relative Reactivities of Air Atoms and Molecules - A review of the literature indicated the best available data on the reactivity of oxygen and nitrogen atoms and molecules with silicon carbide (the primary constituent of siliconized RPP coating) was obtained by Rosner and Allendorf, as reported in references (14) and (15). The data was obtained on the beta form of silicon carbide, which is the same form contained in siliconized RPP. A microwave discharge device was used for generating dissociated species, and specimens consisted of resistance heated filaments of silicon carbide pyrolytically deposited on a tungsten core. True chemical kinetic reaction rate measurements, free of gas phase diffusion phenomena, were obtained by use of high flow velocities ($\approx 10^4$ cm/sec, directed normal to the filaments), low total pressures (≈ 1 Torr) and small specimen diameters (≈ 0.102 mm). Data was obtained for specimen temperatures of 2700°F to 3860°F.

Reaction rates were reported in terms of a dimensionless absorbent atom removal probability, ζ , defined as the ratio of the observed Si or C atom flux, \dot{Z} (Si, c), away from the filament to the impingement rate, \dot{Z}_i of reactant (atoms or molecules) per unit area. The atom removal probability data was converted to absolute mass removal rates per unit area, \dot{M} as shown in Figures 5-5 to 5-7, by use of the Hertz-Knudsen equation

$$\dot{Z}_i = \frac{1}{4} \left(\frac{P_i}{kT} \right) \left(\frac{8kT}{m_i} \right)^{1/2}$$

where m_i = mass reactant species, (i = O, O₂, N, N₂)

k = Boltzmann constant

P_i = pressures of reactant i

T = specimen temperature

Since Rosner and Allendorf's experiments were performed on pyrolytically deposited SiC as contrasted with diffusion coated SiC on RPP, it is important to assess first whether the chemical response of the two materials to oxidation and nitridation are comparable. All of the response data on coated RPP under controlled environmental conditions has been obtained in plasma arc tests with an environment of O, N and N₂. Rosner and Allendorf obtained reaction rate data for these reactants (as well as O₂), and found that both O and N (as well as O₂) are reactive, while N₂ is relatively non-reactive. Below a threshold temperature of about 3050°F their results are correlated reasonably well on an Arrhenius plot of $\ln \dot{M}$ versus $1/T$ for a constant value of pressure. This is in line with theory of absolute reaction rates in reference (13) which indicates,

$$\dot{M}_i = K P_i^n e^{-(E_i/RT)} \quad (3)$$

where, n = reaction order

E_i = activation energy

R = gas constant

K = "constant" whose temperature dependence is very weak compared to the exponential term

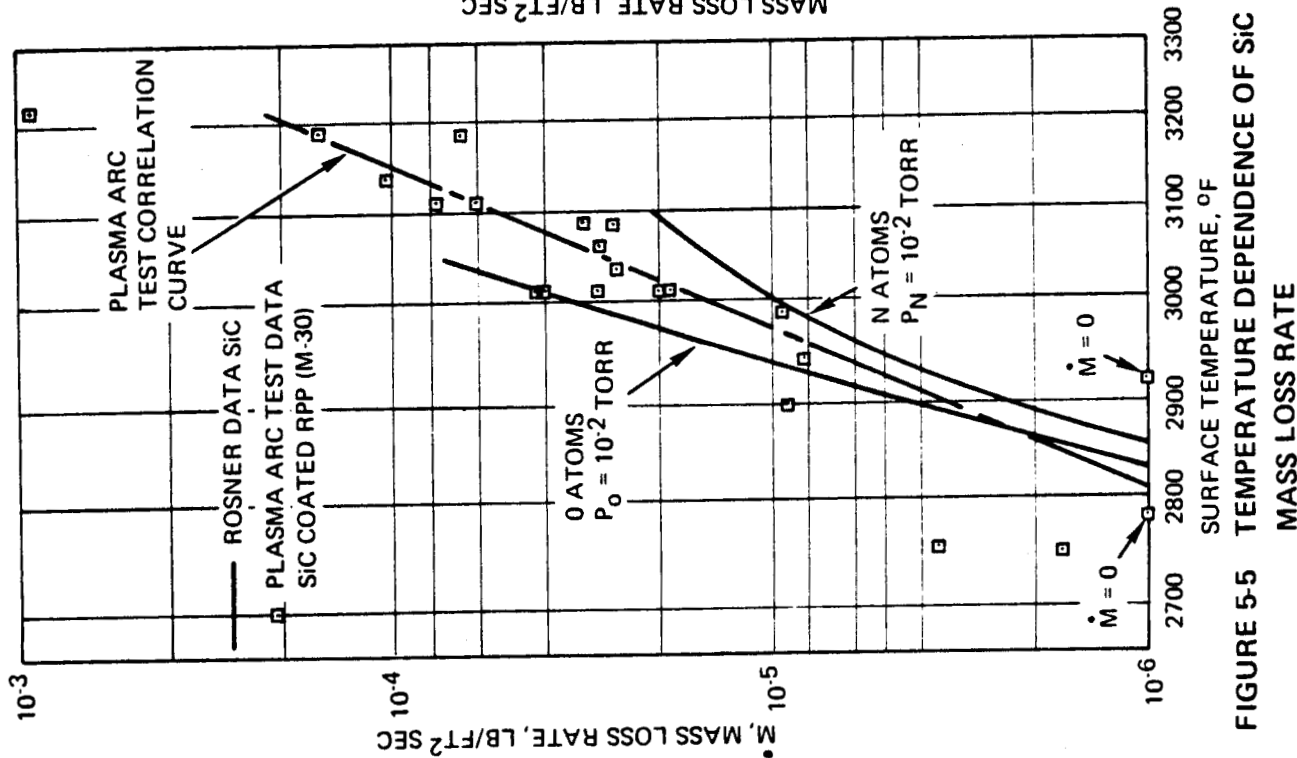


FIGURE 5-5 TEMPERATURE DEPENDENCE OF SiC

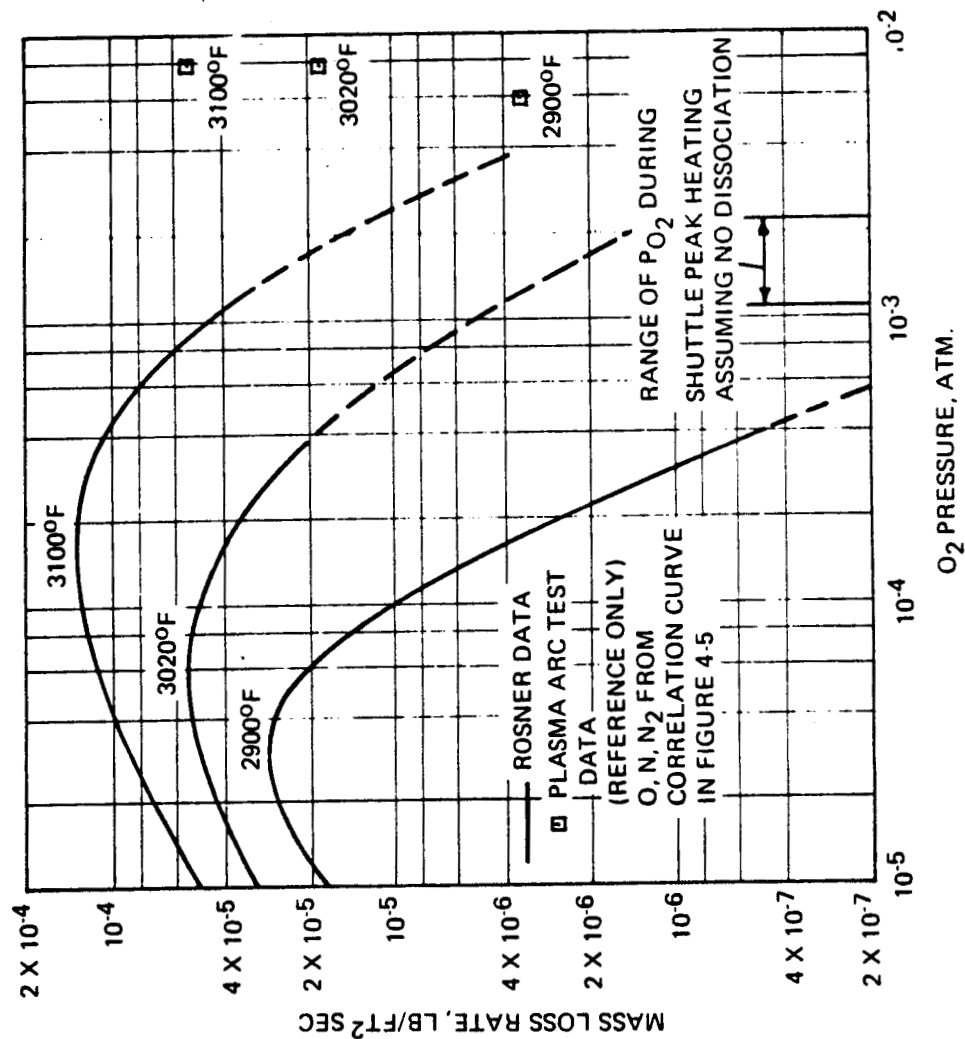


FIGURE 5-6 MASS LOSS RATE OF SiC IN MOLECULAR OXYGEN

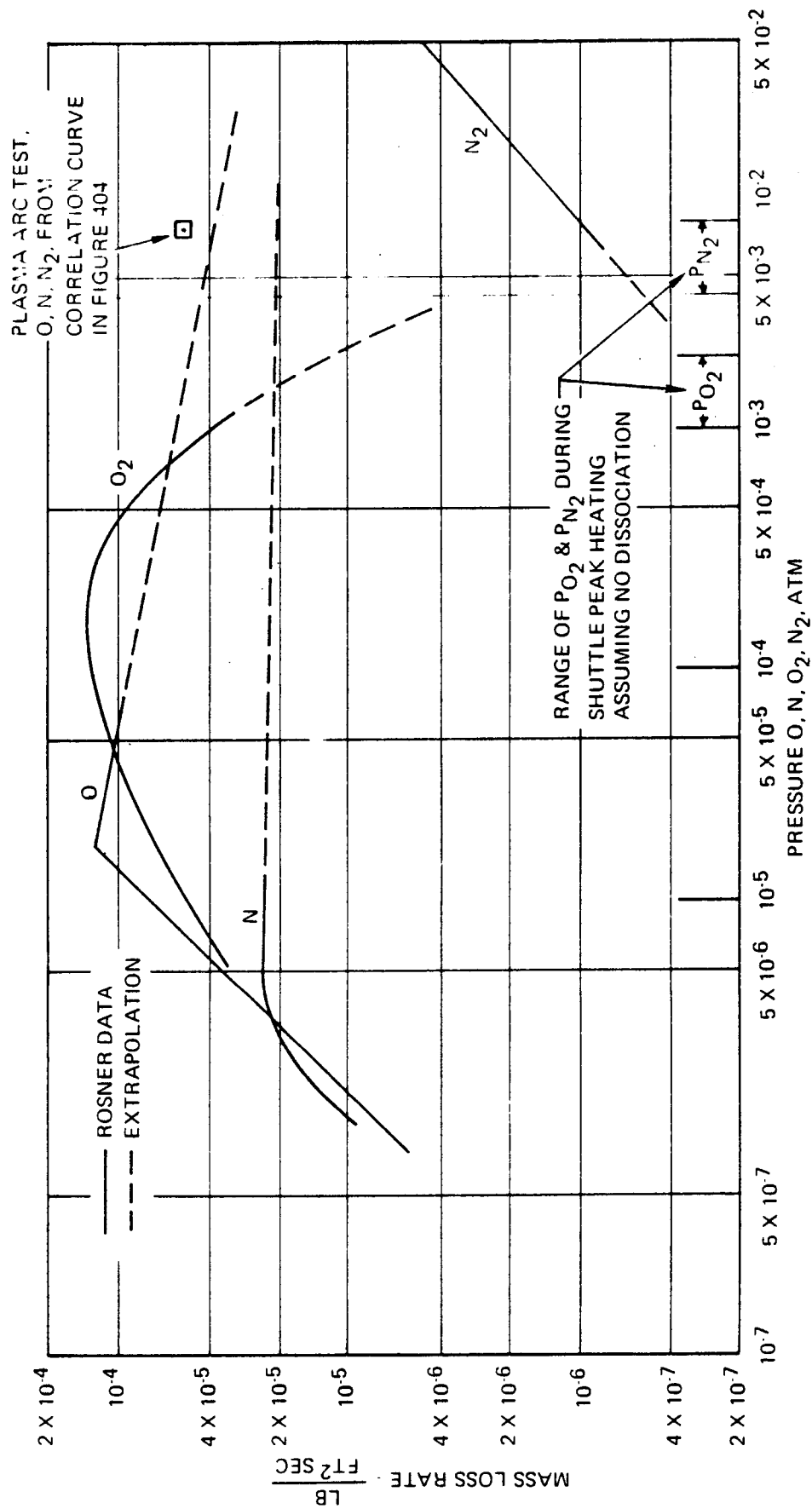


FIGURE 5-7 MASS LOSS RATE OF SiC AT 3100°F

Plasma arc test data for the M-30 SiC coated RPP system were therefore compared with data of Rosner and Allendorf for O and N reactants on an Arrhenius plot with the results shown in Figure 5-5. As mentioned above, this plot is strictly valid only for data corresponding to constant pressure. The plasma test data does cover a range of pressures, but only a very narrow one (factor of two total variation). Rosner's data for O and N reactants in Figure 5-5 corresponds to single value of pressure, but a value orders of magnitude lower than that for the plasma arc test. Hence, only the slopes of the mass loss rates with temperature should be compared, which provides a valid comparison of activation energies E , as shown in equation (3).

It is seen in Figure 5-5 that the slopes of Rosner's data for pyrolytic SiC and the data for coated RPP agree quite well, providing credence to the use of Rosner's data as representative of the relative reactivity of coated RPP to different reactants. It is remarkable that Rosner's mass loss data also agrees reasonably well with the plasma test data in an absolute sense, considering the orders of magnitude difference in pressures. That this is not completely fortuitous can be seen by the data presentation in Figures 5-6 and 5-7.

Figure 5-7 presents Rosner's mass loss data for a constant temperature of 3100°F as a function of pressure. It is seen that above a threshold pressure the dependence of mass loss rate on pressure is very weak, that is, reaction order $n \approx 0$ for N and O reactants. Extrapolation of Rosner's data to plasma test pressure indicates reasonable agreement with plasma test mass loss rate. This provides additional confidence in application of Rosner's data to understanding chemical reactivity of coated RPP.

It will be noted in Figure 5-7 that the mass loss rate of SiC to O_2 actually decreases with increasing pressure above a threshold value of pressure. Rosner explains the weak pressure dependence of SiC mass loss rate in O and N and the negative dependence in O_2 as due to formation of a thin protective layer of silica or oxide of nitrogen on the surface, with the rate limiting mechanism being dissociative evaporation of this film. Such a film would be formed at pressures above some threshold value, with the required pressure increasing with increased surface temperature. This would explain the change in slope of the mass loss versus pressure curves in Figure 5-7. At low pressures the mass loss increases with pressure, indicating bare surface behavior, whereas above some critical pressure the mass loss decreases or becomes independent of pressure, indicating film behavior.

Rosner's data indicates, as shown in Figure 5-7, that a higher pressure is required for film formation in O_2 than in O or N, hence at very low pressures O_2 is more reactive than O or N. However, at the much higher pressures of the plasma arc tests, and of entry, Rosner's data indicates film formation would occur even in O_2 . Hence, the trends of Rosner's mass loss data with increasing pressure indicate O to be more reactive than O_2 at both plasma test and entry pressures at 3100°F . This point is expanded in Figure 5-6.

Figure 5-6 presents Rosner's mass loss rates of SiC in O_2 as a function of pressure for three specific temperatures, compared with plasma arc mass loss rates at these temperatures. It is seen that at 3100°F the mass loss rate of SiC in O_2 at shuttle entry pressures is comparable to the mass loss rates in plasma arc tests. However, at 3020°F the extrapolation of Rosner's data indicates O_2 to be an order of magnitude less reactive, at entry pressures, than the plasma test environment. At 2900°F , O_2 is indicated to be even less reactive, relative to the plasma test environment. It will be noted that the maximum computed radiation equilibrium temperature for entry is 2740°F .

To place this discussion in perspective, if the air at the outer edge of the boundary layer during entry is highly dissociated, then a significant reduction in surface temperature would be expected, due to effects of low catalycity of coated RPP, and surface mass loss rates would be reduced dramatically. If the air is not dissociated, no temperature reduction would occur, but Rosner's data indicates mass loss rates would be far lower than those experienced in the dissociated environment of plasma arc tests. Therefore, application of plasma arc test mass loss rates to the entry environment, in conjunction with the assumption of no temperature relief due to low catalycity, would appear to be highly conservative and unrealistic.

Plasma arc tests in a nondissociated flow are planned for Phase III in the NASA Ames arc heated rectangular duct facility, described in Reference 20, to confirm these tentative conclusions. High total pressures will be required to obtain the necessary heating rates due to the low enthalpy required to avoid dissociation. Realistic partial pressures of O_2 and N_2 will be obtained by use of Argon or Helium diluent. A mixture of O_2 and N_2 is considered necessary since Rosner's results for O and N mixtures in reference (14) indicated significant coupling effects between O and N reactions, which may occur also for O_2 and N_2 . This coupling which occurred at some temperatures and not at others, fortunately resulted in lower mass loss rates than would be predicted by simple addition of loss rates for each species.

Two final points are worth mentioning with respect to Rosner's postulated protective film of silica and nitrogen oxides. Silica is known to be a poor catalyst to atom recombination, hence such a film would explain the low catalyticity of coated RPP in plasma tests. Also, a silica film could exist in liquid form and could, therefore, be sensitive to aerodynamic shear. Since the stagnation heating tests used in Phase I do not generate appreciable surface shear stresses, it was deemed important to explore the possible effects of shear on coating performance. This is discussed in the following section.

5.1.2 Wedge Heating

Stagnation heating plasma arc tests used in Phase I and in the current effort for evaluation of coating performance do not subject the coating to appreciable aerodynamic shear. Due to the high local velocities at the leading edge for the highly swept delta wing configuration, significant shear will be developed. Plasma arc tests were therefore performed using the 30° wedge specimen holder shown in Figure 5-8 in order to evaluate the effects of shear.

Calculations were made of aerodynamic shear for the leading edge and for the wedge heating tests as shown in Figures 5-9 to 5-11 in order to determine the degree of simulation achieved in the tests. Shear was calculated from heating rate \dot{q} , local velocity at boundary layer edge V_1 , and enthalpy difference across the boundary layer ($i_r - i_w$). Using Reynold's analogy,

$$\tau_w = \frac{\dot{q} V_1 P_r^{2/3}}{(i_r - i_w)} \quad (4)$$

- where:
- P_r = Prandtl number evaluated at Eckert's reference enthalpy i^* and local pressure
 - i^* = $i_1 + 0.5 (i_w - i_1) + 0.22 (i_r - i_1)$
 - i_w = air enthalpy at surface temperature and pressure
 - i_r = recovery enthalpy
 - i_1 = local enthalpy at boundary layer edge

Computed shear on the leading edge at the maximum heating locations versus entry time is presented in Figure 5-10. The peak value of 2.33 lb/ft² occurs at 1200 seconds. Shear distribution around the

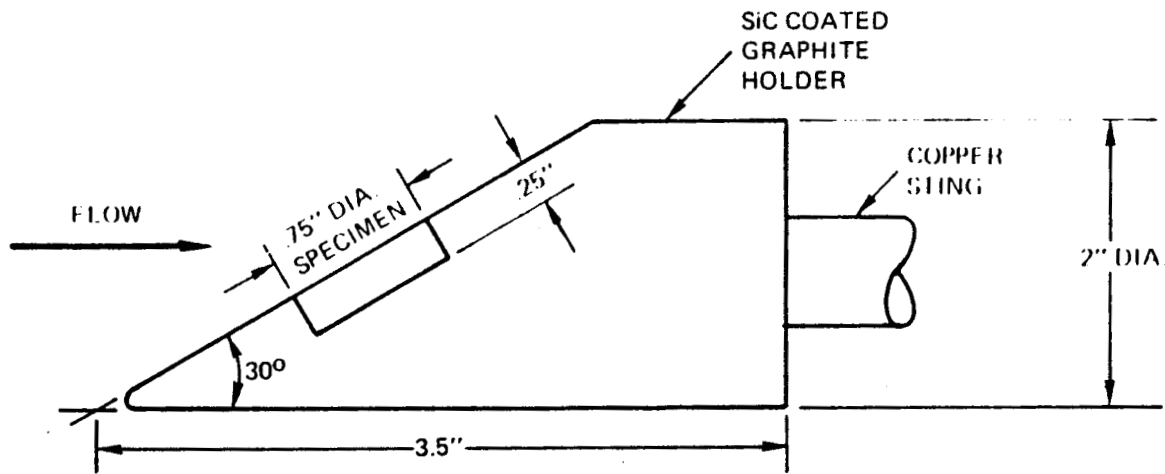


FIGURE 5-8 WEDGE HEATING SPECIMEN HOLDER

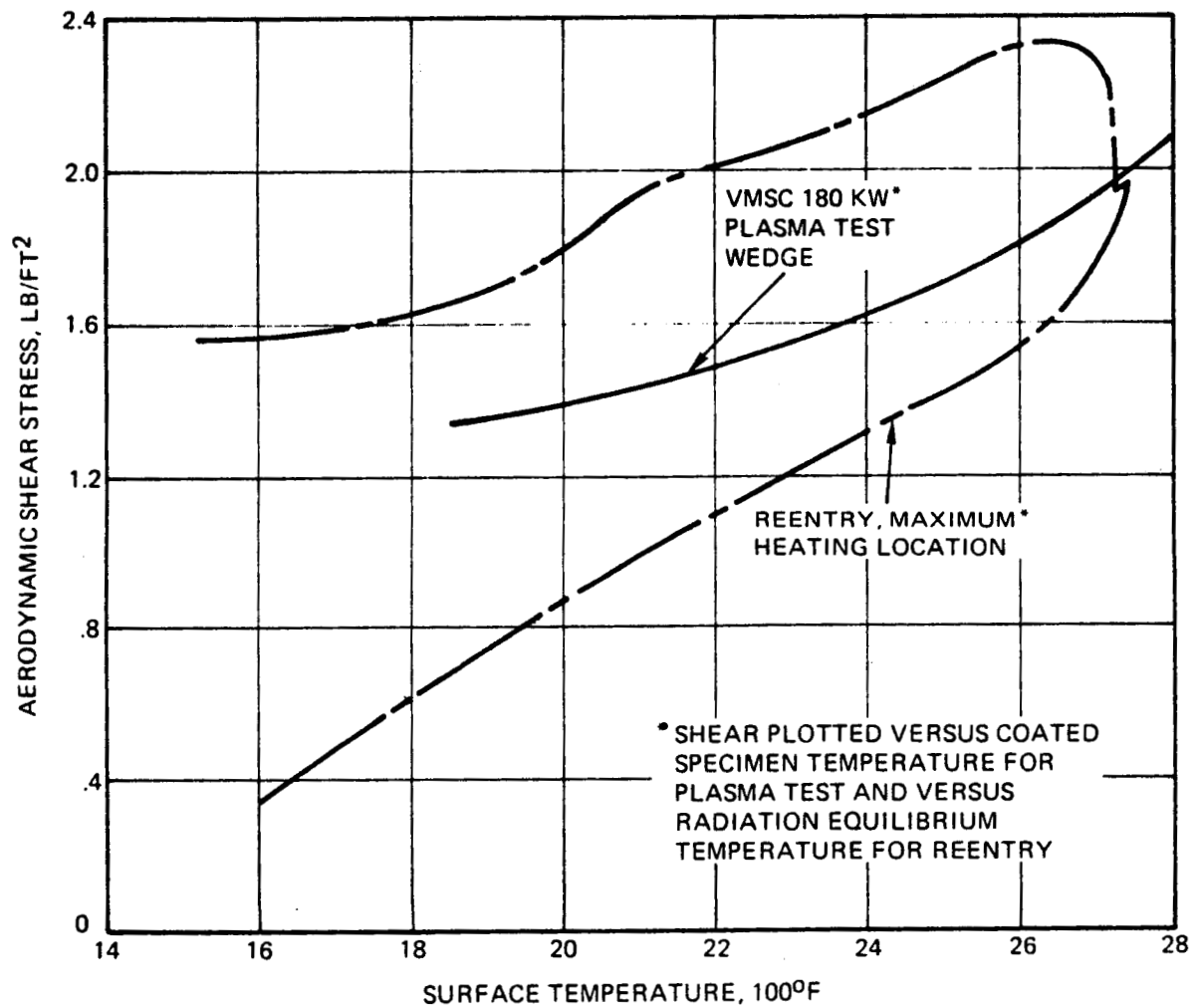


FIGURE 5-9 COMPARISON OF AERODYNAMIC SHEAR ENTRY AND PLASMA ARC TEST

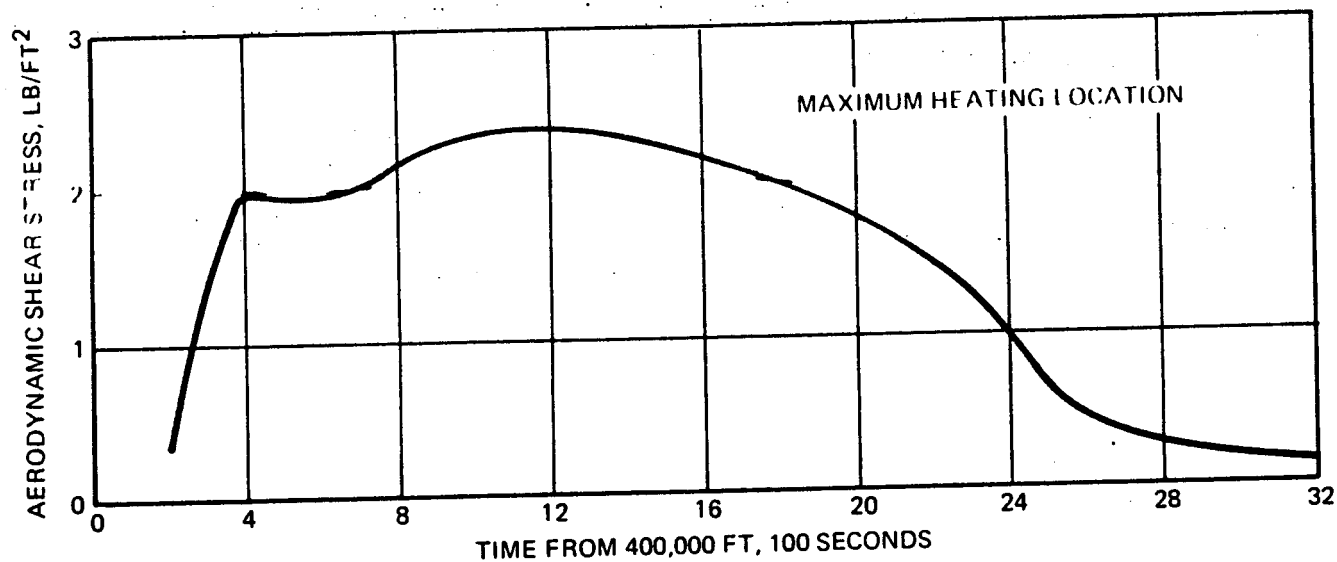


FIGURE 5-10 AERODYNAMIC SHEAR DURING ENTRY

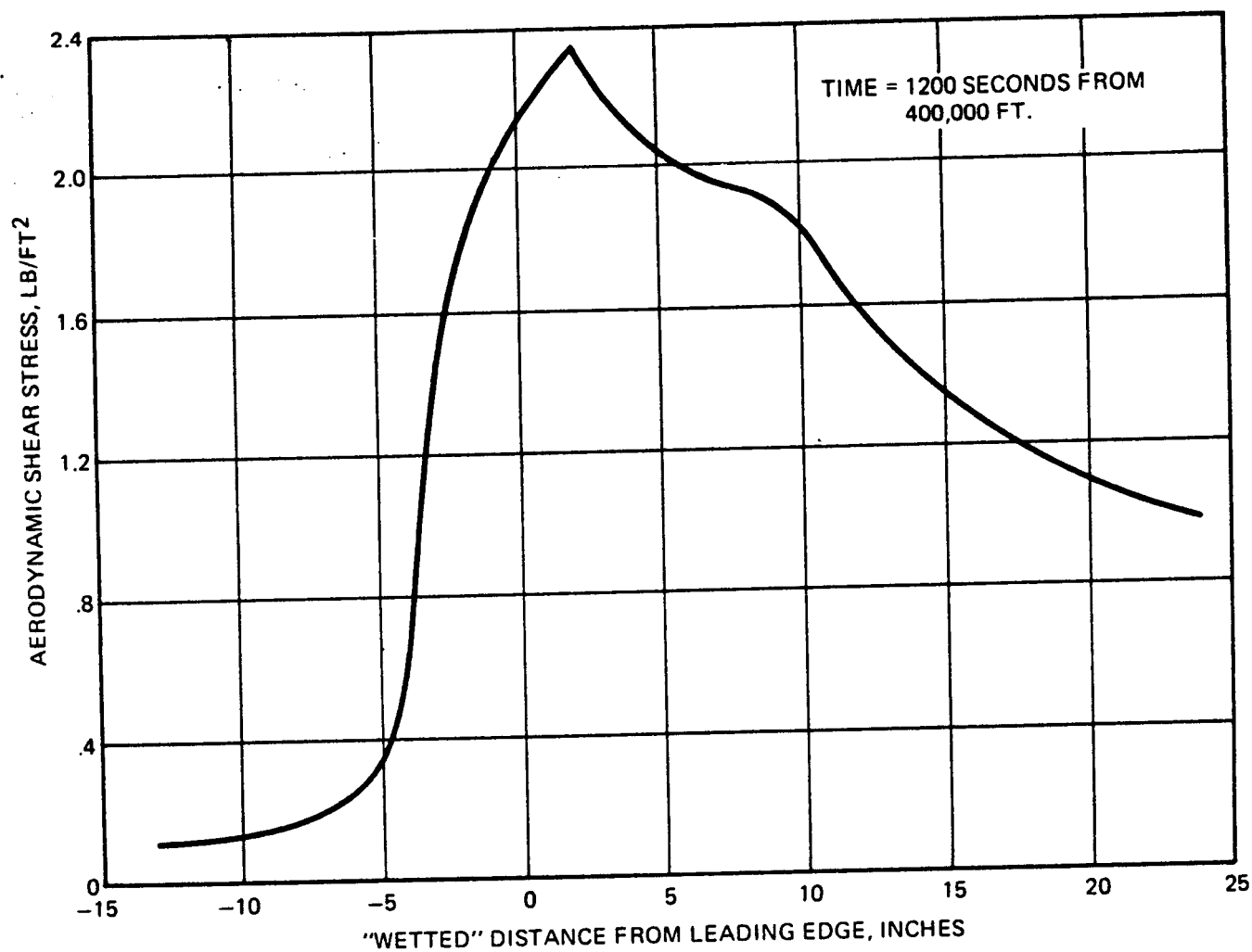


FIGURE 5-11 ENTRY AERODYNAMIC SHEAR DISTRIBUTION

leading edge at 1200 seconds is shown in Figure 5-11 and it is seen that the peak value occurs at the point of maximum heating. Figure 5-9 presents computed leading edge shear at the maximum heating location versus surface temperature throughout entry as compared with computed shear for the plasma arc tests. It is seen that the plasma wedge heating tests provided a reasonable simulation of entry shear, with a peak value in the tests of 2.1 lb/ft^2 compared to 2.33 lb/ft^2 in entry. Future test conditions or wedge angle can be adjusted slightly to more accurately duplicate entry shear.

Wedge heating mass loss data at low temperatures in the range of 1700 to 1950°F are presented in Figure 5-12. Results are shown for a number of SiC coating systems, including 10/60/30 material. None of the materials evaluated in the wedge tests were heat treated. Considering all material systems, the data is widely scattered, ranging from weight gain to weight loss of magnitude $\dot{M}/h = 10^{-3}$. However, for the 10/60/30 system, most data fell around $\dot{M}/h = 10^{-4}$. This value of normalized mass loss is equivalent to the nominal mass loss for the heat treated 10/60/30 coating system at 2480°F in stagnation heating tests. Hence, the data falls far above the mass loss correlation curve for siliconized RPP which was established at higher temperatures for stagnation heating.

In an attempt to isolate whether the unexpectedly high mass loss rates in Figure 5-12 were related to temperature or to the wedge heating conditions, higher temperature wedge tests were performed as reflected in Figure 5-13. This data was obtained in the same temperature range as stagnation heating data. Unfortunately, no data has yet been obtained for the 10/60/30 coating system under these conditions. However, the materials which were evaluated are all of the SiC type. It is seen that wedge heating mass loss rates were an order of magnitude higher than stagnation heating mass loss rates on the same material systems at the same temperatures. Therefore, the high mass loss rates would appear to be a function of wedge heating per se rather than temperature.

As discussed in the section 5.1.4, coating mission life is an inverse function of mass loss rate, hence the high mass loss rates under wedge heating conditions are of definite concern. This is particularly true since the tests represent realistic shear conditions. However, further evaluation will be required before the implication on mission life can be assessed quantitatively. Specifically, further tests will be required to determine whether the mass loss rates in the wedge heating tests can be definitely related to aerodynamic shear, as opposed to pressure for example. Subcontractor wedge heating plasma arc tests are planned in Phase III, as are further tests in the VMSC 180 KW plasma arc tunnel, possibly with

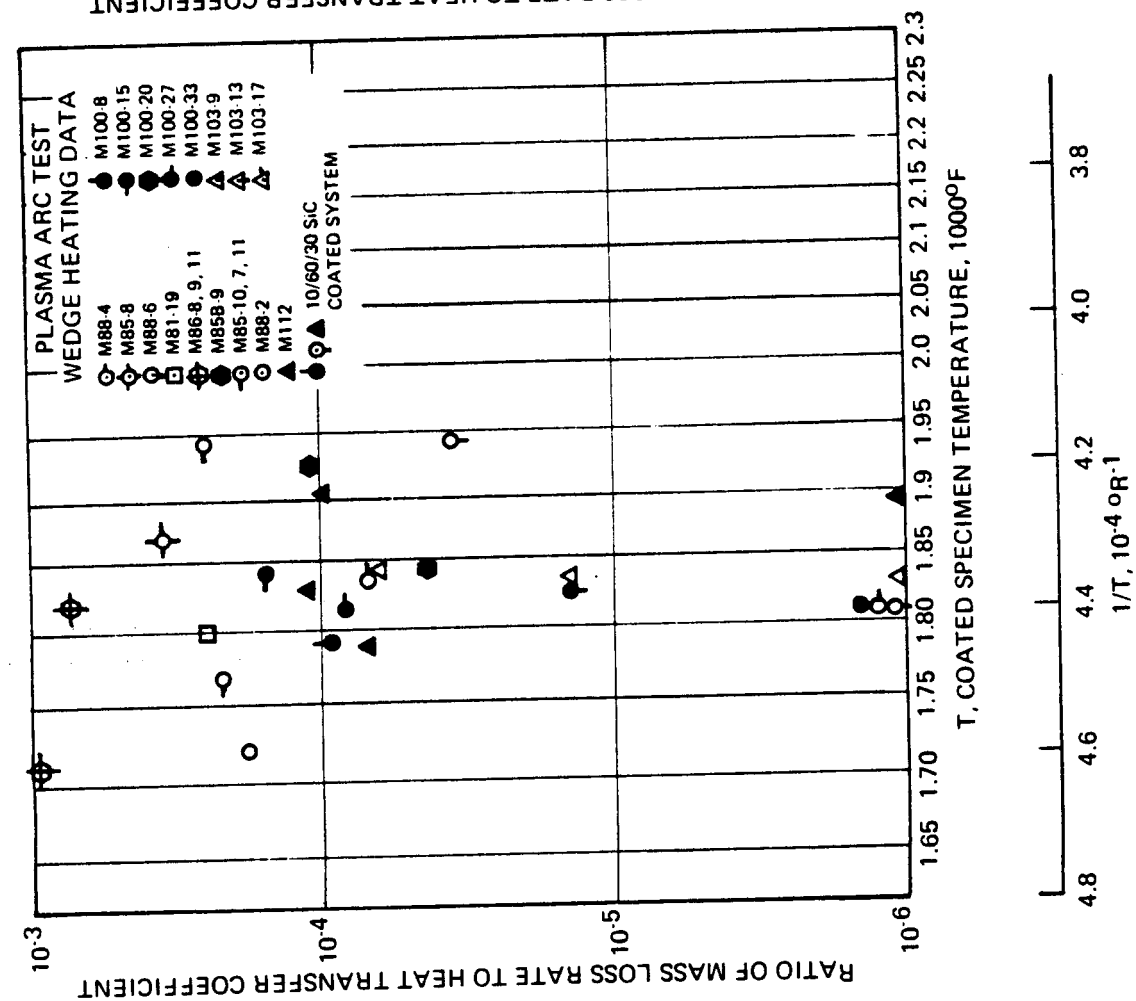


FIGURE 5-12 LOW TEMPERATURE WEDGE HEATING DATA

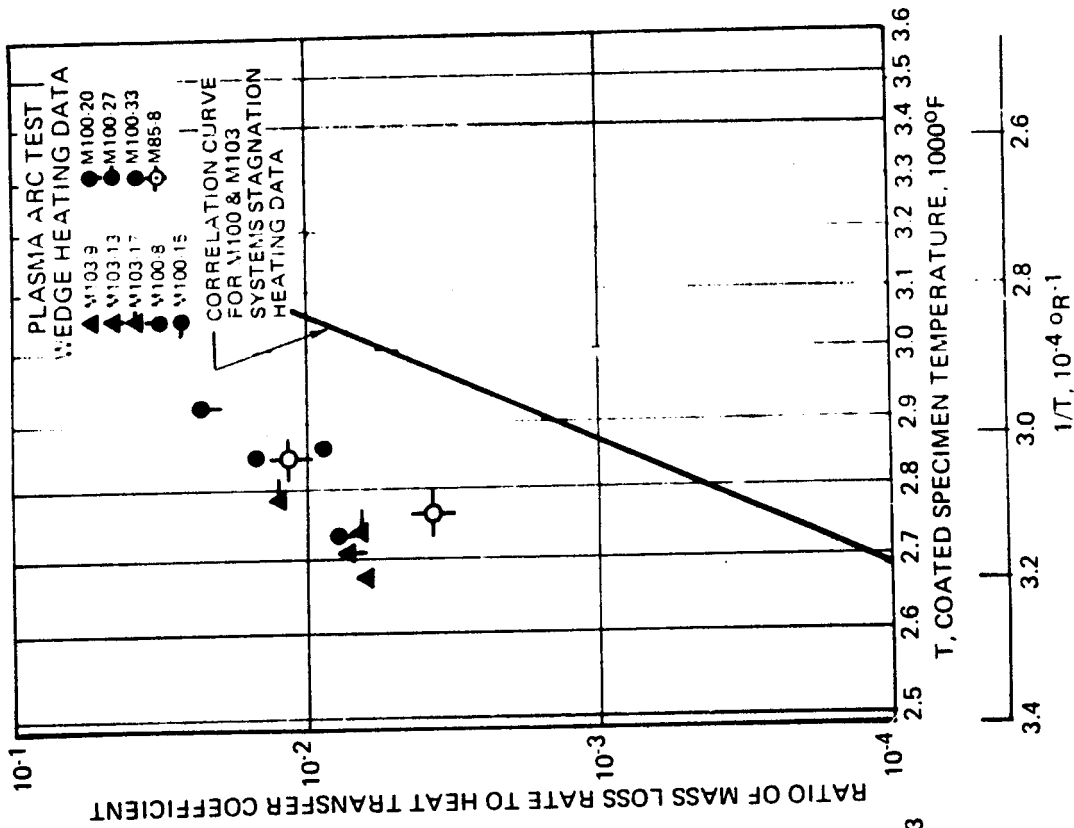


FIGURE 5-13 HIGH TEMPERATURE WEDGE HEATING DATA

different wedge angles to increase shear. Analytical effort is also planned for Phase III to assist in data correlation and interpretation, based upon aerodynamic shear effects on the postulated silica liquid protective layer.

5.1.3 Plasma Arc Evaluation of Heat Treated 10/60/30 Material

Plasma arc tests were performed to evaluate the resistance of the selected, heat treated, 10/60/30 material system to oxidation and other erosion mechanisms under simulated earth atmospheric entry conditions representative of the space shuttle leading edge. A series of 67 tests were performed on 15 coated and 6 bare control specimens in the VMSC 180 KW plasma arc facility with a 1.5 inch exit diameter, Mach 3 nozzle. Test specimens were nominally 0.75 inch diameter by 0.18 inch thick and mounted on a stagnation heating specimen holder with a 1.5 inch diameter silicon carbide coated graphite shroud. The shroud, together with 0.25 inch thick graphite felt insulation behind the specimens, were included to minimize specimen heat losses. Test conditions are summarized in Table 5-1.

TABLE 5-1

PLASMA ARC TEST CONDITIONS

Cold Wall Heat Flux Rate BTU/ft ² sec	Stagnation Enthalpy BTU/Lb	Stagnation Pressure PSIA	Radiation Equilibrium Temperature ($\theta = 0.85$) °F	Coated Specimen Temperature °F	No. of Exposure Cycles	Total Exposure Time Secs.
174	9600	0.420	3910	-	1	90-240
168	8760	0.415	3855	3045-3075	2	1200
162	7870	0.410	3810	3100	2	1200
136	8390	0.400	3650	2910-2970	2-4	3000- 4800
102	6880	0.390	3350	2710-2770	5-6	7200- 10800
73	7450	0.380	3070	2460-2510	5-10	9000- 18000

Stagnation enthalpy was determined by the energy balance method and stagnation pressure was determined by prior calibration with a pressure probe. Surface temperature of each specimen was measured with an

optical pyrometer and corrected for window absorption and emittance effects. Cold wall heat flux rate was inferred from surface reradiation heat flux rate on bare control specimens since calorimeter operation proved unreliable.

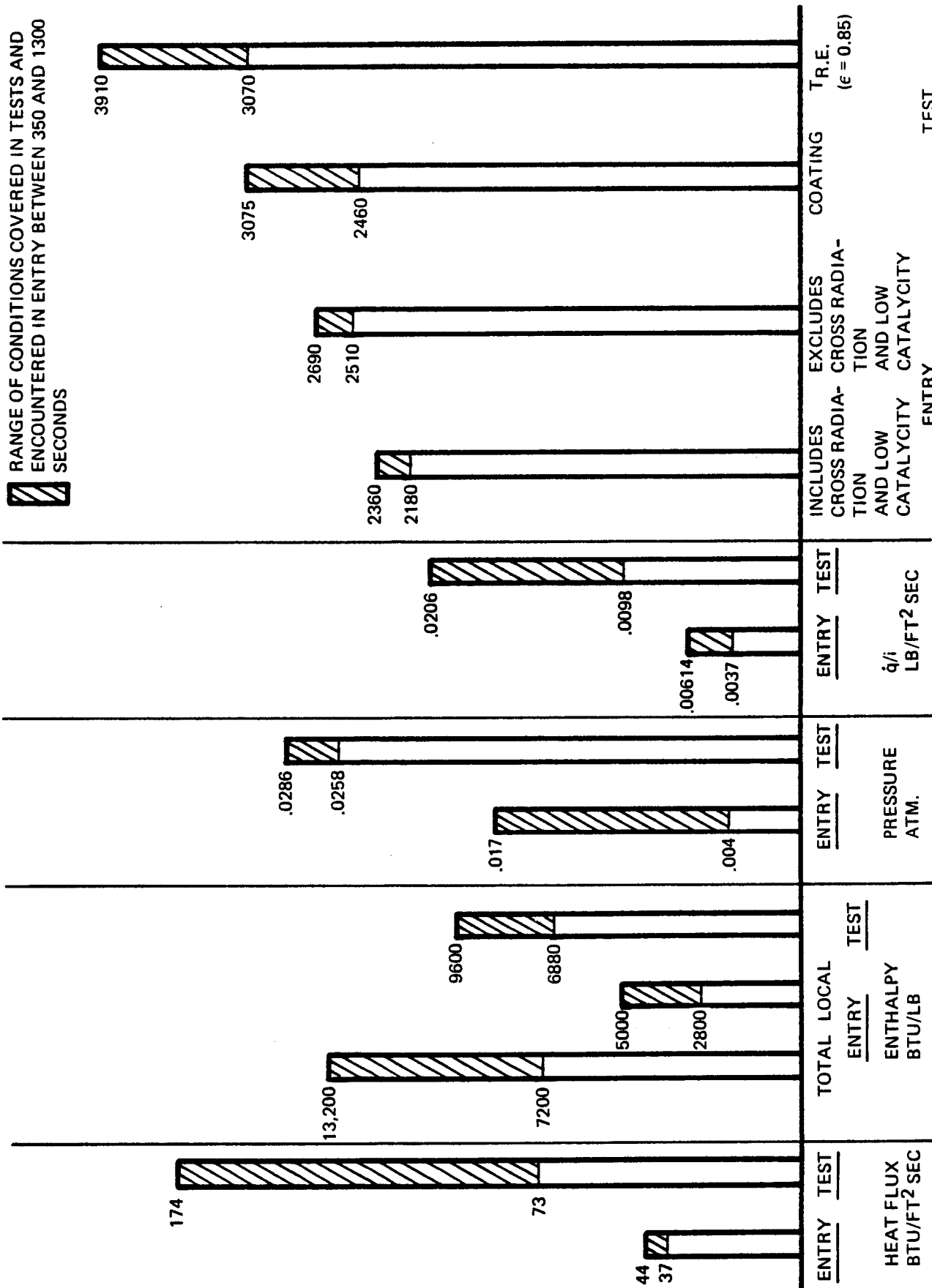
It will be noted in Table 5-1 that total exposure times were quite long, as much as five hours, whereas the largest exposure times in previous tests of siliconized RPP were about 0.8 hour. No coated specimen temperature is given at the 174 BTU/ft² sec heating rate since coating burn through was obtained within 90 to 240 seconds, before specimen temperature had stabilized.

A comparison of test conditions with design entry conditions at the maximum heating location is given in Figure 5-14. The variation of entry conditions corresponds to the entry time period from 350 to 1300 seconds from 400,000 feet altitude. This is the period when the bulk of material mass loss will occur. It is seen that oxidation conditions in the tests were more severe than those expected during entry. This includes surface temperature, pressure, oxygen diffusion rate (as controlled by \dot{q}/i), and concentration of atomic reactant species (as controlled by enthalpy).

Mass loss rates for individual specimen exposure cycles are plotted as a function of specimen surface temperature in Figure 5-15. These loss rates were normalized by surface heat transfer coefficient to reflect the oxidizing potential of the air flow, as was explained in Reference 2. As was expected, based on previous shorter duration testing, the mass loss rates increased strongly with increasing temperature. It is also evident that data scatter is much more severe at the lower temperatures. In early exposure cycles at low temperature, specimens actually demonstrated weight gains, whereas in later cycles weight losses were experienced.

The increasing spread of mass loss data with decreasing temperature is clarified by the data presentation in Figures 5-16 through 5-19. Cumulative mass change is plotted as a function of cumulative exposure time from cycle to cycle. At the lowest heating rate, 73 BTU/ft² sec, there is an initial weight gain, as shown in Figure 5-16, followed by transition to a steady state weight loss. The mass loss rates in Figure 5-1 represent slopes on the mass loss versus time curves in Figures 5-16 through 5-19. At the lower heating rates, these slopes continually change with exposure time, which explains the wide data scatter in Figure 5-15 at low temperature.

 RANGE OF CONDITIONS COVERED IN TESTS AND ENCOUNTERED IN ENTRY BETWEEN 350 AND 1300 SECONDS



SURFACE TEMPERATURE, °F

FIGURE 5-14 COMPARISON OF PLASMA ARC TEST WITH ENTRY HEATING CONDITIONS

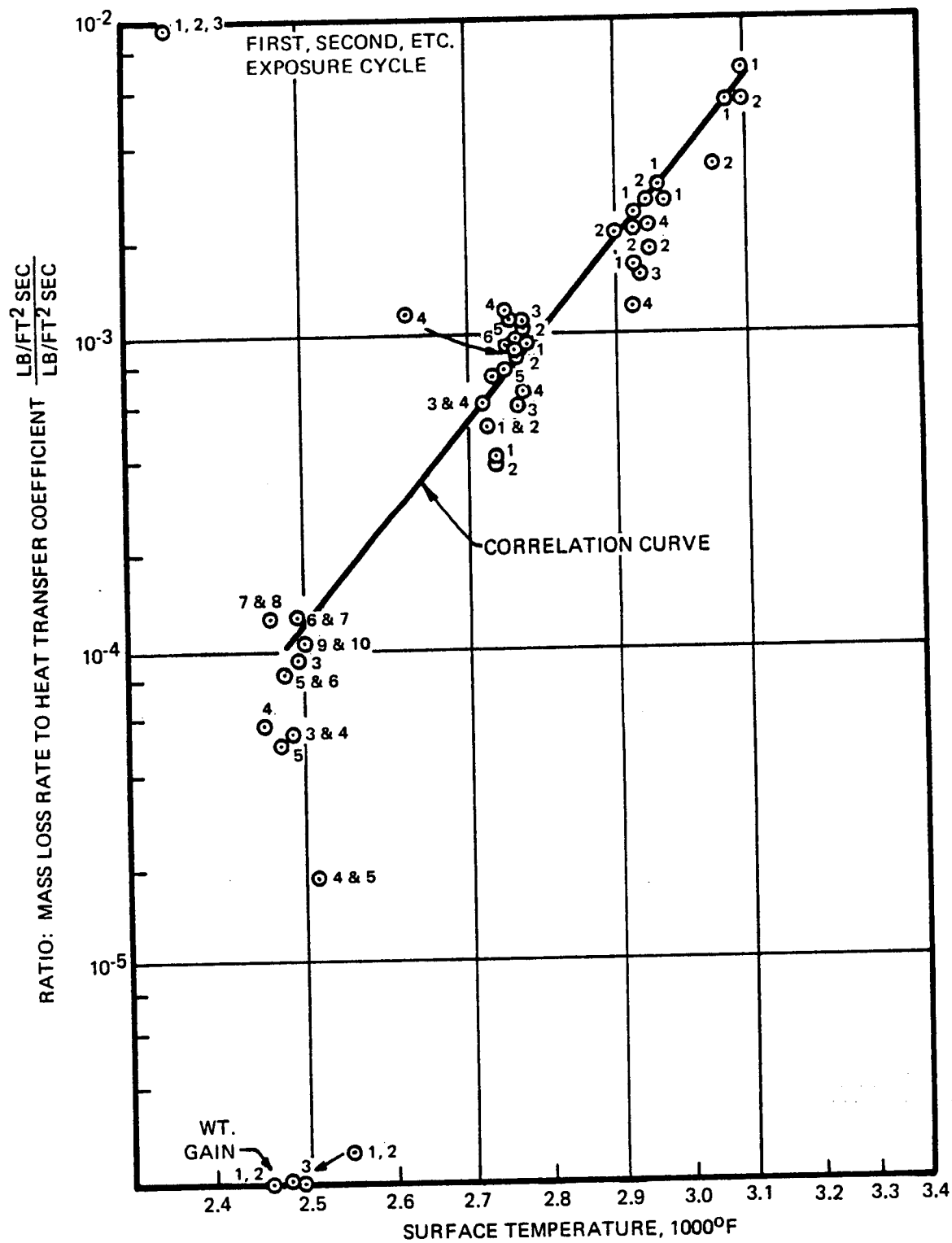


FIGURE 5-15 PLASMA ARC TEST MASS LOSS RATE DATA FOR OXIDATION INHIBITED CARBON-CARBON

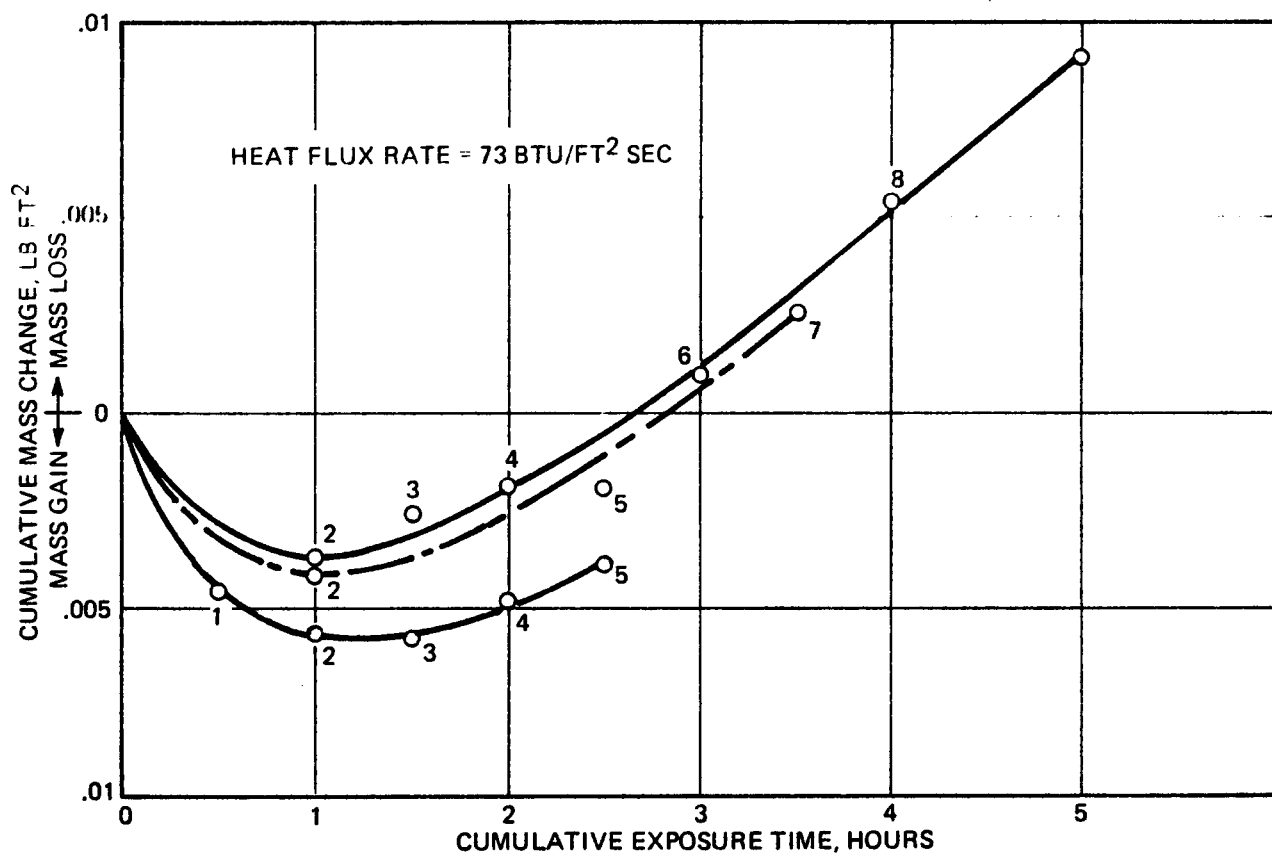


FIGURE 5-16 MASS CHANGE VS TIME FINAL EVALUATION DATA

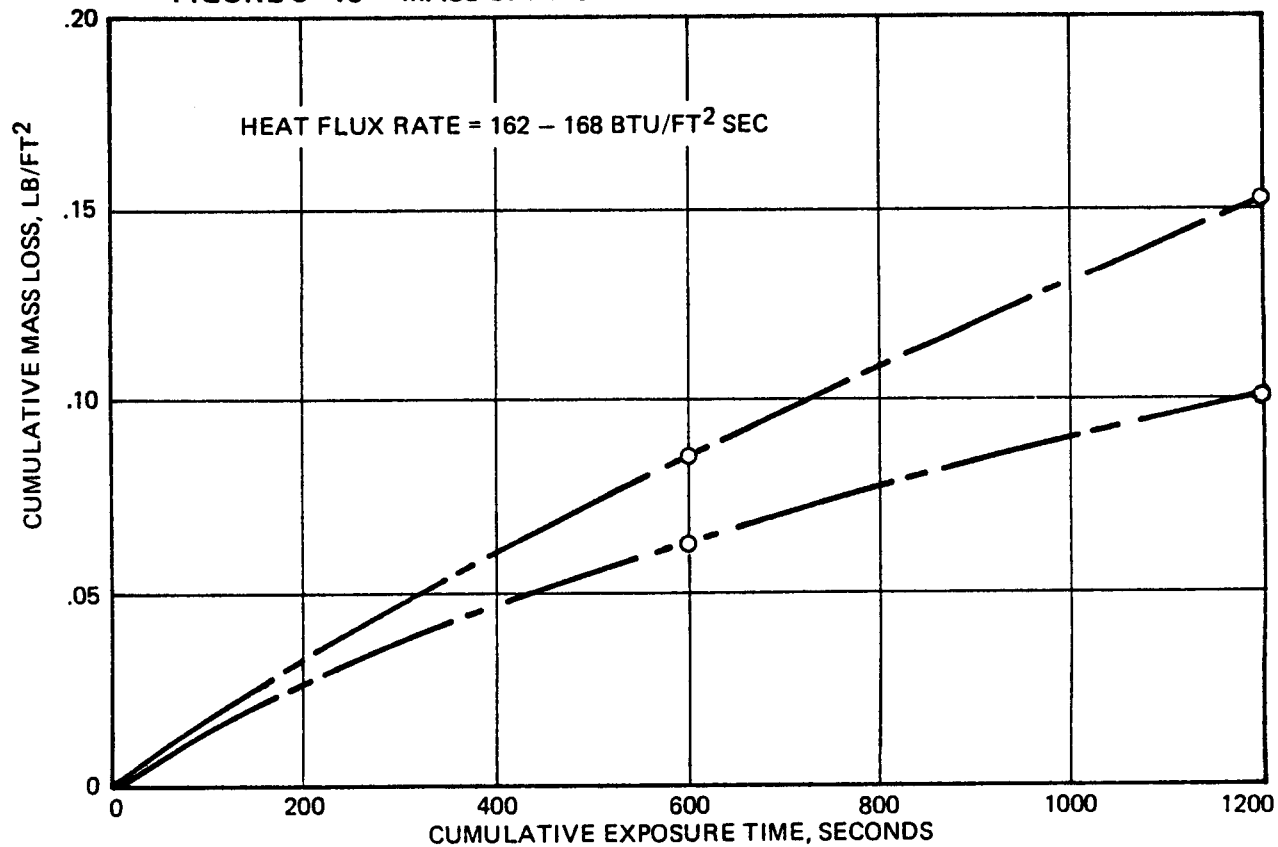


FIGURE 5-17 MASS LOSS VS TIME FINAL EVALUATION DATA

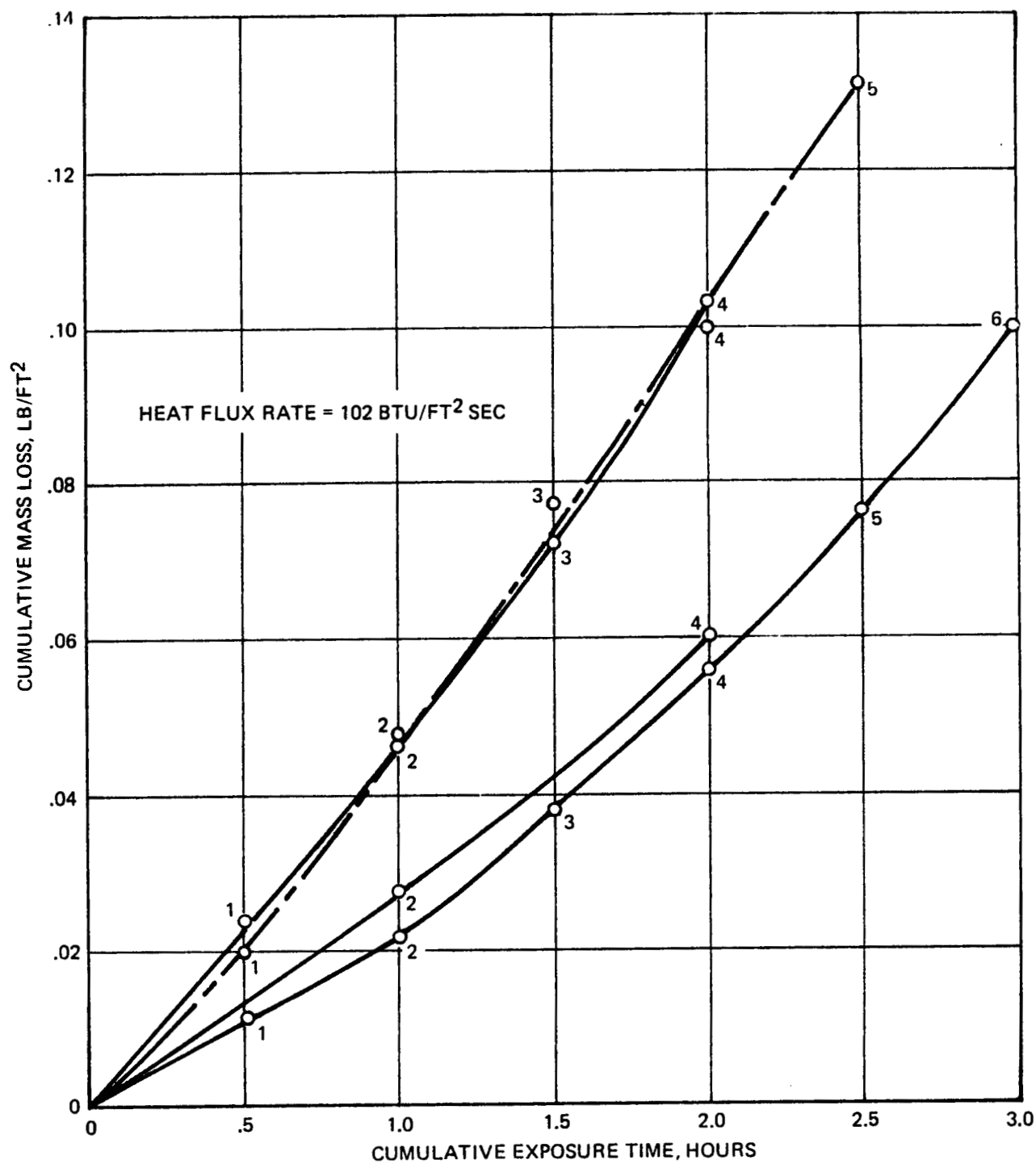


FIGURE 5-18 MASS LOSS VS TIME FINAL EVALUATION DATA

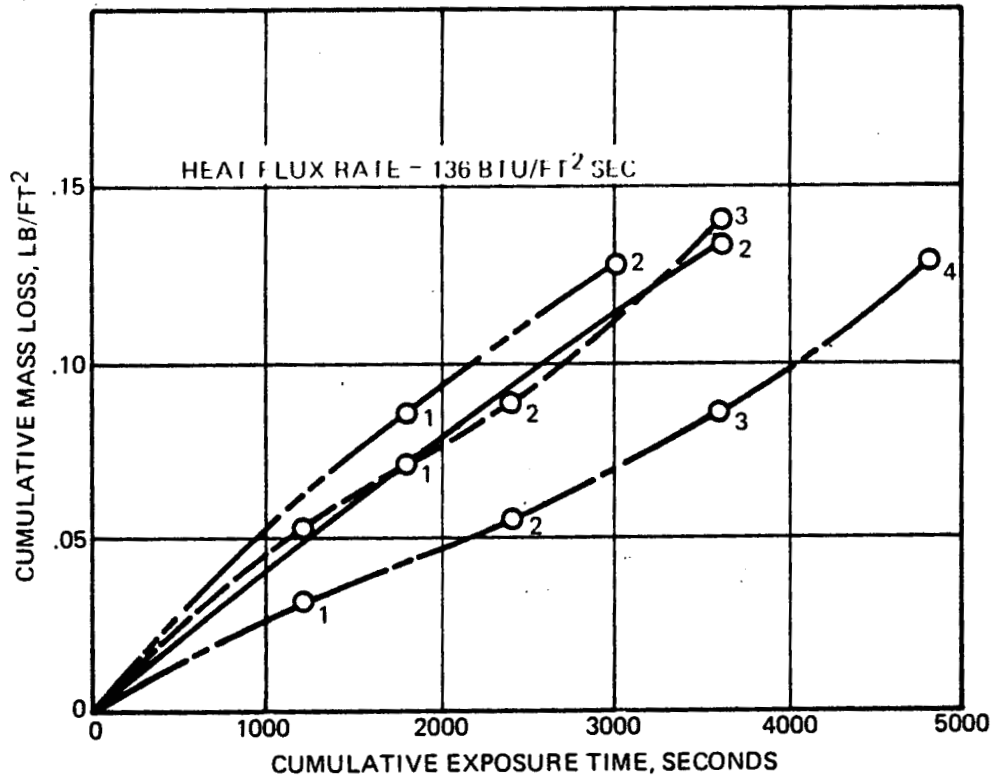


FIGURE 5-19 MASS LOSS VS TIME FINAL EVALUATION DATA

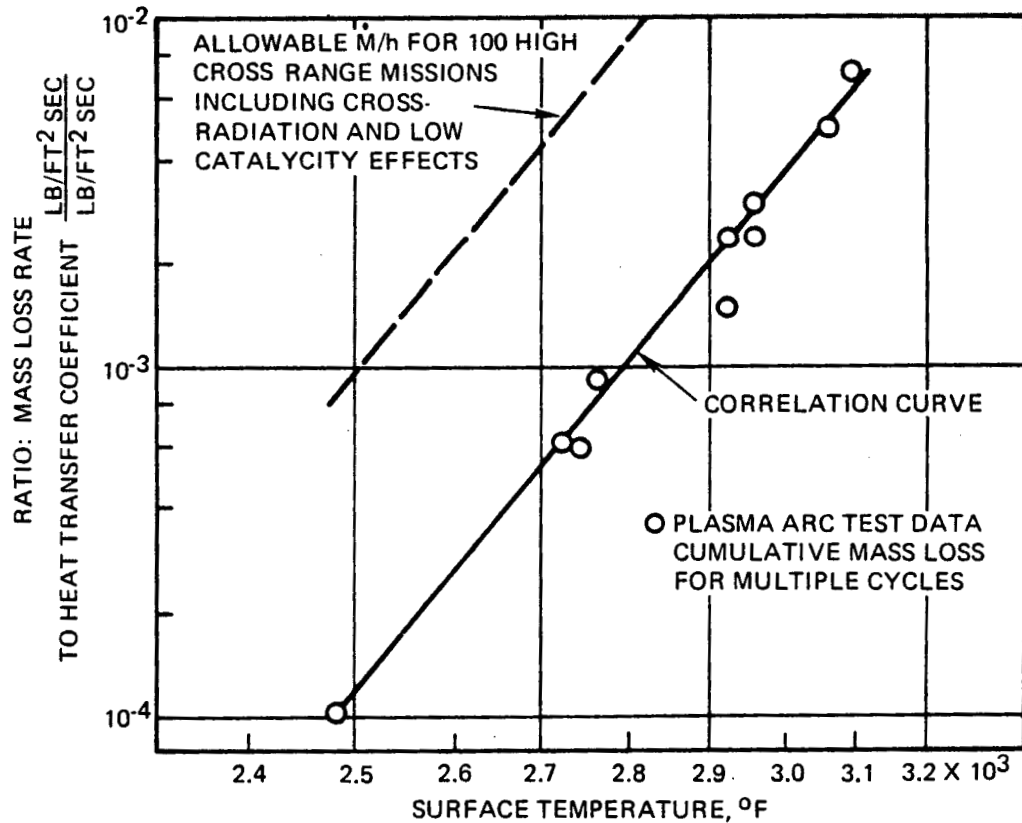


FIGURE 5-20 PLASMA ARC TEST MASS LOSS RATES FINAL EVALUATION DATA

The initial weight gain at low heating rate is presumably due to pickup of oxygen in formation of a silica surface film. This film is continually removed by sublimation, probably at a fairly constant rate. Film formation rate is probably high initially, while the film is thin, but decreases with time as the film thickness increases. Increasing film thickness would be expected to slow the rate of diffusion of oxygen across the film, hence reducing the rate of silica formation. Eventually, a steady state condition is reached where film formation and sublimation rates are equal and film thickness is constant with time.

If the model of coating oxidation described above is correct, it would be expected that steady state film thickness would decrease with increasing mass loss rate at higher heating rates. Hence, the time required to establish steady state mass loss would decrease. This is verified by the mass loss versus time curves in Figure 5-17 through 5-19. No initial weight gain was detected, which indicates that transition to weight loss occurred within the time period of the first heating cycle. Mass loss is nearly linear with time at these higher heating rates, although at 102 BTU/ft² sec there is a trend of slightly increasing mass loss rate with time, as shown in Figure 5-18, possibly reflecting gradual transition to steady state. At the highest heating rates there is a slight reduction in mass loss rate with time, as shown in Figure 5-17, which is not understood.

An average mass loss rate was determined for each of the curves in Figures 5-16 through 5-19, for use in predicting coating mission life capability. Coating life was assumed to be terminated when one-half of the initial coating thickness is lost. This corresponds to a mass loss of 0.083 lb/ft² for the initially 0.02 inch thick, 100 lb/ft³ density coating. For each of the mass loss versus time curves the point was established at which mass loss equals 0.083 lb/ft². The average mass loss rate was then determined to be the slope of a straight line from the origin to the established point. Over the entire useful life of the coating this straight line approximation yields the same cumulative mass loss as the actual experimental curve. It will be noted in Figures 5-16 through 5-19 that sufficient exposure time was employed in the higher heating rate tests to obtain a mass loss in excess of 0.083 lb/ft². At the lowest heating rate, 73 BTU/ft² sec, linear extrapolation to this mass loss was required due to the very low mass loss rate.

The resultant, averaged mass loss rates are presented in Figure 5-20. It is seen that an exponential curve of mass loss rate versus temperature correlates the data quite well, with a small data scatter. At the high temperature end of the data the mass loss rates agree reasonably well with

previous data for siliconized RPP. At the low temperature end the current mass loss rates are considerably higher than previous values. This is due to the fact that previous tests were not of sufficient time duration to obtain steady state values.

Since coating mission life capability is based upon a maximum thickness loss of 0.01 inch, it is necessary to relate the above mass loss data to thickness loss. This relationship is shown in Figure 5-21 which presents measured cumulative thickness loss for each specimen versus measured cumulative mass loss. It is seen that the data is correlated by an apparent coating density of 100 lb/ft³.

5.1.4 Mission Life Prediction for Heat Treated 10/60/30 Material

Predictions were made of coating mission life based upon the plasma arc test data presented in the previous section and predicted aerodynamic heating for the delta wing orbiter. Calculations were made both ignoring effects of low surface catalycity and cross radiation, and including these effects.

In predictions ignoring low catalycity and cross radiation, the radiation equilibrium temperatures at the maximum heating location were used in conjunction with the mass loss correlation curve in Figure 5-20 and calculated heat transfer coefficient, h , for design heating conditions. This resulted in the curve of mass loss rate, \dot{M} , versus entry time in Figure 5-22. This curve was integrated to obtain the total mass loss per unit area for a single mission. The resulting value of 2.54×10^{-3} lb/ft² was computed to be equivalent to 987 seconds of exposure to the temperature and heat transfer coefficient at the time of peak heating. When catalytic effects are included the equivalent exposure time reduces to 729 seconds.

These results were used to predict mission capability as a function of peak surface temperature, with the following relation:

$$N = \frac{\Delta L \text{ Allowable}}{(\dot{M}/h)_{\text{Max}} h_{\text{Max}} t_{\text{EQ}}}$$

where: N = number of missions

$\Delta L \text{ Allowable}$ = allowable total surface recession for N missions

$$= 0.010 \text{ inch} = 0.000833 \text{ feet}$$

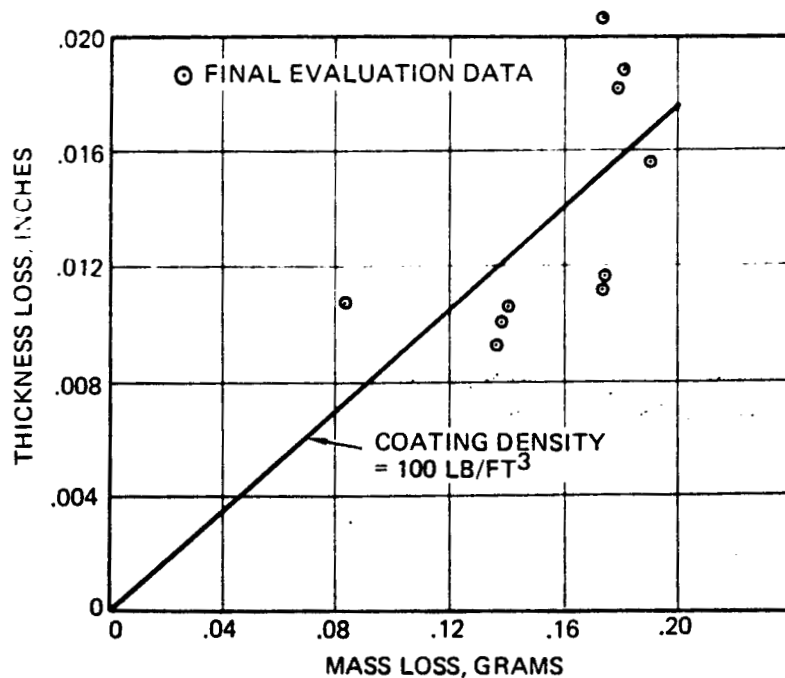


FIGURE 5-21 THICKNESS LOSS VS MASS LOSS SILICONIZED RPP

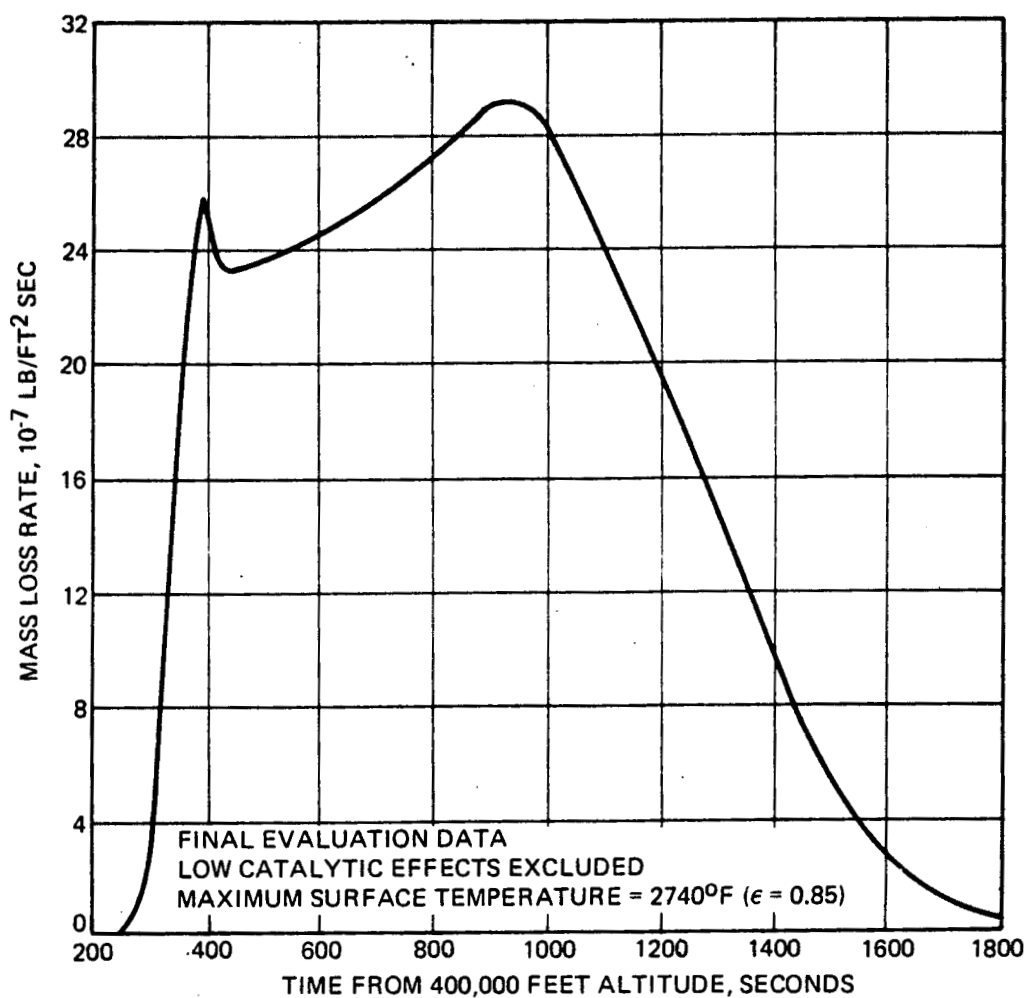


FIGURE 5-22 MASS LOSS RATE DURING ENTRY

- ρ = coating density = 100 lb/ft³
- $(\dot{M}/h)_{\text{Max}}$ = value of \dot{M}/h at time of peak reentry heating, dimensionless
- h_{Max} = value of surface heat transfer coefficient at time of peak reentry heating, lb/ft² sec
- t_{EQ} = equivalent exposure time at $(\dot{M}/h)_{\text{Max}}$ and h_{Max} for single mission = 987 seconds

The allowable total surface recession of 0.010 inch is considered to be a conservative value which would leave about one-half of the initial coating thickness remaining after N missions.

The resulting curve of N versus radiation equilibrium temperature is shown in Figure 5-23. Note that the radiation equilibrium scale corresponds to an emittance of 0.80, which is the reference value most commonly used in specifying temperature distributions on the Orbiter. Since the coating emittance has been measured to be about 0.90 or greater, as reported in Section 5.2.1, actual coating temperature is 80 to 115°F lower than the scale values, even excluding cross radiation and low catalycity effects. At the design heating condition, the peak radiation equilibrium temperature corresponding to $\epsilon = 0.80$ is 2780°F. The predicted high cross range mission capability at this temperature, excluding cross radiation and low catalycity is 47 mission. However, when cross radiation effects are included this is increased to 130 missions. With a mix of high and low cross range missions, total predicted mission life would increase appreciably.

The same procedure was used to predict mission life including low catalycity effects, except that the reduced surface temperature curve from the catalycity analysis, section 5.1.1, was used. This resulted in the relationship shown in Figure 5-24 between coating temperature and radiation equilibrium temperature. This relationship includes effects of low catalycity, cross radiation and coating emittance of 0.90. The resultant mission life prediction in Figure 5-23 indicates 100 mission capability at a peak radiation equilibrium temperature of 3070°F, which corresponds to a surface temperature of 2535°F on the coated material. The plasma arc test data points from Figure 5-20 are transposed onto the mission life curve in order to indicate the range of the curve established by the data.

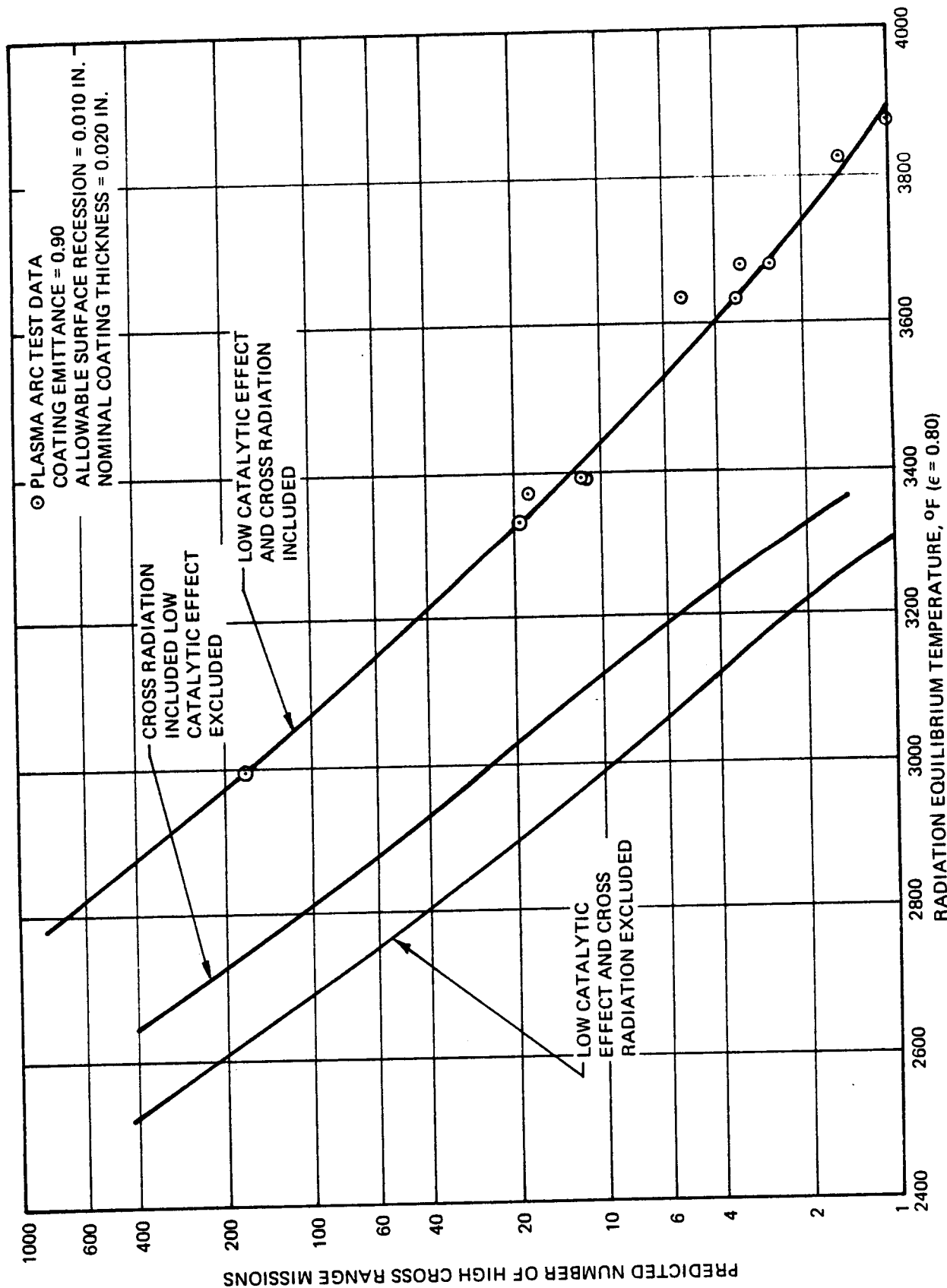


FIGURE 5-23 PREDICTED MISSION CAPABILITY HIGH CROSS RANGE MISSION FINAL EVALUATION DATA

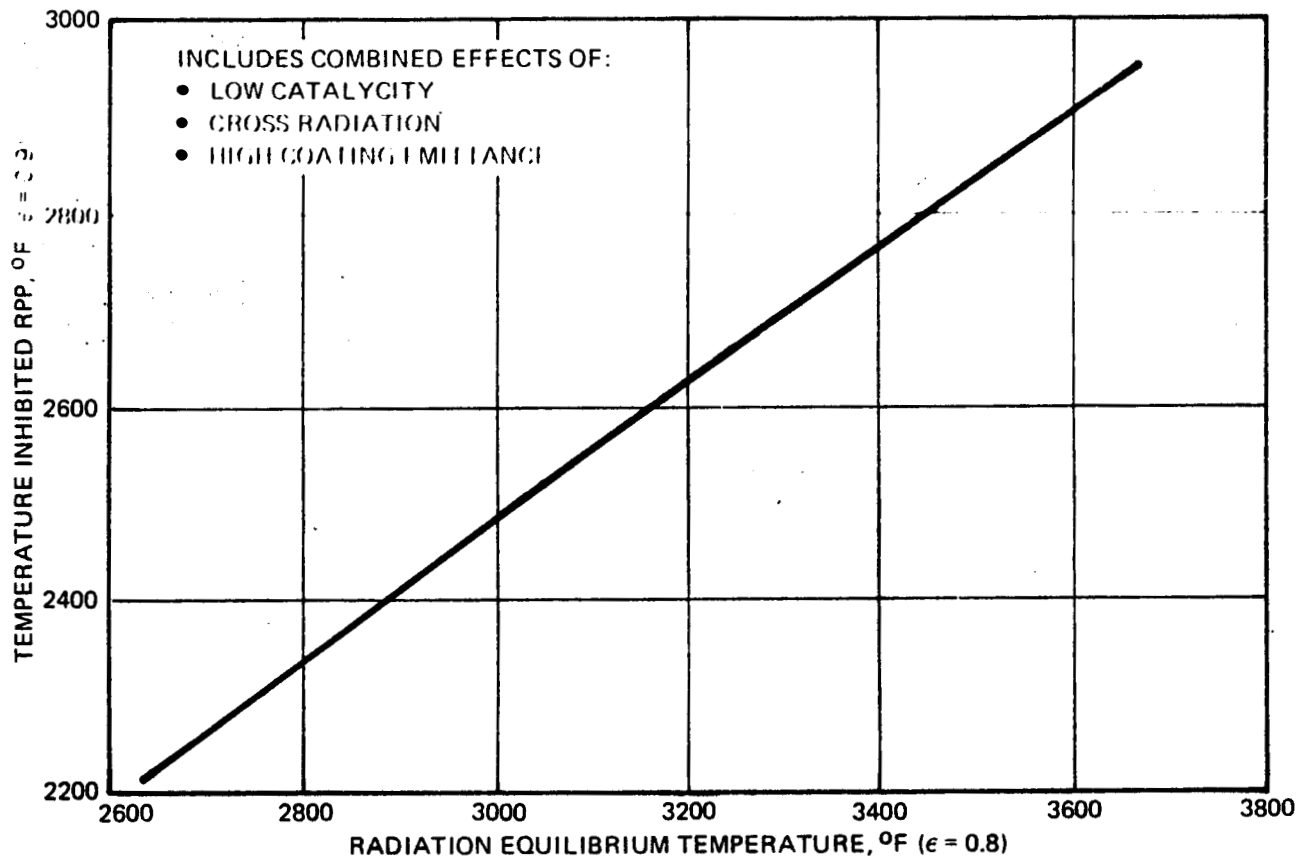


FIGURE 5-24 PEAK TEMPERATURE OF INHIBITED RPP DURING ENTRY VS PEAK RADIATION EQUILIBRIUM TEMPERATURE

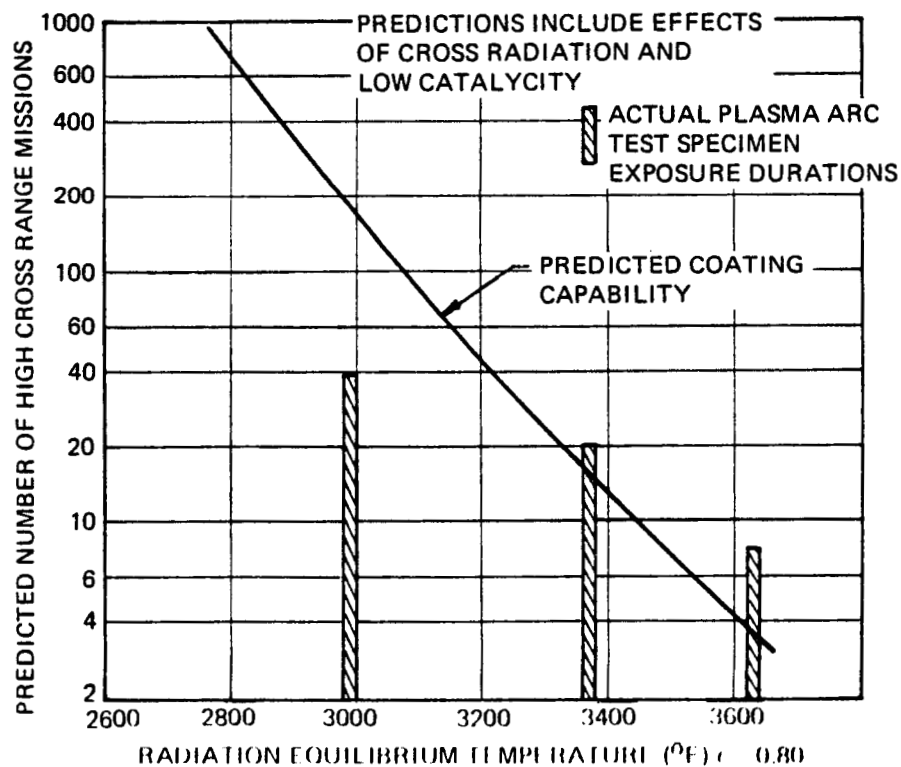


FIGURE 5-25 COMPARISON OF PREDICTED MISSION CAPABILITY WITH ACTUAL EXPOSURE TIMES HIGH CROSS RANGE MISSION

The mission life predictions are compared in Figure 5-25 with the maximum plasma arc test exposure durations. It is seen that specimens were exposed for equivalent numbers of mission cycles well in excess of the predicted curve at the higher temperatures.

The mission life predictions were used to establish an acceptable plasma arc performance for coated RPP. Acceptable performance was defined as an M/h versus temperature curve which results in 100 mission capability for the design heating trajectory, when cross radiation and low catalycity effects are considered. This curve is shown in Figure 5-20, where it is compared with mass loss rates for the heat treated 10/60/30 coating system. It is seen that margin exists to offset potential performance reductions, such as those due to aerodynamic shear.

5.2 PHYSICAL/MECHANICAL PROPERTIES

5.2.1 Physical Properties

Emittance, specific heat and thermal conductivity of the 10/60/30 coated RPP system were measured by Southern Research Institute. The data obtained are presented and compared to values used in thermal analyses, and the relation of each property to design is discussed. The implications of differences between the data and values used in analysis are discussed in section 3.4.

Since the bulk of incident heating is reradiated to space, surface emittance determines the temperature reached by the RPP skin at a given heating rate, and it is therefore of primary importance. Three specimens were included in the emittance measurements which covered the temperature range from 500 to 3150°F. Total normal emittance was measured by comparing the energy received by a radiometer from the sample to that of a black body cavity maintained at the same temperature. Results in Figure 5-26 show that emittance increases with increasing temperature from 0.85 at 500°F to 0.94 at 2000°F and then decreases to 0.90 at 3000°F. The uncertainty limits shown correspond to accuracy of temperature measurements. These measured values are significantly higher than the value of 0.85 used in thermal analyses, and will therefore significantly reduce peak surface temperatures.

Specific heat affects the transient temperature response of the RPP structure and is of secondary importance. A high value increases temperature gradients across ribs and support lugs, which is beneficial from the standpoint of minimizing attachment bolt temperatures; however, it also tends to increase thermal stresses. Nine specimens were included in the specific heat measurements, which employed an adiabatic calorimeter

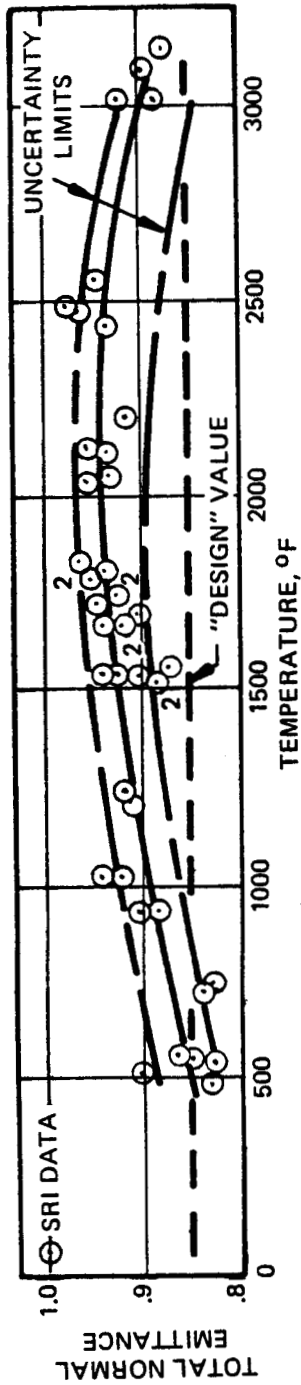


FIGURE 5-26 EMITTANCE OF COATED RPP

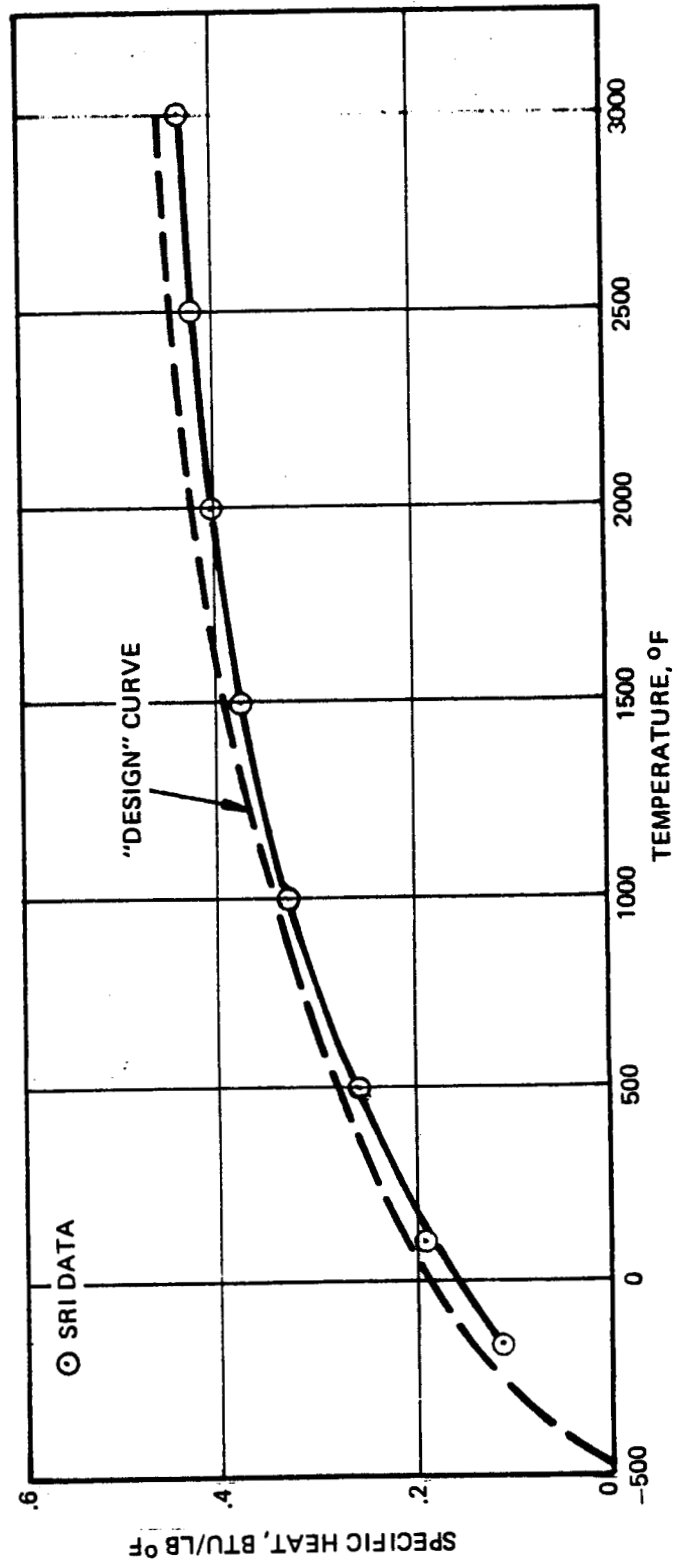


FIGURE 5-27 SPECIFIC HEAT OF COATED RPP

for the temperature range from -150°F to 1000°F and an ice calorimeter for 1000°F to 3000°F . Results in Figure 5-27 show that specific heat increases with increasing temperature from $0.12 \text{ BTU/lb}^{\circ}\text{F}$ at -150°F to 0.43 at 3000°F . These measured values are in good agreement with values used in thermal analyses. The overall uncertainties of the adiabatic and ice calorimeters are $\pm 3\%$ and $\pm 5\%$, respectively.

Thermal conductivity was measured in both the "parallel to lamina" and "normal to lamina" directions. Conductivity in the "parallel to lamina" direction affects transient temperature response of ribs and support lugs. A low value is desired in order to minimize temperature rise of attachment bolts. A high conductivity is desired in the "normal to lamina" direction in order to enhance heat conduction across the skin, which will in turn enhance beneficial cross radiation effects. Measurements were made with a comparative rod apparatus for the temperature range from -250°F to 1800°F and with a radial inflow apparatus for 1500°F to 3000°F . Uncertainty of the measurements is $\pm 5\%$ for the comparative rod and $\pm 12\%$ for the radial inflow apparatus.

Six specimens were included in the "parallel to lamina" measurements, with the results shown in Figure 5-28. Conductivity increases with increasing temperature from $40 \text{ BTU-in/hr ft}^{20}\text{F}$ at -250°F to 115 at 3000°F . It will be noted that one of the specimens had a slightly higher density than the others, which resulted in a significantly higher conductivity. It will also be noted that at 1500°F the measurements made with the two different devices are in substantial agreement. The measured values are about 40% below the value used in thermal analyses, which will reduce attachment bolt temperatures somewhat.

Seven specimens were included in the "normal to lamina" measurements, with the results shown in Figure 5-29. For the lower temperature measurements, six discs were stacked together in order to obtain a greater and therefore more measureable temperature difference across the specimen than would be possible with a single 16 ply thickness. Thin Grafoil was used between discs to minimize interface resistance. Conductivity increases with increasing temperature from a value of $16 \text{ BTU-in/hr ft}^{20}\text{F}$ at -250°F to 51 at 1500°F , and drops to 44 at 3000°F . It will be noted that measurements with the comparative rod and the radial inflow apparatus were overlapping in the 1500°F to 1800°F range, and that agreement between the two devices was good. The measured values are about 36% below the value used in thermal analyses, which very slightly degrades crossradiation effects.

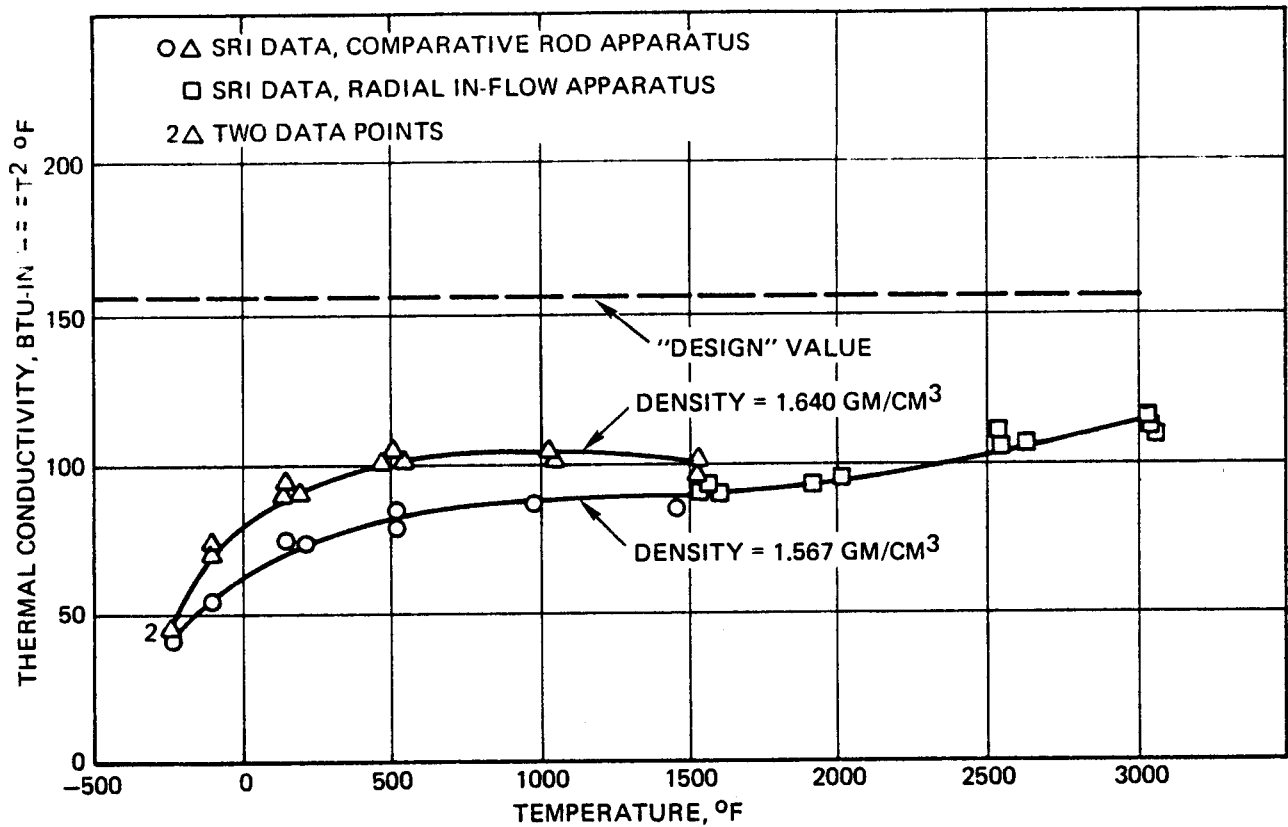


FIGURE 5-28 THERMAL CONDUCTIVITY OF COATED RPP PARALLEL TO LAMINA DIRECTION

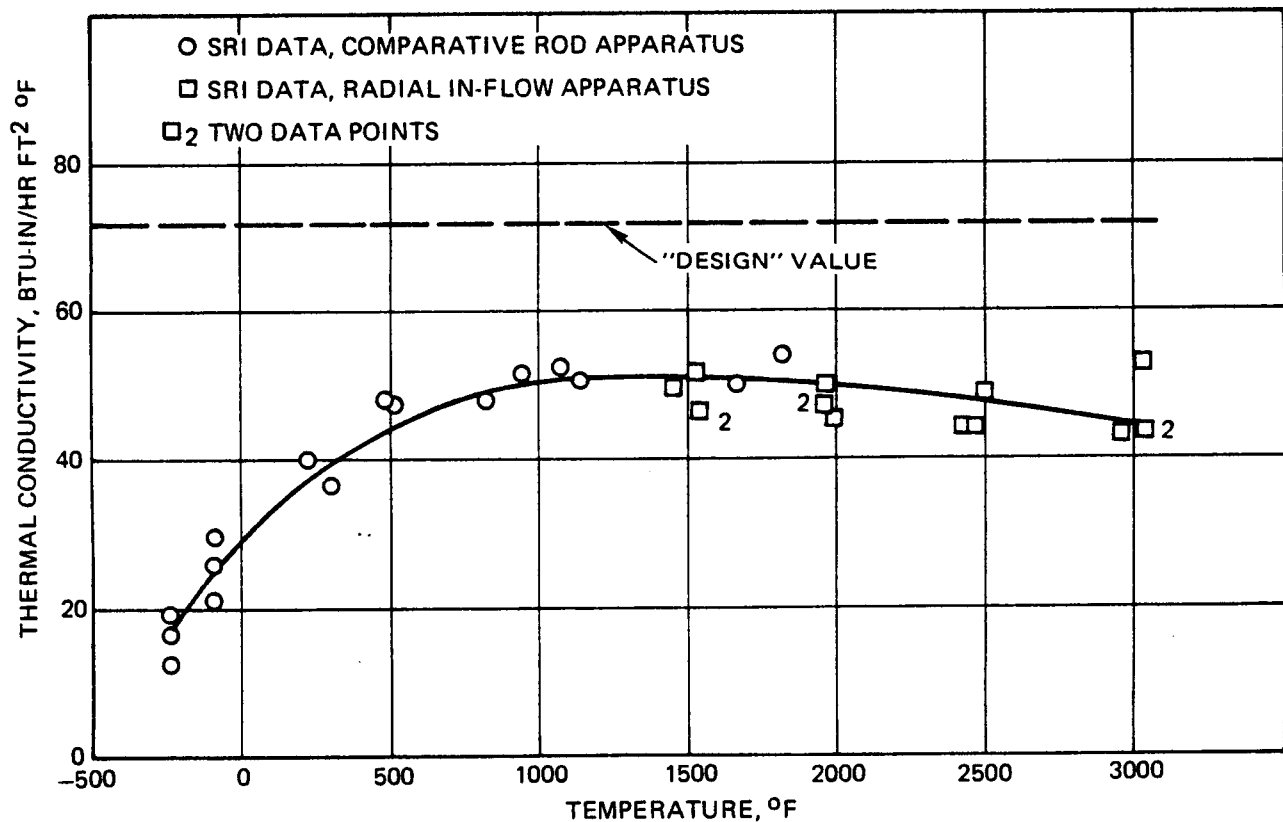


FIGURE 5-29 THERMAL CONDUCTIVITY OF COATED RPP NORMAL TO LAMINA DIRECTION

5.2.2 Mechanical Properties

Mechanical property data were obtained over a wide temperature range and broad spectrum of properties. This permitted evaluation of materials performance throughout the temperature region of application and to ferret out areas that might prove troublesome to successful performance of the material system. All data reported was obtained on coated material, since this is the condition in which the material will be employed and is also the lowest strength condition. Specimens were obtained from 13 ply parallel laminates, since fabrication of specimens from thinner, 9 ply, laminates resulted in warped and unuseable coupons. Elevated temperature static tests were conducted in an inert atmosphere to satisfy limitations imposed by graphite elements of the test facility. Also, testing under oxidation conditions would be meaningless unless mission life conditions were simulated. This was done in separate tests discussed in section 5.2.4. Testing was conducted by the following agencies:

Southern Research Institute (SRI)

Static strength at cryogenic, room, and elevated temperatures in tension, flexure, compression, interlaminar shear (compression-shear) and interlaminar tension.

Vought Aeronautics Company (VAC)

Fatigue testing in tension, flexure, inplane shear, interlaminar (short beam) shear, and interlaminar tension.

Vought Missiles and Space Company (VMSC)

Static room temperature strength in flexure, bearing, interlaminar (short beam) shear and inplane shear.

SRI employed tensile and compression test machines equipped with air bearings on the load grips to minimize misalignment and unwanted bending stresses in axially loaded specimens. A graphite resistance heater tube was employed for elevated temperature tests, where optical strain targets were also used. At cryogenic temperature, strain was measured by extensometer. Fatigue testing at VAC was conducted on Baldwin-Lima-Hamilton Sonntag test machines where the cyclic load, as opposed to deflection, is controlled by a rotating weight. VMSC tests were conducted on a Tinius Olsen tensile test machine. Deflections were recorded using a deflectometer with differential transformer sensor. Specimen configurations for these tests are given in Appendix B.

Strength levels obtained are highly encouraging and decidedly better than for material tested in Phase I. In contrast to Phase I material no low strength regions were noted. Fatigue in particular is outstanding, where applied stress levels exceeding anticipated limit load stress levels withstood beyond 10^6 cycles.

Static Strength - Static strength data for a number of properties is plotted on Figure 5-30 for test temperatures from -250°F to 3000°F . A few of the data points at 3000°F , identified with arrows, represent tests where either the test fixture failed or the specimen bottomed out on the fixture, but the specimen did not fail. The general trend of all properties, except compression in the fill direction, is to increase in strength at elevated temperature. The data obtained at -250°F also exceeds room temperature values so that room temperature strength is generally the lowest achieved. The curves through the test data are "eye balled" as opposed to being mathematically derived. The limited data at a given test condition (3 data points) does not justify a more sophisticated approach at this time.

As noted, only compression strength in the fill direction shows a reduction at 1500°F compared with that at room temperature. The reasons for this are not clear, but the preponderance of data on the other properties would suggest that in fact a reduction in strength may not exist and the difference obtained could be either the result of variations in specimens, specimen warp, or the test technique.

In general the scatter of data is not severe, especially at room temperature, where the leading edge design is critical. No data points fall outside of the range determined by a 33% reduction of typical values as was used in the prototype leading edge design evaluation discussed in Section 3.3.

From the test data and curves the following typical room temperature values (Table 5-2) are obtained. These are not necessarily the average of the room temperature test data but rather the values obtained from each curve fit. In some cases they are biased to the low side. All values are satisfactorily high so that lightweight structure may be designed.

The difference between the two interlaminar shear values is that the compression-shear approach loads a smaller area (see Appendix for specimen configuration) and can develop tensile stress components. The short beam shear value relies on the assumption of a $\frac{VQ}{I}$ beam shear stress distribution across the thickness. However, for the leading edge the lower of the two values may be employed without restriction to design.

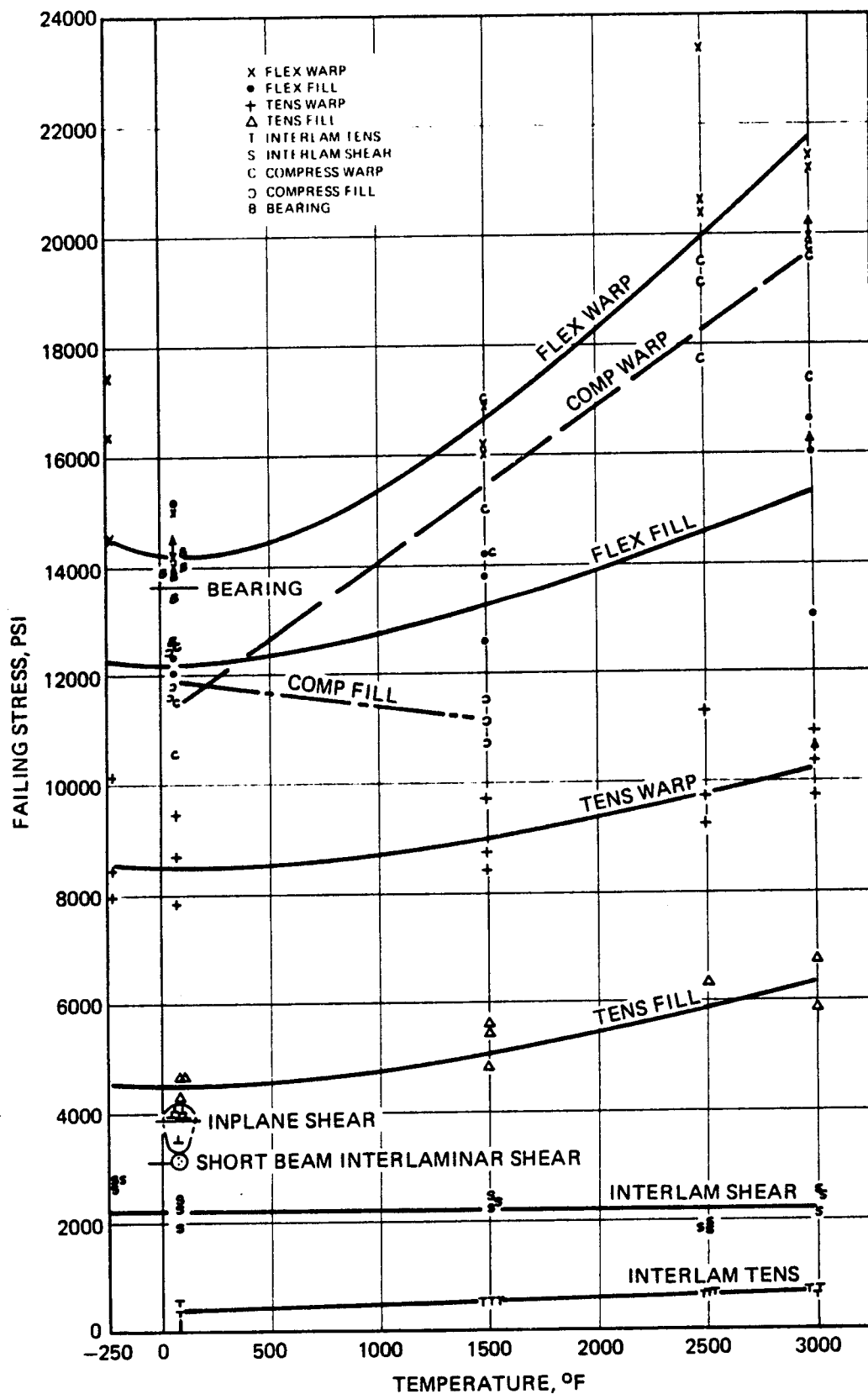


FIGURE 5-30 STRENGTH DATA SILICONIZED RPP HEAT TREATED 13 PLY

TABLE 5-2. TYPICAL ROOM TEMPERATURE STRENGTH VALUES
13-PLY SILICONIZED RPP

PROPERTY	ULTIMATE STRESS, PSI	
	WARP	FILL
Tension	8500	4500
Compression	11500	11900
Flexure	14200	12200
Inplane Shear	3800	3900
Bearing	13500	13800
Interlaminar Shear (Short Beam)		3100
Interlaminar Shear (Compression-Shear)		2200
Interlaminar Tension		400

Bearing, compression, and flexure stresses are high as anticipated. Tensile strength in the warp direction is satisfactory but the fill strength is lower than expected, possibly due to the slight bow in these particular specimens. Inplane shear stress is substantially higher than earlier predictions that were based on interlaminar shear strength. Thus, it appears that the cloth fibers are indeed contributing significantly to the shear strength of the laminate.

Elastic modulus data obtained from these tests are plotted in Figure 5-31. These show a general trend toward increasing modulus with increasing temperature up to about 2500°F, where the curves break over and the elastic modulus reduces. It should be noted that the material has been exposed to temperatures of 3100°F to 3400°F during processing so the reason for a reduced modulus above 2500°F is not clear. However, it has been observed that uncoated RPP shows like behavior in tension and flexure. A rather large data scatter is observed at -250°F where an extensometer rather than optical targets for strain measurement were used. This is believed to be the cause of the scatter, because VMSC has also had unbelievable strain data from extensometers used on RPP. Slippage may be the problem.

The fill direction compression modulus shows an increase with temperature even though the strength, as noted previously, decreases.

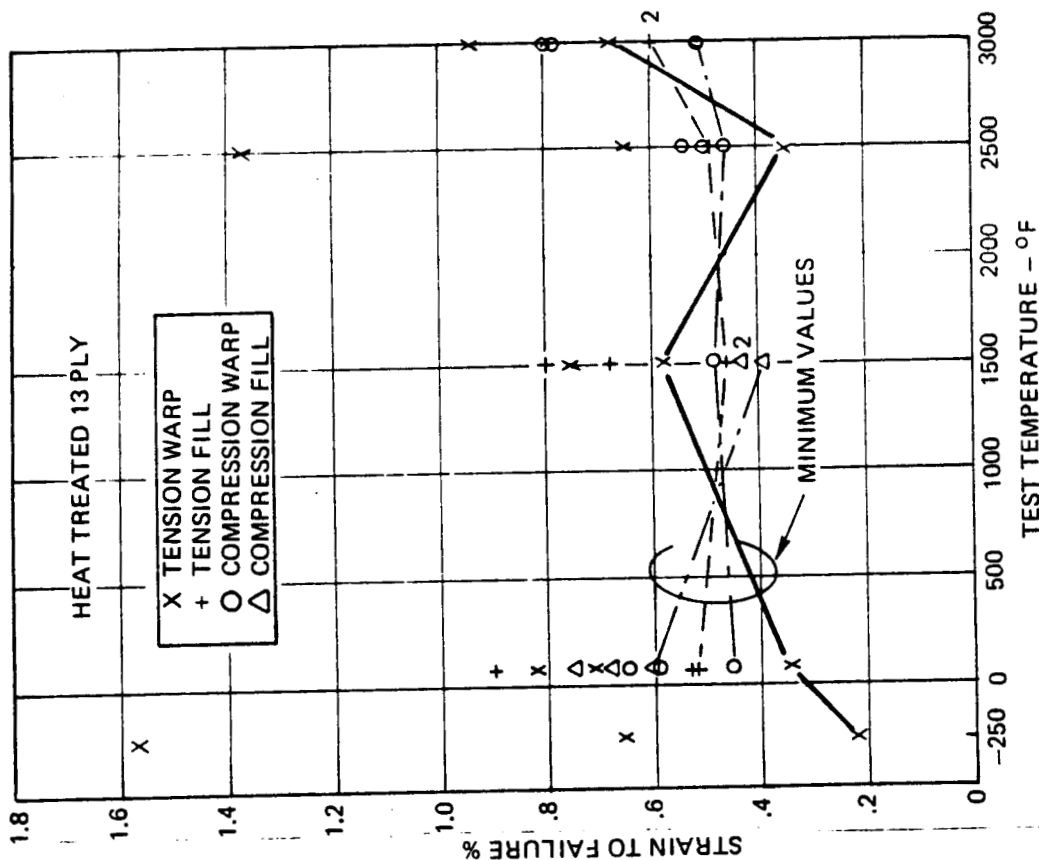


FIGURE 5-31 ELASTIC MODULUS SILICONIZED RPP HEAT TREATED 13 PLY

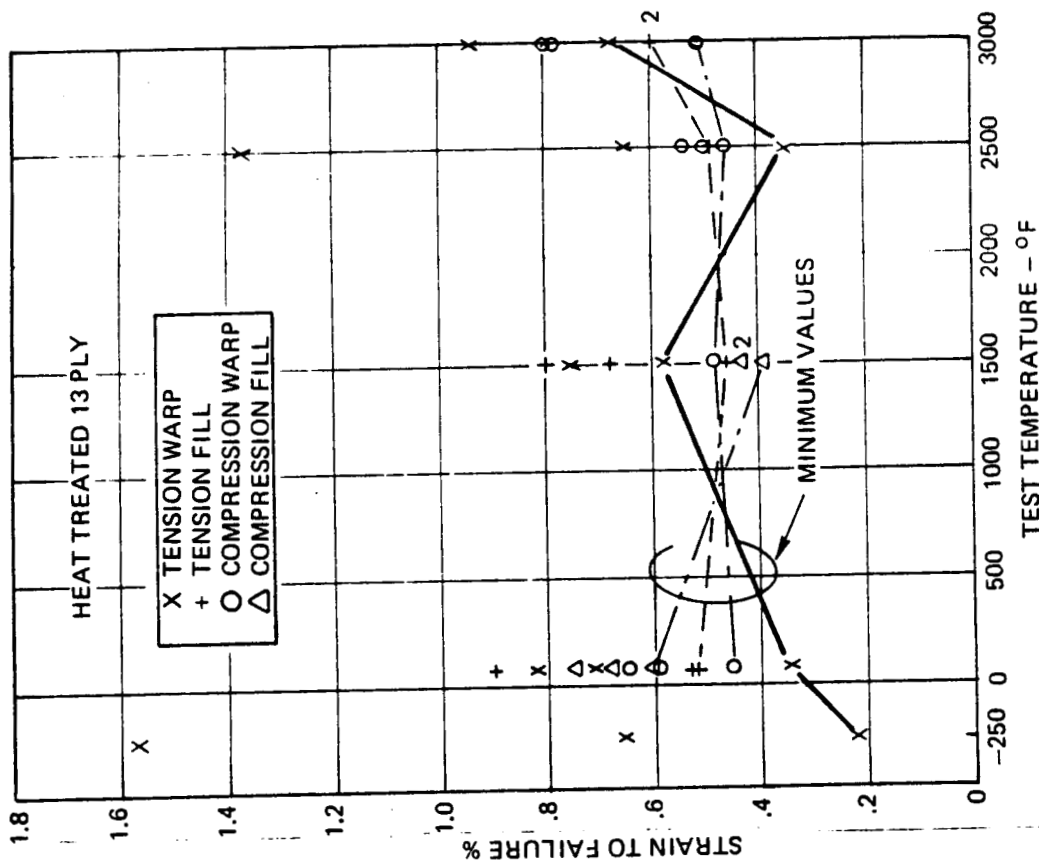


FIGURE 5-32 STRAIN TO FAILURE SILICONIZED RPP TENSION AND COMPRESSION

Tension modulus in the fill direction shows no tendency toward increasing with temperature, but this is not expected to be particularly significant for design.

Strain to failure is of interest to the designer and values have been obtained for tension and compression loads in both the warp and fill directions. These are plotted in Figure 5-32. The minimum values are indicated by the curves drawn through the lower boundaries of the data. At room temperature and above the minimum value is 0.35%. At cryogenic temperature only the tension warp values were obtained but these have a large scatter, varying from 0.22% to 1.57%. This ties in with the comments noted above on elastic modulus measurements at -250°F.

Poisson's ratio of 0.19 was determined by SRI on a coated tension bar loaded in the warp direction at 70°F. By comparison values of 0.23 and 0.20 were measured on bare material at 70°F and 2500°F, respectively. This is a reasonably acceptable value.

Typical stress-strain and load deflection curves for tension, compression and flexure are shown in Figures 5-33 through 5-35, respectively, for 70°F and 2500°F. Coating failure has not been observed to precede substrate failure, although for the high strain indicated for tension at 2500°F it may be possible to generate coating cracks before overall failure. This is rather academic, however, since in practice the maximum design limit stress would not exceed half of the failing stresses shown, because of factors applied to material properties and design loads.

Coefficient of thermal expansion (CTE) for siliconized RPP is relatively low and partly accounts for the low sensitivity to thermal gradients. For example, in the warp direction the CTE is only 1.7×10^{-6} in/in/°F. The difference between warp and fill expansion is only slight. Typical data is given in Figure 5-36 for both the warp and fill directions for 13 ply material. Data for uncoated RPP is shown for comparison. Indications are that coated material expands more in the warp direction than bare, but is little different in the fill direction. Data scatter is indicated by the difference between original and retest data.

Fatigue Strength - Fatigue data was obtained for tension, flexure, inplane shear, interlaminar shear and interlaminar tension. Warp and fill direction loadings were assessed. These tests were exploratory in an attempt to determine the significance of repeated cycling on coated RPP. Results were encouraging in that high stress levels can be applied, while still achieving over 10^6 load applications.

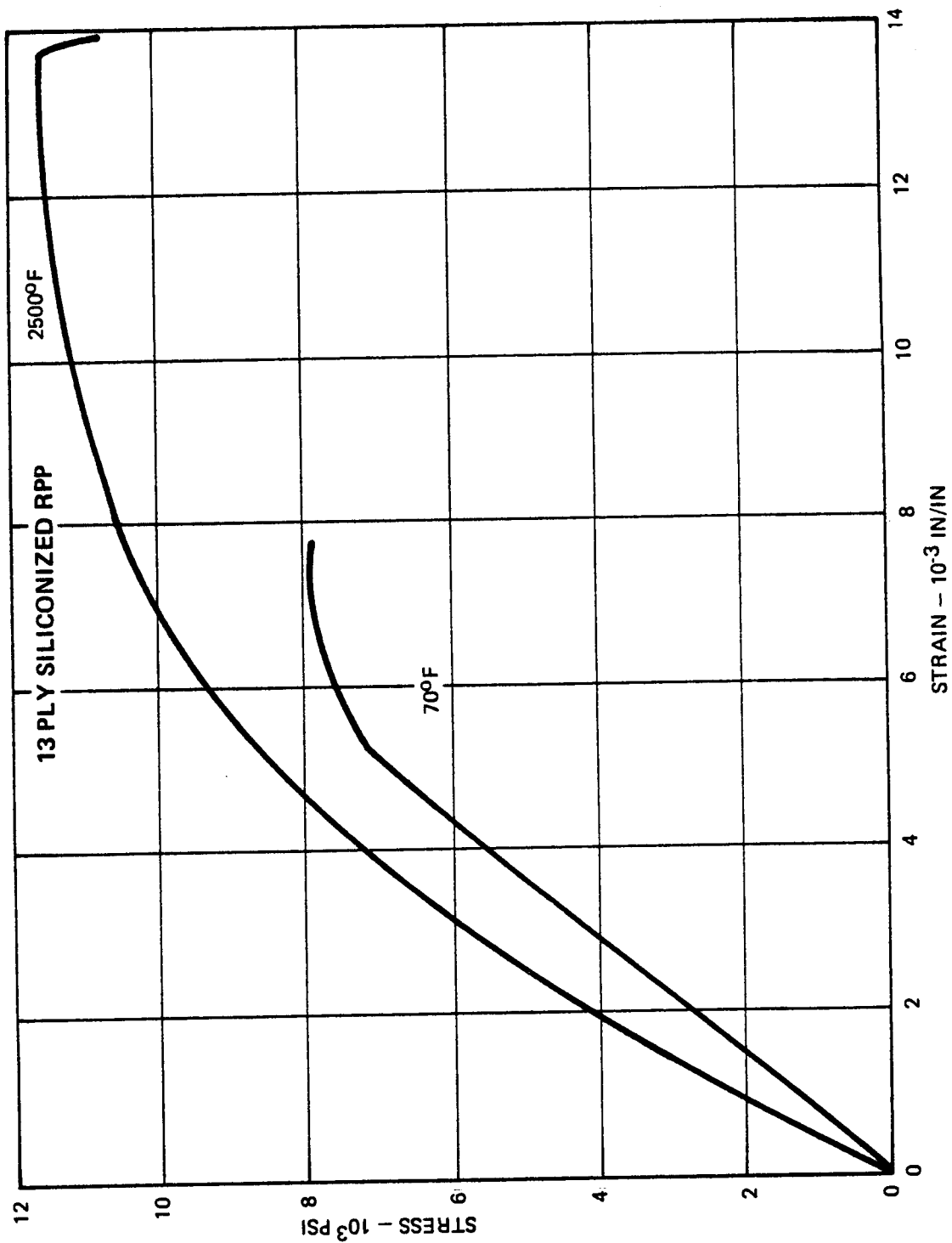


FIGURE 5-33 TYPICAL STRESS-STRAIN CURVES TENSION -WARP

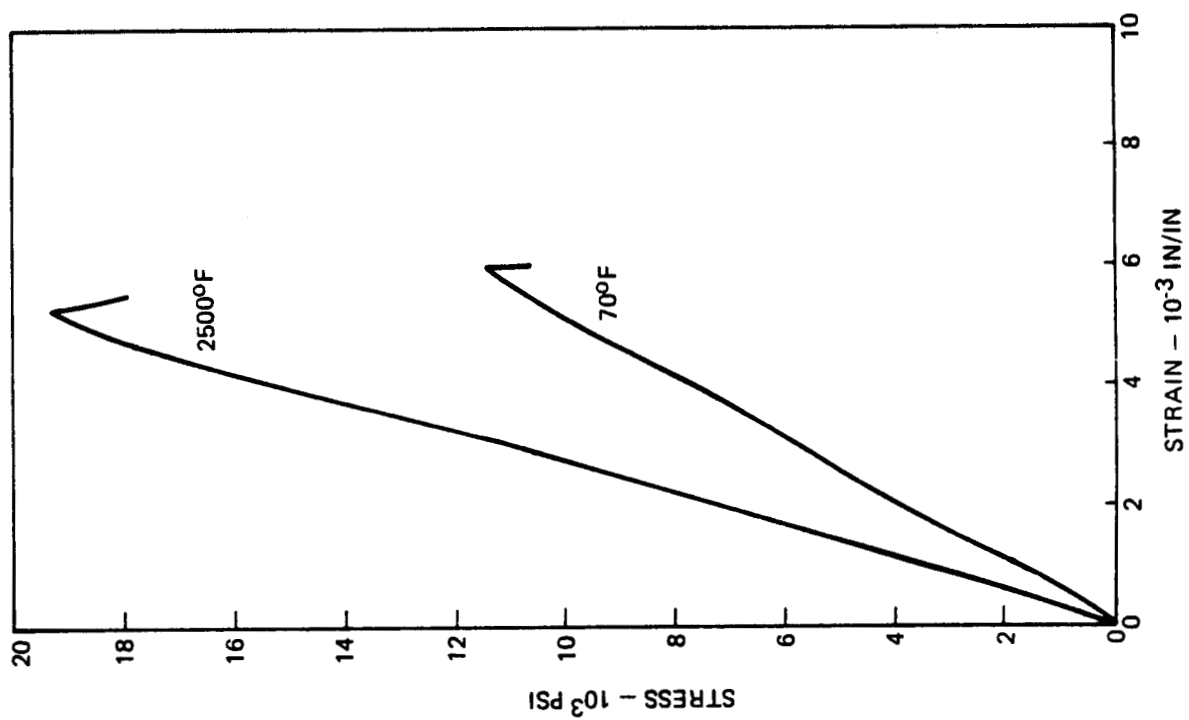


FIGURE 5-34 TYPICAL STRESS-STRAIN CURVES
COMPRESSION - WARP 13 PLY SILICONIZED RPP

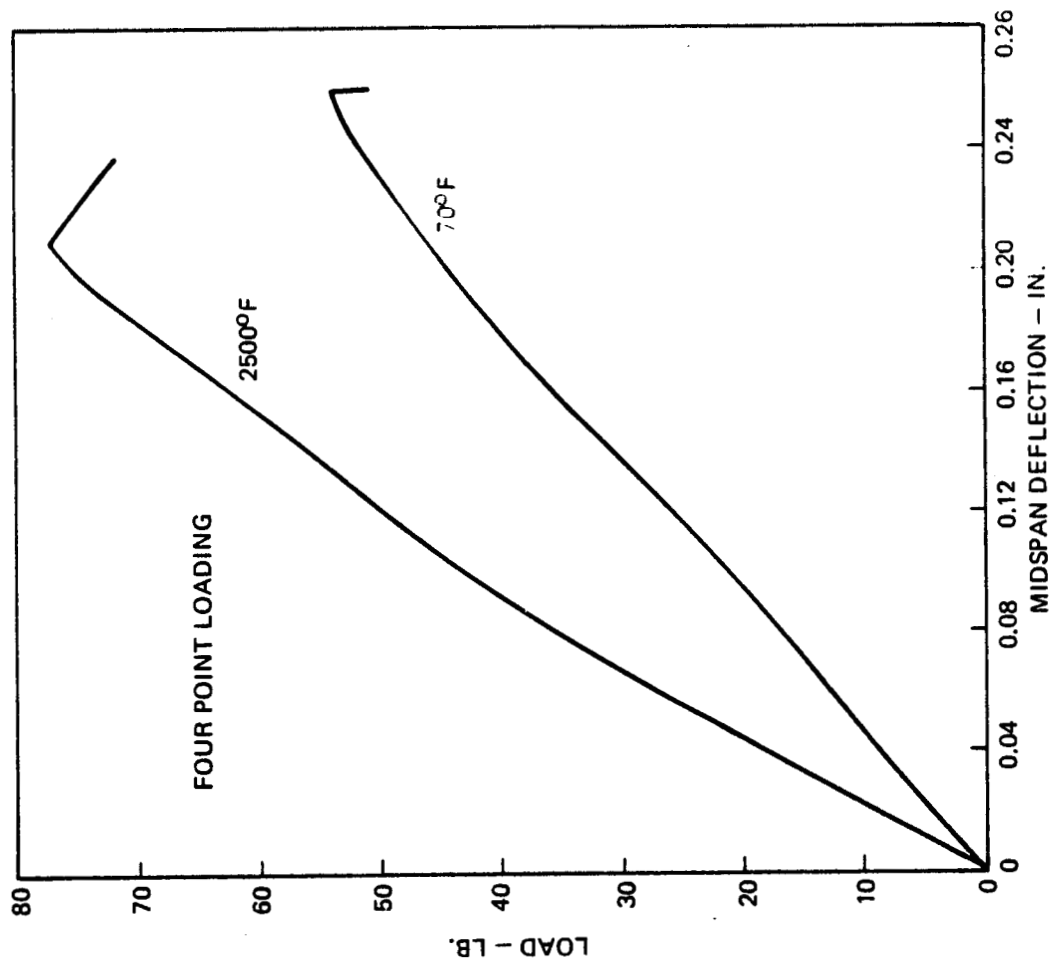


FIGURE 5-35 TYPICAL LOAD-DEFLECTION CURVES
FLEXURE - WARP 13 PLY SILICONIZED RPP

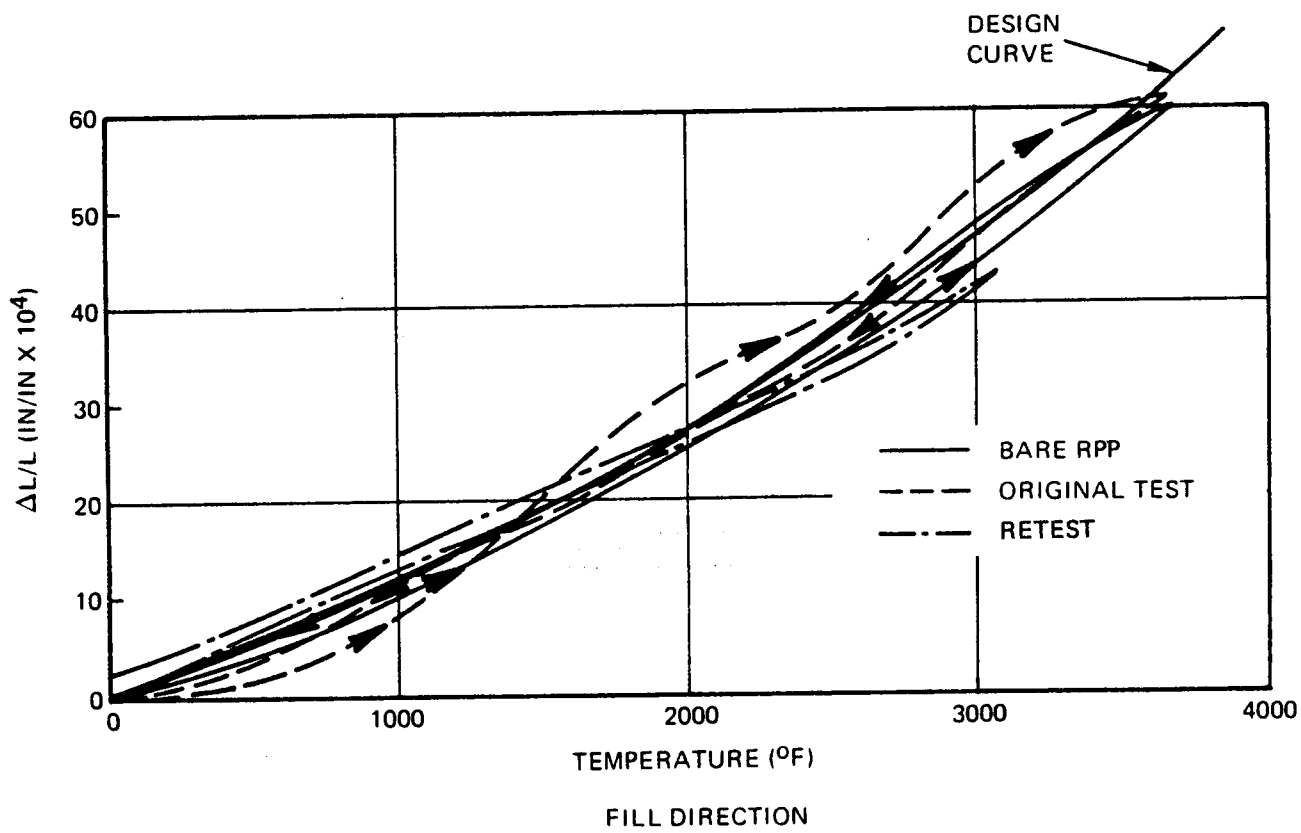
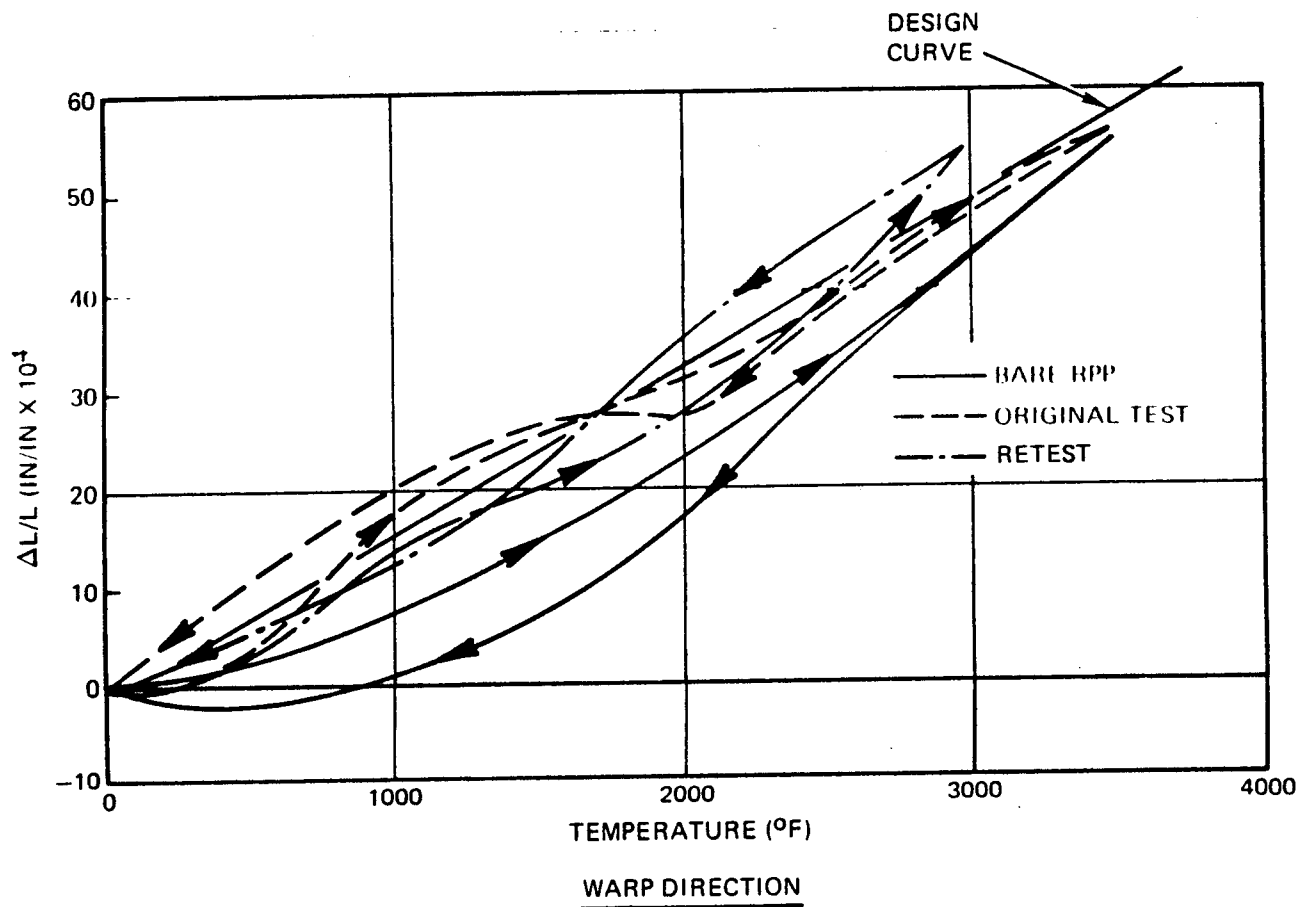



FIGURE 5-36 COEFFICIENT OF THERMAL EXPANSION SILICONIZED RPP

Data is presented in Figures 5-37, 5-38, and 5-39. Several items are particularly worthy of note. First, the transition between early failure and continuous operation is very abrupt. A 5% increase in load can cause the life limit to reduce from 10^6 cycles to less than 10^3 cycles. Also, a few of the high stressed flexure bars produced definite coating cracks (hidden under the load application points), which was classed as failure, but continued to carry the cyclic loads without evidence of general failure. Finally, interlaminar tension, which is probably the most severe loading that can be imposed on RPP, showed a resistance to fatigue failure ($> 10^6$ cycles) at stress levels up to 80% of the typical static failure stress of 400 psi.

On each of the figures a  symbol indicates the maximum limit load stress level that would be expected in any design. This value, 48%, is established assuming a 33% reduction of typical property data to produce design values and an ultimate factor of safety of 1.4. Note that the "endurance" limit lines are far in excess of the design limit stress level. When it is considered that for the Shuttle, limit stress would theoretically be applied on the order of only 100 times in its service life and that applied stresses with high numbers of cycles will be perhaps no greater than 25% (based on vibration analysis estimates) of typical failure stress then fatigue does not appear to be a problem with coated RPP.

Tension and shear fatigue data are shown on Figure 5-37. Applied cycles of up to 8.2×10^6 at 70% stress level were applied without failure. One tension specimen loaded in the fill direction failed after 103,000 cycles at 70% load, but none of the warp specimens failed at this level. If failure did not occur earlier, testing was terminated at the most convenient time above 10^6 cycles but some specimens were tested as high as 8×10^6 cycles.

No observable specimen or coating damage was noticed on the terminated specimens. Four specimens failed early in the test at load levels of 75% and 84%. The low number of cycles involved in these particular tests, and the rate of application (1800 cycles/min.), precluded an accurate assessment of the number of cycles applied. It is estimated that failure occurred at some point less than 1000 cycles. With the limited number of specimens tested the transition curve between 1 cycle (static failure) and the "endurance" limit cannot be established. Therefore the dashed line shown on the figures merely indicates that some unknown transition curve exists.

Three inplane shear specimens were tested, but on the first of these, the loading jig failed, destroying the specimen. The remaining two were cycled at a 70% stress level for 2.0×10^6 and 2.3×10^6 cycles before termination without failure or observable coating damage.

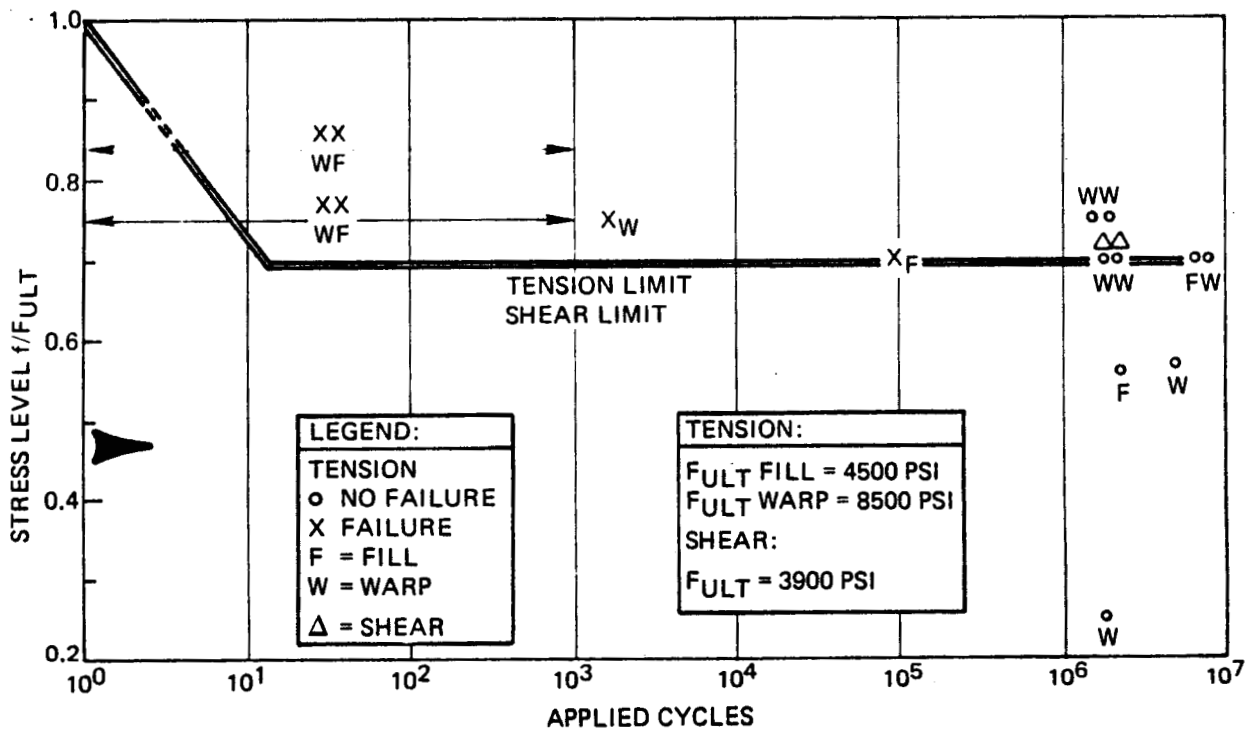


FIGURE 5-37 TENSION FATIGUE AND INPLANE SHEAR FATIGUE $R = 0$

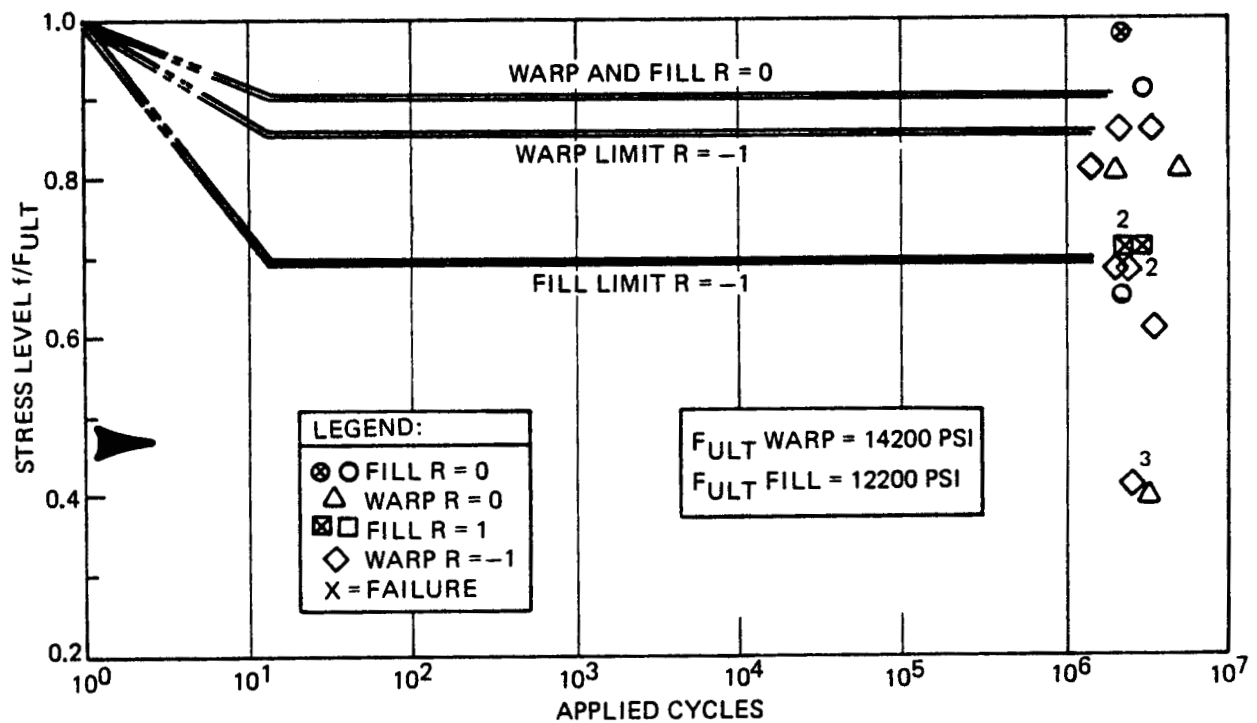


FIGURE 5-38 FLEXURE FATIGUE $R = 0$ AND $R = -1$

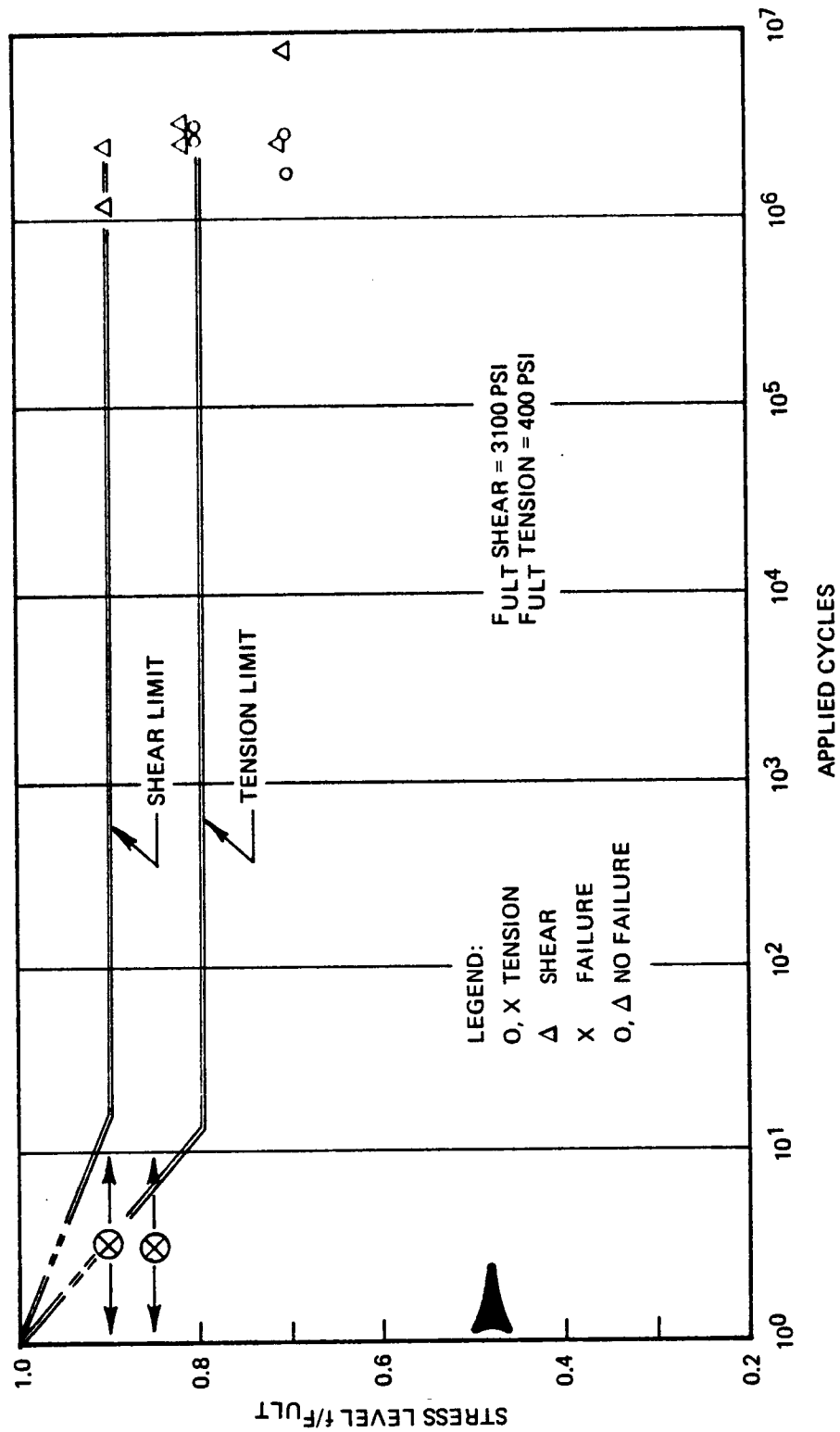


FIGURE 5-39 INTERLAMINAR FATIGUE STRENGTH $R = 0$

All of the fatigue testing except some flexure tests were conducted at load conditions that varied from essentially zero stress to the maximum level. This condition produces a load ratio R (minimum stress \div maximum stress) = 0. Completely reversed stress ($R = -1$), where the maximum compression stress equals the maximum tensile stress, is the most severe loading condition. Flexure fatigue response to this condition is exceptionally good as noted on Figure 5-38. Fill direction stress loading was found to be more severe than for the warp direction. Still, the fill flexure bars withstood in excess of 10^6 cycles under reversed loading at a stress level of 70% of static failure. This is substantially above the expected operating stress level for realistic design. Flexure bars cut in the warp direction withstood even higher stresses (85% of static) without failure. When the severity of testing was reduced to a stress ratio of $R = 0$, the level below which no failures occurred was raised to 90% of static failure.

With the high values being obtained on RPP, interlaminar shear stress is not significant for leading edge design. Fatigue data, shown in Figure 5-39, also indicates that interlaminar shear fatigue is no problem. No failures were obtained at stress levels up to 90% of static failure. These tests were conducted using the short beam shear specimen (Appendix B), the same as that used for VMSC static tests.

Interlaminar tension stress by contrast to interlaminar shear is an area for concern, because bending moments in corners (e.g., the intersection of the curved skin panel and support ribs) can produce relatively high interlaminar tensile stresses. Interlaminar tensile stress is the lowest strength direction of the laminate. It is therefore highly encouraging to find that the fatigue strength in this weak direction is so outstanding. No failures were incurred at stress levels of 80% of static failure when exposed to 2.4×10^6 and 2.6×10^6 cycles. When loaded to 85% and 90% failure occurred within approximately 10 cycles, the exact number being indeterminable. However, considering that a limit stress level not exceeding 48% of static failure is predicted, this critical loading condition appears to be safe from fatigue. This presupposes that corner material is adequately molded to produce sound material. The recognition of the need for sound corner material has prompted a tooling approach employing cast silicone rubber molds that will better ensure quality corners (reference discussion in Sections 7.1.2 and 7.2.1.)

It is logical to question the significance of fatigue loading on the static ultimate strength of the material. Several selected specimens, that had been fatigue loaded in excess of 1.7×10^6 cycles, were statically tested to failure to ascertain the magnitude of strength reduction, if any, after prior cyclic loading. The results were phenomenal. Of the seven specimens tested only one showed a strength reduction from typical values

and this 4.5% change could well have been within normal data scatter. All other failing stresses exceeded typical values obtained as part of the static test program discussed previously. Results are summarized in Table 5-3.

TABLE 5-3. STATIC STRENGTH FOLLOWING FATIGUE CYCLING

<u>Loading</u>	<u>Specimen No.</u>	<u>Stress Ratio, R</u>	<u>Nominal Stress Level, PSI</u>	<u>Cycles Applied</u>	<u>Static Failing Stress PSI</u>	<u>Typical Data Ref. Table 5-2, PSI</u>
Flexure	F-8	-1	5710	2.43×10^6	19000	14200
Flexure	F-9	-1	5710	2.50×10^6	20700	14200
Flexure	F-4	-1	5710	2.49×10^6	19600	14200
Flexure	F-19	-1	8570	3.32×10^6	19800	14200
Inplane Shear	S-8	0	2720	2.33×10^6	3630	3800
Interlam Tens.	TL-/1	0	280	1.74×10^6	702	400
Interlam Tens.	TL-/2	0	280	2.45×10^6	725	400

The indications are that fatigue cycling will not materially weaken the coated laminate, so that strength reductions for the 100 mission service life of the system from the fatigue factor will be minimal if at all.

5.2.3 Joints

The only primary structural joint on the current leading edge design is the support lugs. However, secondary bonding and riveting are also employed to attach trailing edge seal strips to the leading edge segments. For guidance in the design and analysis of these attachment techniques, typical joints were fabricated and structurally tested. In addition, although the concept is not specifically employed on the leading edge design, tension-angle tests were conducted to provide design flexibility to the designer. Tension-angle data may find application to forward fuselage panels or fin leading edge designs. Results of these element tests are summarized in this section. A discussion of the approach to fabrication of bonded and riveted joints is covered in Sections 4.2, 7.1.2, and 7.2.1.

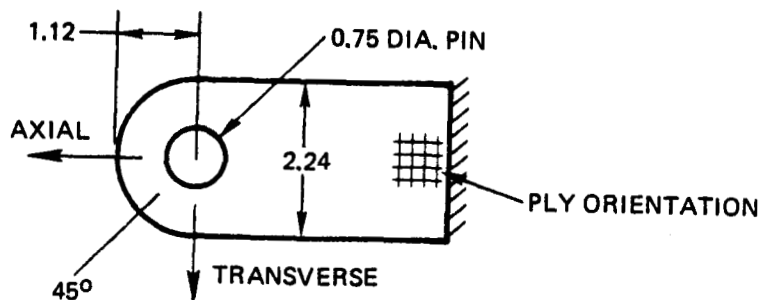
Lug Tests - Lug tests were directed toward the leading edge design concept, where a 0.75 in. dia. lug hole is employed and the layup is cross plied. Bearing stress data on a smaller diameter hole (3/16 in. dia.) is reported in Section 5.2.2.

Cross ply laminates were employed to produce more uniform strength independent of load direction. Laminates from which the lugs were cut were 13 ply in an effort to better correlate lug test results with the tension, shear, and bearing element test data which was also obtained for 13 ply laminates. Unfortunately, the coating depth on the lug specimens was about twice the desired thickness and the results cannot be correlated directly without assumptions on the effect of coating on strength loss.

The test data obtained and the specimen configuration are recorded in Table 5-4. Even with the deep coating (approximately 0.04 in.) the failing strengths for this 13 ply material are far in excess of the maximum ultimate lug load of 266 lb. for the Prototype leading edge, which is applied to 17 ply material.

TABLE 5-4. SUMMARY OF LUG TESTS
13-CROSS PLY LAMINATES

<u>Load Direction</u>	<u>13 Ply Laminate Thickness (In.)</u>	<u>Failing Load (Lb.)</u>
Axial	0.167	485
Axial	0.174	550
Transverse	0.158	603
Transverse	0.157	558
45°	0.154	520
45°	0.155	492



Flexure specimens coated with these lugs produced an average strength of 11550 psi, a 19% reduction when compared against 14200 psi from the SRI tests (Table 5-2). Assuming this ratio holds for tension data and the cross ply tension strength is an average of warp and fill directions, values of $K_t = 0.4$ for axially loaded, and $K_t = 0.9$ for transverse loaded lugs are computed, where K_t is defined as follows:

$$\text{Axial } K_t = \frac{\text{Failing Load}}{\text{Ultimate Tensile Stress} \times \text{Net Tension Area}}$$

$$\text{Transverse } K_t = \frac{\text{Failing Load}}{\text{Ultimate Tensile Stress} \times \text{Average Tension/Shear Area}}$$

It appears that the coated RPP behaves about the same as sand castings in terms of strain concentration effects.

Typical lug failures for the axial, 45° and transverse cases are shown in Figure 5-40. Note that the transverse loaded specimens failed but did not completely separate as the axially and 45° loaded lugs did.

Tension-Angle Tests - Tension angle tests were conducted with parallel and cross ply 17 ply angle specimens with both rectangular washers and washers fitted into the corner radius of the angle. Tension bolt of 1/4" dia. and 1.0 in. wide steel washers were used in the tests. The opposing angle was 0.25 in. thick steel to ensure stiffness. The RPP angle specimens were 1.5 in. long. During test it was noted that the specimens deflected considerably in the spanwise direction, which tended to peak the loads at the bolt location. The effective width of the specimen is probably closer to 1.0 inch rather than the 1.5 in. tested.

A summary of the test data is given in Table 5-5 while photos of the angles after test showing the mode of failure are given in Figures 5-41 and 5-42.

TABLE 5-5. TENSION ANGLE TEST DATA

Direction of Plies	Washer Thickness (In.)	Type Washer	Distance, Edge of Washer To Face of Angle (In.)	Failing Load (Lb.)
Parallel	0.06	Rectangular	0.12	448
Parallel	0.06	Rectangular	0.12	499
Cross	0.06	Rectangular	0.12	487
Cross	0.06	Rectangular	0.12	423
Cross	0.12	Fitted	0	514
Cross	0.12	Fitted	0	638

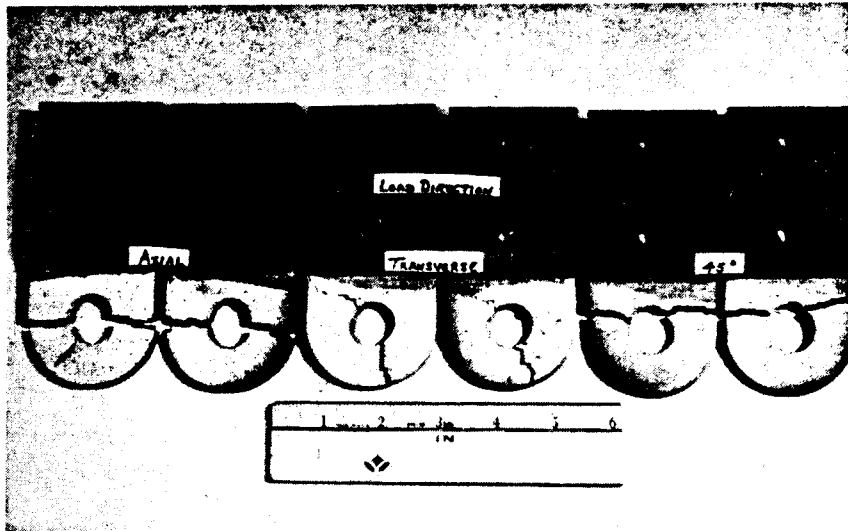


FIGURE 5-40
FAILED LUG
SPECIMENS



FIGURE 5-41
FAILED TENSION
ANGLES – TESTED
WITH WASHER
FITTED TO RADIUS

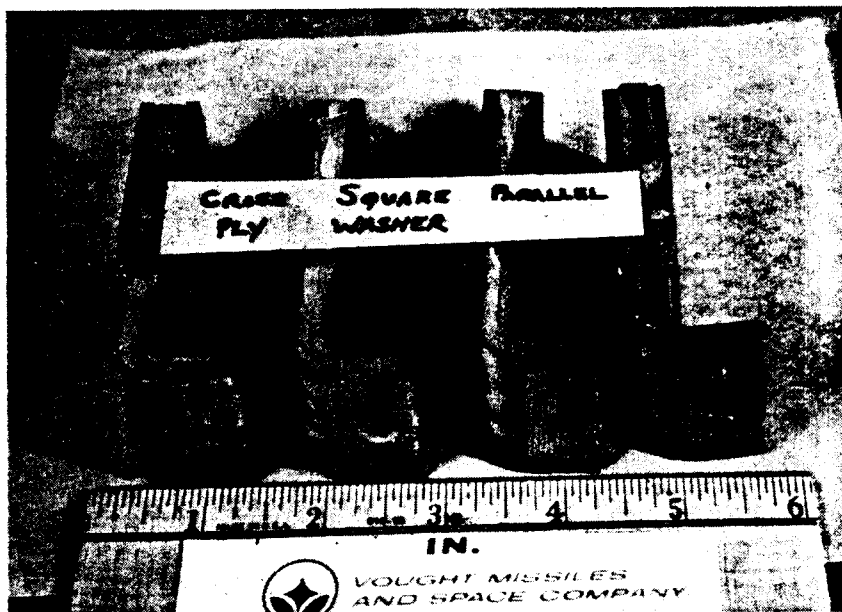


FIGURE 5-42
FAILED TENSION
ANGLES – TESTED
WITH SQUARED
WASHER

The difference between parallel and cross ply laminated angles is not significant as indicated in Table 5-5. The advantage of a thicker and fitted washer is clear from an examination of the data, where the average failing strength is 26% higher than for the cross specimens using the thinner rectangular washer. This is expected.

Failure of the tension angle specimens with rectangular washer typically originated at the inside radius of the angle, propagated to the outside radius and ultimately cracked across the bolthole on a line normal to the angle radius. Failure at the inner radius is prompted by the opening of the corner angle as the specimen deflects under load. With the fitted washer failure occurred in the radius as with the others and also failed through the bolt hole, but parallel to the mold line.

Bonding Tests - Bonded joints are discussed in Section 4.2, where it was noted that bonding in either the as-molded state or after initial pyrolysis are feasible techniques. For leading edge and wing tip panel fabrication, VMSC employed the as-molded bonding approach. These data are reproduced in this section so that typical property data for design application can be located in one section.

Data obtained on bonded specimens are summarized in Table 5-6. These specimens were molded and cured, bonded using WCA prepreg fabric as a scrim cloth with additional R-120 resin applied, recurred, and then pyrolyzed and strengthened by the reimpregnation-repyrolysis approach.

Bond tension strength was obtained with 1.60 in. dia. discs; shear strength was determined with 1.0 in. wide single lap 13 ply laminates, having a 0.5 in. width bond; tension angle data employed 9-ply back to back angles bonded to a 13 ply base plate; and tension peel tests were made with 9 ply back to back bonded angles. Specimen configurations are illustrated in Table 4-4.

Flatwise tension strengths are quite high and are in the range of interlaminar tensile strength values of the laminates. Single lap shear strength is relatively low because considerable rotation of the joints occurred, inducing tensile stresses that lower the average failing stress. With the impressive tensile strength performance there is reason to believe that double lap shear stress values in the 2000 psi range are probable.

Back-to-back tension angle strength is naturally considerably lower than flatwise tension because of the eccentricities and induced peeling loads. Average values are therefore only 1/4 of the flatwise tension values. The significance of peeling stresses is noted by the low peeling loads obtained in the tests. This indicates that this type of design is to be avoided. However,

TABLE 5-6. BONDED JOINT STRENGTH

<u>Type Test</u>	<u>Avg. Failing Load (Lb.)</u>	<u>Average ($\frac{P}{A}$) Failing Stress (PSI)</u>
Flatwise Tension	844	422
	996	498
	988	494
Single Lap Shear	381	762
	386	773
	420	840
Tension Angle	206	103
Back-to-Back	244	122
	208	104
Tension Peel	36	36
	24	24
	20	20



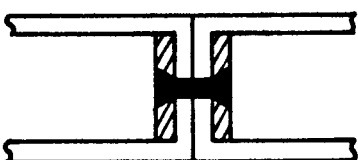
when using back-to-back angles, a viable approach should be possible if care is taken to minimize peeling tendencies. This may involve tapering the legs of angles, using thicker laminates to reduce deflections, and scarfing the thickness at the bond line to obtain flexibility at the edge of the bond. This should reduce stress concentration and peel.

A redundancy feature that can be employed is the introduction of RPP rivets with the bonded joints. These serve two functions: first, they act as tools to clamp the bonded surfaces during fabrication, and second, they service as peel stoppers in the event peel is initiated. Rivets were used in this capacity on the Prototype leading edges. Typical strength data on rivets is given below.

Rivet Tests - The method of fabrication of RPP rivets is covered in Section 4.2. Typical data obtained from rivet tests are included herein primarily to illustrate the potential of rivets. Both shear and tension tests were performed. WCA cloth and various continuous fiber materials were used. Results are shown in Table 5-7.

The single lap shear strength was accompanied by tensile stress components because of joint rotation. Double lap shear stress in the 2000 psi range is noted to be possible while tensile stresses over 1000 psi

TABLE 5-7. TYPICAL RPP RIVETED JOINT STRENGTHS

<u>Configuration</u>	<u>Rivet Material</u>	<u>Failing Shear or Tensile Stress (PSI)</u>	<u>Failing Load (Lb.)</u>
 1/4" DIA RIVET 18 PLY STOCK	WCA	1153	226
	Cloth	1429	280
 3/8" DIA. RIVET 13 PLY STOCK	Hercules HTS	2045	450
	Hercules HMS	1045	230
 3/8" Dia Rivet 13 Ply Stock	Hercules HTS	627	69
	HTS	1125	124
	Hercules AS	1155	127
	Hercules HMS	1580	174

appear feasible. While these values are not spectacular, they represent initial fabrication trials and are sufficiently high to function in conjunction with bonded joints in the redundancy capacity noted above. With modest development it is believed that shear stresses in the 3000 psi range are practical. Predictions on tensile stress projections cannot be made at this time.

5.2.4 Thermal/Oxidation Cycling

In Phase I and in Phase II development tests in a preheated air furnace was used for cycling specimens through the room temperature to 2300 - 2500°F temperature range to obtain a "feel" for thermal/oxidation resistance. This test, which generally consisted of five thermal cycles, each composed of 10 minutes in the hot furnace and 10 minutes outside while cooling, is at best qualitative. There is no way to obtain a direct relation between the furnace test and the effects of the flight environment for 100 missions without having tested specimens to a simulated environment for the required cycles. The furnace test is employed mainly as a comparator of current coating performance to past performance. On the basis of oxygen availability alone it can be estimated that the five cycle test represents upwards of 200 missions, and based on plasma test weight loss could represent even more (reference Section 4.3.2).

In order to establish a more quantitative test a radiant lamp facility was constructed that would operate at reduced oxygen pressures by controlling the nitrogen-oxidation balance to those typical of entry, and permit the application of 100 cycles of a thermal/oxidation environment. The schematic of this facility is given in Figure 5-43.

Specimen temperatures were controlled automatically to follow an entry profile using thermocouples mounted in dummy coated RPP specimens, and a drum programmer which controls the heat lamp power supply. Temperatures up to 2850°F were obtained.

A closed cycle gas flow system was used for economy of operation, and oxygen concentration was controlled to simulate entry oxygen partial pressure. An oxygen analyzer measured O_2 partial pressure, which was controlled manually by adjusting flow rate of O_2 makeup gas. The O_2 makeup replenishes oxygen consumed by the test specimens as well as oxygen which leaks out of the flow system. Nitrogen makeup gas was also provided. A blower was used to circulate the gas at a velocity of 14 ft/sec over the specimen surface. Higher velocities to 45 ft/sec were possible but small specimens cannot be retained in place at the higher velocities. Calculations of oxygen consumption rate indicated that the 14 ft/sec velocity would prevent excessive reduction of oxygen concentration at the specimen surface due either to streamwise concentration gradients or to gradients across the boundary layer. In fact, velocities as low as 5 ft/sec could be tolerated. In order to assure uniformity of flow and heating over the specimens only the central portion of the test section was utilized, and a boundary layer development section was provided upstream of the test section. A heat exchanger was employed to remove heat transferred to the gas in the test section.

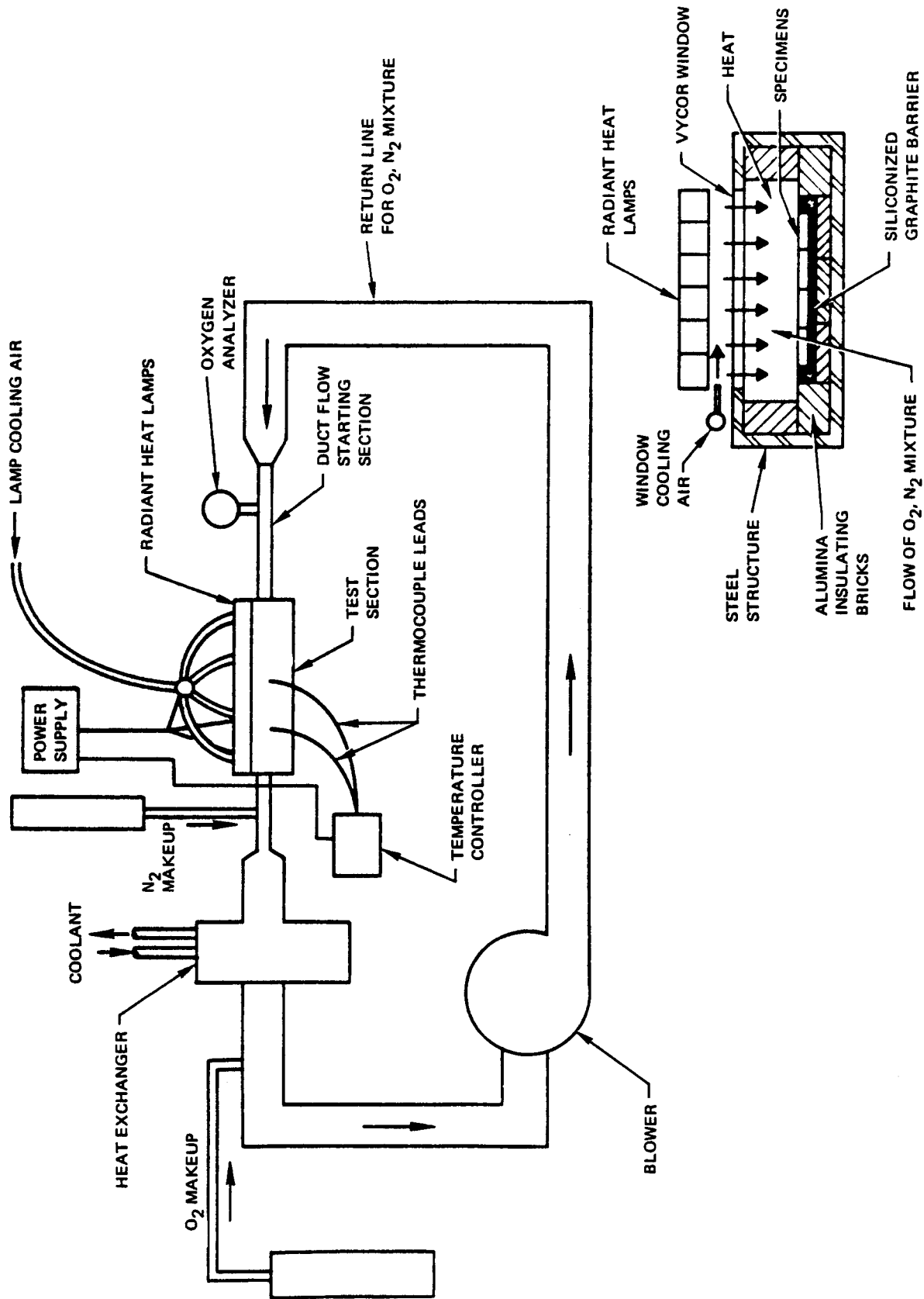


FIGURE 5-43 MISSION THERMAL AND OXIDATION SIMULATOR

Two 10.5 x 10.5 in. windows of high silica glass were positioned between the heat lamps and the test section to seal out lamp cooling air. The test section was lined with alumina insulating bricks to minimize heat losses and a siliconized graphite barrier was placed between specimens and the brick to prevent chemical reaction with the specimen coating.

The time/temperature profile employed in the test was for the high cross range mission. Specimens were brought to the maximum temperature of 2600°F in approximately 5 minutes and held for 15 minutes before reducing temperature. The total cycle was 45 minutes duration. The 2600°F limit was imposed to ensure good lamp life but this temperature is also consistent with the maximum leading edge temperature computed in Phase II, considering internal cross radiation, but excluding low catalytic effects.

Oxygen partial pressure was limited to a maximum of 0.3% to provide an average value for the entry profile. This level was monitored by two instruments upstream of the specimens.

Specimens were cycled for 60 simulated missions with a flexure bar removed and tested after each 20 cycles. Strength after 20 and 40 missions remained high at 13053 psi and 12858 psi respectively. (These specimens had edge coating which reduces apparent strength as compared with the specimens used for design data). However, it was discovered at the 60 cycle checkpoint that air leaks around the Vycor windows was causing excessive subsurface oxidation when the strength fell to 10018 psi. A mapping of the weight losses of the specimens located under each window revealed that significantly higher weight losses were experienced near the window seals than in the center of the window. Since most of the specimens had some portion exposed to the higher oxidation rate, it was pointless to continue the test and all specimens were scrapped.

Efforts to seal the windows in a positive manner were fruitless because when an effective seal was made, the thermal gradients and restraint caused the Vycor windows to crack. Repeated attempts to solve this problem were unrewarding and little confidence existed that the problem could be solved without major rework, high risk, and unacceptable delays. This test facility was therefore abandoned and a new approach was devised.

Since the thermal test rig (Section 7.2.2) proved so successful in the Prototype leading edge entry temperature test, it was decided to adapt this setup for thermal/oxidation cycling tests. The graphite heaters were reconfigured to provide a flat rather than curved heater and installed

into a vacuum chamber that was operated at 3 psig. The installation is pictured in Figure 5-44. A blower and duct arrangement produced air velocity of 17.5 ft/sec hot. Make up oxygen and nitrogen were added to the chamber in a proportion to limit the oxygen partial pressure to the 0.3% desired. Flow rate was such that the 100 ft³ chamber environment was changed in 20 minutes. Oxygen partial pressure was monitored by a gas chromatograph. The temperature profile and controller were the same as that for the radiant lamp facility.

The test environment is illustrated on Figure 5-45. Temperature was controlled to the profile shown with slight roundoff at the corners. Average gas chromatograph readings over the 100-cycles indicate that the oxygen partial pressure varied as noted by the curve labeled "O₂ Test". Computations of the O₂ environment during entry are shown for comparison. It can be seen that O₂ availability during test was conservative during the early portion of entry with the cross over occurring at 18 minutes. Testing was unconservative during the latter portion of the simulated entry condition, but, when it is considered that significant oxidation should occur only above 1000-1500 °F, the average O₂ availability in test represented a good simulation of flight. These temperature/oxidation conditions were applied to the test specimens for 100-cycles.

Specimens tested were from a number of different coating runs and included both heat treated and non heat treated specimens. Test results obtained by VMSC following the 100-cycle exposure are given in Table 5-8. A comparison of this data with the as-fabricated strength given in Table 5-2 and Figure 5-30 reveals that little or no strength loss within expected data scatter is evident in the flexure strength. Compression strength is actually higher than that obtained on as-fabricated material. This, however, is attributed to data scatter or test technique rather than environmental effects.

Note also that non heat treated material behaves similarly to the heat treated material and shows a slightly higher strength after oxidation exposure than the heat treated material. Based on Pereny furnace test data, this is not surprising.

One important aspect to note from these tests is that in this test and the aborted radiant lamp cycling test, little or no coating thickness loss was in evidence (reference Table 5-8). This is because molecular oxygen is less prone to attack the silicon carbide coating and therefore is available to permeate through the coating to oxidize the substrate. Atomic oxygen on the other hand is reactive with silicon carbide, and if this reaction occurs, there is less oxygen available to attack the substrate. To compare molecular against atomic oxygen reactions, a flexure bar was exposed in a plasma arc at 2600 °F surface temperature for 7.1 hours and at a pressure to simulate

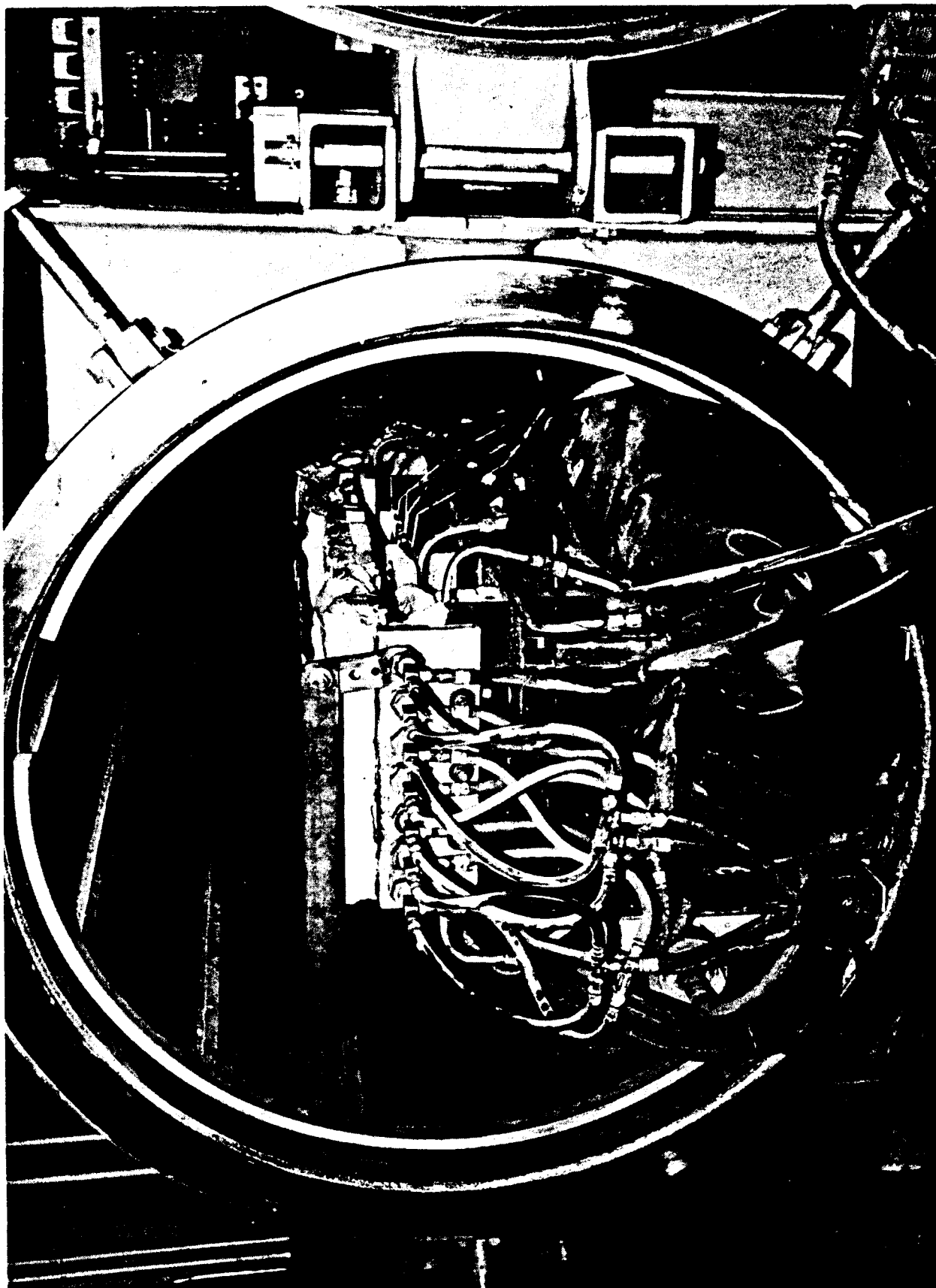


FIGURE 5-44 THERMAL/OXIDATION TEST FACILITY UTILIZING GRAPHITE RESISTANCE HEATER ELEMENTS

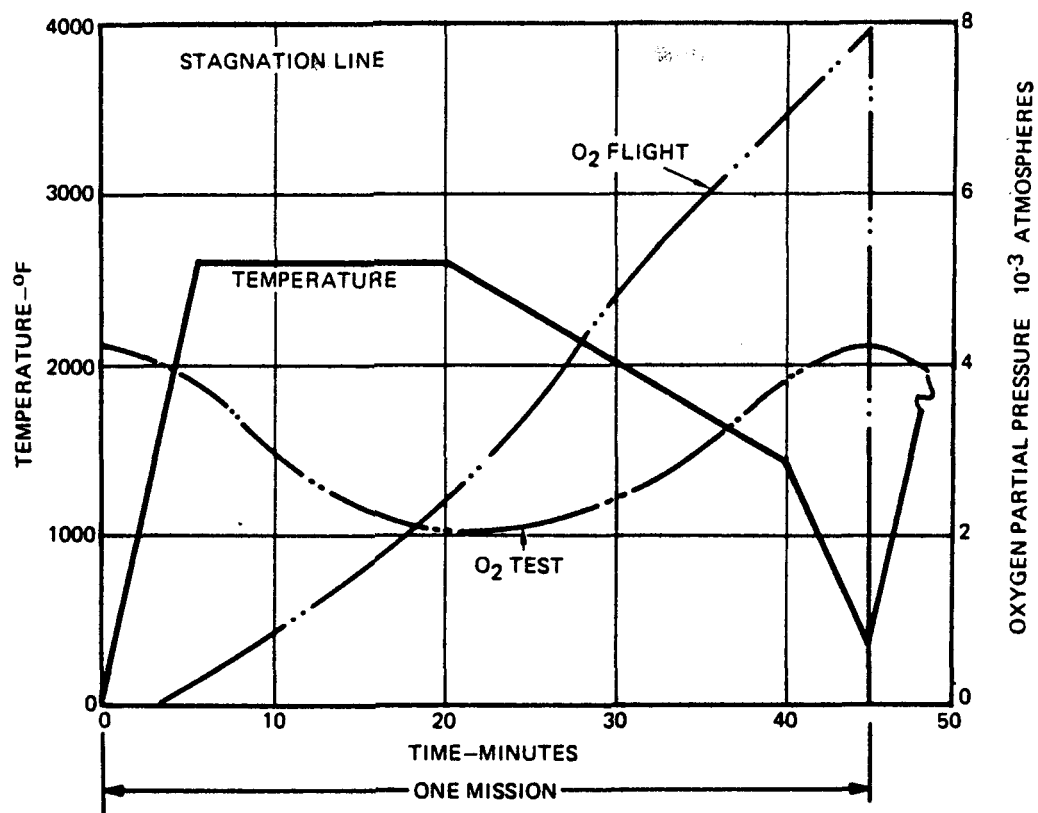


FIGURE 5-45 THERMAL/OXIDATION TEST ENVIRONMENT

TABLE 5-8 SILICONIZED RPP STRENGTH FOLLOWING THERMAL/OXIDATION CYCLING WARP DIRECTION-13-PLY

100- MISSION DATA

SPECIMEN	CONDITION	TEST	FAILING STRESS PSI	THICKNESS CHANGE IN.
M146/155-18	HEAT TREAT	FLEXURE	14200	- 0.001
W10/W13-7		FLEXURE	13400	+ 0.002
W10/W13-8		FLEXURE	15800	+ 0.002
M137/141 F-16		FLEXURE	13800	0.000
M143/144-7		FLEXURE	12400	- 0.002
M146/155-17	HEAT TREAT	FLEXURE	14800	0.000
W10/W13-11		COMPRESSION	15300	- 0.003
W10/W13 FO-8		COMPRESSION	13300	+ 0.004
M145-12		FLEXURE	15700	0.000
M149-1	NON HEAT TREAT	FLEXURE	14100	- 0.003
W6-13		FLEXURE	16800	0.000
M149-3		FLEXURE	16900	- 0.002
		FLEXURE		

about 70 missions. While only a small central portion (approximately 1 inch) of the flexure bar was exposed, it did provide an indication of the effect to be expected. As anticipated, flexure bars in molecular oxygen reacted differently from that exposed to atomic oxygen. The plasma specimen experienced measurable coating erosion (0.019 in.) while the other specimens did not. Substrate attack of the plasma specimen was apparently nill, since the flexure strength after exposure was 14100 psi, and the coating was tightly adherent even though eroded beyond the normal 0.010 in. limit. The control specimen failed at 14200 psi.

Additional thought must be given to the manner in which the siliconized RPP system is evaluated. It is important to the selection of processing (e.g., heat treat or not), and characterization of the material, to test in the most realistic environment, be it primarily atomic, molecular or a mix. If the composition of the entry environment cannot be determined accurately then bounds can be applied to the test environment and the results used in a consistent manner. This is particularly important when testing coating oxidation in an atomic (dissociated) environment, where high heating rates to achieve high temperatures are required because of the low catalytic surface. Yet, the catalytic effects are not considered by most potential users in the evaluation of mission life.

6.0 NON DESTRUCTIVE EVALUATION (NDE) AND INSPECTION

In Phase I a variety of NDE techniques were examined including radiography, ultrasonic through-transmission, ultrasonic pulse-echo, sonicator low-frequency sound, infra-red, and eddy-current. It was determined that x-ray radiography in conjunction with an attenuator (carbon tetrachloride) and ultrasonic through-transmission (C-scan) gave the best results for determining delaminations or low density regions in laminates. Infra red indicated potential but was no better than the other two.

The Phase II effort pursued x-ray and ultrasonic techniques further and sought to establish standards for the in-process evaluation of laminates and completed hardware. Holography was also examined briefly, since this approach is receiving increased emphasis in the NDE field. However, initial attempts have been disappointing with holography, when attempting to thermal stress the RPP.

Results with x-ray and ultrasonic show that these are effective tools for indicating low density regions or delaminated areas at the RPP-2 and RPP-3 states. However, with the large porosity prevalent in the RPP-0 and RPP-1 conditions neither technique is appropriate at these stages and reliance is placed on visual and tap testing. It further appears that the ultrasonic technique will suffice for coated material, while x-ray is effective on coated parts only for edgewise sections such as ribs, beams, or intercostal flanges.

Data has been gathered on flat laminates as well as complex components. Unfortunately only flat laminates have been destructively tested to confirm NDE indications. The components are being used for other purposes and cannot be destroyed at this time. This section of the report summarizes data obtained in the evaluation of laminates throughout the processing steps and documents data obtained on wing tip panel and prototype leading edge components.

6.1 LAMINATE INVESTIGATIONS

6.1.1 NDE Studies

An objective of the Phase II activity was to establish NDE standards for evaluation of bare and coated RPP. Since x-ray and ultrasonic techniques had been proven to be the best candidates examined to date, effort was concentrated on these approaches. Of primary interest was the determination of laminate soundness in both the bare and coated conditions. Attempts to determine coating thickness or establish strength levels of laminates by NDE techniques were beyond the scope of the current effort. Component strength and coating thickness are assessed by destructive test of flexure bars and plasma specimens processed with

the part. The Phase II program was primarily concerned with determining "good" or "bad" as opposed to "how good" or "how bad".

The approach taken was to select a number of panels with suspected defects and follow these through the various processing stages to determine when NDE techniques become effective and how effective. Two groups of laminates were examined as discussed below. The first group, comprised of panels LE #11 and LE #68, were examined as RPP-3, bare and coated. The second group of panels was followed from RPP-0 through RPP-3.

Two large 10 inch x 12 inch bare panels were selected for trial examination. One, panel LE #11, was a 13 ply laminate with a thickness of 0.190 inch, while the other, panel LE #68, was fabricated from 20 plies for a thickness of 0.240 inch. Both panels were examined radiographically, using carbon tetrachloride as an attenuator, and by the ultrasonic technique with water as a couplant.

No defects were observed on panel #LE 11 by radiographic examination and only minor porous areas were observed ultrasonically. Radiographic examination of Panel #LE 68 on the other hand showed large void or porous areas originating at the edges of the panel. Ultrasonic inspection also showed generally porous or void conditions in the same region.

A number of flexure bars, measuring 0.75 inch wide x 5.0 inch long, were taken from each panel. Half of these were tested in the bare condition and the other half were tested in the coated condition. The results listed in Table 6-1, clearly show that the defect indicators do indeed predict areas of low strength. The location of these specimens relative to the indicated defects is illustrated in Figure 6-1 for the LE #68 panel. Flexure values obtained in sound areas of the panel are in agreement with strength data normally expected for RPP panels in these thickness ranges. One conclusion that can be reached is that neither carbon tet nor water has a detrimental effect on either bare or coated RPP strength.

The stress levels produced by the coated and heat treated specimens from the thick panel are higher than expected even though strength of coated thick panels should be higher than for thinner ones. Coating depth on these specimens was about 50% deeper than planned so the high strength cannot be attributed to thin coating. It is surprising that the coated specimens showed no strength reduction compared to bare for panel #LE68.

TABLE 6-1 FLEXURE STRENGTH OF BARE AND COATED RPP
4-POINT LOADING

<u>Panel</u>	<u>Specimen No.</u>	<u>Condition</u>	<u>Flexure Strength PSI</u>
LE #11 (13 plys) (No observable defects)	11-2	Bare	20900
	11-4	↑	21300
	11-6	↑	19300
	11-8	↑	20400
	11-10	↑	20100
	11-12	↑	20900
	11-14	↑	20500
	11-16	↑	19900
	11-18	↓	19900
	11-20	Bare	20600
	11-1	Coated	15100
	11-3	↑	14900
	11-5	↑	12900
	11-7	↑	15000
	11-9	↑	12600
	11-11	↑	16400
	11-13	↑	13500
	11-15	↑	13300
	11-17	↓	12700
	11-19	Coated	13100
LE # 68 (20 Plys) (Defective Panel Ref Figure 6-1)	68-2	Bare	15400*
	68-4	↑	14200*
	68-6	↑	12000*
	68-8	↑	22100
	68-10	↑	21700
	68-12	↑	12300*
	68-14	↑	20800
	68-16	↑	21800
	68-16a	↑	21800
	68-18	↓	21600
	68-20	Bare	22300
	68-1	Coated	10700*
	68-3	↑	17800*
	68-5	↑	9300*
	68-7	↑	22500
	68-9	↑	23200
	68-11	↑	21600
	68-13	↑	-- * gross delam- no test
	68-15	↑	22200
	68-17	↓	23500
	68-19	Coated	21500

* Specimens which were cut from areas noted to be defective by x-ray and ultrasonic inspection.

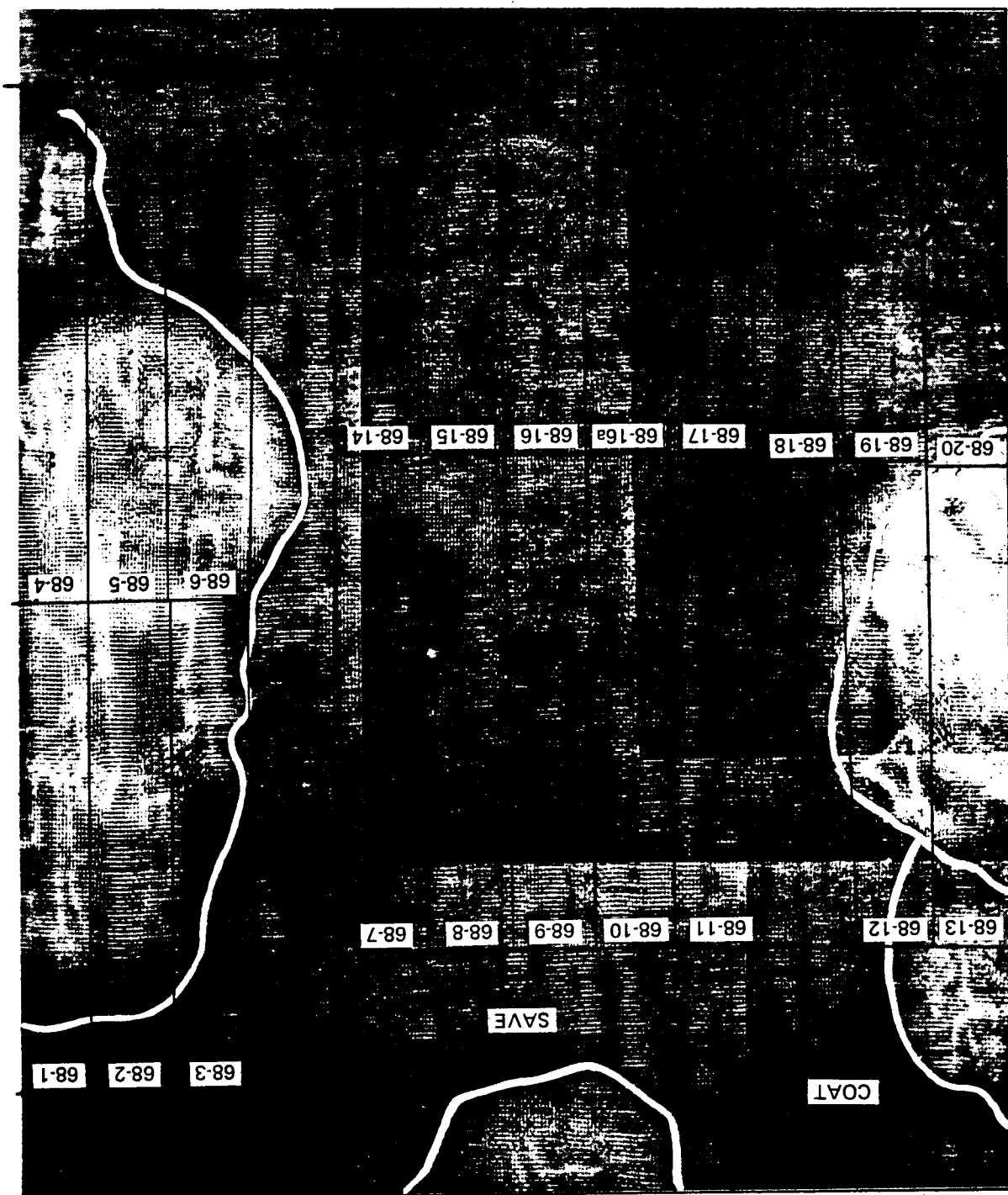


FIGURE 6-1 PHOTOGRAPH OF PANEL NO. LE68 RADIOGRAPHIC FILM, TAKEN AFTER IMMERSION OF PANEL IN CARBON TETRACHLORIDE FOR 30 MINUTES. TEST SPECIMENS ARE SHOWN OVERLAYED.

The coated 13 ply laminate strength is about as expected for the particular furnace run in which these specimens were coated. Coating thickness was in the desired 0.020 in. range. Strength is uniform in both the coated and bare conditions, providing evidence that material appearing sound by x-ray and ultrasonic test does produce good strength.

Five panels, each 10 in. x 10 in. x 13 ply, were selected in the RPP-0 condition for NDE testing because of observed defects which were determined by tapping or visual examination of the edges. These panels were radiographically and ultrasonically examined after each pyrolysis cycle from RPP-0 through RPP-3. Results from one of these panels, number 1-18, which is typical of the others, are shown in Figures 6-2 through 6-8.

In general radiographic data using carbon tet at each processing step were similar, but, as the density of the panel increased, the ability to identify defective areas became easier. Evaluation of defects in the RPP-0 and RPP-1 conditions is not considered feasible because the high degree of porosity at these conditions results in saturation with carbon tet.

Similarly, ultrasonic examination is not feasible in the RPP-0 and RPP-1 conditions because of the high sound absorption or attenuation in these material conditions. However, at the RPP-2 and RPP-3 stages, defective areas become pronounced as the furfuryl alcohol impregnant fills the small voids and increases panel density.

It can be seen that reimpregnation decreases the void because the delaminated region becomes smaller with successive impregnations.

Infrared testing was also performed on some of the five panels but results were not satisfactory because of a malfunctioning dewar in the test equipment. With the recent replacement of the defective dewar, the equipment has been upgraded. A higher sensitivity Barnes Model D-10S, dewar and infrared detector unit has been procured which exhibits less signal to noise ratio. A new X-Y recorder has also been installed on this equipment. Feasibility of infrared evaluation was proven in Phase I efforts, and the equipment modifications should give better defect resolution capabilities in future studies.

A feasibility study is in progress with a G.C. Optronics Model 1306C, holographic unit. This unit has a 15 milliwatt, helium-neon continuous wave laser mounted on a 4 foot x 6 foot table, which has automatic leveling and vibration damping with air cushion devices. An attempt to induce thermal stresses into RPP-3 by heating to 1,000^oF has not produced significant fringe pattern deviations, with known defective areas. The failure to induce thermal stressing of the panels was probably due to the relatively high thermal conductivity and low coefficient of



FIGURE 6-2 PHOTOGRAPH OF RADIOGRAPHIC FILM FROM PANEL # 1-8, RPP-O CONDITION. DETERMINATION OF DELAMINATED AREAS IS NOT POSSIBLE DUE TO SATURATION OF CARBON TETRACHLORIDE THROUGHOUT AVAILABLE POROSITY.

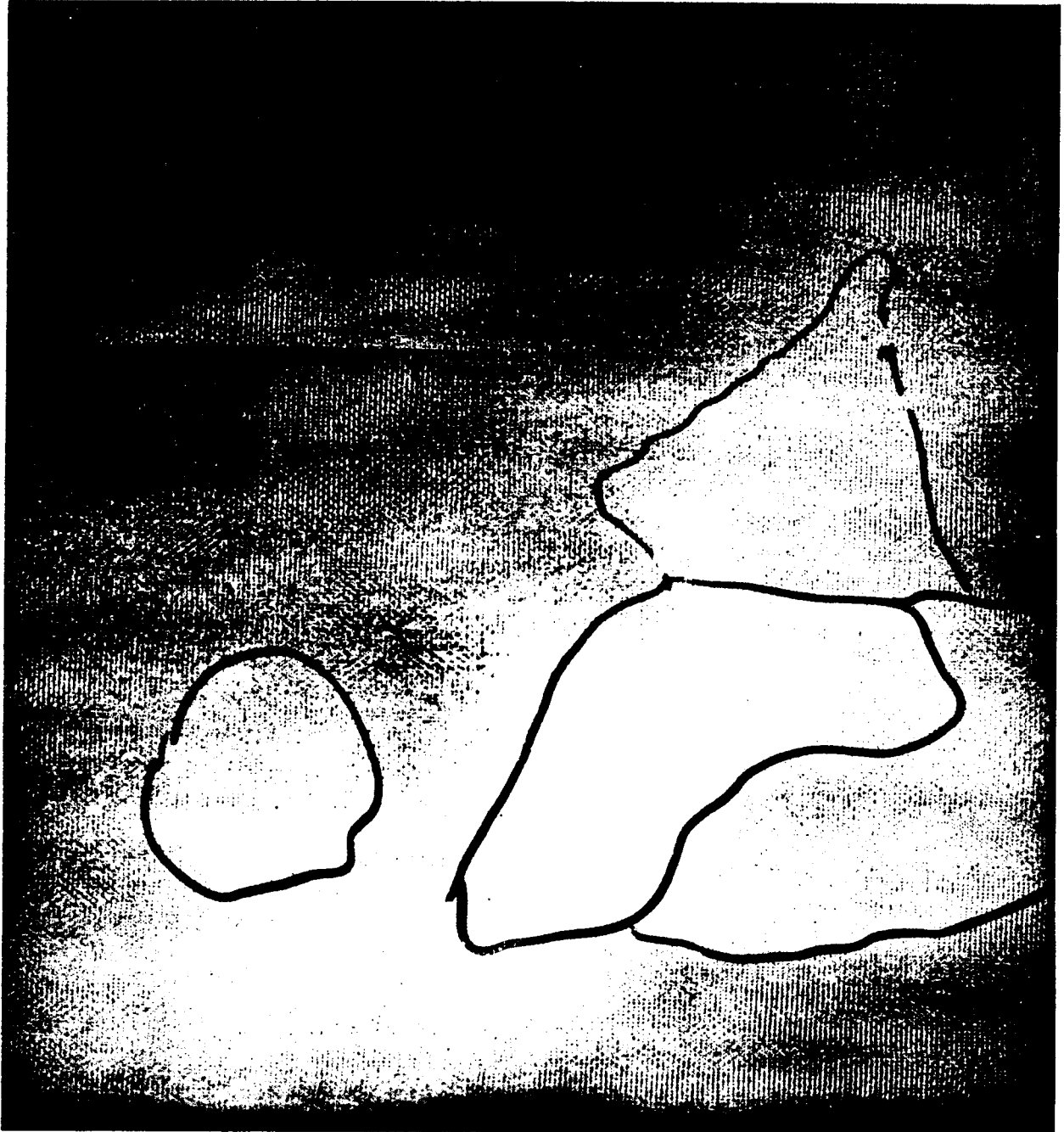


FIGURE 6—3 PHOTOGRAPH OF RADIOGRAPHIC FILM FROM PANEL # 1—8 RPP—1
CONDITION. OUTLINED AREAS WERE NOTED TO BE DELAMINATED BY
VISUAL EXAMINATION AND TAPPING. CARBON TETRACHLORIDE
SATURATION IS EVIDENT IN AVAILABLE POROSITY AND
DELAMINATION.



FIGURE 6-4 ULTRASONIC C-SCAN RECORDING OF PANEL # 1-8, RPP-1 CONDITION. APPROXIMATELY HALF OF THE AVAILABLE POROSITY VOLUME HAS BEEN FILLED BY INITIAL IMPREGNATION. WHITE AREAS ARE POROUS WHICH GIVE HIGH ATTENUATION LEVELS.

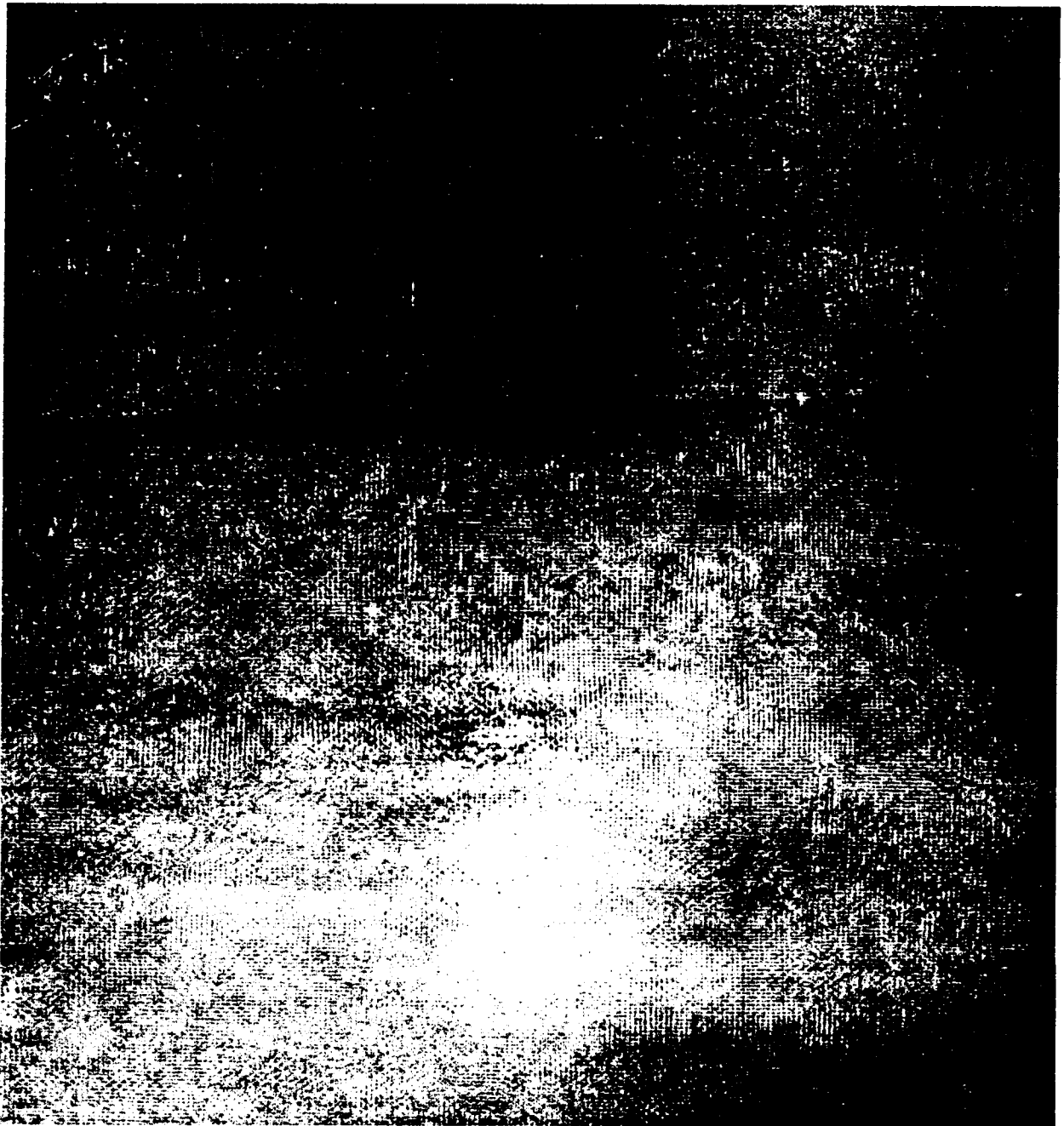


FIGURE 6-5 PHOTOGRAPH OF RADIOGRAPHIC FILM FROM PANEL # 1-8, RPP-2 CONDITION. DELAMINATION AREAS AND THE AVAILABLE POROSITY HAVE BEEN FILLED WITH CARBON TETRACHLORIDE.

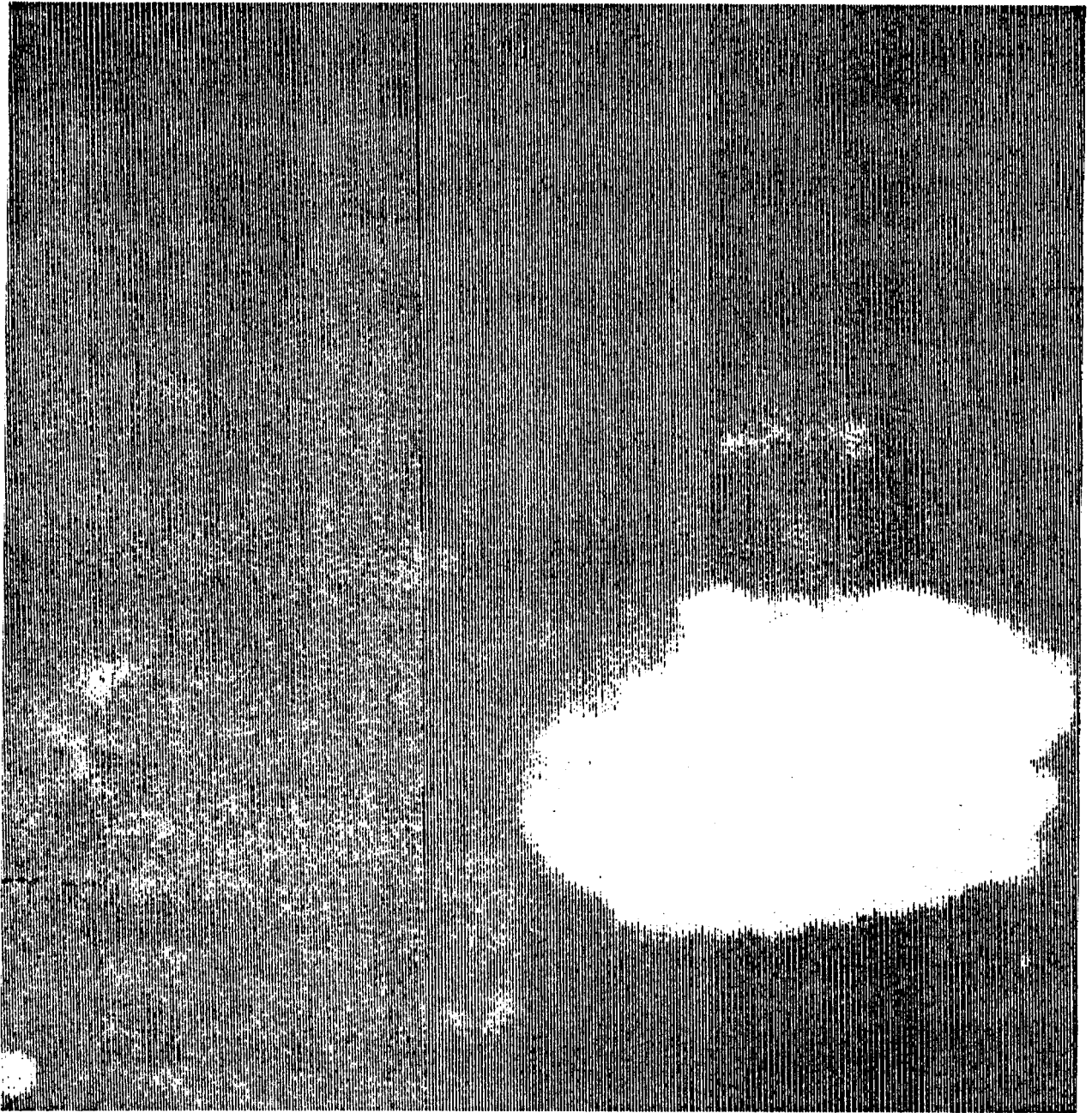


FIGURE 6-6 ULTRASONIC C-SCAN RECORDING OF PANEL # 1-8, RPP-2 CONDITION. RE-IMPREGNATION HAS DECREASED SIZE OF DELAMINATED AREA WHEN COMPARED TO FIGURE 6-4 RPP-1 CONDITION. MAJOR AMOUNT OF AVAILABLE POROSITY VOLUME HAS BEEN FILLED DURING RE-IMPREGNATION.

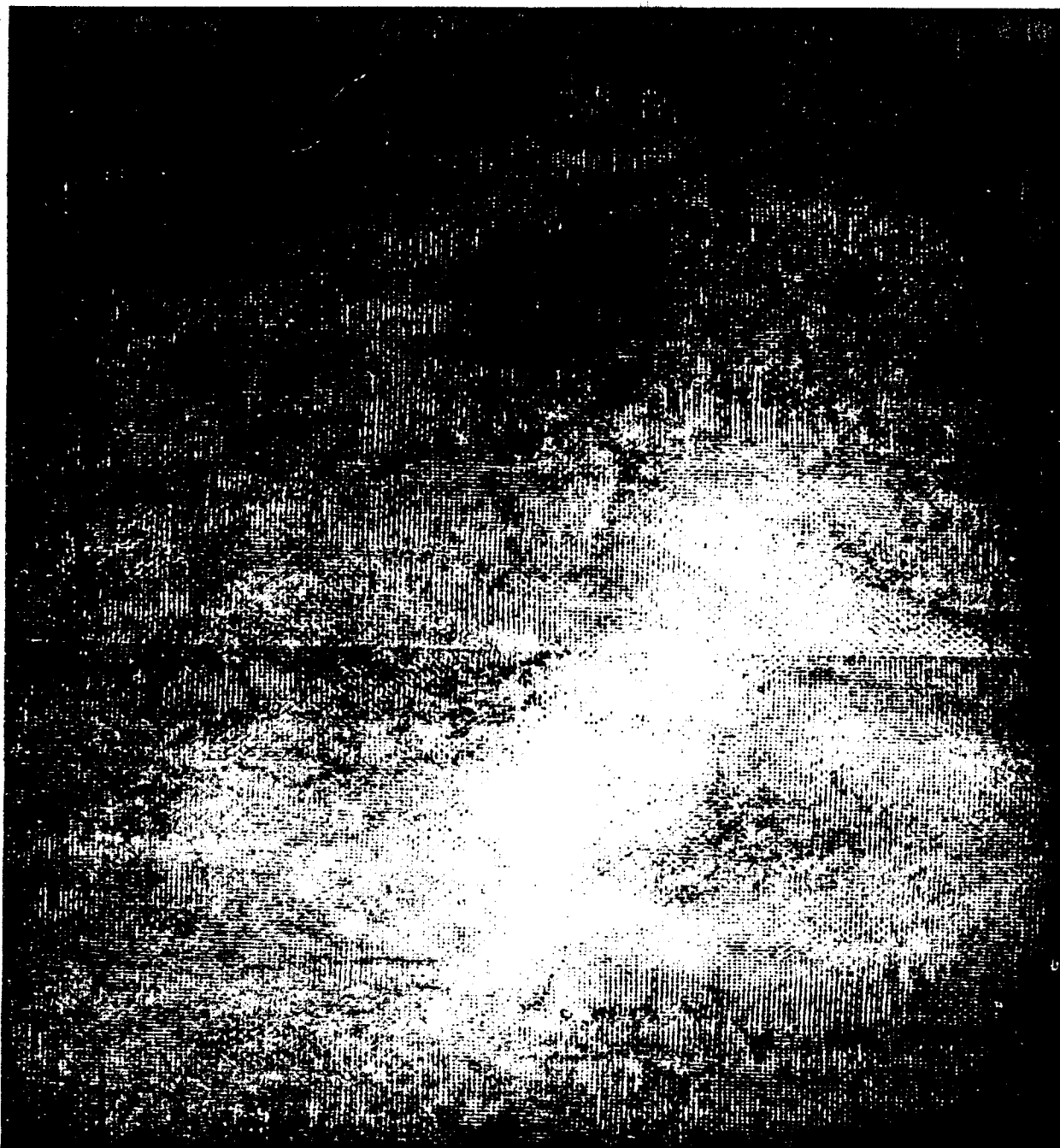


FIGURE 6-7 PHOTOGRAPH OF RADIOGRAPHIC FILM FROM PANEL # 1-8, RPP-3 CONDITION. DELAMINATION AND AVAILABLE POROSITY VOLUME HAS DECREASED IN SIZE WHEN COMPARED TO FIGURE 6-3 AND 6-5, RPP-1 AND RPP-2 CONDITIONS.

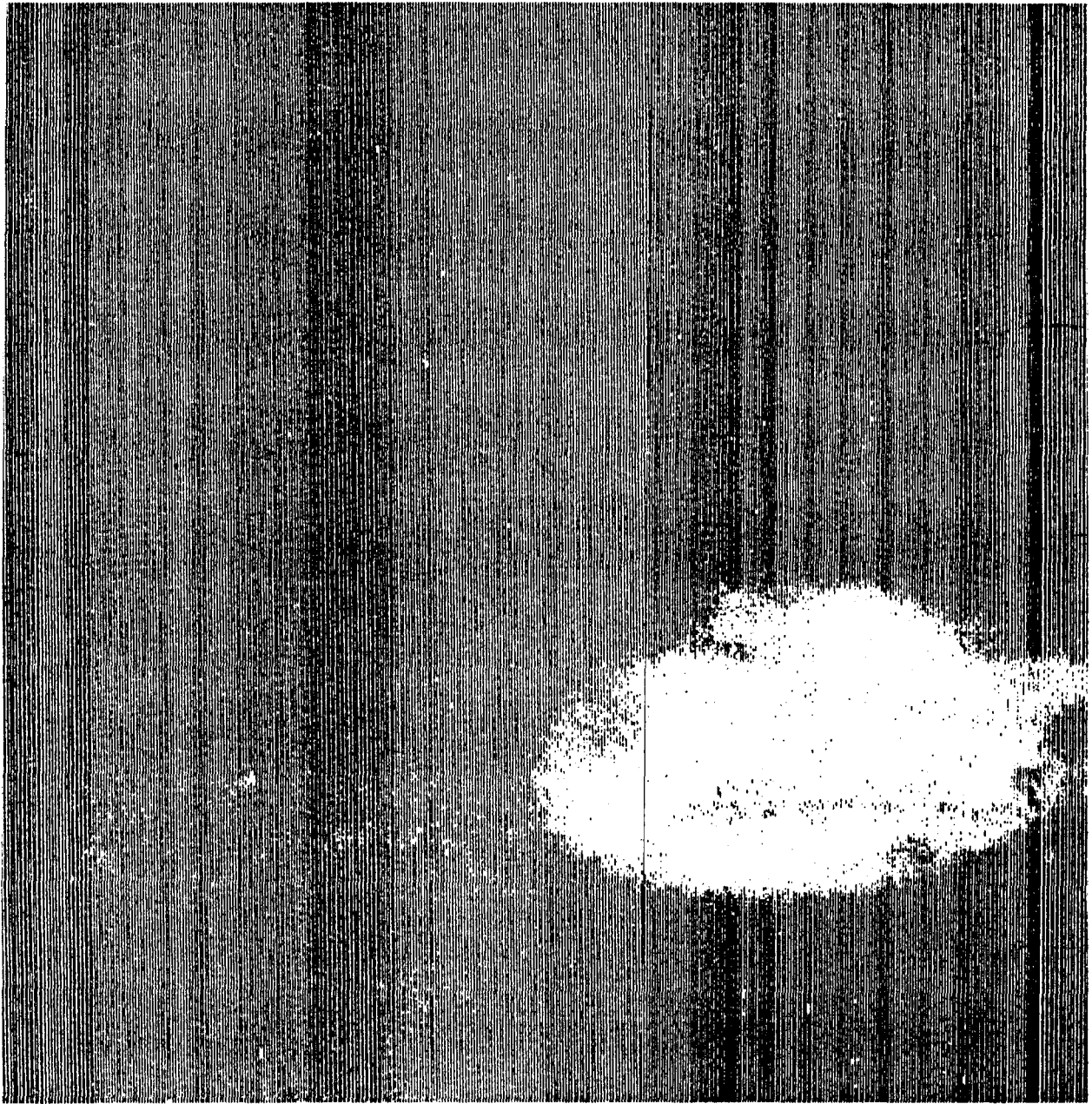


FIGURE 6-8 ULTRASONIC C-SCAN RECORDING OF PANEL # 1-8, RPP-3 CONDITION. RE-IMPREGNATION HAS FURTHER DECREASED SIZE OF DELAMINATED AREA WHEN COMPARED TO FIGURE 6-6 RPP-2 CONDITION.

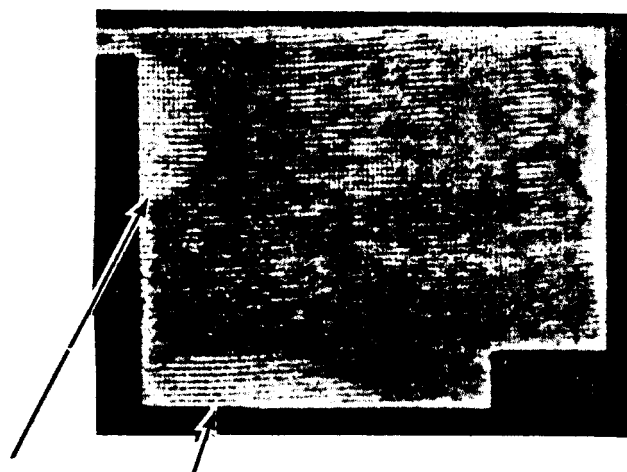
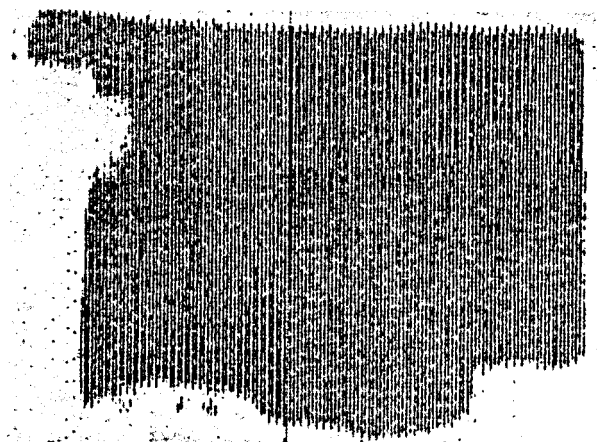
expansion of the RPP-3 material. Another method of stressing the panels, vibration, will be tried in the future. A Krohn-Hite Model DCA-50 power supply is being procured which will drive a transducer through a frequency range from DC to 500 KHz. Two transducers have been ordered; a ceramic crystal - 10,000 to 100,000 KHz, and an electro-mechanical unit with frequencies up to 15,000 KHz. It is expected that excitation of defective panels by vibration stresses will produce observable fringe patterns.

6.1.2 Preliminary Standards

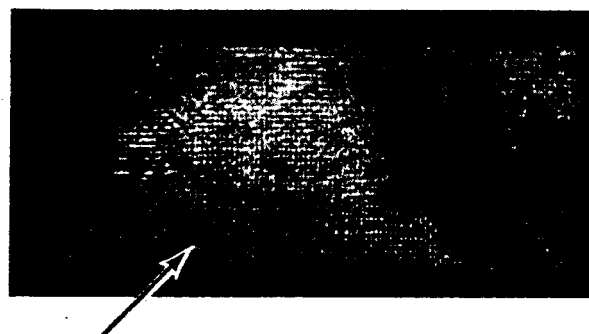
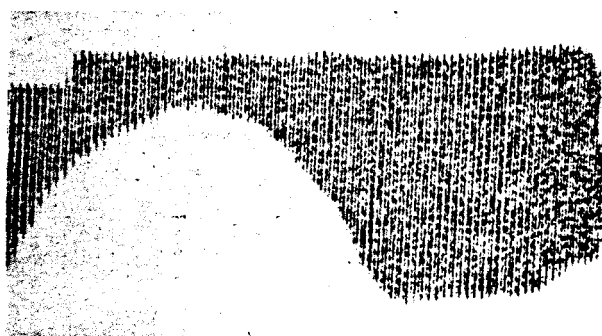
A series of standard samples has been selected containing known defective areas for evaluation of RPP laminates. The types of defects selected are illustrated in Figures 6-9 and 6-10. They are (1) single ply delamination, (2) multiple ply delamination and (3) excessive porosity or low density areas. Flexure strength data taken from various sections of panels with these defects have produced low strength. Data from panel LE # 68 is a typical example. The standards selected were identified by cross sectioning and examination of photomicrographs. Typical examples of defective and good laminate structure are given in Figures 4-2, 4-3 and 4-4. The standards in Figure 6-9 have single type defects, while the panel in Figure 6-10 has both excessive porosity and delaminations. Note that radiographic and ultrasonic inspection gives similar or corresponding defect indications.

Figures 6-11 and 6-12 demonstrate the usage of these standard samples when large panels or assemblies are evaluated. The standard sample is placed next to the panels or assemblies and subjected to ultrasonic or radiographic inspection at the same time and using the same techniques. The standard samples ensure that the panel being inspected has no comparable defect indications, and that the equipment and inspection process is capable of discerning defects of a certain type within a specific sensitivity level.

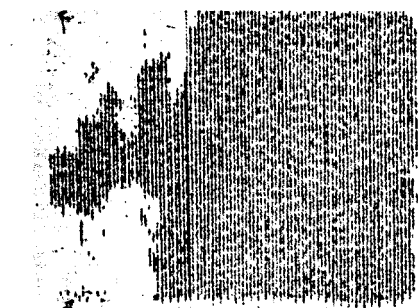
Future phases will extend the NDE data and standards developed in Phase II. These will be up-graded, and a continuing evaluation will refine the relationship of the NDE response data to mechanical properties and microstructure of the laminate. The refinement of these standards will relate acceptance criteria and tolerances to in-process quality control, so that a specification may be issued for various NDE procedures to be used during manufacturing processes evaluation and end item inspection of components.



MULTIPLE PLY DELAMINATIONS

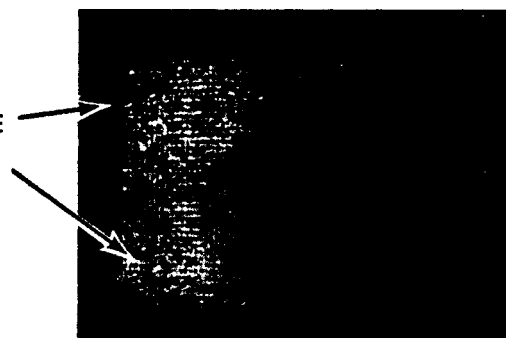


LARGE DELAMINATION – SINGLE PLY



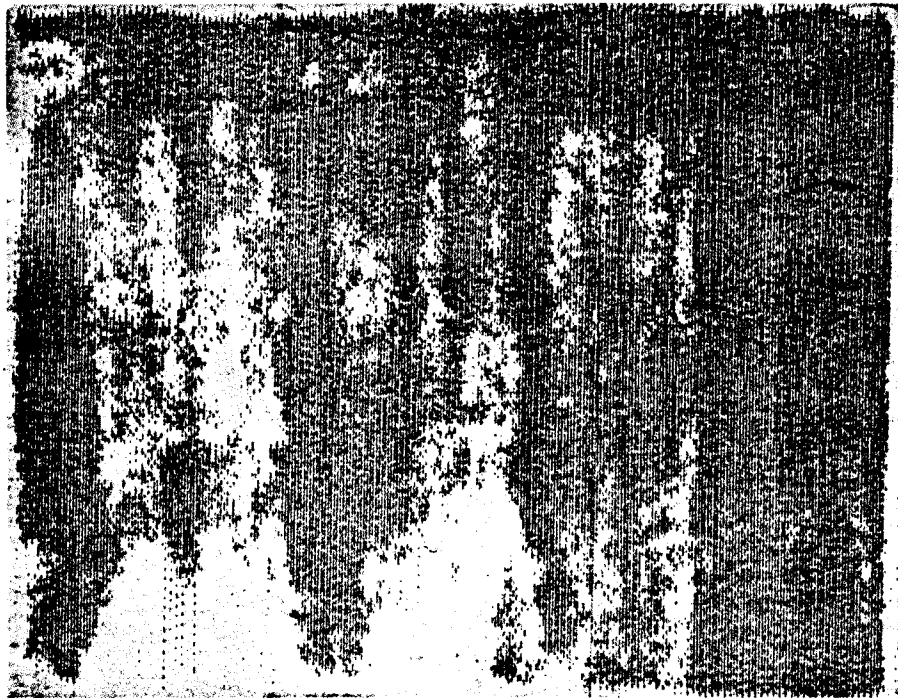
**ULTRASONIC C-SCAN RECORDINGS
5.0 MHz – 100X 3.0 GAIN THROUGH
TRANSMISSION**

**EXCESSIVE
POROSITY**

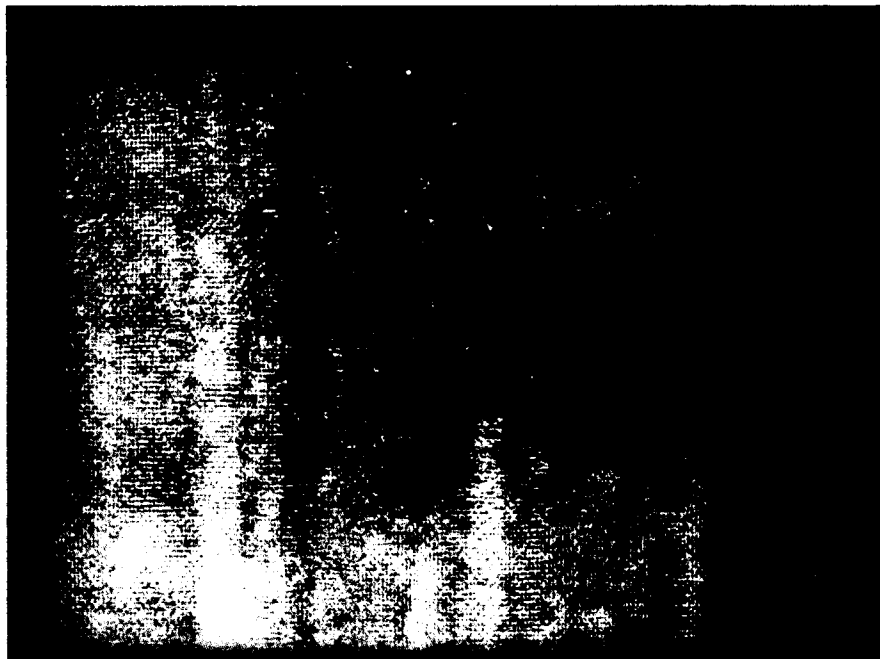


**PHOTOGRAPHS FROM X-RAY FILMS
10 Ma, 25 Kv, 36" FOCAL, 60 SECONDS –
WITH CARBON TETRACHLORIDE
IMMERSION**

FIGURE 6-9 NON-DESTRUCTIVE EVALUATION STANDARD SAMPLES. TYPICAL DEFECTS – LARGE DELAMINATION, MULTIPLE PLY DELAMINATIONS AND EXCESSIVE POROSITY. CORRELATION WAS ESTABLISHED BY VISUAL, PHOTOMICROGRAPHIC, RADIOGRAPHIC AND ULTRASONIC EXAMINATION OF DEFECTIVE AREAS.



ULTRASONIC C-SCAN RECORDING 5.0 MHz – 100X 3.0 GAIN, ½" DIAMETER TRANSDUCER,
THROUGH TRANSMISSION



PHOTOGRAPH OF X-RAY FILMS – 10 Ma, 25 Kv, 36" FOCAL, 60 SECONDS – WITH CARBON
TETRACHLORIDE IMMERSION

**FIGURE 6-10 NON-DESTRUCTIVE EVALUATION STANDARD SAMPLE. DELAMINATIONS
AND POROSITY OF LOW DENSITY AREA DEFECTS.**

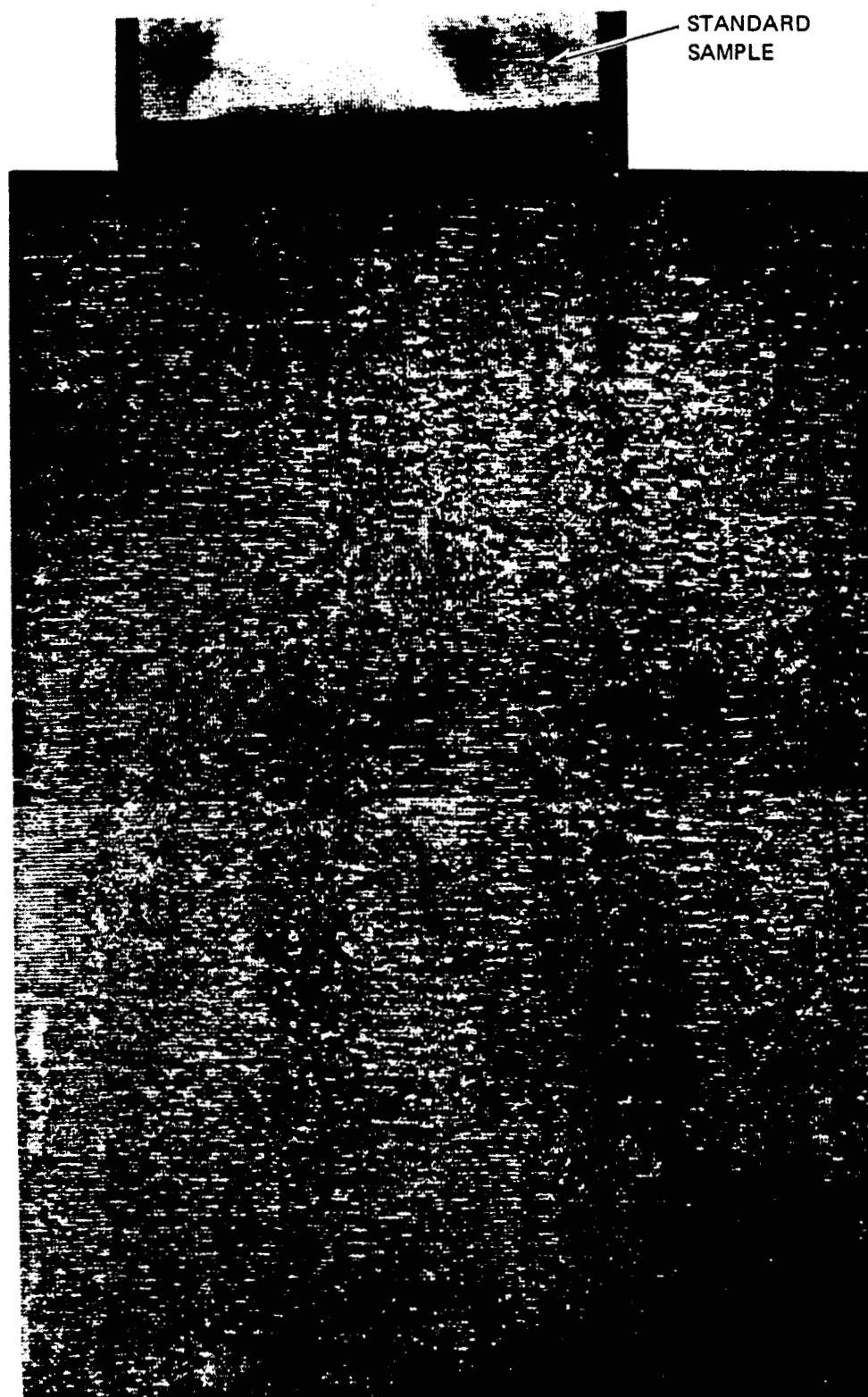


FIGURE 6-11 PHOTOGRAPH OF RPP-3 PANEL FROM RADIOGRAPHIC FILM USING CARBON TETRACHLORIDE IMMERSION WITH STANDARD SAMPLE. NO DEFECTIVE AREAS PRESENT IN PANEL, HOWEVER DEFECTS IN SAMPLE ARE READILY OBSERVED.

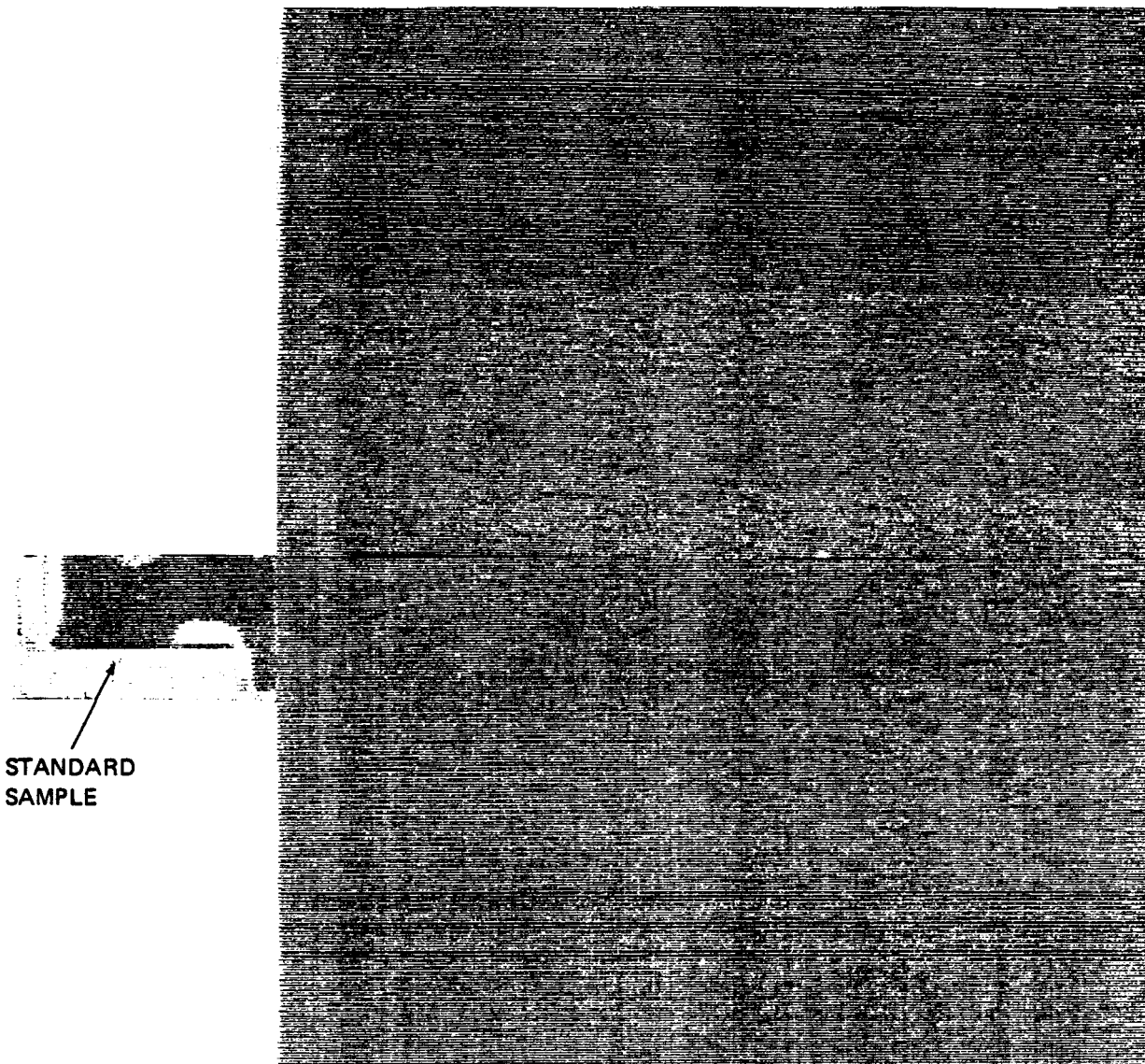


FIGURE 6-12 ULTRASONIC C-SCAN RECORDING OF RPP-3 PANEL WITH STANDARD SAMPLE. NO DEFECTIVE AREAS PRESENT IN PANEL, HOWEVER DEFECTS IN SAMPLE ARE READILY OBSERVED.

Three prototype leading edge assemblies and two wing tip panel assemblies were fabricated in Phase II. These were examined using radiographic and ultrasonic NDE techniques by the Quality Control (Q.C.) organization of VMSC as a means of gathering data on the quality of bare and coated RPP components. The purposes of the Q.C. and NDE functions on Phase II were as follows:

- (1) Ensure that process requirements as defined by specification and drawing were complied with.
- (2) Collect data on the dimensional stability of the hardware during processing.
- (3) Gather data from x-ray and ultrasonic tests for evaluation and comparison with future destructive test.
- (4) Become intimately acquainted with the specific materials and processes for better effectiveness in future phases of the RPP activity.

Since the fabrication of RPP components was developmental and on a "best efforts" basis there were no specific acceptance/rejection criteria established short of gross delamination, warpage or fabrication errors. However, an examination of the data accumulated on the Prototype leading edges, indicates that structural configurations of this size and complexity can be fabricated and controlled to desired tolerances. While some anomalies were noted, in each case they were such that they could be eliminated on future assemblies.

By following the components through the various phases of fabrication and utilizing the data determined from flat panel testing (Section 6.1) it became more clear at what stages of manufacture certain inspection techniques are best suited. For example, x-ray and ultrasonic techniques are not effective in the RPP-0 and RPP-1 state, but light tapping can be employed for gross delamination examination. When the component reaches the RPP-3 stage, both radiographic and ultrasonic techniques appear suitable. As a means of establishing mechanical strength performance at each level of component fabrication, strength data was obtained on representative 13 ply laminates at various stages of processing. This material was molded into flat panels at the time of fabrication of each part and testing was conducted by Q.C., rather than the Engineering. Data obtained from these tests (average of three specimens) are shown in Table 6-2, where typical strength improvement after each reimpregnation is noted. Final RPP-3 strength for flat laminates should normally be

TABLE 6-2 STRENGTH DATA OF COMPONENT TEST PANELS

MAT'L COND.	FLEXURAL STRENGTH DATA*				
	LEADING EDGE ASSEMBLY			WING TIP	
	S/N 1	S/N 2	S/N 3	S/N 1	S/N 2
AUTO CLAVE	20,383	22,025	23,400		19,833
RPP-0	3,800	3,840	4,706	—	4,360
RPP-1	8,343	9,820	10,716	—	8,101
RPP-2	13,210	11,566	16,346	—	12,041
RPP-3	17,666	17,175	18,850	18,830	14,533
COATED	14,538	14,453	13,341	9,465	—

* AVERAGE OF 3 SPECIMENS

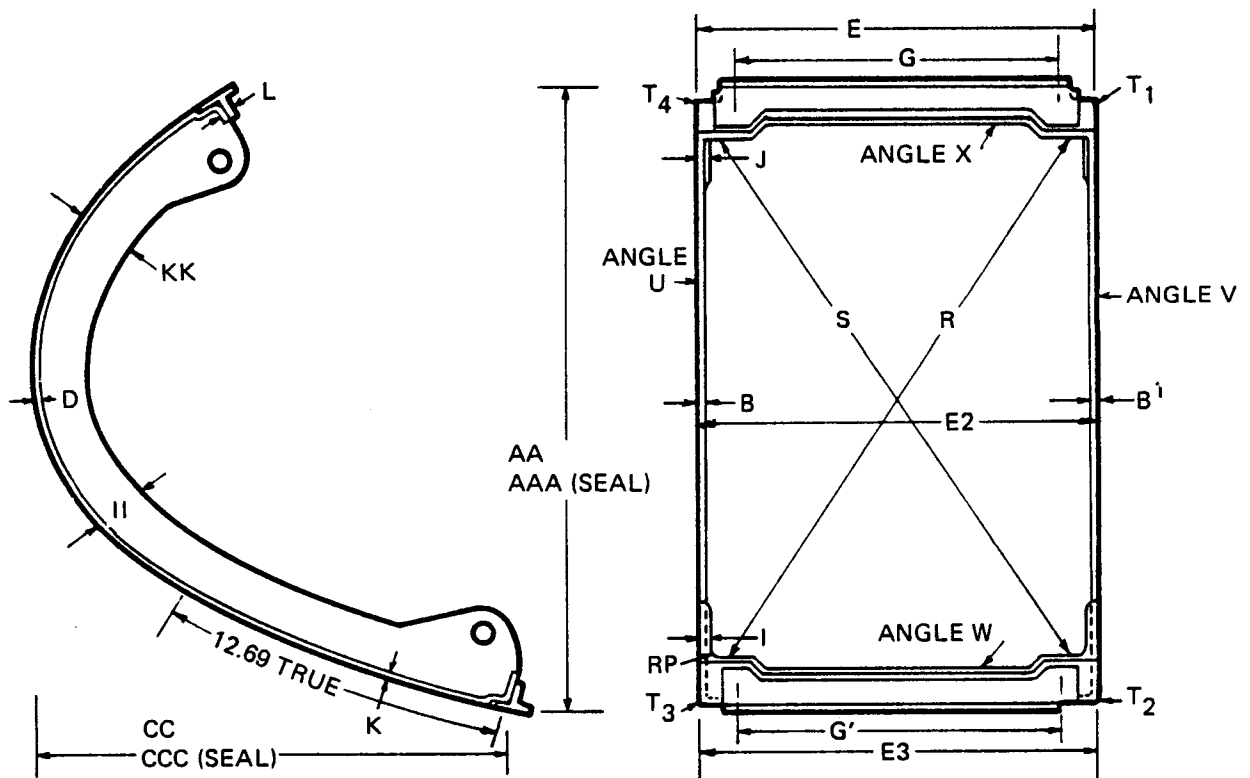


FIGURE 6-13 DIMENSIONAL DATA COLLECTED FOR PROTOTYPE LEADING EDGE

in the range of 18000 to 22000 psi based on recent laminate performance. The test panel for wing tip panel S/N 2 falls somewhat shy of this range for unknown reasons but strength is acceptable for the use intended. This panel was selected as the uncoated unit. All other assemblies appear satisfactorily strong as indicated by test panel strength. Strength after coating for all assemblies is also acceptable and in a range expected.

Dimensional stability of the fabricated articles has been very encouraging, especially during coating, when the parts are relatively unconstrained. Data obtained on the three Prototype leading edge assemblies is summarized in Table 6-3, while the legend for the dimensional data is given in Figure 6-13. The stability of these dimensions is attributed to good restraint tooling, which may have been more sophisticated than required.

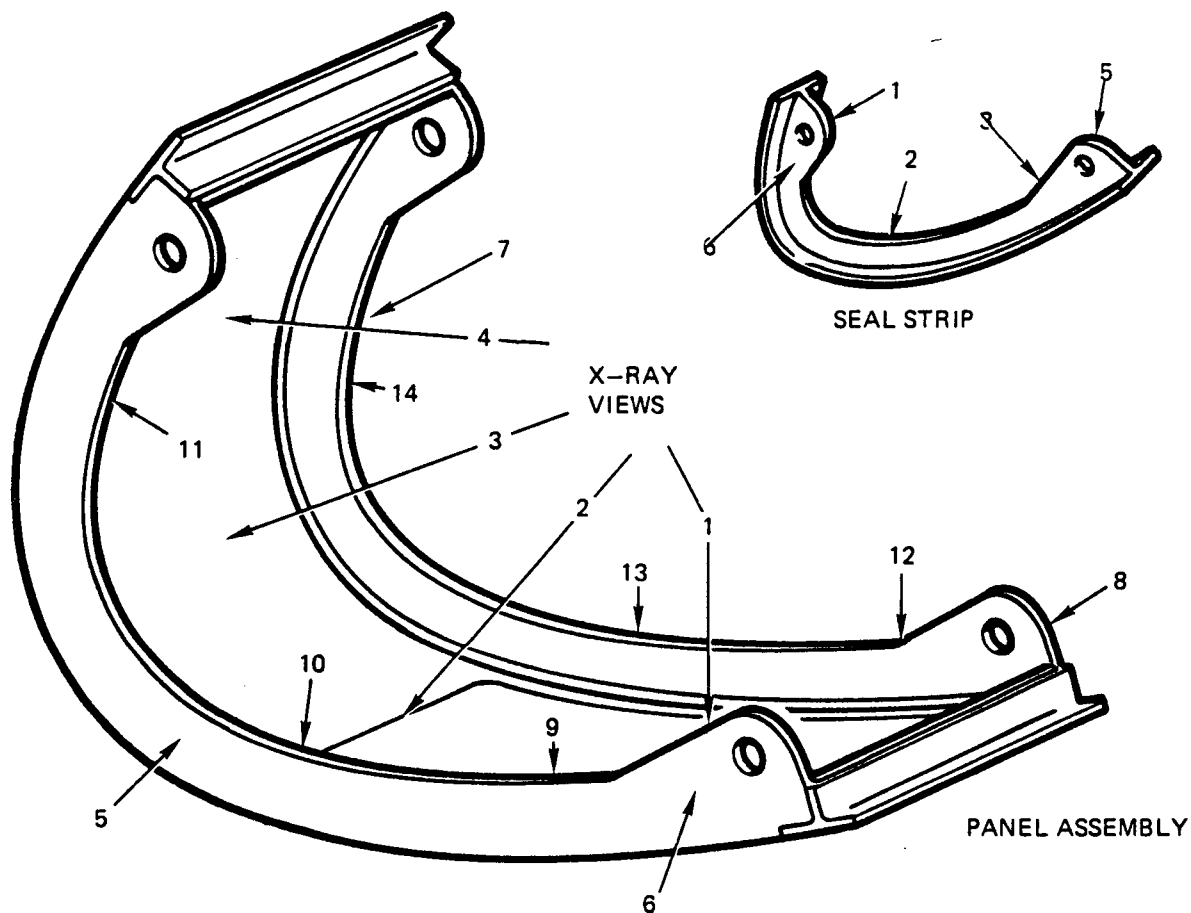
Examination of thicknesses, such as B, B¹, D and K, show typical thickness shrinkage between the as-molded and pyrolyzed condition. Thickness remains stable thereafter, even through coating. Width dimensions (E-1, E-2 and E-3) illustrate the lack of shrinkage in the plane of the laminate. Dimensions R&S indicate the warp free characteristics. Leading edges, S/N-1 and S/N-2, show differences between R&S values in the as molded condition but the differences are decreased in the RPP-3 state. The reason for the difference is that these units were not replaced into the molding tool when the trailing edge seal strips and rivets were cured subsequent to the initial cure of the leading edge layup. This produced moderate initial warp, part of which was removed during pyrolysis by the restraint tooling. Note that on S/N-3 this problem was corrected by using the layup tool during bonding and rivet. Corner angles (U, V, W, X) tend to close during pyrolysis unless prevented from doing so by suitable restraint tooling. The effectiveness of the tooling employed is evident. All other dimensions show close correlation to the desired values, and stability through the coating process.

Selected radiographic and ultrasonic evaluations were made at the RPP-3 stage and after coating as a means of establishing a data bank and gaining experience with RPP/NDE techniques on components. Radiographic data obtained on the Prototype units is illustrated by Figure 6-14.

Typical ultrasonic views of the Prototype leading edges are shown in Figures 6-15 through 6-19. The lower portion of the leading edges in the 14 ply region (view 1) are shown in Figures 6-15, 6-16 and 6-17. Note that low density areas appear on S/N-1 but get progressively better with S/N-2 and S/N-3 indicating improvement with fabrication experience. After coating, low density areas are still in evidence on S/N-1 as illustrated by the trace given in Figure 6-18. This is

Code	Drawing Requirement	S/N - 1				S/N - 2				S/N - 3			
		As		RPP-0		Coated		As		RPP-0		Coated	
		Mold	Coated	Mold	Coated	Mold	Coated	Mold	Coated	Mold	Coated	Mold	Coated
B	0.156 ± .010	.164	.162	.162	.162	.160	.158	.160	.157	.160	.158	.160	.158
B ¹	0.156 ± .010	.166	.155	.155	.155	.163	.154	.163	.154	.160	.158	.160	.158
D	0.156 ± .010	.179	.162	.162	.162	.174	.164	.174	.159	.158	.156	.158	.156
G	11.92 ± .03	11.98	11.98	11.98	11.98	11.92	11.92	11.92	11.98	11.90	11.93	11.90	11.93
G ¹	11.92 ± .03	11.97	11.97	11.97	11.97	11.93	11.93	11.93	11.97	11.93	11.93	11.93	11.93
I	0.221 ± .010	.230	.220	.220	.215	.225	.230	.225	.215	.240	.220	.240	.220
J	0.221 ± .010	.230	.217	.217	.217	.217	.210	.217	.217	.227	.220	.227	.220
E-1	15.00 ± .03	15.05	15.02	15.02	15.01	15.064	15.025	15.064	15.05	15.043	15.042	15.043	15.006
E-2	15.00 ± .03	15.05	15.05	15.05	15.05	15.05	15.04	15.05	15.06	15.063	15.063	15.063	15.004
E-3	15.00 ± .03	15.02	15.03	15.03	15.03	15.012	15.027	15.012	15.04	15.023	15.020	15.023	15.06
K	0.182 ± .010	.220	.210	.210	.195	.194	.186	.194	.183	.185	.183	.185	.182
L	0.286 ± .010	.275	.260	.260	.260	.280	.270	.280	.289	.287	.280	.287	.255
R	-----	27.072	27.58	27.58	27.55	27.27	27.60	27.27	27.575	27.55	27.58	27.55	27.75
S	-----	28.003	27.90	27.77	27.77	28.07	27.97	28.07	27.925	27.57	27.56	27.57	27.76
T ₁	-----	.650	.610	.370	.370	.650	.650	.650	.308	.530	.530	.530	.380
T ₂	-----	.560	.540	.430	.430	.650	.650	.650	.458	.500	.500	.500	.350
T ₃	-----	.580	.560	.500	.500	.500	.500	.500	.476	.523	.515	.523	.495
T ₄	-----	.650	.640	.500	.500	.650	.650	.650	.370	.520	.518	.520	.395
U	90°	91°	90°	90°	90°	90°	90°	90°	90°	90°	90°	90°	90°
V	90°	90°31'	90°	90°	90°	90°	90°	90°	90°	90°	90°	90°	90°
W	90°	90°	90°	90°	90°	90°	90°	90°	90°	90°	90°	90°	90°
X	90°	90°	90°	90°	90°	90°	90°	90°	90°	90°	90°	90°	90°
AA	24.00 ± .03	24.00	24.00	24.00	24.00	24.45	24.200	24.45	24.200	23.875	23.875	23.875	24.24
CC	18.00 ± .03	18.00	18.00	18.00	18.00	18.10	18.10	18.10	18.10	18.25	18.25	18.25	18.07
II	1.44 ± .03	1.58	1.53	1.475	1.475	1.68	1.58	1.68	1.44	1.74	1.76	1.74	1.46
KK	2.30 ± .03	2.35	2.35	2.30	2.30	2.45	2.45	2.45	2.28	2.64	2.64	2.64	2.31
AAA	24.00 ± .03	24.00	24.00	24.00	24.00	24.00	24.00	24.00	24.00	24.00	24.00	24.00	24.00
CCC	18.00 ± .03	18.00	18.00	18.00	18.00	18.00	18.00	18.00	18.00	18.00	18.00	18.00	18.00

TABLE 6-3
PROTOTYPE LEADING EDGE DIMENSIONAL DATA

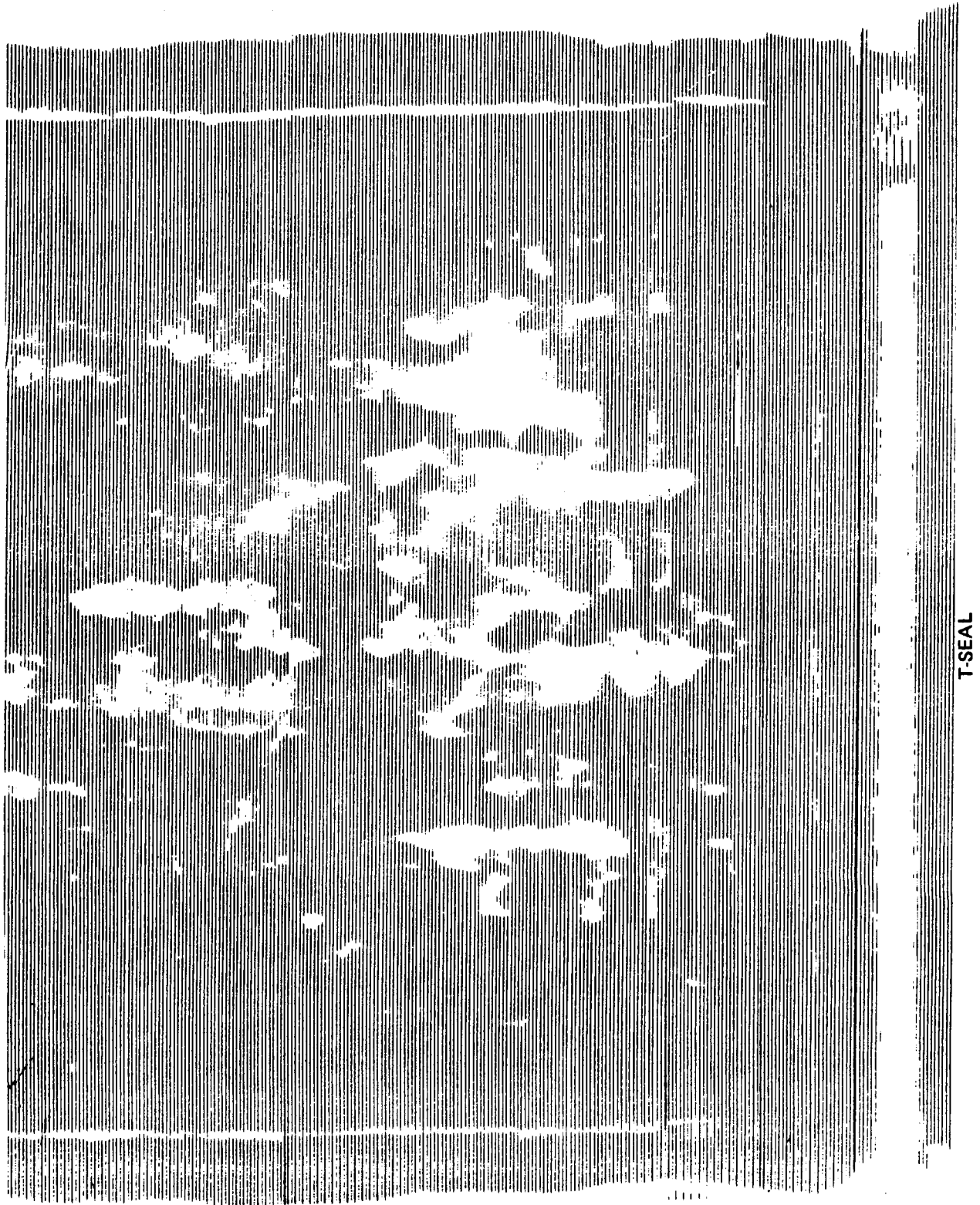


NOTES:

- (1) VIEWS 1 THROUGH 14 ON EACH LEADING EDGE ASSEMBLY
- (2) VIEWS 1 THROUGH 6 TAKEN ON EACH SEAL STRIP
- (3) ULTRASONIC TRANSDUCERS WERE POSITIONED FOR INSPECTION OF AREAS DEPICTED BY VIEWS 1, 2, 3 AND 4 FOR THE PANEL ASSEMBLY AND ALL VIEWS AS SHOWN FOR THE SEAL STRIP
- (4) ALTHOUGH IT IS NOT ILLUSTRATED, THE SAME PROCEDURE OF VIEW SELECTION FOR BOTH X-RAY AND ULTRASONIC WAS USED FOR INSPECTING THE WING TIP ASSEMBLIES

FIGURE 6-14 RADIOGRAPHIC X-RAY VIEWS TAKEN FOR PROTOTYPE LEADING EDGES

RIB

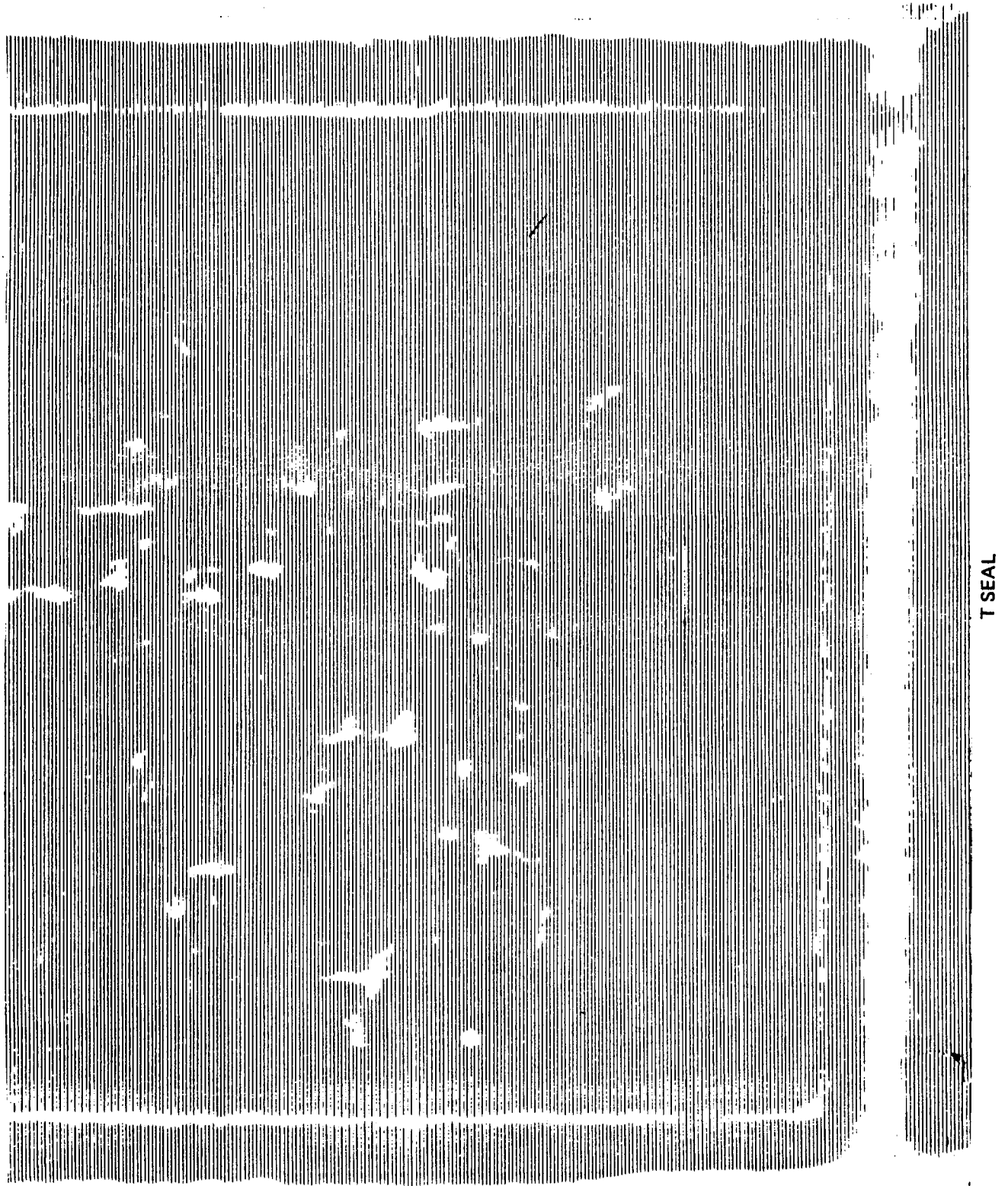


T-SEAL

RIB

FIGURE 6-15 ULTRASONIC C-SCAN RECORDING OF DOUBLER AREA AND T-SEAL BOND OF LEADING EDGE S/N-1 AT RPP-3 STAGE

RIB



RIB

FIGURE 6-16 ULTRASONIC C-SCAN RECORDING OF DOUBLER AREA AND T SEAL BOND OF LEADING EDGE S/N-2 AT RPP-3 STAGE

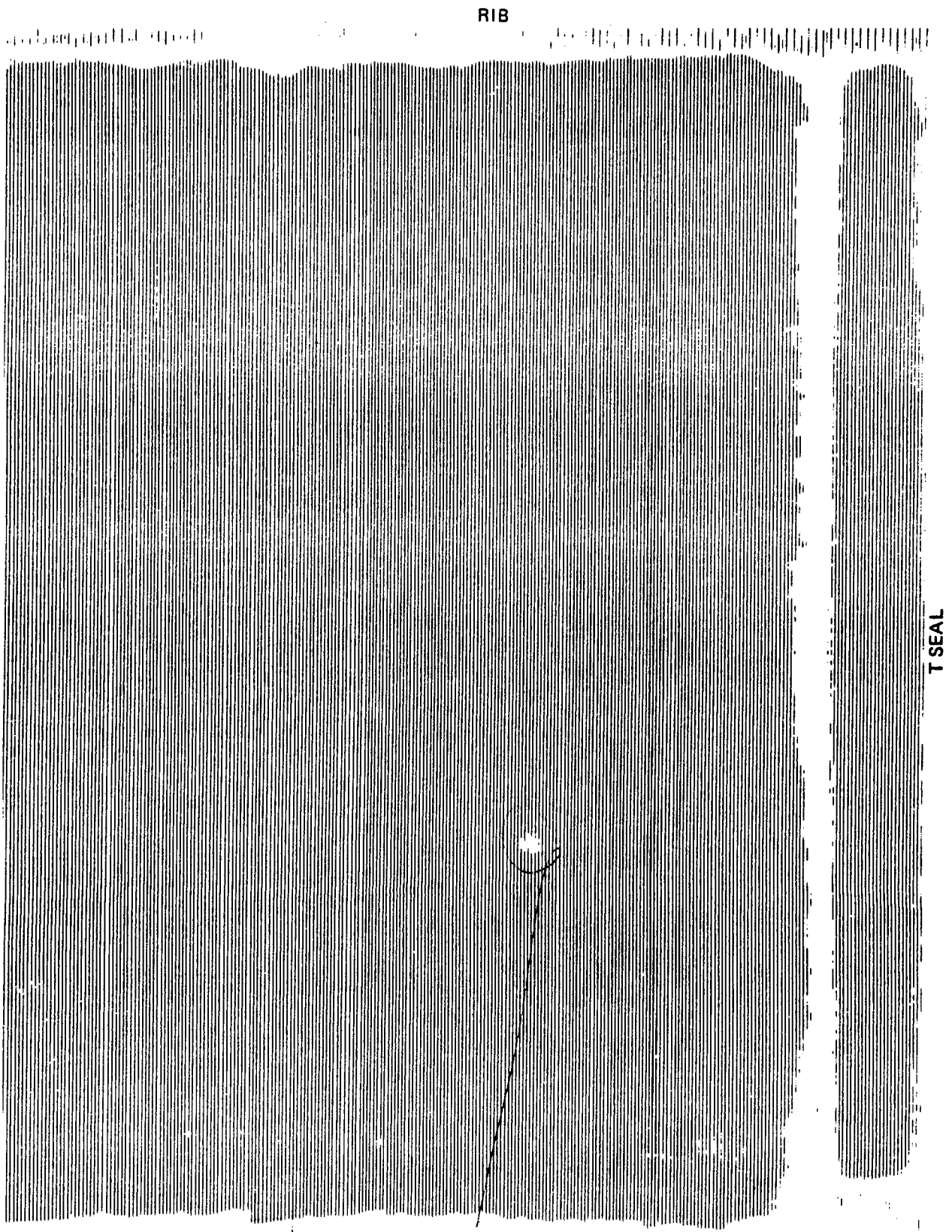
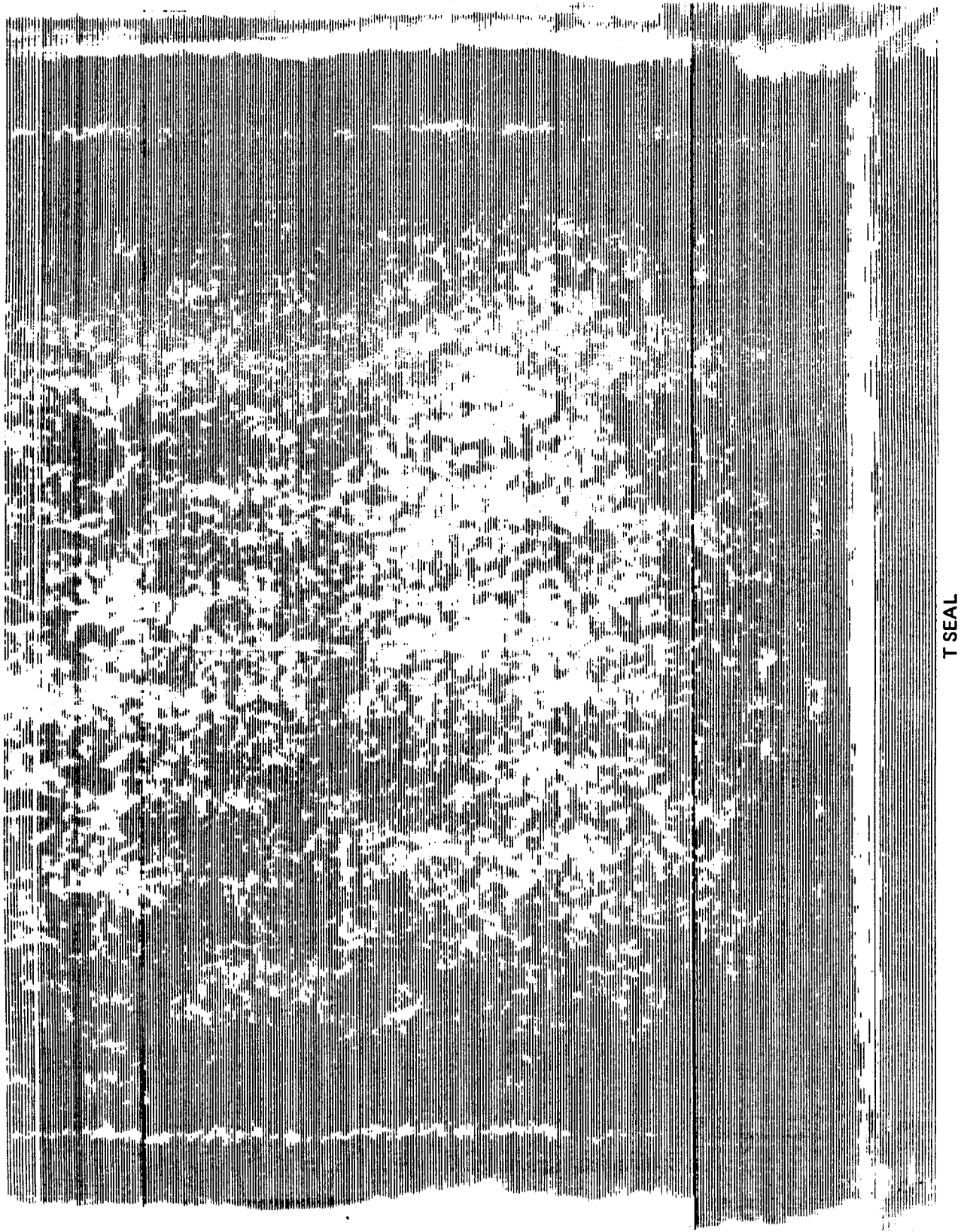


FIGURE 6-17 ULTRASONIC C-SCAN RECORDING OF DOUBLER AND T-SEAL OF LEADING EDGE S/N-3 AT RPP-3 STAGE

RIB



T SEAL

RIB

FIGURE 6-18 ULTRASONIC C-SCAN RECORDING OF DOUBLER AREA AND T-SEAL BOND OF LEADING EDGE S/N-1 AFTER COATING



FIGURE 6-19 ULTRASONIC C-SCAN RECORDING OF LEADING EDGE SEAL STRIP S/N - 1
AT RPP-3 STAGE

significant because it indicates that ultrasonic C-scan may be effective on coated parts, where x-ray techniques are not applicable because the coating masks subsurface defects.

A typical record of the results on a "T" seal strip is shown in Figure 6-19. With the automatic traversing equipment the corner radii of the part are not adequately evaluated. This will require hand held transducers for inspection in these difficult areas. The edges of the part are also not accurately defined with the diameter of transducer used. However, defects at the edges can usually be observed visually and smaller transducers may be employed.

Radiographic examination of the S/N-1 Prototype leading edge is illustrated in Figures 6-20 through 6-22 and is typical of the other leading edges. The bare RPP-3 leading edge is pictured in Figure 6-20, while the coated condition is shown in Figures 6-21 and 6-22. These views correspond to, and can be contrasted with, the ultrasonic traces of Figures 6-15, 6-18 and 6-19. It should be noted that the surface cracks noted on Figure 6-20 are "mud" cracks, a resin rich surface condition in the radius of the part. These areas are normally cleaned up before coating and are not detrimental to the part. No delaminations or porous areas can be observed on the x-rays; however, no attenuator was used on these parts, because it had not yet been determined whether this would be detrimental to coating. Coating thickness is apparent on Figures 6-21 and 6-22 around the edges of the parts. X-ray evaluation identify delaminations if edgewise shots, such as on flanges, can be obtained, but it is not possible to identify these on flat regions without an attenuator. However, even with carbon tet the coating masks subsurface defects as noted above.

Radiographic examination revealed probable local corner delamination where the ribs and beams intersect on leading edges S/N-1 and S/N-3. Also, mud cracking prevailed on all of the parts through RPP-3 processing. The corner delaminations can be improved by better molding tooling, such as the use of RTV rubber precast mold parts. However, these corner regions are apparently not highly loaded and a weakened region at this point may not be severe.

Following coating, some degree of bond delamination of the trailing edge "T" strips was in evidence on all three leading edges. Leading edge S/N 2 was worse than the others but through both boost pressure and entry temperature tests, the severity of delamination by visual inspection remained unchanged. By comparison the bonded intercostals on the coated wing tip panel showed no evidence of delamination during coating. However, improved bonding techniques will be required.

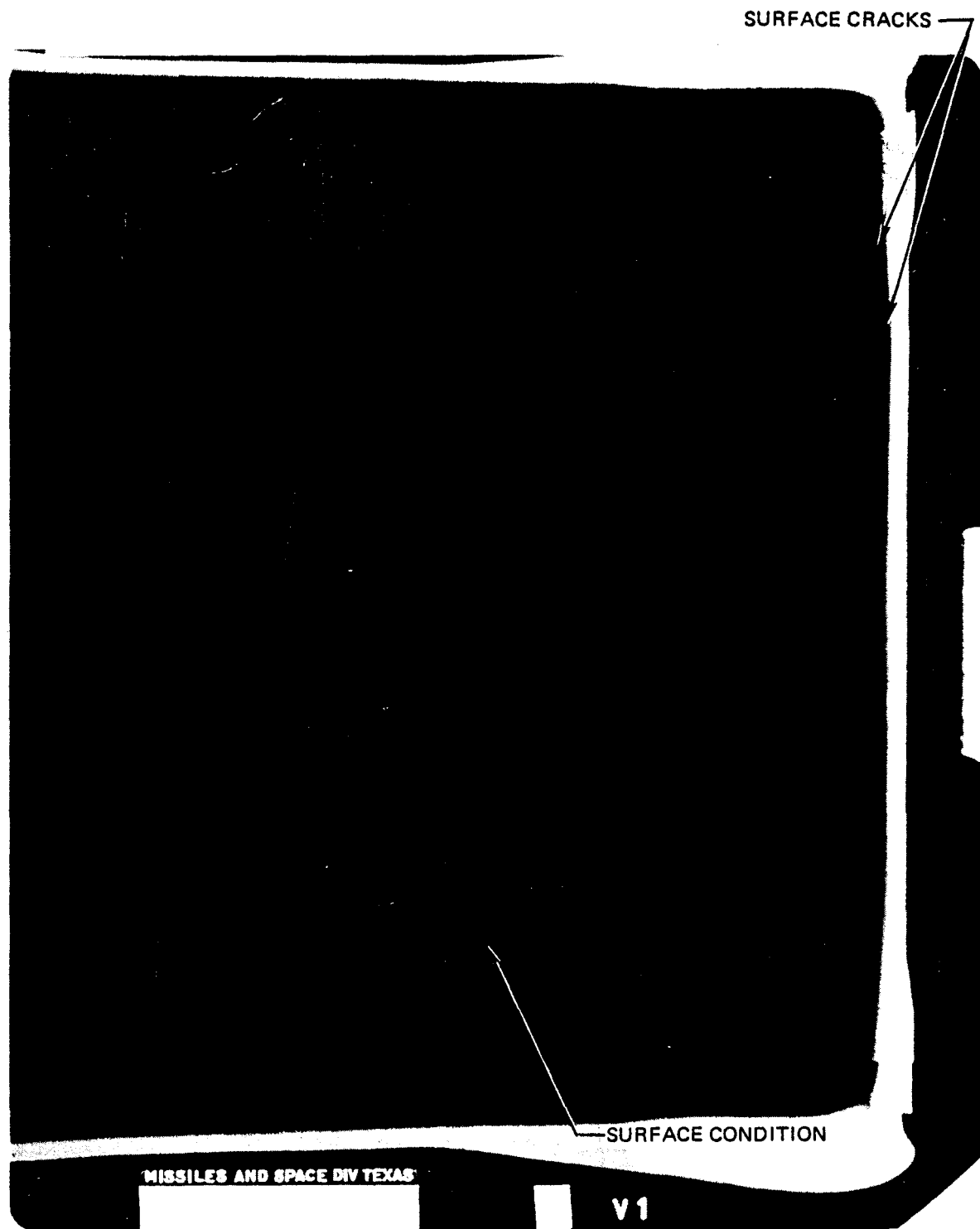


FIGURE 6-20 X-RAY VIEW 1 LEADING EDGE SKIN S/N-1

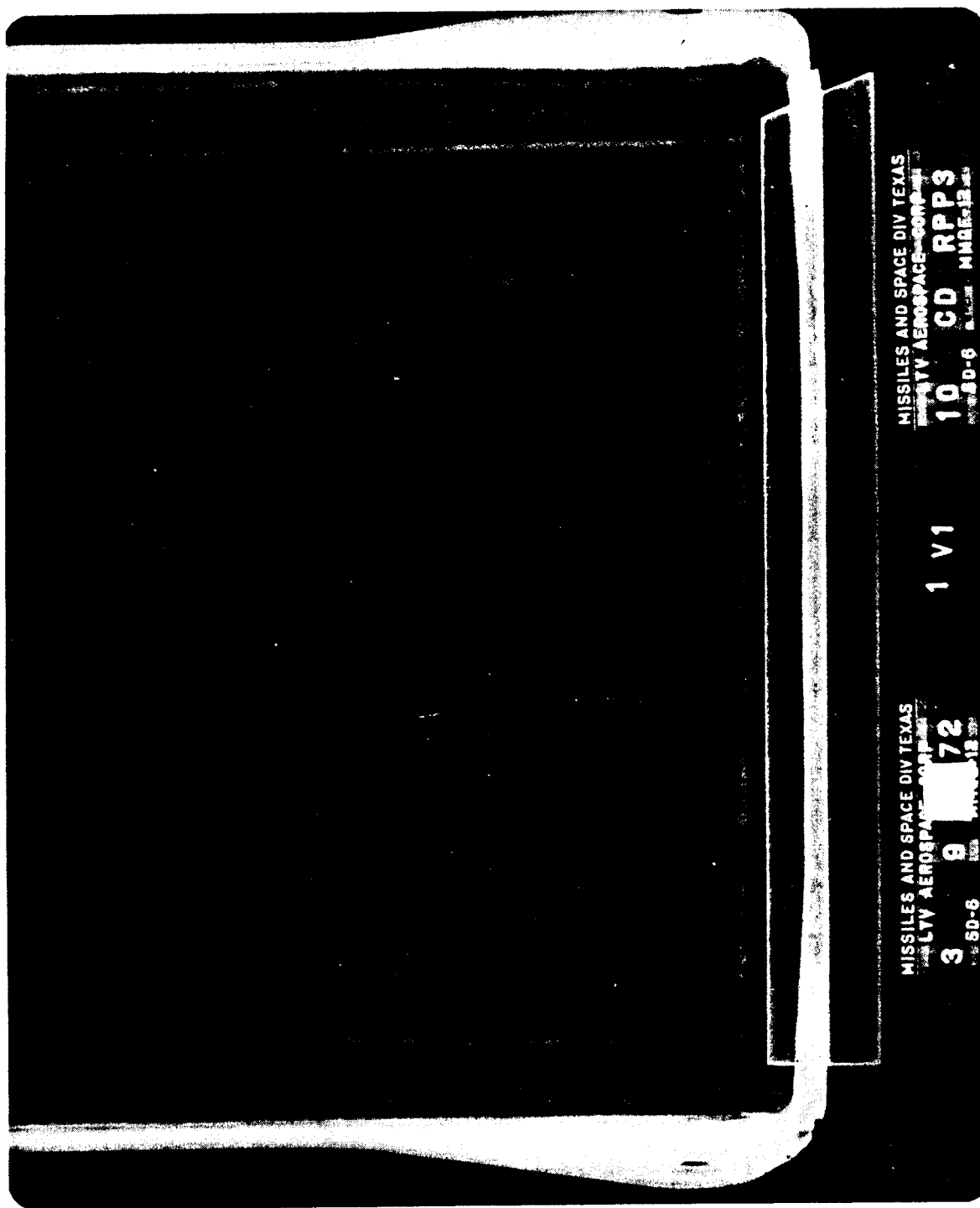


FIGURE 6-21 X-RAY VIEW OF LEADING EDGE S/N-1 AFTER COATING

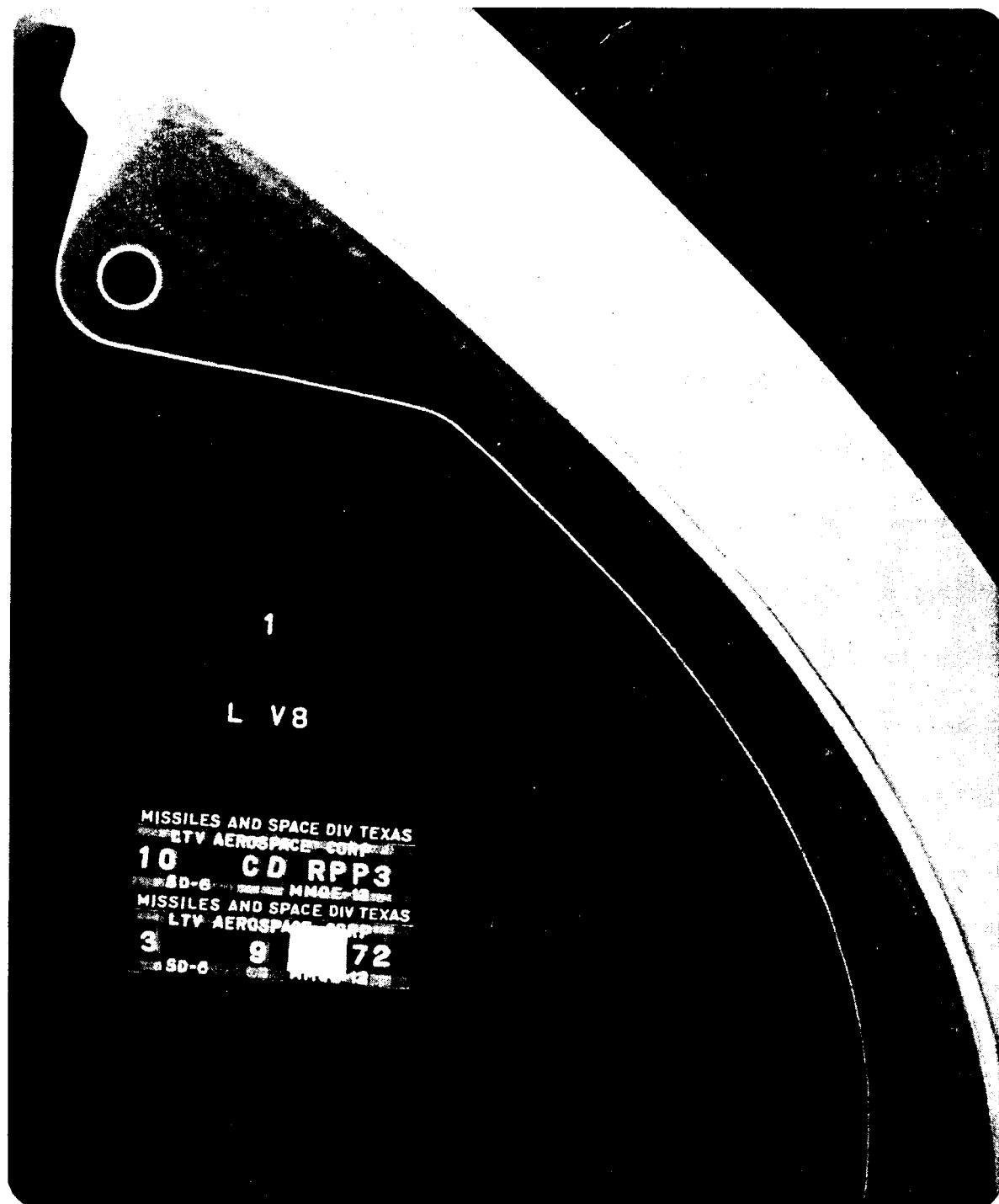


FIGURE 6-22 X-RAY OF LEADING EDGE S/N-1 AFTER COATING

In general the quality of these parts is very good especially considering the fact that these were the first units of this size and configuration fabricated. This is supported by the fact that they passed both load and thermal tests without evidence of failure of any kind.

The wing tip panels were also examined radiographically and ultrasonically, examples of which are given in Figures 6-23 through 6-25. Ultrasonic traces of both wing tip panels are shown in Figure 6-23. Indications are that the S/N 1 panel is quite porous and the intercostal bonds are also porous. This appears improved somewhat on S/N 2 but again the intercostal bond appears unbonded. However, destructive evaluation of these bonded areas will be required to be certain of the meaning of the ultrasonic indicators. Apparently the intercostals are not unbonded because this could be seen by visual examination, especially after coating.

Typical x-rays of the two wing tips are shown in Figures 6-24 and 6-25. S/N 1 has no significant defects. However, S/N 2 on Figure 6-25 shows evidence of delamination along the ribs. This panel was not coated. On both figures the scrim cloth between the two intercostal angles can be observed to wander somewhat and is probably indicating a low density bond. This might require greater clamping pressure to reduce porosity and increase bond strength.

The wing tip panels proved more difficult to fabricate than the Prototype leading edges and the x-ray of Figure 6-25 bears this out. Debulking was a problem with the wing tips because of the small restricted space. A greater span and larger corner radii may improve this situation. Improved debulking aids will be required for future parts of this configuration.

It is important for a better understanding of the applicability of NDE techniques to future efforts that destructive evaluation of these components be performed once they have served their prime purpose. This will dispel much speculation on the significance or severity of a defect indication. It is apparent that x-ray and ultrasonic C-scan techniques will become useful tools in the evaluation of RPP components, but increased emphasis on NDE will be required to produce an effective production operation.

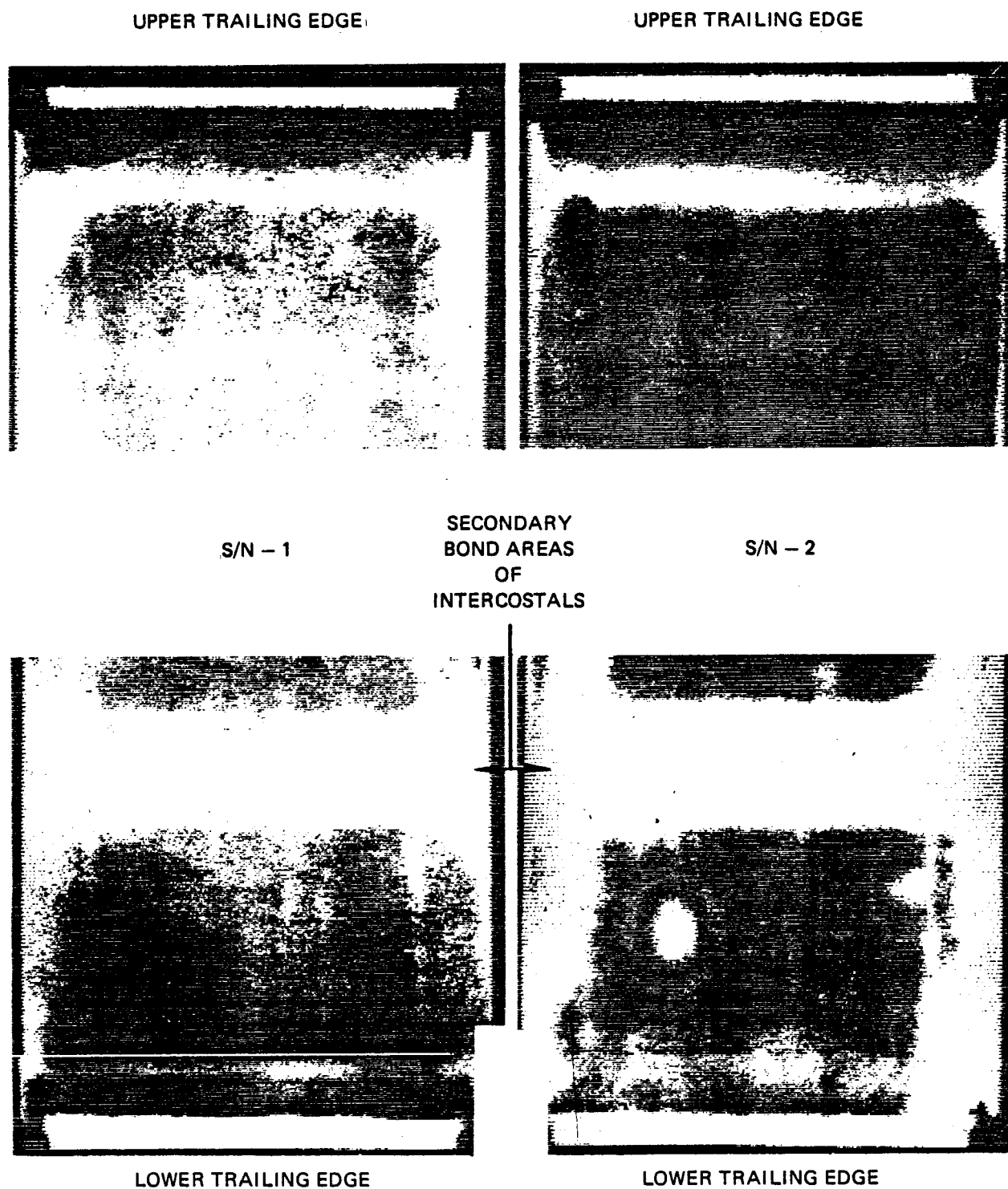


FIGURE 6-23 ULTRASONIC C-SCAN RECORDING OF WING TIPS S/N'S 1 AND 2

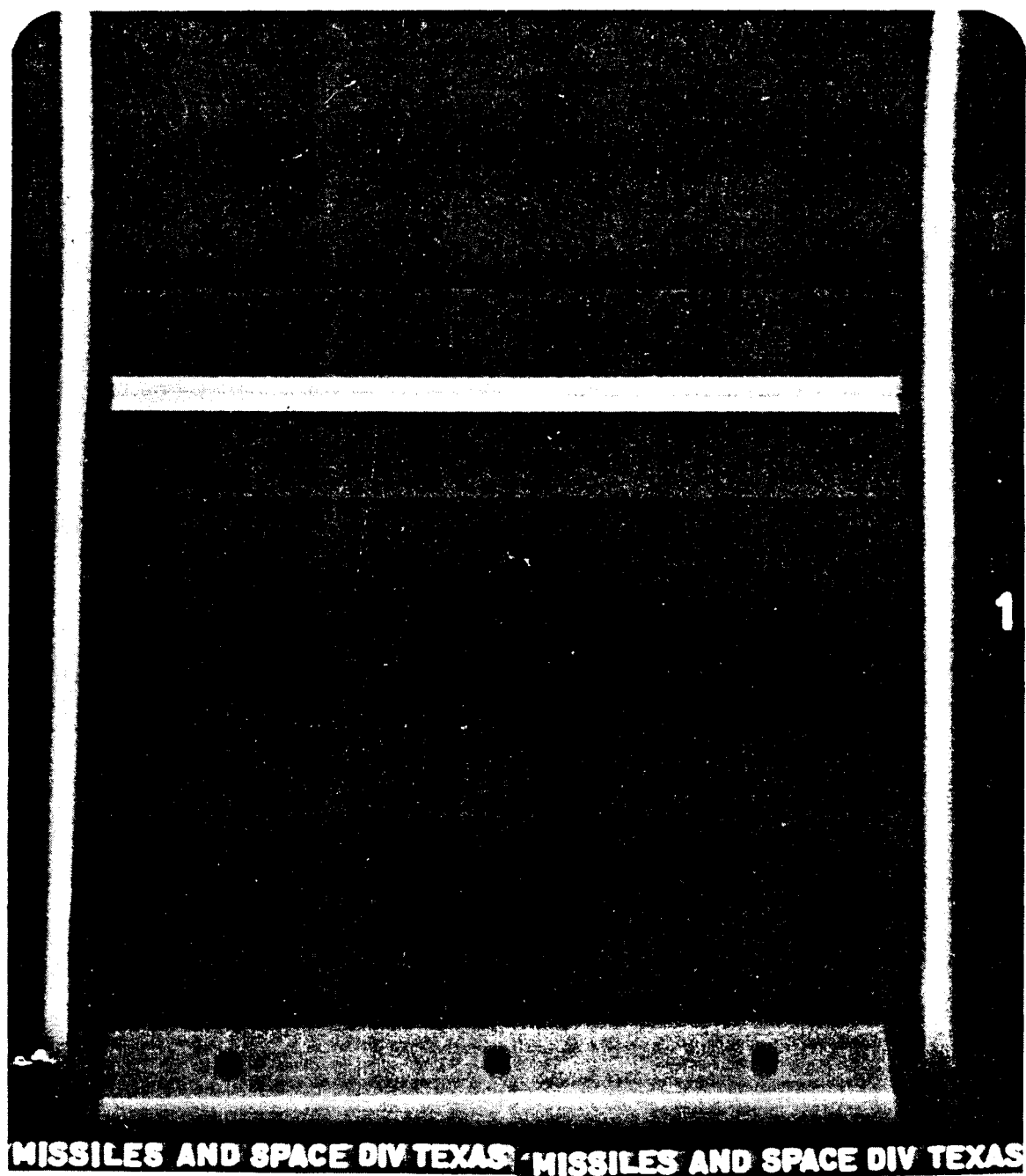


FIGURE 6-24 X-RAY OF WING TIP PANEL S/N-1 SHOWING LOWER SURFACE,
RIBS & INTERCOSTAL — RPP-3

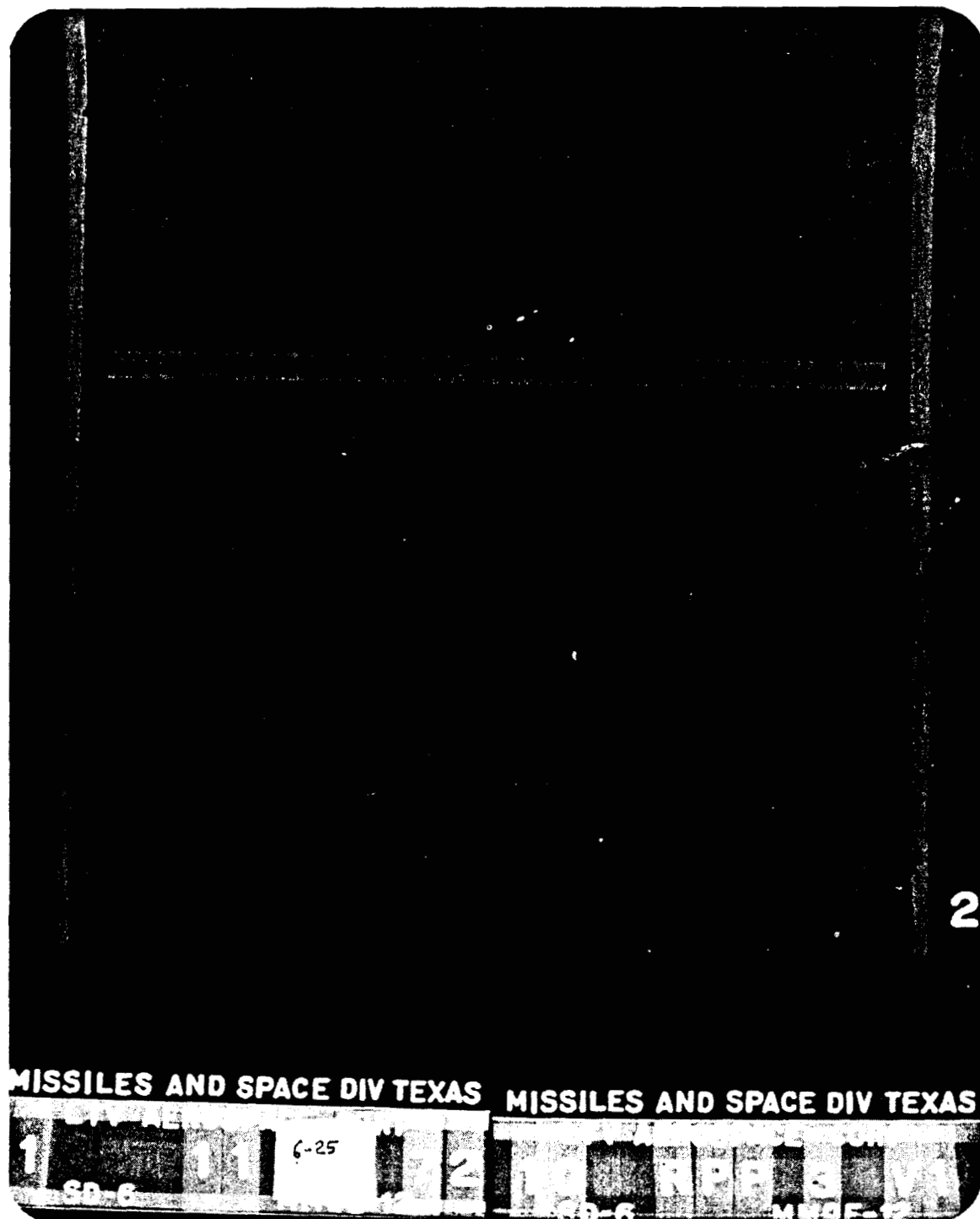


FIGURE 6-25 X-RAY OF WING TIP PANEL S/N-2 SHOWING LOWER SURFACE, RIBS AND INTERCOSTAL RPP-3

7.0 LEADING EDGE HARDWARE

As a demonstration of the ability to fabricate full scale hardware, as a verification of the applicability of analysis tools, and as a means of determining where potential fabrication problems lie, three full scale prototype leading edges and two full scale wing tip panels were successfully fabricated through coating. Two of the prototype leading edges were tested successfully at VMSC to the critical boost load and entry temperatures, while the two wing tip panels will be tested by NASA-MSFC in the 10 MW plasma arc heater. The prototype leading edges represented flight vehicle design and were fully analyzed for thermal, air loads, thermoelastic, and vibrational environments. The test environments applied maximum airloads and thermoelastic stresses without failure.

The wing tip panels by contrast were configured to an existing NASA geometry and were not analyzed, since they will be subjected only to plasma arc exposure. The design concept for support of the wing tip panel permits thermal distortion without inducing significant thermoelastic stresses.

The following sections of the report discuss the features of the test articles, the fabrication techniques employed, and the test results.

7.1 WING TIP LEADING EDGE PANELS

Two RPP wing tip leading edge panels were designed and fabricated for test in a NASA-MSFC plasma arc facility. One of the panels was coated, while the other will be tested bare. The coated panel will be used to assess the performance of the baseline 10/60/30 siliconized system under both stagnation temperature conditions and conditions producing aerodynamic shear. This will provide an opportunity to evaluate coating performance on an RPP component, rather than simply on flat panels normally used for material system evaluation. The test will also (1) indicate the most critical erosion region on a typical leading edge configuration (2) provide temperature data that can be compared against internal cross radiation analysis, and (3) obtain additional data to support analysis of low catalytic effects in stagnation and non stagnation regions.

The bare leading edge will demonstrate erosion rates and erosion patterns around the leading edge. This is important in assessing the uniformity of RPP erosion in a simulated entry environment where both temperature and aerodynamic shear stress variations are encountered.

7.1.1 Design and Instrumentation

The external geometry of the wing tip panels shown in Figure 7-1 is in general accordance with geometry supplied by NASA-MSD. The design is comprised of (1) the wing tip panel, which incorporates integrally fabricated ribs and aft attachment flanges (2) intercostals bonded to the lower surface, (3) end plates to block direct flow of plasma gasses into the wing tip cavity, (4) six thermocouples to measure temperature response in the plasma arc environment, (5) a mounting plate assembly, and (6) a carbon felt insulation shield to protect the mounting plate from overheating.

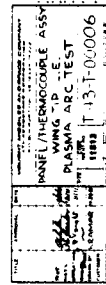
Because airloads are insignificant in the plasma arc test, no structural analysis was conducted. The 13 ply thickness was established on the basis of being comparable to that on which the bulk of the current design data was obtained. This permits more direct correlation between material fabricated in a component and that fabricated as flat panels.

Thermoelastic analysis was not conducted for two reasons: (1) with the low thermal expansion and low elastic modulus of the coated RPP, analyses on other larger full scale assemblies have shown low thermal stresses. It was estimated that relatively low thermal stresses would result on the wing tip panels, as well; and (2) the design approach frees the wing tip at the support flange to allow the rib sections to close slightly as they heat up. This will minimize thermal stresses, but requires loose attachments at the upper or lower support flanges. For plasma arc test conditions, this should be acceptable.

In accordance with NASA request, back to back intercostals were bonded to the lower surface as a demonstration of bonding technique and to assess the integrity of a bonded joint through fabrication and test. While intercostals are no longer planned for the flight vehicle, their application on the small wing tip panels assists in developing bonding technology. Bonding was performed in the as-molded condition in the same fashion as for the trailing edge seal strips for the Prototype leading edge units. Little opportunity was available to optimize the bonding technique because of schedule demands.

Thermocouples were installed into notches drilled into the RPP before coating. Chemical incompatibility of the coating and thermocouple wires is offset by utilizing a barrier of Astroceram. The life limit of this approach has not been established.

Conditions under which the thermocouples must survive are severe. For example, when used with the bare wing tip component, temperatures up to 3400°F are anticipated, while operating in an oxidizing



284-a

atmosphere (although at reduced pressures). The coated component should not exceed 2850°F but the siliconized coating is highly reactive with noble metals at these temperatures and requires protection. Thermal expansion of the part requires some spring technique to permit the thermocouple to stay in contact with the surface to be measured.

The oxidation environment prompted the use of a noble metal, rather than tungsten-rhenium for example. The 3400°F temperature dictated iridium for the thermocouple wires and beryllia for the sheath insulator. Since silicon attacks iridium and other noble metals, a chemical barrier of Astroceram was used to protect the wire. In high temperature measurements, such as will be encountered in the wing tip panel test, it is generally accepted practice to employ rigid, spring loaded, thermocouples to accommodate the thermal expansion involved. While this technique was employed in this program, the configuration of the mounting plate for the thermocouple cartridge becomes complicated as shown by the thermocouple installation in Figure 7-2.

It was felt that a better system might be obtained if a thermocouple could be fabricated with flexural "spring" in the probe portion that would insure continued surface contact as the structure expanded. This could permit a simple, uniform mounting plate for the cartridges. Such a scheme was discussed in reference 6. One company indicated that a flexed probe thermocouple might be a feasible approach to provide the spring action necessary to keep the thermocouple in contact with the part, but attempts to fabricate such a device proved negative so that a return to the coil spring cartridge approach was required.

Coil spring loaded thermocouples were procured from Aero-therm Corp., Mountain View, California. A photograph showing typical units is provided as Figure 7-3, while the cross section is depicted in Figure 7-2. Each thermocouple is comprised of 0.005 in. dia. iridium and iridium-rhodium wires in a double bored 1/16 in. dia. beryllia tube, which acts as an insulator. A 1/8 in. dia. beryllia tube is installed over the first for strength and rigidity. The coil spring, mounted in a stainless steel cartridge, provides a spring load over an excursion of $\pm 1/8$ in. The cartridge is screwed into the mounting block, located in the cool aft region of the wing tip. Mounting block temperature is monitored with ~~copper~~-constantan thermocouples to provide a reference junction temperature for the iridium units. Because iridium and the silicon carbide coating on RPP react at a low temperature, a chemical barrier of Astroceram was employed at the interface. The acceptability of this approach was demonstrated by chemical compatibility tests, conducted in an induction heater to the operating temperatures anticipated.

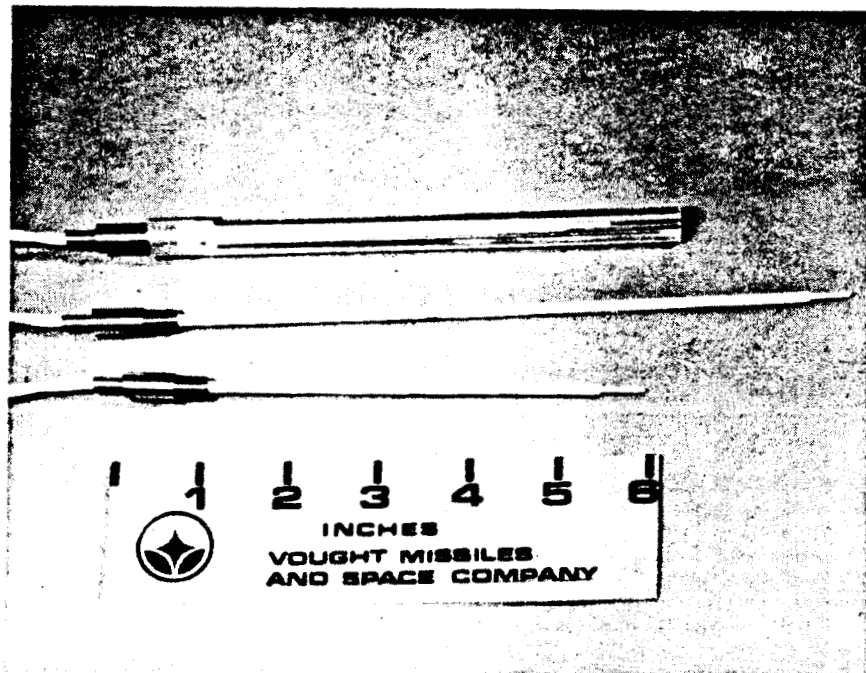
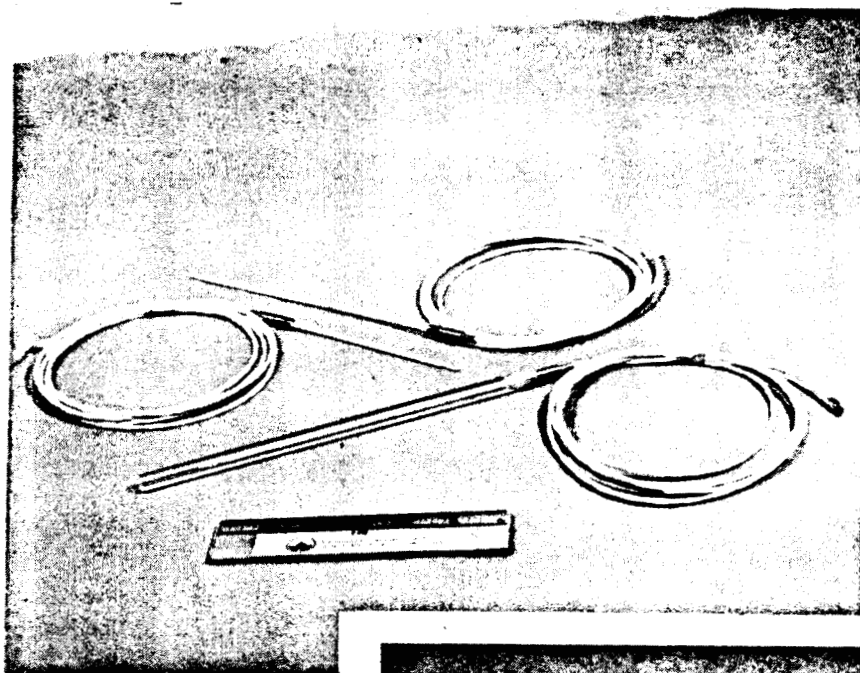


FIGURE 7-3 SPRING LOADED THERMOCOUPLES FOR WING TIP ASSEMBLIES

7.1.2 Fabrication

A female mold was employed in the fabrication of the wing tip panels to ensure a smooth outer surface and enhance the attainment of a wrinkle-free laminate. The mold (Figure 7-4) was made from a rolled and shaped aluminum plate to form the outside curved surface of the part. Aluminum reinforcing ribs were welded to the outside surface to maintain configuration during debulking and cure. Removable aluminum side plates, which facilitate the removal of the part after cure, were attached with 1/4 inch steel bolts to the outside reinforcing ribs. Epon 934, an aluminum filled epoxy, was used to form the mold for the corner or rib radii. The aft section of the mold, which forms the attachment flanges of the wing tip panel, were also removable to permit debulking during lay-up and facilitate removal of the part after cure.

Lay-up began by tailoring the phenolic graphite prepreg to the total overall outside dimensions of the part. These tailored plies were then placed in the mold one ply at a time while hand debulking with a heat gun (150°F) and metal rollers. Additional debulking was performed after each 3 plies of layup using a rubber plunger (Figure 7-4) in a large platen press at 50 psi pressure. After the final ply was placed in the mold, the prepreg graphite, which forms the aft attachment section, was folded into the mold, metal plates were attached and final debulking was performed using the rubber bladder shown in Figure 7-4. This bladder was pressurized to 50 psi for final debulking of the part and also to form the attachment flange section. After final debulking, silicone rubber molds (Figure 7-4) were employed in the radius areas to form the corners and minimize wrinkling.

Perforated cellophane and dry fiberglass cloth was placed over the layup for volatiles removal during cure. The layup and mold were then packaged in a mylar bag which was sealed and evacuated. Autoclave cure was conducted at a pressure of 80 psi, while vacuum was maintained in the mylar bag throughout the cure cycle. The heating profile peaked at 300°F in accordance with the requirements of LTV specification 308-7-10A. After cure, the bag and part were removed from the mold.

A three piece aluminum mold was used to form the internal reinforcing angles (intercostals) for the wing tip. These parts were fabricated through cure like the main wing tip section. After cure and rough trim the reinforcing angles were bonded to the inside surface of the wing tip body (Figure 7-5) using the following procedure. Faying surfaces were sanded with a 240 grit sandpaper to remove the parting film and to deglaze the surface. Liquid R-120 resin was then brushed on all faying surfaces and allowed to dry to remove the excess alcohol. When the resin

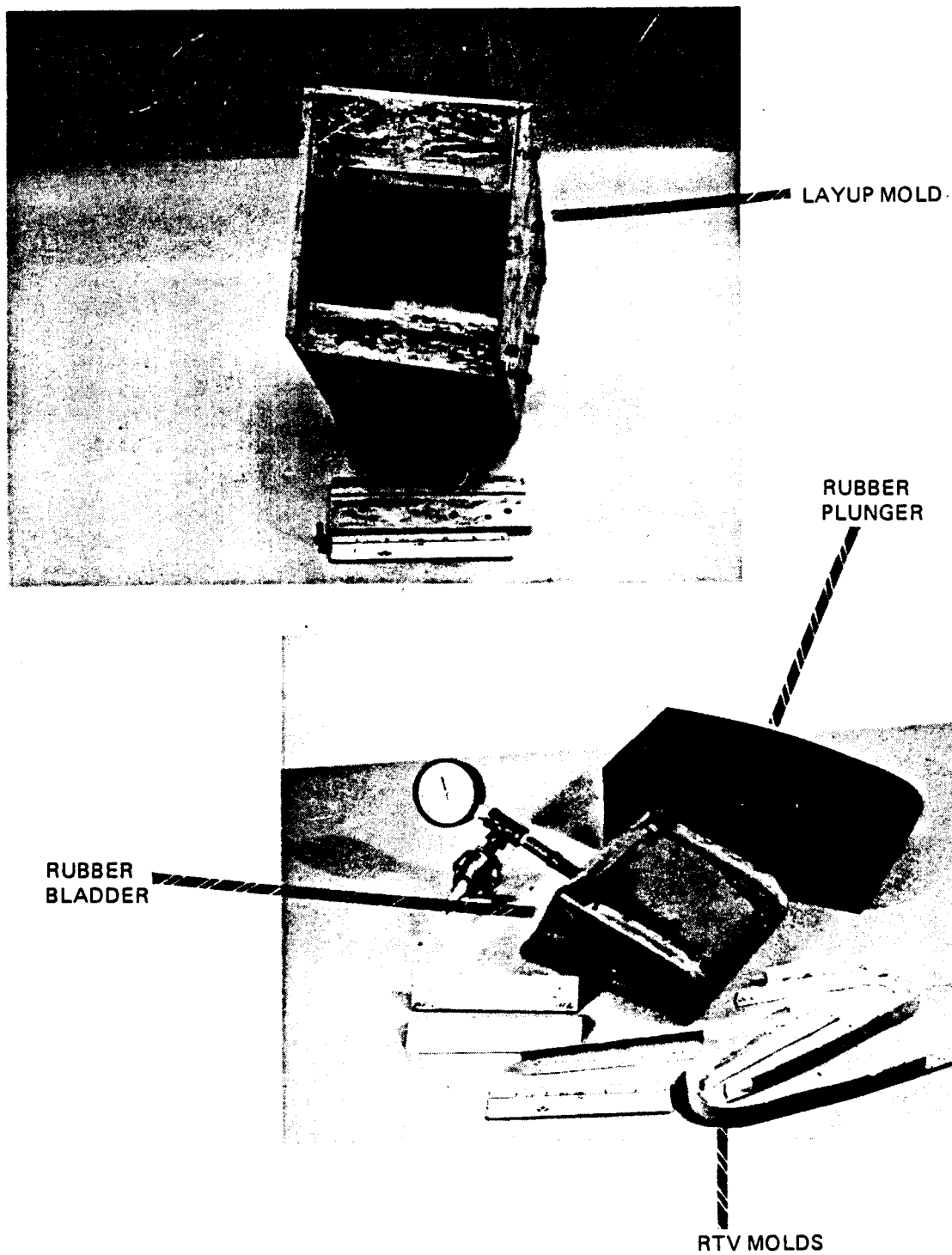


FIGURE 7-4 WING TIP MOLDING TOOLS

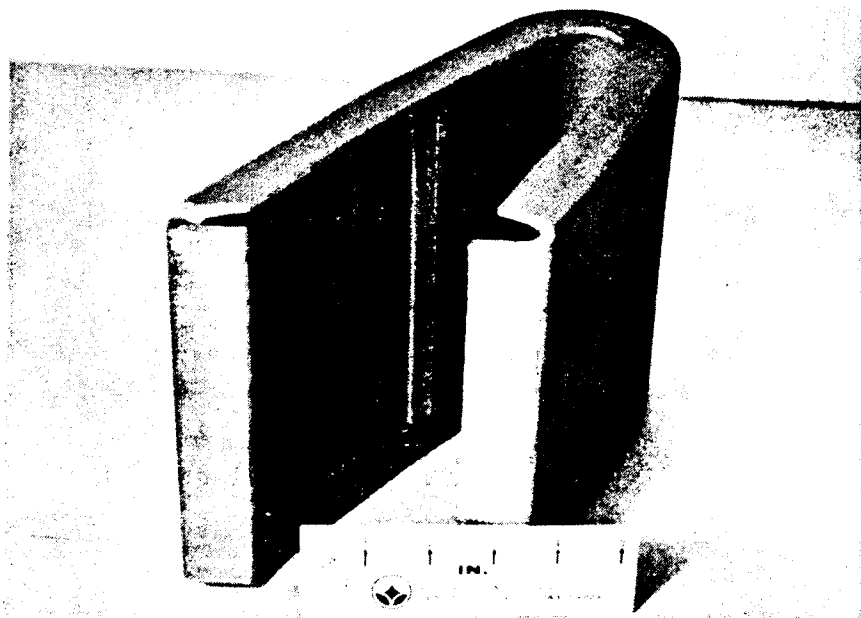


FIGURE 7-5 WING TIP SECTION SHOWING BONDED REINFORCING ANGLES



FIGURE 7-6 GRAPHITE HOLDING FIXTURES FOR PYROLYZATION OF THE WING TIP

became tacky, one ply of WCA/R-120 prepreg cloth was placed between the two angles and also between the angles and the wing tip section. Additional strips of prepreg cloth were placed in the radius areas between the angles to fill and seal the cavity for coating. The bonding layup was then bagged in a mylar bag, evacuated, and cured for two hours at 300°F under vacuum pressure.

The wing tip panel assembly in the as-molded state was then placed in a female graphite holding fixture, conforming to the outside contour of the part (Figure 7-6) for pyrolysis. Additional graphite holding fixtures are placed inside the part in the aft section and around the internal flange areas to eliminate angle closure. Pyrolysis was conducted with the part packed in a stainless steel retort filled with coarse carbon particles which provide high thermal conductivity during pyrolysis and also act as a scavenger for oxygen to produce an oxygen free atmosphere for the part. A 96-hour time-temperature profile is provided by a cam controller to reach the 1500°F pyrolyzation temperature.

The pyrolyzed part, now in the RPP-0 state, was reimpregnated to increase strength. It was placed in a vacuum pressure chamber to remove air from the pores in the part. Subsequently, the chamber was filled with catalyzed furfuryl alcohol and pressurized to 80 psi to force the alcohol into the fine pores.

After removal, the wing tip panel was blotted with paper towels to remove the excess furfuryl alcohol. Autoclave cure of the furfuryl alcohol was limited to two hours at 300°F after which the part was again placed in the graphite holding fixture and pyrolyzed as before. The impregnation and repyrolyzation cycle was performed three times to strengthen the part to the desired RPP-3 state.

The RPP-3 part was then machined to final configuration and washed with isopropyl alcohol in preparation for coating. Coating was conducted in a cylindrical retort and the 10 alumina -60 silicon carbide-30 silicon baseline system pack material. Coating process details are discussed in Section 4.3.2. Heat treating to improve high temperature oxidation resistance was performed at a nominal 3200°F. The coated part is shown in Figure 7-7.

NDE X-ray and ultrasonic evaluations of the wing tip assemblies in the RPP-3 state are covered in Section 6.0. An assembly of the wing tip panels with thermocouples installed is pictured in Figure 7-8. These particular photos are of the uncoated unit, which was the first to be assembled. Care had to be exercised with the fragile thermocouples during installation and they were easily pulled out of their sockets because of the weak spring loading. However, they were equally easy to reinsert.

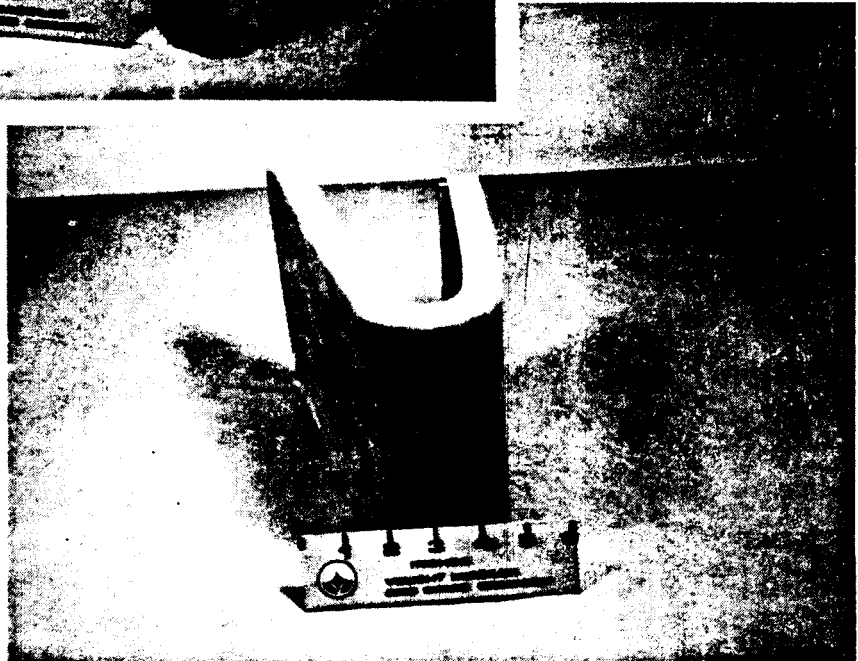
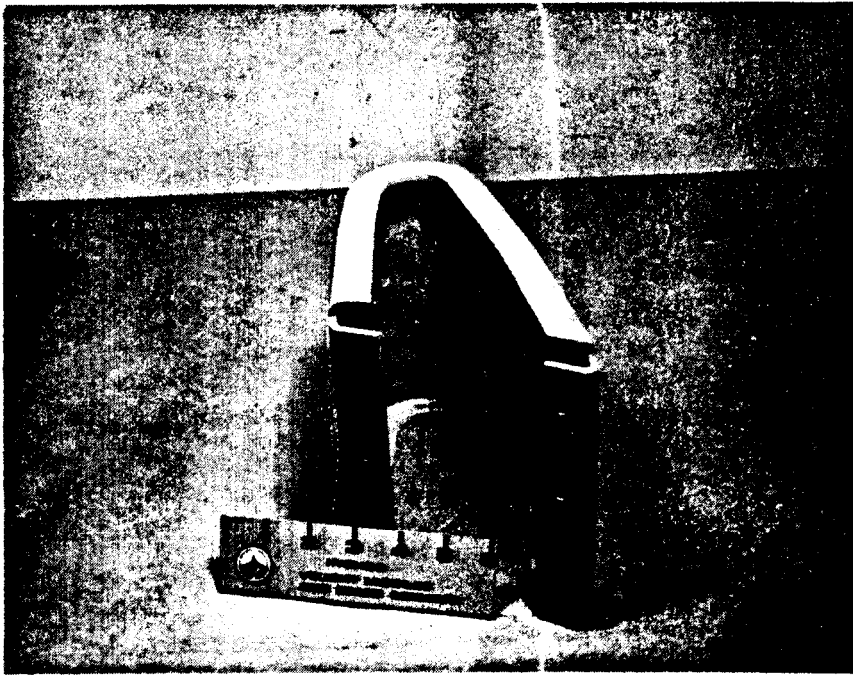


FIGURE 7-7 WING TIP PANEL S/N-1 FOLLOWING COATING

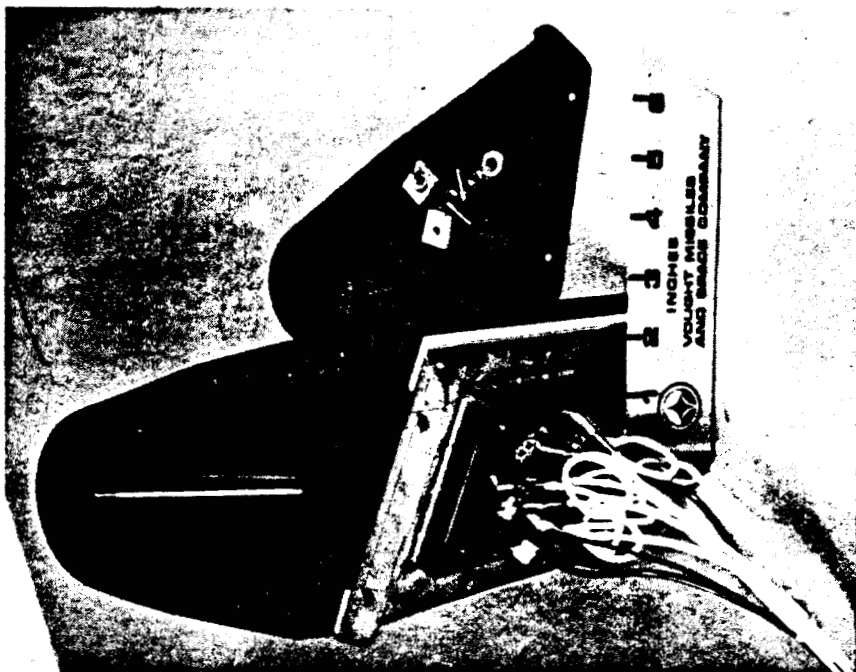


FIGURE 7-8 BARE WING TIP PANEL ASSEMBLY SHOWING THERMOCOUPLE INSTALLATION

7.1.3 Test Plans

As noted previously, the two wing tip panel assemblies are to be tested in the NASA-MSFC 10 MW plasma arc tunnel. A test plan was prepared for NASA-MSFC that contained the following objectives:

- Confirm predicted erosion rate of bare carbon-carbon in a simulated entry environment representative of the space shuttle wing leading edge.
- Determine erosion distribution of bare carbon-carbon around a representative wing section.
- Confirm predicted skin temperature reduction due to cross-radiation.
- Evaluate persistence of low catalytic effects on coated carbon-carbon downstream of the stagnation line.
- Confirm applicability of flat face model plasma test data to a leading edge configuration.
- Establish life limits for the coated wing tip.

The models will be oriented at an angle of attack of 30° to the flow but sweep angle will be 0° . Because of low catalytic effects, the maximum recommended local cold wall heat flux rate for the coated model was raised to 100 BTU/ft² sec to achieve a surface temperature of 2700°F at an enthalpy of 12000 BTU/lb. Multiple cycling was recommended to establish coating life limits on the model. Tests with insulation to prevent internal cross radiation will be compared to those where this heat transfer is not suppressed so that analytical techniques can be verified.

The bare model will be employed both as a "calorimeter" and as a means of establishing empirical erosion rates for comparison with analytical predictions. This data is desirable for further evaluation of uncoated RPP in the entry environment. Erosion rates will also be determined for the coated model at various locations around the wing tip. Thickness changes will be used for this evaluation.

7.2 PROTOTYPE LEADING EDGE

The design and analysis of the prototype leading edge assemblies are covered in Section 3.0, while the NDE and other inspection aspects of fabrication are documented in Section 6.0. This section of the report discusses fabrication of the three prototype leading edge assemblies and

the curved seal strips. In addition the boost pressure loads test and entry temperature test, conducted on the leading edge assemblies, are summarized herein.

7.2.1 Fabrication

The mold for the fabrication of Prototype leading edges (Figure 7-9) was made from a rolled aluminum plate stiffened with welded reinforcing webs, to form the outside curved surface of the part. Machined aluminum strips were riveted and bonded to the curved section for forming the joggles in the outside surface. Shaped aluminum plates were welded to the edges of the curved sections to form the rib areas. Removable end plates were attached with steel bolts to form the end closure (trailing edge beams) and facilitate removal of the part from the mold after cure. Molded sections to form the corner radii of the RPP were made from Epon 934 adhesive. These were replaced for each new part. A three piece aluminum mold was used to form the curved seal strip, Figure 7-10, and consisted of a rolled aluminum plate to form the outside contour and two machined aluminum plates which formed the vertical reinforcing web. The trailing edge "T" section seal mold was a straight three piece aluminum mold like that used for the curved seal strip.

Lay-up of the leading edge prototype began by tailoring the phenolic graphite prepreg cloth to the total outside dimensions of the part. These tailored plies were placed in the mold one ply at a time with hand debulking using a heat gun (150°F) and metal rollers. The placement of the plies, forming of the corners, and the addition of a ply build-up area on the lower surface are described on the Engineering drawings in Sections 3.2 and 3.3.

Special attention was given to debulking the internal radius areas of the layup. Final debulking was accomplished by bagging the entire lay-up and heating to 180°F under vacuum pressure. The vacuum was reduced and the heated part was further debulked using metal rollers. Special shaped rollers were used in the radius areas.

The seal strips were formed by laying-up one half of the tailored plies of prepreg cloth on each curved machined section of the mold. Spacers were placed between the mold sections to eliminate over debulking and three positioning rods were placed in positioning holes in the mold before the two sections were brought together. These sections were then debulked in a platen press. Strips of prepreg cloth were placed in the radius section to fill the gap and the final plies of cloth were layed-up to complete the curved sections of the seal strip. The curved section of the mold was then placed over the lay-up for bagging and cure. Trailing

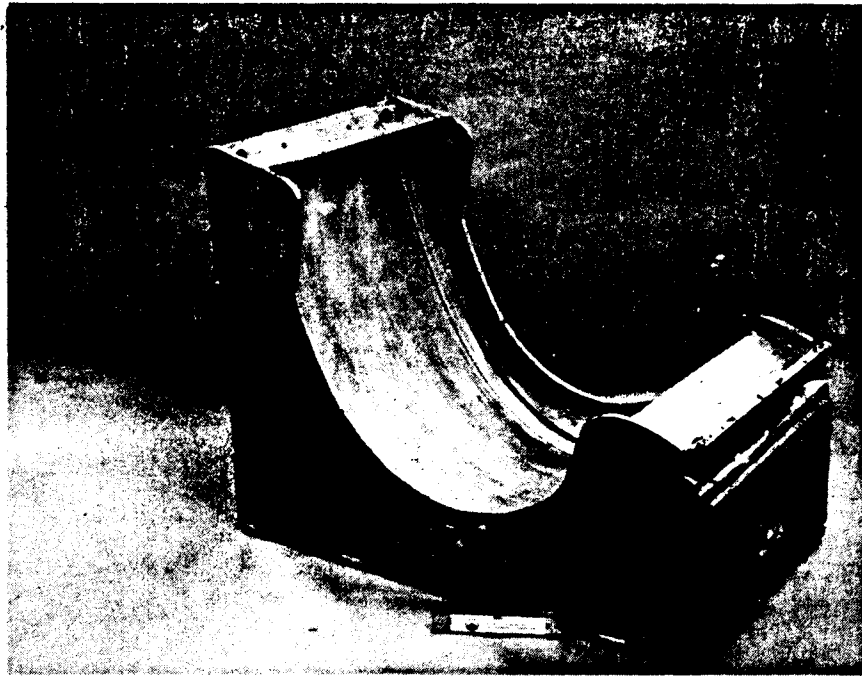


FIGURE 7-9 PROTOTYPE LEADING EDGE LAYUP MOLD

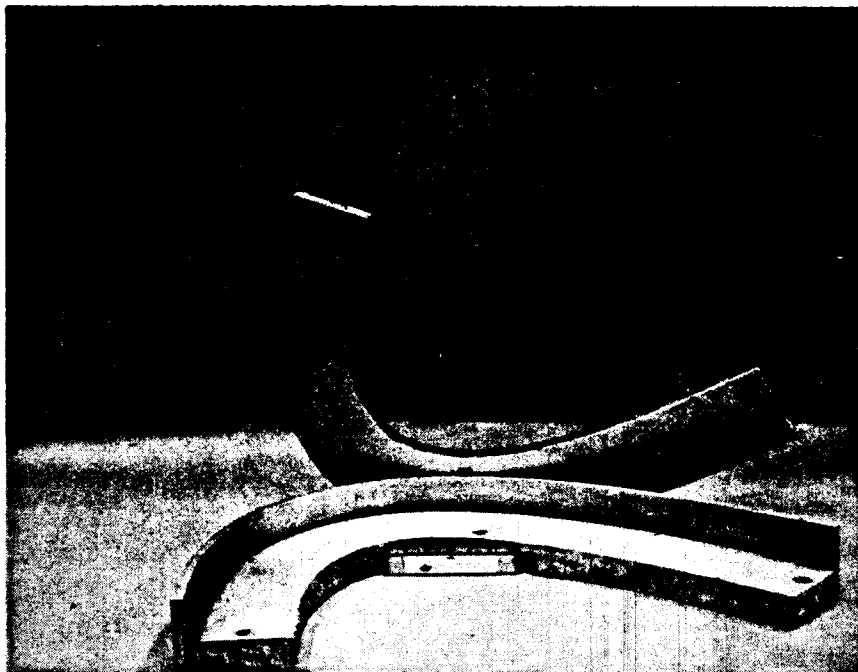


FIGURE 7-10 SEAL STRIP MOLD

edge seal strips were layed-up in a like manner using three piece aluminum tools. All parts were bagged and cured in the autoclave as described in section 7.1.2

After rough machining the aft seal strips were bonded to the main leading edge section in the following manner. Faying edges were sanded with 240 grit sandpaper to prepare a clean bonding surface. The area was cleaned with alcohol, and brush coated with R-120 liquid resin, which was allowed to dry at room temperature. WCA graphite/phenolic prepreg cloth was placed on the main body of the leading edge over the area to be bonded. A slight mismatch in the radius areas was filled with strips of WCA prepreg cloth to eliminate voids. The seal strips were located on the main leading edge section using pilot holes, which were later filled with RPP rivets. An evacuated mylar bag covered the assembly during bond cure at 300°F for two hours. After bonding, the pilot holes were drilled and countersunk in preparation for RPP rivets, Figure 7-11, which were fabricated as follows.

Kreha KCF-100, SY-503 carbon fiber thread was wrapped on an aluminum drum and dip pre-preged with R-120 phenolic resin. Drying of the resin was done at room temperature, while rotating the drum to assure even resin distribution. "B" staging was conducted in a circulating oven for 30 minutes at 180°F. The prepreg threads were then placed in the debulking mold, Figure 7-12, which shaped the threads into a round rod. This rod was then frozen in liquid nitrogen and machined in the frozen state to final dimensions. Pieces were cut to a length that allowed the rod to protrude 1/4" on each side of the section to be riveted. Warming to room temperature then allowed the "B" staged fibers to return to their plyable condition.

Shaped plugs, Figure 7-13, machined from as-cured WCA/phenolic laminates, were used to shape the countersunk heads of the RPP rivets. The protruding prepreg fibers were separated at the center and spread to the outside of the countersunk hole. The shaped plugs, having a brush coat of R-120 phenolic resin, were placed on both sides of the rivet and clamped. Curing of the rivets was conducted in a circulating oven at 300°F for two hours. After cure, the excess plug and fibers were machined off to leave a flush countersunk rivet (Figure 7-11).

Pyrolyzation of the prototype leading edge assembly was performed in a graphite restraining fixture in a carbon particle filled retort shown in Figure 7-14. The prototype leading edge segments were pyrolyzed, and reimpregnated and repyrolyzed three times as described in Section 7.1.2. Figure 7-15 shows a prototype leading edge assembly and seal strip in the RPP-3 state ready for coating.

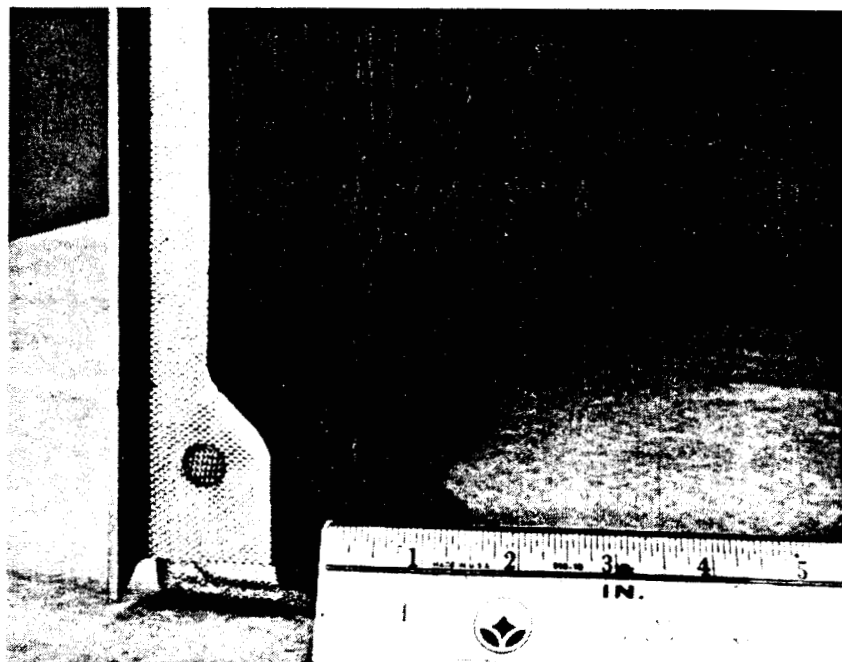


FIGURE 7-11 LEADING EDGE SECTION SHOWING RPP RIVET

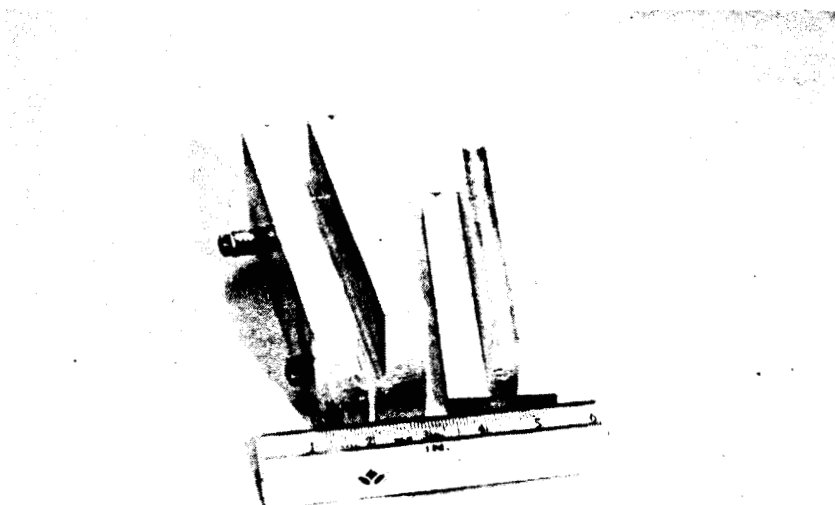


FIGURE 7-12 RIVET DEBULKING MOLD



FIGURE 7-13 AS - CURED PLUG USED TO FORM THE HEAD OF AN RPP RIVET

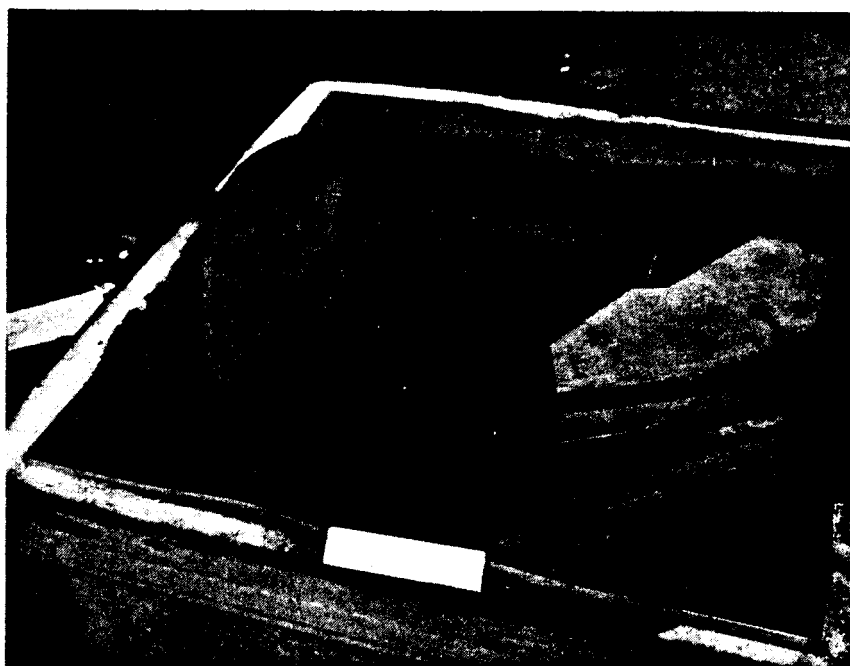


FIGURE 7-14 GRAPHITE RESTRAINING FIXTURES FOR PROTOTYPE LEADING EDGE IN PYROLYZATION RETORT

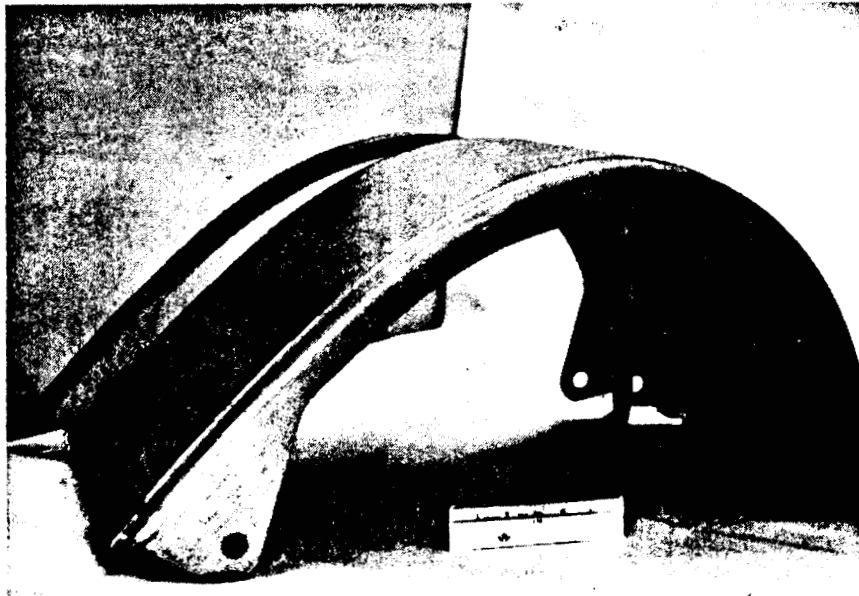


FIGURE 7-15 PROTOTYPE LEADING EDGE ASSEMBLY AND SEAL STRIP READY FOR COATING

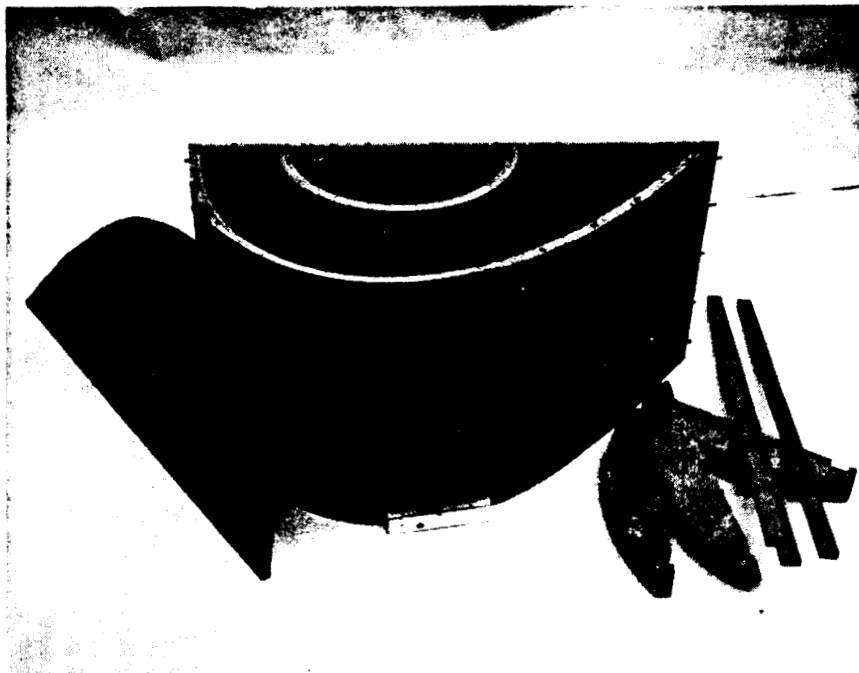


FIGURE 7-16 SHAPED GRAPHITE RETORT USED FOR COATING PROTOTYPE LEADING EDGE ASSEMBLIES

The parts were packed in a 10 alumina - 60 silicon carbide - 30 silicon pack material in a shaped graphite retort, Figure 7-16, and coated in an argon atmosphere at 3050°F for two hours. Parts were readily removed from the pack and cleaned with a stiff bristle brush. Details of the coating process are discussed in Section 4.3.2. Photographs of the coated hardware are shown in Section 7.2.2.

7.2.2 Test

Prototype leading edges were tested to the maximum design airload condition occurring during the boost phase, and to the maximum thermal stress conditions encountered during entry. The purpose of these tests was to demonstrate that the design would indeed meet limit stress conditions for single mission exposure without failure. These tests were used to prove that gross deficiencies in design or fabrication did not exist. Neither time nor funding permitted cycling to validate 100 mission life capability. However, temperature cycling for 100 missions has been conducted successfully by North American Rockwell on the RPP belly panel, which was fabricated and coated by VMSC.

Boost Pressure Test - The most critical design condition for the leading edge occurs at an angle of attack of -5.8° during launch at the period of maximum dynamic pressure. The assumption of 1.0 psi venting lag (Section 3.1) produces a limit pressure differential of 2.6 psi on the lower surface of the leading edge and a very small or essentially zero pressure differential on the upper surface (reference Figure 3-40 for subcase II). This condition is critical for all but the upper trailing edge beam; however, applied stresses on the upper beam are small and not significant. A good representation of the design condition, which was used for test, is a uniform pressure differential of 2.6 psi limit applied from the trailing edge on the lower surface to within 4 in. wrap distance of the geometric stagnation point. This pressure was applied by a bladder, attached to a laminated phenolic block, contoured to match the leading edge. The block and bladder can be seen in the background of Figure 7-17.

Thirty-five strain gages were applied and recorded during test. In addition, four deflections were monitored. Strain gage locations can be seen in Figures 7-17, 7-18, and 7-19. Deflectometer supports and locations can be seen in Figure 7-20. These record rib and panel maximum outward deflections, and inward deflections of both trailing edge beams.

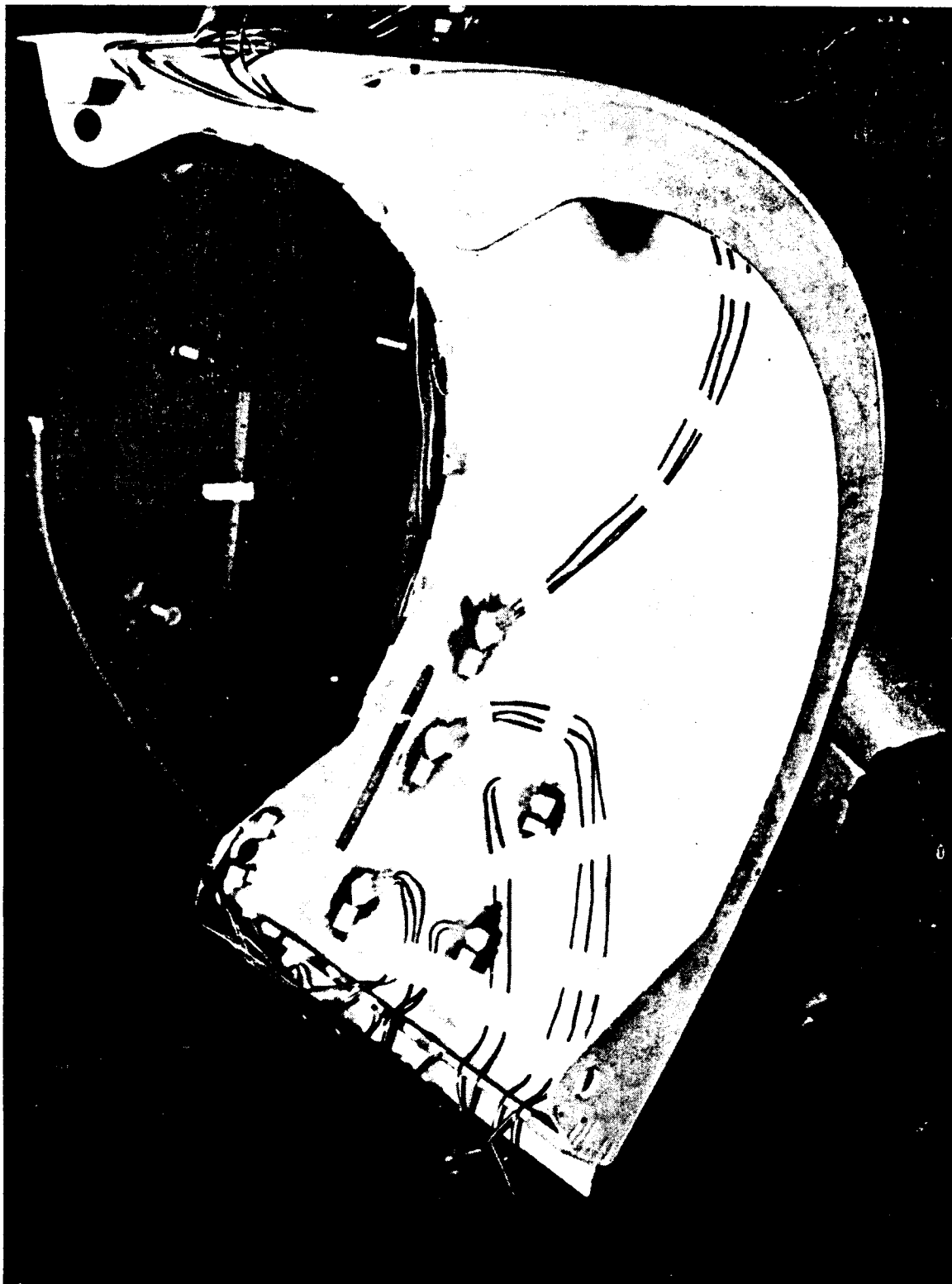


FIGURE 7-17 STRAIN GAGE INSTALLATION BOOST PRESSURE LOAD TEST



FIGURE 7-18 STRAIN GAGE INSTALLATION LOWER PANEL BOOST PRESSURE LOAD TEST

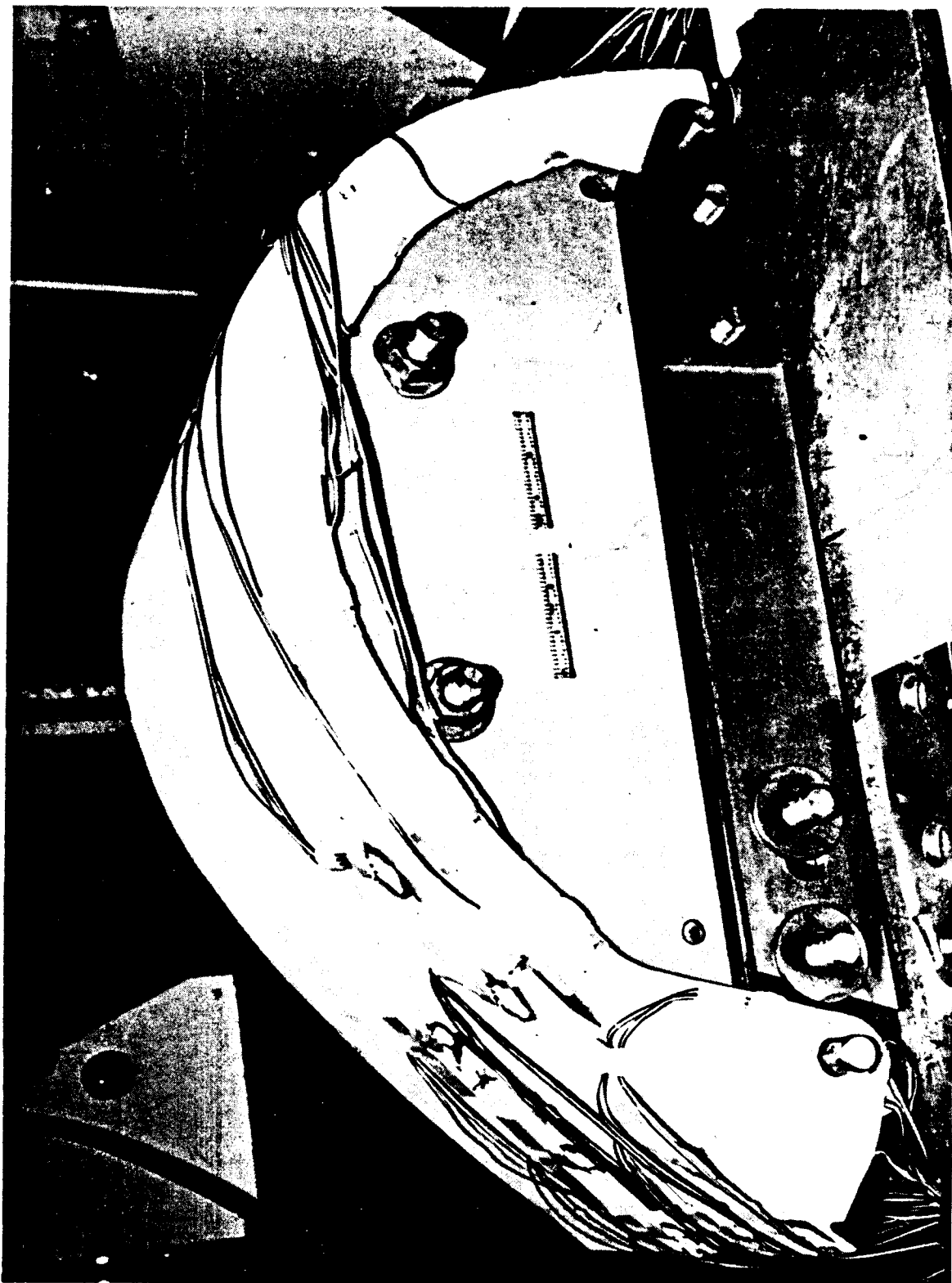


FIGURE 7-19 STRAIN GAGE INSTALLATION RIB AND LUG BOOST PRESSURE LOAD TEST

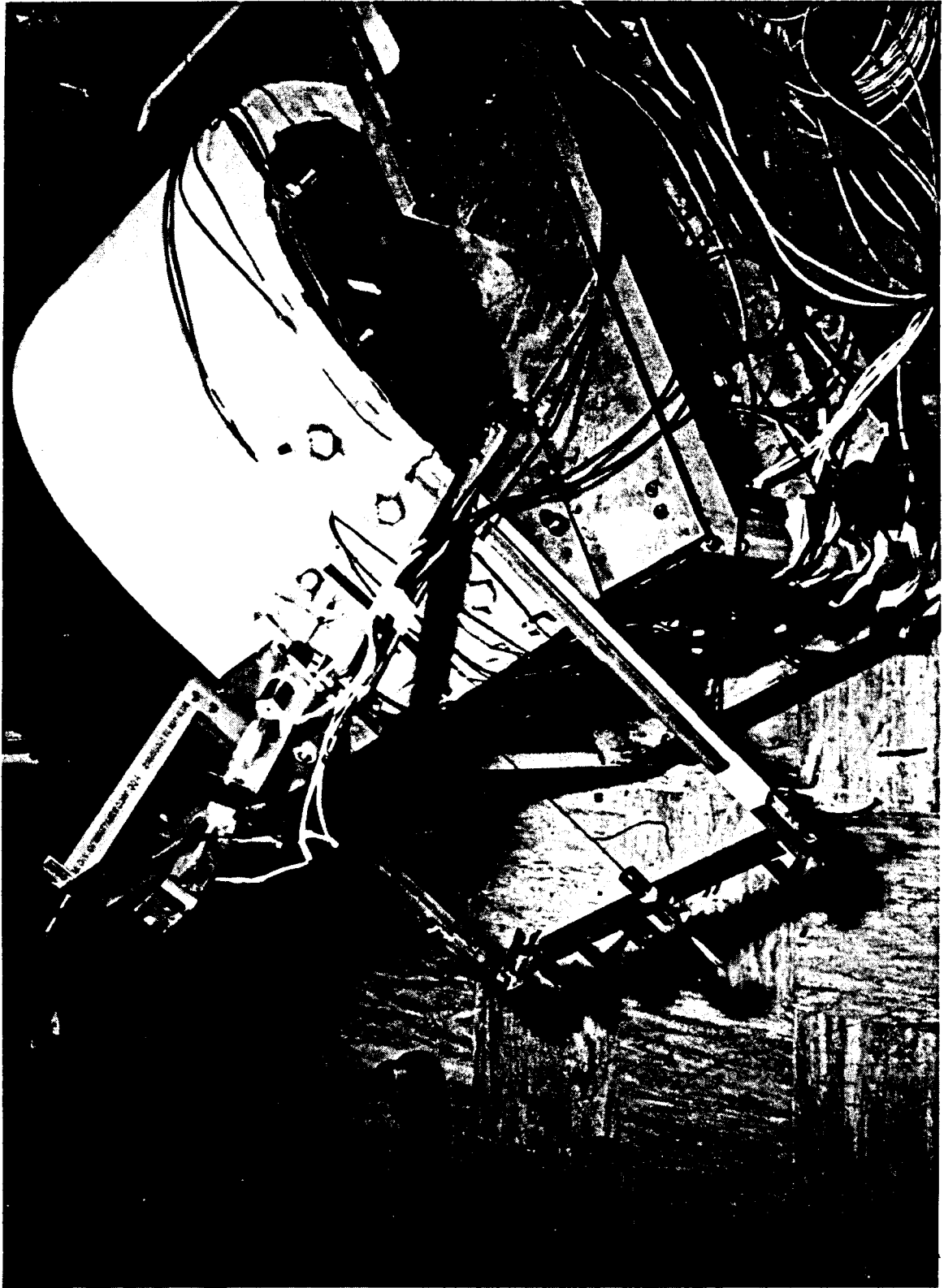


FIGURE 7-20 DEFLECTOMETER INSTALLATION BOOST PRESSURE LOAD TEST

The most significant data to be obtained from the test, according to stress analysis results, is the stress in the upstanding leg of the ribs, skin shear stresses in the lower corner of the panel, and deflections of the rib and panel. These data are shown in Figures 7-21, 7-22, and 7-23 along with bending stress data in the lower skin panel.

Rib stresses computed using the NASTRAN routine are compared against experimentally determined stresses in Figure 7-21. Limit load stresses at the top of the upstanding flange are plotted against the coordinates used in the NASTRAN analysis. Their relationship to the overall panel is indicated in Figure 3-39. Grid point 1 represents the lower trailing edge, while grid point 109 is located at the upper surface trailing edge. Correlation is quite good in the prediction of tensile stresses but compression stresses on the lower portion of the rib were overstated by analysis. The reason for this may be that assumptions of skin effectiveness (width) acting in bending with the rib beam elements was conservative, which could effect the stresses significantly.

A comparison of computed and measured skin stresses are shown in Figure 7-22 for two areas: (1) the maximum bending stresses in the lower panel at the centerline of the leading edge segment and (2) the lower corner of the panel at the beam-rib intersection. At point "A" (Figure 7-22) the chordwise prediction of stresses is close to measured. The axial component of stress is about the same as, but the bending component is lower than predictions. Spanwise stress at point "A" is significantly lower than predicted. This is true of both the axial and bending components of stress. Similarly, at the center of the lower beam the maximum compression stress measured was only 1161 psi compared to a 3060 psi prediction. It isn't clear why this should be, but in general, from examination of measured stresses, the leading edge appears structurally more efficient than NASTRAN analyses would indicate. This is probably due to the curved skin and "picture frame" effect of the ribs and beams, which produce a stiff indeterminate structure.

The maximum shear area at point "B" indicates a higher measured stress than computed, but it must be pointed out that shear modulus data is not available so that isotropic equations were used in reducing rosette strain gage data. This probably results in predicting a higher shear modulus than actual and therefore an overstatement of shear stress. Measured shear stress, reduced in this fashion, is 40% higher than predicted. However, even if strain gage data so evaluated were correct, a margin of safety at ultimate of 23% would exist based on recent shear strength data. Shear modulus data must be obtained, however, before any accurate predictions can be made. Bending data at point "B" tends to indicate that shear stress rather than bending or axial stress dominates at this particular location as predicted by analysis.

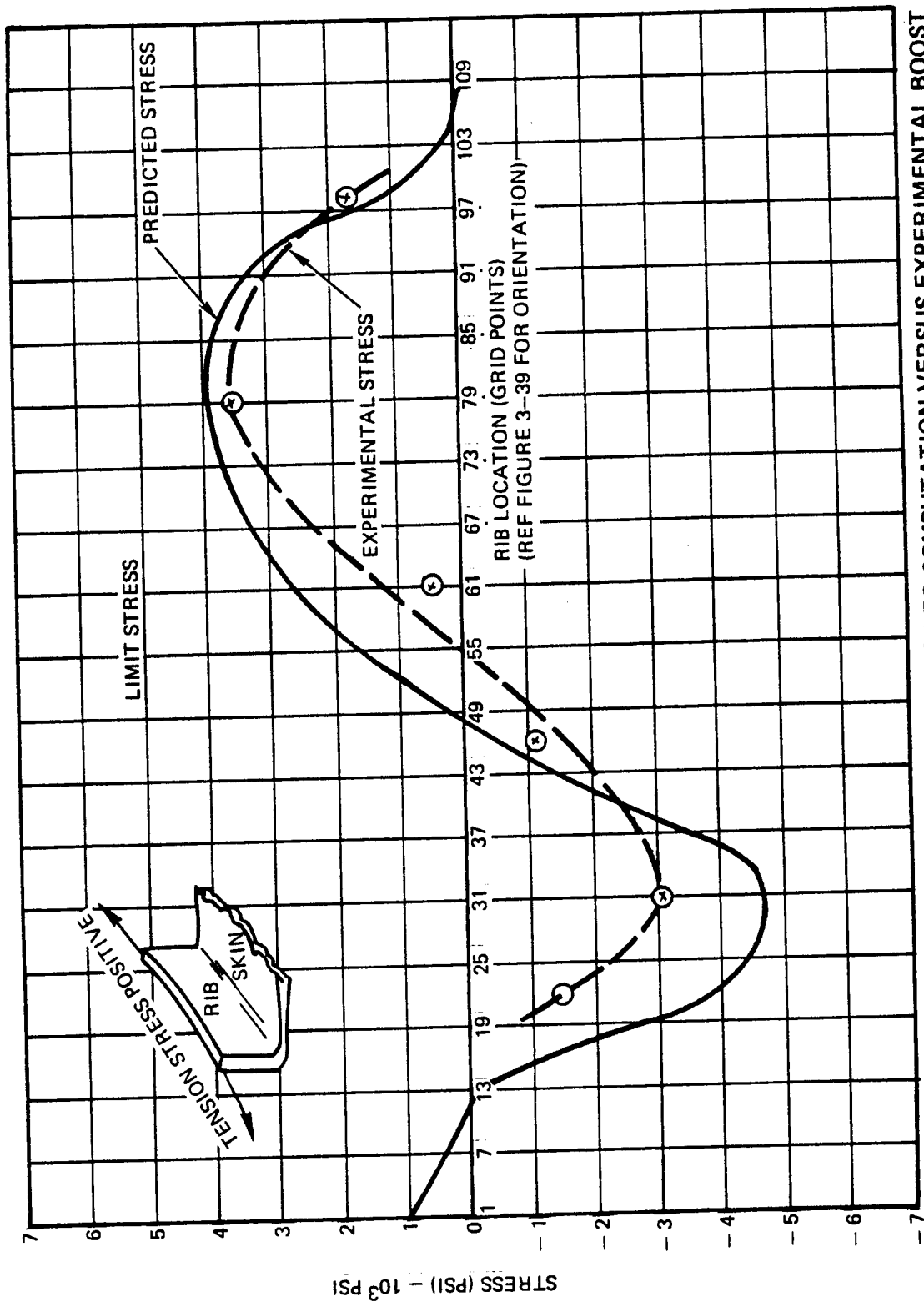


FIGURE 7-21 RIBS STRESSES - UPSTANDING LEG COMPUTATION VERSUS EXPERIMENTAL BOOST PRESSURE LOAD TEST

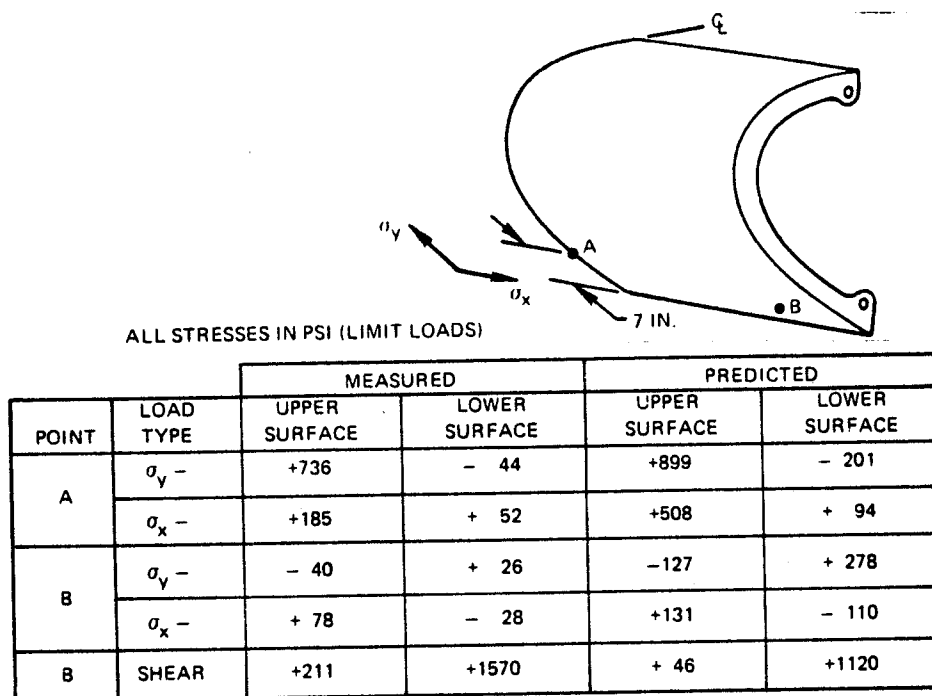


FIGURE 7-22 COMPARISON OF PREDICTED AND EXPERIMENTAL SKIN STRESSES
BOOST PRESSURE LOAD TEST

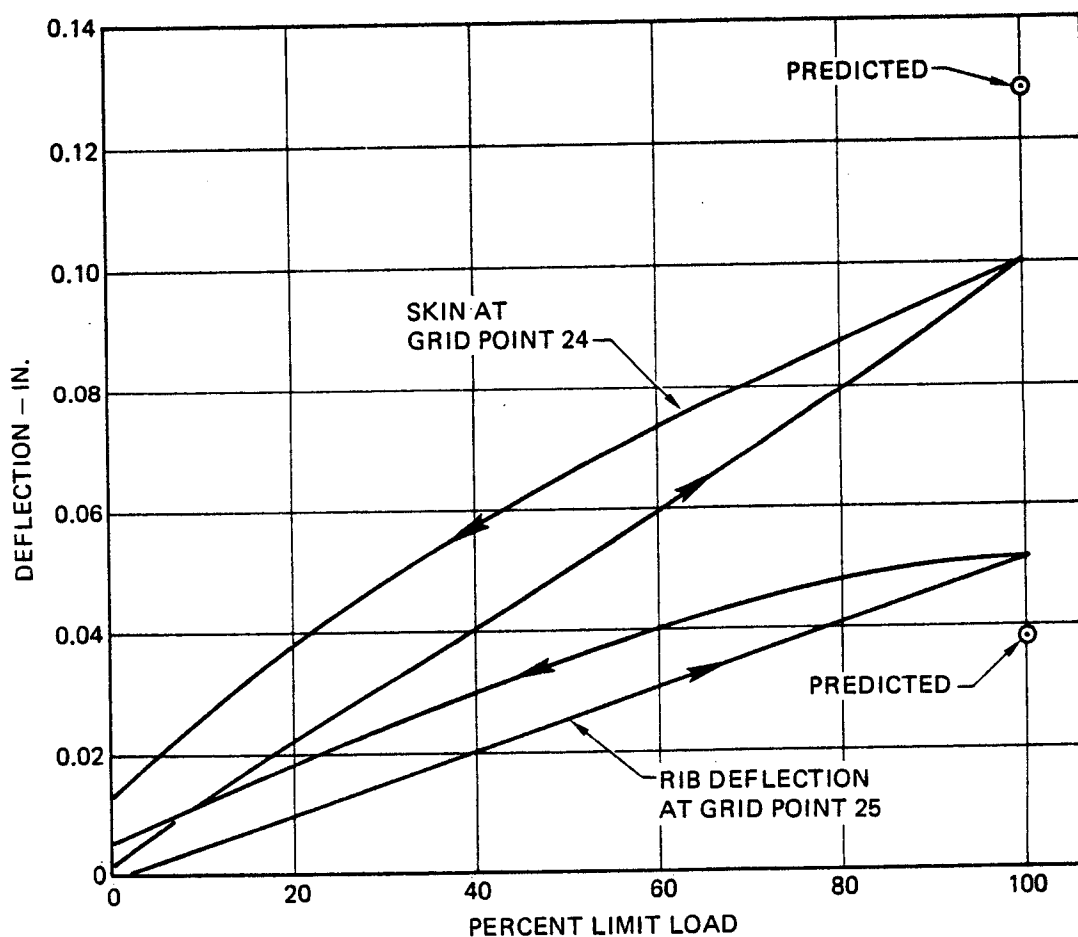


FIGURE 7-23 COMPARISON OF PREDICTED AND MEASURED DEFLECTIONS
BOOST PRESSURE LOAD TEST

Deflections of a rib and the center area of the lower panel are illustrated in Figure 7-23. The prediction of rib deflection was 17% low, while the panel predicted deflection was 28% high. Note that a slight set of 0.005 in. for the rib and 0.013 in. for the panel was experienced after loading to limit stress. This apparently is not uncommon for the RPP material, since it has been noted in specimen flexure testing as well as on the belly panel (reference 9) during static tests conducted by North American Rockwell. Certainly, this is of no consequence as far as fatigue life is concerned because it has been demonstrated by test that the fatigue strength of coated RPP is quite high even under reversed load cycling.

In summary, the proof test was highly successful. No cracks, delaminations, failures or other possible modes of damage were noticed during or after test. While the NASTRAN computations do not predict measured stress values exactly, the analysis is generally conservative. Shear modulus data is required before positive evaluation of the inplane shear data can be made.

Entry Temperature Test - Two leading edge segments, mounted side by side with a seal strip between, were tested to a time-temperature profile simulating entry. Photographs showing the test setup are given in Figures 7-24 and 7-25. Temperature was applied by graphite strip heaters ganged together to produce four independently controlled heating zones. Desired temperatures were those computed for the leading edge assuming an emittance of 0.85 and internal cross radiation effects, but excluding temperature relief from low catalycity.

Only the first eight minutes of entry required simulation because both of the critical thermal stress conditions occur during this period. At about 240 sec after initiation of entry from 400,000 ft., maximum gradients are encountered in the rib and produce maximum rib flange thermal induced tensile stresses. After 400 seconds from entry, maximum temperatures on the leading edge are achieved, and due to the restraint at the still cool lug supports, maximum compressive thermoelastic stresses on the rib flange are produced. At this time maximum thermoelastic stresses in the skin are also experienced, but these are so low as to be insignificant (reference Section 3.5.3).

Because of the high temperatures involved, strain gages cannot be employed for stress measurement. Optical devices are also not amenable to gathering the data desired, since the leading edges are almost completely enclosed during test. Therefore, the test became essentially "go-no go" from a stress standpoint.

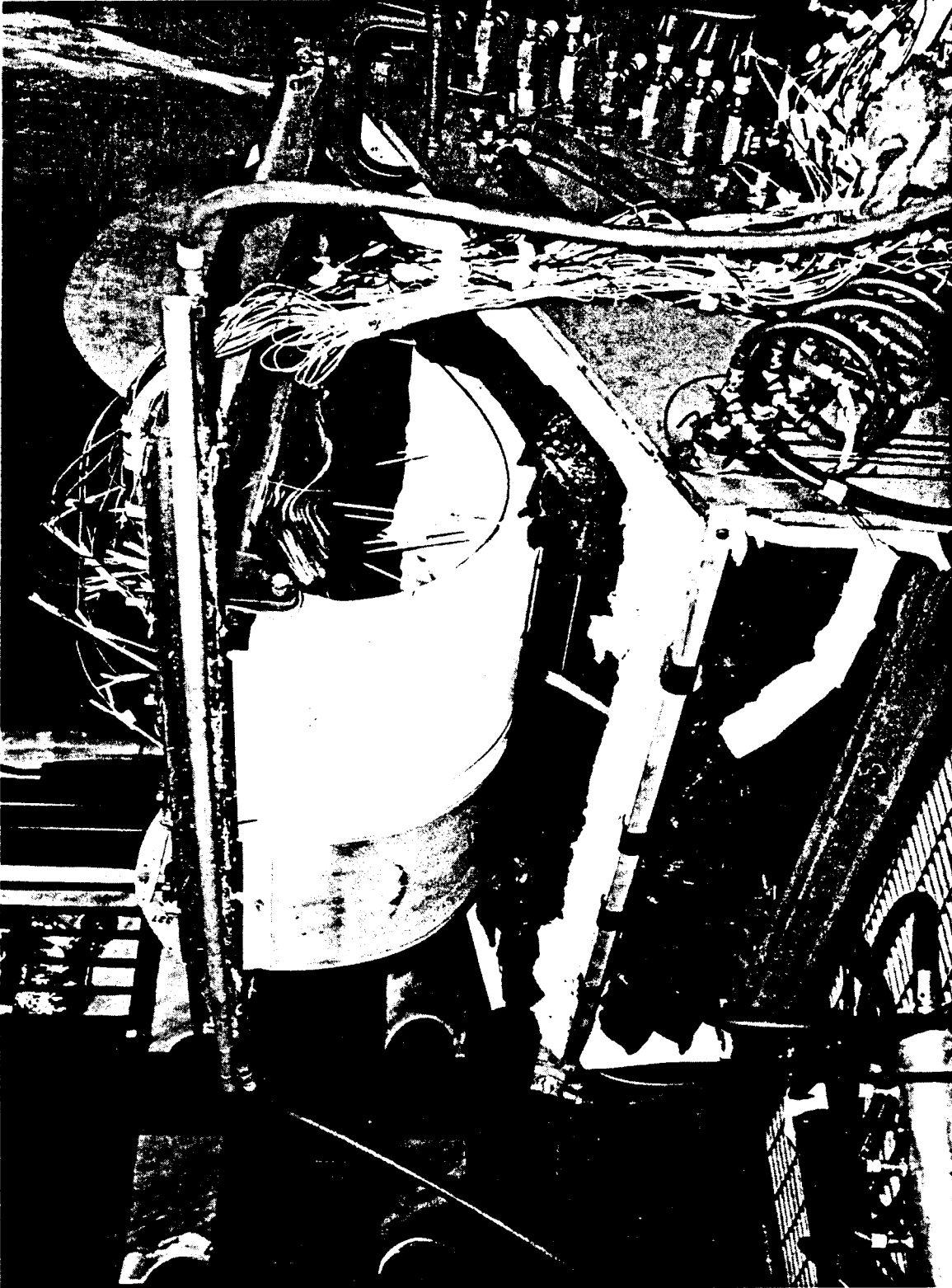


FIGURE 7-24 ENTRY TEMPERATURE TEST SETUP; LEADING EDGES ROTATE INTO HEATER CAVITY FOR HEATING



FIGURE 7-25 ENTRY TEMPERATURE TEST SETUP SHOWING THERMOCOUPLE INSTALLATION ON LEADING EDGE

Examination of the leading edge segments showed no adverse effects from the test. No cracking, delamination, or other possible failures were noted.

Twenty-one thermocouples were monitored during test to ensure sufficient data availability in the event of problems. Their locations are indicated in Figure 7-26. Input temperature of each of the four heat zones was manually adjusted to produce good control to the desired profile which was established at three points around the leading edge. In general, deviations from plan were acceptably small. The front side control thermocouple in the maximum temperature zone (Thermocouple No. 1) did not remain in good contact with the surface so that the true maximum surface temperature, based on estimates using backside temperature data, was probably only 2550°F rather than the 2600°F desired.

Temperature data plots in the controlled regions are shown in Figure 7-27 and are compared against the desired profile at three locations around the leading edge. These correspond to thermocouples nos. 1, 3, and 5 as shown in Figure 7-26. These data show that the test condition was a satisfactory representation of the computed temperatures during entry at both primary thermoelastic stress conditions.

For the maximum rib gradient condition with the calculated stagnation temperature at 1500°F, temperature deviation from desired was no greater than 70°F in the hot region and about 110°F in the cool leeward side of the leading edge as can be seen in Figure 7-27. In trying to achieve the maximum computed leading edge temperatures, which occur at 420 sec on Figure 7-27, manual control of the heat zones produced some delay in achieving the desired temperatures until 500 sec. However, comparing thermocouple data with the planned condition shows the following:

	Planned Temp at 420 sec °F	Achieved Temp at 500 sec °F
Thermocouple #1 (Stagnation)	2600	2625
Thermocouple #3 (Windward side)	2260	2330
Thermocouple #5 (Leeward side)	1775	1670

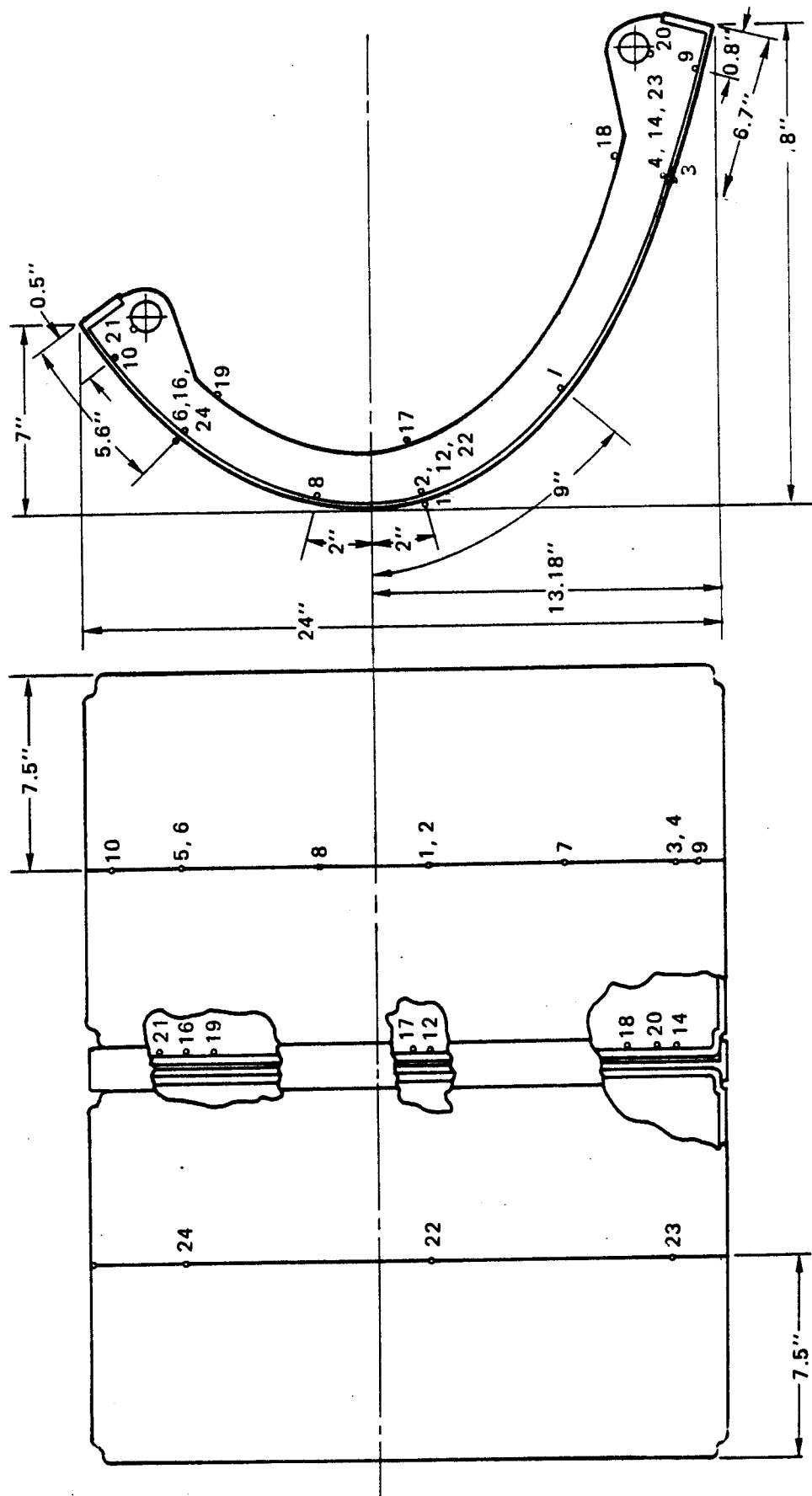


FIGURE 7-26 THERMOCOUPLE LOCATIONS ENTRY TEMPERATURE TEST

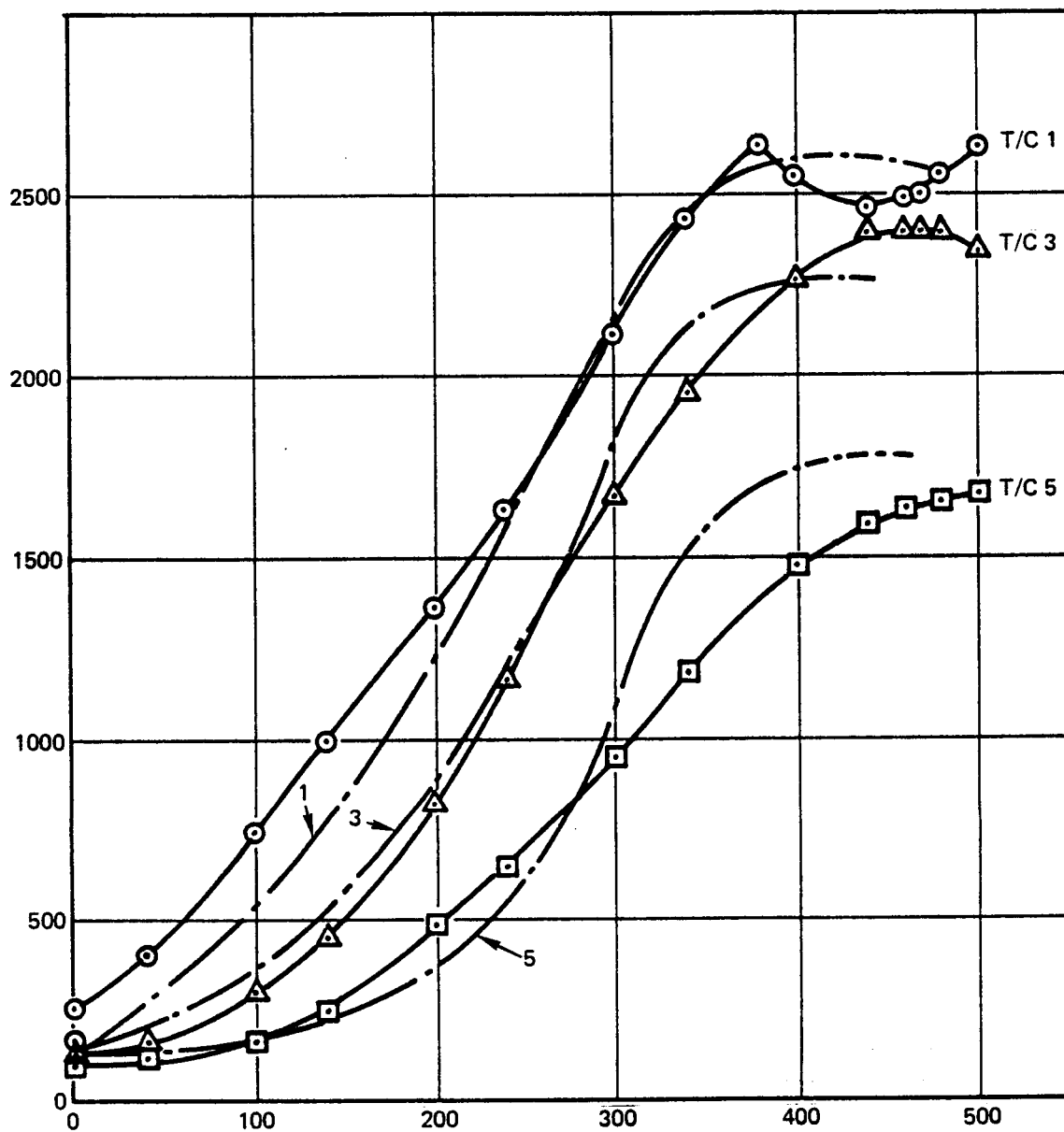


FIGURE 7-27 TEMPERATURE PROFILE DESIRED VS ACTUAL ENTRY TEMPERATURE TEST

This indicates that the greater portion of the leading edge (windward side) was slightly hotter than desired, while the cooler leeward side was about 105°F cooler. Overall the test condition achieved satisfactory temperature levels to demonstrate the adequacy of the leading edge for this condition, which induces maximum compression stresses in the upstanding leg of the ribs.

Other points of comparison between predicted and measured temperatures are given in Table 7-1. This shows the gradients from

TABLE 7-1 COMPARISON OF
PREDICTED AND MEASURED TEMPERATURE
GRADIENTS AT 230 SEC TEST TIME

<u>Condition</u>	<u>Thermocouples</u>	<u>Temperature °F</u>	<u>Meas. Gradient °F</u>	<u>Computed Gradient °F</u>
Across Rib	#12-#17	910 - 720	190	300°F
Skin to Rib	#1-#17	1560 - 720	840	600°F
Across Rib	#14-#18	650 - 560	90	230
Skin to Rib	#3-#18	1050 - 560	490	500
Across Rib	#16-#19	350 - 400	-50	50
Skin to Rib	#5-#19	610 - 400	210	230

the inner edge to the outer edge of the rib and also shows the gradient from the maximum skin temperature at the center of the panel to the inner edge of the rib. These are to be compared with computations of Figure 3-23. Rib gradients are smaller than computed, probably caused by the heat sink effects of the "T" seal strip, which was not included in the calculations for conservatism of stress analyses. Gradients between skin and rib show good correlation with calculation but in the stagnation region a higher gradient was measured than computed. This is not surprising with the heat sink effect of the seal strip.

Temperatures measured at the lug points are not discussed since they do not reflect flight conditions, because the time of test was not meant to duplicate the entire mission, and the insulation used was graphite felt, which is not representative of flight type insulation properties. However, temperature data on the lugs and at other points on the leading edge are given in Appendix C.

The results of this test do verify the adequacy of the leading edge design and material to withstand imposed temperature gradients representative of those computed for flight.

Photographs of the leading edge assemblies following test are given in Figures 7-28 and 7-29. These are shown mounted on the test support structure and after thermocouples and insulation were removed. The dark marks on one of the leading edges are the result of charring of the strain gages used in the boost pressure test, which was conducted prior to the temperature test. Other dark areas on this panel were caused by the graphite felt insulation.



FIGURE 7-28 PROTOTYPE LEADING EDGES - FRONT VIEW FOLLOWING ENTRY TEMPERATURE TEST

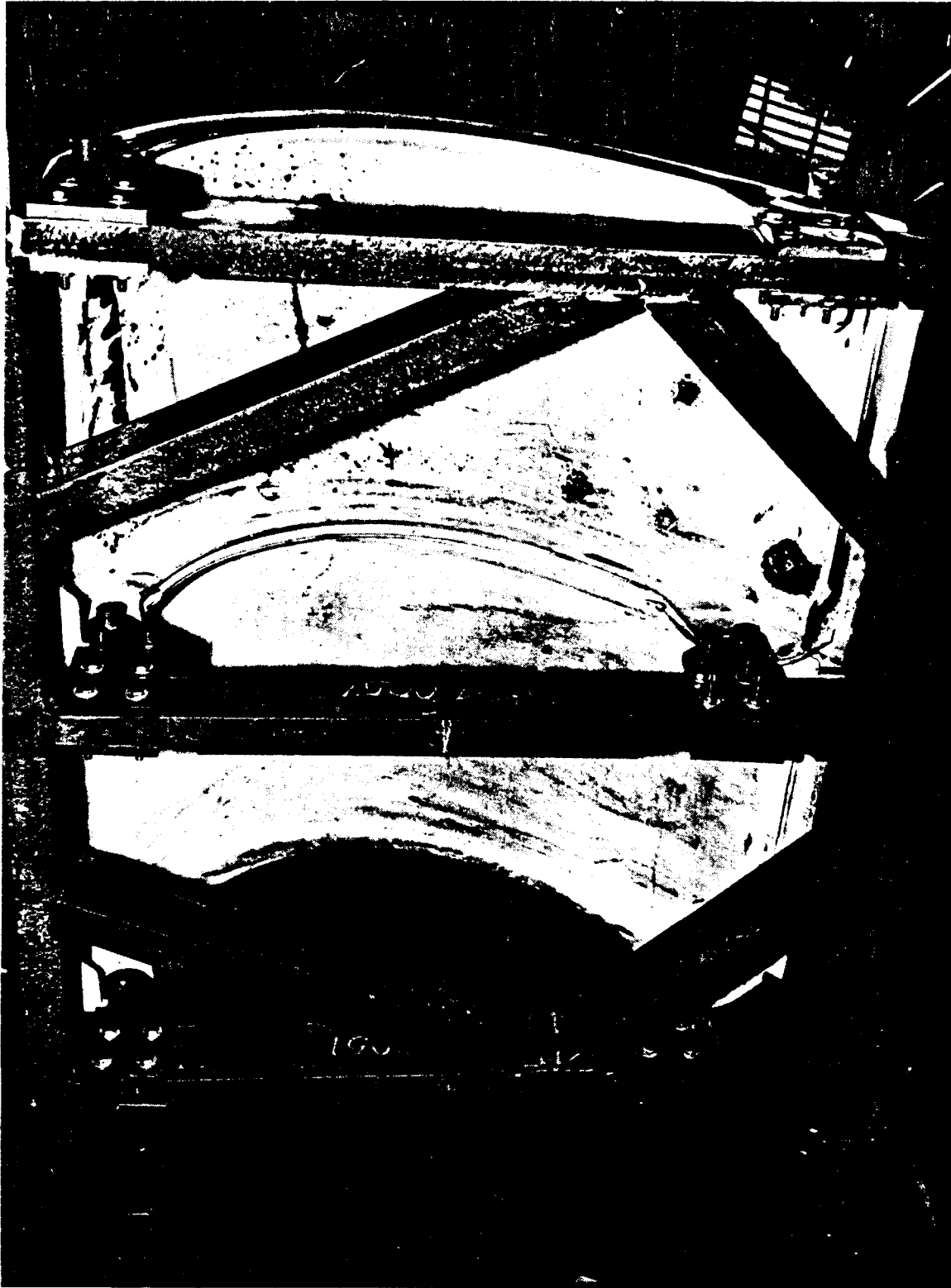


FIGURE 7-29 PROTOTYPE LEADING EDGES - REAR VIEW FOLLOWING ENTRY TEMPERATURE TEST

REFERENCES

1. Contract Statement of Work for NAS9-11224
2. VMSC Rpt No. T143-5R-00044 Development of a Thermal Protection System for the Wing of a Space Shuttle Vehicle, Phase I Final Report
3. VMSC Rpt. No. T143-5R-00060 "Space Shuttle Wing Leading Edge Design Criteria", Phase II, dtd 25 June 1971
4. North American Rockwell Design Data, Letter 71MA3504 dtd 6/4/71
5. 161C Orbiter Wing Surface Pressures, Internal NAR memo dtd 6/25/71
6. VMSC Rpt. No. T143-5R-00087 Development of a Thermal Protection System for the Wing of a Space Shuttle Vehicle, Phase II Quarterly Report
7. "Thermal Property Studies of Oxidation Resistant Carbon-Carbon Material", Battelle Memorial Institute Final Report, March 10, 1971
8. NAR Dynaflex Data, Telecon Message 3 May 1971
9. VMSC Rpt. No. T159-5R-00047 "Oxidation Inhibited RPP Space Shuttle Belly Panel" dtd 31 Jan 1972
10. "Theory of Stagnation Point Heat Transfer in Dissociated Air," "Journal of the Aeronautical Sciences, February 1958
11. Engineering Radiation Heat Transfer by J. A. Wiebelt, Holt Rinehart and Winston, Inc., 1965, Page 88
12. Goulard, R., "On Catalytic Recombination Rates in Hypersonic Stagnation Heat Transfer", Jet Propulsion, November 1958
13. "Computer Program for the Numerical Solution of Nonequilibrium Expansion of Reacting Gas Mixtures, "NASA CR-472, May 1966
14. "High Temperature Kinetics of the Oxidation and Nitridation of Pyrolytic Silicon Carbide in Dissociated Gases, " Journal of Physical Chemistry, Volume 7, No. 9, April 30, 1970

REFERENCES (Cont'd.)

15. "Nitrogen as an Ablative Reactant in Dissociation Air", AIAA Journal, Volume 8, No. 1, January 1970
16. The Theory of Rate Processes, Glasstone, et.al., McGraw Hill Book Co., Inc., New York, N.Y., 1st ed.
17. Inger, G. R., "Nonequilibrium Hypersonic Stagnation Flow with Arbitrary Surface Catalycity Including Low Reynolds Number Effects", International Journal of Heat and Mass Transfer, Vol. 9, No. 8, August 1966, PP 755-772.
18. Chung, P. M.; Liu, S. W. Mirels, H., "Effect of Discontinuity of Surface Catalycity on Boundary Layer Flow of Dissociated Gas", Aerospace Corporation Report No. TDR-69 (2240-20) TN-1, 7 June 1962.
19. Liu, S. W. and Chung, P. M., "Boundary Layer Flow of Dissociated Gas with Arbitrary Distribution of Surface Catalycity", Aerospace Corporation Report No. TDR 269 (4230-40)-4, 21 December 1963
20. "Initial Experience with Two Arc Heated Duct Facilities for AIAA Paper No. 71-262, by M. A. Covington and N. S. Vojvodich

DISTRIBUTION

One (1) copy to:

NASA, Manned Spacecraft Center
Advanced Programs Contract Section
Houston, Texas 77058
Attention: W. M. Chastain/J042

NASA, Manned Spacecraft Center
Advanced Missions Program Office
Houston, Texas 77058
Attention: Wayne Young/HA-JA

Four (4) copies to:

NASA, Manned Spacecraft Center
Technical Information Dissemination Branch
Houston, Texas
Attention: Retha Shirkey/BM6

One (1) copy to

NASA, Manned Spacecraft Center
Management Services Division
Houston, Texas 77058
Attention: John T. Wheeler/BM7

Three (3) copies to:

NASA, Manned Spacecraft Center
Documentation Management Office
Houston, Texas 77058
Attention: Charles M. Grant/BM2

Fifty (50) copies to:

NASA, Manned Spacecraft Center
Project Support Branch
Houston, Texas 77058
Attention: J. E. Pavlosky/ES32

APPENDIX A

MATERIALS TESTS SUMMARY

The data contained in Appendix A is a compilation of furnace coating run parameters for the diffusion systems, flexure strengths of the various diffusion coated systems, and plasma arc test data obtained during the Phase II program. These data are correlated by furnace run number and specific specimen numbers contained in the following tables.

A.1

FURNACE RUNS

The following tables document the furnace runs in which specimens were coated for the leading edge during this reporting period.

TABLE A.1-1 DIFFUSION COATING RUNS
EARLY SERIES

Run No.	System	Specimen Ident	Slurry Composition Weight Percent	Pack Compound Composition Weight Percent	RPP-3 Substrate Condition	Furnace Temp °F	Time at Temp Hours	Wt Gain Due to Coating %
M54						3400	4	
	BS	1-4 13-14	100B	60SiC 40 Si	Not heat treated			13.0
		5-8 15-16	100B	50SiC 50Si				25.6
		9-12 17-18	100B	40SiC 60Si				20.9
M55	BS					3600	4	
		1-10 11-12	100B	50SiC 50Si	Not heat treated			18.4
M56	BS					3900	4	
		1-14 15-16	100B	50SiC 50Si	Not heat treated			23.8
		17-19	32B 68Z _n					4.9
	ZBS	20-23	50B 50Z _n					7.8
	ZBS	24-26	15B 85Z _n					7.9
	ZBS	28-30	2.9B 97.1Z _n					13.2
M57						3900	4	
	BS	1-4	50B ₄ C 50B	50Si 50SiC	Not heat treated	82170		12.5
		5-8	2C 10B					25.7
		9-12	40B ₄ C 40B 20Al ₂ O ₃					19.3
		13-16	75B 25Al ₂ O ₃					12.0
	ZBS	17-20	50B 50Z _n					20.5
		21-24	30Z _n 70B					8.8
		25-28	10Z _n 90B					13.8
M58	BS	1-4	50B ₄ C 50B	50SiC 50Si	Not heat treated	3400	4	20.0
		5-8 33-34	10B 2C					28.3

TABLE A.1-1 DIFFUSION COATING RUNS - EARLY SERIES (Cont'd)

Run No.	System	Specimen Ident	Slurry Composition Weight Percent	Pack Compound Composition Weight Percent	RPP-3 Substrate Condition	Furnace Temp °F	Time at Temp Hours	Wt Gain Due to Coating %
M58 (cont'd)	BS	9-12	40B ₄ C 40B 20Al ₂ O ₃					22.9
		13-16	100B					28.5
		17-20 35	75B 25Al ₂ O ₃					20.1
	ZBS	21-24	2.9B 97.1Z _n					3.1
		25-28 36	50B 50Z _n					18.5
		29-32	90B 10Z _n					9.2
M60	BS	1-6	2C 10B	50Si C 50Si	Not heat treated	3400 3900	2 3	50.0
		7-12	100B					32.6
	ZBS	13-18	50Z _n 50B					20.4
M61	BS with slurry modifications	1-2	-	Boron	Not heat treated	3400	2.5	7.3
		3-4	Boron					7.1
		5-6	Cr					3.5
		7-8	Mo					6.2
		9-10	Hf					6.8
		11-12	Ti					4.1
		13-14	-	B/B ₄ C				3.9
		15-16	B/B ₄ C					10.2
		17-18	Si					4.8
		19-20	Z _n H					6.8
		21-22	Ti					2.6
		23-24	Cr					1.0
		25-26	-	B/SiC				14.3
		27-28	B/SiC					12.3
		29-30	Cr					14.0
		31-32	Si					10.0
		33-34	Z _n H					12.0
		35-36	50Si 50Z _n H					10.4
M62	B switch slurry modifications	1-6	-	50B	Not heat treated	3400	2.5	4.9
		41-42		50SiC				
		7, 8-11	50B					7.4
		43-44	50SiC					
		12, 13-16	C _r					5.9
		17, 18-21	Si					5.7
		22, 23-26	Z _n H					9.2
		27, 28-31	50Si 50Z _n H					6.9
		M60-6	-					- .9
		M60-12	-					- .5
		M60-18	-					- .9
		32-34	W					13.5

TABLE A.1-1 DIFFUSION COATING RUNS - EARLY SERIES (Cont'd)

Run No.	System	Specimen Ident	Slurry Composition Weight Percent	Pack Compound Composition Weight Percent	RPP-3 Substrate Condition	Furnace Temp °F	Time at Temp Hours	Wt Gain Due to Coating %
M62 (cont'd)	BS	35-36	10Z _n H 2B	50B 50SiC	Not heat treated	3400	2.5	8.7
		37-38	10Si 1B					11.8
		39-40	10Z _n H 2(50B/50SiC)					6.5
M63	ZBS	27-30	-	50B	Not heat treated	3400	2.5	15.6
		38-41	50B/50SiC	50SiC				29.0
		61	50Si 50Z _n H	"				41.6
		62-63	-	40B 60SiC				23.8
		82-83	50Si 50Z _n H	40B 60SiC				18.4
		17-18	-	60B 40SiC				7.1
		19	60B 40SiC	"				12.9
		64	50Si 50Z _n H	60B 40SiC				9.2
M65	Siliconi- zed	1, 11, 21	20 20 20 Si/SiC/Al ₂ O ₃	30 20 Si/SiC	Not heat treated	3200 3400	0.5 4.0	11.5
		2-4, 12-14, 22-24	"					20.7
M70	Siliconi- zed	1-4	33Al ₂ O ₃ 33Si 33SiC	70Si 30Al ₂ O ₃	Not heat treated	2900	6.5	45.0
M71	Siliconi- zed	0-9	20 40 40 Al ₂ O ₃ /SiC/Si	70 30 SiC/Si	Not heat treated	3400	4	18.2
M74	Siliconi- zed	4-5	-	33Al ₂ O ₃ 33Si 33SiC	Not heat treated	2900	6.5	24.4
			33Al ₂ O ₃ 33Si 33SiC	70Si 30Al ₂ O ₃				24.7
M79	Siliconi- zed	10-13		20 40 40 Al ₂ O ₃ /SiC/Si	Not heat treated	2900	6	
M81	Siliconi- zed	1-6	-	33 33 33 Al ₂ O ₃ /SiC/Si	Not heat treated	2900	6	14.9
		19-22	-					25.1
		7-12	SiC	70 30 Si/Al ₂ O ₃				22.6
		23-26						22.6
		13-18	33 33 33 Al ₂ O ₃ /SiC/Si					35.0
		27-30						34.2

TABLE A. 1-1 DIFFUSION COATING RUNS - EARLY SERIES (Cont'd)

Run No.	System	Specimen Ident	Slurry Composition Weight Percent	Pack Compound Composition Weight Percent	RPP-3 Substrate Condition	Furnace Temp °F	Time at Temp Hours	Wt Gain Due to Coating %
M82	Siliconized	1-6	20Al ₂ O ₃ 40Si 40SiC	70SiC 30Si	Not heat treated	3400		22.6
		7-9	-	91 3 6 SiC/Al ₂ O ₃ /SiO ₂				25.0
		10-12	91 3 6 Si/Al ₂ O ₃ /SiO ₂	"				26.3
		13-15	-	95SiC/5 SiO ₂				21.6
		16-18	95SiC/5 SiO ₂	"				19.8
		19-21	-	91SiC/9 Al ₂ O ₃				19.7
		22-24	91 9 SiC/Al ₂ O ₃					17.8
		25-26	-	SiC				16.7
		27-28	SiC	"				19.8
		29-30	-	SiO ₂				14.3
		31-32	SiO ₂	"				19.7
		33-34	-	Al ₂ O ₃				14.6
		35-36	Al ₂ O ₃	"				15.5

TABLE A. 1-2 DIFFUSION COATING RUNS ALUMINA/SILICON CARBIDE/SILICON SYSTEMS

Run No.	System	Specimen Identif	Slurry Composition		Pack Composition		RPP-3 Substrate	Silicon Powder	Silicon Carbide Powder	Furnace Temp °F	Coating Time Hrs.	Coating Depth In.	Wt Gain Due to Coating	
			Wt Percent	Wt Percent	Wt Percent	Wt Percent							Wt %	Wt %
M85	Siliconized	1-6	20 Al ₂ O ₃ 40 Si 40 SiC	30 Si 70 SiC			Not heat treated	007	822992	3400	4		20.0	
		7-12	"	"										
M85B	Siliconized	1-3	-	70 SiC 30 Si			Not heat treated	007	822992				26.2	
		4-6	-	1 69 30 Al ₂ O ₃ /SiC/Si									48.5	
		7-9	-	10 60 30 Al ₂ O ₃ /SiC/Si									39.6	
		10-12	-	33 33 33 Al ₂ O ₃ /SiC/Si									52.8	
		13-15	-	20 40 40 Al ₂ O ₃ /SiC/Si									40.8	
		16-18	-	SiC									55.3	
		1-6	33 33 33 Al ₂ O ₃ /SiC/Si	70 Si 30 SiC			3400°F Heat treat	007	822992	3400	4		57.3	
		7-12	"	"			"						20.4	
M86	Siliconized	13-18	"	"			3900°F Heat treat						25.0	
		19-24	"	"			"						16.4	
M88	Siliconized	1-2	-	70 30 SiC/Si			Not heat treated	007	822992	3200	4		27.4	
		3-4	-	1 69 30 Al ₂ O ₃ /SiC/Si									37.0	
		5-6	-	10 60 30 Al ₂ O ₃ /SiC/Si									38.6	
		7-8	-	33 33 33 Al ₂ O ₃ /SiC/Si									40.5	
													36.8	

TABLE A 1-2 DIFFUSION COATING RUNS ALUMINA/SILICON CARBIDE/SILICON SYSTEMS (Cont'd.)

Run No.	System	Specimen Identif	Slurry		Pack		RPP-3 Substrate	Silicon Powder	Silicon Carbide Powder	Furnace Temp of	Coating Time Hrs.	Coating Depth In.	Wt Gain Due to Coating Wt %
			Composition Wt Percent	Composition Wt Percent	Al ₂ O ₃ /SiC/Si	Al ₂ O ₃ /SiC/Si							
M88	Siliconized	9-10	-	20	40	40	Not heat treated	007	822992	3200	4		31.4
		11-13	-	-	-	-	SiC						24.6
		14	-	-	-	-	SiO ₂						13.7
		15-16	-	4	16	40	40						35.4
		17-18	4	16	40	40	30						32.6
		19-20	SiO ₂ /Al ₂ O ₃ /SiC/Si	SiC/Si	SiC/Si	SiC/Si	Not heat treated						29.3
M89	Siliconized	21					Al ₂ O ₃						19.6
		1-12		33	33	33	Not heat treated	007	822992	2900	6		25.8
		1-8					Al ₂ O ₃ /SiC/Si						19.5
		1-4	-	10	60	30	3400°F Heat treat	721	822992	3400	4		15.6
		5-10	-				Al ₂ O ₃ /SiC/Si						21.1
		11-13					Not heat treated						17.9
M91A	Siliconized	1-4	20	40	40	30	3400°F Heat treat	721	822992	3400	4		15.4
		5-10	Al ₂ O ₃ /SiC/Si	SiC/Si	SiC/Si	SiC/Si							22.6
		1-4											13.1
		5-10											24.8
		1-4	30	33	33								25.4
			Al ₂ O ₃ /SiC/Si										34.0
M95A	Siliconized	1-4	-	10	60	30	Not heat treated	721	822992	3200	4		14.0
		13-18	-				Al ₂ O ₃ /SiC/Si						16.9
		5-8	-	1	69	30							13.8
							Al ₂ O ₃ /SiC/Si						8.3
		19-24	-										

TABLE A 1-2 DIFFUSION COATING RUNS ALUMINA/SILICON CARBIDE/SILICON SYSTEMS (Cont'd.)

Run No.	System	Specimen Identif	Slurry Composition Wt Percent	Pack Composition Wt Percent	RPP-3 Substrate	Silicon Powder	Silicon Carbide Powder	Furnace Temp °F	Coating Time Hrs.	Coating Depth In.	Wt Gain Due to Coating Wt %
M95C	Siliconized	9-12	-	33 33 33 Al ₂ O ₃ /SiC/Si	Not heat treated	721	822992	3200	4		8.8
		25-30	-								12.0
M96	Siliconized	5-6, 13-14	-	1 69 30 Al ₂ O ₃ /SiC/Si		721	822992	3400	4		7.6
		19-24	-								11.9
M97A	Siliconized	1-6	-	10 60 30 Al ₂ O ₃ /SiC/Si		721	822992	3000	4		6.4
		7-10	-								6.2
M97B	Siliconized	11-14	-	1 69 30 Al ₂ O ₃ /SiC/Si							6.8
		19-24	-								7.4
M97C	Siliconized	15-18	-	33 33 33 Al ₂ O ₃ /SiC/Si							10.3
		25-30	-								12.9
M100	Siliconized	01-06	-	10 60 30 Al ₂ O ₃ /SiC/Si	Not heat treated	721	822992	3200	4	.017	21.9
		7-12	-		3400°F Heat treat					-	23.8
		41-46	-							.017	24.6
		13-18	-							-	27.9
		61-66	-		3600°F Heat treat					.018	25.4
		19-24	-								31.2
		91-96	-		3900°F Heat treat					.022	23.7
		25-30	-							-	29.3
		5.1-5.6	-		4500°F Heat treat					.017	23.8
		31-36	-							-	31.2
M101	Siliconized	1-2	-	10 60 30 Al ₂ O ₃ /SiC/Si	Not heat treated	721	822992	3200	6	.034	32.8
		3-4	-			468				.023	23.8
		5-9	-			721				-	41.3
		10-13	-			468				-	31.8

TABLE A 1-2 DIFFUSION COATING RUNS ALUMINA/SILICON CARBIDE/SILICON SYSTEMS (Cont'd.)

Run No.	System	Specimen Identif	Slurry Composition Wt Percent	Pack Composition Wt Percent	RPP-3 Substrate	Silicon Powder	Silicon Carbide Powder	Furnace Temp °F	Coating Time Hrs.	Coating Depth In.	Wt Gain Due to Coating Wt %
M103	Siliconized	1-2	-	10 60 30 Al ₂ O ₃ /SiC/Si	Not heat treated	468	822992	3200	6	.062	58.1
		3-4	-				800 RA			.060	55.4
		5-6	-				47058			.054	45.2
		9-12	-				822992			-	62.3
		13-16	-				800 RA			-	60.6
		17-20	-				A7058			-	53.1
M105	Siliconized	S5-S25	-	10 60 30 Al ₂ O ₃ /SiC/Si	Not heat treated	468	822992	3200	4		29.3
		TF1-TF9									19.8
		T1-T18									20.8
		01-07									27.2
		1- 14									26.4
		1-15									37.6
		F1-F15,F17	-							.024	31.0
		C1-C4	-								22.4
		B1-B3	-								23.9
		FF1-FF6	-								28.5
		FF9-FF10									
		A1-A4	-								29.1
		TL1-FL3	-								20.9
		1- 2	-								24.4
M106	Siliconized	3- 6	-	10 60 30 Al ₂ O ₃ /SiC/Si	Not heat treated	468	822992	3200	4		24.4
		1- 3	-								29.7
		011-012 6, 9									24.7
		16-31	-								37.5*

* Avg of Five (5) Specimens

TABLE A 1-2 DIFFUSION COATING RUNS ALUMINA/SILICON CARBIDE/SILICON SYSTEMS (Cont'd.)

Run No.	System	Specimen Identif	Slurry Composition Wt Percent	Pack Composition Wt Percent	Substrate	Silicon Powder	Silicon Carbide Powder	Furnace Temp °F	Coating Time Hrs.	Coating Depth In.	Wt Gain Due to Coating Wt %
M106	Siliconized (Cont'd)	F16, F19-F32	-	10 60 30 Al ₂ O ₃ /SiC/Si	Not heat treated	468	822992	3200	4	.019	24.8
		FF7-FF8	-								24.1
		FF11-FF16	-								
		TL4-TL6	-								21.6
		S26-S28	-								30.4
		E1-E3	-								26.4
		X1-X3	-								19.1
		C1-C2	-								23.0
		1- 2	-								22.0
		1- 3	-								25.8
		F01-F09	-						.023		25.9
		SL1-SL3	-								28.5
M107	Siliconized	T01-T09	-								18.1
		TF10-TF12	-								20.0
		1-2	-	15 55 30 Al ₂ O ₃ /SiC/Si	Not heat treated	468	822992	3200	4	.033	33.1
		7-8	-								42.8
		13-14	-								38.3
		3-4	-	10 60 30 Al ₂ O ₃ /SiC/Si						.031	32.4
		9-10	-							-	60.6
		15-16	-							-	38.7
		5-6	-	5 60 30 Al ₂ O ₃ /SiC/Si						.028	30.8
		11-12	-							-	39.9
		17-18	-							-	37.1
		1	-	10 60 30 Al ₂ O ₃ /SiC/Si	Not heat treated	468	A7058	3100	4		15.8
		31	-								19.0
M108	Siliconized	2	-			468	822992				15.1
		32	-								20.0

TABLE A 1-2 DIFFUSION COATING RUNS ALUMINA/SILICON CARBIDE/SILICON SYSTEMS (Cont'd.)

Run No.	System	Specimen Identif	Slurry Composition Wt Percent	Pack Composition Wt Percent	Substrate	Silicon Powder	Silicon Carbide Powder	Furnace Temp of	Coating Time Hrs.	Coating Depth In.	Wt Gain Due to Coating Wt %
M108	Siliconized	3	-	10 60 30 Al ₂ O ₃ /SiC/Si	Not heat treated	721	822992	3100	4		13.3
		33	-								18.0
		4	-	SiC			RA1500				2.0
		34	-								2.5
		5	-				A7058				2.6
		35	-								5.4
		6	-				822992				2.4
		36	-				822992				3.2
		7	-				RA 800				4.7
M109	Siliconized	1-2	-	10 60 30 Al ₂ O ₃ /SiC/Si	Not heat treated	721	822992	3100	4	.022	25.1
		7-8	-							-	34.6
		3-4	-			468	822992			.024	27.4
		9-10	-							-	40.0
		5-6	-				47058			.027	31.1
		11-12	-							-	43.1
M112	Siliconized	1, 11, 12, 13	-	10 60 30 Al ₂ O ₃ /SiC/Si	Not heat treated	404	A7058	3100	4	-	35.4
		5-8	-							.027	33.4
		2, 3, 14-16	-			468	822992			-	43.6
		6-9	-							.031	37.9
		4, 17-19	-				A7058			-	36.4
		7-10	-							.026	37.2
M113	Siliconized	1N-2N	-	10 60 30 Al ₂ O ₃ /SiC/Si	Not heat treated	404	A7058	3100	2		47.1
		1-2, 7, 9	-								49.9
		3N-4N	-			468	822992				46.6
		3-4, 8, 10	-								50.3
		5N-6N	-				A7058				45.7
		5-6, 11	-								48.9

TABLE A 1-2 DIFFUSION COATING RUNS ALUMINA/SILICON CARBIDE/SILICON SYSTEMS (Cont'd.)

Run No.	System	Specimen Identif	Slurry Composition Wt Percent	Pack Composition Wt Percent	RPP-3 Substrate	Silicon Powder	Silicon Carbide Powder	Furnace Temp °F	Coating Time Hrs.	Coating Depth In.	Wt Gain Due to Coating Wt %
M115	Siliconized	1, 4	-	10 60 30 Al ₂ O ₃ /SiC/Si	Not heat treated	468	A 7058	3100	4		53.9
		1-4	-								55.2
		2-5	-				822992				54.3
		5-8	-								51.1
		3, 6	-			404	A 7058				51.8
		9-12	-								49.9
		7, 8	-			468					29.4
		13-16	-								43.3
		9, 10	-				822992				36.5
		17-20	-								50.7
		11, 12	-				A 7058				36.1
		21-24	-								48.0
M71	Siliconized		1 2 3 Al ₂ O ₃ /SiC/Si	30/70 Si/SiC	Experimental Substrate			3400	4		
		1-16									5.8-23.9
		2-16									5.3-27.0
		3-16									5.7-27.6
		4-16									8.0-35.8
		S1-S4									9.9-16.6
		-7									23.8
		0									56
M116	Siliconized	1-3, 25	-	10 60 30 Al ₂ O ₃ /SiC/Si	Not heat treated	404	113	3100	4		50.4
		13, 16									49.2
		4, 5, 6, 7									52.9
		14, 17									50.6
		8-10, 26									52.4
		15, 18									47.8
M117	Siliconized	5-8	-	10 60 30 Al ₂ O ₃ /SiC/Si	Not heat treated	468	113	3200	4		43.7
		1, 2									44.0

TABLE A 1-2 DIFFUSION COATING RUNS ALUMINA/SILICON CARBIDE/SILICON SYSTEMS (Cont'd.)

Run No.	System	Specimen Identif	Slurry Composition Wt. Percent	Pack Composition Wt Percent	RPP-3 Substrate	Silicon Powder	Silicon Carbide of	Furnace Temp Hrs.	Coating Time In.	Coating Depth In.	Wt Gain Due to Coating Wt %
M117	Siliconized (Cont'd.)	9-12 3,4	--	10 60 30	Not heat treated	404	113				40.5 43.7
M118	Siliconized	1,2 5 7-9 3,4 6 10-12	--	10 60 30 Al ₂ O ₃ /SiC/Si	Not heat treated	468	113	3200	4		38.8 35.8 46.4 33.8 39.2 38.1
M119	Siliconized	A, BN/N D, E, F G, H C	--	M117 Recycled	Not heat treated	--	--	3200	4		19.4
M120	Siliconized	1-3 B1-B6	--	10 60 30 Al ₂ O ₃ /SiC/Si	Not heat treated	468	113	3000	4		17.2 47.7 21.7
M121	Siliconized	1-4 6-8 9-12	--	10 60 30 Al ₂ O ₃ /SiC/Si	Not heat treated	468	113	3150	4		36.0 39.9
M122	Siliconized	1-6 7-10	--	10 60 30 Al ₂ O ₃ /SiC/Si	Not heat treated	468	113	3150	4		39.8 34.4 41.2
M123	Siliconized	1-7 8-11	--	10 60 30 Al ₂ O ₃ /SiC/Si	Not heat treated	468	113	3050	2		49.0 43.8
M124	Siliconized	1-3 11-14	--	10 60 30 Al ₂ O ₃ /SiC/Si	Not heat treated	468	822992	3050	2		19.4 16.5
M125	Siliconized	1-5 B5-510 11, 12	--	10 60 30 Al ₂ O ₃ /SiC/Si	Not heat treated	468	113	3100	2 1/2		19.1 17.5
M126	Siliconized	1,2,5,7 9-11,15-16 21,22 3,4,6,8 12-14,18-20 23,24	--	10 60 30 Al ₂ O ₃ /SiC/Si	Not heat treated	468	113	3150	2		33.5 39.7 29.4
M128	Siliconized	1,2,5,7 11,13-17 3,4,6,8 12,18-22	--	10 60 30 Al ₂ O ₃ /SiC/Si	Not heat treated	468	822992				29.1 33.0
M129	Siliconized	1,2,5,7 9-12 3,4,6,8 13-16	--	10 60 30 Al ₂ O ₃ /SiC/Si	Not heat treated	468	113	3170	2 1/2		28.6 32.5 34.8 39.3 35.9 39.1
						468	822992				35.2 40.8 40.0 43.8

Run No	System	Specimen Identif	Slurry Composition Wt Percent	Pack Composition Wt Percent	RPP-3 Substrate	Silicon Powder	Silicon Carbide C _F	Furnace Temp Hrs.	Coating Time In.	Coating Depth In.	Wt Gain Due to Coating Wt %
M130	Siliconized	1-3, 7, 10, 12 14, 16, 18, 20 21 23, 24, 27-30 35, 36 4, 5, 8, 9, 11, 13 15, 17, 19, 21 25, 26, 31-34 37, 38	--	10 60 30 Al ₂ O ₃ /SiC/Si	Not heat treated	468	113	3100	2 1/2		28.1
M132	Siliconized	1-4, 8-12 B1-B6, B13-B18 5-8, 13-16 B7-B12, B19-B24	--	10 60 30 Al ₂ O ₃ /SiC/Si	Not heat treated	468	113	3090	2 1/2		36.7
M133	Siliconized	1-3, 7-9 B1-B3, B7-B9 B13-B15, B19	--	33 33 33 Al ₂ O ₃ /SiC/Si	Not heat treated	532	00774	2900	6		24.1 28.0
M136	Siliconized	4-6, 10-12 B4-B6, B10-B12 B16-B18, B20 1-6, 13 B1-B6 7-12, 14 7B-12B	--	10 60 30 Al ₂ O ₃ /SiC/Si 30 30 30 Al ₂ O ₃ /SiC/Si	Not heat treated	532	00774	2900 ¹ 3050 3100	2 1 1		20.2 27.8
M137	Siliconized	B2, T5, T9 T10, T14, T16, T18 T0.1-T0.9 TF.1-TF7 1, 6 - 9 S1-S9 S01-S02 1, 2, 4, 6 F1-F6, F8, F11-F13, F15, F16 FF9 1, 2, 6 8-10, 12 B1-B11	--	10 60 30 Al ₂ O ₃ /SiC/Si 10 60 30 Al ₂ O ₃ /SiC/Si	Not heat treated	532	00774	3050	2 1/2		23.1 31.4 20.2 24.3 18.9 21.5 23.1 32.1 18.8 24.7 20.7 21.5 27.6

TABLE A 1-2 DIFFUSION COATING RUNS ALUMINA/SILICON CAR BIDE/SILICON SYSTEMS (Cont'd.)

Run No.	System	Specimen Identif	Slurry Composition Wt Percent	Pack Composition Wt Percent	RPP-3 Substrate	Silicon Powder	Silicon Carbide °F	Furnace Temp Hrs.	Coating Time In.	Coating Depth In.	Wt Gain Due to Coating Wt %
M138	Siliconized	T1, T3, T4, T6-T8, T11-T13, T15, T17	--	10 60 Al ₂ O ₃ /SiC/Si	Not heat treated	532	00774	3050	2 1/2		20.5
		TF1, TF2									20.5
		TL1-TL4									19.6
		1-5, 10-12									20.2
		S10-S15									27.3
		3, 5									17.4
		F01-F09									21.5
		F7, F9, F10, F14									25.0
		FF1-FF8									22.4
		3-5, 7, 11									23.7
		B12-B13									27.0
		B20-B27									
M142	Siliconized	T1-T	--	10 60 Al ₂ O ₃ /SiC/Si	Not heat treated	532	00774	3050	2 1/2		21.8
		TF1-TF4									23.6
		TBP1-TBP4									29.5
		SB1-SB2									20.6
		CF1-CF7									29.9
		C1-C4									25.1
		SL1-SL9									23.5
		TC1-TC4									21.8
		F1-F10									22.9
		1-5									25.1
		B1-B9									31.8
M143	Siliconized	TF5-TF15	--	10 60 Al ₂ O ₃ /SiC/Si	Not heat treated	532	00774	3100	2 1/2		20.8
		SB3-SB8									23.2
		SF1-SF4									17.7
		SL10-SL14									24.4

TABLE A 1-2 DIFFUSION COATING RUNS ALUMINA/SILICON CARBIDE/SILICON SYSTEMS (Cont'd.)

Run No.	System	Specimen Identif	Slurry Composition Wt Percent	Pack Composition Wt Percent	RPP-3 Substrate	Silicon Powder	Silicon Carbide O_F	Furnace Temp Hrs	Coating Time In.	Coating Depth In.	Wt Gain Due to Coating Wt %
M143 (Cont'd.)		F11-F23									25.5
		FF1-FF14									24.4
		6-11									25.5
		B10-B18									31.1
M149 Siliconized		B1-B11	--	10 60 30 $Al_2O_3/SiC/Si$ treated	Not heat	468/532	00774	3100	2 3/4		33.6
		1-9									28.7
		A2-A4									23.4
		B11-B15									24.2
		C1-C3									25.2
M145, Siliconized M146		SB9-SB21	--	10 60 30 $Al_2O_3/SiC/Si$ treated	Not heat	532	00774	3100	3		30.0
		SL15-SL18									27.8
		SF5-SF7									26.8
		FF15-FF22									26.4
		14, 15, 12, 16									30.6
		B20-B23									40.7
		13, 17, 18									24.0
		B24-B26									30.4
		S1-S3									36.1
		SF2, SF6 SF7									26.4
		1, 3									33.3
		B5-B8									41.9
		CF1-CF7									39.2
		B4									37.6
		BF1-BF3									39.6
		F4, F9, F10									27.3
		T1-T11									28.4
		TF1-TF11									24.5
		C1-C3 C5-C7									28.6

TABLE A 1-2 DIFFUSION COATING RUNS ALUMINA/SILICON CARBIDE/SILICON SYSTEMS (Cont'd.)

Run No.	System	Specimen Identif	Slurry Composition Wt Percent	Pack Composition Wt Percent	RPP-3 Substrate	Silicon Powder	Silicon Carbide °F	Furnace Temp Hrs	Coating Time In.	Coating Depth In.	Wt Gain Due to Coating Wt %
M145, M146 (Cont'd.)		SB1-SB5 SB8-SB10 SB-12 FF1,FF3- FF5,FF9- FF13									35.6 30.0
M150	Siliconized	A1 1,2 B,B2 3-6 B3-B6	--	10 60 30 Al ₂ O ₃ /SiC/Si treated	Not heat	468	00774	3100	2 3/4		20.3 24.5 36.5 22.2 39.1
M156	Siliconized	B1-B25 1-8 CPA1-CPA6 CPP1-CPP3 FPP-1-FPP-3	--	10 60 30 Al ₂ O ₃ /SiC/Si treated	Not heat	404	A8784	3100	2 3/4		33.8 30.2 25.4 27.4 24.7
M158	Siliconized	B1-B30 1-3 B31, B32 4-5 B33, B34 6-7	--	10 60 30 Al ₂ O ₃ /SiC/Si treated	Not heat	833	A8784	3100	2 3/4		27.2 23.0 16.1 14.1 23.3 18.2
M161	Siliconized	7-10 B2-B7 11-14 B8-B13 15-16 B14	--	10 60 30 Al ₂ O ₃ /SiC/Si treated	Not heat	833	00776	3100	2 3/4		23.7 30.4 28.5 34.8 29.9 37.2

TABLE A 1-2 DIFFUSION COATING RUNS ALUMINA/SILICON CARBIDE/SILICON SYSTEMS (Cont'd.)

Run No.	System	Specimen Identif	Slurry Composition	Pack Composition	RPP-3 Substrate	Silicon Powder	Silicon Carbide °F	Furnace Temp Hrs	Coating Time In.	Coating Depth In.	Wt Gain Due to Coating Wt %
M163	Siliconized	B ₁ -B ₃	10	60	30 Not heat	055-1	A8784	3100	2 3/4		26.9
		F ₁ -F ₄	Al ₂ O ₃ /SiC/Si	treated							24.8
		B ₄ -B ₆									26.9
		F ₅ -F ₈									25.2
		B ₇ -B ₉									29.1
		F ₉ -F ₁₂									25.9
		B ₁₀ -B ₁₂									33.7
		F ₁₃ -F ₁₆									29.1
		B ₁₃ -B ₁₅									28.4
		F ₁₇ -F ₂₀									26.7
		B ₁₆ -B ₁₈									30.3
		F ₂₁ -F ₂₄	spent pack plus 10% silicon								25.7
M172	Siliconized	B ₁ -B ₆	10	60	30 Not heat	1471	A6220	3100	2 3/4		39.5
		F ₁ -6	Al ₂ O ₃ /SiC/Si	treated							34.7
		W/T									20.6
M165	Siliconized	B ₁ -B ₁₃	10	60	30 Not heat	1471	A6220	3100	2 3/4		13.9
		F ₁ -F ₁₀	Al ₂ O ₃ /SiC/Si	treated							10.4
M166	Siliconized	B ₁ -B ₈	10	60	30 Not heat	1471	A6220	2100	2 3/4		31.4
		F ₁ -F ₈	Al ₂ O ₃ /SiC/Si	treated							27.2
M168	Siliconized	B ₁₀ -B ₁₈	10	60	30 Not heat	1471	A6220	3100	2 3/4		50.6
		F ₁₀ -F ₁₈	Al ₂ O ₃ /SiC/Si	treated							52.7
M169	Siliconized	F ₁ -F ₆	10	60	30 Not heat	1471	A6220	3100	2 3/4		26.6
		B ₁ -B ₈	Al ₂ O ₃ /SiC/Si	treated							32.1
		CPP ₁ -CPP ₃									24.5
		BPP ₁ -BPP ₃									25.6

TABLE A 1-2 DIFFUSION COATING RUNS ALUMINA/SILICON CARBIDE/SILICON SYSTEMS (Cont'd.)

Run No.	System	Specimen Identif	Slurry Composition Wt Percent	Pack Composition Wt Percent	RPP-3 Substrate	Silicon Powder	Silicon Carbide of	Furnace Temp Hrs	Coating Time In.	Coating Depth In.	Wt Gain Due to Coating Wt %
M169 (Cont'd.)		681-6819 B19-B24									16.1 34.9
M171	Siliconized	B7-B9 F1-F9 2,6		10 60 30 Al ₂ O ₃ /SiC/Si	Not heat treated	1471	A6220	3100	2 3/4		26.8 22.7 25.4
W1	Siliconized	1-6 B1-B10 B11-B12	--	10 60 30 Al ₂ O ₃ /SiC/Si	Not heat treated	532	00774				22.9 26.5 25.2
W2	Siliconized	B1-B5 8-13 -2 B6-B7 14, 15		10 60 30 Al ₂ O ₃ /SiC/Si	Not heat treated	468	00774				41.3 32.7 55. 41.9 30.9
W3	Siliconized	HP1, HP2 HB2-1- HB2-24 1, 2 B1, B2 HB6-1 - HB6-6 3-8 B3-B7 T BP C/o	--	10 60 30 Al ₂ O ₃ /SiC/Si	Not heat treated	708	113				19.5 20.1 30.7 39.8 22.9 37.9 44.5 48.2 52.5

TABLE A 1-2 DIFFUSION COATING RUNS ALUMINA/SILICON CARBIDE/SILICON SYSTEMS (Cont'd.)

Run No.	System	Specimen Identif	Slurry Composition Wt Percent	Pack Composition Wt Percent	RPP-3 Substrate	Silicon Powder	Silicon Carbide $^{\circ}\text{F}$	Furnace Temp Hrs	Coating Time In.	Coating Depth In	Wt Gain Due to Coating Wt %
W4	Siliconized		--	10 60 30 Not heat $\text{Al}_2\text{O}_3/\text{SiC}/\text{Si}$ treated	741-385% 404-38.5% 00774 708-23.0%						
		G1-G8			ATJ Graphite Plates						2.3
		1-5									7.5
		T									10.2
		B1-B6									7.3
W5	Siliconized		--	10 60 30 Not heat $\text{Al}_2\text{O}_3/\text{SiC}/\text{Si}$ treated	741-38.5% 00774 404-38.5% 708-23.0%						
		1-6									17.1
		B1-B2									17.0
		B4-B6									
		T									17.5
W6	Siliconized		--	10 60 30 Not heat $\text{Al}_2\text{O}_3/\text{SiC}/\text{Si}$ treated	741-38.5% 404-38.5% 00774 708-23%						
		3, 4, 13									28.0
		B9-B16									33.6
		T									30.5
W7	Siliconized		--	10 60 30 Not heat $\text{Al}_2\text{O}_3/\text{SiC}/\text{Si}$ treated	741-38.5% 404-38.5% 00774						
		1-6									27.7
		B2-B3									32.4
		T									27.1
		E									19.1
		BP									20.2
		U									34.2
		7-10									26.3
		B4-B7									30.2
W8	Siliconized		--	10 60 30 Not heat $\text{Al}_2\text{O}_3/\text{SiC}/\text{Si}$ treated	741-38.5% 404-38.5% 00776 708-23%						
		1-7									24.4
		B1-B7									28.7
		T									26.7

TABLE A 1-2 DIFFUSION COATING RUNS ALUMINA/SILICON CARBIDE/SILICON SYSTEMS (Cont'd.)

Run No.	System	Specimen Identif	Slurry Composition Wt Percent	Pack Composition Wt Percent	RPP-3 Substrate	Silicon Powder	Silicon Carbide of	Furnace Temp Hrs	Coating Time In.	Coating Depth In.	Wt Gain Due to Coating Wt %
W8	(Cont'd.)	E									16.9
		U									34.6
		BP									19.7
W9	Siliconized		--	10 60 30	Not heat Al ₂ O ₃ /SiC/Si treated	404	A8784				41.7
		1-4									44.9
		B1-B3									38.3
		CPV1-CPV16									37.8
		XC28, C28									37.8
		XC48, C48									36.7
		XC68, C68									36.4
		XT9, T9									31.2
		XT5, T5									39.6
		013.8 1-6									54.6
		013.7 1-6									38.7
		013.2 1-6									34.4
		013.4 1-6									53.7
		013.4 1-6									53.5
		013.6 1-6				708	113				42.4
W10	Siliconized	5-6									49.2
		B4-B6									29.6
		XT6, T6									50.7
		013.1 1-6									34.5
		013.3 1-6									
			--	10 60 30	Not heat Al ₂ O ₃ /SiC/Si treated	1471	A8784	3100	2 3/4		31.8
		B1-B3									30.9
		D1-D3									26.1
		Plate									35.2
		E1-E3									30.5
		D1-D3 (cape)									
		S0 ₁ -S0 ₃									36.5
		#14									33.2

TABLE A 1-2 DIFFUSION COATING RUNS ALUMINA/SILICON CARBIDE/SILICON SYSTEMS (Cont'd.)

Run No.	System	Specimen Identif	Slurry Composition Wt Percent	Pack Composition Wt Percent	RPP-3 Substrate	Silicon Powder	Silicon Carbide °F	Furnace Temp Hrs	Coating Time In.	Coating Depth In.	Wt Gain Due to Coating Wt %
W10 (Cont'd.)		SL1									31.5
		C1									24.7
		TL1									28.2
		Panel 1, 2									23.6
		F01-F03									29.7
		F24-F28									33.3
		Q1-Q4									33.4
		T01-T09									30.0
		F1-F3									33.1
		FF1-FF3									34.6
		F01-F09									33.7
		B1-B10									37.5
		1-14									32.6
		11-16			Experi- mental						30.9
		21-26			"						26.2
		31-36			"						28.8
		S1-S4			"						29.3
		0			"						66.5
		41-46			"						32.5
S-1	Siliconized	BPV2- BPV8			RPP-3						30.7
		111-1119									28.0
		B1-B9	10 60 30 Not heat Al ₂ O ₃ /SiC/Si spent pack			532	00774	3100	2 3/4		26.6
		F1-F8	10 60 30 Not heat Al ₂ O ₃ /SiC/Si spent pack						2 3/4		24.9
S-2	Siliconized	B1-B10				532	00774				29.6
		F1-F10									24.6

TABLE A 1-2 DIFFUSION COATING RUNS ALUMINA/SILICON CARBIDE/SILICON SYSTEMS (Cont'd.)

Run No.	System	Specimen Identif	Slurry Composition Wt Percent	Pack Composition Wt Percent	RPP-3 Substrate	Silicon Powder	Silicon Carbide °F	Furnace Temp Hrs	Coating Time In.	Coating Depth In.	Wt Gain Due to Coating Wt %
S-2	(Cont'd.)	X									21.3
		14 ₁ -14 ₃									14.3
		12 ₁ -12 ₃									16.3
		L/E 2									18.1
S-3	Siliconized	B ₁ -B ₉		10 60 30 Al ₂ O ₃ /SiC/Si	Not heat treated	532	00774	3 100	2 3/4		28.9
		F ₁ -F ₉		"	"						21.9
		X									12.8
		14 ₁ -14 ₃		"							10.4
		L/E 3									12.1
S-4	Siliconized	B ₁ -B ₈		10 60 30 Al ₂ O ₃ /SiC/Si	Not heat treated	532	00774	3 100	2 3/4		29.5
		F ₁ -F ₈		"	"						20.6
		ST ₁ -ST ₃		10 60 30 Al ₂ O ₃ /SiC/Si	"						26.9
S-5	Siliconized			"	Not heat treated			3 100	2 3/4		
		B ₁ -B ₁₀		spent pack		532	00774				33.4
		F ₁ -F ₈									24.8
		X									17.9
		14 ₁ -14 ₃									17.6
		12 ₁ -12 ₃									13.0
		L/E 1									17.8
T-1	Siliconized	B ₁ -B ₁₀		10 60 30 Al ₂ O ₃ /SiC/Si		1471	00774				
		F ₁ -F ₁₁		10 60 30 Al ₂ O ₃ /SiC/Si		1471	A6220				14.7
											12.1

TABLE A.1-3 HEAT TREAT RUNS ALUMINA/SILICON CARBIDE/SILICON SYSTEM

Run No.	System	Specimen Identif	Pack Material	Furnace		Weight Change %
				Temp, °F	Time, Hrs.	
M127	Siliconized	M126-8	Carbon felt	3200	3/4	-0.35
		M126-12				-0.26
		M126-20				-0.25
		M127-7				-0.17
		M126-17				-0.20
		M126-9				-0.15
		M125-3				-0.34
		M125-B5				-0.30
		M125-9				-0.24
		M123-9				-0.23
		M123-7				-0.17
M131	Siliconized	M120-B3	Carbon felt	3200	3/4	+0.12
		M120-B4				-0.01
		M121-4				-0.04
		M121-7				+0.06
		M121-11				-0.10
		M122-6				-0.17
		M123-6				-0.04
		M124-5				+0.13
		M124-6				+0.18
		M124-8				+0.03
		M124-12				+0.24
		M124-14				+0.12
		M125-5				+0.22
		M125-7				+0.23
		M129-1				+0.09
		M129-4				+0.05
		M129-9				+0.19
		M129-10				+0.14
		M129-9F				+0.07
		M129-10F				+0.02
		M129-13				+0.26

TABLE A.1-3 HEAT TREAT RUNS ALUMINA/SILICON CARBIDE/SILICON SYSTEM (Cont'd.)

Run No.	System	Specimen Identif	Pack Material	Furnace		Weight Change %
				Temp, °F	Time, Hrs.	
M131 (Cont'd.)	Siliconized	M129-14				+0.23
		M129-19				+0.27
		M129-20				+0.17
		M130-1				0.0
		M130-2				-0.02
		M130-4				-0.09
		M130-5				-0.09
		M130-14				-0.0
		M130-15				0.0
		M130-16				+0.06
		M130-17				+0.15
		M130-23				+0.06
		M130-24				+0.14
		M130-25				0.0
		M130-26				+0.03
		M130-35				+0.05
		M130-36				0.0
		M130-37				+0.02
M134	Siliconized			3200	3/4	
		M133-7				-0.43
		M133-8				-0.48
		M133-11				-0.50
		M133-12				-0.53
		M133-B13				-0.46
		M133-B14				-0.37
		M133-B17				-0.60
		M133-B18				-0.69
		M132-1				-0.22
		M132-8				-0.22
		M132-9				-0.23
		M132-16				-0.28
		M132-B4				-0.32

TABLE A.1-3 HEAT TREAT RUNS ALUMINA/SILICON CARBIDE/SILICON SYSTEM (Cont'd.)

Run No.	System	Specimen Identif	Pack Material	Furnace		Weight Change %
				Temp, °F	Time, Hrs.	
M134	M132-B5	M132-B5		3200	3/4	-0.36
(Cont'd.)	M132-B11	M132-B11				-0.27
	M132-B12	M132-B12				-0.32
	M132-B16	M132-B16				-0.29
	M132-B17	M132-B17				-0.37
	M132-B22	M132-B22				-0.35
	M132-B24	M132-B24				-0.34
M135	Siliconized		Carbon fat	3000	1 1/2	
		M120-85				-0.60
		M121-2				-0.52
		M121-9				-0.53
		M122-4				-0.61
		M123-4				-0.52
		M125-BB				-0.40
		M126-10				-0.19
		M126-13				-0.16
		M126-16				-0.18
		M126-19				-0.17
		M130-12				-0.28
		M130-13				-0.28
		M130-20				-0.26
		M130-21				-0.27
		M130-27				-0.31
		M130-28				-0.52
		M130-32				-0.32
		M130-33				-0.28
		M132-2				-0.27
		M132-7				-0.33
		M132-10				-0.29
		M132-15				-0.30
		M132-B1				-0.39

TABLE A.1-3 HEAT TREAT RUNS ALUMINA/SILICON CARBIDE/SILICON SYSTEM (Cont'd.)

Run No.	System	Specimen Identif	Pack Material	Furnace		Weight Change %
				Temp, °F	Time, Hrs.	
M135 (Cont'd.)	Siliconized	M132-B2	Carbon fat	3000	1 1/2	-0.33
		M132-B9				-0.36
		M132-B10				-0.32
		M132-B13				-0.42
		M132-B14				-0.44
		M132-B19				-0.47
		M132-B21				-0.45
		M133-3				-0.54
		M133-4				-0.56
		M133-9				-0.62
		M133-10				-0.59
		M133-B7				-0.60
		M133-B8				-0.61
		M133-B11				-0.65
		M133-B12				-0.63
M139	Siliconized	M137-10	Carbon felt	3200	3/4	-0.12
		M137-2	"			-0.13
		M137-9	SiC-00774			-0.62
		M137-12	Spent M120 pack			+2.00
		M137-B11	Carbon felt			-0.21
		M137-B1	"			-0.15
		M137-B3	"			-0.83
		M137-B9	"			-0.90
		M138-B20	SiC-00774			-1.15
		M138-B21	Spent M120 pack			+2.10
M141	Siliconized	M137 & M138	Carbon felt	3200	3/4	
		T ₁ -T18				-0.28
		T01-T09				-0.22
		TF1-TF ^o				-0.21

TABLE A.1-3 HEAT TREAT RUNS ALUMINA/SILICON CARBIDE/SILICON SYSTEM (Cont'd.)

Run No.	System	Specimen Identif	Pack Material	Furnace		Weight Change %
				Temp, °F	Time, Hrs.	
M141 (Cont'd.)	Siliconized	TL1-TL4	Carbon felt	3200	3/4	-0.14
		1 - 12				-0.29
		S1-S2				-0.36
		S01-S02				-0.33
		1- 6				-0.27
		F01-F09				-0.41
		F1-F16				-0.26
		FF1-FF9				-0.26
		1, 4, 5, 7, 8, 11				-0.34
		B2-B5, B7, B8				-0.33
		B10-B12				
M144	Siliconized	M142, M143	Carbon felt	3200	3/4	
		2, 3, 5-10				-0.26
		B2, B3, B5- B13, B17, B18				-0.38
		F1-F23				-0.32
		CF1-CF7				-0.41
		FF1-FF14				-0.38
		TF1-TF15				-0.31
		SB1-SB8				-0.46
		T1-T15				-0.33
		SL1-SL14				-0.40
		TC1-TC4				-0.23
		TBP1- TBP4				-0.41
		C1-C4				-0.34
		SF1-SF4				-0.36
		S1-S10				-0.35
M151/153	Siliconized	M149	Carbon felt	3200	3/4	
		B1-B11				-0.40
		1-9				-0.42
		A1-A ₄				-0.40
		B ₁ 1-B ₁ ⁵				-0.45

TABLE A.1-3 HEAT TREAT RUNS ALUMINA/SILICON CARBIDE/SILICON SYSTEM (Cont'd.)

Run No.	System	Specimen Identif	Pack Material	Furnace		Weight Change %
				Temp, °F	Time, Hrs.	
M151/153 (Cont'd.)	Siliconized	M145	Carbon felt	3200	3/4	
		SB9-SB21				-0.66
		SL15-SL18				-0.98
		SF5-SF8				-0.33
		BF1-BF7				-0.57
M155	Siliconized	M145, M146	Carbon felt	3200	3/4	
		T ₅ - T ₁₁				-0.76
		TF ₁ -TF ₁₁				-0.70
		C ₁ -C ₃				-0.67
		C ₅ -C ₇				
		CF1-CF5, CF7				-0.41
		B ₄				-0.44
		BF1-BF3				-0.43
		F ₄ , F ₉ , F ₁₀				-0.20
		S1-S3				-0.48
		SF1, SF6, SF7				-0.50
		1, 3				-0.61
		B5-B8				-0.73
		SB1-SB5				-0.48
		SB8, SB12				
		FF1-FF5				-0.52
		FF9-FF13				
M152	Siliconized + Bare RPP ₃			3400	1/2	
		1, 2(bare RPP ₃) spent pack + felt				+8.7
		5-8(bare RPP ₃)	"			+19.3
		M136-1, 2, 9-10	"			+0.51
		M133-139, W1- B10				
		M136-4, B4	"			+0.72
		M136-1, 10, B2, carbon felt B9				-0.61
		M133-B3, W1- B9				

TABLE A. 1-3 HEAT TREAT RUNS ALUMINA/SILICON CARBIDE/SILICON SYSTEM (Cont'd.)

Run No.	System	Specimen Identif	Pack Material	Furnace		Weight Change %
				Temp, °F	Time, Hrs.	
M157	Siliconized	<u>M156</u>	Carbon felt	3200	3/4	
		B21-B25				-0.52
		CPA1-CPA6				-0.44
		CPP1-CPP3				-0.67
		FPP1-FPP3				-0.50
M159	Siliconized	M158	Carbon felt	3200	3/4	
		B1-B4				-0.54
		2, 3				-0.65
		B31				-0.59
		4, 5				-0.63
		B33				-0.57
		6, 7				-0.34
		W2-14, 15				-0.28
M160	Siliconized		Carbon felt	3200	3/4	
		<u>W-9</u>				
		1-6				-0.57
		B1-B3				-0.47
		XC28, C28				-0.49
		XC48, C48				-0.41
		013.2 1-6				-0.45
		013.3 1-6				-0.65
		013.4 1-6				-0.55
		013.5 1-6				-0.55
		013.6 1-6				-0.90
		013.8 1-6				-0.41
		013.7 1-6				-0.41
		013.1 1-6				-0.64
		XC68, C68				-0.31
		XT9, T9				-0.46
		XT6, T6				-0.25
		XT5, T5				-0.49
		<u>W1</u> -1, 2, 5, 6				-0.68

TABLE A. 1-3 HEAT TREAT RUNS ALUMINA/SILICON CARBIDE/SILICON SYSTEM (Cont'd.)

Run No.	System	Specimen Identif	Pack Material	Furnace		Weight Change %
				Temp, °F	Time, Hrs.	
M160 (Cont'd.)	Siliconized	W2-11, 12	Carbon felt	3200	3/4	-0.40
M162	Siliconized	M161	Carbon felt	3200	3/4	
		B2, B6, B7				-0.92
						-0.64
		B11-B13				-0.70
		12-14				-0.63
		B14				-1.02
		16				-0.62
M164	Siliconized	M163	Carbon felt	3200	3/4	
		F ₁ , F ₂				-.53
		B ₂ , B ₃				-.56
		F ₅ , F ₆				-.37
		B ₅ , B ₆				-.64
		F ₉ , F ₁₀				-.60
		B ₈ , B ₉				-.66
		F ₁₃ , F ₁₄				-.48
		B ₁₁ , B ₁₂				-.52
		F ₂₁ , F ₂₂				-.52
		B ₁₇ , B ₁₈				-.68
M167	Siliconized	M166	Carbon felt	3200	3/4	
		B ₁ , B ₃ , B ₅				-.80
		B ₇				
		F ₁ , F ₃ , F ₅ , F ₇				-.63
M170	Siliconized	M168	Carbon felt	3200	3/4	
		B ₁₁ , B ₁₃ , B ₁₅ , B ₁₇				-.45
		F ₁₁ , F ₁₃ , F ₁₅ F ₁₃				-.33
		M169				
		F ₂ -F ₆				-.52
		B ₂ -B ₈				-.77
		B ₁₉ -B ₂₄				-.81

TABLE A.1-3 HEAT TREAT RUNS ALUMINA/SILICON CARBIDE/SILICON SYSTEM (Cont'd.)

Run No.	System	Specimen Identif	Pack Material	Furnace		Weight Change %
				Temp, °F	Time, Hrs.	
M170 (Cont'd.)	Siliconized	CPP ₁ -CPP ₃	Carbon felt	3200	3/4	-.46
		BPP ₁ -BPP ₃				-.49
		68 ₁ - 68 ₁₉				-.36
M173	Siliconized	M172	Carbon felt	3200	3/4	
		B ₁ -B ₅				-.32
		F ₁ -F ₅				-.49
		W/T				-.37
W13	Siliconized	W-10	Carbon felt	3200	3/4	
		B ₁ -B ₃				-.16
		D ₁ -D ₃				-.26
		Plate				-.94
		E ₁ -E ₃				-.38
		D ₁ -D ₃ (cape)				-.27
		S0 ₁ -S0 ₃				-.40
		14				-.31
		SL ₁				-.37
		C-1				-.34
		TL ₁				-.17
		Panel 1, 2				-.55
		F0 ₁ -F0 ₃				-.21
		F24-F28				-.28
		Q ₁ -Q ₂				-.27
		T0 ₁ -T0 ₉				-.26
		F ₁ -F ₃				-.25
		FF ₁ -FF ₃				-.24
		F0 ₁ -F0 ₉				-.25
		B ₁ -B ₃				-.43
		B ₄ -B ₁₀				
		F ₁ -F ₈ , F ₁₀ - F ₁₄				-.34
		BPV ₂ -BPV ₈				-.27
		11 ₁ -11 ₃ -11 ₅ 11 ₁₉				-.28

A.2

FLEXURE TEST DATA

The following table summarizes all flexure test data conducted on the diffusion coating systems through the reporting period.

TABLE A.2-1
ROOM TEMPERATURE FLEXURE STRENGTHS

SPECIMEN	SIZE, IN.			F_B , psi $\times 10^{-3}$
	LENGTH	WIDTH	THICKNESS	
M54-13	5.0	0.747	0.186	7.13
-14	5.0	0.738	0.195	5.64
-15	5.0	0.751	0.198	7.79
-16	5.0	0.752	0.191	7.12
-17	5.0	0.749	0.186	4.21
-18	5.0	0.742	0.182	6.42
M55-11	5.0	0.754	0.189	9.81
-12	5.0	0.744	0.188	12.1
M56-15	5.0	0.745	0.187	6.08
-16	5.0	0.740	0.190	8.73
M62-1	5.0	0.748	0.204	16.6
-7	5.0	0.747	0.206	16.8
-12	5.0	0.750	0.206	13.8
-17	5.0	0.747	0.210	16.5
-22	5.0	0.751	0.206	16.2
-27	5.0	0.751	0.216	13.1
M63-1	3.0	0.739	0.119	11.4
-4	3.0	0.750	0.122	16.7
-7	3.0	0.741	0.117	8.46
-8	3.0	0.739	0.116	13.9
-11	2.5	0.742	0.070	2.47
-14	2.5	0.742	0.068	13.1
-3	3.0	0.778	0.115	12.7
-6	3.0	0.740	0.118	After 5 Pereny Cycles 15.0
-12	2.5	0.741	0.068	After 5 Pereny Cycles 3.50
-13	2.5	0.740	0.070	After 5 Pereny Cycles 3.30
-16	2.5	0.750	0.069	After 5 Pereny Cycles 6.72 After 5 Pereny Cycles

TABLE A.2-1 (CONT'D.)
ROOM TEMPERATURE FLEXURE STRENGTHS

SPECIMEN	SIZE, IN.			F_B , psi X 10^{-3}
	LENGTH	WIDTH	THICKNESS	
M81-1	5.0	1.007	0.174	22.6
-2	5.0	1.008	0.178	20.3
-3	5.0	1.009	0.178	22.4
-7	5.0	1.007	0.175	19.1
-8	5.0	1.001	0.175	18.2
-9	5.0	1.008	0.177	15.3
-15	5.0	1.010	0.178	16.6
-16	5.0	1.005	0.173	17.1
-17	5.0	1.010	0.168	17.6
M85-1	5.0	1.015	0.157	7.50
-2	5.0	1.021	0.163	6.62
-3	5.0	1.019	0.161	7.39
M86-1	5.0	0.874	0.155	9.29
				Heat Treated 3400°F
-2	5.0	0.978	0.157	8.57
				Heat Treated 3400°F
-3	5.0	0.975	0.157	7.82
				Heat Treated 3400°F
-13	5.0	0.971	0.169	8.24
				Heat Treated 3900°F
-14	5.0	0.976	0.165	8.34
				Heat Treated 3900°F
-15	5.0	1.001	0.168	6.11
				Heat Treated 3900°F
M90-1	5.0	1.003	0.155	7.62
-3	5.0	1.004	0.156	8.45
M91A-1	5.0	0.997	0.154	8.90
-2	5.0	0.999	0.151	7.57
M91C-2	5.0	1.003	0.169	7.45
-3	5.0	1.009	0.169	6.10
M95A-1	5.0	1.015	0.187	10.9
-2	5.0	1.014	0.184	11.7
M95B-5	5.0	1.008	0.183	11.9
-6	5.0	1.013	0.186	12.6

TABLE A.2-1 (CONT'D.)
ROOM TEMPERATURE FLEXURE STRENGTHS

SPECIMEN	SIZE, IN.			F_B , psi $\times 10^{-3}$
	LENGTH	WIDTH	THICKNESS	
M95C-9	5.0	1.014	0.186	13.0
-10	5.0	1.014	0.192	12.7
M96-13	5.0	1.015	0.187	9.92
-14	5.0	1.015	0.182	9.04
M97A-7	5.0	1.014	0.177	19.6
-8	5.0	1.016	0.174	20.1
M97B-11	5.0	1.016	0.182	19.8
-12	5.0	1.016	0.186	20.8
M97C-15	5.0	1.015	0.185	17.7
-16	5.0	1.015	0.185	18.6
M100-01	3.5	0.472	0.165	8.96
-02	3.5	0.442	0.169	8.45
-4-1	3.2	0.472	0.169	8.13
				Heat Treated 3400°F
-4-2	3.5	0.508	0.174	5.36
				Heat Treated 3400°F
-6-1	3.5	0.502	0.170	6.99
				Heat Treated 3600°F
-6-2	3.5	0.502	0.176	6.82
				Heat Treated 3600°F
-6-3	3.5	0.502	0.177	4.25
				Heat Treated 3600°F
-6-4	3.5	0.504	0.172	Plus 5 Pereny Cycles 5.33
				Heat Treated 3600°F
-9-1	3.5	0.500	0.172	Plus 5 Pereny Cycles 7.00
				Heat Treated 3900°F
-9-3	3.5	0.501	0.176	8.00
				Heat Treated 3900°F
-9-2	3.5	0.502	0.169	4.47
				Heat Treated 3900°F
-9-4	3.5	0.503	0.174	Plus 5 Pereny Cycles 3.86
				Heat Treated 3900°F
-5-1	3.5	0.504	0.168	Plus 5 Pereny Cycles 7.67
				Heat Treated 4500°F

TABLE A.2-1 (CONT'D.)
ROOM TEMPERATURE FLEXURE STRENGTHS

SPECIMEN	SIZE, IN.			F_B , psi $\times 10^{-3}$
	LENGTH	WIDTH	THICKNESS	
M100-5-2	3.5	0.504	0.165	6.26
				Heat Treated 4500°F
-5-3	3.5	0.503	0.160	3.26
				Heat Treated 4500°F
				Plus 5 Pereny Cycles
-5-4	3.5	0.505	0.164	2.61
				Heat Treated 4500°F
				Plus 5 Pereny Cycles
M101-1	5.0	0.992	0.172	12.0
-2	5.0	0.970	0.172	11.0
-3	5.0	0.890	0.170	8.32
-4	5.0	0.987	0.180	8.20
M103-1	5.0	0.927	0.172	6.30
-2	5.0	0.926	0.182	7.08
-3	5.0	0.935	0.181	5.13
-4	5.0	0.926	0.162	4.32
-5	5.0	0.925	0.167	5.38
-6	5.0	0.930	0.172	7.50
M105-F2	5.0	0.707	0.152	4.60
-F9	5.0	0.701	0.155	6.48
-F18	5.0	0.707	0.155	11.5
-F3	5.0	0.708	0.155	4.85
				After 5 Pereny Cycles
-F6	5.0	0.702	0.155	4.25
				After 5 Pereny Cycles
-F17	5.0	0.710	0.154	12.9
				After 5 Pereny Cycles
M106-F16	5.0	0.702	0.157	10.2
-F25	5.0	0.707	0.162	7.30
-F09	5.0	0.712	0.157	10.1
-F06	5.0	0.709	0.155	5.29
				After 5 Pereny Cycles
M107-1	5.0	0.976	0.162	8.64
				Fill Direction
-2	5.0	0.940	0.149	18.7
-3	5.0	0.943	0.162	16.7
-4	5.0	0.940	0.170	15.2
-5	5.0	0.934	0.149	19.6
-6	5.0	0.974	0.158	15.1

TABLE A.2-1 (CONT'D.)
ROOM TEMPERATURE FLEXURE STRENGTHS

SPECIMEN	SIZE, IN.			F_B , psi $\times 10^{-3}$
	LENGTH	WIDTH	THICKNESS	
M109-1	5.0	0.961	0.156	8.50
-2	5.0	0.938	0.159	8.70
-3	5.0	0.964	0.154	8.88
-4	5.0	0.941	0.156	9.00
-5	5.0	0.958	0.158	8.75
-6	5.0	0.958	0.164	6.80
M112-5	5.0	1.000	0.189	12.3
-6	5.0	1.004	0.190	12.1
-7	5.0	1.005	0.192	11.0
-8	5.0	1.006	0.192	12.5
-9	5.0	1.005	0.190	10.1
-10	5.0	0.953	0.184	12.0
M113-1	5.0	0.715	0.157	8.94
-2	5.0	0.712	0.156	7.80
-3	5.0	0.702	0.161	7.41
-4	5.0	0.715	0.160	8.60
-5	5.0	0.713	0.160	6.77
-6	5.0	0.724	0.159	8.60
M115-1	5.0	0.786	0.193	8.48
-3	5.0	0.788	0.194	8.11
-4	5.0	0.788	0.194	5.57
-5	5.0	0.788	0.196	5.08
-6	5.0	0.789	0.192	7.47
-7	5.0	0.790	0.195	9.63
-8	5.0	0.790	0.187	13.1
-9	5.0	0.780	0.190	10.9
-10	5.0	0.789	0.190	10.1
-11	5.0	0.783	0.188	11.0
-12	5.0	0.790	0.192	10.3
M30-1-1	5.0	0.775	0.188	10.0
-1-2	5.0	0.775	0.183	9.20
M31-II-1	5.0	0.772	0.182	7.46
-II-5	5.0	0.767	0.178	10.3
M60-1	5.0	0.765	0.187	4.07
-7	5.0	0.748	0.185	7.19
-13	5.0	0.740	0.185	6.36

TABLE A.2-1 (CONT'D.)
ROOM TEMPERATURE FLEXURE STRENGTHS

SPECIMEN	SIZE, IN.			F_p , psi $\times 10^{-3}$
	LENGTH	WIDTH	THICKNESS	
M62-2	5.0	0.750	0.208	14.5
M63-9	5.0	0.745	0.212	10.4
-86	5.0	0.745	0.212	9.64
BARE RPP-3	5.0	0.738	0.213	16.4
M116-13	5.0	0.790	0.196	6.0
-14	5.0	0.782	0.192	7.0
-15	5.0	0.790	0.196	9.1
-16	5.0	0.788	0.193	7.0
-17	5.0	0.789	0.192	5.4
-18	5.0	0.790	0.195	8.1
M117-1	5.0	0.724	0.160	9.7
-2	5.0	0.716	0.161	8.1
-3	5.0	0.707	0.165	9.7
-4	5.0	0.705	0.167	10.0
M118-1	5.0	0.721	0.156	11.8
-2	5.0	0.720	0.157	12.9
-3	5.0	0.723	0.160	8.1
-4	5.0	0.712	0.160	11.3
M119-G	5.0	0.815	0.187	1.6
-H	5.0	0.759	0.186	2.3
M120-1	5.0	0.725	0.158	11.6
-2	5.0	0.727	0.158	9.48
M121-5	5.0	0.726	0.159	13.0
-6	5.0	0.730	0.159	13.2
M122-8	5.0	0.775	0.168	10.1
-9	5.0	0.775	0.164	11.0
M120-3	5.0	0.728	0.155	9.65
				Five Pereny Cycles
M122-7	5.0	0.780	0.150	8.74
				Five Pereny Cycles
M121-8	5.0	0.729	0.158	11.7
				Five Pereny Cycles
M122-10	5.0	0.775	0.169	5.58
				Five Pereny Cycles

TABLE A.2-1 (CONT'D.)
ROOM TEMPERATURE FLEXURE STRENGTHS

SPECIMEN	SIZE, IN.			F_B , psi $\times 10^{-3}$
	LENGTH	WIDTH	THICKNESS	
M123-8	5.0	0.777	0.174	11.1
				Five Pereny Cycles
-10	5.0	0.780	0.170	19.9
-11	5.0	0.776	0.169	20.8
M124-2	5.0	0.730	0.168	19.8
-3	5.0	0.726	0.169	18.8
-1	5.0	0.739	0.170	16.4
				Five Pereny Cycles
M125-1	5.0	0.731	0.169	15.3
-2	5.0	0.740	0.172	14.9
-4	5.0	0.741	0.169	14.3
				Five Pereny Cycles
M126-1	5.0	0.729	0.175	14.8
-2	5.0	0.728	0.175	14.0
-3	5.0	0.728	0.178	14.5
-4	5.0	0.721	0.174	15.3
-5	5.0	0.732	0.174	12.8
				Five Pereny Cycles
-6	5.0	0.710	0.161	19.0
				Five Pereny Cycles
M127-M123-9	5.0	0.781	0.167	20.6
M127-M125-3	5.0	0.734	0.171	11.2
M127-M126-7	5.0	0.716	0.170	15.5
M127-M126-8	5.0	0.714	0.170	15.3
M128-1	5.0	0.727	0.155	15.9
-3	5.0	0.739	0.152	18.2
-7	5.0	0.724	0.154	15.3
-8	5.0	0.724	0.158	17.9
-24	5.0	0.650	0.154	17.6
-26	5.0	0.735	0.157	17.5
-5	5.0	0.737	0.154	9.9
				Five Pereny Cycles
-6	5.0	0.737	0.153	9.5
				Five Pereny Cycles
-25	5.0	0.736	0.157	10.1
				Five Pereny Cycles
-27	5.0	0.739	0.157	12.2
				Five Pereny Cycles

TABLE A.2-1 (CONT'D.)
ROOM TEMPERATURE FLEXURE STRENGTHS

SPECIMEN	SIZE, IN.			F_B , psi $\times 10^{-3}$
	LENGTH	WIDTH	THICKNESS	
M129-2	5.0	0.714	0.162	13.1
-3	5.0	0.715	0.160	16.6
-5	5.0	0.745	0.163	11.8
				Five Pereny Cycles
-6	5.0	0.735	0.164	10.3
				Five Pereny Cycles
M130-8	5.0	0.750	0.158	15.0
-7	5.0	0.750	0.158	16.0
-2	5.0	0.745	0.160	14.3
				Heat Treat
-4	5.0	0.743	0.158	15.5
				Heat Treat
-18	5.0	0.749	0.187	12.6
				Five Pereny Cycles
-19	5.0	0.751	0.180	15.2
				Five Pereny Cycles
-1	5.0	0.746	0.161	11.0
				Heat Treat and
				Five Pereny Cycles
-5	5.0	0.744	0.156	12.0
				Heat Treat and
				Five Pereny Cycles
M132-7	5.0	0.752	0.182	15.1
				Heat Treated 3000°F
-2	5.0	0.743	0.183	12.7
				Heat Treated 3000°F
M132-15	5.0	0.751	0.179	10.9
				Heat Treated 3000°F
				Five Pereny Cycles
M130-20	5.0	0.746	0.188	9.0
				Heat Treated 3000°F
				Five Pereny Cycles
M130-21	5.0	0.746	0.184	10.6
				Heat Treated 3000°F
				Five Pereny Cycles
M132-10	.0	0.750	0.185	13.3
				Heat Treated 3000°F
				Five Pereny Cycles

TABLE A.2-1 (CONT'D.)
ROOM TEMPERATURE FLEXURE STRENGTHS

SPECIMEN	SIZE, IN.			F_B , psi $\times 10^{-3}$
	LENGTH	WIDTH	THICKNESS	
M137-9	5.0	0.769	0.183	9.5 Heat Treated and Five Pereny Cycles
-2	5.0	0.764	0.174	10.0 Heat Treated and Five Pereny Cycles
M138-3	5.0	0.762	0.170	20.1
-7	5.0	0.768	0.181	13.6 Heat Treated and One Pereny Cycle
-4	5.0	0.767	0.173	16.9 Heat Treated and Two Pereny Cycles
-5	5.0	0.764	0.174	11.6 Heat Treated and Three Pereny Cycles
-11	5.0	0.765	0.184	7.8 Heat Treated and Five Pereny Cycles
M137-8	5.0	0.768	0.160	18.2 Heat Treated
M142-4	5.0	0.763	0.167	18.3
M143-11	5.0	0.780	0.171	14.0
M143-8	5.0	0.760	0.168	15.4 Heat Treated and One Pereny Cycle
M142-3	5.0	0.764	0.169	10.2 Heat Treated and Five Pereny Cycles
M142-5	5.0	0.762	0.170	11.1 Heat Treated and Five Pereny Cycles
M143-9	5.0	0.777	0.171	10.0 Heat Treated and Five Pereny Cycles
M142-2	5.	0.773	0.166	15.0 Heat Treated
M143-10	5.	0.785	0.171	13.6 Heat Treated

TABLE A.2-1 (CONT'D.)
ROOM TEMPERATURE FLEXURE STRENGTHS

SPECIMEN	SIZE, IN.			F_B , psi $\times 10^{-3}$
	<u>LENGTH</u>	<u>WIDTH</u>	<u>THICKNESS</u>	
M150-3	5.0	0.733	0.157	15.5
M149-5	5.0	0.732	0.168	13.3
M149-2	5.0	0.725	0.171	Heat Treated
				7.6
				Heat Treated and Five Pereny Cycles
M138-F0-5	5.0	0.714	0.178	11.5
				Heat Treated and Five Pereny Cycles
M130-17	5.0	0.744	0.180	10.1
				Heat Treated and Five Pereny Cycles
M136-3	5.0	0.764	0.153	17.9
-4	5.0	0.765	0.160	Five Pereny Cycles
				6.0
				Heat Treated
M152-2	5.0	0.755	0.154	11.6
M136-1	5.0	.769	0.163	9.0
-2	5.0	.769	0.158	Heat Treated
				6.1
				Heat Treated
M138-F0-7	5.0	.717	0.182	10.1
				Heat Treated and Five Pereny Cycles
M142-1	5.0	.778	0.164	15.5
				Five Pereny Cycles
M138-F0-6	5.0	.715	0.182	9.9
				Heat Treated and Five Pereny Cycles
M143-6	5.0	.777	.157	13.4
				Heat Treated and Five Pereny Cycles

TABLE A.2-1 (CONT'D.)
ROOM TEMPERATURE FLEXURE STRENGTHS

SPECIMEN	SIZE, IN.			F_B , psi $\times 10^{-3}$
	LENGTH	WIDTH	THICKNESS	
M138-F0-4	5.0	.723	.174	9.9 Heat Treated and Five Pereny Cycles
M152-1	5.0	.752	.150	5.5 Five Pereny Cycles
M152-M136-10	5.0	.761	.175	3.9 Heat Treated and Five Pereny Cycles
M156-1	5.0	.732	.163	13.9 Heat Treated
-2	5.0	.737	.159	7.3 Heat Treated and Five Pereny Cycles
-3	5.0	.730	.151	6.3 Heat Treated and Five Pereny Cycles
-5	5.0	.707	.164	6.9 Heat Treated and Five Pereny Cycles
-7	5.0	.823	.163	8.3 Heat Treated and Five Pereny Cycles
M146-13	5.0	.744	.171	11.9 Heat Treated and Five Pereny Cycles
M158-1	5.0	.725	.161	18.2
-2	5.0	.723	.161	20.6 Heat Treated
-6	5.0	.727	.162	15.4 Heat Treated
-5	5.0	.720	.160	19.8 Heat Treated
-3	5.0	.722	.159	4.5 Heat Treated and Five Pereny Cycles
-7	5.0	.726	.158	7.3 Heat Treated and Five Pereny Cycles
-4	5.0	.729	.160	7.5 Heat Treated and Five Pereny Cycles

TABLE A.2-1 (CONT'D.)
ROOM TEMPERATURE FLEXURE STRENGTHS

SPECIMEN	SIZE, IN.			F_B , psi $\times 10^{-3}$
	LENGTH	WIDTH	THICKNESS	
M121-7	5.0	0.726	0.160	11.0 Heat Treated
M129-1	5.0	0.725	0.158	13.5 Heat Treated
M129-4	5.0	0.721	0.163	12.5 Heat Treated
M125-5	5.0	0.732	0.167	11.5 Heat Treated and Five Pereny Cycles
M129-9F	5.0	0.736	0.158	8.7 Heat Treated and Five Pereny Cycles
M129-10F	5.0	0.734	0.156	8.4 Heat Treated and Five Pereny Cycles
M132-4	5.0	0.741	0.175	15.5
-5	5.0	0.756	0.184	13.6
-12	5.0	0.752	0.175	17.4
-13	5.0	0.744	0.175	14.9
-3	5.0	0.751	0.185	13.9
-6	5.0	0.740	0.185	Five Pereny Cycles 13.2
-11	5.0	0.740	0.180	Five Pereny Cycles 16.6
-14	5.0	0.727	0.185	Five Pereny Cycles 12.7
-9	5.0	0.755	0.179	Five Pereny Cycles 15.1
-16	5.0	0.748	0.175	Heat Treated 13.9 Heat Treated
M133-2	5.0	0.740	0.170	15.7
-5	5.0	0.740	0.172	17.7
-1	5.0	0.722	0.163	16.7
-6	5.0	0.737	0.161	Five Pereny Cycles 20.3
-8	5.0	0.746	0.167	Five Pereny Cycles 15.2
-11	5.0	0.746	0.164	Heat Treated 18.4 Heat Treated

TABLE A.2-1 (CONT'D.)
ROOM TEMPERATURE FLEXURE STRENGTHS

SPECIMEN	SIZE, IN.			F_B , psi $\times 10^{-3}$
	<u>LENGTH</u>	<u>WIDTH</u>	<u>THICKNESS</u>	
M133-7	5.0	0.745	0.159	14.0 Heat Treated and Five Pereny Cycles
-12	5.0	0.748	0.163	10.2 Heat Treated and Five Pereny Cycles
M132-1	5.0	0.745	0.171	13.0 Heat Treated and Five Pereny Cycles
M132-8	5.0	0.745	0.172	12.0 Heat Treated and Five Pereny Cycles
M136-8	5.0	0.745	0.171	13.8 Five Pereny Cycles
M136-7	5.0	0.770	0.171	13.1 Five Pereny Cycles
M137-6	5.0	0.766	0.176	16.8
-10	5.0	0.765	0.176	15.9
-12	5.0	0.768	0.180	Heat Treated 13.8 Heat Treated and Five Pereny Cycles
M130-12	5.0	0.752	0.165	18.1 Heat Treated 3000°F
-13	5.0	0.758	0.165	17.8 Heat Treated 3000°F
W1-4	5.0	0.688	0.166	18.4
W5-1	5.0	0.787	0.158	24.6
W2-8	5.0	0.755	0.163	12.9
-9	5.0	0.733	0.165	12.0 Five Pereny Cycles
-14	5.0	0.740	0.162	16.8
W1-3	5.0	0.771	0.158	14.5 Five Pereny Cycles

TABLE A.2-1 (CONT'D.)
ROOM TEMPERATURE FLEXURE STRENGTHS

SPECIMEN	SIZE, IN.			F_B , psi $\times 10^{-3}$
	LENGTH	WIDTH	THICKNESS	
W3-2	5.0	0.774	0.169	8.4
-7	5.0	0.765	0.167	Five Pereny Cycles 10.6
				Five Pereny Cycles
W7-4	5.0	0.757	0.159	16.8
-2	5.0	0.755	0.160	12.8
W6-4	5.0	0.760	0.157	16.7
W3-5	5.0	0.785	0.168	12.7
				Sermetal Treated
W5-2	5.0	0.789	.160	17.9
				Five Pereny Cycles
W3-4	5.0	0.766	.164	13.8
				Sermetal Treated and Five Pereny Cycles
W8-3	5.0	.730	.162	16.6
-7	5.0	.725	.162	16.8
-1	5.0	.729	.160	10.0
				Five Pereny Cycles
-2	5.0	.730	.162	15.8
				Five Pereny Cycles
-4	5.0	.730	.161	10.7
				Five Pereny Cycles
W7-1	5.0	.750	.163	8.4
				Five Pereny Cycles
-3	5.0	.755	.157	14.2
				Five Pereny Cycles
-10	5.0	.750	.170	14.9
				Sermetal Treated and Five Pereny Cycles
W9-1	5.0	.720	.161	12.6
				Heat Treat
-5	5.0	.725	.165	10.5
				Heat Treat
-3	5.0	.722	.161	7.3
				Heat Treat and Five Pereny Cycles

TABLE A.2-1 (CONT'D.)
ROOM TEMPERATURE FLEXURE STRENGTHS

SPECIMEN	SIZE, IN.			F_B , psi $\times 10^{-3}$
	LENGTH	WIDTH	THICKNESS	
W9-6	5.0	.724	.163	5.5 Heat Treat and Five Pereny Cycles
M161-8	5.0	.725	.157	4.7 Heat Treat and Five Pereny Cycles
-9	5.0	.726	.159	4.2 Heat Treat and Five Pereny Cycles
-13	5.0	.721	.157	3.9 Heat Treat and Five Pereny Cycles
-4	5.0	.720	.160	3.2 Heat Treat and Five Pereny Cycles
-16	5.0	.728	.159	3.9 Heat Treat and Five Pereny Cycles
M163-1	5.0	.687	.155	7.5 Heat Treat and Five Pereny Cycles
-3	5.0	.690	.154	14.5 Five Pereny Cycles
-5	5.0	.688	.153	7.6 Heat Treat and Five Pereny Cycles
-7	5.0	.689	.155	13.7 Five Pereny Cycles
-9	5.0	.685	.154	7.1 Heat Treat and Five Pereny Cycles
-11	5.0	.680	.156	13.3 Five Pereny Cycles
-13	5.0	.681	.155	4.8 Heat Treat and Five Pereny Cycles
-15	5.0	.685	.153	17.2 Five Pereny Cycles
-17	5.0	.684	.154	5.3 Heat Treat and Five Pereny Cycles

TABLE A.2-1 (CONT'D.)
ROOM TEMPERATURE FLEXURE STRENGTHS

SPECIMEN	SIZE, IN.			F_B , psi $\times 10^{-3}$
	LENGTH	WIDTH	THICKNESS	
M163-19	5.0	.695	.156	14.7
				Five Pereny Cycles
-21	5.0	.674	.156	4.4
				Heat Treat and
				Five Pereny Cycles
-23	5.0	.687	.157	15.2
				Five Pereny Cycles
M163-2	5.0	.690	.155	17.0
				Heat Treat
-4	5.0	.697	.156	18.5
-6	5.0	.687	.154	18.1
				Heat Treat
-8	5.0	.683	.156	14.0
-10	5.0	.686	.153	17.7
				Heat Treat
-12	5.0	.691	.157	16.1
-14	5.0	.683	.154	15.1
				Heat Treat
-16	5.0	.687	.155	15.8
-18	5.0	.684	.154	14.5
				Heat Treat
-20	5.0	.688	.157	15.0
-22	5.0	.687	.157	14.5
				Heat Treat
-24	5.0	.699	.154	17.8
M165-6	5.0	.702	.156	10.9
				Five Pereny Cycles
M166-1	5.0	.748	.160	15.0
				Heat Treat
-2	5.0	.755	.154	18.4
-5	5.0	.755	.160	19.4
				Heat Treat
-6	5.0	.740	.161	15.6
S2-1	5.0	.731	.156	16.4
-2	5.0	.719	.154	19.0
-7	5.0	.720	.155	15.1
-10	5.0	.715	.155	13.5
				Five Pereny Cycles
S3-1	5.0	.690	.152	14.4
				Five Pereny Cycles

TABLE A.2-1 (CONT'D.)
ROOM TEMPERATURE FLEXURE STRENGTHS

SPECIMEN	SIZE, IN.			F_B , psi X 10^{-3}
	<u>LENGTH</u>	<u>WIDTH</u>	<u>THICKNESS</u>	
S4-1	5.0	.698	.158	11.4 Five Pereny Cycles
T1-1	5.0	.695	.156	19.5 Five Pereny Cycles
W10-9	5.0	.712	.158	18.5
-12	5.0	.716	.158	3.0 Heat Treat and Five Pereny Cycles
-14	5.0	.714	.157	16.3 Heat Treat
W10-F24	5.0	.711	.154	13.1 20 Cycles Radiant Heat Lamp
W10-F25	5.0	.711	.155	12.9 40 Cycles Radiant Heat Lamp
W10-F26	5.0	.711	.150	10.0 60 Cycles Radiant Heat Lamp
W10-1	5.0	.718	.159	7.8 40 Cycles Radiant Heat Lamp
-2	5.0	.721	.152	15.0 20 Cycles Radiant Heat Lamp
M133-3	5.0	.745	.165	16.0 2 Cycles Radiant Heat Lamp
-10	5.0	.742	.167	16.2 2 Cycles Radiant Heat Lamp
M130-16	5.0	.756	.159	16.6 2 Cycles Radiant Heat Lamp
M168-11	5.0	.751	.159	7.2 Heat Treat
-14	5.0	.747	.155	8.0

TABLE A.2-1 (CONT'D.)
ROOM TEMPERATURE FLEXURE STRENGTHS

SPECIMEN	SIZE, IN.			F_B , psi $\times 10^{-3}$
	<u>LENGTH</u>	<u>WIDTH</u>	<u>THICKNESS</u>	
M169-1	5.0	.722	.160	13.4
-6	5.0	.738	.161	12.9
				Heat Treat
W10-11-1	5.0	.757	.206	15.1
				Heat Treat (NDT)
-11-3	5.0	.762	.206	14.9
				Heat Treat (NDT)
-11-5	5.0	.762	.206	12.9
				Heat Treat (NDT)
-11-7	5.0	.764	.203	15.0
				Heat Treat (NDT)
-11-9	5.0	.763	.201	12.6
				Heat Treat (NDT)
-11-11	5.0	.760	.202	16.4
				Heat Treat (NDT)
-11-13	5.0	.759	.203	13.5
				Heat Treat (NDT)
-11-15	5.0	.762	.202	13.3
				Heat Treat (NDT)
-11-17	5.0	.764	.203	12.7
				Heat Treat (NDT)
-11-19	5.0	.762	.201	13.1
				Heat Treat (NDT)
W10-68-1	5.0	.759	.257	10.7
				Heat Treat (NDT)
-68-3	5.0	.764	.256	17.8
				Heat Treat (NDT)
-68-5	5.0	.765	.260	9.3
				Heat Treat (NDT)
-68-7	5.0	.753	.268	22.5
				Heat Treat (NDT)
-68-9	5.0	.753	.270	23.2
				Heat Treat (NDT)
-68-11	5.0	.751	.275	21.6
				Heat Treat (NDT)
-68-13	5.0			No Test
-68-15	5.0	.752	.278	22.2
				Heat Treat (NDT)
-68-17	5.0	.752	.285	23.5
				Heat Treat (NDT)
-68-19	5.0	.750	.290	21.5
				Heat Treat (NDT)

A.3

PLASMA ARC DATA

The following table summarizes all plasma arc test data conducted on the diffusion coated systems of silicon, boron.silicon, and zirconium. boron.silicon types. In addition plasma test data for the melt impregnation hafnium.tantalum coating system are included.

TABLE A.3-1
SUMMARY, PLASMA ARC TEST DATA

HOLDER TYPE	TEST EXPD. NO.	PROCESS	SPECIMEN NO.	COLD WALL HEAT FLUX BTU/FT ² SEC	STAG ENTHAL BTU/LB	STAG. PRESS. PSIA	TIME DURATION SECONDS	CONTROL SPECIMEN TEMP °F	MASS LOSS GRAMS	THICK LOSS IN.	$\frac{\sigma}{N}$	TRUE SURF TEMP °F
Stag	1	B-Si	M54-3	140	8500	.4	300	3430	.5384	.0635		3440
	1	B-Si	M54-7	130	8000	.4	300	3430	.0445	.0		2890
	1	B-Si	M54-11	130	8000	.4	300	3430	.0418	.0005		2890
	1	B-Si	M54-4	130	8000	.4	300	3430				3020
	1	B-Si	M55-3	130	8000	.4	300	3540	.0324	.0	.00491	2890
	1	B-Si	M55-6	130	8000	.4	300	3540		.0015		3050
	2	B-Si	M55-3	130	800	.4	300	3540	.0895	.0015	.0135	2980
	1	BS	M56-2	130	7310	.4	300	3360	.0069	.001	.0008	2790
	1	BS	M56-11	130	7310	.4	300	3360	.01	.0005	.000116	2800
	2	BS	M56-2	130	7310	.4	300	3360	.0077	.0	.000894	2830
	3	BS	M56-2	130	7310	.4	300	3360	.0134	.0005	.00156	2850
	1	BS	M57-2	130	7350	.4	300	3320	.0140	.001	.00162	2740
	1	BS	M57-6	130	7350	.4	300	3320	.0003	.002	.0000348	2730
	1	BS with Al ₂ O ₃	M57-10	130	7350	.4	300	3320	.0100	.001	.00116	2700
	2	BS	M57-2	130	7350	.4	300	3270	.031	.002	.0036	2800
	2	BS	M57-6	130	7350	.4	300	3270	.0117	.001	.00136	2700
	2	BS with Al ₂ O ₃	M57-10	130	7350	.4	300	3270	.0042	.001	.000488	2710
	3	BS	M57-2	130	7350	.4	300	3270	.0779	.0	.00904	2770
	3	BS	M57-6	130	7350	.4	300	3270	.0075	.0	.00087	2730
	3	BS with Al ₂ O ₃	M57-10	130	7350	.4	300	3270	.0121	.001	.001405	2760
	1	BS	M58-6	130	6500	.4	300	3270	.0112	.0035		2690
	1	BS	M58-14	130	6500	.4	300	3270	.0155	.0025		2700
	1	ZBS	M58-26	130	6500	.4	300	3270	.0561	.002		2830
	2	BS	M58-6	70	4320	.36	300	2740	.0	.0		2300
	2	BS	M58-14	70	4320	.36	300	2740	.0	.0		2300
	2	ZBS	M58-26	70	4320	.36	300	2740	.0	.0005		2300
	1	ZBS	M61-36	130	6500	.4	300	3270		.072		3310
	1	BS	M61-32	130	6500	.4	300	3270		.002		2980
	1	BS	M61-26	130	6500	.4	300	3270		.0005		3080
	1	BS	M62-4	130	6500	.4	300	3250		.0025		2700
	1	BS	M62-9	130	6500	.4	300	3250		.0005		2610
	1	BS with Cr	M62-13	130	6500	.4	300	3250		.003		2850
	1	ZBS	M62-23	130	6500	.4	300	3250		.008		2900
	1	ZBS	M62-29	130	6500	.4	300	3250		.0015		2830
	1	ZBS	M62-39	130	6500	.4	300	3250		.0005		2640
	1	ZBS	M62-41	130	6500	.4	300	3250		.0015		2800
	1	BS	M62-43	130	6500	.4	300	3250		.005		2750
Stag	1	ZBS	M62	130	6500	.4	300	3250		.0005		2730
			M60-6									

HOLDER TYPE	TEST EXPD NO	PROCESS	SPECIMEN NO	COLD WALL HEAT FLUX BTU/FT ² SEC	STAG ENTHAL BTU/LB	STAG PRESS PSIA	TIME DURATION SECONDS	CONTROL SPECIMEN TEMP °F	MASS LOSS GRAMS	THICK LOSS IN	$\frac{dH}{dt}$	TRUE SURF TEMP °F
Stag	1	ZBS	M62	130	6500	.4	300	3250		.005		2640
			M60-18									
	1	BS with Cr	M62-14	130	6500	.4	300	3250		.003		2840
	1	BS	M63-21	130	6500	.4	300	3430		.002		2950
	1	BS	M63-27	130	6500	.4	300	3430		.0		2750
	1	ZBS	M63-36	130	6500	.4	300	3430		.0005		2580
	1	ZBS	M63-61	130	6500	.4	300	3430		.0		2640
	1	BS	M63-63	130	6500	.4	300	3400		.0005		2750
	1	BS	M63-66	130	6500	.4	300	3400		.001		2750
	1	ZBS	M63-83	130	6500	.4	300	3400		.0005		2770
	1	BS	M63-29	130	6500	.4	300	3530	.1106	.001		3260
	1	BS	M63-40	130	6500	.4	300	3530	.0531	.002		2830
	1	ZBS	M63-50	130	6500	.4	300	3530	.6636	.0765		3380
	1	Silicon-ized	M65-A	130	6500	.4	300	3530	.0124	.001		2830
	1	"	M65-F	130	6500	.4	300	3530	.0111	.001		2830
	1	"	M65-H	130	6500	.4	300	3530	.1257	.003		3250
	1	"	M65-I	130	6500	.4	300	3530	.0193	.0025		2840
	1	HfTa	HT-27		6170		300	3410		-.0035		3610
	1	HfTa	HT-29		6170		300	3410		-.003		3600
	1	HfTa	HT-31		6170		300	3410		-.005		3690
	1	HfTa	HT-38		6170		300	3410		-.008		3650
	1	Silicon-ized	M65-24		6170		300	3410	.0061	.0005	.000707	2830
	2	HfTa	HT-27		6170		300	3410		-.002		3690
	2	HfTa	HT-29		6170		300	3410		-.002		3650
	2	HfTa	HT-31		6170		300	3410		-.0057		3770
	2	HfTa	HT-38		6170		300	3410		.003		3770
	3	HfTa	HT-27		6170		300	3410		-.001		3760
	3	HfTa	HT-29		6170		300	3410		-.004		3770
	3	HfTa	HT-38		6170		300	3410				3650
	2	Silicon-ized	M65-24		6170		300	3410	.0022	.0005	.000255	2680
	1	"	M79-10		10500		300	3650	.0569	.0067		2990
	1	"	M79-11		10500		300	3650	.0744	.0078		2920
	1	"	M71-6		10500		300	3650	.0342	.005		2840
	1	HfTa	HT-15		10500		300	3650		-.0065		3810
	2	HfTa	HT-15		10500		300	3610				3800
	1	Silicon-ized	M86-10	131	6200	.4	300	3360	.0068	.004	.000789	2950
	1	"	M53-5	129	6200	.4	300	3360	.0031	.0005	.00036	2690
	2	"	M86-10	132	6200	.4	300	3360	.0097	.0015	.001125	2900
	2	"	M53-5	132	6200	.4	300	3360	.0077	.0	.000893	2790
	3	"	M86-10	129	6200	.4	300	3360	.0053	.001	.000615	2790
	3	"	M53-5	132	6200	.4	300	3360	.0063	.0005	.00073	2780
	1	"	M85B-3	127	6500	.4	300	3480	.0124	.0011	.00152	2810
	1	"	M85B-9	127	6500	.4	300	3480	.0025	.0005	.000305	2800
	1	"	M85B-6	131	7150	.4	300	3480	.0157	.001	.00212	2970
Stag	1	"	M85B-12	130	6500	.4	300	3480	.0069	.0	.000845	2860

HOLDER TYPE	TEST EXPO NO	PROCESS	SPECIMEN NO	COLD WALL HEAT FLUX BTU/F ² SEC	STAG ENTHAL BTU/LB	STAG PRESS PSIA	TIME DURATION SECONDS	CONTROL SPECIMEN TEMP °F	MASS LOSS GRAMS	THICK LOSS IN.	$\frac{M}{N}$	TRUE SURF TEMP °F
Stag	1	Silicon-ized	M85B-15	127	6500	.4	300	3480	.0094	.001	.000115	2875
↓	1	"	M85B-18	126	6500	.4	300	3480	.0075	.002	.000916	2900
Stag	1	"	M86-11	60	4440	.36	1800	--	.0134	.0	.000402	2220
Wedge	1	"	M86-9	-	4440	.36	900	--	.0048	.0	.00075	1820
Wedge	1	"	M86-8	-	4060	.36	1800	--	.0131	.0	.000938	1710
Stag	1	"	M85-7	128	6140	.4	300	3560	.0118	.0011		2950
↓	2	"	M85B-3	132	6140	.4	300	3560	.011	.0005	.001272	2850
↓	2	"	M85B-9	130	6140	.4	300	3560	.0045	.0008	.000521	2880
↓	2	"	M85B-6	130	6140	.4	300	3560	.0084	.0	.000972	2860
↓	3	"	M85B-3	132	6140	.4	300	3560	.0118	.003	.001362	2865
↓	3	"	M85B-9	130	6140	.4	300	3560	.0055	.0007	.000636	2900
↓	3	"	M85B-6	130	6140	.4	300	3560	.0108	.001	.001250	2850
↓	1	"	M82-13	132	6140	.4	300	3560	.0285	.002		2930
↓	1	"	M82-19	130	6140	.4	300	3560	.0086	.0013		2930
↓	1	"	M82-25	130	6140	.4	300	3560	.0129	.001		2960
↓	1	"	M82-29	130	6140	.4	300	3560	.0091	.0012		2930
↓	1	"	M82-33	130	6140	.4	300	3560	.0021	.0001		2955
↓	1	"	M81-19	132	6140	.4	300	3430	.0154	.0015	.00178	2830
↓	1	"	M81-25	130	6140	.4	300	3430	.0166	.001	.00192	2890
↓	1	"	M81-30	130.5	6140	.4	300	3430	.0128	.0018	.00148	2850
↓	1	"	M88-15	130.5	6140	.4	300	3430	.0092	.0012		2890
↓	1	"	M88-18	130	6140	.4	300	3430	.0097	.001		2910
↓	1	"	M88-20	130	6140	.4	300	3430	.0147	.0012		2890
↓	1	"	M88-21	130	6140	.4	300	3430	.0095	.0011		2890
↓	1	"	M88-2	130	6140	.4	300	3440	.0095	.0013	.001096	2885
↓	1	"	M88-4	130	6140	.4	300	3440	.0077	.0012	.000890	2890
↓	1	"	M88-6	130	6140	.4	300	3440	.0057	.0018	.000658	2810
↓	1	"	M88-8	130	6140	.4	300	3440	.0083	.0012	.000959	2820
↓	1	"	M88-10	130	6140	.4	300	3440	.0104	.0012	.00120	2820
↓	1	"	M88-12	130	6140	.4	300	3440	.0082	.0008	.000948	2765
↓	1	"	M85B-8	132	5000	.4	300	3540	.0062	.0012	.000585	2830
↓	1	"	M88B-5	130	5000	.4	300	3540	.0114	.0006	.001075	2850
↓	1	"	M85B-2	132	5000	.4	300	3540	.0156	.001	.00147	2875
↓	1	"	M85-11	120	6140	.4	300	3540	.0034	.0007	.000392	2850
↓	2	"	M88-4	130	7900	.4	300	3570	.0174	.0008	.00257	2950
Stag	2	"	M88-6	130	7900	.4	300	3570	.0126	.0008	.00187	2890
Wedge	4	"	M85B-9	23	4250	.36	900	2170	.0003	.0005	.000045	1840
Stag	3	"	M88-4	130	7900	.4	300	3570	.0204	.0017	.00302	2970
Stag	3	"	M88-6	130	7900	.4	300	3570	.0269	.0015	.00398	2950
Stag	1	"	M85-10	130	7900	.4	300	3570	.0153	.0012	.00227	2960
Wedge	4	"	M88-6	23	4250	.36	900	2170	.0016	.0002		1810
Wedge	2	"	M85-10	23	4250	.36	900	2170	.0015	.0003	.000225	1770
Stag	2	"	M88-2	130	7900	.4	300	3570	.0212	.001	.00314	2930
↓	2	"	M88-8	130	7900	.4	300	3570	.0104	.0012	.00154	2880
↓	2	"	M81-19	130	7900	.4	300	3570	.032	.0025		2950
↓	3	"	M88-2	130	7900	.4	300	3570	.0163	.001	.00242	2930
↓	3	"	M88-8	130	7900	.4	300	3570	.0225	.0016	.00333	3000
Stag	3	"	M81-19	130	7900	.4	300	3570	.0314	.0013		2910
Wedge	4	"	M88-2	23	4250	.36	900	2170	.0012	.0001	.000181	1720
Wedge	4	"	M81-19	23	4250	.36	900	2170	.0017	.0	.000256	1800
Stag	2	"	M85B-8	140	7250	.4	300	3650	.0194	.0012	.00245	2970

HOLDER TYPE	TEST EXPD. NO.	SPECIMEN PROCESS	SPECIMEN NO.	COLD WALL HEAT FLUX BTU/FT ² SEC	STAG. ENTHAL. BTU/LB	STAG. PRESS. PSIA	TIME DURATION SECONDS	CONTROL SPECIMEN TEMP °F	MASS LOSS GRAMS	THICK LOSS IN.	$\frac{H}{T}$	TRUE SURF TEMP °F
Stag	3	Silicon-ized	M85B-8	150	7400	.4	300	3830	.0244	.0021	.00293	3050
	2	"	M85B-2	150	7400	.4	300	3830	Coating burn thru			3820
	2	"	M85B-5	150	7400	.4	300	3830	.0315	.0024	.00378	3110
	1	"	M90-6	130	7900	.4	300	3570	.0142	.0009	.0021	2875
	1	"	M91A-10	130	7900	.4	300	3570	.0101	.0011	.0015	2860
	1	"	M91C-10	130	7900	.4	300	3570	.0230	.0015	.00341	2910
	1	"	M92-10	130	7900	.4	300	3570	.0062	.0004	.00092	2860
	1	"	M92-13	130	7900	.4	300	3570	.0114	.0011	.00169	2910
	1	"	M93	130	7900	.4	300	3570	-.0564	.0015		2875
			M91B-10									
	1	"	M93B-10	130	7900	.4	300	3570	.0206	.0015	.00306	2900
	1	"	M93A-10	130	7900	.4	300	3570	-.034	.001		2880
Stag Wedge	1	"	M85-8	22	4440	.36	900	2130	-.0021	.0001	.00035	1870
Wedge	4	"	M88-4	22	4440	.36	900	2130	.0005	.0001		1810
Stag	2	"	M91A-10	130	7000	.4	300	3510	.0107	.0004	.00141	2880
	2	"	M91C-10	130	7000	.4	300	3510	.0101		.00133	2930
	2	"	M92-10	130	7000	.4	300	3510	.0116	.0004	.00153	2970
	2	"	M92-13	130	7000	.4	300	3510	.0071	-.0008	.000934	2830
	2	"	M93-	130	7000	.4	300	3510	.0903	.0001		2955
			M91B-10									
	2	"	M93B-10	130	7000	.4	300	3510	.0184	.001	.00242	2920
	2	"	M93A-10	130	7000	.4	300	3510	.1075	.0019		2950
	2	"	M90-6	130	7000	.4	300	3510	.0124	.0002	.00164	2865
	3	"	M91A-10	130	7000	.4	300	3510	.0112	.001	.001472	2945
	3	"	M91C-10	130	7000	.4	300	3510	.0174	.0013	.00228	2915
	3	"	M92-10	130	7000	.4	300	3510	.0101	.0013	.00133	2970
	3	"	M92-13	130	7000	.4	300	3510	.0058	.0017	.000762	2875
	3	"	M93	130	7000	.4	300	3510	.0168	.0017	.00220	2990
			M91B-10									
	3	"	M93B-10	130	7000	.4	300	3510	.0211	.0016	.00278	2900
	3	"	M93A-10	130	7000	.4	300	3510	.0407	.0026	.00535	2975
	3	"	M90-6	130	7000	.4	300	3510	.0096	.0008	.00126	2905
	2	"	M85-7	60	4620	.36	300	--	-.0010	.0		2500
Stag	3	"	M85-7	60	4620	.36	300	--	-.0007	.0		2450
Wedge	5	"	M88-4	22	4620	.36	900	2130	.0004	.0008	.0000697	1835
Wedge	3	"	M85-10	22	4620	.36	900	2130	.0015	.0004	.000264	1945
Wedge	5	"	M88-6	22	4670	.36	900	2130	.0002	.0003	.0000351	1945
Wedge	5	"	M853-9	22	4675	.36	900	2130	.0006	.0	.000105	1925
Stag	4	"	M85-7	72	4675	.36	900	--	-.0029	.0002		2440
Wedge	5	"	M85-7	40	7000	.40	300	2590	.0009	.0004	.000384	2250
Stag	6	"	M85B-9	90	5050	.39	300	3240	.0041	.0006	.000561	2730
	6	"	M88-4	90	5050	.39	300	3240	.0058	.0	.000795	2500
	4	"	M85-10	90	5050	.39	300	3240	.0007	.00001	.0000958	2650
Stag	6	"	M88-6	90	5050	.39	300	3240	.0018	.0005	.000246	2645
Wedge	2	"	M85-8	48	10000	.44	300	2760	-.002	.0		2510
Stag	1	"	M95A-18	130	6000	.4	900	3520	.0205	.0014	.00077	2800
	6	"	M85-7	90	6000	.39	300	3220	.0008	.0	.00013	2670
	1	"	M95B-24	90	6000	.39	900	3220	.0057	.0007	.000309	2690
	1	"	M95A-16	90	6000	.39	900	3220	.0024	.0013	.00013	2575
	1	"	M95C-30	90	6000	.39	900	3220	.0246		.001335	2540
	1	"	M96B-24	90	6000	.39	900	3220	.0005	.0051	.0000271	2540
	1	"	M97-4	130	6400	.4	300	3480	Specimen burned up			3420
	1	"	M97-22	130	6400	.4	600	3480	Specimen melted			2980
Stag	1	"	M97-28	130	6400	.4	600	3480				2890

HOLDER TYPE	TEST EXPO. NO.	SPECIMEN PROCESS	NO.	COLD WALL HEAT FLUX BTU/FT ² SEC	STAG. ENTHAL. BTU/LB	STAG. PRESS. PSIA	TIME DURATION SECONDS	CONTROL SPECIMEN TEMP °F	MASS LOSS GRAMS	THICK LOSS IN.	$\frac{M}{T}$	TRUE SURF. TEMP °F
Stag	1	Silicon-ized	M100-12	130	6400	.4	900	3460	.0188	.0022	.000753	2850
↓	1	"	M100-13	130	6400	.4	900	3460	.0210	.002	.00084	2795
↓	1	"	M100-24	130	6400	.4	900	3460	.0072	.0018	.000288	2790
↓	1	"	M100-24	130	6400	.4	600	3460	.0139	.0026	.000556	2805
Stag	1	"	M100-31	130	6400	.4	900	3460	.0159	.0023	.000637	2850
Wedge	3	"	M85-8	86.9	13750	.46	600	3280	.0594	.003	.0115	2860
Stag	1	"	M101-5	130	6500	.4	900	3540	.056		.00228	2940
↓	1	"	M101-10	130	6500	.4	600	3540	.0604	.0065	.00245	2955
↓	2	"	M100-12	130	6500	.4	300	3540	.0279	.0026	.0034	2970
↓	2	"	M100-13	130	6500	.4	300	3540	.0538	.0054	.00777	3050
↓	2	"	M100-24	130	6500	.4	300	3540	.0243	.0028	.00296	2955
↓	2	"	M100-25	130	6500	.4	300	3540	.0289	.002	.00417	2965
↓	2	"	M100-31	130	6500	.4	300	3540	.0232	.0038	.00335	2960
↓	2	"	M101-5	130	6500	.4	300	3540	.0254	.003	.0031	2960
↓	2	"	M101-10	130	6500	.4	300	3540	.0194	.0093	.00236	2975
Stag	1	"	M100-8	28	4770	.36	900	2310	.0004	.0001	.0000555	1820
Wedge	1	"	M100-15	28	4770	.36	900	2310	-.0005	.0001		1810
Wedge	1	"	M100-20	28	4770	.36	900	2310	-.0018	.0001		1885
Wedge	1	"	M100-27	28	4770	.36	900	2310	.0004	.0		1795
Wedge	1	"	M100-33	28	4770	.36	900	2310	.0012	.0		1870
Stag	1	"	M103-12	130	7700	.4	900	3535	.0622	.0062	.0030	2860
↓	1	"	M103-20	130	7700	.4	900	3535	.0433	.0056	.00209	2855
↓	1	"	M103-16	130	7700	.4	900	3535	.0757	.0075	.00366	2965
↓	2	"	M103-12	130	7700	.4	300	3535	.0299	.0058	.00432	2860
↓	2	"	M103-20	130	7700	.4	300	3535	.0339	.0032	.0049	2930
Stag	2	"	M103-16	130	7700	.4	300	3535	.0302	.0025	.00436	2955
Wedge	1	"	M103-9	28	4770	.36	900	2315	-.0022	-.0001		1800
↓	1	"	M103-13	28	4770	.36	900	2315	-.0016	.0012		1800
↓	1	"	M103-17	28	4770	.36	900	2315	-.0021	.0001		1850
↓	1	"	M101-7	28	4770	.36	900	2315	-.0007	.0003		1845
↓	1	"	M101-12	28	4770	.36	900	2315	-.0021	-.0011		1850
↓	1	"	M101-12	28	4770	.36	900	2315	-.0021	-.0011		1850
↓	2	"	M103-9	28	4770	.36	900	2315	.0005	.0001	.0000693	1840
↓	2	"	M103-13	28	4770	.36	900	2315	.0001	-.0008	.00001385	1835
↓	2	"	M103-17	28	4770	.36	900	2315	.0	.0002	.0	1830
↓	2	"	M100-8	28	4770	.36	900	2315	.0007	.0001	.000097	1795
↓	2	"	M100-15	28	4770	.36	900	2315	.0011	.0	.000152	1840
↓	2	"	M100-20	28	4770	.36	900	2315	.0001	.0001	.00001385	1825
↓	2	"	M100-27	28	4770	.36	900	2315	.0006	.0003	.0000831	1815
↓	2	"	M100-33	28	4770	.36	900	2315	-.0005	.0		1805
↓	2	"	M101-7	28	4770	.36	900	2315	-.0001	.0001		1850
↓	2	"	M101-12	28	4770	.36	900	2315	.0001	.0		1815
↓	4	"	M85-8	83.7	13750	.46	300	3250	.0094	.0005	.00377	2770
↓	3	"	M103-1383.7	13750		.46	300	3250	.0159	.0	.00636	2680
↓	3	"	M103-1783.7	13750		.46	300	3250	.0169	.0008	.00676	2730
↓	3	"	M100-2083.7	13750		.46	300	3250	.0189	.0026	.00746	2730
↓	3	"	M100-3383.7	13750		.46	300	3250	.0192	.002	.00768	2730
↓	4	"	M103-1383.7	13750		.46	300	3250	.0181	.0025	.00724	2710
↓	4	"	M103-1783.7	13750		.46	300	3250	.0306	.0001	.01225	2790
↓	4	"	M100-2083.7	13750		.46	300	3250	.0568	.0052	.0227	2925
Wedge	4	"	M100-3383.7	13750		.46	300	3250	.0373	.0028	.01492	2850

HOLDER TYPE	TEST EXPO. NO.	SPECIMEN PROCESS	NO	COLD WALL HEAT FLUX BTU/FT ² SEC	STAG. ENTHAL. BTU/LB	STAG. PRESS. PSIA	TIME DURATION SECONDS	CONTROL SPECIMEN TEMP °F	MASS LOSS GRAMS	THICK LOSS IN.	$\frac{\Delta T}{h}$	TRUE SURF. TEMP °F
Stag	1	Silicon- ized	M106 20E LE 20-24	130	7500	.4	300	3480	Coating burned up within 1 min			3480
	1	"	M105 20B LE 26-7	130	7500	.4	240	3480	"			3420
	1	"	M107-8	130	7500	.4	900	3620	.0765	.006	.00358	2965
	1	"	M107-10	130	7500	.4	900	3620	.0528	.0063	.00248	2945
	1	"	M109-9	130	7500	.4	900	3620	.0560	.0049	.00263	2975
	1	"	M109-8	130	7500	.4	900	3620	.0347	.0023	.00163	2955
	1	"	M105 20B	130	7500	.4	900	3620	.0989	.0077	.00464	3000
	1	"	M109-11	130	7500	.4	900	3620	.0578	.004	.00271	3010
	1	"	M107-12	130	7500	.4	900	3620	.288	.0117	.00604	3040
	1	"	M108-33	130	7500	.4	900	3620	.0058	.0027	.000272	2890
	1	"	M108-32	130	7500	.4	900	3620	.0314	.0029	.00147	2975
	1	"	M108-31	130	7500	.4	300	3620	Burned thru			2995
	1	"	M105- 20C-14	130	7500	.4	900	3700	Burned thru			3040
	1	"	M106 20E	130	7500	.4	900	3700	.0674	.004	.00316	2955
	1	"	M106- 20D	130	7500	.4	900	3700	.0641	.009	.0030	2880
	1	"	M106- 20E	130	7500	.4	900	3700	.0455	.0038	.00214	2955
	1	"	M105- 20A	130	7500	.4	900	3700	.0421	.0	.00197	2890
	2	"	M108- 33	130	6750	.4	300	3550	.0096	.0001	.00135	2870
	3	"	M108- 33	130	6750	.4	300	3540	.0027	.0019	.000342	2880
	1	"	M105 -20C-15	130	6750	.4	900	3540	.0702	.0065	.00296	2910
	1	"	M112-1	130	6740	.4	300	3540	.0242	.0016	.00306	3020
	1	"	M112-2	130	6750	.4	300	3540	.0039	.0007	.000494	2850
	1	"	M112-4	130	6750	.4	300	3540	.0080	.0009	.001012	2945
	1	"	M112-12	130	6750	.4	300	3540	.0043	.0	.000545	2890
	1	"	M112-15	130	6750	.4	300	3540	.0075	.0009	.00095	2925
	1	"	M112-18	130	6750	.4	300	3540	.0020	.001	.000253	2870
	4	"	M108-33	130	6750	.4	300	3540	.0146	.0009	.00185	2965
	2	"	M112-2	130	6750	.4	300	3540	.0102	.0009	.00129	2955
	2	"	M112-12	130	6750	.4	300	3540	.0020	.0007	.000253	2850
	2	"	M112-18	130	6750	.4	300	3540	.0142	.0007	.00180	3020
	1	HfTan	HT-84	130	7300	.4	600	3620				3920
	1	"	HT-81	130	7300	.4	600	3620				3410
	1	"	HT-82	130	7300	.4	600	3620				3940
	2	"	HT-84	130	7300	.4	600	3620	Coating flaked off			3980
	2	"	HT-81	130	7300	.4	600	3620				3960
	2	"	HT-82	130	7300	.4	600	3620				4100
	3	"	HT-81	130	7300	.4	600	3620				3810
Stag	3	"	HT-82	130	7300	.4	600	3620				4190

HOLDER TYPE	TEST EXPO. NO.	SPECIMEN PROCESS	SPECIMEN NO.	COLD WALL HEAT FLUX BTU/FT ² SEC	STAG. ENTHAL. BTU/LB	STAG. PRESS. PSIA	TIME DURATION SECONDS	CONTROL SPECIMEN TEMP °F	MASS LOSS GRAMS	THICK LOSS IN.	$\frac{\delta}{R}$	TRUE SURF. TEMP °F
Stag	2	Silicon-ized	M112-1	130	7300	.4	300	3620	.0428	.0038	.00588	3110
	2	"	M112-2	130	7300	.4	300	3620	.0068	.0012	.000934	2980
	2	"	M112-4	130	7300	.4	300	3620	.0244	.0034	.00335	3060
	3	"	M112-12	130	7300	.4	300	3620	.0070	.0003	.000962	2970
	2	"	M112-15	130	7300	.4	300	3620	.0263	.002	.00361	3100
Stag	3	"	M112-18	130	7300	.4	300	3620	.0096		.00132	3030
Wedge	3	"	M112-2	28	5250	.36	900	2310	.0005	.0001	.0000693	1790
Wedge	4	"	M112-12	28	5250	.36	900	2310	.0008	.0002	.000111	1830
Wedge	4	"	M112-2	28	5250	.36	900	2310	.0	.0002		1890
Wedge	5	"	M112-12	28	5250	.36	900	2310	.0007	.0002	.000097	1910
Stag	1	"	M113-2	130	7300	.4	300	3590	.0219	.0031	.00301	2990
	1	"	M113-4	130	7300	.4	300	3590	.0220	.0023	.00302	2980
	1	"	M113-5	130	7300	.4	300	3590	.0130	.0022	.001786	2940
	1	"	M113-10	130	7300	.4	300	3590	.0221	.0015	.00304	3110
	1	"	M113-11	130	7300	.4	300	3590	.0287	.0016	.00394	3110
	1	"	M115-3B	130	7300	.4	300	3590	.0223	.0018	.00307	3120
	1	"	M115-7B	130	7300	.4	300	3590	.0208	.0024	.00286	3110
	1	"	M115-11B	130	7300	.4	600	3590	.0140	.0012	.000961	2870
	1	"	M115-15B	130	7300	.4	600	3590	.0137	.0015	.000941	2960
	1	"	M115-19B	130	7300	.4	600	3590	.0120	.0018	.000825	2910
	1	"	M115-23B	130	7300	.4	600	3590	.0254	.0024	.00176	2980
	2	"	M113-2	130	7300	.4	300	3590	.0135	.0023	.001854	2920
	2	"	M113-4	130	7300	.4	600	3590	.0244	.0030	.00168	2930
	2	"	M113-5	130	7300	.4	600	3590	.0142	.0010	.000975	2840
	2	"	M113-10	130	7300	.4	600	3590	.0279	.0045	.00192	2890
	2	"	M113-11	130	7300	.4	600	3590	.0200	.0009	.00137	2880
	1	"	M116-1	130	6850	.4	600	3510	.0238	.0032	.00153	2940
	1	"	M116-6	130	6850	.4	600	3510	.0347	.0031	.00224	2960
	1	"	M116-26	130	6850	.4	600	3510	.0424	.0039	.00273	2980
	1	"	M116-9	130	6850	.4	600	3510	.0196	.0038	.00126	2910
	1	"	M117-7	130	6850	.4	600	3510	.0506	.0022	.00326	2910
	1	"	M117-11	130	6850	.4	600	3510	.0296	.0043	.00190	2940
	1	"	M118-9	130	6850	.4	600	3510	.0454	.0055	.00292	2960
	1	"	M118-12	130	6850	.4	600	3510	.0371	.0043	.00239	2910
	1	"	M119-3	130	7400	.4	600	3570	.0122	.0008	.000795	2870
	1	"	M120B-2	130	7400	.4	600	3520	.0012	.0003	.0000773	2680
	1	"	M121-1	130	7400	.4	600	3520	.0133	.0033	.000857	2830
	1	"	M122-1	130	7400	.4	600	3520	.0206	.0027	.00134	2840
	1	"	M123-2	130	7400	.4	600	3670	.0212	.0020	.00147	2840
	1	"	M123-5	130	7400	.4	600	3670	.0228	.0029	.001585	2850
	1	"	M123-3	130	7400	.4	300	3670	.0154	.0010	.00214	2850
	2	"	M123-3	130	7400	.4	300	3670	.0418	.0085	.00590	2820
	2	"	M123-2	130	7400	.4	600	3670	.0129	.0011	.000896	2870
	2	"	M123-5	130	7400	.4	600	3670	.0138	.0015	.000959	2870
	1	"	M124-11	130	7400	.4	600	3670	.0049	.0013	-	2730
	2	"	M124-11	130	7400	.4	600	3670	.0137	.0021	.000952	2820
	1	"	M124-13	130	7400	.4	600	3670	.0263	.0027	.00183	2860
	2	"	M124-13	130	7400	.4	600	3670	.0240	.0016	.00167	2880
Stag	1	"	M125-6	130	7400	.4	600	3620	.0245	.0021	.00170	2840

Specime
had hol
drilled
through
coating

HOLDER TYPE	TEST EXPT. NO.	SPECIMEN PROCESS	NO.	COLD WALL HEAT FLUX BTU/FT ² SEC	STAG. ENTHAL. BTU/LB	STAG. PRESS. PSIA	TIME DURATION SECONDS	CONTROL SPECIMEN TEMP °F	MASS LOSS GRAMS	THICK LOSS IN.	$\frac{Q}{A}$	TRUE SURF. TEMP °F
Stag	2	Silicon- ized	M125-6	130	7400	.4	600	3620	.0124	.0006	.000862	2820
	1	"	M125-10	130	7400	.4	600	3620	.0168	.0026	.00117	2820
	2	"	M125-10	130	7400	.4	600	3620	.0322	.0026	.00224	2880
	1	"	M126-23	130	7400	.4	600	3620	.0252	.0021	.00175	2830
	2	"	M126-23	130	7450	.4	600	3580	.0375	.0046	.00263	2920
	3	"	M126-23	100	6360	.39	600	3390	.0025	.0009	.000194	2660
	1	"	M126-21	130	7400	.4	600	3620	.0212	.0017	.00147	2830
	3	"	M126-21	100	6360	.39	600	3390	.0031	.0010	.000241	2650
	1	"	M126-18	130	7400	.4	600	3620	.0285	.0031	.00198	2810
	2	"	M126-18	130	7450	.4	600	3580	.0584	.0057	.00408	2930
	3	"	M126-18	100	6360	.39	600	3390	.0056	.0019	.000435	2650
	1	"	M126-15	130	7400	.4	600	3620	.0143	.0035	.000994	2780
	2	"	M126-15	130	7450	.4	600	3580	.0451	.0046	.00316	2895
	3	"	M126-15	100	6360	.39	600	3390	.008	.0017	.000622	2700
	1	"	M126-14	130	7400	.4	600	3620	.0272	.0029	.00189	2830
	2	"	M126-14	130	7450	.4	600	3580	.0411	.0042	.00288	2910
	3	"	M126-14	100	6360	.39	600	3390	.0036	.0007	.000280	2620
	1	"	M126-11	130	7400	.4	600	3620	.0177	.0019	.00123	2790
	2	"	M126-11	130	7450	.4	600	3580	.0674	.0051	.00471	2950
	3	"	M126-11	100	6360	.39	600	3390	.0056	.0013	.000435	2610
	4	"	M126-11	100	6450	.39	600	3390	.0082	.0002	.000646	2600
	4	"	M126-23	100	6450	.39	600	3390	.0045	.0019	.000354	2640
	1	"	M127-17	130	6500	.4	600	3640	.0327	.0024	.0020	2930
	2	"	M127-17	100	6450	.39	600	3390	.0004	.0003	.0000315	2690
	3	"	M127-17	100	6450	.39	600	2290	.0049	.0003	.000385	2700
	1	"	M127-85	130	6500	.4	600	3640	.0119	.0040	.000726	2900
	2	"	M127-85	100	6450	.39	600	3390	.0000	.0002	0	2690
	3	"	M127-85	100	6450	.39	600	3390	.0011	.0002	.0000867	2660
	1	"	M127-7	130	6500	.4	600	3640	.0196	.0018	.00120	2900
	2	"	M127-7	100	6540	.39	600	3390	.0002	.0003	.0000158	2650
Stag	3	"	M127-7	100	6450	.39	600	3390	.0002	.0005	.0000158	2565
Wedge	4	"	M137-7	97	15100	.46	270	3390	.0202	.0004	.00855	2980
Wedge	4	"	M126-21	97	15100	.46	240	3390	.0508	.0027	.0242	2940
Stag	1	"	M127-12	130	6500	.4	600	3640	.0187	.0020	.00114	2890
	2	"	M127-12	100	6450	.39	600	3390	.0008	.0002	.0000630	2650
	3	"	M127-12	100	6450	.39	600	3390	.0040	.0000	.000315	2670
	1	"	M129-12	130	6500	.4	600	3640	.0404	.0039	.00247	2850
	1	"	M129-16	130	6500	.4	600	3640	.0219	.0020	.00134	2830
	1	"	M130-41	130	6400	.4	600	3640	.0128	.0020	.000782	2720
Stag	1	"	M130-42	130	6500	.4	600	3640	.0281	-	.00172	2870
Wedge	2	"	M130-42	62	9400	.44	300	2960	.0033	.0003	.001225	2525
Stag	1	"	M130-30	130	6500	.4	600	3640	.0603	.0042	.00368	2930
Wedge	2	"	M130-30	62	9400	.44	300	2960	.0008	.0000	.000296	2515
Wedge	5	"	M127-7	62	9400	.44	300	2960	.0002	.0002	.0000741	2620
Wedge	5	"	M126-11	62	9400	.44	240	2960	.0000	.0001	0	2380
Stag	1	"	M130-31	130	6500	.4	600	3640	.0230	.0016	.001405	2800
	1	"	M131-1	130	6360	.4	600	3610	.0132	.0013	.00079	2840
	1	"	M131-2	130	6360	.4	600	3610	.0151	.0011	.000904	2850
	1	"	M131-4	130	6360	.4	600	3610	.0134	.0016	.000802	2910
	1	"	M131-5	130	6950	.4	600	3610	.0188	.0024	.00123	2950
Stag	1	"	M131-3	130	6360	.4	600	3610	.0060	.0008	.000359	2860
Wedge	2	"	M131-3	71	10000	.44	300	3080	-.0004	.0005	-	2525

HOLDER TYPE	TEST EXPO. NO.	SPECIMEN PROCESS	SPECIMEN NO.	COLD WALL HEAT FLUX BTU/FT ² SEC	STAG. ENTHAL. BTU/LB	STAG. PRESS. PSIA	TIME DURATION SECONDS	CONTROL SPECIMEN TEMP °F	MASS LOSS GRAMS	THICK LOSS IN.	$\frac{\delta}{T}$	TRUE SURF. TEMP °F
Stag	1	Silicon-ized	M131-6	130	6950	.4	600	3610	.0193	.0032	.00126	2950
	1	"	M131-7	130	6950	.4	600	3610	.0204	.0013	.001335	2950
	1	"	M131-9	130	6950	.4	600	3610	.0243	.0028	.00159	3000
	1	"	M131-10	130	6900	.4	600	3740	.0193	.0023	.00125	2950
	1	"	M131-11	130	6900	.4	600	3740	.0259	.0037	.00168	2960
Stag	1	"	M131-8	130	6950	.4	600	3610	.0152	.0021	.000994	2950
Wedge	2	"	M131-8	71	10000	.44	300	3080	.0019	.0001	.000654	2700
Stag	1	"	M131-12	130	6900	.4	600	3740	.0121	.0015	.000785	2930
Wedge	2	"	M131-12	71	10000	.44	300	3080	-.0005	-.0003	-	2570
Stag	1	"	M89-3	130	6900	.4	600	3740	.0863	.0066	.0056	3020
	1	"	M89-5	130	6900	.4	600	3740	.1527	.0151	.0099	2910
	1	"	M89-7	130	6900	.4	300	3740	.0903	.0082	.01172	3050
	1	"	M89-10	130	6900	.4	600	3740	.1323	.0119	.00858	2900
	1	"	M132-B6	130	6130	.4	600	3590	.0507	.005	.00292	2970
	1	"	M132B15	130	6130	.4	600	3590	.0317	.0029	.00183	2910
	1	"	M132-23	130	6130	.4	600	3620	.0321	.0023	.00185	2910
	1	"	M133-B2	130	6130	.4	600	3620	.0572	.0053	.00330	2890
	1	"	M133B15	130	6130	.4	600	3620	.1010	.0025	.00581	2970
	1	"	M133B16	130	6130	.4	600	3620	.0290	.0054	.00167	2870
	1	"	M132-22	130	6130	.4	600	3620	.0213	.0020	.00123	2930
	1	"	M132B17	130	6130	.4	600	3620	.0186	.0008	.00107	2870
	1	"	M132-B5	130	6130	.4	600	3620	.0202	.0012	.00116	2950
	1	"	M133-14	130	6130	.4	600	3620	.0553	.0017	.00318	2930
	1	"	M132-87	130	6130	.4	600	3590	.0343	.0022	.00198	2890
	2	"	M132-B7	130	6130	.4	600	3620	.0538	.0045	.00310	2940
	3	"	M132-B7	130	6130	.4	600	3620	.0687	.0069	.00396	2950
	4	"	M132-B7	100	5000	.39	600	3390	.0129	.0018	.000786	2650
Stag	5	"	M132-B7	100	5000	.39	600	3390	.0101	-.0019	.000616	2690
Wedge	6	"	M132-B7	63	10000	.44	300	2980	.0037	.0025	.00143	2600
Wedge	7	"	M132-B7	63	10000	.44	300	2980	.0056	-.0056	.00216	2590
Stag	1	"	M133-B5	130	6130	.4	600	3620	.0610	.0067	.00351	2950
Stag	2	"	M133-B5	130	6130	.4	600	3620	.0441	.0046	.00254	2920
Stag	3	"	M133-B5	130	6130	.4	600	3620	.0499	.0069	.00288	2860
Stag	4	"	M133-B5	100	5000	.39	600	3390	.0523	.0019	.00319	2910
Stag	1	"	M132B12	130	6130	.4	600	3620	.0252	.0022	.00145	2970
Stag	2	"	M132B12	130	6130	.4	600	3620	.0184	.0017	.00106	2980
Stag	3	"	M132B12	130	6130	.4	600	3620	.0144	.0014	.00083	2950
Stag	4	"	M132B12	100	5000	.39	600	3390	-.0009	.0004	-	2690
Stag	5	"	M132B12	100	5000	.39	600	3390	.0011	.0002	.0000671	2770
Wedge	6	"	M132-B12	63	10000	.44	300	2980	.0020	.0005	.000774	2630
Wedge	7	"	M132-B12	63	10000	.44	300	2980	.0019	.0001	.000735	2590
Stag	1	"	M133-B4	100	5000	.39	600	3390	.0109	.0016	.000665	2690
Stag	2	"	M133-B4	100	5000	.39	600	3390	.0075	.0006	.000458	2670
Wedge	3	"	M133-B4	63	10000	.44	300	2980	.0026	.0000	.0010	2650
Wedge	4	"	M133-B4	63	10000	.44	300	2980	.0024	.0009	.00093	2670
Stag	1	"	M133-18	130	6130	.4	600	3620	.0207	.0008	.00119	2930
	2	"	M133-18	130	6130	.4	600	3620	.0210	.0026	.00121	2970
	3	"	M133-18	130	6130	.4	600	3620	.0179	.0010	.00103	2950
	4	"	M133-18	100	5000	.39	600	3390	.0046	.0000	.00028	2780
Stag	5	"	M133-18	100	5000	.39	600	3390	.0027	.0004	.000165	2710
Wedge	6	"	M133-18	63	10000	.44	300	2980	.0008	.0004	.00031	2620
Wedge	7	"	M133-18	63	10000	.44	300	2980	.0106	.0000	-	2640

(Coatin
borned
throug

{ Spec. chippe

HOLDER TYPE	TEST EXP. NO.	SPECIMEN PROCESS	NO.	COLD WALL HEAT FLUX BTU/FT ² SEC	STAB. ENTHAL. BTU/LB	STAB. PRESS. PSIA	TIME DURATION SECONDS	CORRECTED SPECIMEN TEMP °F	MASS LOSS GRAMS	THICK LOSS IN.	$\frac{L}{T}$	TRUE SURF. TEMP °F
Stag	1	Silicon-ized	M136-12	130	7250	.4	600	3570	.0220	.0034	.0015	2850
	2	"	M136-12	130	7250	.4	600	3570	.0243	.0025	.00166	2860
	1	"	M136-6	130	7250	.4	600	3570	.0409	.0030	.00280	2840
	1	"	M136-8	130	7250	.4	600	3570	.0226	.0015	.00154	2810
	1	"	M137-B6	130	7130	.4	600	3610	.0487	.0050	.00326	2880
	1	"	M135-M132-B19	130	7130	.4	600	3610	.0182	.0028	.00122	2850
	1	"	M135-M132-B19	130	7130	.4	600	3610	.0212	.0022	.00142	2870
	1	"	M135-M130-32	130	7130	.4	600	3610	.0469	-	.00314	2960
	1	"	M138-B13	130	7130	.4	600	3610	.0287	.0036	.00193	2900
	2	"	M138-B13	130	7130	.4	600	3610	.0289	.0035	.00194	2860
	3	"	M138-B13	130	7130	.4	600	3610	.0321	.0044	.00216	2890
	2	"	M137-B6	130	7130	.4	600	3610	.0614	.0050	.00411	2890
	1	"	M139-M137-3	130	7130	.4	600	3610	.0206	.0008	.00138	2850
	2	"	M139-M137-3	130	7130	.4	600	3610	.0170	.0011	.00114	2870
	1	"	M139-M137-11	130	7130	.4	600	36.0	.0267	.0008	.00179	2880
	2	"	M139-M137-11	130	7130	.4	600	3610	.0154	.0020	.00103	2890
	1	"	M139-M138-20	130	7130	.4	600	3610	.0216	.0042	.00145	2810
	2	"	M139-M138-20	130	7130	.4	600	3610	.0301	.0061	.00202	2840
	1	"	M139-M138-21	130	7130	.4	600	3610	.0502	.0026	.00336	2830
	2	"	M139-M138-21	130	7130	.4	600	3610	.0545	.0004	.00366	2850
	1	"	M141-M137-7	130	7130	.4	600	3610	.0267	.0031	.00179	2910
	2	"	M141-M137-7	130	7130	.4	600	3610	.0252	.0024	.00169	2950
	3	"	M141-M137-7	130	7130	.4	600	3610	.0224	.0026	.00150	2960
Stag	4	"	M141-M137-7	130	7130	.4	600	3610	.0227	.0014	.00152	2990
Stag	1	"	M141-M138-22	130	7130	.4	600	3610	.0252	.0018	.00168	2950
	2	"	M141-M138-22	130	7130	.4	600	3610	.0130	.0006	.000872	2970
	3	"	M141-M138-22	130	7130	.4	600	3610	.0232	.0031	.00156	2990
	4	"	M141-M138-22	130	7130	.4	600	3610	.0158	.0003	.00106	2940
	5	"	M30,H4	130	7130	.4	600	3610	.0232	.0035	.00156	2950
Stag	6	"	M30,1-18	130	7130	.4	600	3610	.0100	.0006	.00067	2920

HOLDER TYPE	TEST EXPO. NO.	SPECIMEN PROCESS	NO.	COLD WALL HEAT FLUX BTU/FT ² SEC	STAG. ENTRAL STU/LB	STAG. PRESS. PSIA	TIME DURATION SECONDS	CONTROL SPECIMEN TEMP °F	MASS LOSS GRAMS	THICK LOSS IN.	$\frac{Q}{T}$	TRUE SURF. TEMP °F
Stag	4	Silicon-ized	M30, I-16	130	7130	.4	600	3610	.0162	.0027	.00109	2970
	1	"	M151-21	130	7140	.4	600	3600	.0265	-	.00178	2940
	2	"	M151-21	130	7140	.4	600	3600	-	.0035	-	2960
	1	"	M149-B5	130	7140	.4	600	3640	.0337	.0044	.00226	3000
	1	"	M149B10	130	7140	.4	600	3640	.0282	.0039	.00189	2980
	1	"	M158-25	130	8390	.4	600	3640	.0415	.0038	.00328	2870
	1	"	M158-1									
	1	"	HT M159	130	8390	.4	600	3640	.0270	.0020	.00213	2910
	1	"	M158-31									
	1	"	HT M159	130	8390	.4	600	3640	.0289	.0030	.00228	2890
Stag	1	"	M158-33									
	1	"	HT M159	130	8390	.4	600	3640	.0472	.0035	.00372	2950
Stag	1	"	W9-6/									
	1	"	M160	130	8390	.4	600	3630	.0438	.0046	.00346	2950
	1	"	W9-1/									
	1	"	M160	130	8390	.4	600	3630	.0445	.0044	.00352	2950
Stag	1	"	W9-2/									
	1	"	M160	130	8390	.4	600	3630	.0353	.0035	.00279	2950
	1	"	M163-2									
	1	"	M164HT	130	8390	.4	600	3630	.0187	.0020	.00148	2940
	1	"	M136-17	130	8390	.4	600	3630	.0419	.0042	.00331	2950
	1	"	M163-14									
	1	"	M164HT	130	8390	.4	600	3630	.0271	.0031	.00214	2950
	1	"	M163-11									
	1	"	M164HT	130	8390	.4	600	3630	.0356	.0024	.00282	2950
	1	"	M163-8									
	1	"	M164HT	130	8390	.4	600	3630	.0313	.0028	.00247	2950
	1	"	S1-9									
	1	"	M164HT	130	8390	.4	600	3630	.0561	.0055	.00443	2950
	1	"	S1-9									
	1	"	M164-8	130	8390	.4	600	3630	.0358	.0053	.00283	2950
	1	"	M163-5									
	1	"	M164HT	130	8390	.4	600	3630	.0261	.0020	.00206	2950
Stag	1	Hf-Ta	HT-89	130	7400	.4	600	3600				3100
	2	Hf-Ta	HT-89	130	7400	.4	600	3600				3980
	3	Hf-Ta	HT-89	130	7400	.4	600	3600				3980
	4	Hf-Ta	HT-87	130	7400	.4	600	3600				4080
	1	Hf-Ta	HT-90	130	6500	.4	300	3380				3370
	2	Hf-Ta	HT-90	130	6500	.4	300	3380				3890
	3	Hf-Ta	HT-90	130	6500	.4	300	3380				4010
	4	Hf-Ta	HT-90	130	6500	.4	300	3380				4030
	5	Hf-Ta	HT-90	130	6500	.4	300	3380				4080
	1	Hf-Ta	HT-93	130	7130	.4	300	3610		-.0010		3195
	2	Hf-Ta	HT-93	130	7130	.4	300	3610		-.0055		3420
	3	Hf-Ta	HT-93	130	7130	.4	300	3610		-.0021		3400
	4	Hf-Ta	HT-93	130	7130	.4	300	3610		-.0006		3430
	5	Hf-Ta	HT-93	130	7130	.4	300	3610		-.0036		3450
Stag	6	Hf-Ta	HT-93	130	7130	.4	300	3610		-.0054		3710

TABLE A.3-2
SUMMARY, PLASMA ARC TEST FINAL EVALUATION DATA
HEAT TREATED 10/60/30 MATERIAL

HOLDER TYPE	TEST EXPO. NO.	SPECIMEN NO.	COLD WALL HEAT FLUX Btu/ft ² Sec	STAG. ENTHAL. Btu/lb	STAG. PRESS. PSIA	TIME DURATION SECONDS	MASS LOSS GRAMS	THICK. LOSS IN.	$\frac{\dot{M}}{h}$	TRUE SURF. TEMP. °F	COMMENTS
Stag	1	Control 1	136	8390	0.40	180	0.7794	0.0803	0.225	3650	
	1	M150/51-B1	136	8390	0.40	1800	0.0964	0.012	0.00241	2930	
	2	"	136	8390	0.40	1800	0.0846	0.0086	0.00212	2930	
	1	M137/M141									
		B-4									
	2	"	136	8390	0.40	1200	0.0432	0.009	0.00162	2930	
	3	"	136	8390	0.40	1200	0.0318	-0.0025	0.00119	2930	
	4	"	136	8390	0.40	1200	0.0415	0.0021	0.00156	2940	
	1	M137/M141/									
		B-2									
	2	"	136	8390	0.40	1200	0.0714	0.0074	0.00268	2970	
	3	"	136	8390	0.40	1200	0.0494	0.0029	0.00185	2950	
	1	M156-1, HT	136	8390	0.40	1200	0.0706	0.0053	0.00265	2950	
	2	M156-1, HT	136	8390	0.40	1200	0.1179	0.0098	0.00294	2960	
	1	Control 2	73	7450	0.38	240	0.0562	0.0014	0.00210	2910	
	1	M137/M141/B-5	73	7450	0.38	1800	0.8003	0.084	0.300	3070	
	2	"	73	7450	0.38	1800	-0.0063	0.0001	(-)	2460	
	3	"	73	7450	0.38	1800	-0.0016	0.0000	(-)	2460	
	4	"	73	7450	0.38	1800	-0.0002	0.0002	(-)	2480	
	5	"	73	7450	0.38	1800	0.0014	0.0002	5.81x10 ⁻⁵	2460	
Stag	1	M137/M141/B-8	73	7450	0.38	1800	0.0012	0.0003	4.98x10 ⁻⁵	2490	Specimen chipped
	2	"	73	7450	0.38	1800	-	-	-	2485	
	3	"	73	7450	0.38	1800	-0.0052	0.0009	(-)	2480	
	4	"	73	7450	0.38	1800	-	-	-	2495	
	5	"	73	7450	0.38	1800	0.0026	0.0009	5.40x10 ⁻⁵	2475	
	6	"	73	7450	0.38	1800	-	-	-	2480	
	7	"	73	7450	0.38	1800	0.0040	0.0011	8.3x10 ⁻⁵	2475	
	8	"	73	7450	0.38	1800	-	-	-	2465	
	9	"	73	7450	0.38	1800	0.0060	0.0005	12.45x10 ⁻⁵	2465	
	10	"	73	7450	0.38	1800	-	-	-	2495	
	1	M145/151-153	73	7450	0.38	1800	0.0051	0.0002	10.6x10 ⁻⁵	2500	
	2	"	73	7450	0.38	1800	-	-	-	2500	
	3	"	73	7450	0.38	1800	-0.0057	.0012	(-)	2470	
	4	"	73	7450	0.38	1800	.0022	.0003	9.14x10 ⁻⁵	2490	
	5	"	73	7450	0.38	1800	-	-	-	2520	
	6	"	73	7450	0.38	1800	.0009	.0003	1.87x10 ⁻⁵	2495	
	7	"	73	7450	0.38	1800	.006	.0007	12.45x10 ⁻⁵	2520	
	1	Control 3	102	6880	0.39	210	.9804	.0544	0.274	3350	
	1	M137/M141/B10	102	6880	0.39	1800	.0150	.0025	4.12x10 ⁻⁴	2730	
	2	"	102	6880	0.39	1800	.0145	.0018	3.99x10 ⁻⁴	2730	

TABLE A.3-2

SUMMARY, PLASMA ARC TEST DATA (Continued)

HOLDER TYPE	TEST EXPO. NO.	SPECIMEN NO.	COLD WALL HEAT FLUX Btu/ft ² Sec	STAG ENTHAL. Btu/lb	STAG PRESS. PSTA	TIME DURATION SECONDS	MASS LOSS GRAMS	THICK. LOSS IN.	$\frac{M}{h}$	TRUE SURF. TEMP. °F	COMMENTS
Stag	3	M137/M141/B-10	102	6880	0.39	1800	.0220	.0017	6.05x10 ⁻⁴	2760	
	4	"	102	6880	0.39	1800	.0241	.0010	6.64x10 ⁻⁴	2765	
	5	"	102	6880	0.39	1800	.0282	.0010	7.76x10 ⁻⁴	2745	
	6	"	102	6880	0.39	1800	.0329	.0013	9.05x10 ⁻⁴	2755	
Stag	1	M138/M141/B-23	102	6880	0.39	1800	.0327	.0029	9.00x10 ⁻⁴	2760	
	2	"	102	6880	0.39	1800	.0302	.0025	8.30x10 ⁻⁴	2760	
	3	"	102	6880	0.39	1800	.0350	.0028	9.63x10 ⁻⁴	2760	
	4	"	102	6880	0.39	1800	.0432	.0024	11.9x10 ⁻⁴	2745	Coating burned through
	5	"	102	6880	0.39	1800	.1465	.0009	-	2760	
	1	M145/151-20	102	6880	0.39	1800	.0269	.0034	7.4x10 ⁻⁴	2730	
	2	"	102	6880	0.39	1800	.0383	.0038	10.52x10 ⁻⁴	2770	
	3	"	102	6880	0.39	1800	.0399	.0037	11.0x10 ⁻⁴	2770	
	4	"	102	6880	0.39	1800	.0317	.0037	8.72x10 ⁻⁴	2760	
	5	"	102	6880	0.39	1800	.0419	.0036	11.5x10 ⁻⁴	2760	
Stag	1	M138/M141/B-24	102	6880	0.39	1800	-	-	-	2730	Mass and thickness loss
	2	"	102	6880	0.39	1800	.0375	.0061	5.16x10 ⁻⁴	2715	measurements
	3	"	102	6880	0.39	1800	-	-	-	2710	are for two
	4	"	102	6880	0.39	1800	.0442	.0047	6.08x10 ⁻⁴	2720	cycles. Coating
	5	"	102	6880	0.39	1800	-	-	-	2740	burned through
	6	"	102	6880	0.39	120	.0936	.0030	-	2750	in last cycle.
Stag	1	Control 4	174	9600	0.42	180	-	.1036	-	3910	Coating burned through
	1	M150/51-B2	174	9600	0.42	240	-	-	-	-	*
	1	M149/51,153-B9	174	9600	0.42	90	.0797	.0930	3.58x10 ⁻²	3810	
	1	Control 5	162	7870	0.41	180	.1155	.0097	6.85x10 ⁻³	3100	
	1	M145/151-23	162	7870	0.41	600	.0916	.0076	5.43x10 ⁻³	3105	
	2	M145/151-23	162	7870	0.41	600	.8390	.0906	0.202	3855	
	1	Control 6	168	8760	0.415	180	.850	.0064	5.42x10 ⁻³	3075	
	1	M145/151-22	168	8760	0.415	600	.0529	.0037	3.37x10 ⁻³	3045	
Stag	2	M145/151-22	168	8760	0.415	600	-	-	-	-	

* Some coating left at end of run, but temperature did not stabilize and run was terminated.

A. 4

PERENY FURNACE TEST DATA

The following table summarizes the test data obtained on diffusion coated systems in Phase II after exposure to "x" cycles in a Pereny furnace operating at one atmosphere conditions. The test is conducted by placing the specimens into the preheated furnace (nominally maintained at 2300°F unless otherwise noted) for 10 minutes, withdrawing and allowing 10 minutes to cool (to approximately 1000°F), then reinserting into the furnace. Heat and cool phases constitute one cycle. Normally, data is obtained after the 1st and 5th cycles. Some specimens were tested for 6 and 10 cycles as noted.

TABLE A. 4-1

WEIGHT CHANGE DURING THERMAL CYCLE AT 2300°F
(When 6th Cycles are listed it is at 2500°F or 2600°F)

Run No.	% Weight Change				Sample Size
	1st	5th	6th	10th	
M54-1	-2.2	-15%		-27.1	3/4" dia.
2	-2.1			-28.8	
5	-1.7	-7.5		-13.2	
6	-1.6			-14.2	
9	-2.4	-17.5		-30.3	
10	-1.8			-23	
13	-1.3			-17.5	1 x 5"
14	-1.1			-21	
15	-1.1			-16.3	
16	- .28			-14.6	
17	-			-19.9	
18	-5.5			-27.0	
M55-1	- .8				3/4" dia.
4	- .7	- 3.9			
8	-2.9	-21.8			
11	-2.0	-14.0			1 x 5"
M56-1	- .7	- 6.3			3/4" dia.
6	-6.3	- 7.4			
10	+5.1	+ .1			
15	- .8	- 7.6			3/4" x 5
17	+ .08	-28.0			3/4" dia.
20	+1.2	-18.8			
24	-5.5	-19.1			
28	-4.8	-26.6			
M57-17	-1.2	-16.0			3/4" dia.
21	-1.2	-17.0			
25	-1.4	-17.9			
M58-3		- 7.6	-9.2		3/4" dia.
7		- 1.7	-2.0		
11		- 6.7	-7.9		
15		- 2.2	-2.5		
19		- 8.0	-9.6		
22		-18.5	-22.0		

TABLE A.4-1 (Cont'd.)

Run No.	% Weight Change				Sample Size
	1st	5th	6th	10th	
M58-31		-19.2	-22.8		
M59-36		+ 5.3	+ 5.6		3/4" dia.
32		+ 6.1	+ 6.8		
27			+21.7		
M60- 3	- .4	- 2.0	- 2.2		3/4" dia.
9	- .8	- 4.3	- 4.8		
15	- 1.7	-12.9	-15.4		
M61- 1	+ 5.2	+ 7.6	+ 6.7		3/4" dia.
3	+ 3.3	+ 5.0	+ 4.5		
13	+ 5.6	+ 6.7	+ 5.3		
15	+ 9.5	+11.4	+10.1		
25	+ 2.0	+ 2.7	+ 2.2		
27	+ 4.3	+ 5.7	+ 5.1		
5	+10.1	+12.4	+10.6		
23	+ 8.9	+10.8	+ 9.7		
29	+ .2	+ 8.0	+ 7.3		
7	+ 4.4	+ 1.9	+ .6		
9	+14.3	+13.8	+10.5		
11	+ 4.0	+ 3.9	+ 4.4		
17	+ 5.4	+ 4.8	+ 2.7		
19	+ 9.9	+11.7	+ 9.5		
21	+ 6.8	+ 6.4	+ 4.7		
31	+ 3.1	+ 3.5	+ 3.0		
33	+ 2.2	+ 2.2	+ 1.4		
35	+ 4.2	+ 5.4	+ 4.4		
M62- 4	+ 6.9	+10.3	+10.5		3/4" dia.
9	+ 5.8	+ 8.0	+ 8.2		
13	+ 9.6	+15.0	+14.5		
19	+ 1.3	+ .2	+ .7		
23	+ 6.3	+ 9.9	+ 9.5		
24	+ .6	+ .6	+ .8		
29	+ 4.3	+ 5.8	+ 5.3		
32	+ 4.4	+ 5.4	+ 4.8		
35	+11.7	+17.5	+17.0		
37	+ 6.2	+ 8.8	+ 8.3		
39	+11.0	10.8	+15.6		

TABLE A.4-1 (Cont'd)

Run No.	% Weight Change				Sample Size
	1st	5th	6th	10th	
M62-41	+ 5.6	+ 7.3	+ 7.5		3/4" dia.
43	+ 8.5	+11.5	+11.6		
M60-6	+ .5	- .1	- .4		
12	- 8.6	-12.7	-12.2		
M63-10	+ 7.9	+ 4.5			1 x 5"
87	+ 3.0	+ 4.5			3/4" dia.
72	+ 2.6	+ 5.6			
63	+ 7.0	+11.6			
66	+ 1.7	+ 2.3			
17	+ .8	+ .4			
60	- .1	- 1.6			
21	+12.4	+18.5			
51	+ 0.5	- 1.3			
27	+ 2.4	+ 2.9			
31	- .2	- .9			
26	+ 1.3	+ .06			
M71- 4	- 6.0				3/4" dia.
5	- 5.8				
M72-HA 2-18	+ .9	+ .7			2" x 2"
M74- 1	+ .06	- 7.2			2" x 2"
3	+ .08	- 2.1			
4	+ .3	- 1.8			
7	+ .3	- 1.4			
8	+ .03	- 2.8			
9	+ .2	- 1.6			
M81-20	+ 1.3	+ .3			
23	+ .9	- 1.6			
27	+ .8	- 6.9			
M82- 8	+ .03	- 1.2			3/4" dia.
10	+ .02	- 1.5			
15	+ .01	- 2.4			
16	+ .02	- 1.7			

TABLE A.4-1 (Cont'd.)

Run No.	% Weight Change				Sample Size
	1st	5th	6th	10th	
M82-20	+ .004	- 2.8			3/4" dia.
22	- .01	- 3.5			
26	- 1.3	- 8.7			
27	- 1.0	- 7.8			
30	- 1.2	-11.5			
34	- 1.0	-16.9			
35	- .8	- 9.3			
M85-12	- .8	- 7.3			3/4" dia.
M85B-1	+ .1	+ .3			3/4" dia.
4	+ .08	- 1.4			
7	+ .5	- .8			
10	+ .4	+ 1.0			
13	+ .2	- .4			
16	- .6	- 3.0			
M86- 7	- 4.2	-23.7			3/4" dia.
20	- 5.6	-30.0			
M88- 1	+ .9	+ .5			
3	+ .8	+ 1.5			
5	+ 1.3	+ 1.4			
7	+ 1.3	+ .9			
9	+ .8	+ .6			
11	- .3	- .5			
13	- 1.5	- 9.4			
16	+ .9	+ .2			
17	- .01	- 2.7			
19	- .2	- 3.9			
M90- 5	- 1.3	-10.4			3/4" dia.
M91A-9	-10.3	-48.5			3/4" dia.
M91C-9	- 1.0	- 4.3			
M92- 9	- 1.0	- 9.2			
12	- 7.5	-13.5			

TABLE A.4-1 (Cont'd.)

Run No.	% Weight Change				Sample Size
	1st	5th	6th	10th	
M93-M91B-9	+ 2.7	+ 3.3			3/4" dia.
M95A-17	- 6.3	-26.2			3/4" dia.
B-23	- 5.9	-23.5			
C-29	- 7.0	-25.1			
M96B-23	- 7.7	-26.7			3/4" dia.
M97A- 6	-12.0	-41.1			3/4" dia.
B-24	- 9.5	-43.6			
C-30	- 6.3	-31.0			
M100- 7	- 3.0	-12.9			3/4" dia.
14	- 2.6	-10.5			
19	- 2.1	- 9.7			
26	- 3.1	-12.8			
32	- 2.6	-11.1			
M101- 6	+ 1.7	+ 2.0			3/4" dia.
11	+ 1.3	+ .7			
M103-11	+ 1.9	+ 4.8			3/4" dia.
15	+ 2.0	+ 1.0			
19	+ 1.8	+ 3.6			
M106-F06	- 1.2	- 8.9			.7 x 5"
23	+ .4	- 4.8			
M107-13	+ 1.4	+ .7			1 x 1"
15	+ 1.9	+ .7			
17	+ 1.3	- 1.6			
M108- 1	- .1	- 7.0			1 x 1"
2	- .4	- 7.5			
3	- .9	-11.5			
M105-F3	- .4	- 6.0			.7 x 5"
F6	- .7	- 6.9			
F17	- .3	- 3.1			

TABLE A.4-1 (Cont'd.)

Run No.	% Weight Change				Sample Size
	1st	5th	6th	10th	
M109- 7	- .7	- 8.5			3/4" dia.
10	+ .5	- 2.9			
12	+ .5	- 3.5			
M112- 3	- .4	- 2.9			3/4" dia.
11	- 1.1	- 7.2			
14	+ .3	- 1.2			
17	- 1.0	- 5.9			
M113- 1	+ .4	+ .1			3/4" dia.
3	+ 1.7	+ 1.7			
6	+ 1.1	- .9			
9	+ 2.2	+ 3.3			
M115-4B	+ 1.1	+ .8			3/4" dia.
8B	+ 1.2	+ 1.4			
12B	+ .4	- 1.7			
16B	+ .4	- 2.9			
20B	+ 1.2	+ .8			
24B	- .1	- 5.3			

TABLE A. 4-2

WEIGHT CHANGE DURING THERMAL CYCLE AT 2300°F

Run No.	<u>% Weight Change</u>		% Wt. Gain in Coating	Sample Size
	1st	5th		
M116-3	+1.0	+ .2	50.5	3/4" Dia.
7	+1.2	+1.4	52.7	
10	+1.3	+1.6	52.8	
M117-8	+1.8	+2.2	44.6	3/4" Dia.
12	+1.7	+1.7	41.6	
M118-5	+1.8	+1.9	42.8	3/4" x 1/2"
6	+1.6	+ .9	39.2	
M120-B1	+1.9	+1.8	36.3	3/4" Dia.
3	+3.0	+3.0	36	3/4" x 5"
M121-8	+1.7	+1.0	33.7	3/4" x 5"
12	+1.8	+2.3	39.5	3/4" x 1/2"
M122-2	+2.1	+3.9	50.7	3/4" Dia.
5	+1.9	+3.4	47.1	3/4" Dia.
7	+1.4	+2.1	45.5	3/4" x 5"
10	+1.4	+2.1	45.6	3/4" x 5"
M123-1	+ .4	-3.5	18.8	3/4" Dia.
8	+ .2	-4.1	16.4	3/4" x 5"
M124-1	+1.2	-1.0	19.4	3/4" x 5"
4	+1.4	-1.4	21.1	3/4" x 2
7	+1.2	- .4	15.0	3/4" x 1
9	+1.0	- .2	23.7	3/4" x 3
10	+ .1	- .8	13.0	3/4" x 2
M125-4	+1.3	+1.1	34.1	3/4" x 5
11	+2.9	+2.7	28.7	1" x 1 1/4"
12	+1.1	+ .9	30.2	1" x 1 1/4"

TABLE A.4-2

WEIGHT CHANGE DURING THERMAL CYCLE AT 2300°F

Run No.	<u>% Weight Change</u>		% Wt Gain in Coating	Sample Size
	1st	5th		
M126-5	+ .6	- .7	27.8	3/4" x 5"
6	+ .5	- .3	26.8	3/4" x 4-5 "
22	+1.0	+1.2	36.5	3/4" Dia.
24	+1.0	+ .8	35.5	3/4" Dia.
25	+ .7	+ .6	32.5	3/4" x 2 "
26	+ .8	+ .3	35.5	3/4" x 2 "
M128-5	- .4	-2.5	31.9	3/4" x 5 "
6	- .3	-1.9	34.8	3/4" x 5 "
17	-.01	-1.6	40.2	3/4" Dia.
22	-.02	-1.8	39.7	3/4" Dia.
25	-.04	- .3	36.7	3/4" x 5 "
27	-.03	-1.1	38.1	3/4" x 5 "
M129-5	+ .7	+ .6	38.8	3/4" x 5"
6	+ .6	+ .06	36.7	3/4" x 5"
17	+ .8	+ .8	37.8	3/4" x 1 1/2"
18	+ .7	+ .2	37.6	3/4" x 1 1/2"
M130-18	+ .8	+ .04	28.3	3/4" x 5"
19	+ .8	- .09	25.9	3/4" x 5"
40	+1.3	+1.3	35.9	3/4" Dia.
43	+1.3	+1.1	35.0	3/4" Dia.
M132-3	+ .3	- .4	25.7	3/4" x 5"
6	+ .5	- .3	25.2	3/4" x 5"
11	+ .5	- .08	29.9	3/4" x 5"
14	+ .6	- .03	30.7	3/4" x 5"
B3	+1.1	+ .2	37.2	3/4" Dia.
B8	+1.2	+ .4	35.9	3/4" Dia.
B18	+1.3	+1.0	38.9	3/4" Dia.
B20	+1.4	+ .8	38.5	3/4" Dia.
M133-1 (1/1/1)	+ .4	+ .8	23.2	3/4" x 5"
6	+1.1	+1.3	25.7	3/4" x 5"
B1 (1/1/1)	+1.4	+1.4	30.3	3/4" Dia.

TABLE A.4-2

WEIGHT CHANGE DURING THERMAL CYCLE AT 2300°F (Cont'd.)

Run No.	<u>% Weight Change</u>		% Wt. Gain in Coating	Sample Size
	1st	5th		
M133-B6	+1.4	+1.4	26.0	3/4" Dia.
M136-3 (1/1/1)	+ .8	- .3	19.9	3/4" x 5
7	+1.0	+ .6	25.6	3/4" x 5
B3 (1/1/1)	+1.2	+ .7	28.4	3/4" Dia.
B7	+1.2	+ .6	29.4	3/4" Dia.
W1-3	+ .6	- .9	23.2	3/4" x 5"
W2-9	+ .7	- .9	32.8	3/4" x 5"
X1	+ .5	-1.2	33.3	3/4" x 2 1/2"
X2	+ .5	-1.0	31.1	3/4" x 2 1/2"
X3	+ .1	-1.2	32.6	3/4" x 2 1/2"
W3-2	- .3	-3.8	30.9	3/4" x 5"
7	+ .5	- .3	37.1	3/4" x 5"
W4-2	- .5	-7.5	7.0	3/4" x 5"
W5-2	+ .04	-2.5	14.8	3/4" x 5"
M142-1	+ .5	- .3	23.7	3/4" x 5"
W7-1	+ .6	- .4	34.2	3/4" x 5"
3	+ .4	-1.9	23	3/4" x 5"
P1	+ .4	-1.7	33.8	3/4" x 2 1/2"
W8-1	+ .8	- .7	33.6	3/4" x 5"
2	+ .4	-1.8	21.3	3/4" x 5"
4	+ .2	-2.3	27.1	3/4" x 5"
M163-3	+ .4	- .3	24.6	3/4" x 5"
7	+ .4	- .4	25.6	3/4" x 5"
11	+ .7	- .2	26.1	3/4" x 5"
15	+ .4	- .4	28.1	3/4" x 5"
19	+ .5	- .3	26.5	3/4" x 5"
23	+1.3	- .3	26.6	3/4" x 5"

TABLE A.4-2

WEIGHT CHANGE DURING THERMAL CYCLE AT 2300°F (Cont'd.)

Run No.	<u>% Weight Change</u>		% Wt. Gain in Coating	Sample Size
	1st	5th		
T1-1	+ .2	-1.4	17.7	3/4" x 5"
M165-6	-1.1	-8.0	16.2	3/4" x 5"
M166-4	+ .3	- .5	22.6	3/4" x 5"
M168-10	+ .4	+1.1	51.1	3/4" x 5

TABLE A. 4-3

WEIGHT CHANGE OF HEAT TREATED SPECIMENS
DURING THERMAL CYCLE AT 2300°F

Run No.	HT Run No.	<u>% Weight Change</u>		% Wt. Gain in Coating	Sample Size
		1st	5th		
M125-9	M127	- .3	-3.6	37.9	3/4" Dia.
M126-9	M127	- .5	-4.7	33.7	3/4" Dia.
20	M127	- .6	-5.2	35.2	3/4" Dia.
M125-5	M131	+ .2	-1.7	30.9	3/4" x 5"
M129-9F		+ .4	+ .02	45.8	
M130-5		- .05	-2.5	25.4	
1		+ .06	-2.1	27.6	
M129-10F		+ .4	- .1	40.9	3/4" x 5"
19		+ .6	- .4	40.4	3/4" x 1 1/2"
20		+ .5	- .5	39.2	3/4" x 1 1/2"
M124-5		- .7	-7.2	21.2	3/4" x 1"
8		-1.4	-9.2	13.9	3/4" x 1"
6		- .8	-8.1	17.4	3/4" x 1"
M121-11		- .4	-2.5	41.0	3/4" x 1/2"
M120-B3		+1.1	+ .9	40.8	3/4" Dia.
M130-17		- .3	-3.3	26.8	3/4" x 5"
M132-1	M134	+ .02	-2.6	27.6	3/4" x 5"
8		+2.5	-2.1	27.7	3/4" x 5"
B4		+ .2	-2.7	38.1	3/4" Dia.
B11		+ .3	-3.1	35.9	
B16		+ .2	-4.3	33.3	
B24		+ .1	-4.3	33.6	3/4" Dia.
M133-7		+ .01	-3.3	20.1	3/4" x 5"
12		+ .06	-3.4	26.2	3/4" x 5"
13		+ .2	-5.4	27.1	3/4" Dia.
17		- .06	-4.8	30.1	3/4" Dia.
M130-20	M135 (3000°F)	+ .07	-1.6	32.1	3/4" x 5"
21		- .04	-2.5	27.3	3/4" x 5"
27		+ .5	-2.1	21.9	3/4" Dia.
33		+ .2	-3.3	38.6	3/4" Dia.
M132-10	M135 (3000°F)	- .06	-2.3	27.4	3/4" x 5"

TABLE A.4-3 (cont'd.)

Run No.	HT Run No.	<u>% Weight Change</u>		% Wt. Gain in Coating	Sample Size
		1st	5th		
M132-15	M135	- .01	-2.3	31.2	3/4" x 5"
B2	(3000°F)	+ .3	-3.3	33.8	3/4" Dia.
B10		+ .4	-2.5	35.9	3/4" Dia.
M138-F _o -4	M141	-1.4	-8.6	19.7	3/4" x 5"
5		-1.1	-6.6	22.2	
6		-1.2	-7.6	19.7	
7		-1.0	-6.3	21.9	
M138-4		-1.5	(-3.1)	17.4	
			2 cycles		
5		-1.3	(-4.2)	19.7	
			3 cycles		
7		-1.0	--	23.2	
11		-1.5	-9.3	17.5	
B12		-1.2	-9.2	30.1	3/4" Dia.
M137-2	M139	- .5	-5.2	20.8	3/4" x 5"
9		- .3	-4.0	22.2	3/4" x 5"
12		+ .3	-1.6	18.9	3/4" x 5"
B9		-1.0	-8.4	26.5	3/4" Dia.
M142-3	M144	- .1	-1.2	32.7	3/4" x 5"
5		- .1	-3.5	21.8	
M143-8		- .1	--	26.9	
9		+ .02	-2.4	27.9	
6		- .3	-3.2	24.2	3/4" x 5"
M149-2	M151/	- .5	-4.6	29.4	3/4" x 5"
9	M159	- .2	-3.1	29.5	3/4" x 4 1/2"
M150-7	M151/ M153	- .2	-3.7	23.7	3/4" x 2 1/2"
M136-10	M152	-2.6	-14.4	21.8	3/4" x 5"
M146-13	M151/153	+ .07	-1.5	27.9	3/4" x 5"
M156-2	M157	- .9	-5.8	31.4	3/4" x 5"
3		-1.1	-6.8	28.7	
5		- .7	-5.1	31.3	
7		- .6	-4.6	31.5	3/4" x 5"

TABLE A. 4-3 (Cont'd.)

Run No.	HT Run No.	<u>% Weight Change</u>		% Wt. Gain in Coating	Sample Size
		1st	5th		
M158-3	M159	-2.9	-12.2	23.2	3/4" x 5"
W9-3	M160	- .004	-3.4	42.3	3/4" x 5"
6	M160	+ .05	-3.4	43.4	3/4" x 5"
M161-8	M162	-2.1	-9.5	22.8	3/4" x 5"
9		-1.8	-12.8	24.7	
13		-1.7	-9.5	27.6	
14		-1.7	-9.8	29.5	3/4" x 5"
M163-1	M164	-1.6	-10.9	24.5	3/4" x 5"
5		-1.5	-9.7	23.4	
9		-1.2	-8.7	26.2	
13		-1.5	-8.1	31.1	
17		-1.4	-8.7	28.6	
21	M164	-1.3	-9.5	25.1	3/4" x 5"
W10-12	W13	-1.4	-9.7	34.5	3/4" x 5"
13	W13	-1.1	--	34.5	3/4" x 5"
M166-7	M167	- .5	-3.7	29.8	3/4" x 5"
M68-12	M170	- .2	-1.1	40.6	3/4" x 5"
M169-2	M170	-1.0	-6.3	28.3	3/4" x 5"

TABLE A. 4-4

WEIGHT CHANGE DURING THERMAL CYCLE AT 2300°F
FOR USED PACK MATERIALS

Run No.	% Weight Change		% Wt Gain in Coating	Sample Size
	1st	5th		
M119-A	- .7	-8.3	19.8	3/4" Dia.
B	- .8	-9.2	19.8	3/4" Dia.
X1-X	+ .6	-1.7	22.1	3/4" x 2.5"
M152-1	-2.4	-18	8.7	3/4" x 5"
M152(M136-9)	-1.8	9.8	24.6	3/4" x 5"
M158-4	-2.3	-11.8	14	3/4" x 5"
(M159HT)				
7	-2.2	-11.0	18.4	3/4" x 5"
(159HT)				
M161-16	-1.3	-8.2	29.9	3/4" x 5"
(M162 HT)				
S1-2	- .05	-2.8	23/4	3/4" x 5"
6	-1.1	-6.2	36.5	3/4" x 5"
(M164HT)				
8	-1.7	-9.4	26.7	3/4" x 5"
(M164HT)				
S2-10	+ .01	-2.1	27.1	3/4" x 5"
S3-1	- .01	-2.0	27.6	3/4" x 5"
S4-1	- .3	-3.5	24.4	3/4" x 5"

TABLE A.4-5

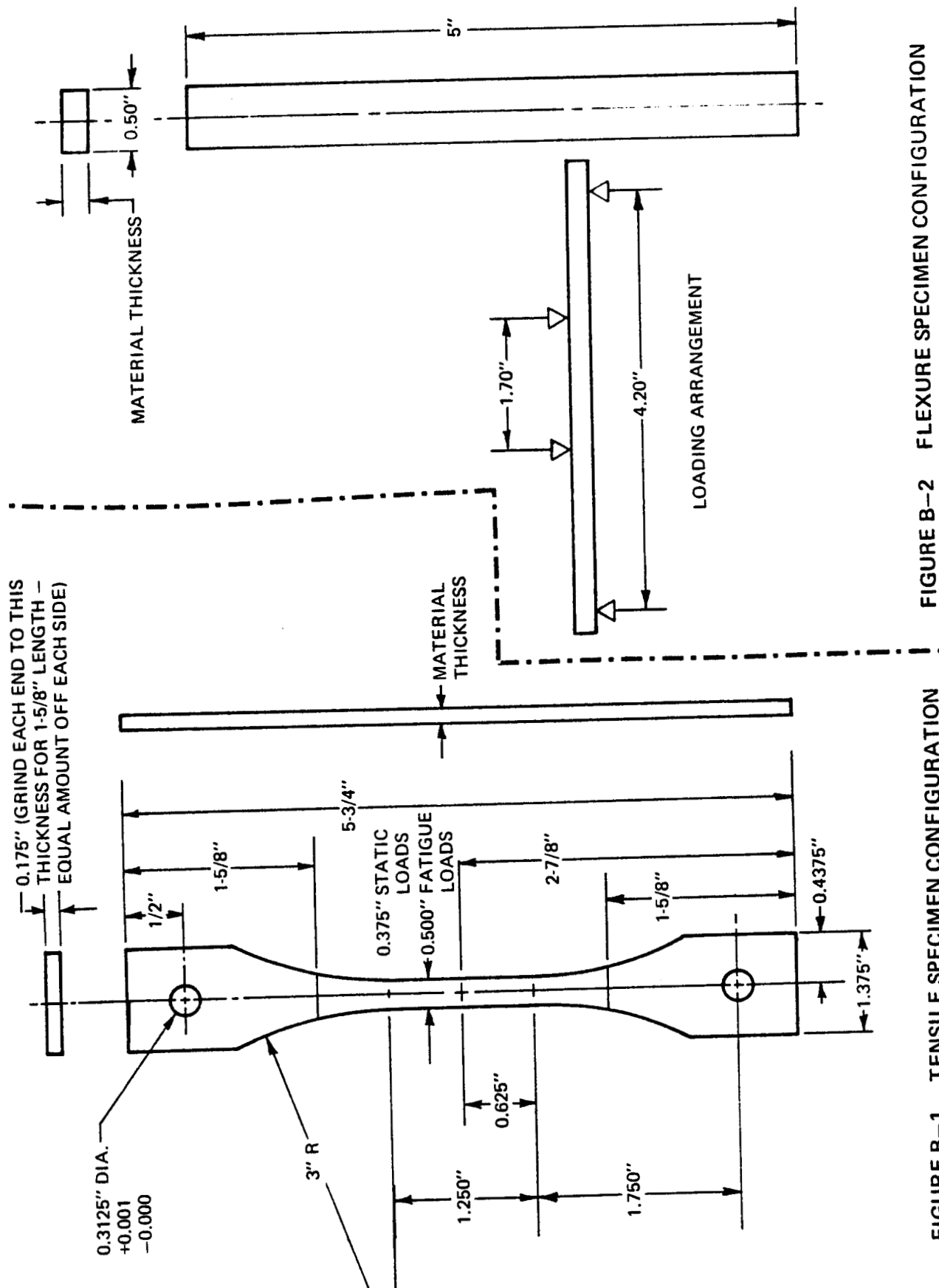
THERMAL TREATMENTS AFTER COATING APPLIED

Specimen	Thermal Treatment		% Weight Change		
	Atmosphere	Time/Temp	Thermal Treatment	1st	5th
M57-3	N ₂	1 hr/1600°F	- 1.4	-1.64	
7			- .15	- .89	
23			- .1	-1.5	
M59-31	N ₂	1 hr/1600°F	+ .8	+1.6	
M61-10	O ₂	1 hr/1600°F	+24.0	+ .3	0
12			+20.9	+ .04	- .3
20			+20.1	+ .3	+ .2
22			+23.9	- .2	- .02
6			+28.1	+ .4	+ .2
8			+22.3	+ .2	- .4
16			+15.9	- .2	- .01
18			+13.7	- .8	-1.3
4			+26.5	-1.0	+ .4
24			+17.0	- .4	- .6
M62- 5	O ₂	1 hr/1600°F	+ 7.6	- .8	-1.7
10			+7.0	- .7	-1.7
25			+10.9	- .6	-1.0
30			-28.3	-2.9	-7.4
33			+ 7.6	- .6	-1.6
36			+10.8	- .5	-1.0
38			+ 1.4	- .5	-1.1
40			+18.8	- .5	-1.1
14			+11.5	+ .06	-1.1
15			+ 9.3	+ .9	+ .5

APPENDIX B

TEST SPECIMEN CONFIGURATION

Test specimens used in the conduct of static and fatigue tests to establish design data are shown in Figures B-1 through B-9. Configurations B-1, B-2, B-3, B-5 and B-6 were used in the SRI tests from -250°F through 3000°F. Configurations B-1, B-2, B-4, B-7, B-8 and B-9 were used by VMSC in static and fatigue testing.



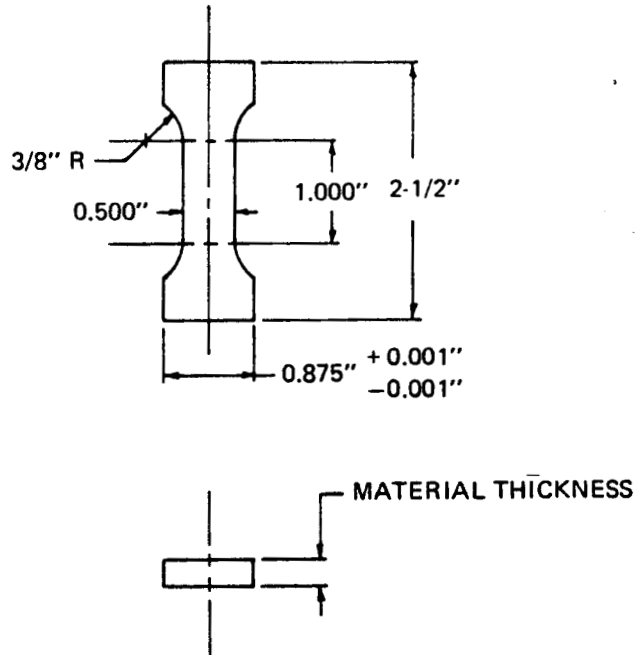


FIGURE B-3 AXIAL COMPRESSIVE SPECIMEN CONFIGURATION

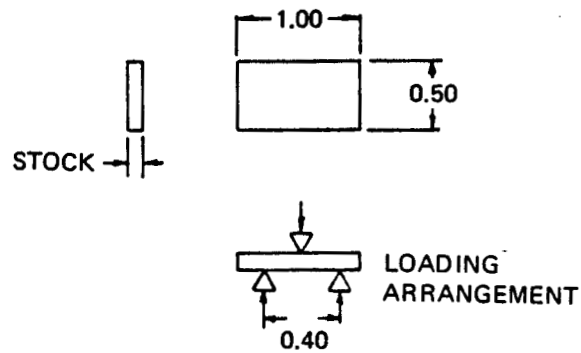


FIGURE B-4 INTERLAMINAR SHEAR SPECIMEN CONFIGURATION (SHORT BEAM SHEAR) VMSC TESTS

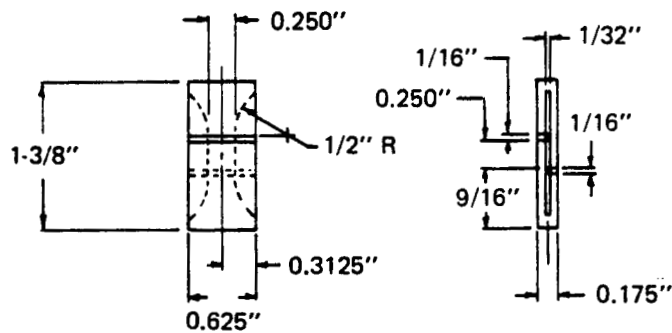


FIGURE B-5 INTERLAMINAR SHEAR SPECIMEN CONFIGURATION (COMPRESSION/SHEAR) SRI TESTS

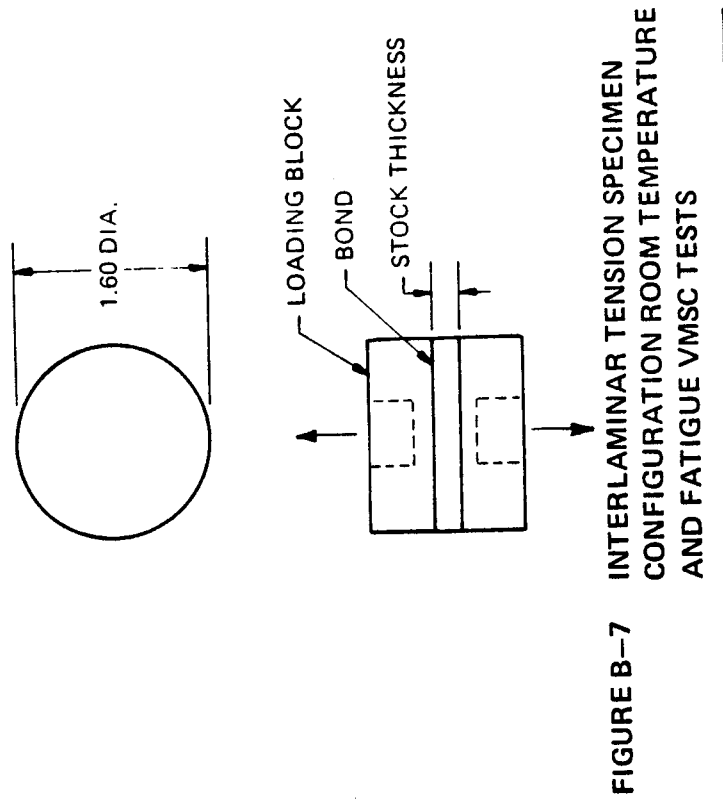


FIGURE B-7 INTERLAMINAR TENSION SPECIMEN CONFIGURATION ROOM TEMPERATURE AND FATIGUE VMSC TESTS

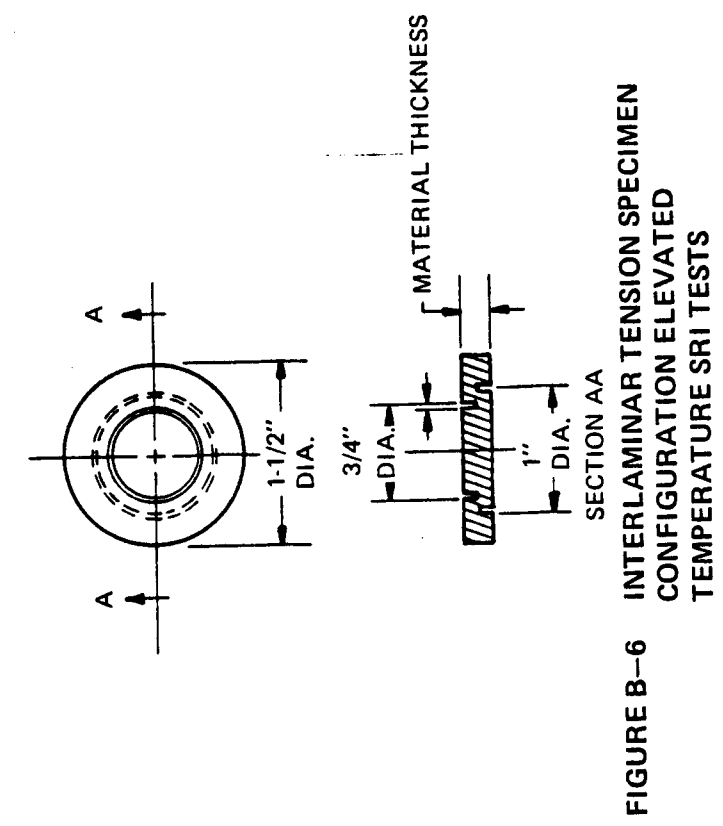


FIGURE B-6 INTERLAMINAR TENSION SPECIMEN CONFIGURATION ELEVATED TEMPERATURE SRI TESTS

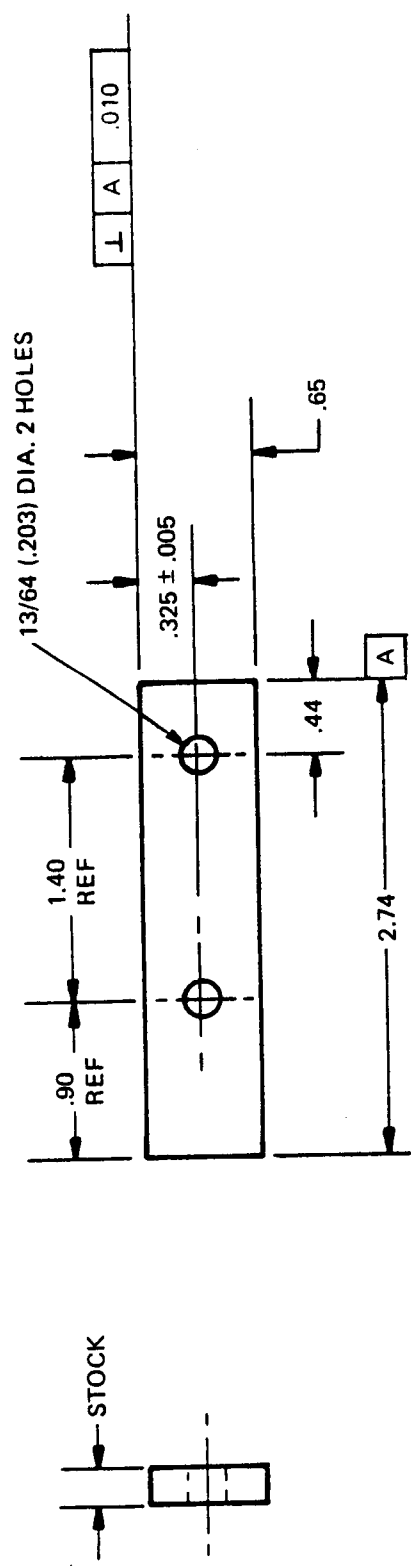


FIGURE B-8 BEARING SPECIMEN

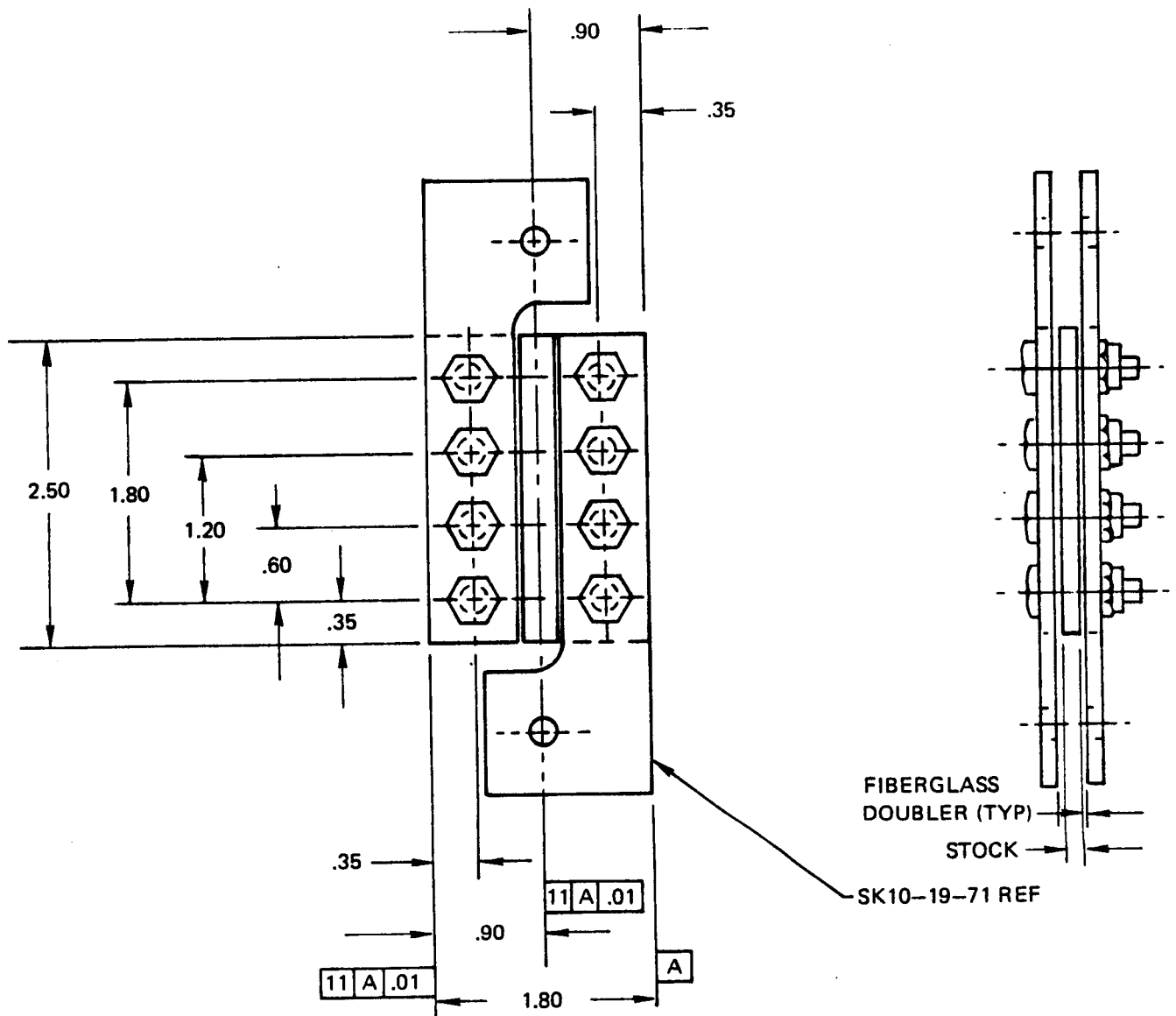


FIGURE B-9 INPLANE SHEAR SPECIMEN

APPENDIX C PROTOTYPE LEADING EDGE TEST DATA

Prototype leading edges were tested to the critical boost pressure condition and the entry temperature conditions. Pertinent data obtained from these tests are included in this appendix. A discussion of the tests is provided in section 7.2.2.

Strain gage locations are illustrated in Figure C-1, while output stresses at 100% of limit load (2.6 psi burst pressure) are listed in Table C-1. The output is given in stress which was converted from measured strain using the following elastic moduli:

Tension Warp - 1.4×10^6 psi
Tension Fill - 1.4×10^6 psi
Compression Warp - 2.1×10^6 psi
Compression Fill - 1.5×10^6 psi

Temperature time histories for the entry temperature test are given in Figures C-2 through C-7. Locations of the thermocouples are shown in Figure 7-26. Note on the temperature plots that the elapsed time scale has been shifted to correspond to $T = 0$ being start of entry for correlation with Figure 7-27.

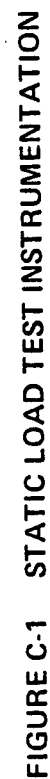


TABLE C-1. STRESS OUTPUTS
BOOST PRESSURE TEST
LIMIT LOAD (100%)

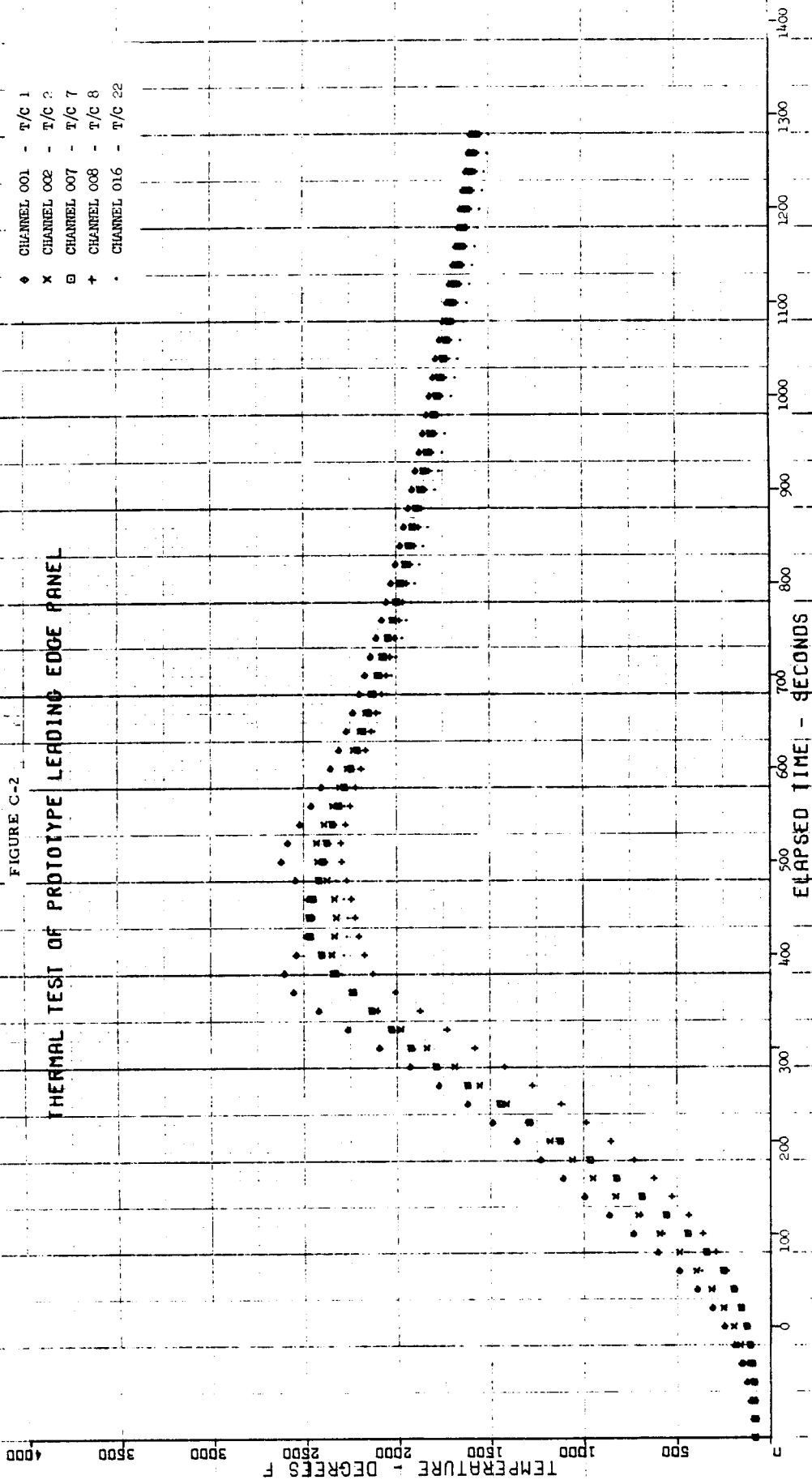
DAY 001 TIME 010:04:59
RECORD 0009

CH 001 + 1716	PSI A-1	CH 002 + 3565	PSI A-2
CH 003 - 953	PSI A-3	CH 004 + 474	PSI A-4
CH 005 - 1109	PSI A-5	CH 006 + 77	PSI A-6
CH 007 - 3051	PSI A-7	CH 008 - 1465	PSI A-8
CH 009 - 357	PSI A-9	CH 010 - 0	PSI A-10
CH 011 + 7	PSI A-11	CH 012 - 31	PSI A-12
CH 013 - 1161	PSI A-19	CH 014 - 143	PSI A-20
CH 015 - 397	PSI A-21	CH 016 - 566	PSI A-22
CH 017 - 85	PSI A-23	CH 018 - 171	PSI A-24
CH 019 + 53	PSI A-25	CH 020 - 29	PSI A-26
CH 021 - 0	PSI A-27		
CH 022 - 44	PSI T-28A	CH 023 + 52	PSI T-28B
CH 024 + 736	PSI T-29A	CH 025 + 185	PSI T-29B
CH 026 - 81	PSI T-30A	CH 027 + 157	PSI T-30B
CH 028 + 368	PSI T-31A	CH 029 + 67	PSI T-31B
CH 030 - 1	PSI T-32A	CH 031 + 23	PSI T-32B
CH 032 + 132	PSI T-33A	CH 033 + 51	PSI T-33B
CH 034 - 35	PSI T-34A	CH 035 - 3	PSI T-34B
CH 036 - 102	PSI T-35A	CH 037 + 183	PSI T-35B
CH 038 + 26	PSI R-36A	CH 039 + 500	PSI R-36B
CH 040 - 28	PSI R-36C	CH 042 - 69	PSI R-37B
CH 041 - 40	PSI R-37A	CH 045 - 273	PSI R-38B
CH 043 + 78	PSI R-37C	CH 048 + 262	PSI R-39B
CH 044 - 38	PSI R-38A	CH 051 - 307	PSI R-40B
CH 046 + 0	PSI R-38C	CH 054 + 183	PSI R-41B
CH 047 + 131	PSI R-39A		
CH 049 + 105	PSI R-39C		
CH 050 + 78	PSI R-40A		
CH 052 + 53	PSI R-40C		
CH 053 + 53	PSI R-41A		
CH 055 + 51	PSI R-41C		
CH 056 - 100	M-IN D-45	CH 057 - 51	M-IN D-46
CH 058 + 8	M-IN D-47	CH 059 - 11	M-IN D-48

- (1) See Figure C-1 for Strain Gage Location
- (2) M-In = Milli-inches

♦ CHANNEL 001 - T/C 1
 x CHANNEL 002 - T/C 2
 □ CHANNEL 007 - T/C 7
 + CHANNEL 008 - T/C 8
 • CHANNEL 016 - T/C 22

FIGURE C-2
 THERMAL TEST OF PROTOTYPE LEADING EDGE PANEL



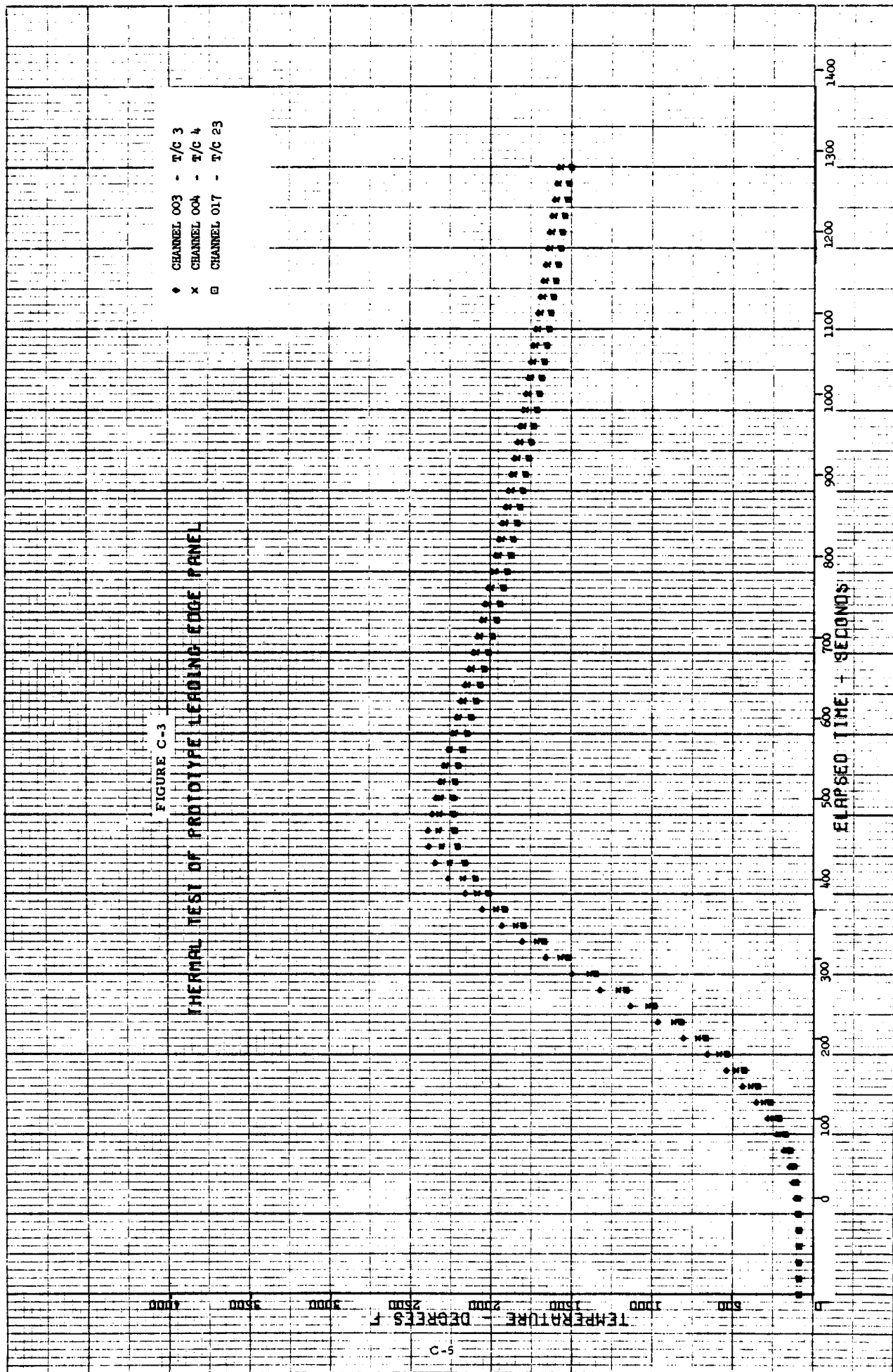
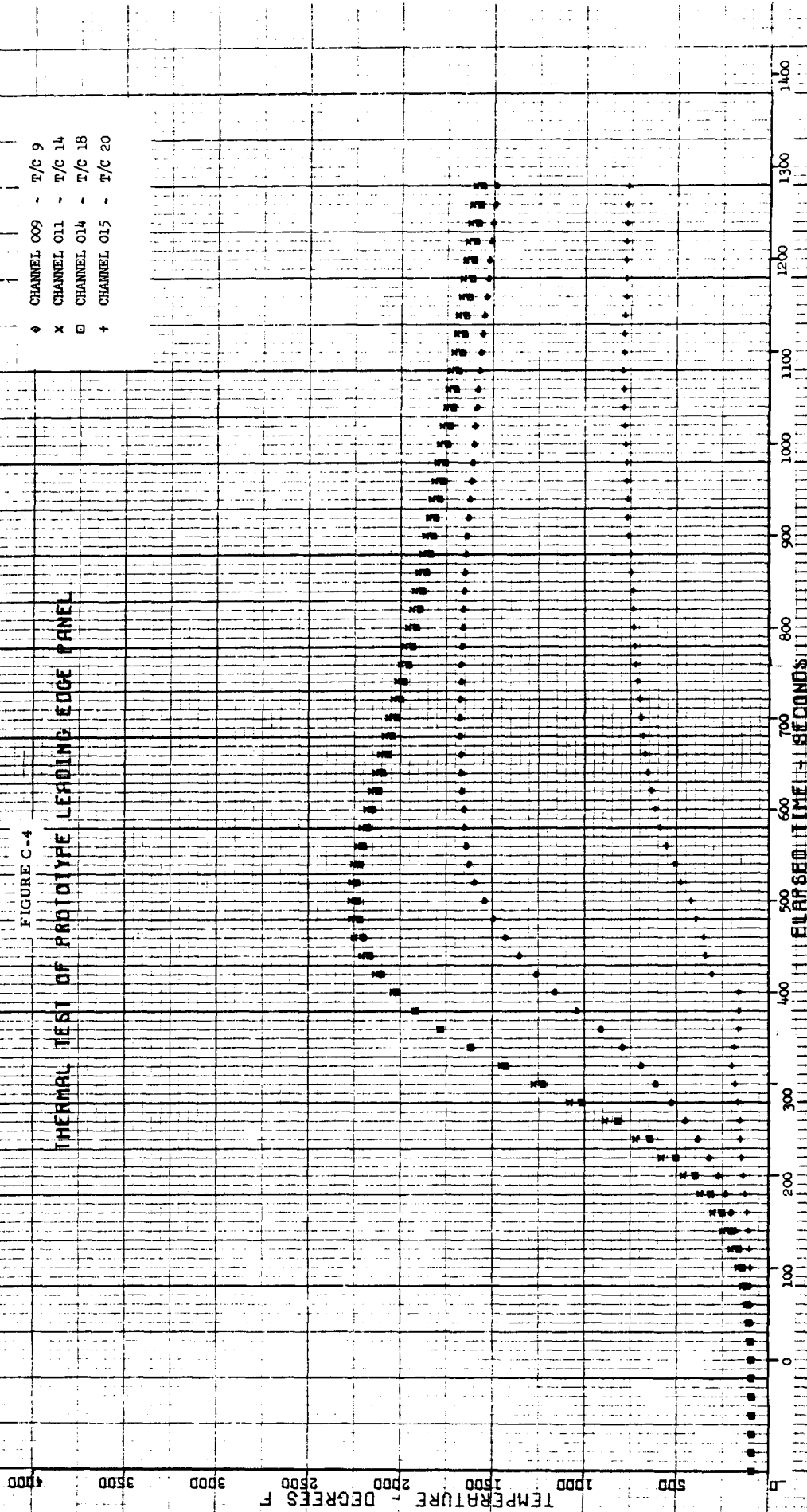
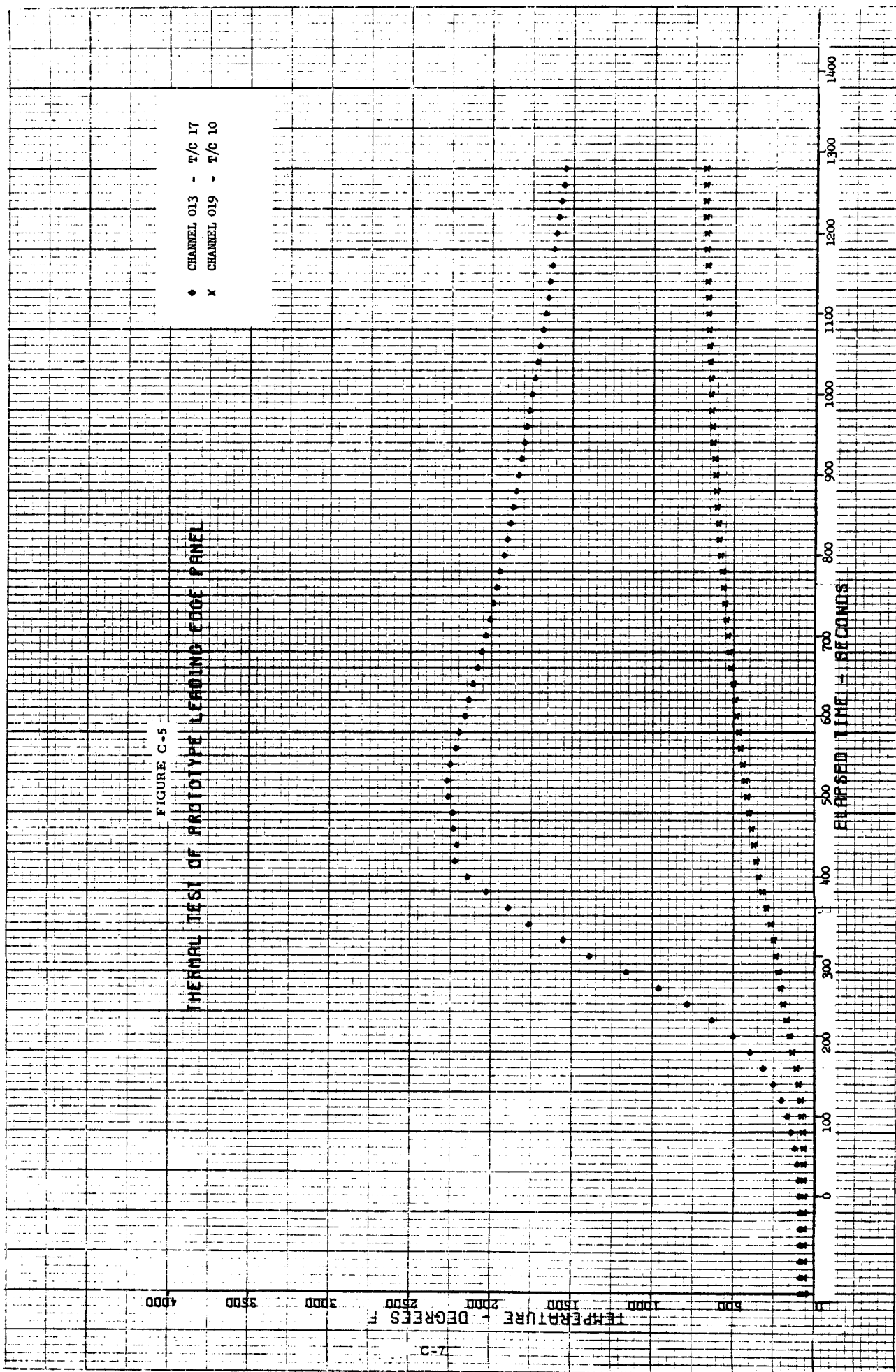


FIGURE C-4
THERMAL TEST OF PROTOTYPE LEADING EDGE PANEL

♦ CHANNEL 009 - T/C 9
 x CHANNEL 011 - T/C 14
 □ CHANNEL 014 - T/C 18
 + CHANNEL 015 - T/C 20





TEMPERATURE - DEGREES F

C-8

FIGURE C-6

THERMAL TEST OF PROTOTYPE LEADING EDGE PANEL

- ◆ CHANNEL 005 - T/C 5
- × CHANNEL 006 - T/C 6
- CHANNEL 018 - T/C 24

ELAPSED TIME - SECONDS

0 100 200 300 400 500 600 700 800 900 1000 1100 1200 1300 1400

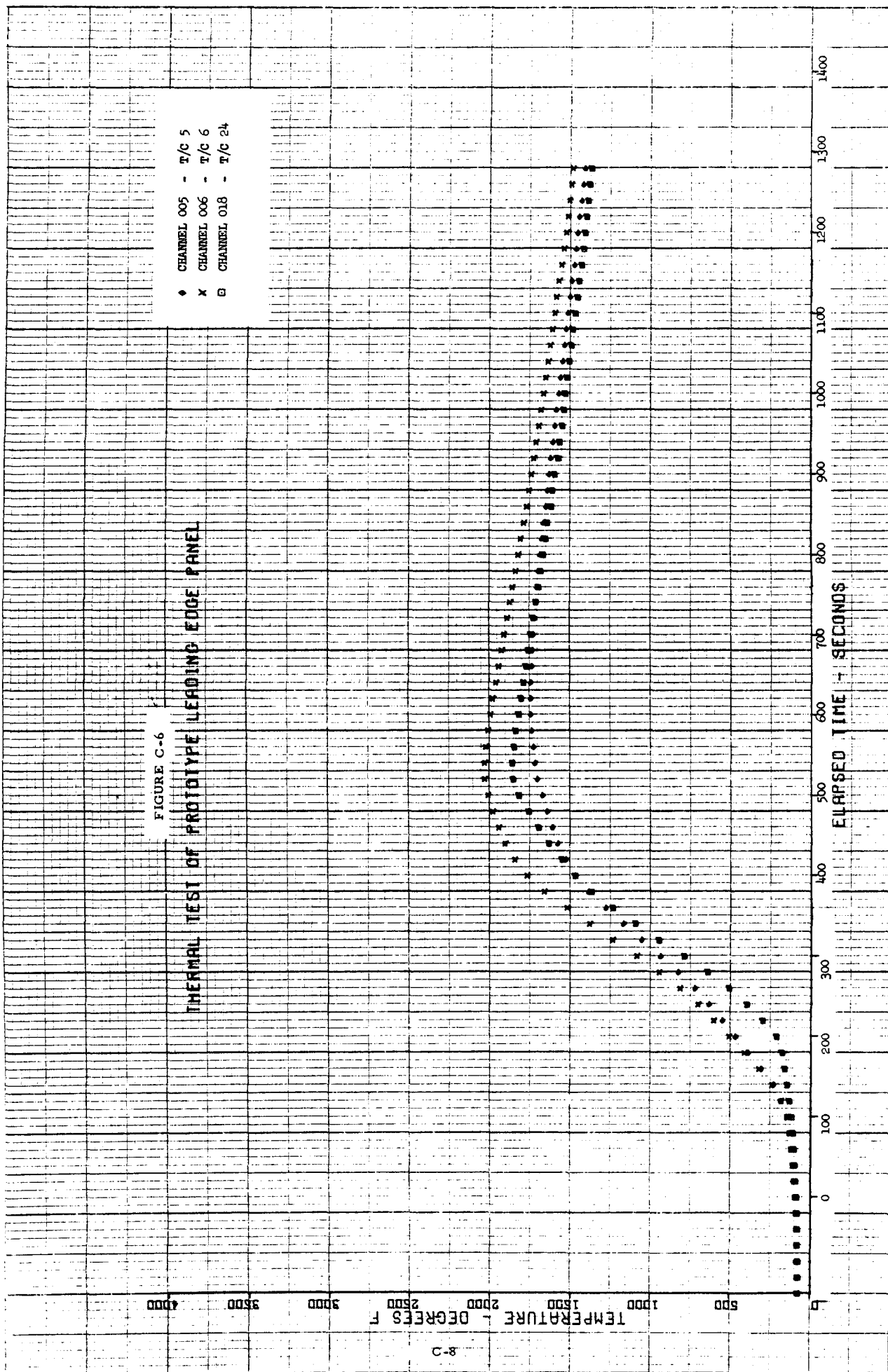


FIGURE C-7

THERMAL TEST OF PROTOTYPE LEADING EDGE PANEL

- CHANNEL 10 - T/C 12
- × CHANNEL 12 - T/C 16
- CHANNEL 20 - T/C 19
- + CHANNEL 21 - T/C 21

